

NMR Spectroscopic Investigations and Method Development in Photocatalysis and Medicinal Chemistry

Dissertation

zur Erlangung des Doktorgrades der Naturwissenschaften

(Dr. rer. nat.)

der Fakultät für Chemie und Pharmazie

der Universität Regensburg



vorgelegt von

Nitschke Philipp

aus Neubrandenburg

im Jahr 2019

Die vorliegende Dissertation beruht auf Arbeiten, die zwischen Februar 2016 und Juni 2019 am Arbeitskreis von Frau Professor Dr. Ruth M. Gschwind am Institut für Organische Chemie der Universität Regensburg durchgeführt wurden.

Promotionsgesuch eingereicht:	Juni 2019
Die Arbeit wurde angeleitet von:	Prof. Dr. Ruth M. Gschwind
Promotionsausschuss:	
Vorsitzender:	Prof. Dr. Alexander Breder
1. Gutachter:	Prof. Dr. Ruth M. Gschwind
2. Gutachter:	Prof. Dr. Remco Sprangers
3. Prüfer:	Prof. Dr. Werner Kremer

Danksagung

Als erstes möchte ich mich bei meiner Doktormutter Frau. Prof. Dr. Ruth M. Gschwind für die vielen interessanten Themen und den damit einhergehenden, zahlreichen Diskussionen herzlichst bedanken, welche diese Arbeit in ihrer endgültigen Form entscheidend geprägt haben.

Darüber hinaus bedanke ich mich bei Prof. Dr. Remco Sprangers für die Übernahme des Zweitgutachtens und bei Prof. Dr. Werner Kremer in seiner Rolle des dritten Prüfers. Auch möchte ich bei Prof. Dr. Alexander Breder bedanken, welcher das Amt des Vorsitzenden ausfüllt.

Einen großen Dank auch an alle meine ehemaligen und aktuellen Kollegen, von denen sich nicht wenige von Kollegen zu Freunden entwickelten. Danke für ein langjährig wunderbares Arbeitsklima und die schöne gemeinsame Zeit. Danke Nele Berg, Johannes Gramüller, Florian Hastreiter, Kerstin Rothermel, Veronica Scheidler, Willibald Stockerl, Verena Streitfredt, Dr. Johnny Hioe, Dr. Lokesh Nanjundappa, Dr. Matej Zabka, Dr. Juliand Greindl, Dr. Andreas Seegerer, Daniel Schneider, Dr. Nils Sorgenfrei, Dr. Hanna Bartling, Dr. Michael Haindl, Dr. Fabio Morana und Dr. Carina Koch.

Des Weiteren bedanke ich mich bei Frau Ulrike Weck und Frau Nikola Kastner-Pustet, die einem das Leben aus organisatorischer Sicht um vieles leichter gemacht haben. Auch gilt mein Danke der ganzen NMR-Abteilung; Dr. Ilya Shenderovic, Herrn Fritz Kastner, Frau Anette Schramm und Frau Georgine Stühler.

Weiterer Danke geht an alle meine Kommilitonen und Freunde, welche mich durch mein Studium und die Zeit danach, bis zum heutigen Tage unterstützt haben und allgemein für eine großartige Zeit gesorgt haben.

Der größte Dank fällt dennoch meinen lieben Eltern, Bärbel und Dirk sowie meinem engsten Familienkreis zu, die mich mein ganzes Leben unterstützten. Ich danke euch.

**NMR Spectroscopic Investigations and
Method Development in Photocatalysis
and Medicinal Chemistry**

Table of Contents

1	Introduction and Outline	1
1.1	NMR spectroscopy as a tool in photochemistry	1
1.2	NMR in drug discovery	3
2	Combination of Illumination and High Resolution NMR Spectroscopy: Key Features and Practical Aspects, Photochemical Applications, and New Concepts	7
2.1	Abstract.....	8
2.2	Introduction	11
2.3	Illumination methodology for NMR spectroscopy.....	14
2.3.1	Illumination sources in NMR spectroscopy	14
2.3.1.1	LASERs as illumination source in NMR spectroscopy	14
2.3.1.2	LEDs as illumination source in NMR spectroscopy	16
2.3.2	Illumination approaches in photo-NMR.....	18
2.3.2.1	<i>Ex situ</i> illumination in photo-NMR.....	18
2.3.2.2	<i>In situ</i> illumination in photo-NMR.....	22
2.3.2.2.1	Illumination from the bottom or side	25
2.3.2.2.2	Illumination from the inside	28
2.3.2.2.3	Illumination from the top.....	32
2.4	Other illumination approaches and special apparatus for photo-NMR	34
2.4.1	UVNMR.....	34
2.4.2	UVNMR-illumination.....	36
2.4.3	FlowNMR-illumination	39
2.4.4	NMR on a Chip-illumination.....	41
2.4.5	EPRNMR-illumination	43
2.4.6	Illumination apparatus for solution state NMR to study heterogeneous photocatalysis	43
2.4.7	Illumination apparatus for solid state NMR	46

2.5	Applications of photo-NMR	48
2.5.1	Homogeneous photocatalysis	48
2.5.1.1	Flavin catalyzed photo oxidation of benzyl alcohol.....	48
2.5.1.2	Photocatalytic cross-dehydrogenative coupling reaction	52
2.5.1.3	Photoinduced and Lewis acid activated selective single C(sp ³)-F bond cleavage in trifluoromethylarenes	56
2.5.1.4	Visible-light-mediated liberation and <i>in situ</i> conversion of fluorophosgene.....	58
2.5.1.5	Photoinduced McMurry-type reaction.....	63
2.5.1.6	Photoinduced dark catalytic cycle	66
2.5.2	Heterogeneous catalysis.....	71
2.5.2.1	Photocatalytic oxidation of toluene inside the NMR tube.....	71
2.5.2.2	TiO ₂ , catalysed C-C coupling	73
2.5.3	Photoassisted polymerization reactions	75
2.5.3.1	Rapid monitoring of visible light-mediated controlled polymerization .	75
2.5.3.2	Light-on/off studies of photo-mediated controlled radical polymerization	77
2.5.4	Photoswitches.....	79
2.5.4.1	Spiropyran ↔ merocyanine.....	79
2.5.4.2	Multiple-state photochromic system	83
2.5.4.3	Photoswitchable rotamers.....	87
2.5.5	New methods and concepts in <i>in situ</i> illumination NMR	90
2.5.5.1	Unusual photoswitch for modulating spin multiplicity.....	90
2.5.5.1.1	Light sensitive MRI agent.....	90
2.5.5.1.2	Photoinduced reversible acceleration of T ₁ -relaxation (PIRAT)	93
2.5.5.2	Photochemical pump with NMR detection: generated synchronized coherence on microsecond time scale.....	95

2.5.5.2.1	Kinetics of hyperpolarized metal dihydrides	96
2.5.5.3	DTS-hv: decrypting transition state combinations by light.....	99
2.5.5.4	Internal light intensity and quantum yield determination	103
2.6	Conclusion and Outlook	107
2.7	References.....	109
3	Combined in situ illumination-NMR-UV/Vis Spectroscopy: A New Mechanistic Tool in Photochemistry.....	123
3.1	Abstract.....	125
3.2	Introduction	127
3.3	Results and Discussion	130
3.4	Conclusion	136
3.5	References.....	137
3.6	Supporting Information.....	139
3.6.1	Setup	139
3.6.1.1	General information.....	139
3.6.1.2	Electronic setup	139
3.6.1.3	Spectroscopy setup.....	141
3.6.1.4	Automation and modification of pulse sequences.....	144
3.6.1.5	Comparison of reaction rates – conventional LED illumination setup vs new combined LED UVNMR-illumination setup	148
3.6.2	Summary of conPET processes and investigators of aryl halides with PDI as photocatalyst	151
3.6.2.1	Summary of conPET processes.....	151
3.6.2.2	Investigations of the photoreduction of aryl halides with PDI as photocatalyst	153
3.6.2.2.1	General information	153
3.6.2.2.2	Assignment of starting materials, photocatalyst and products	155

3.6.3	Investigations of a common photoswitch.....	158
3.6.3.1	Assignments of 1 and its open form 2.....	159
3.6.3.2	NMR and UV/Vis build up and decay curves of 2.....	162
3.6.3.2.1	Isomerization experiments at 300 K.....	162
3.6.3.2.2	Isomerization experiments at 180 K.....	165
3.6.3.3	Photodegradation	165
3.6.4	References	167
4	Photoinduced Dehalogenation of Aryl Halides with Perylene Bisimides Investigated by (UV)NMR Spectroscopy – What is the catalyst?.....	169
4.1	Abstract	170
4.2	Introduction.....	171
4.3	Results and Discussion.....	174
4.3.1	Test system	174
4.3.2	<i>In situ</i> NMR and UV/Vis measurements under illumination	175
4.4	Conclusion.....	192
4.5	References	194
4.6	Supporting Information.....	199
4.6.1	Materials.....	199
4.6.2	Combined UVNMR-illumination measurements	199
4.6.2.1	Preparation of the blank sample for the UVNMR-illumination measurements.....	199
4.6.2.2	Blank sample measurements.....	200
4.6.2.3	Sample preparation	200
4.6.2.4	UVNMR-illumination measurements	200
4.6.3	Regular <i>in situ</i> NMR illumination measurements.....	201
4.6.3.1	Sample preparation	201
4.6.3.2	<i>In situ</i> NMR measurements.....	201

4.6.4	Photo-CIDNP Experiments.....	202
4.6.5	<i>Ex situ</i> NMR end point measurements	202
4.6.6	UV/Vis measurements (under illumination)	202
4.6.7	Test background reaction of 4-bromo-acetophenone	203
4.6.8	¹ H assignments of relevant starting materials and products	203
4.6.9	Titration experiments.....	205
4.6.10	UVNMR compared to regular UV/Vis	207
4.6.11	Photo-CIDNP effects of the vinyl species 3	207
4.6.12	<i>In situ</i> NMR profiles of 2-chloro-benzonitrile 6	208
4.6.13	UV/Vis experiments.....	210
4.6.14	Signal broadening of the perylene core signals of PDI under illumination.....	212
4.6.15	NMR behavior of PDI with and without the presence of 1 under illumination	213
4.6.16	Re-aeration experiments.....	213
4.6.17	Prolonged illumination of PDI in the presence of 4-bromoacetophenone 1...	214
4.6.18	UV/Vis measurements of PDI in the presence of 4-bromo-acetophenone 1 .	215
4.6.19	¹ H reaction profiles with PDI-TEA pre-irradiation	216
4.6.20	Comparison of the ¹ H reaction profiles with PDI and PDI-TEA pre-irradiation	217
4.6.21	<i>Ex situ</i> NMR measurements to compare the performance of the photocatalysts PDI and PTCDA	218
4.6.22	References	220
5	Visible-Light-Mediated Liberation and <i>In Situ</i> Conversion of Fluorophosgene	221
5.1	Abstract.....	223
5.2	Introduction	225
5.3	Results and Discussion	228
5.4	Conclusion	237

5.5	References	238
5.6	Supporting Information.....	240
5.6.1	Materials and methods.....	240
5.6.2	Nuclear magnetic resonance spectroscopy.....	240
5.6.3	Gas chromatography and gas chromatography coupled with mass spectrometry	240
5.6.4	Mass spectrometry.....	241
5.6.5	Preparation of the photocatalyst P3	241
5.6.6	General procedure of the preparation of carbonates and urea derivates	241
5.6.7	Cyclovoltammetric data of P3, 2a and 2b (in MeCN) – Figure S1-3	242
5.6.8	Transient spectroscopy and further mechanistic discussion	243
5.6.8.1	2D transient absorption spectrum	243
5.6.8.2	Data analysis	244
5.6.9	Verification of the radical cation and radical anion spectra of P3 via spectro-electro chemistry	245
5.6.10	Investigation of the catalytic active species via online irradiation	246
5.6.11	NMR spectroscopic investigations	246
5.6.11.1	Materials	246
5.6.11.2	Sample preparation for <i>in situ</i> NMR illumination measurements	247
5.6.11.3	Sample preparation for <i>ex situ</i> NMR illumination measurements	247
5.6.11.4	NMR measurements.....	247
5.6.11.5	<i>In situ</i> NMR illumination measurements.....	247
5.6.11.6	<i>Ex situ</i> NMR illumination measurements.....	248
5.6.11.7	Processing and evaluation.....	248
5.6.11.8	NMR assignments	249
5.6.11.9	Relevant spectra for the assignments of the two conformations of the key fluorointermediate (F-I1 and FI-2)	251

5.6.11.9.1	Conformations of F-I1 and FI-2	254
5.6.11.10	Illuminated NMR reaction profiles	255
5.6.11.10.1	<i>In situ</i> NMR reaction profiles	255
5.6.11.10.2	<i>Ex situ</i> reaction profiles	259
5.6.11.10.3	<i>In situ</i> reaction profiles without 1a	260
5.6.11.11	Off cycle equilibrium and role of water	263
5.6.12	References	266
6	Investigation of Ligand Receptor interactions by Small Molecule Guided NMR spectroscopy: Interactions of Histamine and H2R Antagonists with membrane bound H2R.....	269
6.1	Introduction	271
6.1.1	Ligand based NMR methods in drug discovery for the investigation receptor – ligand interactions	275
6.1.1.1	Saturation transfer difference (STD).....	275
6.1.1.2	(Exchange) transferred NOE (trNOE).....	278
6.1.1.3	Water-ligand observed via gradient spectroscopy (WaterLOGSY) ..	279
6.1.1.4	Inter-ligand NOE pharmacophore mapping (INPHARMA)	281
6.1.1.5	Relaxation based methods: T1 ρ and T2.....	282
6.2	Results and Discussion	284
6.2.1	Investigations of the Histamine-H2 receptor by ligand based NMR methods	284
6.2.2	The Histamine receptor test system for the ligand based NMR experiments	284
6.2.3	Ligand based NMR investigations of the membrane bound hH2R-G _{saS} ..	286
6.2.3.1	INPHARMA experiments.....	286
6.2.3.2	Experimental considerations for STD experiments with the H2R membrane system	286
6.2.3.3	STD experiments with the H2R membrane system	289

6.2.3.3.1	STD with high protein and high ligand concentration	293
6.2.3.3.2	STD with high protein and low ligand concentration.....	294
6.2.3.3.3	STD with low protein and high ligand concentration.....	295
6.2.3.3.4	STD with low protein and low ligand concentration	296
6.2.3.3.5	STD competition experiments.....	297
6.3	Conclusion and outlook.....	299
6.4	Supporting Information.....	300
6.4.1	Membrane preparation of the SF9 cell membranes	300
6.4.2	GTPyS-assays.....	300
6.4.3	NMR reference spectra of the ligands for assignment and purity control	301
6.4.4	General membrane sample preparation for NMR.....	302
6.4.4.1	General procedure.....	302
6.4.4.2	Other procedures.....	302
6.4.5	STD experiments	302
6.5	References	304
	Conclusion.....	313
	Glossary.....	317

1 Introduction and Outline

1.1 NMR spectroscopy as a tool in photochemistry

In the last decade photocatalysis has emerged as one of the major research fields in chemistry^[1-4]. Especially synthetic applications present an impressive amount of research and novel approaches^[5]. But to sustain this growth a fundamental understanding of the underlying mechanisms in photocatalytic reactions is of utmost importance^[6]. Besides the dominating methods to investigate photocatalytic processes such as (ultrafast) UV/Vis spectroscopy^[7-11] and EPR spectroscopy^[12,13], NMR spectroscopy has established itself as a valuable and complementary method. Since the discovery of the photo-chemically induced dynamic nuclear polarization (photo-CIDNP) effects, which can yield information about the initial photoexcitation^[14,15] in the early 1960s, NMR has evolved into a versatile tool in photochemistry that can provide information about solvent effects^[16], aggregation^[17] and intermediates^[18-23] in photocatalytic reactions. The second chapter of this thesis serves as an elaborate introduction of NMR as a tool in photochemistry. In a first part, this chapter discusses established approaches in photo-NMR such as *ex situ* and *in situ* NMR illumination techniques as well as common light sources. Furthermore, a range of special illumination setups and techniques are presented, which push the boundaries of illumination NMR. In the second part, case studies focusing on *in situ* illumination NMR are presented addressing the topics of homogeneous and heterogeneous photocatalysis, photoswitches, photoinitiated polymerizations and new concepts for *in situ* illumination NMR in detail. In addition, the evolution of NMR in photocatalysis is surveyed ranging from first recordings of reaction profiles to the elucidation of complex reaction mechanisms.

Although NMR has established itself as a valuable tool to study photocatalytic systems, there is still room for improvements in terms of methods and applications. The third chapter supports this statement and introduces a triple combination of UV/Vis spectroscopy, NMR spectroscopy and *in situ* illumination (UVNMR-illumination) as a new tool for the investigation of photosystems. This fully automated system enables the simultaneous investigation of UV/Vis and NMR active species i.e. paramagnetic and diamagnetic species (with the additional option to illuminate the sample in case of photosystems). As a result, for the first time, time coherent reaction profiles from UV/Vis and NMR can be plotted against each other under the same conditions. The applicability

Introduction

of this UVNMR-illumination setup is verified by the investigation of two test systems from the research fields of photowswitches and photocatalysis. First, the isomerization behavior of a photoswtichable spiropyran^[24] is surveyed at different temperatures and second, a consecutive photoinduced electron transfer (ConPET) process is analyzed^[25].

The fourth chapter continues the studies from chapter three and dwells deeper into the investigations of ConPET processes. The principle of ConPET relies on the ability of the respective photocatalyst to use the energy of two photons for chemical reactions^[25,26]. Therefore, the photocatalyst needs the ability to form stable radical anions (or radical cations), which can be excited a second time resulting in excited radical anions with increased redox potentials. ConPET processes have gained much popularity in synthesis^[25–30] but the mechanistic proposal of the two photon excitation was highly discussed after its initial presentation. Recently, the mechanism of ConPET could be verified for the photocatalyst rhodamine 6G by means of single molecule spectroscopy^[31], but the mechanistic proposal for the initial ConPET process, which describes the dehalogenation of aryl haldies with perylene bisimide (PDI) as photocatalyst was lately challenged^[32]. Therefore, this chapter investigates this PDI promoted reaction in detail by means of elaborate UVNMR-illumination, *in situ* NMR illumination and UV/Vis spectroscopic studies. These examinations yielded insights about electron-donor-acceptor (EDA) complexes, the generation of the stable PDI radical anion and the presence of a long initiating phase, which suggests various interaction of PDI with itself. Combining these results, a new mechanistic proposal could be presented, which is based on physical interactions (stacks/aggregates) between PDI and the PDI radical anion.

Chapter five presents a cooperative study, which focused on the development and investigation of the light induced activation of C-OCF₃ bonds. The chapter first describes the design of a synthetic approach, which suggested that after C-OCF₃ activation, fluorophosgene is liberated *in situ* and further incorporated into various substrates. Therefore, extensive mechanistic studies were carried out, which included *ex situ* and *in situ* illumination NMR studies, transient spectroscopy and radical trapping experiments to check this hypothesis. Combining these different and complementary mechanistic methods, an elaborate mechanistic proposal could be made, which confirms the *in situ* liberation of fluorophosgene and is i.a. based on the detection of a charge-transfer complex of the photocatalyst, the unambiguous assignment of fluorophosgene-substrate intermediates and the identification of an unproductive water-dependent dark cycle.

1.2 NMR in drug discovery

G-protein coupled receptors are important, ubiquitous, transmembrane structures in our body^[33]. They present the biological target molecule of around 25 % of all available drugs on the market^[34,35] and up to date over 800 GPCRs could be identified^[36]. Hence, besides desire to understand the mechanistic behavior of these complex biological targets, there is an ongoing demand to identify new, active substances with ever increasing selectivity and activity.

In the last decades, NMR spectroscopy has established itself as one of the most spread and effective tools in drug discovery and is employed in every phase of drug design ranging from full assignment of the identified target molecule^[37], early fragment screening^[38–41] to detailed structure activity relationship studies^[37,38] and in vivo imaging tests^[42]. Therefore, it is no surprise that also GPCRs as high priority structures have been objects of major interest for NMR spectroscopic studies^[43]. Yet, GPCRs present themselves as challenging endeavors for solution NMR due to their nature as transmembrane proteins, which makes them difficult to stabilize and due to their inherently high molecular weight, which can be a major issue in solution NMR. Especially the investigation of GPCRs in parental membrane systems has been rarely presented. Parental membranes that incorporate GPCRs (e.g. from SF9 or HEK cells) are closer to the natural environment of GPCRs than artificial membranes or nanodiscs but usually lack the stability of the GPCR inside the membrane. Despite this drawback several systems were published in the last years^[44,45]. These studies focused on ligand based NMR techniques such as saturation transfer difference (STD) and interligand NOE pharmacophore mapping (INPHARMA). Ligand based NMR methods are usually independent of the molecular weight of the biological target^[38,39] and therefore fit to investigate GPCRs in membrane systems. The last chapter of this thesis, first surveys common ligand based NMR methods and their characteristics. Second, a ligand based NMR study focusing on STD (and INPHARMA) of the human Histamine-H2 receptor (H2R), which is incorporated in a parental membrane system (from SF9 cells) is presented. The chapter discusses preparative sample preparation, buffer systems as well as practical considerations of ligand based NMR experiments. In addition, extensive STD studies are conducted, which probe the effects of known, commercially available H2R antagonists such as ranitidine and famotidine and the hormone histamine in presence of membrane systems with and without H2R.

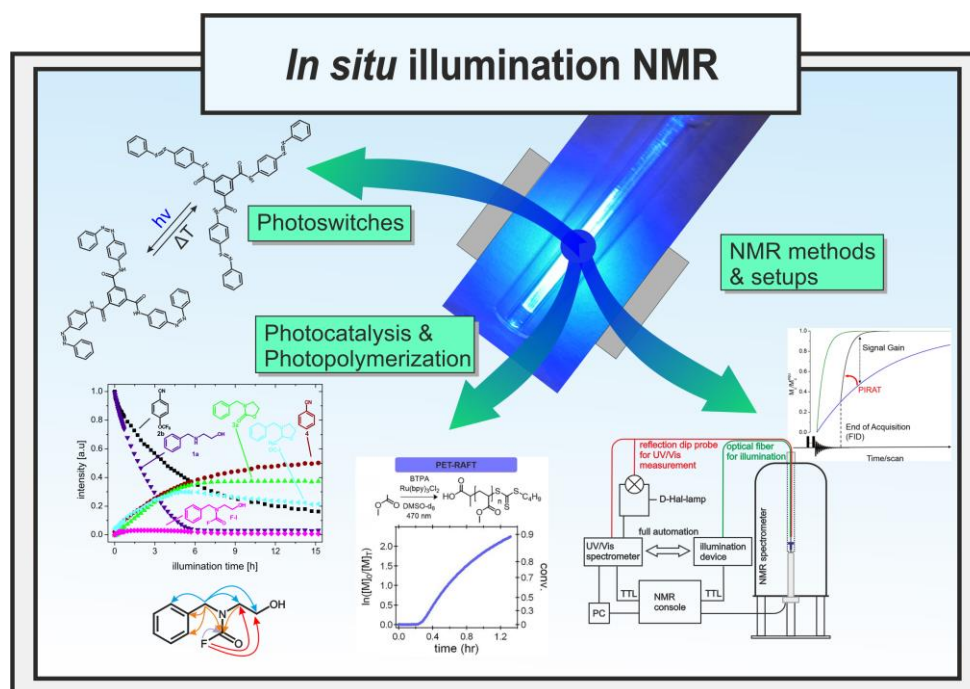
- [1] K. Zeitler, *Angew. Chem. Int. Ed.* **2009**, *48*, 9785–9789.
- [2] N. A. Romero, D. A. Nicewicz, *Chem. Rev.* **2016**, *116*, 10075–10166.
- [3] R. C. McAtee, E. J. McClain, C. R. J. Stephenson, *Trends Chem.* **2019**, *1*, 111–125.
- [4] L. Marzo, S. K. Pagire, O. Reiser, B. König, *Angew. Chem. Int. Ed.* **2018**, *57*, 10034–10072.
- [5] B. König, *European J. Org. Chem.* **2017**, *2017*, 1979–1981.
- [6] L. Buzzetti, G. E. M. Crisenza, P. Melchiorre, *Angew. Chem. Int. Ed.* **2019**, 3730–3747.
- [7] C. G. S. Lima, T. D. M. Lima, M. Duarte, I. D. Jurberg, M. W. Paixão, *ACS Catal.* **2016**, *6*, 1389–1407.
- [8] J. Sun, Y. He, X. De An, X. Zhang, L. Yu, S. Yu, *Org. Chem. Front.* **2018**, *5*, 977–981.
- [9] J. Wang, G. Burdzinski, J. Kubicki, M. S. Platz, *J. Am. Chem. Soc.* **2008**, *130*, 11195–11209.
- [10] E. Riedle, M. K. Roos, S. Thallmair, C. F. Sailer, N. Krebs, B. P. Fingerhut, R. de Vivie-Riedle, *Chem. Phys. Lett.* **2017**, *683*, 128–134.
- [11] U. Megerle, M. Wenninger, R.-J. Kutta, R. Lechner, B. König, B. Dick, E. Riedle, *Phys. Chem. Chem. Phys.* **2011**, *13*, 8869.
- [12] G. Liu, S.-H. Liou, N. Enkin, I. Tkach, M. Bennati, *Phys. Chem. Chem. Phys.* **2017**, *19*, 31823–31829.
- [13] M. Goswami, A. Chirila, C. Rebreyend, B. de Bruin, *EPR Spectroscopy as a Tool in Homogeneous Catalysis Research*, Springer US, **2015**.
- [14] M. Goez, in *Annu. Reports NMR Spectrosc.*, Elsevier Ltd., **2009**, pp. 77–147.
- [15] M. Goez, in *Hyperpolarization Methods NMR Spectrosc.*, **2012**, pp. 1–32.
- [16] C. Feldmeier, H. Bartling, K. Magerl, R. M. Gschwind, *Angew. Chem. Int. Ed.* **2015**, *54*, 1347–1351.
- [17] J. Dađová, S. Kümmel, C. Feldmeier, J. Cibulková, R. Pažout, J. Maixner, R. M. Gschwind, B. König, R. Cibulka, *Chem. A Eur. J.* **2013**, *19*, 1066–1075.
- [18] D. Petzold, P. Nitschke, F. Brandl, V. Scheidler, B. Dick, R. M. Gschwind, B. König, *Chem. A Eur. J.* **2019**, *25*, 361–366.
- [19] H. Bartling, A. Eisenhofer, B. König, R. M. Gschwind, *J. Am. Chem. Soc.* **2016**, *138*, 11860–11871.
- [20] K. Chen, N. Berg, R. Gschwind, B. König, *J. Am. Chem. Soc.* **2017**, *139*, 18444–18447.
- [21] A. Mills, C. O'Rourke, *J. Org. Chem.* **2015**, *80*, 10342–10345.
- [22] D. Lehnherr, Y. Ji, A. J. Neel, R. D. Cohen, A. P. J. Brunskill, J. Yang, M. Reibarkh, *J. Am. Chem. Soc.* **2018**, *140*, 13843–13853.

- [23] N. Lokesh, A. Seegerer, J. Hioe, R. M. Gschwind, *J. Am. Chem. Soc.* **2018**, *140*, 1855–1862.
- [24] J. Piard, *J. Chem. Educ.* **2014**, *91*, 2105–2111.
- [25] I. Ghosh, T. Ghosh, J. I. Bardagi, B. König, *Science* **2014**, *346*, 725–728.
- [26] I. Ghosh, B. König, *Angew. Chem. Int. Ed.* **2016**, *55*, 7676–7679.
- [27] M. Poznik, B. König, *React. Chem. Eng.* **2016**, *1*, 494–500.
- [28] M. Neumeier, D. Sampedro, M. Májek, V. A. de la Peña O’Shea, A. Jacobi von Wangelin, R. Pérez-Ruiz, *Chem. A Eur. J.* **2018**, *24*, 105–108.
- [29] L. Zeng, T. Liu, C. He, D. Shi, F. Zhang, C. Duan, *J. Am. Chem. Soc.* **2016**, *138*, 3958–3961.
- [30] A. Graml, I. Ghosh, B. König, *J. Org. Chem.* **2017**, *82*, 3552–3560.
- [31] J. Haimerl, I. Ghosh, B. König, J. Vogelsang, J. M. Lupton, *Chem. Sci.* **2019**, *10*, 681–687.
- [32] M. Marchini, A. Gualandi, L. Mengozzi, P. Franchi, M. Lucarini, P. G. Cozzi, V. Balzani, P. Ceroni, *Phys. Chem. Chem. Phys.* **2018**, *20*, 8071–8076.
- [33] H. B. Schiöth, M. C. Lagerström, *Nat. Rev. Drug Discov.* **2008**, *7*, 339–357.
- [34] R. C. Stevens, V. Cherezov, V. Katritch, R. Abagyan, P. Kuhn, H. Rosen, K. Wüthrich, *Nat. Rev. Drug Discov.* **2013**, *12*, 25–34.
- [35] J. P. Overington, B. Al-lazikani, A. L. Hopkins, *Nat. Rev. Drug Discov.* **2006**, *5*, 993–996.
- [36] J. L. Sharman, H. E. Benson, A. J. Pawson, V. Lukito, C. P. Mpamhanga, V. Bombail, A. P. Davenport, J. A. Peters, M. Spedding, A. J. Harmar, *Nucleic Acids Res.* **2013**, *41*, 1083–1088.
- [37] Y. Li, C. Kang, *Molecules* **2017**, *22*, 1399.
- [38] T. Sugiki, K. Furuita, T. Fujiwara, C. Kojima, *Molecules* **2018**, *23*, 1–27.
- [39] M. J. Harner, L. Mueller, K. J. Robbins, M. D. Reily, *Arch. Biochem. Biophys.* **2017**, *628*, 132–147.
- [40] D.J. Abraham, *Burger’s Medicinal Chemistry and Drug Discovery*, John Wiley & Sons, Inc., Hoboken, NJ, USA, **2003**.
- [41] R. Powers, *J. Med. Chem.* **2014**, *57*, 5860–5870.
- [42] B. Ross, T. Tran, P. Bhattacharya, D. M. Watterson, N. Sailasuta, **2011**, 93–114.
- [43] I. Shimada, T. Ueda, Y. Kofuku, M. T. Eddy, K. Wüthrich, *Nat. Rev. Drug Discov.* **2019**, *18*, 59–82.
- [44] R. P. Venkitakrishnan, O. Benard, M. Max, J. L. Markley, F. M. Assadi-Porter, in *Membr. Protein Struct. Dyn.* (Eds.: N. Vaidehi, J. Klein-Seetharaman), Humana Press, Totowa, NJ, **2012**, pp. 47–63.
- [45] S. Bartoschek, T. Klabunde, E. Defossa, V. Dietrich, S. Stengelin, C. Griesinger,

Introduction

T. Carlomagno, I. Focken, K. U. Wendt, *Angew. Chem. Int. Ed.* **2010**, *49*, 1426–1429.

2 Combination of Illumination and High Resolution NMR Spectroscopy: Key Features and Practical Aspects, Photochemical Applications, and New Concepts



Philipp Nitschke, Nanjundappa Lokesh and Ruth M. Gschwind

Progress in Nuclear Magnetic Resonance Spectroscopy

accepted June 2019

DOI: 10.1026/j.pnmrs.2019.06.01

Philipp Nitschke, Lokesh Nanjundappa and Ruth M. Gschwind all participated in the creation of the manuscript and took part in the literature collection.

Adapted with permission from *Prog. Nuc. Mangn. Res. Spectrosc.* Source of this chapter: <https://www.sciencedirect.com/science/article/pii/S0079656519300238?via%3Dihub#f0275>

2.1 Abstract

In the last decade, photochemical and photocatalytic applications have developed into one of the dominant research fields in chemistry. However, mechanistic investigations to sustain this enormous progress are still relatively sparse and in high demand by the photochemistry community. UV/Vis spectroscopy and EPR spectroscopy have been the main spectroscopic tools to study the mechanisms of photoreactions due to their higher time resolution and sensitivity. On the other hand, application of NMR in photosystems has been mainly restricted to photo-CIDNP, since the initial photoexcitation was thought to be the single key to understand photoinduced reactions. In 2015 the Gschwind group showcased the possibility that different reaction pathways could occur from the same photoexcited state depending on the reaction conditions by using *in situ* LED illumination NMR. This was the starting point to push the active participation of NMR in photosystems to its full potential, including reaction profiling, structure determination of intermediates, downstream mechanistic studies, dark pathways, intermediate sequencing with CEST etc. Following this, multiple studies using *in situ* illumination NMR have been reported focusing on mechanistic investigations in photocatalysis, photoswitches, and polymerizations. The recent increased popularity of this technique can be attributed to the simplicity of the experimental setup and the availability of low cost, high power LEDs. Here, we review the development of experimental design, applications and new concepts of illuminated NMR. In the first part, we describe the development of different designs of NMR illumination apparatus, illuminating from the bottom/side/top/inside, and discuss their pros and cons for specific applications. Furthermore, we address LASERs and LEDs as different light sources as well as special cases such as UVNMR(-illumination), FlowNMR, NMR on a Chip etc. To complete the discussion on experimental apparatus, the advantages and disadvantages of *in situ* LED illumination NMR versus *ex situ* illumination NMR are described. The second part of this review discusses different facets of applications of inside illumination experiments. It highlights newly revealed mechanistic and structural information and ideas in the fields of photocatalysis, photoswitches and photopolymerization. Finally, we present new concepts and methods based on the combination of NMR and illumination such as sensitivity enhancement, chemical pump probes, experimental access to transition state combinations and NMR actinometry. Overall this review presents NMR spectroscopy as a complementary tool to UV/Vis spectroscopy in mechanistic and structural investigations of photochemical processes. The review is presented in a way that is intended to assist the photochemistry and photocatalysis community in adopting and

understanding this astonishingly powerful *in situ* LED illumination NMR method for their investigations on a daily basis.

2.2 Introduction

In the last decade, light-driven chemistry and particularly the photocatalytic applications have witnessed a nearly exponential growth[1–6]. This growth can be attributed to multiple factors, (i) increased awareness among chemists of the use of solar energy, (ii) availability of low cost and high power LEDs covering the whole spectral range, (iii) generalization of concepts in visible light photoredox catalysis coupled with quick follow up by chemists for synthetic applications and (iv) recognition of the advantages of photochromic systems in modulating physical and chemical properties of molecules or materials.

Despite this enormous growth in photochemical applications, structural and mechanistic investigations are still sparse and in high demand from the photochemistry community. To sustain this growth it is necessary to study the underlying mechanisms of photochemical processes and to have evidence-driven reaction development and optimization. Historically, UV/Vis spectroscopy[7–12] and EPR spectroscopy[13–15] have been the main spectroscopic tools used to study the mechanisms of photoreactions due their higher time resolution and sensitivity. The combination of regular and ultrafast UV/Vis spectroscopy provides information about the chromophore and its photoexcited states[11], the formation of electron donor acceptor (EDA) complexes [16–18], and energy transfer to other species[19]. EPR has been used to observe radical species (paramagnetic species) in chemical processes[13]. Compared to these methods, traditional NMR methods have inherently lower time resolution and sensitivity, and therefore fail to characterize photoexcited states. However, the discovery of the photo-CIDNP effects has facilitated NMR participation in the mechanistic elucidation of photoreactions via indirect detection of radical pairs and biradicals[20,21]. Applications of photo-CIDNP NMR were and are still further explored to follow the connecting pathways among precursors, paramagnetic intermediates and products[22]. The use of LASER pulses in photo-CIDNP NMR has enabled time resolved photo-CIDNP measurements to access life times of short lived radical pair species[23]. Despite this huge impact of photo-CIDNP NMR in photoreactions, the full potential of NMR methods in terms of structure elucidation of intermediates has not so far been tapped in photocatalysis. On the other hand, many NMR methods are well established in mechanistic investigations of chemical reactions and dynamics despite the inherent limitations of traditional NMR spectroscopy such as low sensitivity and time resolution. Particularly *in situ* NMR has been successfully applied in the detection of intermediates[24,25], studies of weak

interactions[26,27], aggregation[28] and to extract kinetic and thermodynamic data for regular organic reactions[29,30].

The biased, limited applicability of traditional NMR methods in photoreactions has mainly been due to a prevalent focus on mechanistic studies in photocatalysis investigating initial photoexcited states and short radical species. The downstream pathways and intermediates after the initial photoexcitation were most often overlooked.

In 2015, the Gschwind group proved for the first time the possibility of different reaction pathways starting from the same photoexcited state by using *in situ* LED illumination NMR [31]. This investigation showed that downstream pathways and intermediates can be just as important to understand photocatalytic mechanisms as insights into the initial photoexcitation. This remarkable observation led to two changes in photomechanistic studies: (i) inclusion of mechanistic investigations of downstream pathways and intermediates in photocatalysis, and (ii) possible opportunities to expand the applicability of NMR methods to their full potential in mechanistic and structural investigation of photochemical processes.

The emergence of low cost, high power LEDs for *in situ* illumination NMR further boosts the applicability of *in situ* LED illumination NMR in photoreactions. Subsequently the Gschwind group has extensively used and showcased the *in situ* LED illumination NMR technique in mechanistic investigations of various photocatalytic reactions, by effectively incorporating both traditional and advanced NMR methods [31–35]. In addition they have also developed sequential light-on and light-off sequences, which give critical information about light-dependent and dark pathways as well as light-dependent intermediates [32]. There are also significant *in situ* LED illumination investigations reported from other groups. Thiele's group has explored the technique to study different types of photochromic systems[36]. Recently Merck has adopted the technique to measure quantum yields and to carry out an elaborate study of the mechanism of photoinduced iron complex catalyzed reactions[37,38]. Hawker's group has explored the technique for light-induced controlled radical polymerization[39–41]. Duckett's group has developed and applied an *in situ* LASER photochemical pump for hyperpolarization and kinetic measurement of organometallic compounds[42,43]. Recently, this simple yet more effective technique of *in situ* illumination NMR has received more attention from the synthetic community of both academia and industry.

In this review we give an overview of the methodology developed so far for *in situ* illumination NMR. We then discuss the pros and cons of the various methods, and highlight important applications of NMR illumination in photochemistry, photocatalysis,

photochromic systems and photopolymerizations, and more particularly in mechanistic studies of photochemical processes. To keep this review to a moderate size, we mainly focus on high resolution solution NMR, which highlights new advantages and concepts. We excluded photo-CIDNP studies from the application part, as good reviews and book chapters are already available in the literature exclusively focusing on photo-CIDNP[20,21,44]. We also excluded biomolecular studies from this review.

The review is mainly organized into two parts: illumination methodology for NMR spectroscopy and applications of illumination NMR. The methodology part will discuss different illumination sources and the development of the most common experimental designs, while also showcasing some special arrangements exclusively designed for photo-NMR. The application part is further divided into subsections, discussing homogenous photocatalysis, heterogeneous photocatalysis, light-assisted CRP polymerization, photoswitches and new concept/method developments.

2.3 Illumination methodology for NMR spectroscopy

2.3.1 Illumination sources in NMR spectroscopy

Basically, every option of illumination source, including our sun, has found its way into photochemistry and photocatalysis[45–48]. For the combination of NMR spectroscopy with illumination mainly LASERs[22,49–57], xenon halogen lamps[58–61] and LEDs[31,36,39,62–66] are employed. Looking back at four decades of illuminated NMR, most of the typical designs use LASERs and/or LEDs. Additionally, these illumination sources represent the two extremes in terms of light intensity, costs, maintenance, and application fields. Therefore, this review concentrates in the following on LASERs and LEDs and does not discuss xenon lamps explicitly. First the principle illumination sources and then their incorporation into the various experimental arrangements is presented.

2.3.1.1 LASERs as illumination source in NMR spectroscopy

Light amplification by stimulated emission of radiation (LASERs) presented the first dominating illumination source that was combined with NMR spectroscopy. This is, of course, attributed to beneficial properties inherent to LASERs for photochemical applications [67]. Especially two properties set LASERs apart from the available halogen lamps or light bulbs at that time, namely monochromatic wavelength emission[68] and extremely high light intensity. The monochromatic emission allows for irradiation of photoactive species with maximum selectivity. This is of special importance in mixtures of photoactive compounds with different absorption windows. Furthermore, LASERs can be precisely incorporated into various optical designs without appreciable power dissipation. This enables both full control over the optical output and high light intensities. As an additional advantage, LASER systems were continuously improved as LASERs found their way into every field of research within the sciences e.g. physics[68], physical chemistry[69], biology[68,70,71] and medicine[68,70,71]. This demand led to a strong response from industry resulting in many commercially available LASER designs, LASER bundles, and optics that e.g. promote efficient coupling to fiber optics and can be individually adapted to the investigated system. As a result, LASERs provide optimal properties regarding output power, pulse amplitudes and time resolution even without any homemade modifications. Especially the very high light intensity of LASERs is a key point for many investigations in photochemistry, because the behavior of photosystems is generally proportional to the light intensity in terms of kinetics (photoreactions) and photo-CIDNP effects[72]. As a result, LASERs can overcome critical sensitivity

problems. Especially, in photo-CIDNP and time resolved photo-CIDNP studies the requirement for high light intensities and extremely high time-resolution has made LASERs the light source of choice during recent decades[20,49,73–75].

However, experiments with LASERs have several drawbacks, too. First of all, they are very costly in comparison to other illumination sources. For example, today one LED can be purchased for a few Euros while even the price of cheap LASER is easily higher than 1000 Euro. This is especially an issue when multiple excitation wavelengths and therefore multiple LASERs are required for a project, as this further increases costs. In addition, experiments with LASER usually involve highly sensitive equipment using various lenses and mirrors[23,76,77]. Hence, they require careful adjustment and fine tuning for every experiment to provide optimal results.

Special issues for the application of LASERs arise for mechanistic investigations and reaction profiles in batch photocatalysis. Here, the ability of LASERs to maximize the light output rather poses a restriction than an overall benefit, because all photocatalysts will “photobleach” (photodegrade) under prolonged light exposure[78–80]. Especially for slow batch reactions (hour to day timescale) employing homogeneous, small molecule photocatalysts, LASERs can literally “burn holes” into the investigated samples, hampering prolonged investigations and reaction profiles of the same sample¹. Flow systems, micro reactors or rotation of the NMR tube can circumvent these problems connected with photobleaching using a new region of the sample for each LASER shot. As a result, in these designs, the high light intensity of LASERs can be an advantage also in photocatalysis. Another issue for NMR mechanistic investigations of photocatalytic reactions with LASERs is the direct comparability with synthetic results concerning e.g. yields, reactivities, and stereoselectivities, since most of the synthetic applications are conducted with LEDs[1,3,45,81–83] or xenon lamps[81] and not with monochromatic LASERs.

In summary, LASERs provide the strongest light source with utmost wavelength selectivity and time resolution. Therefore, in photosystems requiring these light specifications, such as photo-CIDNP or time resolved photo-CIDNP effects, LASERs are the logical and optimal method of choice. For mechanistic investigations of slow photocatalytic batch reactions the power of LASERs is not always beneficial mainly due

¹ From the authors' experience, new high power LED sources used in synthesis are also reaching power outputs that simply destroy the photocatalysts instead of further accelerating the investigated reaction.

to photobleaching of the catalysts. Therefore, in photocatalysis, sometimes the high costs of LASERs cannot be justified by additional mechanistic insights.

2.3.1.2 LEDs as illumination source in NMR spectroscopy

Light emitting diodes (LEDs) emerged as the second dominating illumination source for NMR investigations within the last decade. This trend is well-grounded for several reasons. The first one is Haitz' law, which predicted an exponential growth in LED output power in combination with an exponential decline in costs for LEDs[84,85]. This prediction was even surpassed during the last decades resulting in availability of a vast number of high power LEDs at low costs ranging from the UV-C throughout the whole VIS region and even to the IR regime[86,87]. The second reason was the emergence of photocatalysis as a skyrocketing new research field in chemistry[1–3,5,6,88–90] and the increased level of interest of the community to discover new photoswitchable systems[91–94]. Third, already the first NMR investigation in photocatalysis by the Gschwind group showed that after an identical photoexcitation, totally different mechanistic pathways are possible and NMR is able to add mechanistic information not accessible to time resolved UV/Vis spectroscopy[31]. This and other studies showed the importance of the mechanism downstream from the photoexcitation step, and paved the way to extended NMR investigations in photocatalysis[32–34,38]. Besides investigations solely focused on NMR spectroscopy, NMR is also often used in a supporting role or in the expansion of insight to photosystems previously probed using synthesis, UV/Vis or EPR. Hence, especially comparability of batch/flow synthesis and NMR based investigations is important. Since most of the investigations in synthesis are conducted with LEDs as illumination source[1,3,45,81–83] it is only natural that NMR spectroscopy would follow in the same manner. Furthermore, LEDs are almost insignificant in cost (< 3€ in the Vis region per LED can be easily found online). As most LED-NMR designs allow for quick exchange of LEDs, it is affordable and easy to assemble an arsenal of LEDs providing every wavelength from deep UV to the near IR region. Additionally, LEDs can be operated in a pulsed mode instead of continuous illumination. Using short light pulses (ms range), one can significantly increase the applied current through the LED. This results in higher light output of the LED for the duration of the pulse. For example, the Gschwind group showed that the recommended maximum current for continuous operation of a blue light Cree XP-E2 LED can be increased nine fold using a pulse width of 1 ms[95]. Simultaneous photo-CIDNP experiments revealed that the increase of the current is still directly proportional to the light output, indicating that time resolved photo-CIDNP studies might also be accessible with LEDs. This makes LEDs the

“all-rounder” for the investigation of photosystems by NMR as they can be used straight-forwardly for every system, e.g. photoreactions, photoswitches and steady state photo-CIDNP. In addition, LED-based designs usually don't require any adjustment or optimization on each run in the way that would be needed for LASERs as LEDs are much more robust. This makes LED-based apparatus very flexible, cheap and straight-forward.

Nevertheless, LEDs also have some restrictions and disadvantages. Although, LEDs are nowadays ubiquitous, they haven't found their way into the sciences in a similar way as LASERs yet. This results in a lack of commercially available high precision equipment to set up LED illumination systems so far. As a consequence most NMR-LED illumination apparatus is still built in house. Only recently, a first commercially available system has been presented online by GoldstoneScientific. Many of the home built designs were published in the last decade[39,95–97]; they are all unique in their own way and will be discussed more thoroughly in section 2.3.2 and 2.4.

A second serious problem with LEDs is their varying output power that can deviate by $\pm 50\%$, as well as significant deviations of peak wavelengths (± 10 nm), which can be found in datasheets for the different LEDs. In-house-performed measurements determining output power and peak wavelength showed that even purchased LEDs from the same manufacturer-batch and -type can still have significant deviations ($\pm 20\%$; ± 5 nm). This, of course can massively impede reproducibility of any investigation if an LED has to be replaced. Hence, it is of the utmost importance to carefully choose the LED by production number at purchase to guarantee that all LEDs are from the same batch. The batch properties of LEDs can usually be accessed in their datasheet provided by the manufacturer. This significantly increases reproducibility, but we would still recommend to measure output power and peak wavelength individually for every LED in order to achieve good results.

Additionally, LEDs in the UV-C and UV-B region (> 320 nm) need special considerations, although they are not the main focus in photochemistry/-catalysis. To date, the costs of UV-C and UV-B LEDs can be up to several hundred Euros for the highest output powers, negating the main benefit of LEDs as cost efficient illumination source. Furthermore, from the authors' experience these LEDs can pose serious challenges when it comes to heat dissipation, raising the need for special LED boards and larger cooling blocks/systems to avoid reduced output powers and potential shifts of the wavelength maximum.

For the comparison of LEDs to LASERS it has to be mentioned that a narrower bandwidth rivaling that of LASERS can also be achieved with LEDs employing various high- and low-pass filters in customized setups as an upgrade option, if high wavelength specificity is needed. However, the use of filters results in a significantly reduced LED output power (up to >90 % as wavelength selectivity increases, from the authors' experience).

In summary, LEDs are a cheap, flexible and easy to use illumination source that can be used in every photo-NMR application yielding reliable and reproducible results. Disadvantages of LEDs are mostly that they require home-built apparatus; they have limited reproducibility between different LEDs and a reduced cost-efficiency ratio for LEDs in the UV-C, UV-B (and IR) range. Furthermore, if maximum light intensity is needed, LEDs still don't compete with LASERS. However, if light intensity isn't a limiting or major factor, LEDs represent the ideal choice for investigations of photosystems.

2.3.2 Illumination approaches in photo-NMR

Next to the choice of the illumination source, it is crucial to decide how to properly guide the light to/into the investigated sample. This review will present various experimental designs that can be divided into two main, light-guiding groups: *ex situ* and *in situ* illumination. *Ex situ* illumination describes the execution of, for example, the photoreaction in an external vessel after which small aliquots or the whole reaction mixture are transferred to the NMR tube/system. In contrast, the term *in situ* illumination implies the initial reaction container (e.g. the NMR tube) is also used for the NMR investigations and placed inside the NMR spectrometer before illumination. Hence, an *in situ* sample is a totally closed system allowing for mechanistic studies without any interference due to sampling.

It should be noted that some unique situations such as flow experiments can't be unambiguously categorized as either *ex situ* or *in situ*, and these are discussed in detail in section 2.4.

2.3.2.1 *Ex situ* illumination in photo-NMR

The *ex situ* illumination approach for the investigation of photosystems by NMR comprises the execution of a photoprocess in an external container from which small samples or the whole mixture are taken at certain, defined points and inserted into to the NMR spectrometer for further measurement. Especially for the investigation of

photoreactions and photoswitches on a minute to hour to day time-scale, *ex situ* illumination can be the method of choice. On the other hand, *ex situ* illumination is not at all recommended for studies that investigate short lived transient species, such as in photo-CIDNP studies[20].

Ex situ illumination is definitely the most straightforward method to investigate a photoreaction by NMR spectroscopy as it doesn't require any special apparatus or modification of the NMR spectrometer or other NMR components in any way. The big advantage here is the fact that the reaction container for the photoreaction is exactly the same as that used in the synthetic batch approach[32,34]. This can eliminate the issue of comparability between synthesis and analytics, offering the same sample volume and concentration, the same light intensity/light source and the ability to stir the sample. The *ex situ* approach has also proved itself indispensable if gases are essential reactants. A lot of photocatalytic systems require aerobic conditions as they are dependent on oxygen as terminal oxidant[90,98–100]. In contrast to open *ex situ* approaches, in closed *in situ* arrangements all the oxygen is rapidly consumed and as a result the catalytic cycle stops, the overall conversion is low, comparability to synthesis is a problem, and valuable information on oxygen dependent intermediates is lost. Gases are also often generated as reaction products in photocatalysis, e.g. decarboxylations generate CO₂ and diazonium salts often liberate N₂ [1,6]. In such cases, an *ex situ* arrangement can be easily adjusted to provide a continuous supply/exhaust of gas, whereas for most *in situ* arrangements this is very complicated to achieve. Therefore, *ex situ* NMR reaction profiles are ideal to monitor the overall reaction progress of the major reactants and products especially if gases play a role. Furthermore, *ex situ* NMR investigations can also be used as an “end-point-assay” to screen reactions conditions by analyzing the crude mixture after illumination[34].

Of course, *ex situ* NMR investigations also have some drawbacks. The main issue is dead time. At least a minute passes from taking a sample from the reaction vial, transferring it to the NMR tube and NMR spectrometer to the acquisition of an NMR spectrum, even if the process is optimized[32,34]. Hence, information on short lived² intermediates can be completely lost and in some cases even tracking the overall reaction progress might be impeded if the investigated reaction is very fast (minute time scale)[101]. From the authors' own experience, some reactions already showed ~30 % conversion at the measurement of the starting point, by just carrying the sample from the lab to the NMR spectrometer while exposing it to ambient light. Hence, it is

² Here, short lived refers to a second to minute time scale.

recommended to always keep the investigated samples shaded from external light sources, i.e. to wrap the sample in aluminum foil and/or to use ambered NMR tubes. Furthermore, some reactions show induction periods of several minutes resulting in a delayed product or intermediate formation. Such induction periods are easily missed in experiments with *ex situ* approaches, especially if the delay prior to the initial timepoints is too long. For example, the *ex situ* and *in situ* reaction profiles in Fig. 1 and Fig. 2 both show the product formation of **3a**. The *in situ* profile (Fig. 2) **3a** clearly shows a sigmoidal progression, whereas in the *ex situ* profile (Fig. 1) the sigmoidal progression in the formation of **3a** is not detected due to the long time delay between the first measurement points. Clearly, information from induction periods can be critical for a correct interpretation of mechanistic data and also in cases such as *in situ* formation/modulation of the catalytic species[102] or in presence of interfering substances (e.g. O₂ quenching the excited state of the photocatalyst), which have to be consumed before the reaction can start [103].

Another concern is the act of sample taking. One new NMR sample has to be prepared for each new timepoint, as online monitoring is not possible. This restricts the number of points that can be taken as the investigated sample is depleted over time. Many photoreactions are executed in a very low volume of 0.2-2 mL[83,104–106], and upscaling might be an issue as optical density can be a problem at larger volumes[4]. A conventional 5 mm NMR tube needs a sample volume of at least 400 μ L (preferably 600-700 μ L) to provide good NMR spectra. As a consequence, direct sample extraction of the full NMR volume required is sometimes not an option in photoreactions. To circumvent this, one can take small aliquots from the reaction vial (10-100 μ L) and dilute them with the corresponding solvent for NMR measurements[34]. This can increase the number of points provided by one sample tremendously, but it also poses the threat that dilution might change the conditions inside the sample, and in addition severe sensitivity problems can arise. Depending on the dilution factor, concentrations inside the sample can be changed by an order of magnitude and this most probably shifts key reaction intermediates below the NMR detection limit, since even highly populated intermediates are often only present to around 10 % or less (relative to the initial concentration of the starting material)[32,34]. Furthermore, introducing new solvent can carry additional water, oxygen and/or other impurities into the sample, potentially damaging reaction intermediates and disturbing the mechanistic pathway.

Another, second option is to prepare several separated samples (e.g. 6x1-2 mL vials) for parallel reactions (Fig. 1; bottom left)[32]. This allows one to take the full required NMR volume at every timepoint. A disadvantage of using parallel samples is the usual

systematic error of sample preparation (slightly different volumes, concentrations, possible degree of water and/or oxygen etc.) that may affect the acquired results. When parallel illumination sources are used, a photoreaction specific error might also build up; as mentioned in section 2.3.1.2 power output and peak wavelength of LEDs can significantly differ and thus the reaction progress within the different vials might vary, as photoreactions are usually proportional the light exposure[72].

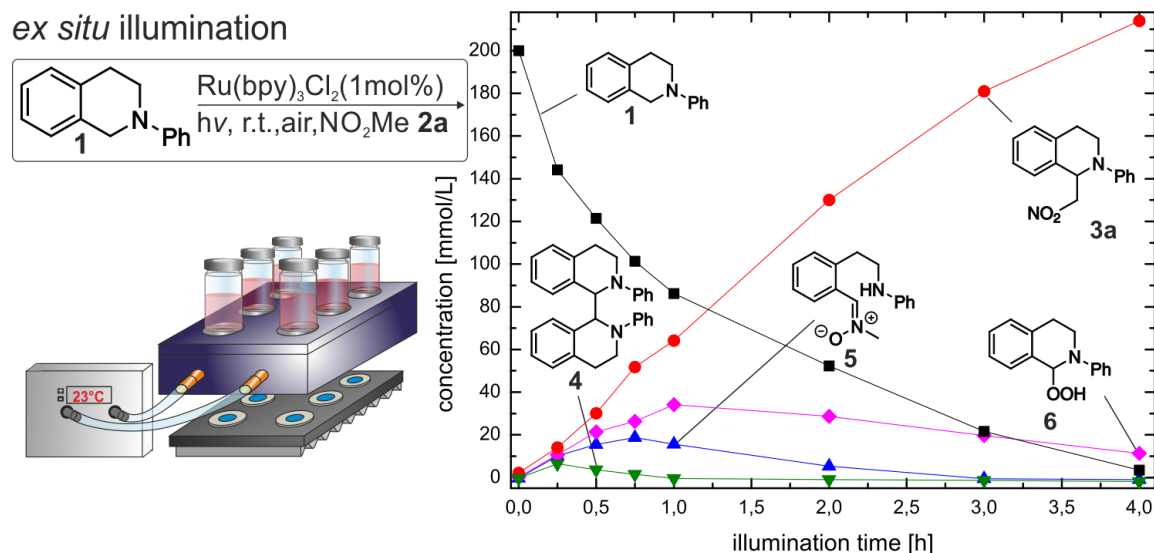


Fig. 1: The *ex situ* illumination approach to investigate the photocatalytic Aza-Henry reaction of isoquinolines by NMR[32]. Samples are directly taken from the batch reaction to be recorded in the NMR spectrometer. Due to the aerobic conditions, one can readily detect intermediate **6**, which stems from the reaction of **1** with O_2 as terminal oxidant and is not observed with “quasi” anaerobic *in situ* conditions (see Fig. 2). Spectra measured at 600 MHz.

For the investigation of photoswitches, *ex situ* NMR is rather limited and heavily dependent on the system. If the state of the photoswitch induced by light is stable or if thermal back isomerization is slow (> minutes) tests can be executed. But for many photoswitches thermal back isomerization is fast and these switches require direct monitoring of the process with *in situ* illumination NMR[107,108].

In summary, *ex situ* NMR illumination investigations are a flexible and straightforward approach to study slow photoreactions, starting material and product profiles as well as long lived photoswitches to screen reaction conditions. Therefore, *ex situ* studies are an attractive choice for the tracking of photoreactions, since only the typical apparatus for photochemical reactions/catalyses is required. Furthermore, *ex situ* is so far a basic and indispensable tool in case gasses (oxygen, nitrogen etc.) are involved in the reaction,

either as starting materials, terminal oxidant or products. On the other hand, *ex situ* illumination fails for the detection of short lived reaction intermediates and is inappropriate for photosystems such as photoswitches with fast thermal back relaxation or photo-CIDNP studies. To study very short lived intermediates, dark cycles and photoswitches etc. *in situ* NMR studies are recommended.

2.3.2.2 *In situ* illumination in photo-NMR

Photo-NMR investigations are referred to as *in situ* illumination, if the initial reaction container (e.g. the NMR tube) is used for the NMR investigations and placed inside the NMR spectrometer from the beginning. Therefore, especially when illuminated from inside the tube (see section 2.3.2.2.2), the sample represents a closed system for the whole duration of the illumination and the conducted reaction is not exposed to any outside factors besides light. This excludes the introduction of possible systematic errors arising from sample transfer such as the introduction of water and oxygen or the loss of gaseous products. Typical examples from the authors' group are photoreactions which require triethylamine (TEA) or N,N-diisopropylethylamine (DIPEA) as sacrificial electron donors[34,108]. Both release acetaldehyde as a secondary product during the reaction. From the authors' experience, most of or all acetaldehyde is lost during *ex situ* sample transfer, because it is gaseous at room temperature. During *in situ* illumination the same acetaldehyde is readily monitored³. The big advantage of *in situ* illumination is the ability to monitor any NMR detectable process online and to start NMR acquisition immediately after or during the illumination. This makes it possible to gain access to short lived or transient species on the NMR time scale, which would be elusive with the *ex situ* illumination approach. Furthermore, many more timepoints can be collected, providing refined reaction profiles compared to *ex situ* illumination (Fig. 1 vs Fig. 2). Another big advantage of *in situ* setups is the possibility to automate the process instead of having to carry out tedious manual sampling. Besides the hardware required for NMR acquisition, the NMR console generally possesses custom Real-time Clock Pulse (RCP) outputs, which can be connected to external systems e.g. the illumination device [95,108]. Hence, the NMR console can be used as a central control hub triggering and sequencing all external, connected systems. In terms of photo-CIDNP studies and the investigation of photoreactions this means absolute time control over the interplay of data acquisition and illumination. *In situ* measurements also allow for detailed investigations of photoswitches with a short thermal back-isomerization. Here, two options are possible

³ It should be noted that at very high concentrations of acetaldehyde, information can also be lost in the *in situ* setups because bubbles may form.

for investigating the structure and properties of a thermally unstable photostate. For photoswitches that do not decompose under prolonged light exposure, the unstable state can be detected under continuous illumination, i.e. in the photostationary state (PSS). In case of degradation of the photoswitch under continuous illumination or too fast thermal back-isomerization at room temperature, the NMR spectrometer can be used as a cooling unit. Then, the thermal back-isomerization can be decreased or even stopped using very low temperatures and thus the stabilized state can be investigated in depth even after short illumination times[107,108].

Of course, *in situ* illumination also comes with some restrictions and drawbacks. The first one is a reduced light intensity compared to *ex situ* batch reactions. Although *in situ* illumination setups have improved over the last decades, they still lose large amounts of light due to fiber optics or mirror systems (especially LED setups usually lose at least 80 % of the initial light intensity)[95,96]. As a result, reaction times of photoreactions can be significantly slower compared to *ex situ* illumination. From the authors' experience, reactions are usually slower by a factor of 2-3 when carried out *in situ*. In addition, there might be issues if some reaction components, e.g. starting materials and/or intermediates, are not completely soluble or precipitate during the reaction. Because of the absence of stirring, insoluble reaction components or products elude NMR detection, sink to the bottom of the tube, and are not further available for the reaction. As a result not only are the NMR profiles incomplete but confusing offsets of *in situ* and synthetic batch reactions may occur. For some *in situ* arrangements, sample spinning is still possible (especially if the illumination is from the bottom/side see section 2.3.2.2.1). But in the authors' experience spinning is not enough to keep most of the precipitating components within the region of the rf coils. Furthermore, arrangements illuminating from the top or bottom have a serious problem with optical density because the light has to penetrate a couple of centimeters in order to illuminate the whole sample (see section 2.3.2.2.1 and 2.3.2.2.3). Another drawback of *in situ* systems is their limited commercial availability, although this issue might be slowly removed.

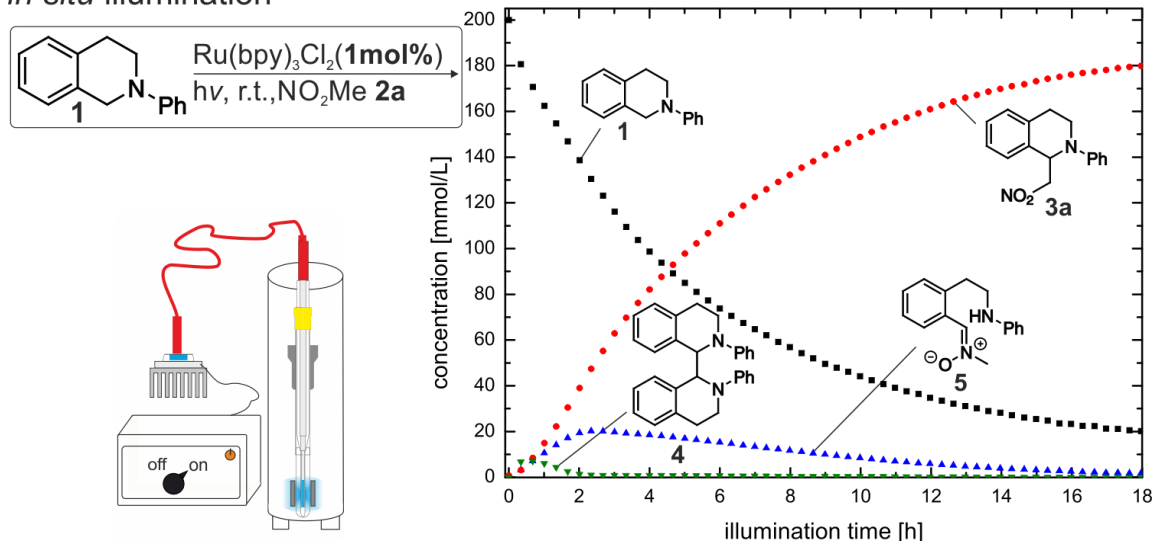
in situ illumination

Fig. 2: The *in situ* illumination approach to investigate the photocatalytic Aza-Henry reaction of isoquinolines by NMR[32]. The whole reaction is executed inside the NMR tube, enabling much more detailed monitoring of the reaction progress compared to the *ex situ* approach (see Fig. 1). Here, illumination is provided by a glass fiber connected to an LED illumination source. The glass fiber is directly introduced into the NMR tube via a coaxial glass insert and is sandblasted at its bottom to provide uniform illumination. Spectra measured at 600 MHz.

In terms of specific experimental arrangements for providing *in situ* illumination, it is no surprise that the first *in situ* designs were already developed in the 1970/80s for the investigation of photo-CIDNP effects. These were improved over the years and today three approaches can be distinguished for *in situ* illumination:

- illumination from the bottom/side (Fig. 3 B)
- illumination from the inside (Fig. 3 A/1)
- illumination from the top (Fig. 3 A/2)

Illumination from the top/inside most often involves direct connection to the NMR tube with light being guided through the sample bore of the magnet. In contrast, illumination from the bottom/side usually requires modifications of the NMR probe, with light literally passing through the probe, and typically lacks direct connection to the NMR tube. Although being improved over the years, newer designs still follow these approaches to illuminate the sample, and most of them will be discussed in the following.

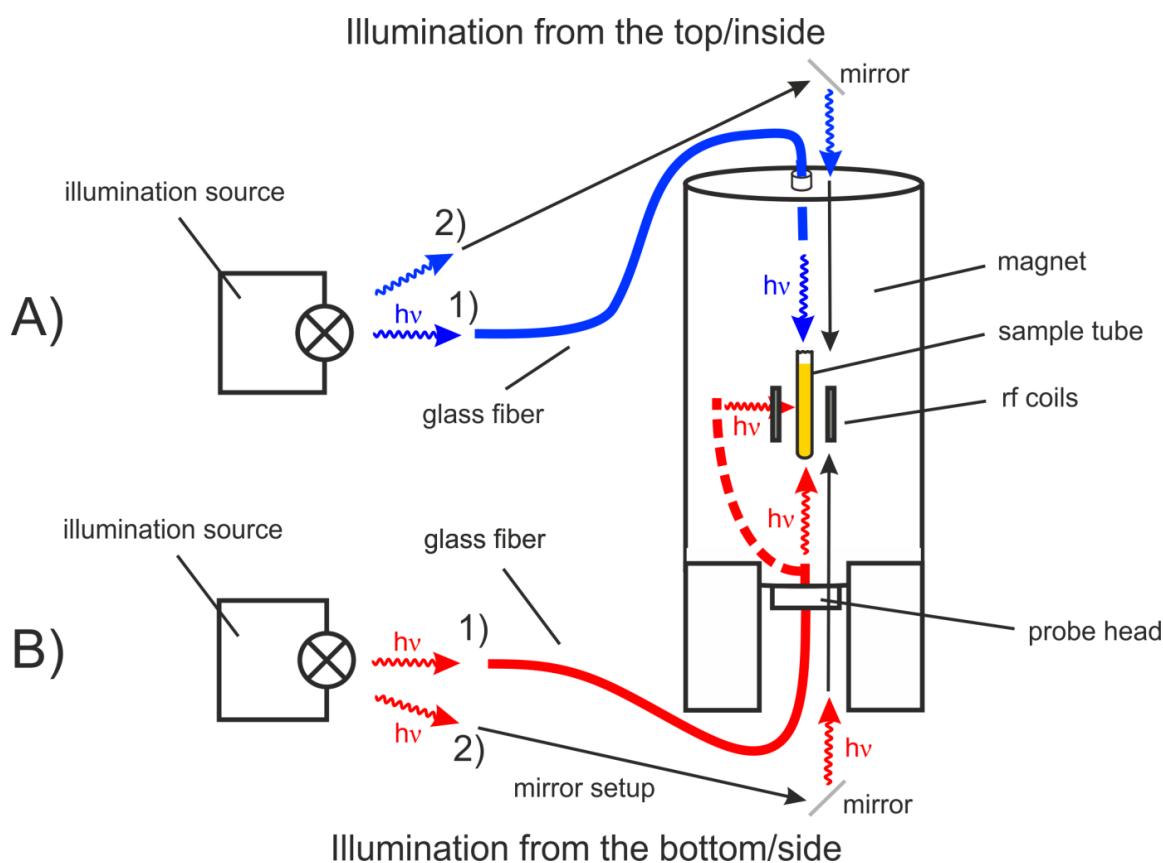


Fig. 3: Principal approaches for *in situ* irradiation of an NMR sample illuminating from the top, inside, side or bottom. A) Illumination from the top/inside. The optical systems are sometimes connected to the NMR tube and led through the sample bore. B) Illumination from the bottom/side. The fiber optics are led through the probe to enable light access to the NMR sample. Optionally, the designs (both from bottom/side and top) can include mirror systems (2) in addition to or instead of fiber optics (1).

2.3.2.2.1 Illumination from the bottom or side

One of the first *in situ* illumination designs was introduced by Kaptein's group in 1978[109,110]. Here, an argon ion LASER was incorporated into the probe of a Bruker 360 MHz spectrometer, illuminating the sample from the bottom for the investigation of photo-CDINP effects in proteins. Even in 1978, illumination control was already automated via the NMR console, providing this advantage of *in situ* illumination. In 1981 Miller *et al.* presented a comparable arrangement, which also illuminated the sample from the bottom with the help of a nitrogen LASER[111]. The design of Kaptein's group was later improved again in 1982[21]. The newer version switched from illumination through the bottom to illumination from the side (Fig. 4). Here, the NMR probe was equipped with a quartz glass stick, which mounted a cylindrical mirror inside the NMR spectrometer in order to guide the light. This improved the light transfer from the argon

LASER to the sample, because now the illumination focused directly on the NMR sensitive region within the rf coils, reducing optical density problems. These two principal approaches to illuminate the sample from the bottom or through the side of the NMR tube remained throughout the years. Newer designs, e.g. as presented by the Duckett[42,43] and Gscheidt[77,112] groups, differ only in the type of LASER or how the mirror/glass rod system is put together. Similar illumination types from the bottom are also employed in special arrangements such as FlowNMR-illumination, NMR on a Chip-illumination and UVNMR. These arrangements of illumination are described below in section 2.4.

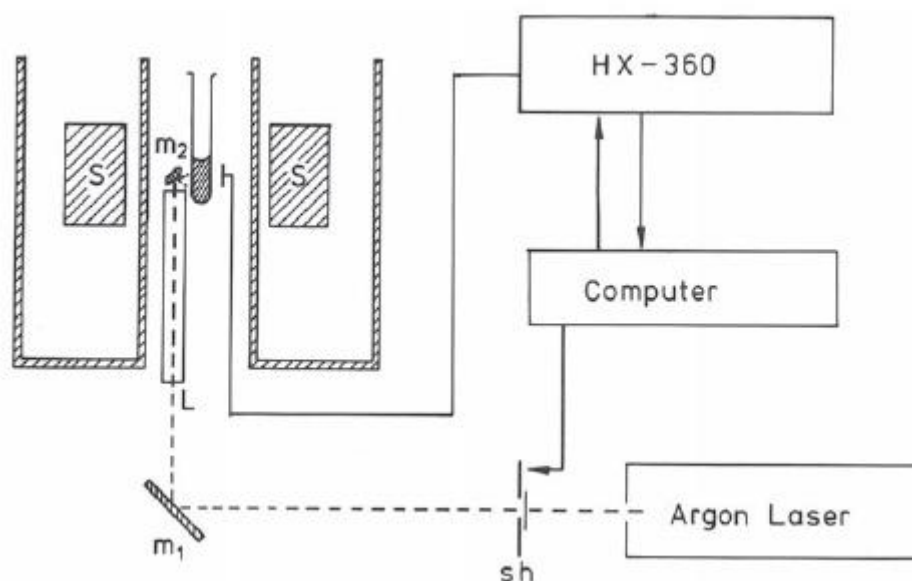


Fig. 4: Schematics of the experimental design for photo-CIDNP experiments presented by the Kaptein group in 1982[21], in which light enters through a hole drilled in the NMR probe. The setup utilizes a quartz glass light guide and a cylindrical mirror to illuminate the sample from the side in the region of the rf coils. The sample can be spun to increase field homogeneity, and the full sample volume is provided for measurements, because no inserts etc. are needed inside the NMR tube.

In general, *in situ* illumination from the bottom or side has the advantage of a fixed light source and hence illumination pathway. This increases reproducibility of the results and avoids the need for any equipment to be attached to the NMR tubes. Hence, it is possible to spin the sample, which increases field homogeneity and possibly keeps some insoluble material necessary for further conversion in the region of the rf coils. Furthermore, spinning can be used to improve homogeneous illumination for arrangements with continuous illumination from the side. It is also possible to couple the

spinning frequency with intense light pulses to use fresh compartments of the sample and thus avoid photobleaching. On a practical note, sample preparation doesn't have to be changed compared to a regular NMR measurement. This is especially advantageous for samples, which are air and/or moisture sensitive and have to be prepared in a glove box or under inert atmosphere. There, the handling for *in situ* designs with inner tubes is far more laborious. Additionally, illumination of a regular NMR sample provides the full sample volume in the region of the rf coils, whereas this can be significantly reduced in some *in situ* designs where illumination is from the inside. This is an advantage in terms of NMR sensitivity, but the experimenter has to be very careful about optical density issues.

As an unavoidable disadvantage, to the authors' knowledge all actual *in situ* designs with illumination from the bottom/side need modified NMR probes. For the insertion of the illumination guide holes have to be drilled, potentially damaging the costly probe. In addition, for illumination from the bottom, and still more so when from the side, it is increasingly difficult to accommodate the hardware needed for illumination as modern spectrometers and probes are much more geometrically constrained[23]. Therefore, most often simple, old and/or cheap probes are used, which do not provide the highest level of NMR performance. Furthermore, modification of the probe significantly reduces experimental flexibility as there is most often only one modified probe available at one particular field strength. As a result, such designs are valuable for groups focusing on special aspects of photocatalysis, photoswitches or photo-CIDNP limited to defined molecular classes. In addition, designs that illuminate from the bottom might have some real issues regarding optical density, especially in photocatalysis. The distance from the bottom of the NMR tube to the top of the sample can be several centimeters (4-5 cm). According to Lambert Beer's law an exponential decrease of light intensity from bottom to the top takes place, which is expected to be significant over this distance. Depending on the individual concentration and absorbance of the investigated system, sometimes the light might barely reach the active layer between the rf coils; however diffusion and especially convection helps overcome this problem.

In summary, *in situ* illumination from the bottom or side is a reliable illumination approach with good reproducibility due to a fixed light path. As a result it is ideal for long term investigations of similar or comparable systems. But, *in situ* illumination from the bottom/side comes with the unavoidable necessity for major probe modifications (drilling), with the potential for damage to the costly probe.

2.3.2.2.2 Illumination from the inside

Experimental designs using illumination from inside the sample were developed shortly after the first experiments using illumination from the bottom or side. A first approach by Lerman *et al.* was presented as early as 1980[113]. It described the use of a 0.4 mm thick and 30 m long quartz optical fiber with the raw end of the fiber directly placed in the NMR tube above the region of the rf coils and the other end connected to a krypton LASER. This concept was picked up and elaborated by Berliner *et al* in 1984[114] (Fig. 5 A). They also employed an optical fiber (0.2 mm, compared to the 0.4 mm of Lerman *et al.*), but instead of putting the fiber directly into the solution they additionally inserted a 2 mm stem coaxial insert which hosted the optical fiber. Furthermore, the end of the fiber was stripped to improve illumination and was positioned at the center of the rf coils, which yielded the best illumination results (however, since the end of the fiber was stripped but not treated any further, most if not all of the light is still emitted downwards through the tip of the fiber). In some of their samples they raised the light fiber and the coaxial glass insert above the region of the rf coils to avoid shimming problems. This version of “inside illumination” essentially represented the state of the art for two decades, and the only modification was a special arrangement adding a flow/injection setup through the NMR tube introduced and refined by the Hore group from 1997 to 2003[115–117]. In 2000 the Schwalbe group improved the homogeneity of illumination inside the NMR tube by placing a pencil shaped quartz Shigemi tip just below the tip of the optical fiber[118–120]. Another step to improve illumination from the inside was shown by Kuprov *et al.* in 2004[121]. By etching the end-part of the optical fiber inside the NMR tube the light output of the fiber was switched from downward to uniform illumination in all directions. Furthermore, the position of the fiber itself was changed such that the fiber covered the whole region of the rf coils, rather than being positioned with its tip being either above the rf coils or at their center (see also Fig. 5 A vs B). This resulted in a uniform illumination of the whole active region along the z-axis during NMR measurements.

When LEDs were introduced as an alternative light source (see section 2.3.1.2), several groups started also to combine LEDs and glass fibers for *in situ* inside illumination, but to the authors' knowledge haven't published the experimental designs explicitly. However, in these designs typically shutters were used between the LEDs and the glass fiber to switch the light-on and -off. Due to this spacing a lot of the light was lost for the illumination of the sample and the main drawback of these early combinations of LEDs and glass fibers was the very low light intensity, which hampered investigations in

photosystems. Here, the breakthrough came when the Gschwind group developed an LED glass fiber combination that offered a huge increase in light output [95]. In this optimized design, the main innovation was that the LED was directly attached to the optical fiber and that even the silicon lens of the LED was removed in order to minimize the distance between LED and glass fiber. This reduction of distance compared to the shutter-based design resulted in an increase of light intensity by around a factor of 30. Furthermore, it was shown that the edging of the end tip of the glass fiber can be achieved by sandblasting instead of using hazardous compounds like hydrofluoric and sulfuric acid. It is also possible to treat the end of the glass fiber with a diamond file and/or abrasive paper. Sandblasting can easily blast off fiber tips with a small diameter (< 1 mm) while diamond files give one much more control over the roughening process and do not break the glass fiber so easily. Roughening with a diamond file or abrasive paper can be performed with an illuminated fiber tip, which gives a constant visual confirmation of the level of abrasion. This optimization of the homogeneous illumination from the tip again results in a factor around 3 in increased illumination intensity compared to a raw fiber in the region of the rf coils. A further factor important for the light intensity is the heating up of the LED during illumination, which restricts the LED performance for continuous illumination or long, strong light pulses. Therefore, the LED itself was set on a customized cooling block for heat dissipation while being powered by a home-built transistor unit. Additionally, the Gschwind group showed that by using short light pulses followed by delays the LED can be made to “overshoot” to increase the temporal light output, which is in principle similar to the effects of duty cycles in NMR. This combination of reasonable light intensities for photocatalysis, low costs for the LED setup, non-hazardous treatment of the fiber tip, and the ability to obtain valuable mechanistic insight into photocatalysis[31] paved the way for a comeback of *in situ* photo-NMR in photocatalysis and photoswitches. The design has been widely adopted and was reproduced multiple times[64,122,123]. It was even reproduced in industry e.g. Merck[37,38,64] and AstraZeneca (personal communication). By now the apparatus can be bought commercially online (GoldsteinScientific). In 2017 Dolinski *et al.* showed, that the glass fiber can also be centered in the NMR tube with a cheap Teflon insert as an option to replace the coaxial glass inserts of the previous designs[39].

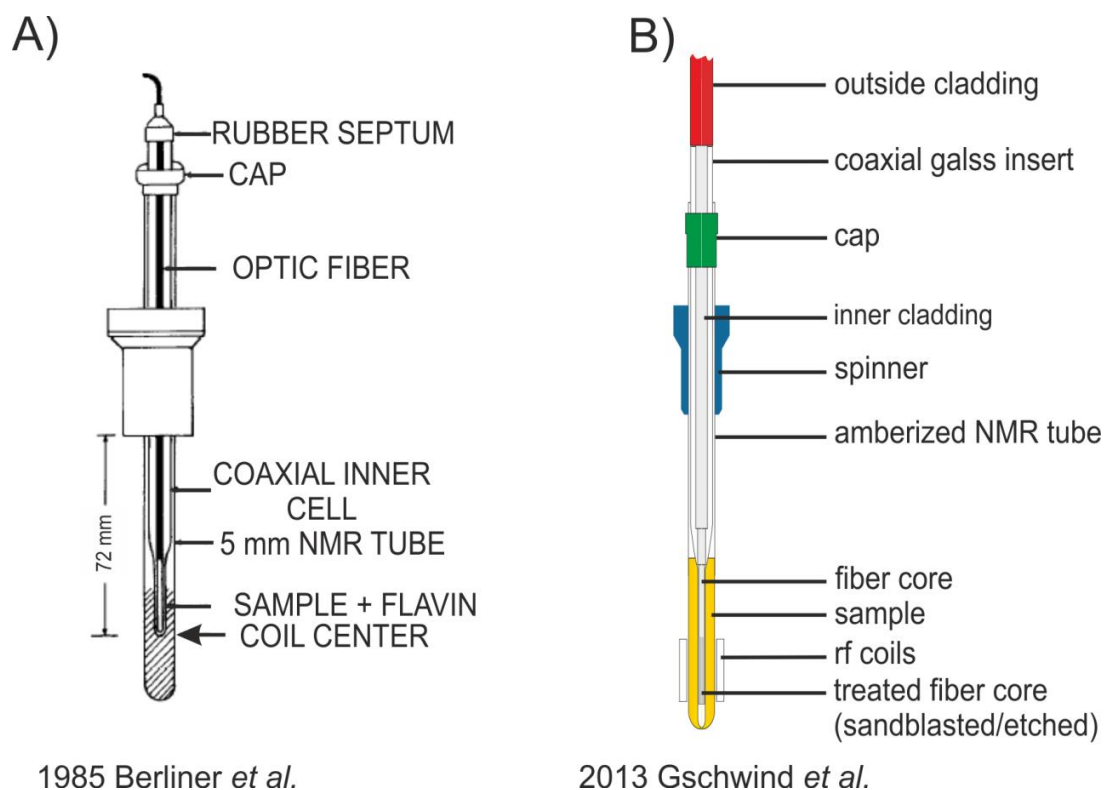


Fig. 5: Schematics for *in situ* illumination from the inside of the NMR tube. A) *In situ* illumination setup presented by Berliner *et al.* in 1985[114] B) *In situ* illumination setup presented by Gschwind *et al.* in 2013[95]. The main difference is the positioning and treatment of the end tip of the glass fiber, which only covers half the rf coil region and only illuminates downwards in the Berliner design, while in the Gschwind design it covers the whole rf region and illuminates in all directions due to sandblasting of the fiber tip.

The biggest advantage of illumination from the inside compared to other *in situ* designs (top, bottom, side) is its flexibility. The apparatus requires no modification of any NMR hardware, especially not of the probe. Within minutes, a user can take the apparatus to any available solution NMR spectrometer, at any field strengths and with any cryo-probes, to start investigations under illumination. The time required to set up experiments is mostly determined by the sample preparation and is nearly analogous to the sample preparation time needed for batch reactions. However, when inert and/or water free conditions are required, the handling of the glass fiber inside the glove box is more laborious. Another advantage is the high degree of uniform illumination. Due to the treatment of the fiber tip, the light is emitted in all directions throughout the sample and reaches the whole region within the rf coils. It is interesting to consider the advantages and disadvantages of using the coaxial insert. One might argue that it is a disadvantage, as the active sample volume is reduced significantly. But this might also be a blessing in disguise for photoreactions, since the active layer that the light has to penetrate is also

reduced significantly[51]. For example, using a 5 mm NMR tube (usual inner diameter of 4 mm) with a 1 mm diameter glass insert results in a length of the light path through the sample of 1.5 mm. Switching to a 3 mm diameter glass insert reduces the length of the light path to 0.5 mm (meanwhile the sample volume needed in the NMR tube goes from ~450 μ L to ~300 μ L). This can eliminate or at least reduce complications arising for highly concentrated samples when the optical density is too high, which is a significant issue for designs illuminating from the top or bottom⁴. It also enables the use of comparable concentrations to the synthetic approach, which is often a problem for other techniques such as UV/Vis spectroscopy. Furthermore, this approach can also decrease the time needed for full product conversion, as the same amount of light can be used for a reduced sample volume (note that some photoreactions take up to 12-24 h in batch and *in situ* the light intensity is further reduced). The same principle is of course valid for photoswitches in order to reach the photostationary state (PSS) as fast as possible. Another advantage of the glass insert is that it can be straightforwardly cleaned after the reaction. The insert is very robust and can be cleaned like any other glassware. In contrast, if the glass fiber is put directly into the reaction solution, it also has to be cleaned after every reaction, increasing the risk of breaking the sensitive fiber. Furthermore, direct use of the fiber in solution might lead to local, extreme temperatures on the surface of the fiber. This can result in side reactions and/or contamination of the glass fiber. Similar to other *in situ* designs, full automation for the interplay of illumination and NMR acquisition is standard.

Nonetheless, *in situ* illumination from the inside still has some drawbacks compared to other *in situ* systems. Due to the positioning of the glass fiber throughout the rf coils, shimming can be an issue as the glass fiber is never perfectly straight. Sometimes the sample has to be repositioned (lifted up and down) in order to get good shimming results. But from the authors' experience, this is rather an issue with older consoles (TCUII and older for Bruker systems) and almost a negligible issue on newer systems (AvanceNeo). Next, due to the coaxial glass insert, the active volume in the region of the rf coils is reduced. As mentioned before, this can also be seen as an advantage but can of course also be a disadvantage if very low concentrations are investigated and S/N becomes a limiting factor. Additionally, as the fiber is directly attached to the NMR tube, sample spinning is not possible and reactions requiring or producing gases are problematic. Due to the glass insert there is usually almost no free space left in the NMR tube. Hence, gas input, removal or storage is hardly possible for high sample

⁴ It is to be noted, that the insertion of a quartz glass insert can also be used for *in situ* illumination from the side to decrease optical density issues[110].

concentrations with the designs shown in Fig. 5. However, the authors' experiences with reactions that produce gases (decarboxylations etc.) showed that so far such a gas evolution inside the sample only pushed some drops of the reaction mixture through the Parafilm out of the NMR tube, without damaging the apparatus. Additionally, gas bubbles can form, which cause a deterioration in the line width due to field inhomogeneity. However, if carrying out such experiments, please consider that the effect and destructiveness of gas evolution can be extremely different depending on the individual reaction and the design of the LED apparatus.

In summary, *in situ* illumination from the inside is extremely flexible and can be used with any solution NMR spectrometer. In addition, it provides a high degree of uniform illumination and the use of a glass insert can reduce optical density issues and reaction times. In contrast, insertion of the glass fiber can cause some problems with shimming and gas-forming reactions can be an issue at high concentrations. But the success and spread of illumination from the inside clearly shows that it has by now established itself as the main approach to investigate photocatalysis and photoswitches by NMR spectroscopy.

2.3.2.2.3 Illumination from the top

In 2005, Kuprov *et al.* developed a dedicated LASER system with illumination from the top to study time resolved photo-CIDNP effects (Fig. 6)[23]. The design used a mirror/prism system to guide the light of a 355 nm, high power Nd:YAG LASER into the NMR sample, through the sample bore. This mirror/prism approach is similar to mirror/prism systems from the bottom (see section 2.3.2.2.1) but avoids the need for probe modifications and hence adds the flexibility to use any solution NMR spectrometer. The high power Nd:YAG LASER is capable of creating 100 mJ, 10 ns light pulses to achieve maximum sensitivity for time resolved photo-CIDNP effects. This created the necessity for this mirror/prism system, because with these power outputs the 100 mJ pulses literally destroyed optical fiber systems such as those usually used for illumination systems that lead through the sample bore. Other options to guide the light, e.g. long, fused silica light pipes and liquid light guides were also ruled out due to other issues such as impractical handling or high losses of light. The design uses three prisms to redirect the LASER beam directly into the NMR magnet from the top. The NMR tube hosts a 20 cm, fused silica rod with polished ends for two reasons. First, it effectively transfers the light into the sample and second, it serves as an airtight seal to protect oxygen sensitive samples. It is to be noted that these glass rods can also be damaged by the high power output of the LASER, making it necessary to replace them regularly.

But they are easily replaced and of low cost. In addition, the equipment is also automated to control the interplay of light pulses and NMR acquisition.

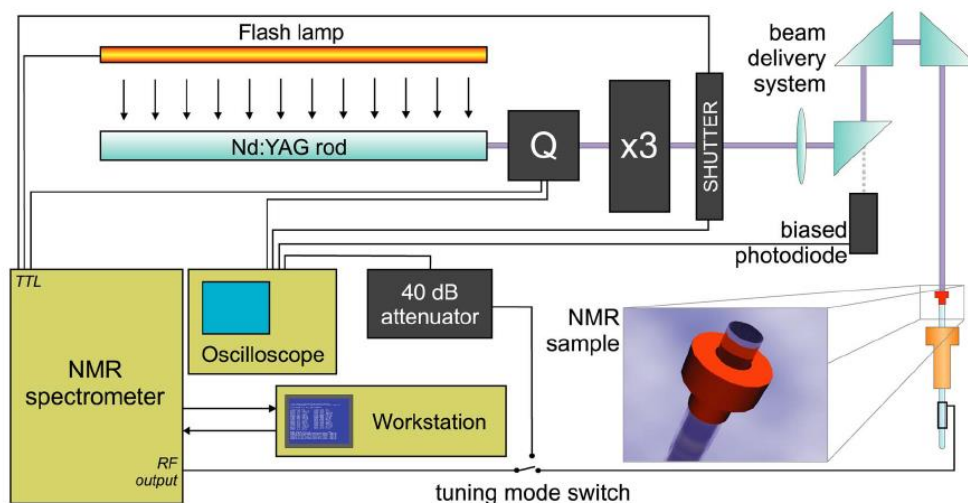


Fig. 6: The LASER system with illumination from the top as described by Kuprov *et al.* for time resolved photo-CIDNP experiments[23]. The design uses a 355 nm Nd:YAG LASER and the emitted light is guided via a prism system, which requires three prisms. The NMR tube is filled with a fused silica rod, which acts both as a light guide and airtight seal for oxygen sensitive samples. The NMR console is used as a central control hub to automate the interplay of NMR acquisition and light pulses.

The biggest advantage of such a design using illumination from the top is its flexibility, similarly to *in situ* illumination from the inside. It can be used with any solution NMR spectrometer, albeit setting up experiments takes longer than with fiber-based designs because the prism system has to be adjusted regularly due to horizontal drift of the magnet. In addition, the use of prisms is the only approach that can withstand a prolonged exposure to high power LASERS.

But in contrast, the approach of illumination from the top has issues in terms of optical density. Similar to illumination from the bottom (see section 2.3.2.2.1), the light has to pass through outer parts of the sample before reaching the sensitive region between the rf coils. Especially for highly concentrated samples, the light might not penetrate deeply enough to actually reach the active layer effectively.

In summary, Kuprov *et al.* presented a highly flexible LASER-based design, which can be used with any solution NMR spectrometer. The design provides tremendous light output and presents an ideal tool for the investigation of time resolved photo-CIDNP effects.

2.4 Other illumination approaches and special apparatus for photo-NMR

2.4.1 UVNMR

The first special case we examine in this section is that of UVNMR. Although this apparatus doesn't include any illumination besides the light from UV/Vis measurements, it still merits coverage in this review for two reasons. First, it is a direct precursor of the UVNMR-illumination design discussed elsewhere in this review, and second, it introduces UV/Vis to NMR, which is a widely used analysis tool in photochemistry. In 2009 Tolstoy *et al.* introduced this novel combination of NMR and UV/Vis spectroscopy, which allowed the simultaneous acquisition of NMR and UV/Vis spectra from the same sample inside the NMR spectrometer[124]. Here, the NMR probe was equipped with a guiding channel that allowed for insertion of a commercially available UV/Vis reflection probe. This is similar to designs already discussed using illumination from the bottom (see section 2.3.2.2.1), but instead of an optical light guide fiber it uses optical UV/Vis fibers. This UV/Vis reflection probe consists of seven optical fibers. Six fibers act as illumination fibers connected to a halogen/deuterium light source that promote the investigated molecules from ground to excited state. The seventh (last) fiber takes care of the UV/Vis detection as it is connected to an UV/Vis spectrometer (Fig. 7 A). Each individual fiber has a diameter of 200 μm . The design reported in 2009 used a regular NMR tube for the measurements, but the design of the NMR tube was changed in 2011[125]. The initial regular NMR tube was manually modified by replacing the originally round bottom by a flat, polished glass bottom to provide a better transition from sample to reflection dip probe. The NMR tube was placed centrally, directly above the UV/Vis reflection probe. The design requires a reflective system to guide the light from the six illumination fibers back into the detection fiber. In this case an optical polytetrafluoro-ethylene (PTFE) insert was chosen which is directly inserted into the NMR tube. The shape of the insert was also optimized between 2009 and 2011 resulting in a flat bottomed cylindrical insert that is mounted on top of two small spacers (Fig. 7 B). This refined reflective system leads to a fixed active layer of 0.2 mm for the UV/Vis measurements (= optical path length 0.4 mm), while not affecting the active layer for NMR measurements between the rf coils.

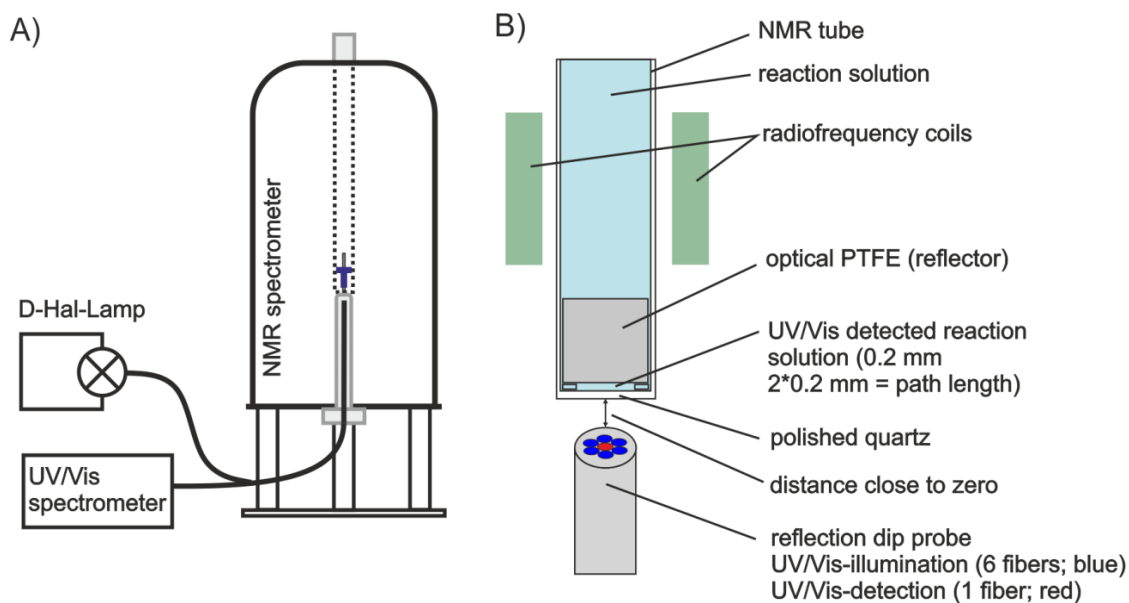


Fig. 7: Schematics of the UVNMR design presented by Tolstoy *et al.*[124,125] A) The NMR probe head has a drilled hole for a fiber based UV/Vis reflection dip probe connected to a UV/Vis spectrometer and a D-Hal-light source. B) Details of the NMR/UV/Vis arrangement inside the magnet. The tube is modified with a flat quartz glass bottom which is placed right on top of the reflection dip probe. The design used optical PTFE for reflection of the UV/Vis light leading to an optical path length of 0.4 mm.

This UVNMR system is optimal for the investigation of thermodynamic equilibria, e.g. hydrogen bond systems, as was shown by Tolstoy and Limbach *et al.* [125], and it provides reliable and reproducible UV/Vis and NMR results. On the other hand this arrangement has the typical restrictions and inconveniences of all experiments employing illumination from the bottom (see section 2.3.2.2.1). The first is the need to drill through the NMR probe, with the risk of damage and the usual restriction in terms of different field strengths, cryo-probes etc. Apart from the hardware complications there is the complication that within the sample under investigation, the active layer of UV/Vis and the bulk compartment used for NMR measurements are basically separated, i.e. diffusive exchange is very limited. For static equilibria this is not an issue; however in the case of dynamic systems such as reactions, deviations of the reaction progress between the two compartments might be possible.

It should be mentioned that a UVNMR design existed before the system of Tolstoy *et al.* mentioned by Gaeva *et al.* in 2006[61]. Here, a commercially available UV/Vis dip probe was put raw into an NMR tube, which also allowed the acquisition of NMR and UV/Vis spectra from the same system. This design was used to investigate a stable spiro-based photoswitch which was subjected to *ex situ* illumination beforehand[61]. Hence, this

arrangement could be described as a combination of NMR, UV/Vis spectroscopy and *ex situ* illumination, although the combination of all three was sequential rather than simultaneous. Unfortunately, this design was only very briefly described, therefore will not be discussed further here.

In summary, the UVNMR experimental design discussed here constitutes a valuable combination of UV/Vis and NMR spectroscopy and is ideal for the investigation of static systems. Many of the required parts of the apparatus are commercially available and reasonably straightforward to put together. The approach comes with some disadvantages, such as the need to drill through the NMR probe as well as a questionable performance regarding dynamic systems, but is the clear method of choice for investigations of static systems by UV/Vis and NMR spectroscopy.

2.4.2 UVNMR-illumination

In 2018, the Gschwind group published a new combination of UV/Vis spectroscopy, NMR spectroscopy and illumination termed UVNMR-illumination[108]. This experiment essentially elaborates and combines two existing systems; their *in situ* NMR illumination unit [95] and the UVNMR design introduced by Tolstoy *et al.*[124,125]. The new design focused on four areas:

- making dynamic systems accessible for UVNMR measurements
- introducing illumination to the combination of NMR and UV/Vis spectroscopy to enable investigations in photochemistry
- providing a highly flexible system that can be used with any solution NMR spectrometer
- introducing automation for the simultaneous control of UV/Vis measurements, NMR measurements, and illumination

The organization of components inside of the NMR tube was inspired by our *in situ* NMR illumination system[95]. A regular, 5 mm, thin walled NMR tube (optionally ambered to reduce the effect of transient light if investigating photosensitive systems) serves as reaction vessel (Fig. 8 A). A coaxial glass insert with an inner diameter of 3 mm provides space for optical systems. Here, the insert is filled with two optical fiber systems. First, it hosts an illumination fiber with a cleared and sandblasted or abraded tip which guides light from an LED directly into the sample under investigation. Secondly, a commercially available UV/Vis reflection dip probe is positioned right next to the illumination fiber. This dip probe is essentially a fiber bundle consisting of 7 fibers, where 6 fibers effect

illumination and are attached to a halogen/deuterium illumination source. The seventh fiber is connected to a UV/Vis spectrometer (Avantes) and works as a detection fiber. All 7 fibers in the reflection dip probe have a diameter of 100 μm . The resulting fiber bundle occupies 1 mm in diameter inside the glass insert. An optical PTFE insert at the bottom of the NMR tube is used as a reflector. The position of the coaxial glass insert is variable due to a customized, airtight screw cap; hence the distance between UV/Vis reflection dip probe and reflector can be adjusted at will. A distance between reflection dip probe and reflector of 1 mm is recommended, resulting in an active layer of 2 mm for the UV/Vis measurements.

The NMR console (Bruker) was used as a central control unit to combine NMR, UV/Vis and illumination. It is directly connected to the UV/Vis spectrometer and the illumination by cables carrying two, individual Real-time Clock Pulse (RCP) outputs of the IPSO unit (Fig. 8 B). The RCP outputs operate on Transistor-Transistor Logic (TTL) and send either an up or down (“yes” or “no”) signal to an external source. Therefore, the LED can be remotely switched on and off by the first TTL signal. Furthermore, the second TTL signal triggers a single measurement at the UV/Vis spectrometer. The signal switch from up to down can be executed by command lines anywhere in the NMR pulse sequence. Hence, illumination, UV/Vis and NMR measurements can be sequenced at will. Of course, manual control of illumination, UV/Vis spectrometer and NMR or separate usage of all three aspects is also an option.

It should also be noted that the NMR spectrometer can be used as heater or cooling unit giving the option to acquire UV/Vis spectra over a large temperature range (here tested in the range 180-323 K).

Combination of illumination and NMR

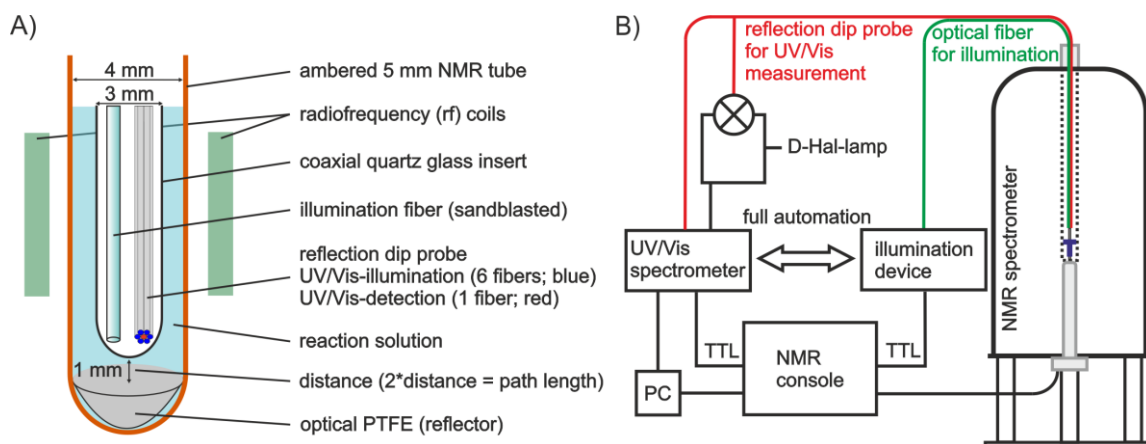


Fig. 8: Schematics of the UVNMR-illumination design introduced by the Gschwind group[125] A) The optionally ambered NMR tube hosts a coaxial quartz glass insert which contains two fiber optical systems: a fiber for illumination connected to an LED-illumination device and a UV/Vis reflection dip probe connected to a UV/Vis spectrometer and a D-Hal-lamp. Optical PTFE is used as a reflector. The measured path length can be adjusted manually and is usually around 2 mm. B) Schematics of all devices involved for the UVNMR-illumination experiment. The NMR console acts as central control unit triggering light on/off as well as the NMR and UV/Vis measurements.

This design was successfully applied in dynamic systems such as photocatalysis and for the investigation of photoswitches. Additionally, the goals were fulfilled to present a flexible, automated UVNMR unit that gives the additional option of sample illumination. The system consists of mostly commercially available parts and needs no modification of the NMR spectrometer.

Although expanding possible applications for UVNMR (and illumination) this design also comes with some restrictions and room for improvement. It should be noted that the Lambert-Beer-law can't be taken into account directly as the optical PTFE has diffuse reflection properties hampering absolute quantification by UV/Vis spectroscopy; however, relative quantification works. But this is only an issue for paramagnetic species because the NMR measurements can of course be used for quantification of all diamagnetic components. Furthermore, it is challenging to keep the distance from the coaxial quartz glass insert to the PTFE reflector constant between separate experiments and shimming is sometimes affected just by the sheer number of objects inside the tube.

In summary, the Gschwind group presented a triple combination of NMR, UV/Vis and illumination, which can be employed for static and dynamic systems including photochemical systems such as photocatalysis and photoswitches. The arrangement

can be used with any solution NMR spectrometer and can be fully automated if necessary.

2.4.3 FlowNMR-illumination

FlowNMR has recently been a field of increased attention and application, both in high field NMR spectroscopy and bench top NMR systems[126,127]. Mainly focusing on reaction monitoring, it is no surprise that some FlowNMR systems were combined with illumination making FlowNMR accessible for photoinduced systems. Simpson's group in 2016/17[59,128] and Hintermair's group in 2018[97] recently developed FlowNMR-illumination systems and showed their application in photochemistry. Simpson's group combined a commercially available 250 μ L injection FlowNMR probe (Bruker) with a home built illumination system employing a xenon light source from OceanOptics next to the reaction container. This approach combines the main advantages of *ex situ* and *in situ* NMR illumination studies. Due to the external reaction container, stirring and high light exposure is possible, while still keeping the reaction in a closed system and enabling online monitoring. A drawback of Simpson's design is the need of a FlowNMR probe decreasing the flexibility of the system. The FlowNMR-illumination design presented by the Hintermair group circumvents this issue by inserting the whole flow system from above through the sample bore (Fig. 9) [97]. This design utilizes an InsightMRflow tube from Bruker inside the magnet, an HPLC pump (JASCO PU-2085 Plus), a reaction container and an LED light source and combines all in a single system. This arrangement is not permanently bound to one spectrometer, since the flow tube is inserted from the top.

Another flow system, specialized for the investigation of photo-CIDNP effects, was presented by Fedin *et al.* in 1999[76]. The design initially collects the sample in a photochemical cell inside an auxiliary magnet (0-70 mT). Here, the sample is irradiated with an excimer LASER at 308 nm to build up photo-CIDNP polarization. Afterwards to sample is transferred into the NMR spectrometer for acquisition. The transfer time is around one second.

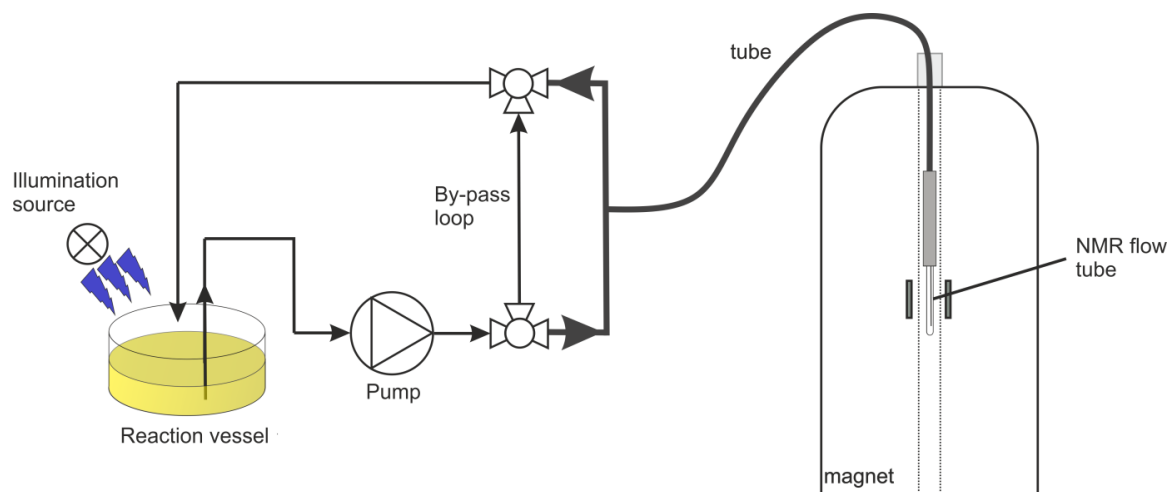


Fig. 9: Schematics of the FlowNMR-illumination design presented by Coombes *et al.*[97] The reaction vessel is directly illuminated and connected to a flow system, which leads through the NMR spectrometer enabling online monitoring of the reaction.

Such FlowNMR-illumination systems provide unprecedented accuracy for online monitoring of photoreactions combined with high light exposure, but the flow systems also come with some drawbacks. It is apparent that these systems require very high volumes in comparison to the regular *ex situ* and *in situ* approaches. Just the tubing in Hintermair's group setup holds ~5 mL, and reaction volumes of around 20 mL are recommended[97]. This might be an issue in terms of cost (some photocatalysts cost hundreds to thousands of Euros even in the milligram range). Most synthetic photoreactions are conducted in the low mL range (0.2-2 mL [83,104–106]) and straightforward increase to 20 mL might not work. On a related note, Dutta *et al.* mentioned that cleaning of the flow system can be troublesome and time consuming[128].

In summary, the FlowNMR-illumination systems present a fascinating, new tool for the investigation of photoreactions that shows significant advantages compared to the regular *ex situ* and *in situ* approaches. The designs combine online monitoring with a homogenous reaction mixture under high light exposure. But one has to take care the investigated system is suited to the approach in terms of cost and scalability of the reaction due to the high volume requirements.

2.4.4 NMR on a Chip-illumination

Another field of research that gained more attention in recent years is the miniaturization of NMR probes and detection volumes, often called “NMR on a Chip”. In 2018 the Gomez and Velders groups described the combination of their customized NMR on a Chip probe with two fiber guided illumination designs, which can be operated either statically or in flow[96]. The first arrangement shows the applicability of illumination systems for NMR on a Chip by generating various photo-CIDNP effects. Here, the rf microcoils are embedded within a Vis-transparent, polydimethylsiloxane (PDMS) polymer[129], which in turn is placed on a 3D-printed polylactic acid (PLA). The Chip system described allows for volumes in the low μL range. A 1 mm internal diameter optical fiber is directly inserted into the PLA holder resulting in an effective distance of 2 mm from fiber end to NMR detected layer. The glass fiber itself is attached to a low power LASER emitting at 455 nm. With this initial design it could be shown that restrictive parameters in photo-CIDNP investigations like uniform illumination of the sample and increasing optical density for highly concentrated samples can be circumvented effectively.

In the same year the Gomez and Velders groups presented a second fiber-based design which improved the overall light output of the initial setup and also introduced LED illumination as a second illumination option besides LASERs (Fig. 10 A)[63]. Furthermore, the field of application was extended to include investigation of photoreactions. The Chip system also varied changing from a PDMS polymer to glass Chips made from D263 glass, which showed a transmission of >90 % in the investigated wavelength regions. This new Chip version also allowed for significantly lower volumes, transitioning from the μL to the nL range (detection volume: 25 nL) and thereby minimizing optical density effects[63]. Analogous to the first system, the Chip was placed on top of a customized Chip holder, while the optical fiber system was switched from a glass to a plastic optical fiber system. This created the opportunity to upscale significantly the fiber diameter to 5 mm (compared to 1 mm in the previous glass fiber design). The fiber diameter is considerably wider than the inner diameter of the microcoil (250 μm). As a result, critical obstacles such as non-uniform illumination are easily overcome beside the increased light output of the thicker fiber. The fiber is fixed on the NMR Chip holder right above the NMR detection volume by a customized adapter. The “input” end of the plastic fiber is either attached to a LASER or LED illumination setup. The light LASER Diode (LD) system was mounted in a collimation tube to focus the emitted light directly into the optical fiber. A Teflon frame was used to align the LASER

beam. This LED illumination design deserves somewhat more attention as it is a novel approach using the power of an LED array rather than just a single LED, thereby increasing potential light transmission into the investigated sample significantly. In total 28 LED bulbs are mounted on a customized, printed circuit board (PCB) and the LEDs are interconnected in blocks of six. A hole is drilled in the center of the PCB accommodating the optical fiber. A concave mirror was placed in front of the LED array to focus the emitted light back into the core of the fiber system (Fig. 10 B). PCB and mirror were placed in an adjustable aluminum box, which allowed for flexible positioning of all components by a railing system. In addition, the aluminum box is equipped with a fan to dissipate heat.

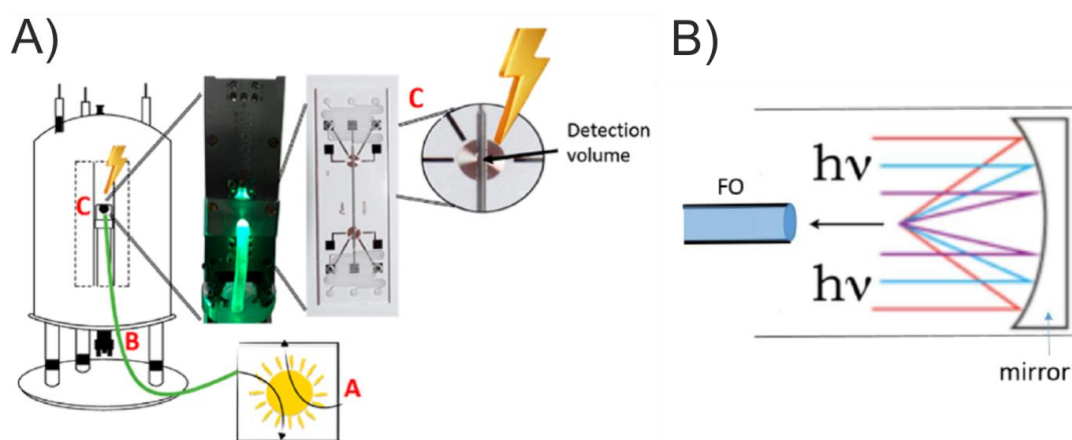


Fig. 10: A) Schematics of the NMR on a Chip illumination setup introduced by Velders *et al.* The NMR magnet contains a customized NMR microfluidic probe operating in the μL to nL scale[63]. The probe also provides space to host fiber optics with diameters from 1-5 mm for directly illuminating the sample on the Chip system. B) Schematic representation of the LED illumination system used by the Gomez and Velders groups. A concave mirror is used to collimate the light of 28 LEDs in a single fiber, which drastically increases the light output to the investigated sample.

The Gomez and Velders groups presented practical combinations of illumination and NMR on a Chip[63,96]. The systems can be operated in flow or can be investigated as a static sample with very small volumes (nL- μL). Furthermore, the designs are available for different Chip sizes and materials and have been tested with different fiber sizes and LEDs or LASERS. Due to the favorable ratio of sample to illumination source diameter (light source \gg sample) and high light intensities, obstacles such as non-uniform illumination and optical density can be avoided. This was demonstrated on various systems ranging from photo-CIDNP investigations to the observation of photoreactions. Yet, a downside is that essentially every part of the apparatus is manually modified or

self-made from the start, ranging from the probe head over the NMR on a Chip system to the whole illumination setup. The Chip system itself can be produced very cheaply using 3D printing. Despite that, combination of the system with commercial NMR on a Chip designs (e.g. Bruker) might be an issue in the future.

In summary, NMR on a Chip with illumination expands the combination of NMR and illumination systems considerably, providing very high light intensities and significantly reduced optical density issues while only requiring very low amounts of sample (nL- μ L).

2.4.5 EPRNMR-illumination

In 2017 the Bennati group[130] presented an interesting triple combination of low field NMR, EPR spectroscopy and illumination. Just like UVNMR-illumination, it combines two prominent spectroscopic methods and can readily provide information about diamagnetic and paramagnetic species, in addition to the option to illuminate the sample.

This triple combination of EPR, NMR spectroscopy and LASER flash illumination was used to create optically driven liquid DNP effects within the solvent after excitation of a fullerene nitroxide system, which replaced microwave irradiation.

2.4.6 Illumination apparatus for solution state NMR to study heterogeneous photocatalysis

Besides homogeneous photocatalysis, heterogeneous photocatalysis with TiO_2 as photoactive substance has seen tremendous growth in recent years[98]. Hence, it is no surprise that NMR studies also focused on the investigation of these interesting systems. Especially the Mills *et al.* group presented a variety of approaches to open the field of heterogeneous photocatalysis for investigations with high resolution solution NMR spectroscopy. Since 2011 the Mills *et al.* group have reported the use of sol-gel titanium-coated NMR tubes to investigate heterogeneous, photocatalytic systems monitoring oxidations and C-C coupling reactions (see section 2.5.2)[58,131–133]. To uniformly coat the NMR tube a few drops of a self-made titanium paste are put into the NMR tube and spread by shaking. Then the tube is placed in a mechanical spinner and rotated at 1000 rpm for 5 min. Subsequent application of vacuum followed by a drying process at 450 °C for 90 minutes completes the coating process.

The photoreactions investigated are conducted completely inside the NMR tube with a reaction volume of 1 mL[58,133]. To deliver light into the sample the Mills group presented two distinct approaches (Fig. 11). The first is illumination of the whole NMR

tube outside the NMR spectrometer in a customized UV-photoreactor[133]. Here, the photoreactor consists of two sets of 6 x 8 W black light UV lamps (365 nm) arranged in a hemispherical cylinder. In combination, the two hemispheres completely envelop the irradiated NMR tube. Furthermore, the NMR tube is connected to a mechanical spinner, which increases homogeneous illumination. Additionally, an aluminum reflector around the photoreactor maximizes light output. After illumination starts the NMR tube is periodically taken from the photoreactor to the NMR spectrometer to conduct the NMR investigations[133]. The second illumination approach is the *in situ* illumination of the sample with fiber optical systems from within the NMR tube[58]. This approach is similar to the *in situ* illumination of NMR tubes from the inside presented in section 2.3.2.2.2. However, in this case, the coaxial quartz glass insert is omitted because the solvents used (e.g. water) are not detrimental to the glass fiber. A xenon-arc lamp combined with a monochromator provides light at 365 nm[58]. Both approaches come with the pro and cons of other systems that are investigated by *ex situ* and *in situ* illumination (see section 2.3.2). *Ex situ* illumination ensures a higher light exposure but cannot be used to detect short lived intermediates due to the dead-time for the transfer to the NMR spectrometer. *In situ* illumination provides real-time, online information from the system but has significantly reduced light output. Additionally, for the systems investigated by Mills *et al.* oxygen was needed as a reactant, which can only be present at low concentration in the *in situ* system, resulting in significantly diminished concentration of all reactants (down to 1 mM)[58].

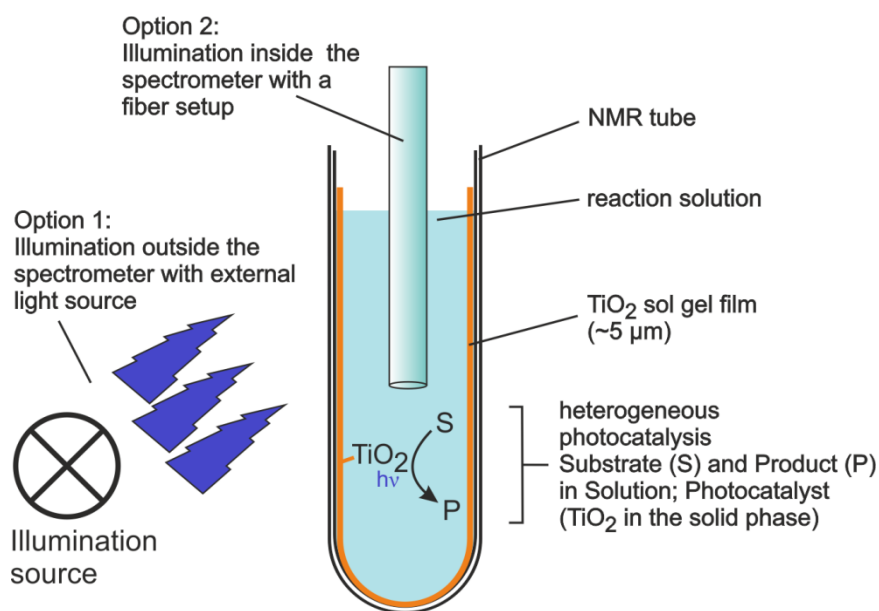


Fig. 11: Schematic representation of the titanium dioxide coated NMR tubes for heterogeneous photocatalysis described by Mills *et al.* The whole NMR tube is uniformly coated with a TiO₂ sol gel film with a thickness of approximately 5 μm[58,133]. Mills *et al.* described two illumination approaches to conduct the photoreactions. Under option 1 the whole NMR tube is illuminated outside the spectrometer by putting the NMR tube into a UV-photoreactor, which also allows for tube spinning ensuring homogeneous illumination[133]. Under option 2 the sample is illuminated *in situ* inside the NMR tube by utilizing fiber optics analogous to the designs discussed in section 2.3.2.2.2[58].

A design similar to the *in situ* approach of Mills *et al.*[58] was used by Wang *et al.* in 2016[60]. It also utilizes fiber optics located inside the NMR tube, but instead of one fiber that is sandblasted at the tip it uses a bundle of 7 fibers that only illuminate downwards and are placed above the sample. Furthermore, instead of a fixed coating, they used Pd/TiO₂ micro-particles which float inside the reaction solution.

In summary, Mills and Wang *et al.* showed that heterogeneous photocatalysis can be readily approached with high resolution, solution NMR spectroscopy: Using TiO₂ coating or particles and *ex situ* and *in situ* NMR illumination approaches, they provided new insights into photoreactions using TiO₂ as photoactive species.

2.4.7 Illumination apparatus for solid state NMR

Combinations of NMR and illumination have also found their way into solid state NMR spectroscopy, enabling a considerable number of research topics and approaches. However, giving a detailed description of this area would go beyond the scope of this review.

An interesting combination of illumination and solid state NMR was presented by Hwang *et al.* in 1997/98[134,135]. Here, a special, home-built NMR probe was used based on a design of Gay *et al.*[136]. This was further elaborated by the introduction of a light pipe into the probe which directly emitted the light into the sample through a small gap (10 mm) in the rf coils (Fig. 12 A). The light pipe was connected to a 300 W xenon-arc lamp (ILC Technology), which was combined with a dichroic mirror to confine the emitted wavelength to the desired range.[134,135] The reactions investigated using this approach mainly focused on systems with TiO₂ as photoactive species[137–142]. Another handy approach was presented by the Matysik group in 2017 describing an aerodynamic field-cycling arrangement[143]. Here, an optical fiber is used to illuminate the sample from the side but illumination and measurements actually are conducted at different positions and at different times inside the magnet. A gas flow system lifts the sapphire rotor up to the position of the glass fiber where illumination takes place. Afterwards, the gas flow stops, the rotor is positioned back in the stator, and spinning and NMR measurements start. This design was used to test the magnetic field dependence of solid state photo-CIDNP effects and thus to draw conclusions on the field-dependent behavior of solids.

A UVNMR combination was also introduced to solid state NMR in 2004 by Hunger *et al.* (Fig. 12 B)[144]. The design is based on a 7 mm MAS NMR probe from Bruker, which was remodeled to fit an injection/flow system presented by Horvath *et al.* in 1995 [145]. Additionally, the MAS rotor was equipped with a quartz glass window, which allowed for the combination of the MAS rotor with a UV/Vis reflection dip probe. This approach was used to track the conversion of methanol on dealuminated zeolite[144].

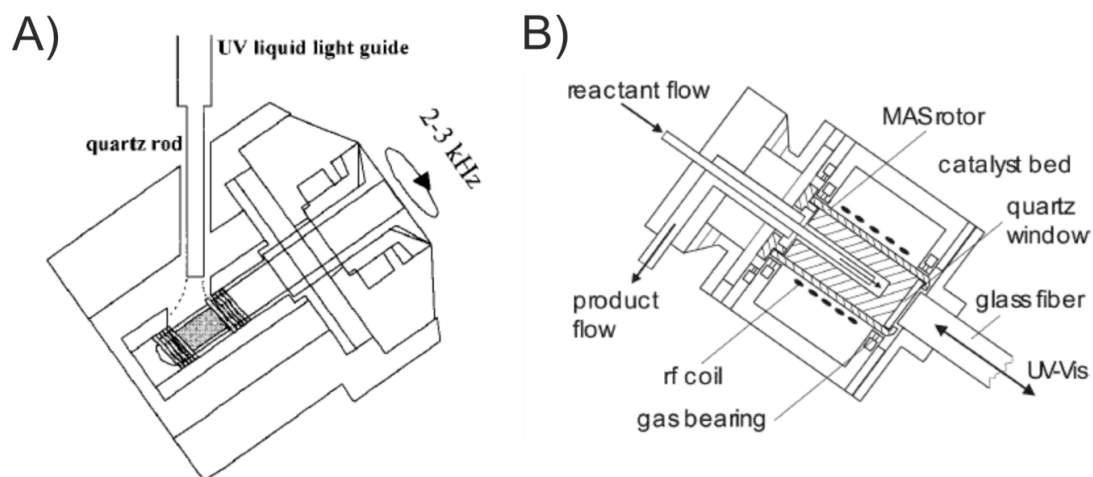


Fig. 12: Schematics of different NMR-illumination systems for solid state NMR A) Schematics of Hwang *et al.* showing a home-built MAS probe modified to accommodate an optical pipe system to deliver light into the sample[134]. B) Schematics of the UV/Vis solid state NMR combination by Hunger *et al.* showing a modified MAS probe to include a reactant flow system as well as a quartz glass window, which is connected to a UV/Vis reflection dip probe[144].

2.5 Applications of photo-NMR

2.5.1 Homogeneous photocatalysis

LED-based NMR illumination devices are simple and powerful tools, which provide access to valuable and rich kinetic and structural insights into photochemical reactions at atomic resolution.

2.5.1.1 Flavin catalyzed photo oxidation of benzyl alcohol

Until 2015, the *in situ* illumination NMR technique was mostly applied to observe photo-CIDNP effects; this was consistent with the common consensus view, that the key to understand photochemistry lies entirely in the initial photoexcitation step. In 2015, the Gschwind group determined reaction profiles for a photocatalytic reaction by using *in situ* LED illumination NMR, which revealed strongly solvent dependent rates and yields, resulting from the modulation of the electron transfer mechanism in a flavin catalysed photoreaction [31]. For the first time, this study proved that two different reaction pathways can arise from an identical photoexcited state during photocatalysis depending on the experimental conditions. Despite the extensive and excellent ultra-fast time resolved UV/Vis spectroscopic mechanistic studies by Dick and Riedle[11], this switch between an inefficient one-electron transfer mechanism and a more effective two-electron transfer mechanism had not previously been uncovered. This work showed that, in spite of its inherent limitations, such as low time resolution and insensitivity, NMR spectroscopy can provide information about photocatalytic mechanisms that are key to the reaction outcome but were not accessible from UV/Vis spectroscopy. Therefore, this study has changed the approach of photosynthetic practitioners to include investigation of the downstream pathways after the photoexcitation step in photocatalytic mechanistic studies. Thus, this remarkable observation by NMR in photocatalytic mechanistic studies successfully complements UV/Vis studies, and more importantly it encourages a more active use of NMR spectroscopy in mechanistic investigations of photocatalysis.

In principle, flavin derivatives are known to catalyse diverse biochemical reactions and can act as both one-electron and two-electron mediators in redox reactions depending on the stability of the semiquinone radical inside the protein[146]. In synthetic photocatalysis flavin derivatives are well explored and the mechanism of flavin-catalysed photooxidation of benzylic alcohol has been studied in-depth by time resolved UV/Vis spectroscopy[11], revealing the initial photoexcited states and the significance of triplet

states for product formation (Fig. 13). However, whether one or two flavin molecules are necessary to conduct the overall two-electron, two-proton reaction was unclear. UV/Vis spectroscopy is perfectly adequate to monitor events within the photocatalyst, but is most often blind to events within the substrate or product. As a result, the reason for the highly solvent dependent rate and yield was not previously understood.

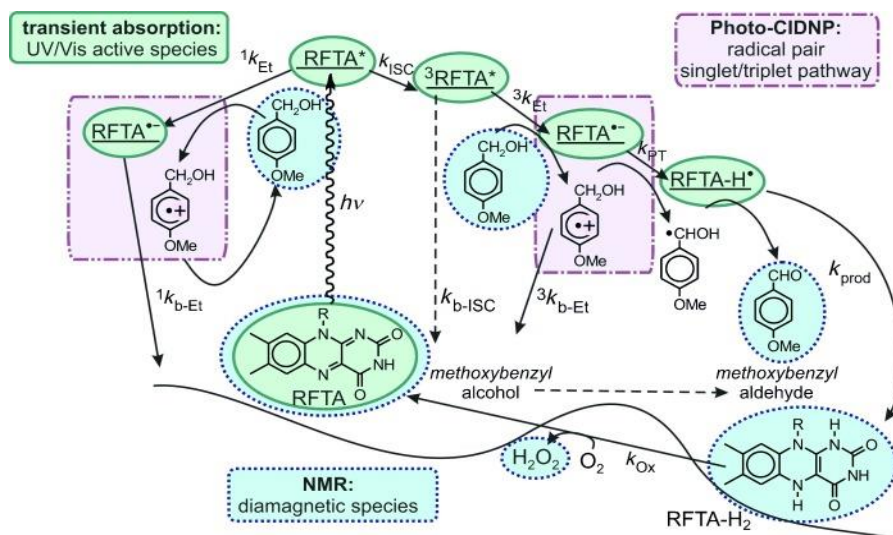


Fig. 13: Detailed photocatalytic cycle of RFTA-catalysed photo oxidation of benzyl alcohol obtained by complementary data from UV/Vis and *in situ* illumination NMR. The initial excited states and radicals are detected by UV/Vis spectroscopy. Complementary kinetic information about substrate, product, RFTA (catalyst) and reduced RFTA-H₂ was obtained from NMR. Photo-CIDNP effects corroborate UV/Vis studies via detection of radical pairs.

In contrast, NMR spectroscopy is inadequate to detect directly the initial photoexcited states but works well to detect diamagnetic substrates and products. To connect the substrate/product cycle and the photocatalytic cycle it was in addition necessary to make the photocatalyst transformation NMR-detectable (Fig. 13). For this purpose, we selected riboflavin tetraacetate (RFTA) as photocatalyst for the oxidation of methoxy benzyl alcohol (MBA) in two solvents, CD₃CN (slow reaction) and CD₃CN/D₂O (1:1; fast reaction). To interrupt the catalytic cycle, which means observing and following the reduced form of the catalyst, the samples were deoxygenated and the recovery of the reduced photocatalyst was interrupted. In each solvent both photo-CIDNP and NMR kinetic data of substrate, product, oxidized and reduced form of the photocatalyst were acquired using the Gschwind group *in situ* illumination NMR approach (blue LED light, see Fig. 14).

In pure CD_3CN , the authors observed photo-CIDNP effects in the catalyst, which corroborated the presence of zwitterionic radical pairs in the reaction pathway as had been predicted by UV/Vis studies[11] (Fig. 14 G). For the photo-CIDNP signals of RFTA and reduced RFTA- H_2 , the typical and expected opposite phase was detected characteristic of the two halves of the catalytic cycle and corroborating the longer lived triplet state being the reactive pathway. By far more informative, i.e. complementary to the UV/Vis spectroscopy results, were the observed kinetic NMR data, since our efficient LED *in situ* illumination approach provides a light intensity strong enough for photo-CIDNP effects and simultaneously low enough to be non-destructive even to small homogeneous photocatalysts in solution. Therefore, we could record a full reaction profile by NMR and to the best of the authors' knowledge this was the first full *in situ* NMR reaction profile recorded of a homogeneous photocatalysis reaction. The data in pure CD_3CN , presented in Fig. 14 E, shows a 1:1 linear relationship in the initial kinetics between conversion from RFTA into RFTA- H_2 and the increase of the benzyl aldehyde product. Thus, just the plain NMR-detected reaction kinetics of starting material, product and catalyst conversion revealed a formal two-electron process in pure CD_3CN (as this requires one molecule of RFTA for one molecule of MBA oxidation), which could not be established by UV/Vis spectroscopy.

In the case of $\text{CD}_3\text{CN}/\text{D}_2\text{O}$ (1:1), no photo-CIDNP effects were detected, most probably due to rapid separation of the zwitterion radical pair followed by individual counterion stabilization. Upon illumination, the classical NMR spectra showed broadened peaks for both RFTA and RFTA- H_2 , whereas peaks for starting material, product, and solvent remained sharp. These broadened peaks from both RFTA and RFTA- H_2 remained even after illumination was turned off. Similar observations of distance-dependent line broadening with respect to a radical centre had already been made for flavin mononucleotide (FMN) ring systems in deoxygenated solutions and indicate an exchange line broadening with a semiquinone radical. By far more exciting was the kinetic NMR data shown in Fig. 14 F for reaction in $\text{CD}_3\text{CN}/\text{D}_2\text{O}$. Compared to pure CD_3CN , an extremely fast product formation (i.e 50 % yield just in 10 min compared to 4 hours in CD_3CN , Fig. 12 F), an almost immediate, complete drop of the RFTA signals and a slightly delayed formation of the reduced RFTA- H_2 were detected. This reaction profile is characteristic for the presence of an NMR silent, stabilized intermediate. Based on the line broadening and the reaction profile, the authors deduced the presence of an anionic semiquinone radical intermediate, which was additionally confirmed by UV/Vis spectroscopy. Thus, again just based on the reaction profiles, it was revealed that RFTA in $\text{CD}_3\text{CN}/\text{D}_2\text{O}$ acts as a formal one-electron oxidation agent for the oxidation of MBA.

The comparison between the two solvents shows that the mechanism between one-electron and two-electron transfer pathways can be switched even after an identical photoexcitation step, depending on the experimental conditions.

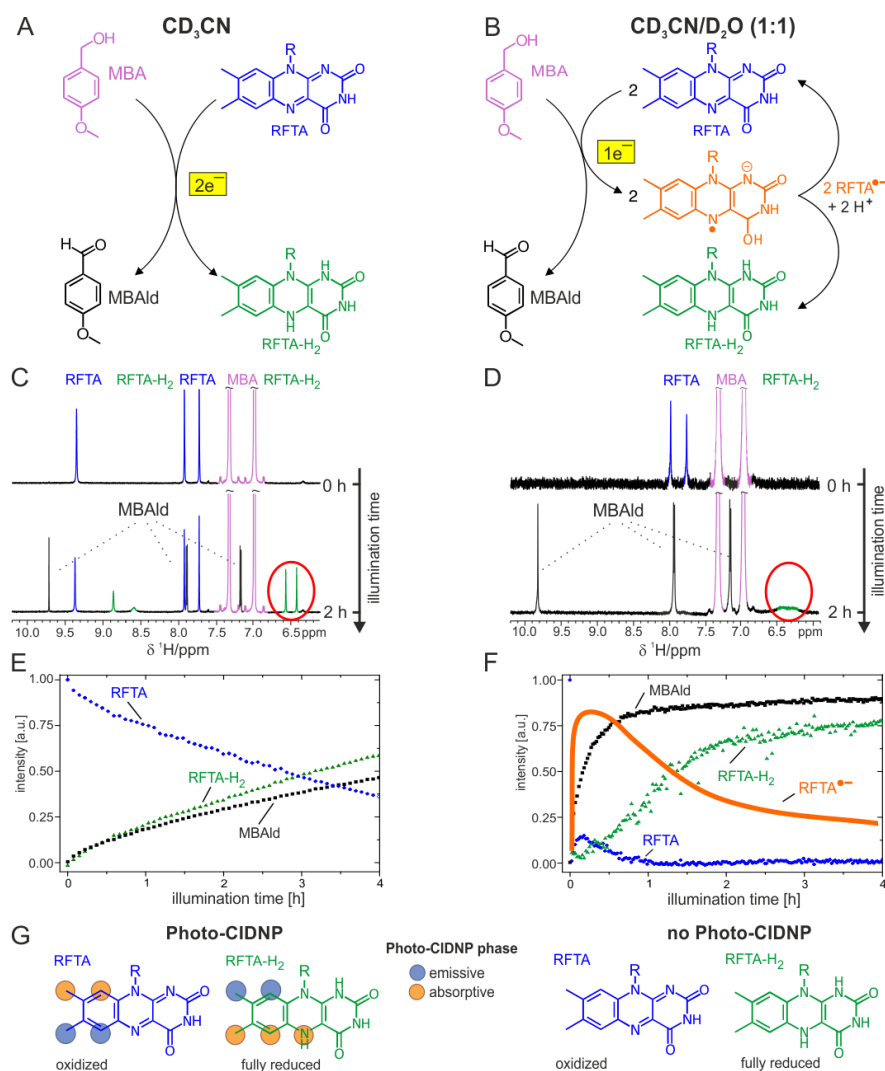


Fig. 14: Mechanistic elucidation of two solvent dependent mechanisms starting from the same RFTA excited state by *in situ* illumination NMR reaction profiles. In CD_3CN an inefficient two-electron transfer is detected, while the addition of water allows for an efficient one-electron transfer mechanism. Spectra measured at 600 MHz.

Overall, this study shows several key aspects of modern mechanistic investigations in photocatalysis. No doubt, time-resolved UV/Vis remains key method for characterising the initial photoexcited states. However, NMR spectroscopy is the method of choice to investigate reaction pathways downstream from the initial photoexcitation, and even plain NMR-based kinetic profiles of starting materials, products and/or catalyst conversion can reveal information inaccessible to UV/Vis studies. This study showed the initial excited states and downstream mechanism both have equal importance for the

effectiveness of a photocatalytic reaction. That means UV/Vis and NMR spectroscopic investigations provide complementary information and should be combined in modern photocatalytic studies. In addition, if possible and necessary, other spectroscopic methods such as EPR should be included to gain further direct information about radical species. This study demonstrated a complementary and strengthening approach of combined spectroscopic methods in flavin derivative photocatalysis.

2.5.1.2 Photocatalytic cross-dehydrogenative coupling reaction

After highlighting the significance of obtaining *in situ* illumination NMR reaction profiles of reactants, products, and the photocatalyst for mechanistic investigation in a flavin photocatalytic reaction, in 2016 the Gschwind group raised the potential of the *in situ* illumination NMR technique to investigate the next level of complexity [32]. For the first time, this work involved observation, monitoring and structural characterization of multiple intermediates in photocatalytic reactions, requiring a far higher degree of photocatalytic conversion and NMR sensitivity. Additionally, these studies highlighted new ideas for accessing additional mechanistic information, such as the application of sequential light-on and -off techniques. These sequential steps enabled the Gschwind group to differentiate between light-dependent and light-independent pathways, as well as to address the need of the photocatalyst for light-dependent pathways or the stability of intermediates towards light. Another remarkable output of this study was to showcase the potential of *in situ* illumination NMR to differentiate between hydrogen atom transfer pathways and proton transfer pathways, which complements UV/Vis studies (it was not observable by UV/Vis spectroscopy) and had never been addressable previously.

The photocatalytic cross-dehydrogenative coupling (CDC) reaction of N-aryltetrahydroisoquinolines (THIQ) is one of the most exploited reactions for various synthetic transformations [147,148]. Many intermediates have previously been detected [147,149–151]. However, the sequence of these intermediates remained ambiguous, and especially the question of hydrogen atom transfer (HAT) versus proton transfer remained unsolved. By combining extensive NMR studies with UV/Vis studies, EPR and synthetic applications the Gschwind group revealed a highly complex mechanistic picture of this reaction, involving overall five parallel reaction pathways. For this very detailed mechanistic investigation of the photocatalytic cross-dehydrogenative coupling (CDC) reaction of N-aryltetrahydroisoquinolines (THIQ), both *in situ* and *ex situ* LED illumination NMR were combined (Fig. 15 A and 15 B). During the initial investigations using classical solvents such as DMF and *in situ* LED illumination, the oxygen dependent reaction stopped after the consumption of all the oxygen dissolved in

solution, which resulted in very low yields (lack of oxygen) and restricted any further investigations of intermediates. Realising the anaerobic nature of the *in situ* setup, the solvent was switched to nitromethane to replace oxygen as the terminal oxidant. This made it possible additionally to observe the influence of oxygen on mechanistic pathways, intermediates, rates and yields.

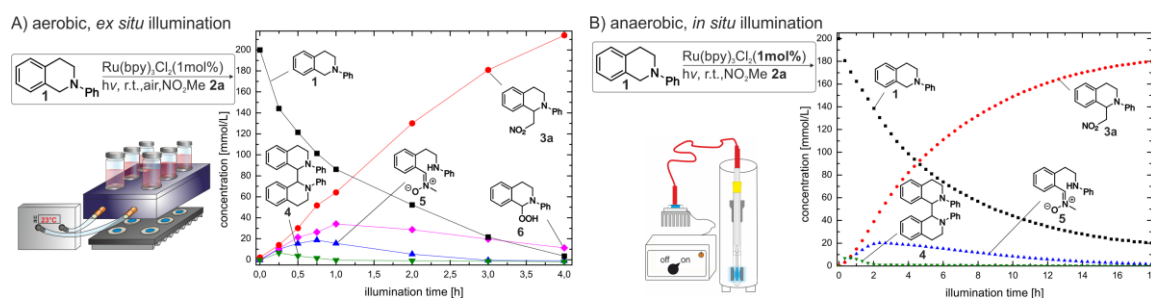


Fig. 15: A) Reaction profile obtained from *ex situ* illumination under aerobic conditions. B) Reaction profile obtained from *in situ* illumination under anaerobic conditions. Spectra measured at 600 MHz.

For the *in situ* anaerobic reaction conditions with nitromethane as terminal oxidant, two key intermediates could be identified, the dimer of THIQ **4** and the first ring opened intermediate **5**, which had not previously been detected (Fig. 15 B). Formation of both intermediates and product were suppressed by addition of TEMPO, indicating a radical mechanism for intermediate formation and a deprotonation pathway with nitromethane as terminal oxidant. Under aerobic reaction conditions in the *ex situ* approach a significantly faster reaction process was observed. This was due to O_2 causing increased efficiency of catalyst turnover via oxidation of the catalyst and further involvement of the amine radical cation in follow up reactions. This was evident as it was possible to observe an additional relatively highly concentrated intermediate THIQ-OOH **6** (Fig. 15 A), which was later shown to be produced via a hydrogen atom abstraction pathway (see Scheme 1 B) Furthermore, the appearance of THIQ dimers and the intermediate **5** proved again an unexpected deprotonation of amine cation radicals (Fig. 15 A) even in aerobic conditions. This was significant as amine cation radicals are prone to oxidation in presence of O_2 , which is the thermodynamically favourable process ($(E_{red}(O_2/O_2\cdot^-) = -0.75 \text{ V vs SCE } (E_{ox}(Et_2N^+\text{CHCH}_3/Et_2N^+=\text{CHCH}_3) = -1.12 \text{ V vs SCE})$) and shows that with nitromethane as solvent both principal pathways, the oxygen dependent and the nitromethane induced, are active.

To elucidate the effect of light on the mechanistic pathway of the intermediates, sequential light-on/off experiments were carried out in both aerobic and anaerobic conditions. From reaction profile information, optimal time periods were selected to

accumulate high amounts of intermediates prior to switching off the light. The observed reaction profiles show directly which of the intermediates require light for their further transformation and which are light-independent. Thus, Fig. 16 reveals that the intermediates **5** and **6** transform into product via a light-independent reaction, while the concentration of dimer **4** remains constant in the dark. Additional investigations with and without photocatalyst showed that for dimer **4**, a whole photocatalytic oxidation step is required (Fig. 16 C). Beside the detection of reaction intermediates and their kinetic profiles in classical mechanistic studies using NMR spectroscopy, these light-on/off studies are unique in photocatalytic systems and add extremely valuable information for determining mechanisms.

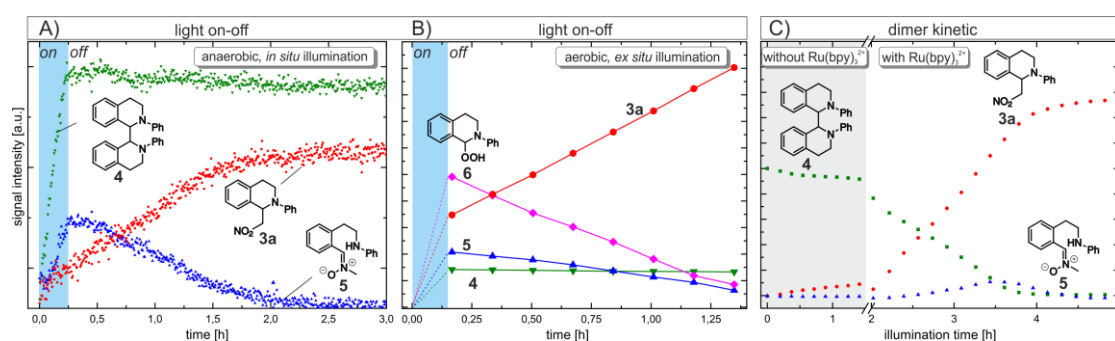


Fig. 16: Reaction profiles during the light-on and -off sequences under anaerobic *in situ* illumination A) and aerobic *ex situ* illumination B) and light-on/off dimer kinetics C). Spectra measured at 600 MHz.

Another big question in photocatalysis is how the photoreaction proceeds even in the absence of photocatalyst, which is quite often observed, albeit most often together with a photocatalytic reaction at a reduced speed. These photocatalyst-free reactions occur most often due to the formation of an electron donor acceptor (EDA) complex, which itself allows for a very slow, inefficient electron transfer (see Scheme 1 A background reaction in the dark). Upon illumination electron transfer is by far faster (see Scheme 1 B light-induced background reaction). However the key question is the potential of these uncatalyzed pathways to prevent electron back transfer. Therefore, exactly this point was studied. The formation of an EDA complex between THIQ and MeNO₂ was quickly evident as the addition of THIQ to the colourless nitromethane **2a** resulted in a pale yellow mixture. Furthermore, and most importantly, in the absence of oxygen these background reactions stopped while in the presence of oxygen iminium ion **2** and THIQ hydroperoxide **6** appeared as reaction intermediates. That means, firstly, that for an effective uncatalyzed reaction the electron has to be transferred to a third partner (here O₂) to prevent electron back transfer. Second, the O₂⁻ acts exclusively as a

hydrogen atom acceptor and induces the iminium pathway, while the radical pathway is absent and no dimer **4** or open intermediate **5** appears; these observations were also corroborated by additional investigations.

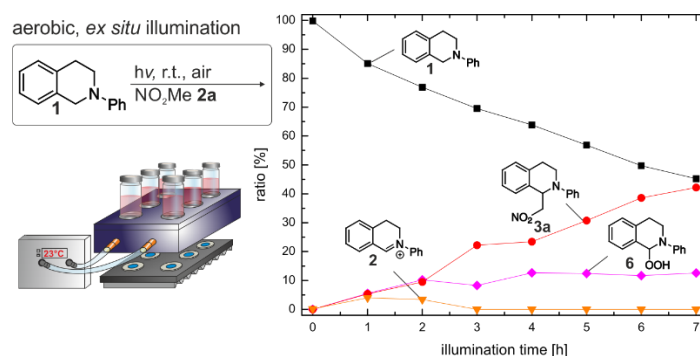
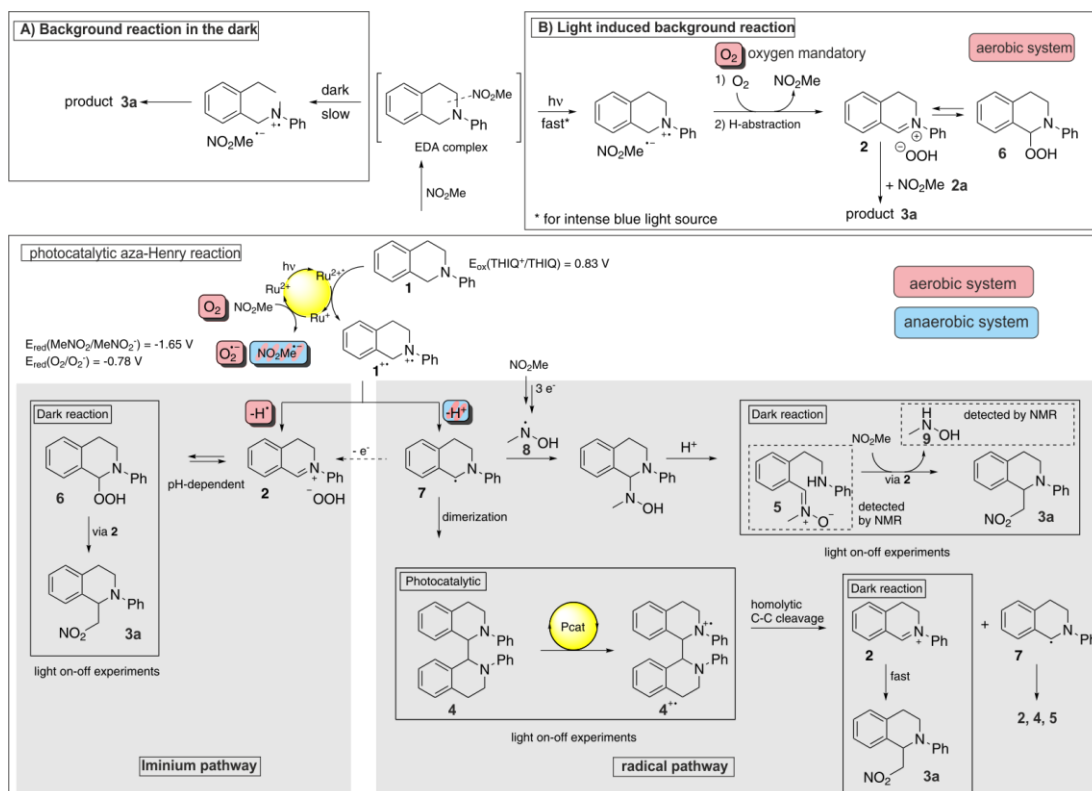


Fig. 17: The reaction profile of this photoreaction in absence of photocatalyst shows the formation of an EDA complex between THIQ and MeNO₂ under aerobic conditions. Spectra measured at 600 MHz.

Overall, from this extensive NMR study of the photocatalyzed Aza-Henry reaction of N-aryltetrahydroisoquinolines, five parallel mechanistic reaction pathways were elucidated, which are summarized in Scheme 1. For the first time, separate pathways for hydrogen atom transfer and proton transfer were revealed for a photocatalytic reaction. While oxygen as terminal oxidant induces hydrogen atom abstraction, nitromethane as terminal oxidant initiates a radical pathway that splits again into two paths, depending on the radical recombination partner. Furthermore, two photocatalyst-free reactions could be identified, with the light-induced reaction being by far more effective. We believe that in photocatalysis such complex reaction schemes with several parallel pathways each having different reaction rates/effectiveness occur by far more frequently than is realised. However, the investigation described here shows that an in-depth mechanistic investigation can reveal most of them.

Scheme1: Detailed mechanistic pathway of the photocatalyzed Aza-Henry reaction of N-aryltetrahydroisoquinolines.



2.5.1.3 Photoinduced and Lewis acid activated selective single C(sp³)-F bond cleavage in trifluoromethylarenes

Fluorine containing organic molecules have been the subject of special interest, particularly in the pharmaceutical industry[152]. Therefore, the development of economical, catalytic routes for the generation of fluoro-organic molecules under mild conditions is in high demand. Especially, a single C-F bond cleavage starting from a CF₃ group furnishing aryl difluoroalkyl compounds represents an important but so far elusive synthetic conversion in photocatalysis. In 2017, the Gschwind group studied a new synthetic protocol developed by the König group for the selective monodefluorination of trifluoromethylarenes under mild conditions using a combination of visible light photocatalysis and Lewis acid activation (Fig. 18 A) [33]. The mechanistic investigation in this work highlights the application of the *in situ* LED illumination NMR technique to visualize the Lewis acid/base activation in a reaction via ¹¹B, ¹⁹F and ¹H NMR measurements.

This study was designed to test the possibility of activating trifluoromethylarenes by photocatalytic SET reduction to convert them into their corresponding radical anion.

From this radical anion, F^- could be removed by Lewis acid activation of the borenium cation $TMP-Bpin^+$ formed *in situ* as Lewis acidic activator. The main objective of this study was to elucidate the nature of the activation step involved in this unusual photocatalysis. Screening studies revealed that both pinacolborane (HBpin) and the sterically hindered, α -H atom-free amine 2,2,6,6-tetramethylpiperidine (TMP) are essential for an effective reaction (no product formation occurs without HBpin or TMP). Therefore, the *in situ* illumination NMR studies concentrated on the identification of the HBpin and TMP derived intermediates and the observation of the interactions between the substrates and these Lewis acid base pairs. The identification and assignment of the various ^{11}B signals were the main challenges of this study. Due to the small chemical shift range of the ^{11}B signals combined with their broader linewidths no direct magnetization transfer from neighbouring NMR active nuclei could be detected, making it necessary to synthesize accessible intermediate species and side products to allow valid assignments to be determined. Furthermore, for the identification of additional transient species, important information about their combined chemical shifts (^{11}B , 1H , ^{13}C , ^{19}F) were taken from the reaction kinetics. This made the *in situ* detection and identification of the borenium cationic species (**13'**, Lewis acid activation) possible (Fig. 18 B, top), which was identified as the crucial activator in the reaction pathway. This was confirmed by ^{11}B spectra of the independently prepared borenium species (Fig. 18 B, bottom), while 1H - 1H NOESY spectra confirmed directly the existence of the protonated species (Fig. 18 C). It was also possible to verify an interaction between the neutral substrate trifluoromethylarenes and the borenium cationic species **13** via 1H - 1H NOESY spectra. However, this showed an interaction mainly with the $-CN$ group and not with the CF_3 group. Therefore, the interaction between the key CF_3 group and the Lewis acid activator most probably occurs at the stage of the NMR-invisible radical anion after the photoreduction step. Combining these key points with data from other synthetic mechanistic investigations, such as radical quenching and trapping, the authors proposed the catalytic cycle shown in Fig. 18 D.

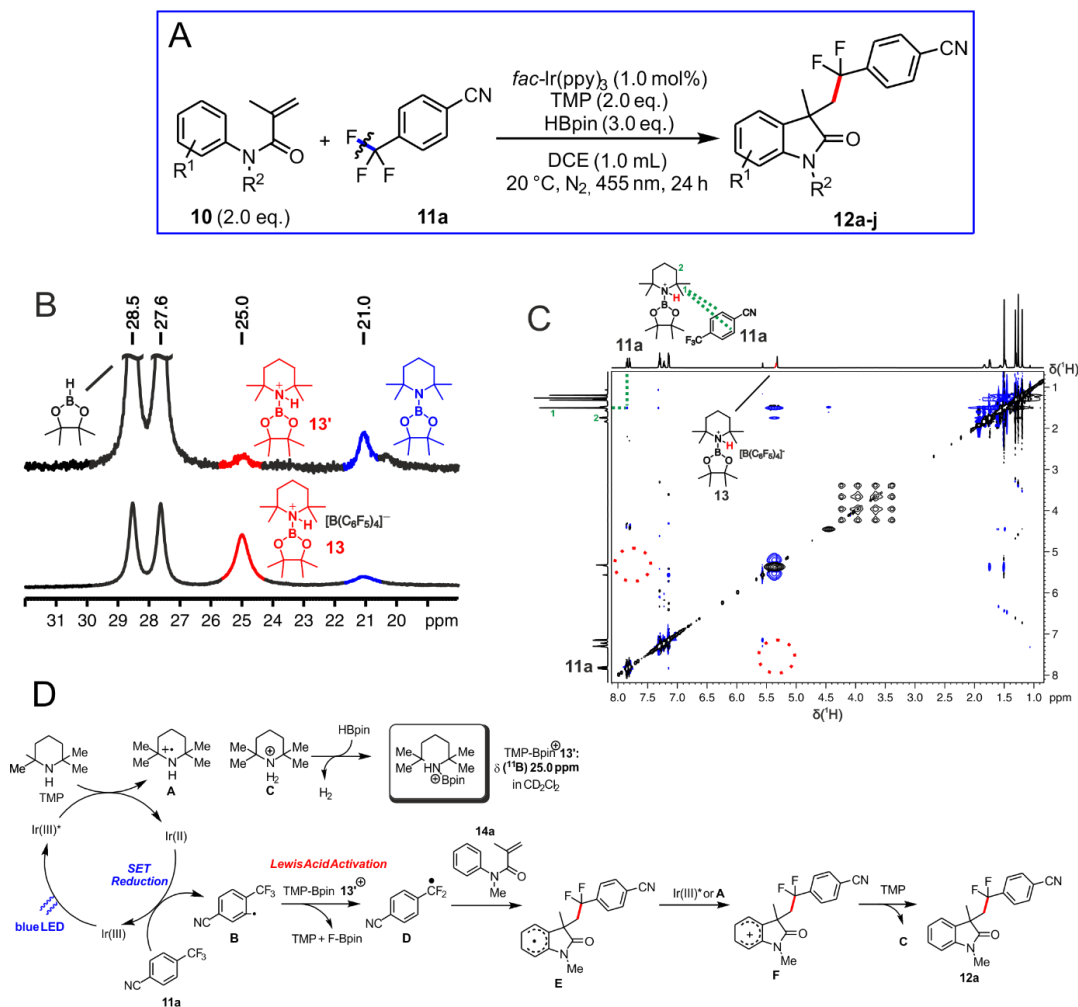


Fig. 18: (A) Optimised reaction conditions for visible light-mediated photocatalysed and Lewis acid activated aryldefluoroalkylation. (B) Identification of the *in situ* generated borenium cationic species **13'** by comparing the ¹¹B NMR spectra of the photocatalytic reaction (top) and the independently synthesised TMP-Bpin⁺ **13** (bottom). The elimination of the F⁻ ion from the reduced radical substrate is the key step in the reaction. (C) The ¹H-¹H NOESY spectrum shows the interaction between the activated Lewis acid and CN side of the substrate not the CF₃ group (see green dotted lines compared to red empty circles). This suggests that the interaction with the CF₃ group takes place on the level of the radical anion. (D) Overall proposed photocatalytic cycle including the description of Lewis acid activation, based on the observed NMR and synthetic evidence. Spectra measured at 600 MHz.

2.5.1.4 Visible-light-mediated liberation and *in situ* conversion of fluorophosgene

In 2019, in collaboration with B. König's group, the Gschwind group presented mechanistic studies of the photocatalytic *in situ* generation and conversion of fluorophosgene using a combination of extensive *ex situ* and *in situ* NMR studies,

transient spectroscopy and radical trapping experiments[34]. The impact of this study on synthetic work was that it made the activation of C-OCF₃ bonds under mild photocatalytic conditions accessible. The innovation of this reaction was the nature of the activated reactive species, being the anion and not the radical in a reductive photocatalysis. In typical reductive photocatalytic mechanisms the initial radical anions fragment into unreactive ionic leaving groups such as halides, pseudo halides or cyanides, while the remaining neutral radicals are predominant in the productive reaction pathway. In contrast, this reaction was designed to generate such a highly reactive ionic species (here: trifluoromethanolate; O-CF₃⁻) that the productive reaction pathway is propagated by the anion instead of the radical. Trifluoromethanolate fragments into F⁻ and fluorophosgene, which in turn yields an NMR-detectable key intermediate with various starting materials (e.g. aminoethanols) and later on the desired products.

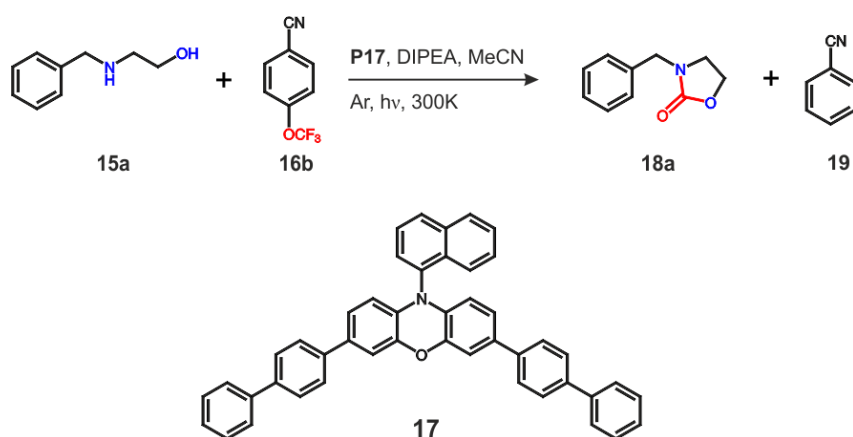


Fig. 19: Reaction scheme for the initial optimization and test reactions for the overall NMR investigation used by the Gschwind and König groups[34]. General reaction conditions: **15a** (0.1 mmol); **16b** (1.05 equiv); **17** (2 mol %); DIPEA (3 equiv) in CD₃CN under inert atmosphere irradiated by 400 nm light.

Synthetic optimization, including screening of photocatalysts, starting materials and amount of base led to the following synthetic conditions: trifluoromethoxybenzene (**16b**) as fluorophosgene precursor, **17** as photocatalyst and DIPEA as electron donor. Furthermore, photoexcitation was achieved by irradiation at 400 nm and the reaction was conducted in acetonitrile under inert atmosphere at room temperature (300 K for NMR investigations). Regarding the mechanistic investigations, first transient spectroscopy probed the initial photoexcitation. Only with the high concentrations applied under synthetic conditions (2 mM) does the photocatalyst **17** form a CT-complex dimer (consisting of the radical cation and anion of **17**). DIPEA then quenches the radical cation of **17** (Fig. 20 A). As a consequence, the radical anion of the photocatalyst is able

to reduce **16b** to its radical anion. This radical anion of **16b** subsequently fragments into trifluoromethanolate and a benzonitrile radical, which could be readily detected by radical trapping experiments with N-methylpyrrole and allylbenzene (Fig. 20 B). Next, the power of NMR spectroscopy came into full effect by detecting various downstream intermediates and products (see Fig. 20 C and D). First, *ex situ* and *in situ* NMR reaction profiles corroborated the fragmentation of trifluoromethanolate into fluorophosgene via detection of F⁻. Next, *in situ* reaction kinetics showed the conversion of the starting material into benzonitrile (**16b** → **19**). Furthermore, one key intermediate **F-I** was detected stemming from the reaction of the liberated fluorophosgene and starting material **15a**, which could be assigned unambiguously with support from ¹⁹F-¹³C HSQC and ¹H-¹⁹F HMBC spectra. The reaction progression also suggested this carbonyl fluoride intermediate **F-I** as a direct precursor to the desired product **18a**. A second intermediate **OC-I** was key to understanding a second parallel downstream process after the photoexcitation step. In this parallel mechanism, the starting material **15a** reacts with acetaldehyde, which is an unavoidable secondary product of DIPEA, to form the intermediate **OC-I**. Further *ex situ* NMR tests and *in situ* kinetics provided evidence that **OC-I** is in a water-dependent equilibrium with the starting material **15a**, allowing for continuous formation of the product **18a** from **OC-I** as long as fluorophosgene is provided. *Ex situ* NMR tests also showed that addition of extra water can almost completely suppress the formation of **OC-I** resulting in a cleaner and accelerated reaction.

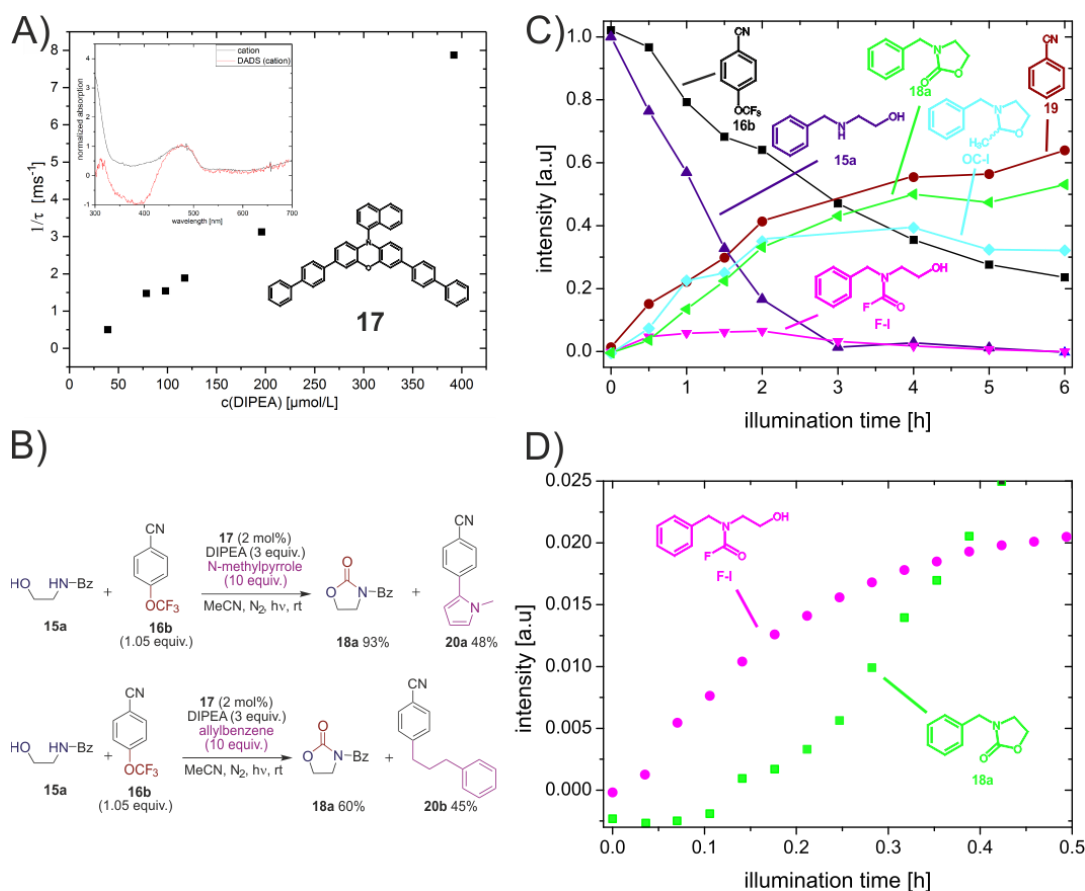


Fig. 20: Overview of the mechanistic investigations described by the Gschwind and König groups[34]. A) Transient spectroscopy yielded a Stern-Volmer plot showing the quenching of the **17** radical cation by increasing DIPEA concentration; as a result the **17** radical anion is free in solution and available for further reactions e.g. with **16b**. B) Radical trapping experiments showed the presence of a benzyl radical. C) and D) Combined *ex situ* and *in situ* NMR spectroscopy give a detailed insight into the reaction progression of all diamagnetic reactants and products, resulting in the detection of various intermediates (**OC-I** and **F-I**). Spectra measured at 600 MHz (C) and 500 MHz (D).

These mechanistic investigations combining NMR spectroscopy, transient spectroscopy and radical trapping experiments enabled a comprehensive picture to be obtained for the dominant reaction pathway and revealed an off-cycle equilibrium in the dark that retards the reaction. In Fig. 21 the full mechanistic cycle is given. First, **17** is excited under light exposure of 400 nm LEDs. A resulting CT-complex dimer leads to the generation of **17⁺⁺** and **17^{-•}**. **17^{-•}** is quenched by **16b** yielding **16b^{-•}** which readily fragments into an aryl radical and trifluoromethanolate. The trifluoromethanolate decomposes into fluorophosgene and F⁻. The nucleophilic, starting material **15a** reacts with the available fluorophosgene resulting in a carbonylfluorine-intermediate (**F-I**) and downstream,

intramolecular cyclization leads to the desired product **18a**. **17⁺** is regenerated under consumption of DIPEA. The aryl radical forms benzonitrile **19** by abstraction of hydrogen from DIPEA. The main pathway is accompanied by a second, off-cycle pathway. Stemming from DIPEA, acetaldehyde is liberated downstream which can react with **15a** to give **OC-I**. The intermediate **OC-I** is in a water-dependent equilibrium with **15a** and as long as fluorophosgene is provided **18a** can be generated from **OC-I**.

Overall, combining different and complementary mechanistic methods, in this study nearly every step in a complex photocatalytic reaction could be elucidated. In addition, a parallel pathway leading to a side product was revealed. However, once the reaction mechanism had been understood, it became possible to reduce significantly the influence of this off-cycle equilibrium, especially the influence of water.

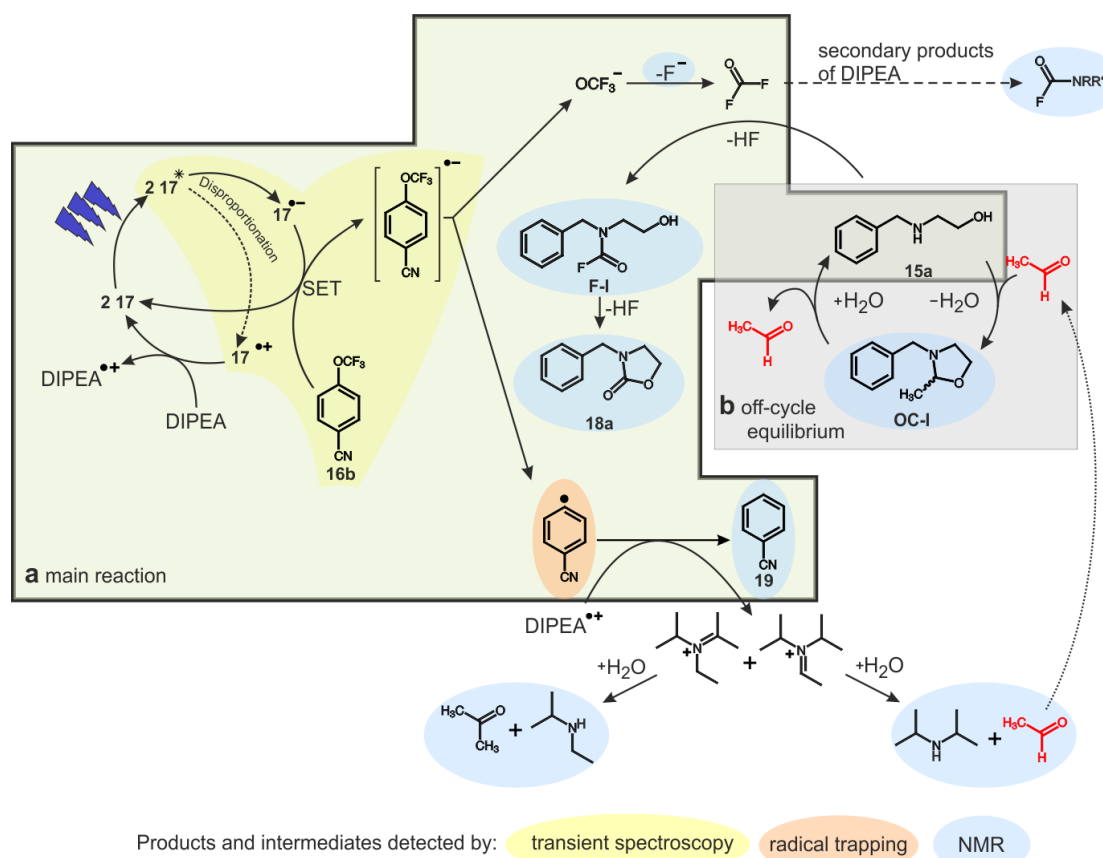


Fig. 21: Mechanistic proposal of the in situ liberation of fluorophosgene determined by the Gschwind group in cooperation with the König group[34]. A combination of NMR spectroscopy, transient spectroscopy and radical trapping gave insight into every step of the reaction ranging from the initial excitation to the final product formation.

2.5.1.5 Photoinduced McMurry-type reaction

Very recently, the König group developed an unprecedented photocatalytic McMurry-type reaction (Fig. 22), in which an unexpected transformation from benzaldehydes into stilbene derivatives occurred instead of the expected straightforward ketyl radical coupling [35]. This led the Gschwind group to carry out an extensive *in situ* LED NMR spectroscopic study to understand this unusual reaction pathway. One of the biggest challenges faced in this work was the fact that regular NMR reaction profiling of intermediates could not be used because there were multiple reaction intermediates present at extremely low concentration. The reaction utilizes a diboron reagent, which in principle can be used as an NMR reporter to follow the reaction pathway. However, from the Gschwind groups' previous experience we knew (see section 2.5.1.3) that the interpretation of transient ^{11}B NMR signals demands intensive synthesis of individual intermediates to validate the assignment of the intermediates and that ^{11}B is quite insensitive. Therefore, the strategy was to use a substrate with selective ^{13}C labelling at the reaction centre (carbonyl position) enabling the chemical modulations predominantly at the carbonyl position to be followed. In addition, this approach complemented our recently introduced use of the popular Chemical Exchange Saturation Transfer (CEST) technique to reaction mechanisms of small molecules[25], which was applied here for the first time in mechanistic studies of photocatalysis. First, proton coupled and decoupled ^{13}C measurements were used as the main methods to characterize transient intermediates assisted by theoretical calculations. This simple but very effective method allowed direct specification of the number of protons at the reaction centre within the intermediates, enabling their partial characterization.

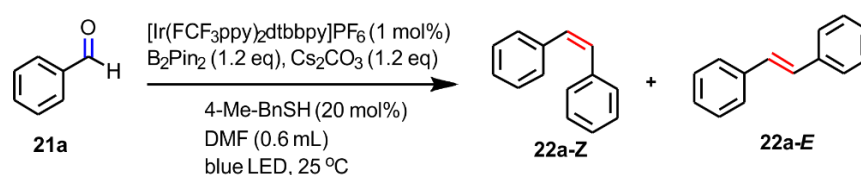


Fig. 22: Reaction scheme for photoinitiated carbonyl-metathesis: deoxygenative reductive olefination of aromatic aldehydes *via* photoredox catalysis.

The measured ^{13}C NMR spectrum from an *in situ* LED illuminated NMR experiment after 18 h of irradiation is shown in Fig. 23 A. The spectrum shows multiple peaks, including several very low intensity signals corresponding to the different intermediates. Assignments for key intermediates in addition to the starting materials and products are highlighted. A systematic analysis was carried out to assign these active intermediates. Initially, the broadened line corresponding to the carbonyl of the benzaldehyde substrate

suggested the formation of a ketyl radical that was in fast exchange with benzaldehyde on the NMR time scale. However, an additional broadened peak of a transient intermediate was also observed at around 75 ppm (Fig. 23 B), which could not initially be assigned or connected with any other exchanging species. Therefore, the CEST method was applied to identify the chemically exchanging species (Fig. 23 B'). Surprisingly, the broadened chemically exchanging peak identified via CEST linked the substrate benzaldehyde and the line broadened intermediate, which was later assigned to a 3-membered cyclic key intermediate (**F**). This was the first intermediate detected by NMR in this photocatalysis reaction, and this showed that CEST can be used as a high-sensitivity variant of EXSY to identify the sequence of intermediates in a reaction. In addition, it showed that CEST can be effectively applied even in a two-step exchange process mediated via a short lived radical species. The structure of this first 3-membered cyclic key intermediate (**F**) was characterized by measuring ^1H coupled and decoupled ^{13}C spectra at low temperature and was corroborated by theoretical calculations (Fig. 23 B). This was the first report of detection of this intermediate, which had not been possible by traditional NMR methods due to its transient nature. Subsequently, the next connected carbanion intermediate (**G**) was detected with the use of coupled and decoupled ^{13}C spectra and theoretical calculations (Fig. 23 C). The subsequent intermediate **H** was identified via parallel synthesis of the pure compound (Fig. 23 D). To get an impression of the complexity of the reaction mixtures under investigation and the multitude of species with similar chemical shifts or possible chemical shift combinations in such photocatalytic reactions, a ^1H - ^{13}C HSQC of the reaction mixture is presented in Fig. 24. The extent of chemical shift overlap is not dissimilar to that expected for small proteins, and without specific ^{13}C labelling as applied in this study, assignments would have been extremely difficult to make. Furthermore, this demonstrates that an assignment strategy using exclusively chemical shifts from theoretical calculations to identify the intermediates would be insufficient. Therefore, the authors recommend including all possible additional information from the sequence of the intermediates, as here, from CEST experiments and parallel synthesis of pure compounds.

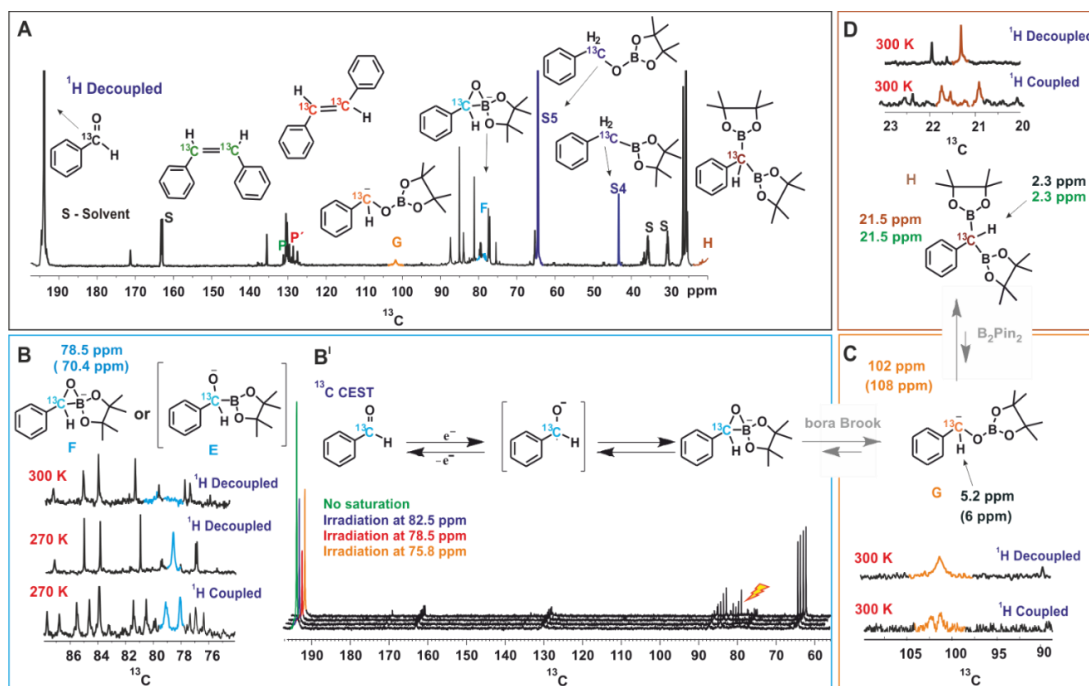


Fig. 23: (A) The *in situ* LED NMR ^{13}C spectrum of the reaction mixture after 18 h of illumination reveals an extremely complex mixture of species in this McMurry type reaction; the assigned peaks are marked with corresponding colours. (B) Transient intermediate **F**, stabilized and characterized at 270 K from ^1H decoupled and coupled ^{13}C spectra. (B') ^{13}C CEST spectra connecting benzaldehyde and primary key intermediate **F**. (C) Identification of α -oxyboryl carbanion **G** from ^{13}C and ^1H chemical shifts. (D) NMR identification of another intermediate **H** in the reaction mixture, using ^{13}C chemical shift. Spectra measured at 600 MHz.

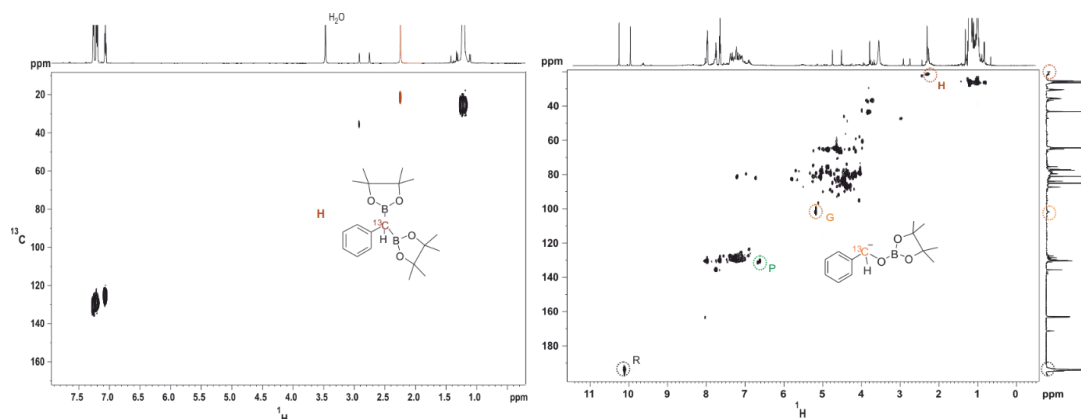


Fig. 24: Comparison of *in situ* LED NMR ^1H - ^{13}C HSQC spectra of a pure intermediate **H** (left) and the reaction mixture (right). The high number of peaks and the overlap of peaks even in this 2D spectrum of the reaction mixture illustrates the extent of the complexity in studying reaction intermediates. In the reaction mixture, the intermediates **G** and **H** as well as the product **P** are marked. Spectra measured at 600 MHz field.

By combining these sequential intermediates observed in *in situ* LED illumination NMR experiments along with evidence obtained from quenching and synthetic studies, the following photocatalytic cycle (Fig. 25) was proposed. Initially the B₂pin₂ (Bis(pinacolato)diboron) activates the substrate aryl aldehyde, which undergoes single electron transfer (SET) reduction by the photocatalyst. In the next step, the reduced radical anion binds to the base reacted B₂pin₂, which forms intermediate **E** or **F** in the key step of the SET reaction. The connectivity between **F** and the substrate was evaluated by CEST NMR. The intermediate **F** on undergoing "boraBrook" rearrangement forms intermediate **G**, which was again detected by NMR. The carbanion **G** reacts again with B₂pin₂ and forms **H**, which was also observed by NMR. In a subsequent step intermediate **H** reacts with the base Cs₂CO₃ to form the carbanion **I**. In the last step carbanion **I** binds to another aryl aldehyde substrate to form stilbene derivatives.

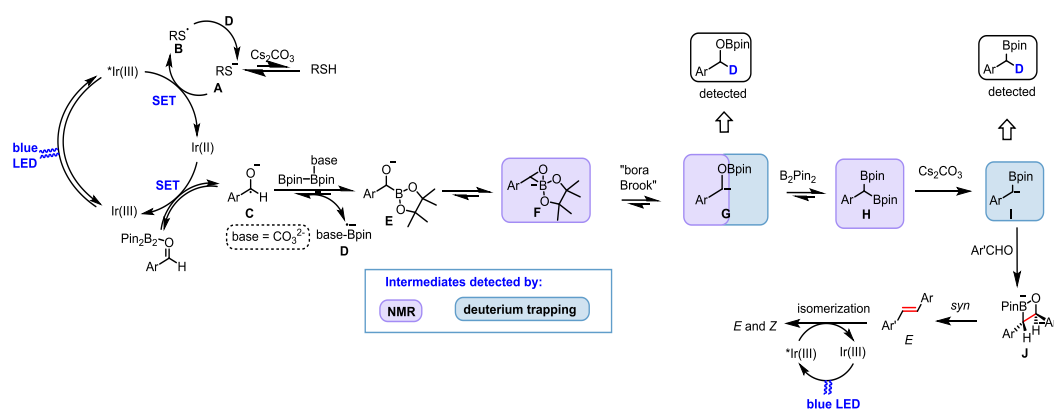


Fig. 25: Proposed photocatalytic cycle for photoinitiated carbonyl-metathesis newly developed by the Gschwind group, based on *in situ* NMR studies, synthesis of proposed intermediates and quenching experiments.

2.5.1.6 Photoinduced dark catalytic cycle

In 2018, another impressive application of *in situ* LED illumination NMR in mechanistic studies was reported by Lehnher *et al* from Merck[38]. One of the main highlights of this study was the first use of *in situ* LED illuminative NMR to observe the dynamics of a gaseous species (here CO) during the reaction. In general, generation of large amounts of gases inside the NMR tube often causes severe problems, e.g. inhomogeneity (shimming problems), backward reaction and possible escape of gas, which makes it difficult to observe. Here, the generated gaseous species is from the pre-catalyst equilibrium and not from the product formation. Therefore, only tiny amounts of gas are produced and the closed system used for illumination is an advantage rather than a

disadvantage. The advantage of the closed system was later extended to *ex situ* synthesis as well.

In this work, the authors carried out a systematic investigation to understand the reaction mechanism of their newly developed photoinduced iron-catalyzed cycloisomerization of alkynols to cyclic enol ethers using *in situ* LED-NMR. The four possible products of this catalytic reaction are shown in Fig. 26 and obtaining selectivity especially for the desired product **24a** was very challenging. The reaction was catalysed by the iron carbonyl complex $\text{LFe}(\text{CO})_3$ (L = tetraphenylcyclopentadienone represented as **cat-CO** in Fig. 27 A). It was known to the authors that the pre-catalyst $\text{LFe}(\text{CO})_3$ needs to be activated by removing one of the CO groups. This could be achieved either by (1) heat, (2) oxidant (e.g., Me_3NO), or (3) light. The details of the selectivity and the yield under different conditions are tabulated below (Table 1 and 2). Without light, either the wrong selectivity or low yields were obtained. However, by using light the authors could obtain 100 % selectivity and yield for **24a**. Surprisingly, N_2 purging, which was an established method to remove CO, could only achieve 45 % conversion. In contrast, the closed vessel, which used light to remove CO, resulted in 100 % conversion. This intrigued the authors to further investigate the effect of light.

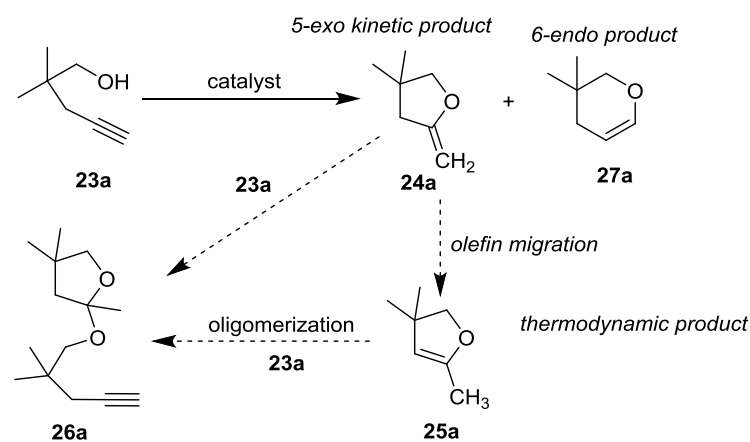


Fig. 26: Possible product distribution for cycloisomerization of alkynol. Here **24a** is the kinetic product, **27a** and **25a** are thermodynamic products.

Table 1 Testing different conditions for selectivity and yield without light.

No	temp [°C]	oxidant	base	2a:3a:4a	Yield %
1	RT	Me ₃ NO	–	96:1.4:2.8	25
2	RT	–	K ₂ CO ₃	90:1.7:8.0	7
3	RT	Me ₃ NO	K ₂ CO ₃	99:0.05:0.8	24
4	RT	–	–	0:0:100	5
5	70	Me ₃ NO	–	3.5:32:65	100
6	70	–	K ₂ CO ₃	91:3.9:4.7	31
7	70	Me ₃ NO	K ₂ CO ₃	96:4.0:0.15	14
8	70	–	–	0:0:100	8

Table 2 Testing N₂ purge and solvent effect on yield and selectivity with light.

No	λ nm	condition	solvent	2a:3a:4a	Yield [%]
1	450	N ₂ purge	d ₈ -toluene	100:0:0	45
2	450	closed vial	d ₈ -toluene	100:0:0	100
3	450	closed vial	CD ₂ Cl ₂	99:0.05:0.8	100

Initially, the authors hypothesized that the light induces CO dissociation from the pre-catalyst LFe(CO)₃ generating a functional catalyst containing both a Lewis acidic and a Lewis basic moiety, as shown in the mechanism in Fig. 27 A. To validate this proposal, the authors first measured the quantum yield of value 3 using their earlier developed actinometer [37] and eliminated any solvent effects on the selectivity via testing the reaction in both CD₂Cl₂ and toluene, obtaining the same results (Table 2). Next, they measured *in situ* NMR kinetic profiles of reactant and products under continuous illumination, yielding the results shown in Fig. 27 B. The reaction profile obtained showed

an induction period, which was in line with the prediction that the initial CO dissociation generates the activated catalyst $\text{LFe}(\text{CO})_2$. Furthermore, from the observed sharp peaks in the NMR spectra throughout the reaction, they concluded that paramagnetic species were absent.

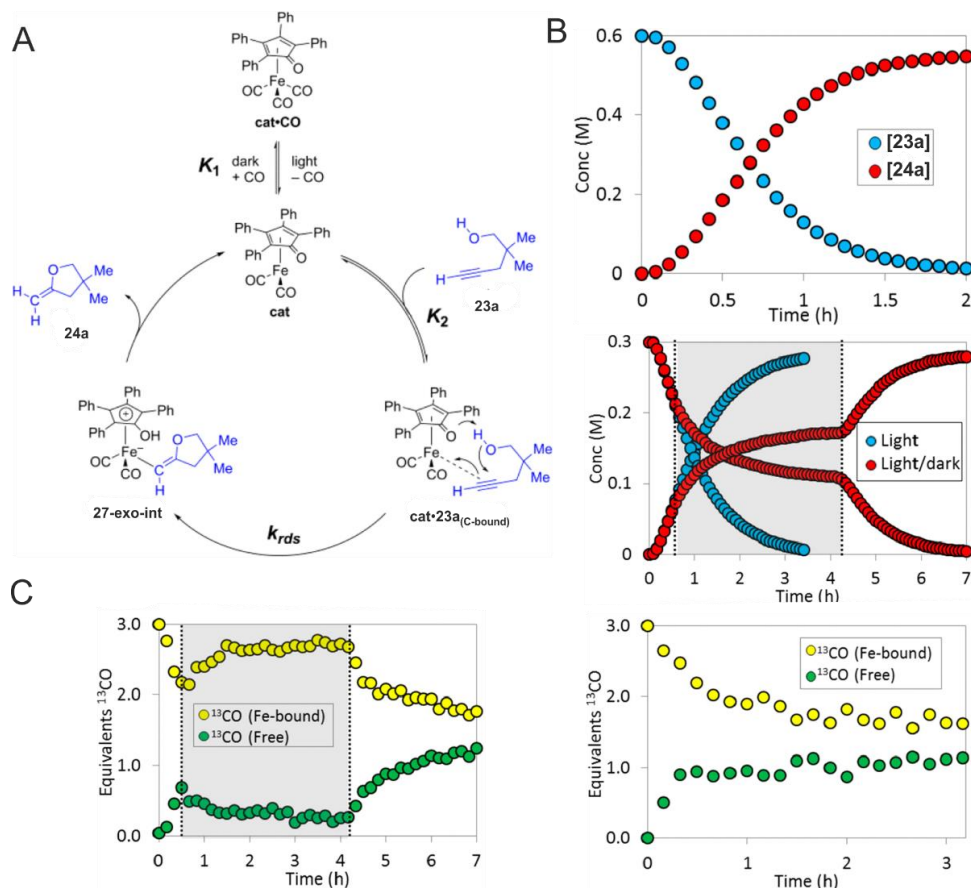


Fig. 27: (A) Postulated photoinduced catalytic cycle, describing pre-activation of the catalyst and also the presence of both Lewis acidic and Lewis basic moieties. (B) Observed reaction profile for product and reactant concentrations; the initial induction period indicates pre-activation of the catalyst. (C) Visualization of photoinduced activation of the catalyst by the dynamics of bound and unbound *in situ* ^{13}CO during the light-on and -off steps. The initial increase in free ^{13}CO suggests a pre-activation light-induced step via removal of CO group. The increase in bound CO during the light-off period indicates a deactivation step in the dark. The shaded area corresponds to the period with the light-off. Spectra measured at 500 MHz.

To check the effect of the light, the authors also obtained a reaction profile for reactant and product during a sequential light-on, light-off and light-on sequence (Fig. 27 B). When the light was switched off after the initial illumination, the rate of the reaction decreased but did not stop completely, indicating the presence of a dark reaction

pathway. Turning the light-on again, the reaction rate accelerated significantly after an induction period. Using labelled ^{13}CO , the authors could also monitor the free ^{13}CO ($\delta_{\text{C}} = 184.2$ ppm) and catalyst bound ^{13}CO ($\delta_{\text{C}} = 208.8$ ppm) during this sequence (Fig. 27 C). The dynamics of CO showed i) during illumination an increase in free CO and a decrease in bound CO; ii) after turning off the light, a gradual decrease of free CO and a gradual increase of bound CO; iii) on turning the light-on again an increase in free CO and a decrease of bound CO similar to that during the initial illumination period. From these observations, the authors concluded that illumination mainly helps in activating the catalyst by removing the CO group. Further, the reaction proceeds even in the dark. However, free CO deactivates the catalyst by binding back on the catalyst under dark conditions. This was in line with the observed quantum yield value of 3. That means that after activation of the catalyst each molecule on average can go through 3 catalytic cycles before CO binds back on the catalyst in the dark.

To validate the hypothesis that an activated catalyst acts as both Lewis acidic and Lewis basic moiety, the authors carried out DOSY experiments at a high concentration of catalyst (22.5 mM) under continuous illumination. As expected, the authors observed a small diffusion coefficient matching with a dimer structure, as shown below, which strongly supports their hypothesis that their activated catalyst has a dual Lewis acidic and Lewis basic character.

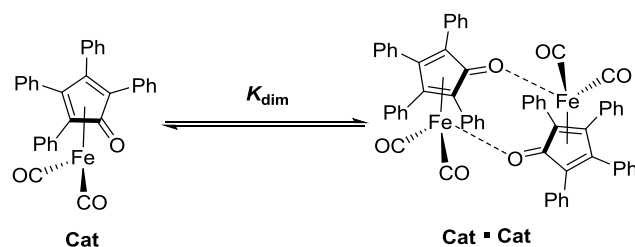


Fig. 28: Possible catalyst dimer structure depicting both Lewis acidic and Lewis basic moieties.

Overall, in this elegant study the authors managed to observe quantitatively the gaseous species during a photocatalysis reaction, which is very challenging using closed *in situ* illumination setups. Furthermore, using the signature of the ^{13}CO dynamics during a light-on and -off sequence, they accessed critical information about the activation and deactivation of the photocatalyst.

2.5.2 Heterogeneous catalysis

In general, the use of semiconductor photocatalysts (SPCs) in synthesis has gained immense interest due to their high surface area and activity. Common SPCs are TiO_2 and doped- TiO_2 . In addition to high level selectivity and performance under mild conditions, SPCs are non-degradable and reusable. Based on SPCs, many organic synthetic applications such as formation of carbon–carbon and carbon–heteroatom bonds as well as cyclisation, reduction and oxidation reactions have been reported in the literature.

2.5.2.1 Photocatalytic oxidation of toluene inside the NMR tube

In general, the progress of a SPC reaction is monitored by *ex situ* sampling of the reaction mixture and subsequent analysis using HPLC and/or NMR. NMR monitoring of heterogeneous reaction mixtures, particularly of photocatalytic heterogeneous reaction mixtures, is very difficult due to the inhomogeneity of the solution. Hence, it most often requires *ex situ* purification and filtering before the NMR measurements. This procedure is very time consuming as it requires pre-treatment. Furthermore, it is error prone, especially for following the reaction progress. To overcome these problems, in 2012 Mills and O'Rourke reported the development of a smart solution based on an *in situ* NMR method [133]. This study highlights the first NMR reaction monitoring and reaction profile of a heterogeneous photocatalytic reaction using the NMR tube as a reaction vessel (see section 2.4.6). In this new approach, the inner surface of the NMR tube was coated with a thin layer of semiconductor material (in this case TiO_2 , shown in Fig. 29 A). Then, the photocatalysis was carried out inside the NMR tube but outside the NMR spectrometer to allow for *ex situ* illumination with light from the outside of the tube. For mixing, the NMR tube was agitated by fixing it to a stirrer and for measurements the stirring was regularly interrupted and the NMR tube was transferred into the NMR spectrometer. The authors illustrated this method using the oxidation of toluene catalysed by TiO_2 in CD_3CN . The recorded ^1H spectra of the reaction mixture at different time points are shown in Fig. 29 B. The toluene concentration [(t, 7.24 ppm), (d, 7.17 ppm), (t, 7.14 ppm)] reduces with time, as the toluene is oxidised to benzaldehyde [(s, 9.98 ppm), (d, 7.87 ppm), (t, 7.66 ppm), (t, 7.55 ppm)], which in turn is further oxidised to benzoic acid [(d, 7.97 ppm), (t, 7.59 ppm), (t, 7.46 ppm)]. The authors also observed a minor peak at 7.3 ppm corresponding to benzene, which was generated in negligible amounts. The maximum amount of benzaldehyde and benzoic acid observed are 27% (45 min) and 41% (75 min), respectively. Based on the observed reaction profile (Fig. 29 C), the

authors proposed the mechanism shown in Fig. 29 D. The initial hydroxide radicals are generated from TiO_2 .

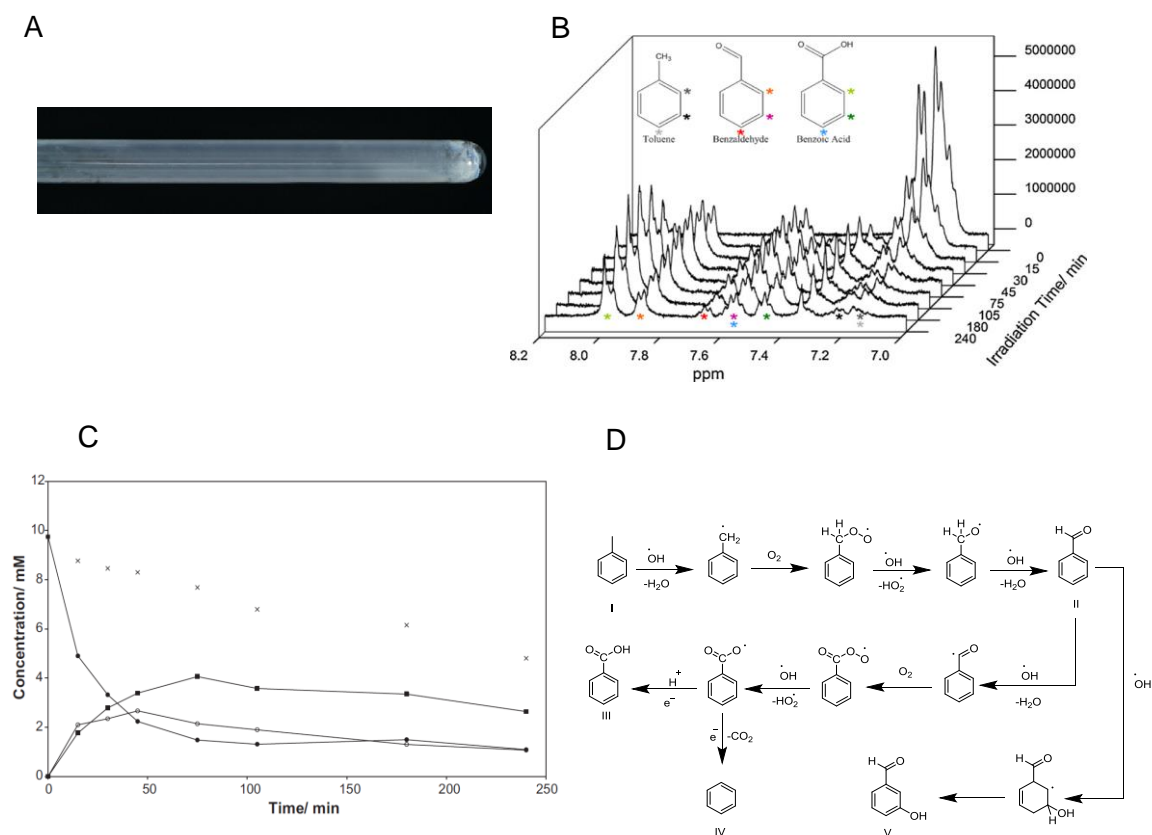


Fig. 29: Heterogeneous photocatalytic oxidation of toluene: (A) Photograph of the NMR tube with TiO_2 coating on the inner surface. (B) ^1H NMR spectra at different times of irradiation. (C) Reaction profile of substrate toluene (\bullet), products benzaldehyde (\circ) and benzoic acid (\blacksquare), and sum of all these concentrations (\times). The decrease in concentration of the sum of all these species potentially indicates degradation. (D) Proposed mechanism for the oxidation. Spectra measured at 500 MHz.

This study shows that detailed NMR monitoring of heterogeneous photocatalytic reactions is possible. The approach discussed here operates without any *ex situ* sampling or additional treatments, such as filtering.

2.5.2.2 TiO₂, catalysed C-C coupling

In a subsequent study, Mills and O'Rourke applied their titania-coated *in situ* NMR method to investigate a detailed mechanism for the photocatalytic carbon–carbon coupling of phenoxyacetic acid with N-substituted maleimides[131]. This study also highlights the advantages of systematically studying the individual photochemical and photocatalytic reactions of each reactant. This enabled the authors to understand and modulate the observed product distribution in the desired hetero carbon–carbon coupling reaction. In principle, this heterogeneous photocatalysed reaction should give both the hetero adduct **28** and the cyclic heteroproduct **29** (Fig. 30 A). However, the NMR analysis revealed additional products **30**, **31** and the maleimid dimer **33** (Fig. 30 A). To understand these side reactions, the authors studied the photochemical and the photocatalytic reactions of two substrates (phenoxy acetic acid and N-substituted maleimide) individually. In the case of phenoxyacetic acid without photocatalyst, the authors did not observe any absorbance at 365 nm and, as expected, no photochemical reaction was observed. Upon addition of TiO₂, the authors observed a photocatalytic reaction of phenoxyacetic acid to yield anisole **30** and 1,2-diphenoxyethane **32** (Fig. 30 B). The second reactant, N-substituted maleimide, itself absorbs at 365 nm and undergoes a photochemical 2+2 addition reaction without photocatalyst to yield the dimer **33**. In the presence of TiO₂, the N-substituted maleimides undergo an additional photocatalytic reaction to give N-succinimide **31**. Thus, in the presence of TiO₂ both products **30** and **31** are generated (Fig. 30 C). All of these individual reactions are competitive during the photocatalytic carbon–carbon coupling of phenoxyacetic acid with N-substituted maleimides (Fig. 30 A).

Combination of illumination and NMR

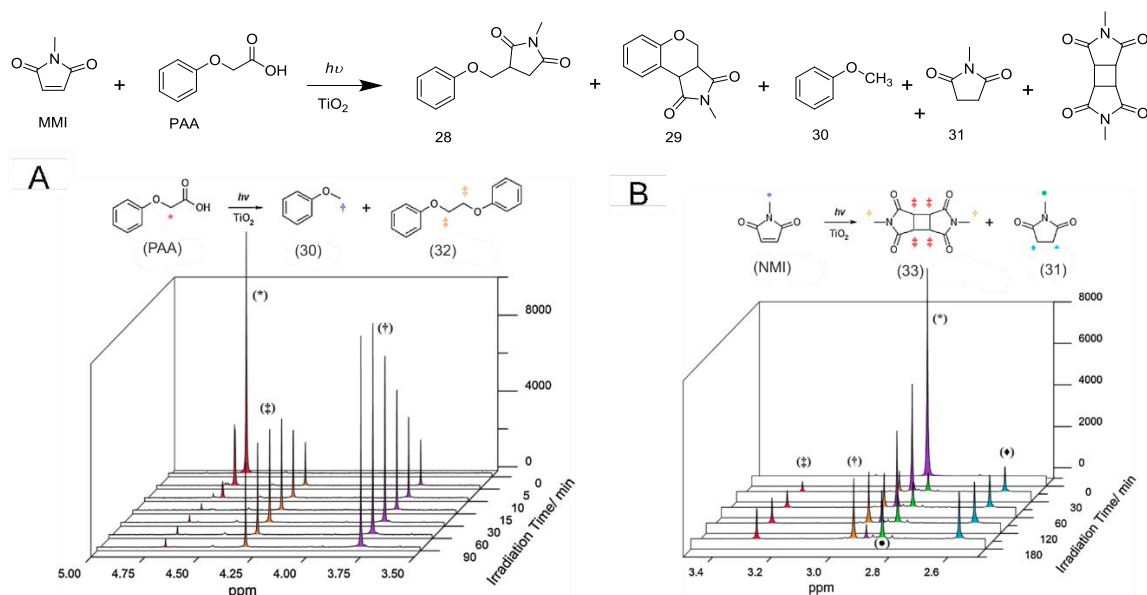


Fig. 30: (A) Observed product distribution in photocatalytic C-C coupling of phenoxyacetic acid with N-substituted maleimides. Individual photochemical reactions of the substrates reveal side reactions: (B) Photochemical reaction of phenoxyacetic acid and its ¹H NMR spectra measured during the reaction. (C) Photochemical reaction of N-substituted maleimides and its ¹H NMR spectra measured during the reaction. Spectra measured at 400 MHz.

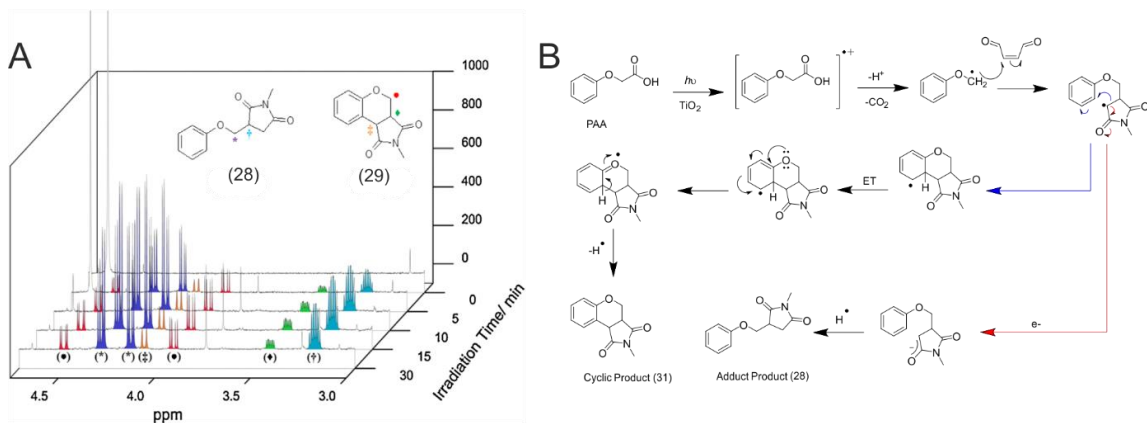


Fig. 31: Photocatalytic C-C coupling of phenoxyacetic acid with N-substituted maleimides: (A) Monitoring of the product formation via ¹H NMR spectra. (B) Proposed mechanism for the expected main products. Spectra measured at 400 MHz.

Therefore, the authors attempted to reduce this side product formation and to improve the yield of the desired C-C couplings by switching off the direct photochemical reaction of maleimid dimer III. This was done by using their earlier developed sol-gel titania coated NMR tubes. They irradiated the TiO₂ layer from outside, which worked not only as a catalyst but also as a UV filter. This minimised the direct absorbance by the

N-N-substituted maleimides and their side reaction, resulting in improved hetero C-C coupling yields. Further, by varying the SCP material composition they could even obtain different product distributions. Overall they obtained their highest yield of 74 % hetero C-C adduct **28** by using sol-gel and coating the inner side of the NMR tube (glass container) with 100 % anatase titania. The *in situ* NMR spectra of the optimized photocatalytic reaction are shown in Fig. 31 A.

This study shows the occurrence of multiple parallel reaction pathways in heterogeneous photocatalysis, which leads to a complex product distribution. By a systematic investigation using coated NMR tubes from which detailed mechanistic information was obtained, the authors were successful in improving the catalytic process.

2.5.3 Photoassisted polymerization reactions

2.5.3.1 Rapid monitoring of visible light-mediated controlled polymerization

The development of controlled radical polymerization (CRP) techniques facilitated the design of complex polymers with predefined molecular weight and low dispersity. Among these, the visible-light mediated CRP technique particularly attracted immense interest due to its mild operational conditions and spatiotemporal control[153]. In this regard *in situ* LED NMR plays a vital role in studying and optimizing these light assisted CRP reactions. In 2017, Craig J. Hawker and his group showed for the first time the application of *in situ* LED NMR experiments to monitor polymerization reactions[40]. For this purpose, the authors developed an *in situ* LED NMR arrangement suitable for polymerization monitoring with illumination from the top/inside (see Fig. 32 B). This study showed the significance of reaction profiling and the sequential light-on/off technique for temporal control and optimization of the polymerization conditions.

Initially, the authors investigated the controlled radical polymerization of N,N'-dimethylacrylamide (DMA, as the monomer) and 2-(butylthiocarbonothioyl) propionic acid (BTPA, as the chain transfer agent) (Fig. 32 A). In this light-assisted CRP reaction, tris(2,2-bipyridyl)dichlororuthenium(II) ($\text{Ru}(\text{bpy})_3\text{Cl}_2$) was used as a water-soluble photocatalyst for a photoelectron transfer reversible addition-fragmentation chain transfer (PET-RAFT) polymerization. It was known that the presence of oxygen in the reaction solution retards the propagation of the polymerization. Therefore, initial degassing was necessary for fast polymerization. Alternatively, the authors hypothesised that sodium ascorbate could be used to accelerate polymerization, since sodium ascorbate can reduce singlet oxygen. To validate this hypothesis, they carried out

systematic *in situ* LED-NMR reaction profiling (Fig. 32 C). This showed an initial induction period, which was followed by an accelerated polymerization (best seen on the blue curve in Fig. 32 C). This induction period was due to the presence of oxygen. After the reduction of oxygen by sodium ascorbate the polymerization process started. Next they tested the effect of light intensity on the reaction rate and dispersity. The polymerization rate increased almost linearly with the light intensity (Fig. 32 C and 32 D). However, an increase in dispersity was also observed with increasing light intensity (Fig. 32 D). Therefore, this study showed that the light intensity has to be optimized to obtain a good balance between high rates and low dispersity. The authors also tested the temporal control of the reaction by using sequential light-on and -off steps (Fig. 32 B) within an *in situ* LED illumination NMR arrangement. In contrast to the systems with dark reaction pathways discussed previously (see section 2.5.1.2), here no reaction in the dark was detected, resulting in excellent temporal control (Fig. 32 E).

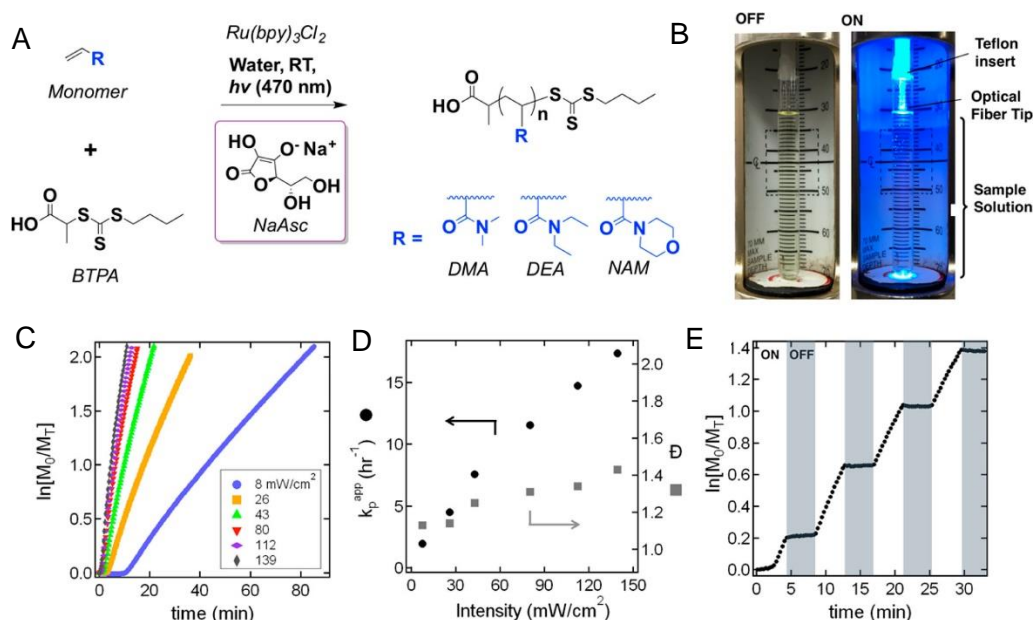


Fig. 32: *In situ* NMR monitoring of PET-RAFT. A) Reaction scheme. B) *In situ* LED NMR sample apparatus. C) Reaction kinetics at different light intensities, where M_0 and M_T are the concentration of the monomer at time zero and T , respectively. D) Apparent propagation rate constants (k_p^{app}) and dispersity of the resulting polymers with respect to light intensity. E) Temporal control testing.

Overall, the authors successfully developed an *in situ* illumination NMR experimental design and protocol for monitoring and optimizing visible light mediated polymerization reactions. This allowed the authors to implement precise on and off light cycles and accurately measure the corresponding kinetics of polymerization in an easy and fast way. This in turn enabled them to verify their proposed hypothesis and thereby

accelerate polymerization of an oxygen-containing reaction mixture by using reductive additives.

2.5.3.2 Light-on/off studies of photo-mediated controlled radical polymerization

As mentioned above, controlled radical polymerization (CRP) reactions have offered great control in synthesising diverse polymers. Temporal control is an important characteristic of CRPs. In addition to other stimuli, application of light to carry out CRPs is advantageous[153]. Light-assisted CRPs can provide greater temporal control than other stimuli as it is particularly easy and fast to turn on and off the light. However, the presence of additional dark pathways can complicate the temporal control in these reactions.

After initial validation of the *in situ* LED NMR method for monitoring polymerization (see section 2.5.3.1), the Hawker team next investigated three different types of light-induced CRP polymerization reactions as well as the suitability of different conditions for temporal control[41]. To check the presence of dark pathways in these light-induced CRP polymerizations, the authors applied light-on and -off sequential procedures, which facilitated monitoring and improved the temporal control of the processes. Three different types of light-initiated controlled polymerized reactions were investigated: photoinduced electron/energy transfer reversible addition–fragmentation chain transfer (PET-RAFT) polymerization, Cu-free atom transfer radical polymerization (Cu-free ATRP) and Cu-mediated atom transfer radical polymerization (ATRP).

For PET-RAFT temporal testing, the authors carried out the polymerization of methyl acrylate (MA) in DMSO (Fig. 33 A). After an induction period due to consumption of residual oxygen, the kinetics showed linear conversion (up to 30-40 %). On application of sequential light-on and -off steps in the linear region, nearly ideal temporal control was shown, i.e. during light -off almost no polymerization occurred and upon light-on a linear reaction progress was observed (Fig. 33 D). Next, the authors tested the temporal control in a Cu-free ATRP for the polymerization of methyl methacrylate and observed a similar temporal control as in the case of RFTA (Fig. 33 B and D). One significant difference was that the rate of the reaction was significantly faster in PET-RFTA than in the Cu-free ATRP polymerization.

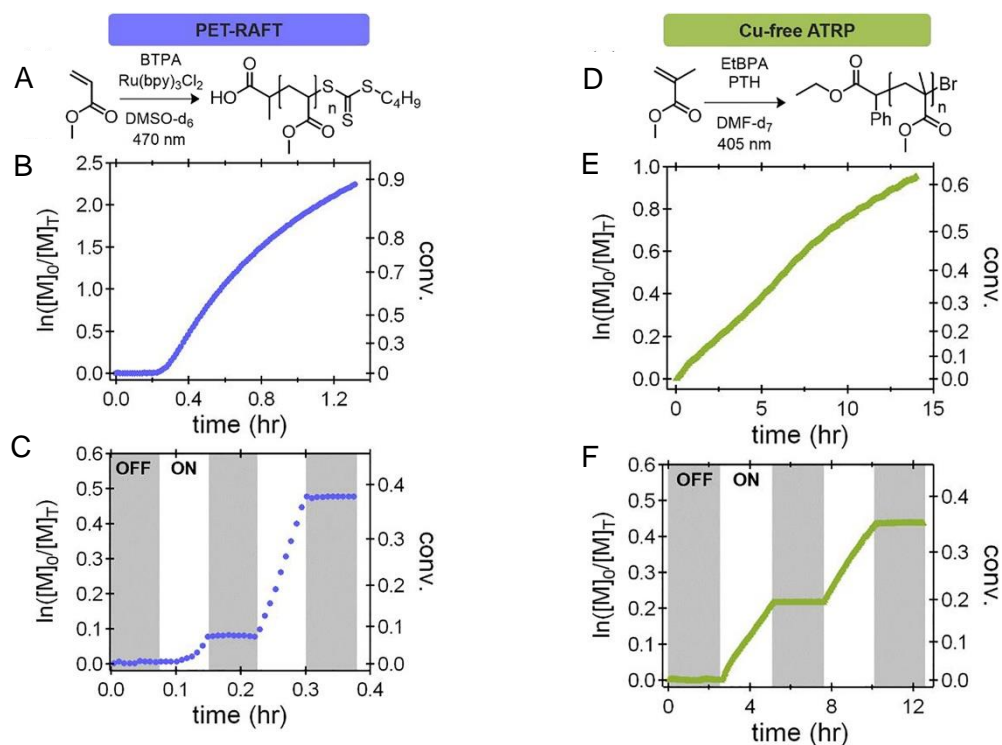


Fig. 33: Temporal control in CRPs. PET-RAFT polymerization (left; blue) A) polymerization scheme for methyl acrylate (MA) and tris(2,2'-bipyridyl)dichlororuthenium(II) hexahydrate. B) Polymerization reaction profile. C) Temporal control testing for the PET-RAFT. Cu-free ATRP (right; green) D) polymerization of methyl methacrylate (MMA) and 10-phenylphenothiazine. E) Polymerization reaction profile. F) Temporal control testing. Spectra measured at 600 MHz.

However, in the third reaction, the Cu-mediated ATRP polymerization in organic solvents, the reaction does not completely shut down during light-off steps, i.e. temporal control was not achieved (Fig. 34 B). This revealed the presence of a dark pathway in the third reaction. In fact this was due to the existence of residual Cu(I) even in the dark, which was responsible for the residual polymerization. To enhance the temporal control in this Cu-mediated ATRP, immediate consumption of Cu(I) was needed. Therefore, the authors screened for different ligands, and for combinations of aqueous solvent and salts such as CuBr_2 and NaBr for the immediate consumption of Cu(I). For a combination of CuBr_2 and NaBr in aqueous solution, excellent temporal control was achieved in *in situ* LED-NMR (Fig. 34 B).

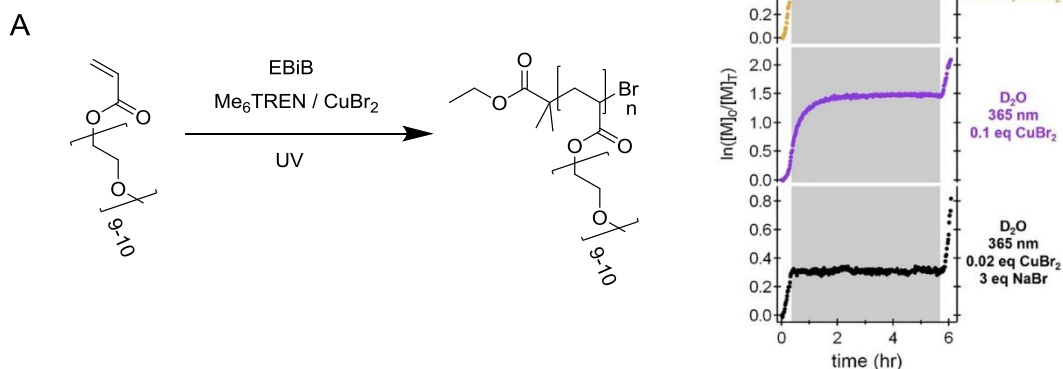


Fig. 34: Switching off the dark pathway: (A) Cu-mediated polymerization of poly(ethylene glycol) methyl ether acrylate (PEGA) macromonomers. (B) Temporal control testing by sequential light-on and -off steps under different conditions. Spectra measured at 600 MHz.

Overall the study highlights the advantages of the *in situ* LED illumination NMR technique in monitoring and optimizing light-stimulated CRP reactions. Even in the presence of unwanted dark cycles the authors were able to suppress these dark pathways by changing reaction conditions.

2.5.4 Photoswitches

Another research group that recently started using *in situ* LED illumination NMR experiments extensively is that of Thiele [36,39,62,107]. Beside a few applications in polymerizations and photocatalysis [122,154,155], so far they mainly focused on photochromic switches due to their importance in polymers, materials, and molecular machines. Significant examples include the investigation of multi photoisomers and rotamers[36,62] which cannot be studied by UV-Vis spectroscopy. Each study highlighted different advantages of the *in situ* LED illumination NMR technique over *ex situ* and UV/Vis spectroscopy, which are discussed in the following section. Another special type of photoswitch from the Herges group for spin multiplicity modulation is also discussed in section 2.5.5.1.

2.5.4.1 Spiropyran ↔ merocyanine

In 2016, the Thiele and Gschwind groups in collaboration explored the *in situ* LED illumination NMR technique to study meta stable photochromic systems [107]. In this

work they tested *in situ* kinetic measurements versus *ex situ* measurements and also different light sources for the *in situ* experiment. The study showcases the advantages of *in situ* LED illumination NMR over *ex situ* NMR in terms of kinetic measurements and the acquisition of longer, conventional ^{13}C and 2D NMR spectra for meta stable isomers, which would otherwise not be possible in *ex situ* illumination due to fast thermal back isomerization. The study also highlights the combined application of low temperature and continuous light illumination to enhance the population of the meta stable photoisomer.

The authors chose a spiropyran photochrome system for the investigation, which on illumination switches between a closed spiropyran form and an open merocyanine form (Fig. 35 A). Spiropyran photochrome based applications in materials, polymers and MRI agents are well explored to modulate their physical and chemical properties[155,156] However, the underlying structure-property relationship of this light-responsive spiropyran-polymer was poorly understood. This was due to the missing structural and kinetic information of the open meta stable merocyanine form. To understand this structure-property relationship of the spiropyran photoswitch, both *ex situ* and *in situ* techniques were applied to measure kinetics during light-on and -off experiments as well as 2D experiments.

Upon irradiation with light at 365 nm, the cyclic form of spiropyran **34** switches to the thermally less stable and more conjugated open merocyanine form **35** (Fig. 35 A). Due to the thermal instability of the metastable merocyanine (half-life as low as 13 s), this unstable molecule was very difficult to study by *ex-situ* NMR.

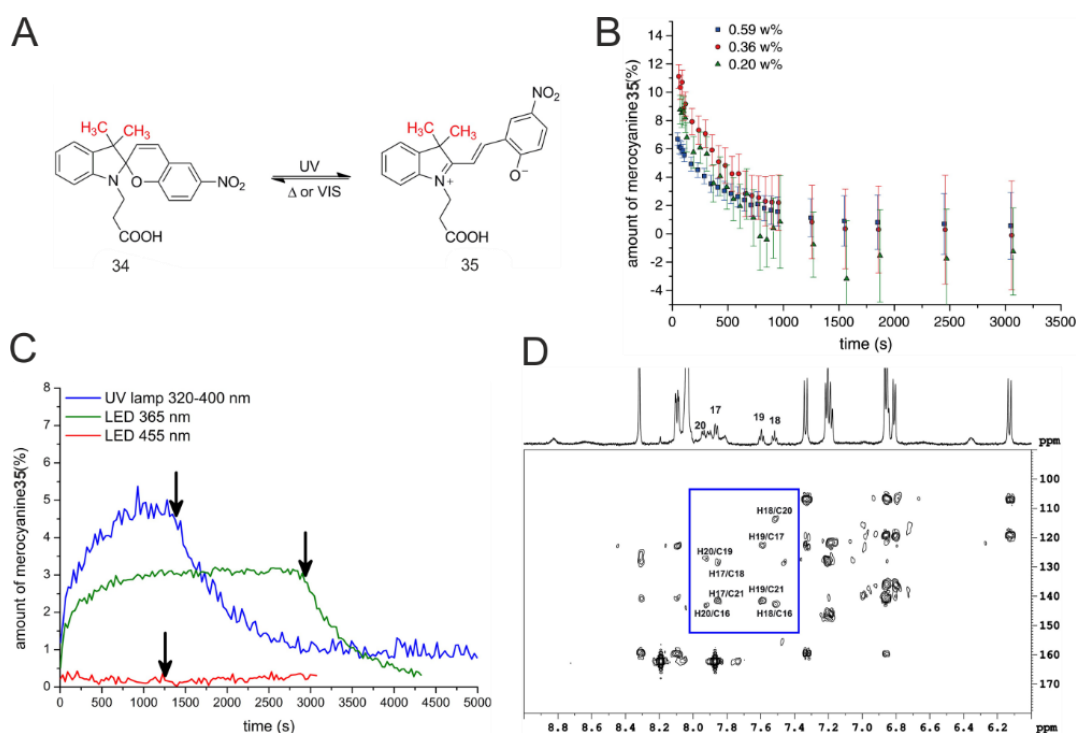


Fig. 35: (A) Spiropyran \leftrightarrow merocyanine photoswitch. (B) Thermal relaxation of the meta stable merocyanine back to the spiropyran after 10 min of *ex situ* irradiation. (C) *in situ* LED illumination (LED λ = 365 nm) NMR monitoring the spiropyran ring opening, the PSS and the thermal relaxation of the meta stable merocyanine. (D) 2D HMBC NMR spectrum of spiropyran **34** (intense signals) and merocyanine **35** (signals in the box) in DMF- d_7 at 255 K under continuous irradiation. Spectra measured at 600 Hz.

On extensive screening of the reaction in different solvents, a maximum half life time of 402 s for merocyanine in DMSO was found, which facilitated acquisition of *ex situ* NMR data. However, from the *ex situ* NMR studies in DMSO after irradiation of spiropyran for 10 min it was possible to monitor the thermal back reaction (Fig. 35 B). From the *in situ* LED NMR setup, as expected more information could be obtained, including the ring opening kinetics, the PSS and also the thermal back reactions (Fig. 35 C and Table3). This highlights the advantages of the *in situ* arrangement over *ex situ* NMR in studying photochromic systems. In both *ex situ* and *in situ* studies, the authors could obtain rate constants and half-life times for the meta stable merocyanine by exponential curve fitting, which shows similar thermal relaxation (Table 3). The influence of concentration and different light sources on the rate and half life time of merocyanine was tested in the *in situ* setup. At higher concentrations, a slightly higher rate and a shorter half-life for the merocyanine were observed (Table 3). Furthermore, in the *in situ* experiment, replacing the LED with a UV lamp resulted in a slightly slower rate and a longer half-life.

Table 3: Measured thermal relaxation of merocyanine after irradiation with different light sources at different concentrations in DMSO-d₆ at 300 K; the starting points corresponds to the arrows in Fig. 35 C.

Irradiation procedure	Concentration	Light source	10 ⁻³ k ₁ /s	τ _{1/2} /min	R ²
<i>ex situ</i> NMR	0.59 wt. %	UV lamp	2.36 ± 0.14	4.90	0.99
<i>ex situ</i> NMR	0.36 wt. %	UV lamp	2.16 ± 0.16	5.35	0.99
<i>ex situ</i> NMR	0.20 wt. %	UV lamp	1.91 ± 0.19	6.05	0.97
<i>in situ</i> NMR	0.30 wt. %	UV lamp	1.76 ± 0.06	6.56	0.97
<i>in situ</i> NMR	0.30 wt. %	LED 365 nm	1.99 ± 0.08	5.81	0.99
UV/VIS	0.05 mg/ml	UV lamp	1.7	6.80	0.99

In the next step, the very challenging task of measuring 2D NMR experiments for the meta stable form in the *in situ* arrangement was achieved. For that, a significant concentration of merocyanine **35** over a longer period of time is required. This was achieved by a combination of continuous irradiation and low temperature measurements. Due to the low temperature the thermal back relaxation was reduced and also partial stabilization of merocyanine **35** was achieved. Thus, by continuous irradiation at 255 K a constant, significant concentration of merocyanine was maintained. This allowed ¹³C chemical shifts and 2D HSQC, HMBC, and NOESY spectra of merocyanine to be obtained for the first time. The measured HMBC spectra are shown in Fig. 35 D; the blue rectangle frames the peaks of merocyanine **35**.

In this investigation the *in situ* LED illumination NMR measurements were validated against *ex situ* NMR measurements using the example of a spiropyran ↔ mesocyanine system, highlighting some advantages of the *in situ* LED illumination NMR regarding initial kinetics, PSS and low temperature stabilisation of thermally metastable isomers.

2.5.4.2 Multiple-state photochromic system

After validation of the *in situ* illumination LED-NMR technique for the investigation of photochromic systems, the Thiele group expanded the method to investigate more complex photoswitches, e.g. multiple state photochromic systems [62]. Despite the extensive application of UV/Vis spectroscopy in the study of photochromic systems, the spectral overlap of some of the multiple state photoswitches is so severe that UV/Vis spectroscopy fails to distinguish the multiple photoisomers or to analyse their photokinetic properties. For example, the UV/Vis spectra of benzene-1,3,5-tricarboxamide (BTA) **36** is shown in Fig. 36 B. Here, the authors took the advantage of high resolution NMR spectroscopy to carry out a systematic investigation that successfully identified multiple photoisomers and measured their photokinetic properties. Very impressively, the authors obtained both kinetic and thermal stability data for all the photoisomers.

As a model system for NMR investigation, exactly this benzene-1,3,5-tricarboxamide (BTA) **36** with three azobenzene units (Fig. 36 A) was chosen, which shows four photoisomers, i.e all trans(**ttt**), trans-trans-cis(**ttc**), trans-cis-cis(**tcc**) and all cis(**ccc**) (Fig. 37). As expected, at thermal equilibrium the authors observed mainly the **ttt** isomer and a minor proportion of the **ttc** isomer (7%) (Fig. 37 A). After *in situ* NMR UV irradiation for 3.5 hrs, the **ccc** isomer was observed as the most populated (Fig. 37 B). After several days in the dark, additionally the other two isomers (**ttc**, **tcc**) were observed (Fig. 37 C). The aromatic and NH protons of benzene-1,3,5-tricarboxamide in BTA **36** showed well resolved chemical shifts for all four photoisomers. To assign the overlapping azobenzene peaks, the authors applied state of the art assignment techniques including 2D ASAP HSQC and BIRD pureshift HSQC, HMBC and also ^1H - ^{15}N experiments.

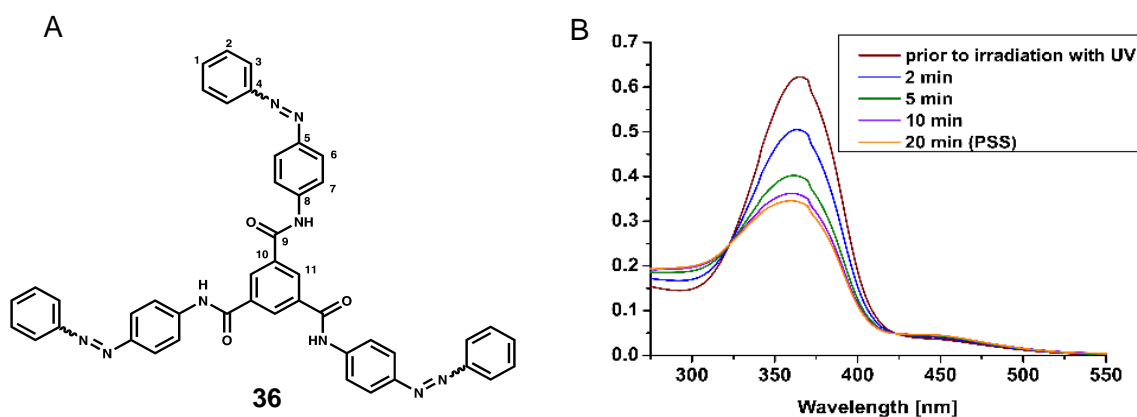


Fig. 36: UV/Vis spectral overlap of multiple state photoswitches (A) Chemical structure of the most stable photoisomer of BTA **36** at room temperature before irradiation. (B) The UV/Vis spectra of a 4 μM solution of BTA **36** before and during the irradiation with UV light ($\lambda = 365 \text{ nm}$) in DMSO show the severe overlap of the absorption that prevents any further investigation.

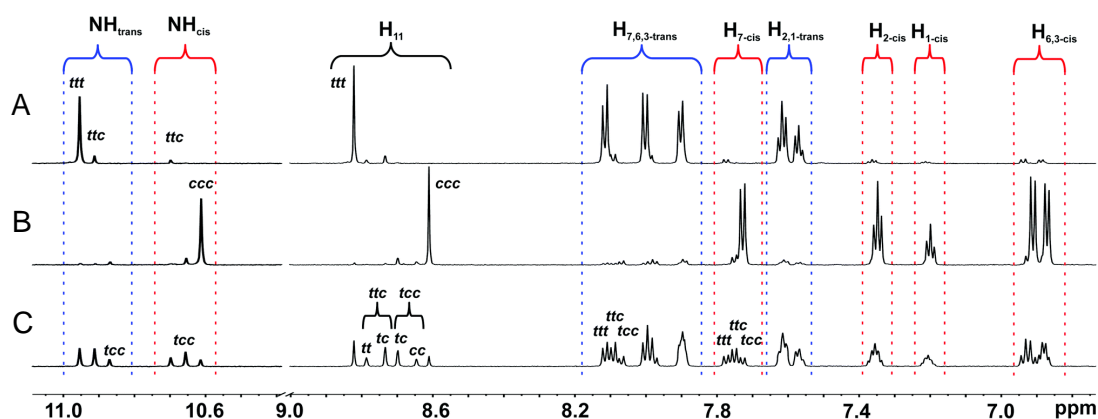


Fig. 37: Controlled *in situ* ^1H NMR visualization of multiple state photoisomers of BTA **36** in $\text{DMSO-}d_6$ at 300 K. A) Prior to irradiation the **ttt** isomer is the major component. B) After 3.5 h of continuous *in situ* irradiation with UV light ($\lambda = 365 \text{ nm}$) the **ccc** isomer is the major component. C) Several days after turning off the UV light source a mixture of all four isomers was obtained. Spectra measured at 600 MHz.

The excellent separation of the ^1H chemical shifts of the 4 photoisomers shown in Fig. 37, allowed the authors to measure the kinetics of all photoisomers during both irradiation and thermal relaxation (Fig. 38 A and 38 B). During the irradiation, the concentration of the initial major isomer **ttt** decreased exponentially and it subsequently disappeared completely (half-life 11 h), whereas **ttc** increased suddenly upon switching on the irradiation and then gradually decreased to 1 %. Both **tcc** and **ccc** increased

exponentially after start of the illumination and later reached saturation values of 13% and 83%, respectively.

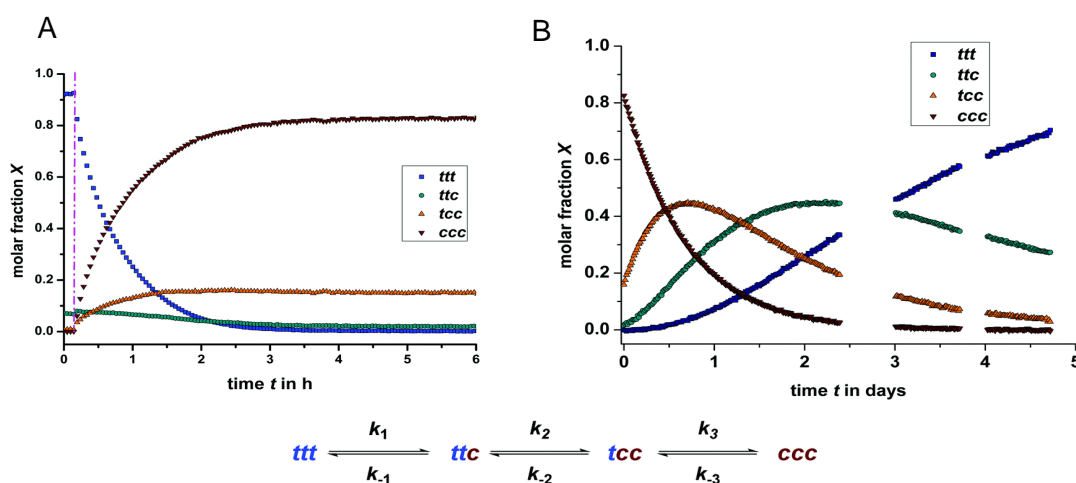


Fig. 38: (A) Kinetics of photoisomers during continuous irradiation with UV light ($\lambda = 365$ nm), extracted from the integrals of the resonances H_{11} in $DMSO-d_6$. The dashed line in the beginning indicates the start of illumination (B) Kinetics of photoisomers during thermal relaxation in $DMSO-d_6$ at 300 K. Measured at 600 MHz.

However, the authors observed more complex kinetic behaviour during the thermal back reaction, as shown in Fig. 38 B. The initial major populated **ccc** isomer drops exponentially reaching almost zero. In contrast, **tcc** and **ttc** initially increased exponentially reaching maxima of 43 % and then decreased. However, **tcc** and **ttc** develop at different rates; **tcc** develops far faster than **ttc**. The kinetic pattern obtained showed a linear dependence on the number of *cis* moieties in the isomer, i.e. the higher the number of *cis* units, the faster the corresponding thermal back relaxation (see Table 4). This indicates independent isomerization events for all three double bonds, possibly due to the larger distance between the azo units. From the rates so obtained the authors could back-calculate the concentrations of all four isomers at thermal equilibrium, which for two isomers are below the NMR detection limit (see Table 5).

Table 4: Measured thermal back relaxation rate showing linear dependence on *cis* moieties.

Reaction step	k [day^{-1}] (from H_{11} int.)	k [day^{-1}] (from NH int.)
k_{-1}	0.509	0.478
k_{-2}	0.978	0.970
k_{-3}	1.486	1.465

Table 5: Calculated concentration of photoisomers below the NMR detection level.

Photoisomer	X from integral [%]	X calculated from k [%]
<i>ttt</i>	~93	93.43
<i>ttc</i>	~7	6.40
<i>tcc</i>	—	0.17
<i>ccc</i>	—	0.00001

This study showcased the advantages of high resolution NMR spectroscopy over UV/Vis spectroscopy in an impressive way for the investigation of multiple-state photoswitches. The authors successfully obtained very detailed kinetic information for all four photoisomers, highlighting the potential of *in situ* LED illumination NMR experiments that feature the broader chemical shift dispersion of NMR spectra versus the severe signal overlap in some UV/Vis spectra.

2.5.4.3 Photoswitchable rotamers

In 2018, the Thiele group in collaboration with Dračinský and Procházková reported another impressive investigation by *in situ* LED illumination NMR on a special case of photochromes, i.e. photoswitchable rotamers [36]. Considering the recent emerging trend for the development of photoswitchable drugs, the authors very cleverly selected a biologically important class of compounds, azopyrimidines derivatives, as model systems for their investigation (Fig. 39 A). Similarly to azobenzenes, azopyrimidines are also photoswitchable between *trans* and *cis* forms, and the UV/Vis spectra of selected compounds at thermal equilibrium are shown in Fig. 39 B). The introduction of intramolecular hydrogen bonds (IMHBs) in azo derivatives significantly influences molecular physio-chemical properties such as reactivity, lipophilicity, solubility, membrane permeability, acidity and biocompatibility[157,158]. In a similar way, IMHBs in azo derivatives also dramatically change their photochemical properties and can hamper the formation of the *cis* isomer. In this study the authors investigated the modulation of these *trans* and *cis* populations by introduction of intramolecular hydrogen bonds. In the *trans* form these azopyrimidines can further form two types of rotamers, which are photoswitchable (see Fig. 39 A). However, the visualization and monitoring of these rotamers by UV/Vis spectroscopy was not possible due to spectral overlap. Again, the higher spectral resolution of *in situ* LED illuminated NMR not only facilitated the visualization of these rotamers but even allowed determination of kinetics and hence the rotation barriers of these rotamers.

For this investigation, the authors selected three types of photoswitchable azopyrimidines based on the number of hydrogen bond donors (Fig. 39 A) (i) without any hydrogen bond donor (Fig. 39 A, compound **37**), (ii) with a single hydrogen bond donor (Fig. 39 A, compound **38**) and (iii) with two hydrogen bond donors (Fig. 39A, compound **39-44**).

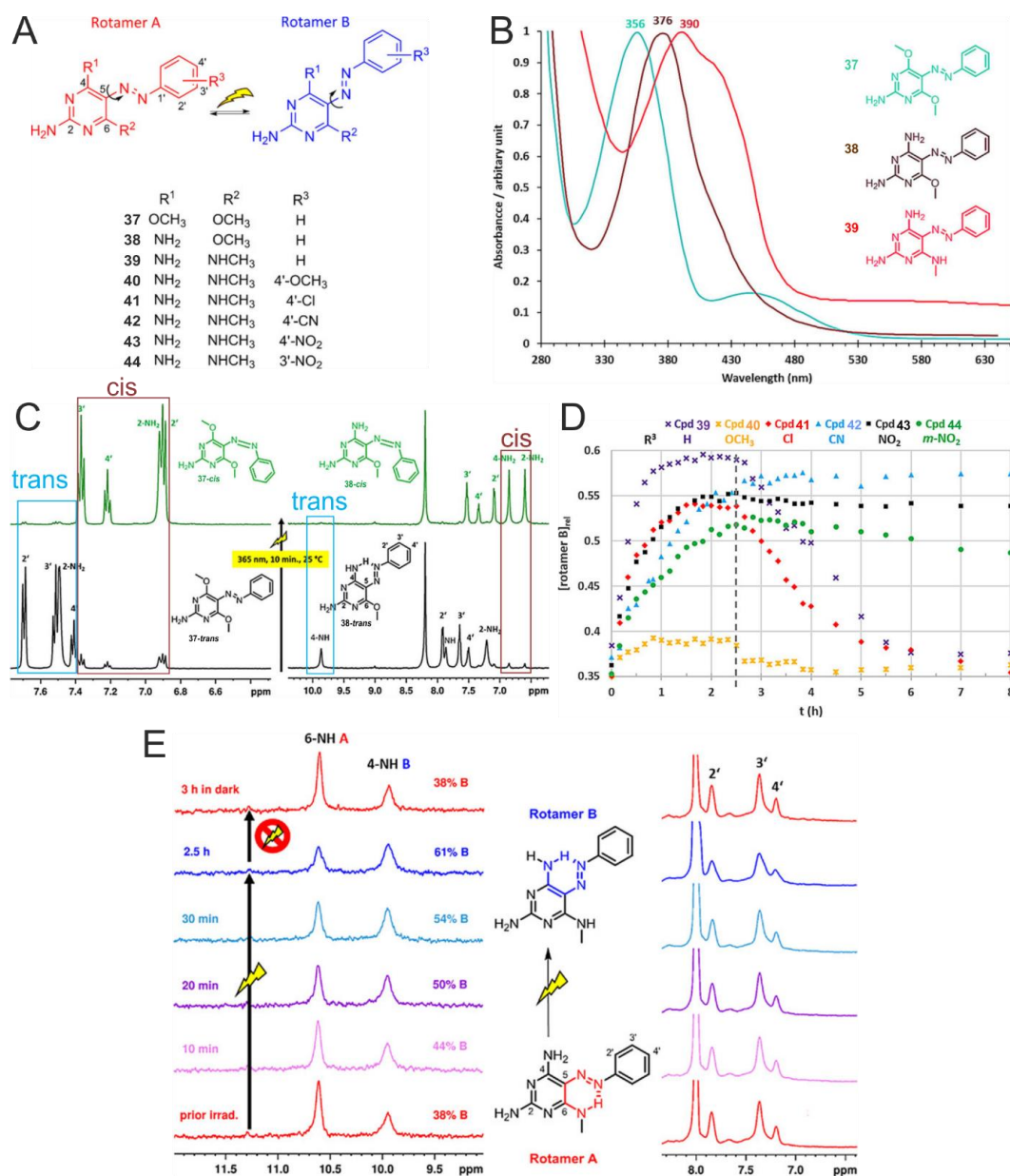


Fig. 39: Influence of hydrogen bonds on the photophysical properties of isomers and rotamers (A) Selected azopyrimidine systems with no intramolecular hydrogen bonds (IMHB) (**37**), a single IMHB (**38**) and two IMHBs (**39-44**). (B) UV-visible absorption spectra of compounds **37-39**. (C) *In situ* LED NMR spectra before and after irradiation of compound **37** and **38** (D) Influence of substituents on rotational barrier. The relative rotational barriers are measured by thermal relaxation analysis after switching off the irradiation, i.e. the longer the rotamer thermal relaxation the larger the rotational barrier. (E) *In situ* NMR spectra of the population of the two *trans* rotamers of compound **39** at different irradiation times (at $-110\text{ }^{\circ}\text{C}$). Spectra measured at 500 MHz.

For compound **37**, which does not possess a hydrogen bond donor, an IMHB is not possible and the authors observed two absorption maxima in the UV/Vis spectra (356

and 450 nm, Fig. 39 B), showing 20% of the *cis* form at room temperature under thermal equilibrium. Similar populations were also detected in the ^1H NMR spectra (Fig. 39 C left bottom). For compound **38**, which has one NH donor, one strong IMHB is expected in the *trans* form and again the *cis* isomer population is considerably smaller (Fig. 39 B and 39 C). In contrast, no *cis* isomer was detected in the spectrum of compound **39**, which can have two stable rotamers for the *trans* isomer.

On *in situ* irradiation of compounds **37–39** with UV light (365 nm) (2 mM solutions in DMF- d_7) at room temperature (25 °C), the authors observed significant differences in the time resolved *in situ* NMR spectra revealing different photophysical properties for the compounds. Compound **37**, with no IMHB, shows almost complete conversion to the *cis* isomer within 10 minutes of irradiation (Fig. 39 C). For **38** the thermal back relaxation is extremely slow and the observed half-life ($\tau_{1/2}$) was around 11.5 days, indicating a relatively high barrier (Table 6). Compound **38** with one IMHB can form a more stabilized *trans* form (rotamer B, Fig. 39 C, right); however within 10 min of irradiation again an almost complete conversion to the *cis* form was observed. In contrast to compound **37**, thermal back relaxation of **38** was far faster with a half-life time of 5 hrs, i.e. this compound has a relatively low barrier.

Table 6: Experimentally obtained and calculated activation barrier for *cis* to *trans* thermal back relaxation.

Cmpd.	No. of IMHB donors	$\Delta G^\ddagger_{\text{exp}}$ [kcal mol $^{-1}$]	$\Delta G^\ddagger_{\text{calc}}$ [kcal mol $^{-1}$]
37	0	25.9	28.2
38	1	23.5	24.2
39	2	–	16.4

For compound **39**, no *cis* form was observed even after long irradiation times and at low temperature (-110 °C). Instead of the *cis* isomer, at low temperature the authors could observe two sets of peaks corresponding to the two rotamers A and B in a *trans* form (Fig. 39 E), with their ratio changing with irradiation time and temperature. Subsequently, the authors measured the rotational barrier between these rotamers of compound **39** by following the thermal back-relaxation. In a next step they measured the rotational barriers for different substituents in the compounds **39–44** (Fig. 39 D). The highest rotational barrier was found for compound **6** and was explained via push-pull effects i.e.

the conjugately connected electron donating group at one end and electron accepting group at other end can induce strong double bond character, resulting in larger rotational barrier.

This study shows detailed investigations of the influence of intramolecular hydrogen bonds and substituents on photophysical properties of azopyrimidines using the *in situ* LED illumination NMR technique, which effectively complements UV/Vis spectroscopic studies. The study shows not only photoresponsive *trans cis* isomerization, but also photorotamers, which to our knowledge is very rarely described.

2.5.5 New methods and concepts in *in situ* illumination NMR

2.5.5.1 Unusual photoswitch for modulating spin multiplicity

In 2011, Herges's group developed an unusual reversible photoswitch for the modulation of spin multiplicity [159]. This was achieved by covalently attaching a photochromic azopyridine to a Ni porphyrin (Fig. 40 A), which was photoswitched between *cis* and *trans* form. The azopyridine in *cis* form is coordinated to Ni²⁺ (Coordination Number 5) leading to a paramagnetic state, while the *trans* azopyridine form does not coordinate to Ni²⁺ (Coordination Number 4) and therefore leads to a diamagnetic state (Fig. 40 A). This enabled the authors to achieve photoswitchable diamagnetic ↔ paramagnetic status reversibly at ambient temperature.

The photoswitch was tested over 100000 cycles, demonstrating an exceptional stability and reversibility (Fig. 40 A). By exploiting this excellent diamagnetic ↔ paramagnetic reversible photoswitching property of this Ni-porphyrin based system, the authors designed two applications: (i) a light responsive MRI agent and (ii) a sensitivity boost in NMR experiments. Both are discussed below.

2.5.5.1.1 Light sensitive MRI agent

Smart, or stimuli-responsive, MRI agents are advantageous due to their selective responsiveness towards physiological conditions and biological molecules. These paramagnetic MRI agents are specifically responsive towards pH, temperature, enzymes and ions. However, light responsive MRI agents have been less thoroughly explored despite their potential for greater spatiotemporal control.

Therefore, Herges's group exploited their above-mentioned Ni porphyrin based diamagnetic ↔ paramagnetic reversible photoswitch to develop a light sensitive MRI

contrast agent. As discussed above, in this Ni porphyrin photoswitch the paramagnetic condition was achieved by photoswitching the attached azopyridine to the *cis* form, which then shows a higher downfield shift for the pyrrole protons (Fig. 40 C). However, it was recognised that not all the *cis* forms resulted in paramagnetic complexes. The *cis* form of azopyridine can both coordinate or not coordinate (Fig. 40 B), and only when coordinated to Ni²⁺ does the *cis* form lead to a paramagnetic complex. In order to develop a reliable, photoswitchable MRI agent it is crucial to improve the azopyridine coordination to Ni²⁺, and therefore the authors screened different substituted azopyridines. This was cleverly done by exploiting the Hammett correlation, allowing the authors to favour the coordinated form by introducing an electron donating group at the para position in the pyridine of azopyridine. A maximum of up to 89 % of the co-ordinated form was found for a MeO substitution (Fig. 40 C), and very interestingly the authors also noted a high conversion to the *cis* form (>95 %). The quantification of these associated complexes for different substituted azopyridines was done by monitoring higher downfield chemical shifts of the pyrrole protons (no coordination: around 8.9 ppm; fully coordinated around 53 ppm; see Fig. 40 C), which was facilitated by *in situ* LED illumination NMR.

After successful improvement in the paramagnetic condition of the complex, the authors measured the relaxivities for these differently associated complexes and as expected found the highest relaxivity for the MeO substituted complex, that with the maximum *cis* coordination.

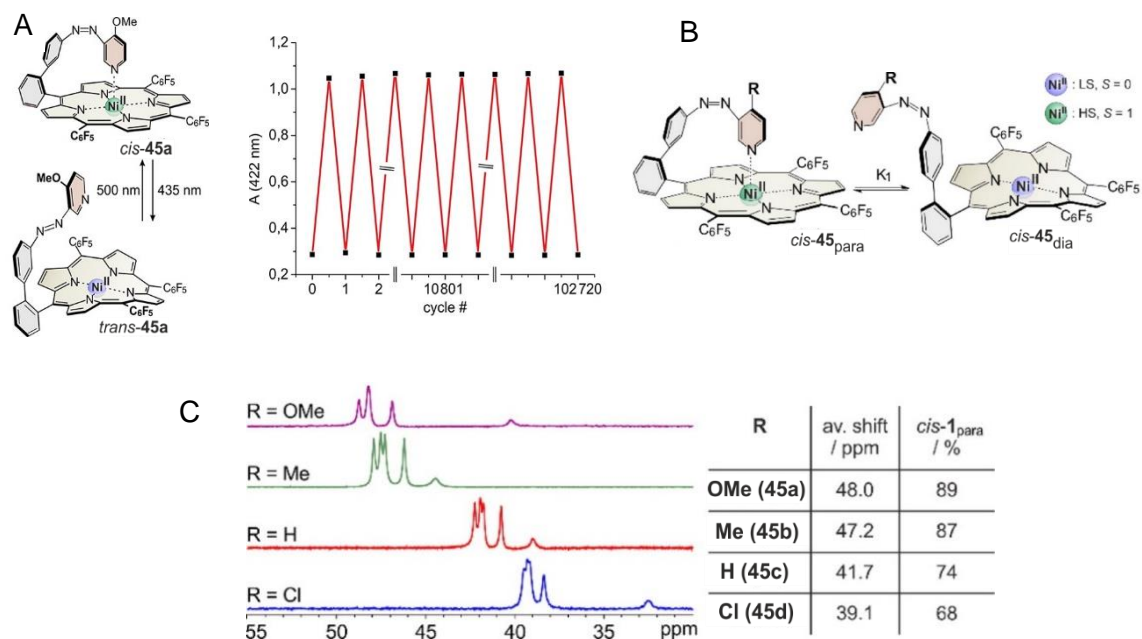


Fig. 40: Azopyridine-attached Ni-porphyrin photoswitch modulating spin multiplicity. (A) Photoswitching of diamagnetic \leftrightarrow paramagnetic states via azopyridine *cis* \leftrightarrow *trans* isomerization has immense photostability, as shown on the plot of UV/Vis absorption at 422 nm as a function of the number of switching cycles. (B) Possible equilibrium between the coordinated *cis*-paramagnetic and the non-coordinated *cis*-diamagnetic complexes (C) *In situ* LED NMR spectra and quantification of different substituent effects on the extent of the coordinated form in the *cis* isomer. Spectra measured at 600 MHz.

Table 7: Substituent dependent relaxivity measurements facilitated by the *in situ* LED illumination NMR experiment. Measured at 200 MHz.

R (compd)	$R_1/\text{mM}^{-1} \text{s}^{-1}$	
	at 500 nm	at 435 nm
MeO (45a)	0.159	0.045
Me (45b)	0.155	0.029
H (45c)	0.121	0.018

2.5.5.1.2 Photoinduced reversible acceleration of T₁-relaxation (PIRAT)

The other reported application of this photoswitchable diamagnetic ↔ paramagnetic complex is sensitivity enhancement in NMR [112]. Sensitivity is an inherent problem in NMR. In general sensitivity is improved by acquiring more transients. However, longer nuclear relaxation times significantly limit the number of transients that can be acquired in a given time. In principle relaxation can be accelerated by introducing paramagnetic species, but at the cost of line broadening. In 2018, Gescheidt's group in collaboration with Herges's group exploited the above described reversible paramagnetic ↔ diamagnetic property of Ni complexes to boost the NMR sensitivity. Very significantly, the method boosts sensitivity, while still maintaining narrow line widths. This paramagnetic relaxation enhancement (PRE) was achieved via reversible paramagnetic ↔ diamagnetic (spin cross over) photoswitching in an *in situ* LED illumination NMR experiment. The authors implemented the idea by synchronising reversible photoswitching of the azopyridine within the Ni complexes from *trans* (low spin, S=0, diamagnetic) to *cis* (high spin, S=1, paramagnetic) within the NMR pulse sequence. This synchronised pulse sequence (PIRAT) is shown in Fig. 41 A. During the RF irradiation and acquisition, the electronic spin state was maintained as diamagnetic to ensure narrow line widths, while during the interscan delay the spin state was photoswitched back to paramagnetic to accelerate nuclear relaxation. This enabled a higher number of scans to be acquired in a given time and hence improved sensitivity. This is very advantageous, especially in 2D NMR experiments. The predicted effect of PIRAT sequence on T₁ and sensitivity enhancement is shown in Fig. 41 B.

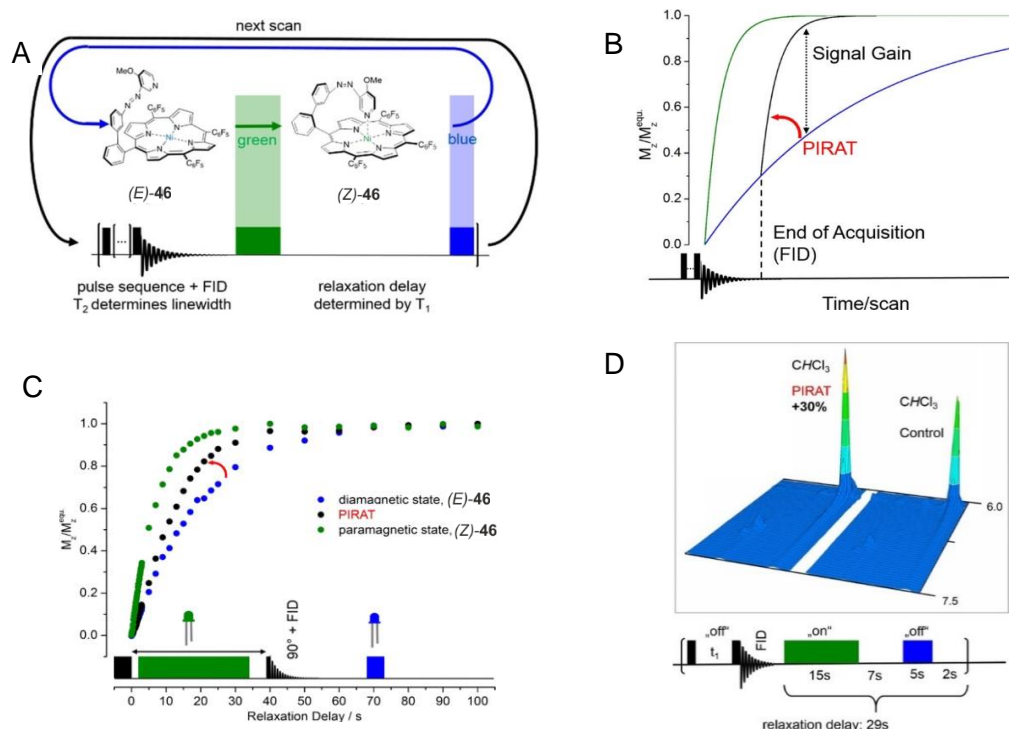


Fig. 41: New concept for sensitivity enhancement using spin-state sensitive photoswitches (A) PIRAT pulse sequence. (B) Predicted PIRAT effect on T_1 and signal sensitivity. (C) T_1 saturation recovery measurement of 10 % $CHCl_3$ in toluene- d_8 under PIRAT, diamagnetic and paramagnetic conditions. (D) Comparison of signal sensitivity of a 2D COSY for 10 % $CHCl_3$ in toluene under normal and PIRAT conditions. Spectra measured at 200 MHz.

To illustrate the principle the authors prepared a sample of 10% $CHCl_3$ in toluene- d_8 ($CHCl_3$ has particularly slow relaxation). By synchronizing the pulses of a saturation recovery experiment with on and off paramagnetic states, the authors could obtain the results shown in Fig. 41 C. The sensitivity enhancement was illustrated in a 2D COSY for the same sample and the authors could observe 30% enhancement in sensitivity, which is shown in Fig. 41 D.

The study shows the proof of a new concept for sensitivity enhancement facilitated by the *in situ* LED illumination NMR setup and highlights the possibility of new method developments by combining different concepts with the *in situ* LED illumination NMR platform.

2.5.5.2 Photochemical pump with NMR detection: generated synchronized coherence on microsecond time scale

NMR spectroscopy provides dynamics information over a wide range of timescales. However, despite their limited structural accessibility, UV/Vis, IR and Raman spectroscopy are the preferred methods to follow faster dynamic processes due to their better sensitivity and time resolution. Thus, numerous pump–probe methods have been reported based on these fast techniques. In contrast to traditional NMR methods, time resolved photo-CIDNP NMR can provide faster dynamics information with high sensitivity and time resolution [22,23].

Inspired by these concepts and owing to the greater level of structural detail accessibility by NMR, in 2014 the Duckett and Perutz groups in collaboration developed a photochemical pump probe with NMR detection to follow faster dynamics with better sensitivity and time resolution [42,43]. The method combines *in situ* photolysis and hyperpolarization from *para* hydrogen. Thus, first an initial short laser pulse (ns) is used to dissociate effectively *ortho*-H₂ from the ruthenium complex. In the subsequent time delay the dissociated *ortho*-H₂ is replaced by *para*-H₂, which is applied at 3 atm pressure to support the formation of the hyperpolarized complex (almost 100 % polarization just in 0.1 ms, see Fig. 42 A and B). The resulting spectrum is shown in Fig. 42 C.

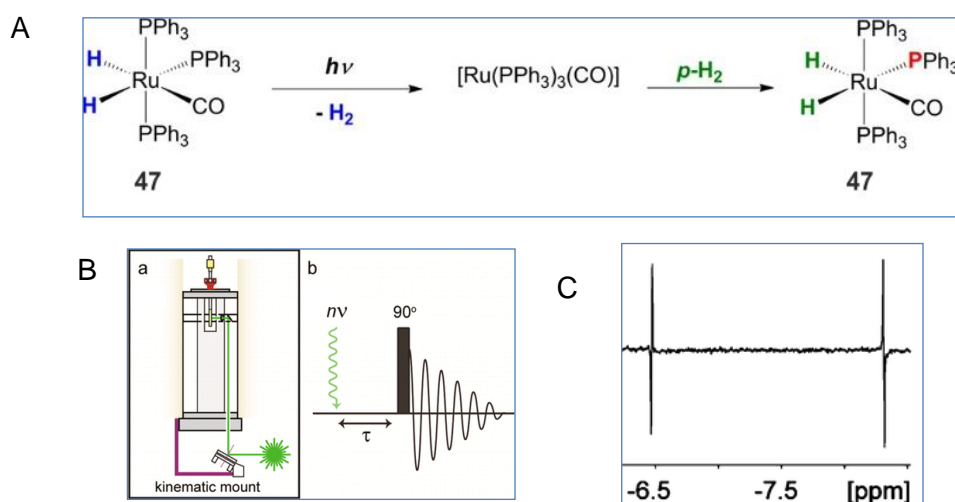


Fig. 42: Combination of photodissociation and hyperpolarization: (A) Photochemical reaction of compound **47** with *para*-H₂ (B) *in situ* LASER NMR irradiation apparatus and NMR pump–probe sequence (C) Single-LASER shot, single 90° rf pulse, *para*-H₂ enhanced $^1H\{^{31}P\}$ NMR spectrum at the hydride region of complex **47** with $\tau = 0.05$ ms. Spectra measured at 600 MHz.

Unlike in thermal PHIP polarization, the technique generates a synchronised coherence. Due to this faster polarization, the authors could observe both longitudinal and ZQ states, as illustrated for complex **47**. The ZQ modulation shown in Fig. 43 A was accessed via a systematic incrementation of the time delay between the LASER pulse and rf pulse (Fig. 42 B). The observed modulation in complex **47** was an exponential decay of a sinusoidal wave with a frequency equal to the chemical shift difference of the two hydrides (Fig. 43 A). In this technique the authors could select observation either of longitudinal magnetization or of ZQ by selecting the rf pulse angle. A two dimensional spectrum similar to a conventional spectrum was also obtained, which shows peaks at $\Delta\delta = \pm$ ZQ (Fig. 43 B). This was in contrast to the thermal PHIP polarization, where only longitudinal magnetization was accessible.

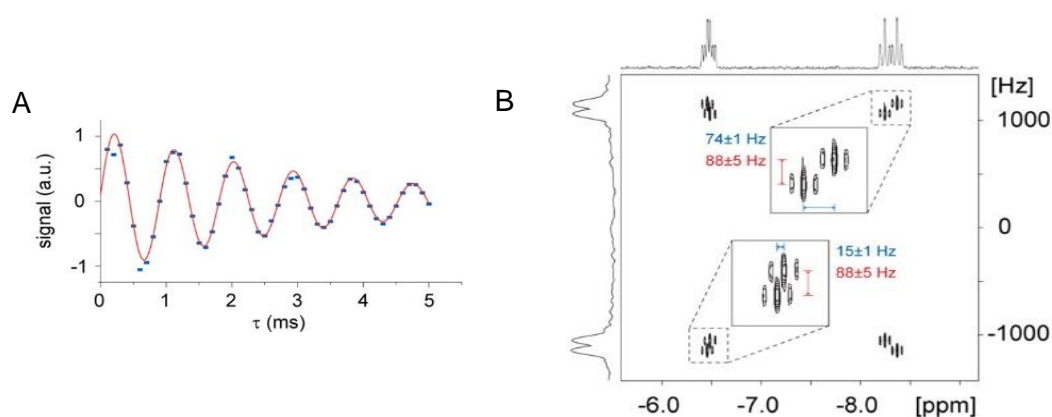


Fig. 43: Fast photoinduced coherence allows for zero quantum detection: (A) Integrals of the $^1\text{H}\{^{31}\text{P}\}$ hydride signal upon variation of the delay τ up to 5 ms. Red line: fit to exponentially decaying sine wave at the zero quantum frequency. (B) 2D ^1H pump–probe NMR spectrum of **47**, in which the vertical dimension corresponds to the evolution during τ . Spectra measured at 600 MHz.

The study establishes the proof of a new concept for observation of fast dynamics with high sensitivity by combining a photochemical pump and NMR detection, which was facilitated by an *in situ* LASER illumination NMR setup.

2.5.5.2.1 Kinetics of hyperpolarized metal dihydrides

After successfully establishing their chemical pump probe with NMR detection (see section 2.5.5.2), the Perutz and Duckett groups used the *in situ* LASER illumination NMR experiment to investigate the kinetics of metal hydride formation for $\text{Ir}(\text{H})_2\text{I}(\text{CO})(\text{PPh}_3)_2$ **48**, which is derived from the iodide analogue of Vaska's complex, $\text{IrI}(\text{CO})(\text{PPh}_3)_2$ **49**

(Fig. 44) [42]. The authors used a single LASER pulse for the kinetic measurements and applied multiple LASER pulses to detect additional intermediates. In the presence of *para*-H₂ at 3 atm and 298 K, the authors observed no polarization, which indicates the stability of the Ir(H)₂(CO)(PPh₃)₂ **48** at room temperature. At 335 K the authors did observe polarization due to the exchange of H₂ with the *para*-H₂. The observed hyperpolarized spectrum is shown in Fig. 44 C. The enormous sensitivity gain in comparison to normal spectra is clearly visible in Figs. 44 E and C.

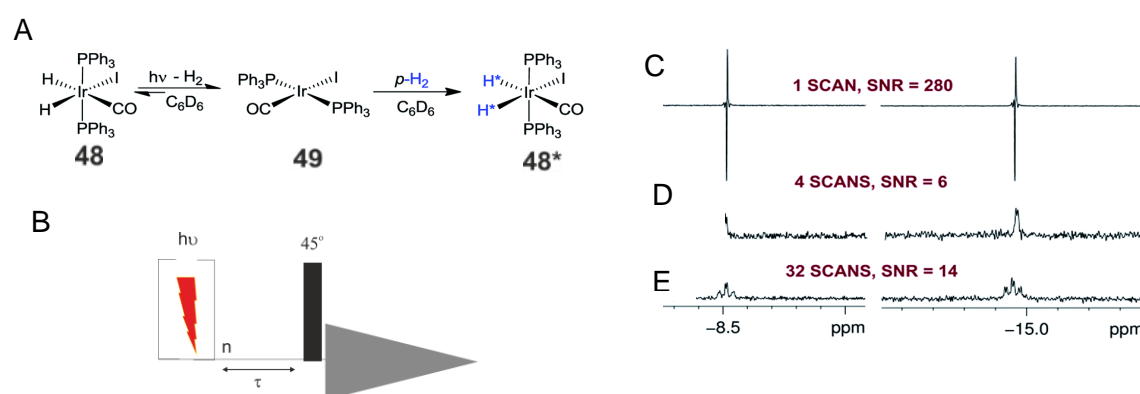


Fig. 44: (A) Reaction scheme for LASER induced reductive elimination of H₂ and oxidative addition of *p*H₂ for Ir(H)₂I(CO)(PPh₃)₂ (B) Photochemical pump and NMR probe pulse sequence Hydride region of a series of ¹H NMR spectra of **48** in C₆D₆ (Right side). (E) The signals are fully relaxed prior to collection (32 scans, SNR = 14) without any decoupling and not polarized (D) The relaxed signals are ³¹P decoupled (4 scans, SNR = 6) but not polarized. (C) The signals are hyperpolarized and ³¹P decoupled (1 LASER pulse, 1 scan, SNR = 280). The values of SNR in (D) and (C) indicate an enhancement factor of 93. Spectra measured at 600 MHz.

In a subsequent step, the authors carried out LASER initiated (355 nm irradiation) reductive elimination of H₂ and oxidative addition of *para*-H₂ to Ir(H)₂I(CO)(PPh₃)₂. The polarized hydrides are observed after a time delay on application of a 45° rf pulse (Fig. 44 C). Unlike in the case of the ruthenium complex RhCl(CO)(PPh₃)₂ discussed in the last section, the authors observed only longitudinal spin order I_zS_z, but no ZQ coherences. The fact that the ZQ coherence of the hydride is dephased indicates a rather slow addition of *para*-H₂. The plot of intensity development versus time delay between the LASER pulse and the rf pulse is shown in Fig. 45 B, which gives the direct concentration dependence in the absence of relaxation as shown for the previous

example of the ruthenium complex $\text{RhCl}(\text{CO})(\text{PPh}_3)_2$ (Fig. 43 A). In the presence of relaxation as in this example, the exponential increase can be fitted to the equation shown in Fig. 45 C.

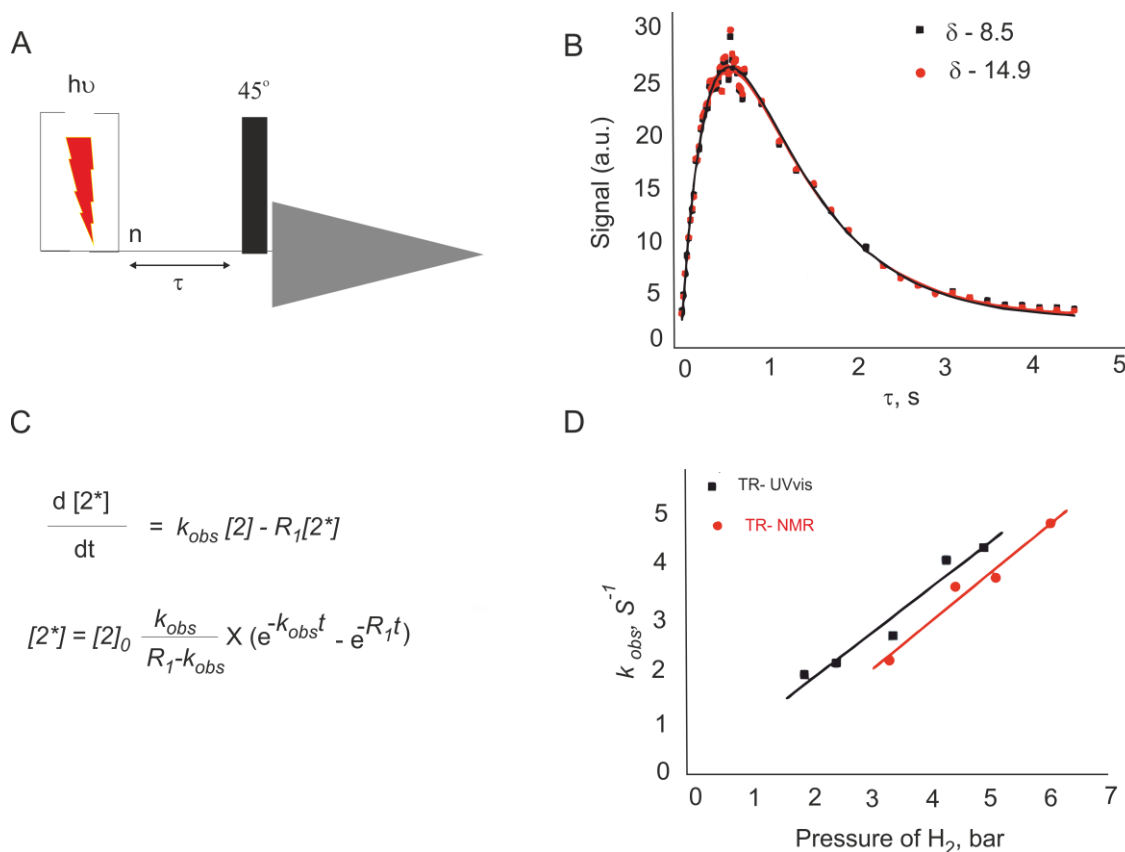


Fig. 45: Monitoring millisecond dynamics of reductive elimination of H_2 and oxidative addition of $p\text{-H}_2$ to $\text{Ir}(\text{H})_2\text{I}(\text{CO})(\text{PPh}_3)_2$. (A) 2D LASER pump-NMR probe pulse sequence for kinetic measurement. (B) Build-up of intensity with time, which directly shows the formation of the H_2 associated complex. (C) Kinetic equation to extract k_{obs} from the data (D) Plot of k_{obs} vs pressure of *para*- H_2 to determine the second order rate constant k_2 . Spectra measured at 600 MHz.

From the 2D experiment after fitting the data to the equation, the authors determined a k_{obs} of $2.1 \pm 0.2 \text{ s}^{-1}$ for H_2 oxidative addition under 3.31 bar of *p*- H_2 . Under excess $p\text{-H}_2$ the reformation of **48** was a pseudo first order reaction. By varying the pressure of H_2 the authors could calculate the k_2 second order rate constant from the different values of k_{obs} . A plot of k_{obs} vs. pressure is given in Fig. 45 D. The second order rate constant k_2 for the regeneration of **48** in the presence of hydrogen as determined from this analysis was $3.26 \pm 0.42 \times 10^2 \text{ M}^{-1} \text{ s}^{-1}$ (with the solubility of H_2 taken as $2.9 \times 10^{-3} \text{ M atm}^{-1}$) at 298 K. This was in good agreement with literature values. To detect other intermediates in the

system, the authors carried out a multiple LASER pulse irradiation. This consists of 48 LASER pulses at 10 Hz repetition rate. After 32 LASER shots, two by-products were observed (Fig. 46). The authors could identify and assign both by-products shown in Fig. 46. They have identified both **48***a and **50***, identification of the new complex **50*** was confirmed by using excess of PPh₃.

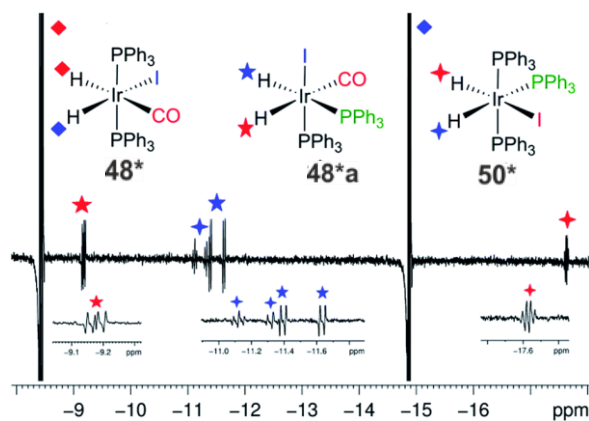


Fig. 46: Generation and detection of additional intermediates by a multiple pulse LASER pump probe experiment. The authors identified **50*** by using excess of PPh₃. Spectra measured at 600 MHz.

In summary, the authors successfully developed a chemical pump probe with NMR detection for higher time resolution and higher sensitivity by combining photolysis and PHIP hyperpolarization concepts. This technique allowed them to follow different faster dynamics associated with organo-metallic complexes, which was illustrated for two complexes.

2.5.5.3 DTS-hv: decrypting transition state combinations by light

Information about transition states is key to understanding reaction mechanisms. However, due to the indefinitely short lifetime of transition states, theoretical calculations are the method of choice to address active transition state combinations and structures of transition states. Experimental information about transition states is very rare, and mainly provided by kinetic isotope effects, which again have to be interpreted using theoretical calculations. In 2017, the Gschwind group developed a concept to address transition state combinations exclusively by experimental investigations, the principal scheme for which is given in Fig. 47 [160]. The prerequisite for the application of this method is an enantioselective catalysis or reaction, in which the major and minor chiral products emerge from the two sides of a pre-equilibrium (see Fig. 47 left side), e.g. Z and E isomers in stereoselective transformations of double bonds. The difficult but key

point is that a stimulus should exist, which exclusively changes the concentrations within this pre-equilibrium but changes nothing else in the whole catalytic mechanism. This is called the decrypter or the external stimulus, being orthogonal to the remaining mechanism. When this condition is met, it is exclusively the concentrations of A and B that change, whereas all other rate constants remain identical. Furthermore, the equilibration of A and B needs to be the rate determining step, or at least contribute to the rate determining step. Given these conditions, i.e. that the overall rate is affected by the change in the concentrations of A and B, the rates and the ee values of the enantioselective catalysis change in a characteristic way for the different transition state combinations, then the experimenter can directly read out the mechanistic pathway. The main challenge is to find an experimental parameter that can act as an orthogonal decrypter, since most of the experimental parameters, such as temperature or concentrations, change a multitude of steps within the reaction mechanism.

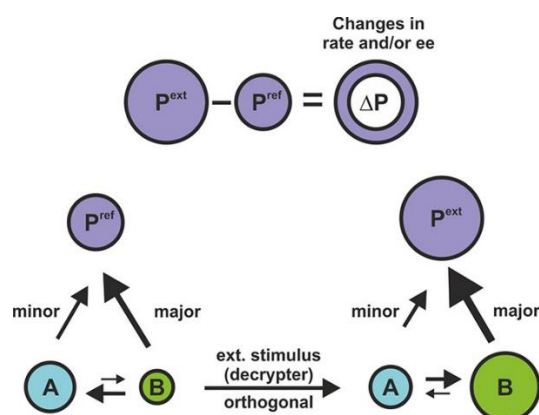


Fig. 47: General scheme showing the principle by which information about transition states can be accessed.

In the field of Brønsted acid catalysis the Gschwind group found such a system in merging their structural NMR investigations of the binary catalyst substrate complexes and their NMR spectroscopic hydrogen bond investigations of these complexes with their *in situ* illumination unit, photoisomerization experience and low temperature methods to make thermally labile photoisomerization states detectable. They called this novel approach Decrypting Transition States by Light (DTS-hv), since light was used as an external decrypter and exploited the influence of E and Z photoisomerization of imines on the reaction rates and the enantiomeric excess (ee). The NMR spectroscopic structural and hydrogen bond investigations of the chiral phosphoric acid TRIP and arylsubstituted imines as substrates revealed that, in contrast to earlier assumptions, there is a slow isomerization between E and Z isomers in these binary complexes, which is a prerequisite that photoisomerization may contribute to the rate determining step.

This point turned out to be critical for understanding the detailed nature of the reaction mechanism, since it opened up the possibility of testing photoisomerization with light as external decrypter in the reactions of these catalyst substrate complexes. Therefore, the photoisomerization was first tested on both free imines and binary complexes (see Fig 48) and indeed, LED-based experiments using illumination at 365 nm were successful in demonstrating photoisomerization of both.

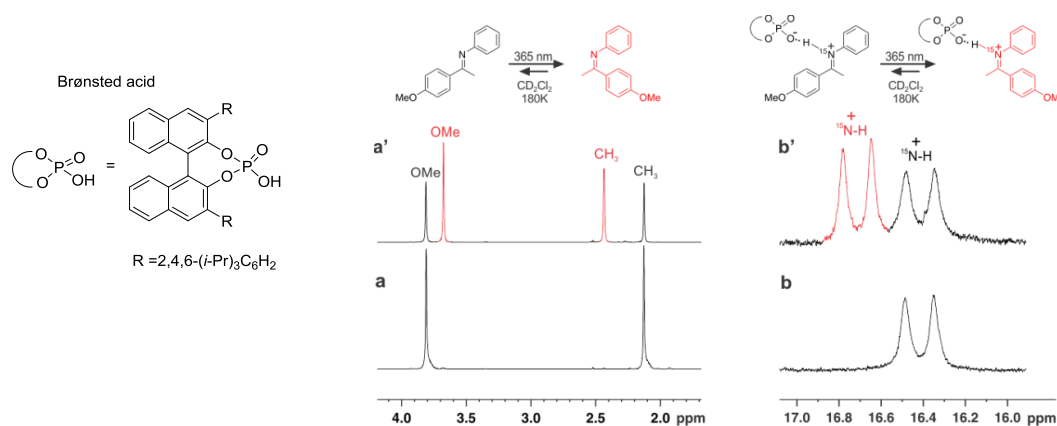


Fig. 48: *In situ* LED NMR ¹H spectra of photoinduced isomerization of imine in presence and absence of Brønsted acid catalyst. Spectra measured at 600 MHz.

Next the effect of such a photoisomerization on stereoselective transformations of double bonds was analysed (see Fig. 49). According to textbook chemistry any double bond can exist in E or Z configuration. Furthermore, the nucleophile (or similarly the electrophile in other reactions) can approach from the top or from the bottom. In combining these possibilities statistically overall eight transition state combinations result (including the differentiation between major and minor pathways). However, usually the stereochemistry (R or S) of the major product of such an enantioselective catalysis is known simply from chiral HPLC analysis and this reduces the eight possible transition state combinations to four leading to the stereochemistry of the known major product. For example, using the transition state nomenclature developed by Himo and Goodman[161-163] for Brønsted acid catalysed stereoselective transformations and assuming the R being the stereochemistry of the major product, four transition state combinations **Type I Z**/Type I E, **Type I Z**/Type II Z, **Type II E**/Type I E, **Type II E**/Type II Z are possible. In each of these transition state combinations the first pathway given in bold letters denotes the energetically lower transition state towards the major R product, while the second transition state leads to the minor product S. Furthermore, Type I denotes attack from the bottom, while Type II stands for attack from the top. Now the effect of photoisomerization of the E imine into the Z imine on rates and ee-values is

explained for the four different transition state combinations (see Fig. 49 B). For **Type I Z/Type II Z** photoisomerization increases the concentration of the reactive Z imine and thus the overall reaction rate. However, the ee-value is constant, because both major and minor product are formed over Z-transition states. Similarly, for **Type II E/Type I E** transition state combinations the ee-value is not affected but the overall rate is reduced due to the depletion of the E imine population. In the case of the mixed transition state combinations **Type I Z/Type I E** and **Type II E/Type II Z** both rates and ee-values are affected, with the first one being the optimum for catalysis by increasing both rate and ee, while the latter is the worst case decreasing both.

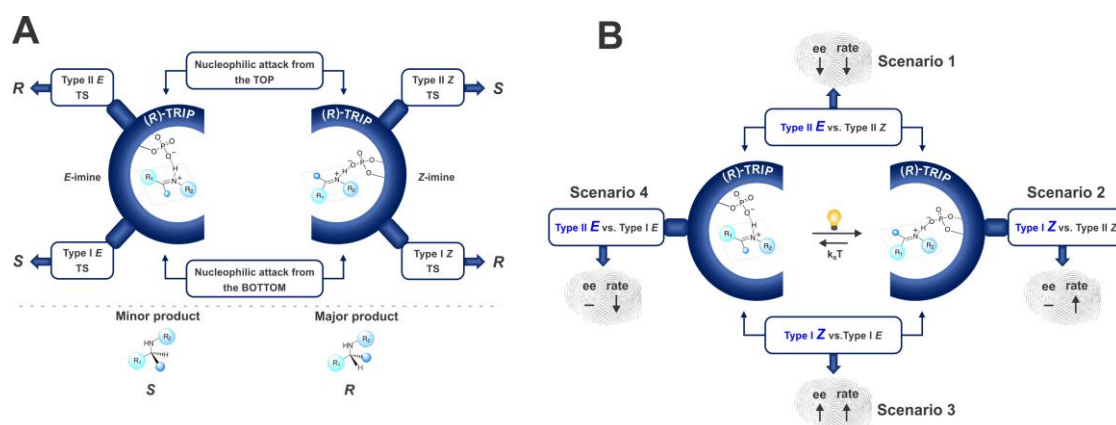


Fig. 49: Graphical illustration of reaction model (A), and possible scenarios for observed major enantiomeric product R (B).

For the case of Brønsted acid catalysed stereoselective reduction of imines with Hantzsch ester as reductant and the R-amine as major product, a **Type I Z/Type I E** transition state combination was predicted by theoretical calculations, while a **Type II E/Type I E** combination was predicted for the transformation of aldimines. Therefore, next the effect of photoisomerization was tested on two synthetic model systems, the asymmetric transfer hydrogenation of imines with Hantzsch ester and an asymmetric alkylation of aldimines under conditions typically used in synthetic applications. On photoisomerization of ketimines from E to Z an increase in rate (yield) and similar ee values (Fig. 50 A) were observed for a multitude of ketimine systems. This revealed that the transition state combination that is active is from scenario 2, **Type I Z/Type II Z**, which represents a deviation from the predictions of theoretical calculations. Our structure investigations of the binary complexes together with theoretical calculations revealed the reason of this offset, which is the slow isomerization of E imines to Z imines directly visible in the NMR spectra of the binary complexes (see Fig. 50 B), which had been assumed to be fast in the previous calculations. In contrast to the ketimine case, a

drop in rate and almost no change of *ee* value was observed for aldimines, revealing that for them scenario 4 is active, i.e a **Type II E**/Type I E, as previously predicted by theoretical calculation.

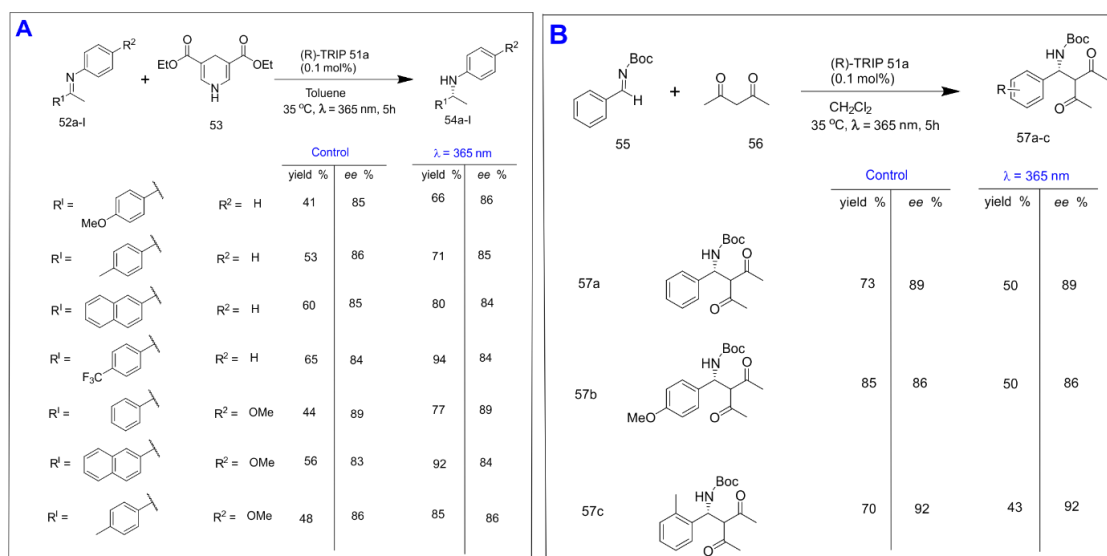


Fig. 50: (A) Relative comparison of rate and *ee* in Brønsted acid catalysed asymmetric hydrogenation of ketimines under standard conditions and during photoisomerization (B) Relative comparison of rate and *ee* in Brønsted acid catalysed asymmetric alkylation of aldimines under standard conditions and during photoisomerization.

Overall, this approach is a general and unprecedented method to get experimental insight into transition state combinations during stereoselective catalysis and was the first of its kind to use light to access mechanistic information about transition state combinations in light-independent organo-catalysis. The revealed the breadth of the DTS-hv method and hints at possible expansion to other systems.

2.5.5.4 Internal light intensity and quantum yield determination

Quantum yields are fundamental mechanistic parameters in describing photocatalysis, providing key information about the photochemical process or the photoinitiated free radical polymerization. Usually external measurements were applied to determine both quantum yields and light intensities. However, the observed absolute light intensity inside the NMR tubes in the *in situ* NMR illumination apparatus is always different from that externally measured. Therefore, using the externally measured intensity for quantitative analysis can lead to errors. In 2018 Ji *et al.*, developed an elegant method for quantifying quantum yield and internal light intensity inside the *in situ* illuminated NMR tube[37]. Such internal light intensity measurements will be very advantageous in

monitoring and optimising the apparatus, especially for testing new LEDs and optical fibres, and as well as to monitor degradation of LEDs and fibres. Furthermore, the method will greatly assist in maintaining similar illumination conditions throughout an investigation or in accounting for any errors. The measurement of quantum yields by using the *in situ* LED NMR method as described below is another advantage of this approach as it makes it possible to determine this key parameter in photocatalysis under exactly the same conditions as the NMR measurements.

The reported method is simple, easy to conduct and measurements can be done on a single sample, which minimises the experimental error. The authors illustrated the method using the known ferrioxalate (for 200-500 nm range) and *o*-nitrobenzaldehyde (365 nm) chemical actinometers (an actinometer is a system for measuring the photon flux in a light beam, in this case by exploiting a photochemical reaction of previously known quantum yield). In addition they have introduced a new actinometer, 2,4-dinitrobenzaldehyde (2,4-DNBA), for the 440 nm range. Initially, the method involves the rate measurement of the photochemical reaction for a known actinometer (for example *o*-nitrobenzaldehyde, 300-400 nm, $\phi = 0.5$) as a function of concentration. These data are then fitted to equation 1 to extract the intensity of the light I_0 and molecular absorptivity (ϵ), in case both are required (Fig. 51). When only I_0 is required, e.g for recalibration of LEDs, one can also use the simpler equation 2 to extract I_0 with a single highly concentrated solution (i.e. under zeroth order condition). Once the light intensity (I_0) of the LED has been established in this way, one can analyse the reaction of interest so as to extract its quantum yield by measuring the rate under zeroth order conditions and applying equation 2.

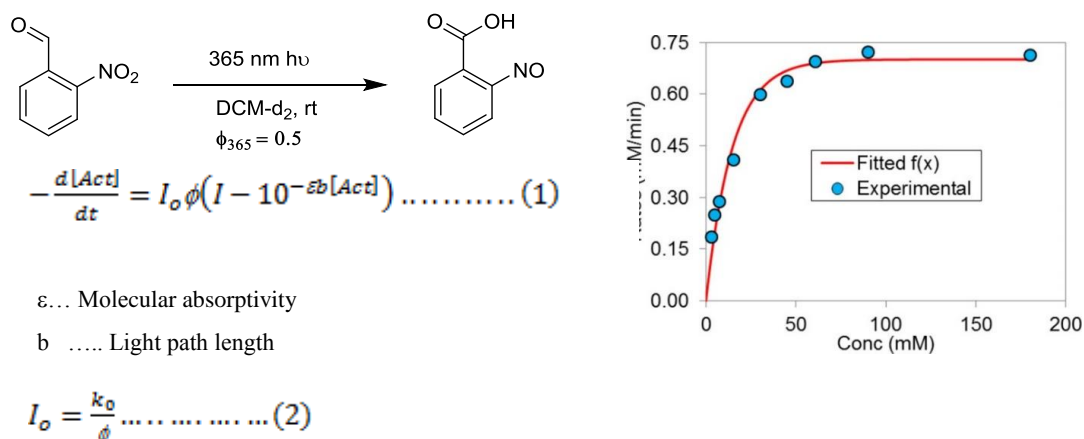


Fig. 51: Protocol for internal intensity and quantum yield measurement inside the NMR tube. The above reaction scheme shows the photochemical reaction of a known chemical actinometer (*o*-nitrobenzaldehyde). Initially, a plot of photochemical reaction rate for *o*-nitrobenzaldehyde versus concentration is obtained and fitted to equation (1) to determine light intensity and molecular absorptivity (ϵ) for the particular apparatus being used. Subsequently, the rate constant at zeroth order condition (i.e. at high concentration of photocatalyst or substrate) for the reaction of interest is measured and, together with the I_0 value determined using the measurements with the actinometer, used to calculate the quantum yield according to equation 2. Spectra measured at 600 MHz.

The method was illustrated for the photocatalytic C–H fluorination of leucine methyl ester, which is shown in Fig. 52. First I_0 was determined by using *o*-nitrobenzaldehyde (300–400 nm $\phi = 0.5$) as an actinometer. The authors obtained the intensity of light (I_0 , $23.4 \mu\text{einstein L}^{-1} \text{s}^{-1}$) and also the molecular absorptivity (ϵ , $265 \text{ M}^{-1} \text{cm}^{-1}$) by fitting measured rates with different concentrations to equation 1 of Fig. 51.

In the next step the authors measured the quantum yield for photocatalytic C–H fluorination of leucine methyl ester (Fig. 52) and determined the quantum yield to be 0.22 by using the known intensity of light and the measured rate of the fluorination under zeroth order condition. In addition, they compared rates at two concentrations of the catalyst, 2.5 and 10 mol %, and found similar rates, thus confirming that the assumption of zeroth order condition was valid.

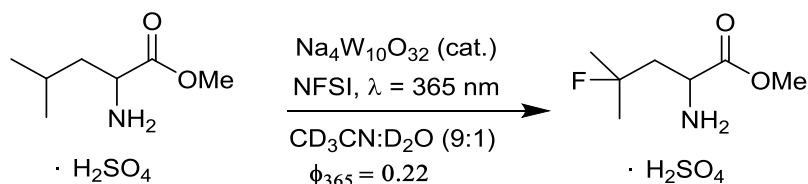


Fig. 52: Photocatalytic C-H Fluorination of leucine methyl ester, as used to illustrate quantum yield measurement inside the NMR tube (see text). The obtained quantum yield was 0.22.

Unfortunately, the *o*-nitrobenzaldehyde NMR actinometer cannot absorb in the visible region. To measure quantum yields in the visible region (440 nm) with a diamagnetic actinometer, the authors developed an additional chemical actinometer 2,4-dinitrobenzaldehyde (2,4-DNBA), which gives a quantum yield of 1 at 365 nm and 0.08 at 440 nm. To illustrate the utility of this new actinometer, they measured the quantum yield of the photocatalytic dehydrogenation reaction shown in Fig. 53. In this case, the photocatalyst absorbs at 440 nm, and the obtained quantum yield based on 2,4-dinitrobenzaldehyde is 0.38, close to the value of 0.4 obtained from standard ferrioxalate method.

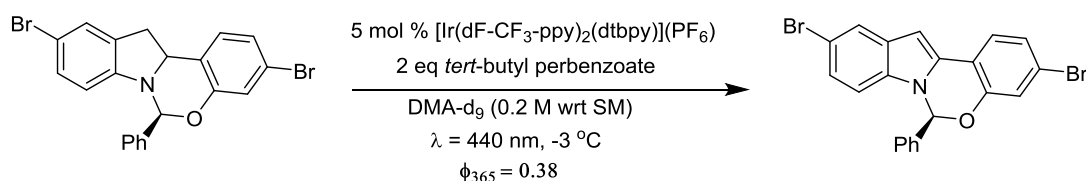


Fig. 53: Illustration of quantum yield measurement inside the NMR tube in the visible region using a newly developed chemical actinometer (2, 4-dinitrobenzaldehyde). This was demonstrated using photocatalytic indoline oxidation, and the quantum yield obtained was 0.38.

The *in situ* quantum yield determination method discussed above is expected to be very valuable as an alternative tool to calibrate *ex situ* optical experiments, especially in cases where *in situ* experiments are already established. Furthermore the method can be very useful in calibration of LEDs and fibres, which can assist in reproducibility of the photochemical process.

2.6 Conclusion and Outlook

The application of light to drive organic reactions and transformations in photocatalysis and photoswitches has seen an exponential growth in the last decade. Although the vast number of synthetic approaches is impressive, there is still significant scope for improvement with respect to the characterization of structural and mechanistic aspects of these reactions. This review surveys the growing significance of NMR spectroscopy in investigations of light-driven systems, as a complementary method to established techniques such as EPR and UV/Vis spectroscopy.

In the experimental part we present the emergence of LASERs and LEDs as the dominating light sources for NMR investigations and discuss their pros and cons depending on the desired application. Here it becomes clear, that LASERs are the illumination source of choice if maximum light intensity and wavelength selectivity is needed (e.g. photo-CIDNP studies). In contrast, LEDs represent the “allrounder” amongst illumination sources and can be applied as illumination source in any NMR investigation (e.g. photocatalysis, photoswitches, steady state photo-CIDNP etc.). In addition, *ex situ* and *in situ* techniques are listed and explained as general approaches for illuminated NMR investigations. While *ex situ* techniques are straight-forward and become the method of choice if an investigated system consumes or produces gases, the *in situ* technique has established itself as the preferred option if detailed studies about reaction progression and/or (short lived) intermediates are required. Furthermore, the comprehensive discussion of *in situ* illumination NMR from the bottom/side, from the inside, and from the top showed that the initial designs, which were presented in the late 1970s and early 1980s, were in principle not changed. Nevertheless, over the last decades refinements such as the position or treatment of the glass fiber sometimes drastically increased the performance of the system. Comparing all *in situ* approaches, it is evident that (especially in combination with LEDs) *in situ* illumination from the inside has established itself as the most widely applicable arrangement for illuminating NMR samples. Nevertheless, illumination from the bottom/side and the top are still commonly used for applications that require maximum light output (photo-CIDNP). In addition, special designs such as UVNMR(-illumination), flow systems, NMR on a Chip etc. push the boundaries of illumination NMR spectroscopy. The creativity and number of these approaches show that photo-NMR still has a lot of untapped potential and will most likely continue to grow in the future.

The applications part shows elaborate case studies in the field of photocatalysis, photoswitches and new methodical approaches in *in situ* illumination NMR. We survey the evolution of *in situ* illumination NMR as an investigation tool being solely focused on photo-CIDNP studies (not discussed in this review) towards a broadly applicable method for mechanistic investigations in photosystems. Nowadays, especially in photocatalysis, illumination NMR provides detailed information about reaction kinetics, solvent effects, intermediate structures and exchange processes, which are readily combined with information gained from EPR and transient spectroscopy. The development of these investigations in photocatalysis and the different aspects in terms of NMR techniques are exemplified on various studies. In addition, we highlight the *in situ* investigation of photoswitches. Here, *in situ* illumination NMR became a valuable tool to simultaneously gain structural and quantitative insights. Furthermore, some prominent examples from photoinitiated polymerization studies are discussed. At last, we present a selection of novel NMR illumination techniques that focus on different aspects of NMR spectroscopy. These include photoswitches that generate paramagnetic species to proliferate T1 relaxation properties, a photoisomerization approach that can give experimental insight into transition state combinations and a novel technique to determine quantum yields by *in situ* illumination NMR. Although illumination NMR has seen tremendous growth in the recent decade, we think that the potential of the developed techniques and applications have only scratched the surface so far and we will witness a continuous rise of NMR as a method in photodriven systems in the future

2.7 References

- [1] I. Ghosh, L. Marzo, A. Das, R. Shaikh, B. König, Visible Light Mediated Photoredox Catalytic Arylation Reactions, *Acc. Chem. Res.* 49 (2016) 1566–1577. doi:10.1021/acs.accounts.6b00229.
- [2] B. König, Photocatalysis in Organic Synthesis - Past, Present, and Future, *European J. Org. Chem.* 2017 (2017) 1979–1981. doi:10.1002/ejoc.201700420.
- [3] L. Marzo, S.K. Pagire, O. Reiser, B. König, Visible-Light Photocatalysis: Does It Make a Difference in Organic Synthesis?, *Angew. Chemie Int. Ed.* 57 (2018) 10034–10072. doi:10.1002/anie.201709766.
- [4] L. Buzzetti, G.E.M. Crisenza, P. Melchiorre, Mechanistic Studies in Photocatalysis, *Angew. Chemie Int. Ed.* (2019) 3730–3747. doi:10.1002/anie.201809984.
- [5] K. Zeidler, Photoredox Catalysis with Visible Light, *Angew. Chemie Int. Ed.* 48 (2009) 9785–9789. doi:10.1002/anie.200904056.
- [6] M. Majek, A. Jacobi von Wangelin, Mechanistic Perspectives on Organic Photoredox Catalysis for Aromatic Substitutions, *Acc. Chem. Res.* 49 (2016) 2316–2327. doi:10.1021/acs.accounts.6b00293.
- [7] Y. Zhang, J. Kubicki, M.S. Platz, Ultrafast UV–Visible and Infrared Spectroscopic Observation of a Singlet Vinylcarbene and the Intramolecular Cyclopropanation Reaction, *J. Am. Chem. Soc.* 131 (2009) 13602–13603. doi:10.1021/ja905992p.
- [8] J. Wang, G. Burdzinski, J. Kubicki, M.S. Platz, Ultrafast UV–Vis and IR Studies of *p*-Biphenyl Acetyl and Carbomethoxy Carbenes, *J. Am. Chem. Soc.* 130 (2008) 11195–11209. doi:10.1021/ja803096p.
- [9] P.K. Verma, F. Koch, A. Steinbacher, P. Nuernberger, T. Brixner, Ultrafast UV-Induced Photoisomerization of Intramolecularly H-Bonded Symmetric β -Diketones, *J. Am. Chem. Soc.* 136 (2014) 14981–14989. doi:10.1021/ja508059p.
- [10] E. Riedle, M.K. Roos, S. Thallmair, C.F. Sailer, N. Krebs, B.P. Fingerhut, R. de Vivie-Riedle, Ultrafast photochemistry with two product channels: Wavepacket motion through two distinct conical intersections, *Chem. Phys. Lett.* 683 (2017) 128–134. doi:10.1016/j.cplett.2017.02.086.
- [11] U. Megerle, M. Wenninger, R.-J. Kutta, R. Lechner, B. König, B. Dick, E. Riedle, Unraveling the flavin-catalyzed photooxidation of benzylic alcohol with transient absorption spectroscopy from sub-pico- to microseconds, *Phys. Chem. Chem. Phys.* 13 (2011) 8869. doi:10.1039/c1cp20190e.
- [12] J. Xue, H.L. Luk, S. V. Eswaran, C.M. Hadad, M.S. Platz, Ultrafast infrared and UV-vis studies of the photochemistry of methoxycarbonylphenyl azides in solution, *J. Phys. Chem. A.* 116 (2012) 5325–5336. doi:10.1021/jp3025705.
- [13] M. Goswami, A. Chirila, C. Rebreyend, B. de Bruin, *EPR Spectroscopy as a Tool in Homogeneous Catalysis Research*, Springer US, 2015. doi:10.1007/s11244-015-0414-9.
- [14] K.C. Christoforidis, M. Louloudi, E.R. Milaeva, Y. Sanakis, Y. Deligiannakis, EPR study of a novel [Fe-porphyrin] catalyst, *Mol. Phys.* 105 (2007) 2185–2194.

- doi:10.1080/00268970701749260.
- [15] T. Risse, D. Hollmann, A. Brückner, In situ electron paramagnetic resonance (EPR) -a unique tool for analysing structure and reaction behaviour of paramagnetic sites in model and real catalysts, *Catalysis* 27 (2015) 1-32. doi:10.1039/9781782622697-00001.
- [16] C.G.S. Lima, T.D.M. Lima, M. Duarte, I.D. Jurberg, M.W. Paixão, Organic Synthesis Enabled by Light-Irradiation of EDA Complexes: Theoretical Background and Synthetic Applications, *ACS Catal.* 6 (2016) 1389–1407. doi:10.1021/acscatal.5b02386.
- [17] B. Liu, C.H. Lim, G.M. Miyake, Visible-light-promoted C-S cross-coupling via intermolecular charge transfer, *J. Am. Chem. Soc.* 139 (2017) 13616–13619. doi:10.1021/jacs.7b07390.
- [18] J. Sun, Y. He, X. De An, X. Zhang, L. Yu, S. Yu, Visible-light-induced iminyl radical formation: Via electron-donor-acceptor complexes: A photocatalyst-free approach to phenanthridines and quinolines, *Org. Chem. Front.* 5 (2018) 977–981. doi:10.1039/c7qo00992e.
- [19] I. Ghosh, R.S. Shaikh, B. Kçnig, Communications Photocatalysis Very Important Paper Sensitization-Initiated Electron Transfer for Photoredox Catalysis *Angew. Chemie Int. Ed.*, 56 (2017) 8544–8549. doi:10.1002/anie.201703004.
- [20] M. Goetz, Chapter 3 Photo-CIDNP Spectroscopy, in: *Annu. Reports NMR Spectrosc.*, 1st ed., Elsevier Ltd., 2009: pp. 77–147. doi:10.1016/S0066-4103(08)00403-1.
- [21] R. Kaptein, Photo-CIDNP Studies of Proteins, in: *Biol. Magn. Reson.*, Springer US, Boston, MA, 1982: pp. 145–191. doi:10.1007/978-1-4615-6540-6_3.
- [22] M. Goetz, I. Sartorius, CIDNP Determination of the Rate of In-Cage Deprotonation of the Triethylamine Radical Cation, *J. Phys. Chem. A.* 107 (2003) 8539–8546. doi:10.1021/jp030244g.
- [23] I. Kuprov, M. Goetz, P.A. Abbott, P.J. Hore, Design and performance of a microsecond time-resolved photo-chemically induced dynamic nuclear polarization add-on for a high-field nuclear magnetic resonance spectrometer, *Rev. Sci. Instrum.* 76 (2005) 84103. doi:10.1063/1.2010287.
- [24] M.B. Schmid, K. Zeitler, R.M. Gschwind, The elusive enamine intermediate in proline-catalyzed aldol reactions: NMR detection, formation pathway, and stabilization trends, *Angew. Chemie Int. Ed.* 49 (2010) 4997–5003. doi:10.1002/anie.200906629.
- [25] N. Lokesh, A. Seegerer, J. Hioe, R.M. Gschwind, Chemical exchange saturation transfer in chemical reactions: A mechanistic tool for NMR detection and characterization of transient intermediates, *J. Am. Chem. Soc.* 140 (2018) 1855–1862. doi:10.1021/jacs.7b12343.
- [26] J. Greindl, J. Hioe, N. Sorgenfrei, F. Morana, R.M. Gschwind, Brønsted Acid Catalysis-Structural Preferences and Mobility in Imine/Phosphoric Acid Complexes, *J. Am. Chem. Soc.* 138 (2016) 15965–15971. doi:10.1021/jacs.6b09244.
- [27] N. Sorgenfrei, J. Hioe, J. Greindl, K. Rothermel, F. Morana, N. Lokesh, R.M.

- Gschwind, NMR Spectroscopic Characterization of Charge Assisted Strong Hydrogen Bonds in Brønsted Acid Catalysis, *J. Am. Chem. Soc.* 138 (2016) 16345–16354. doi:10.1021/jacs.6b09243.
- [28] J. Daďová, S. Kümmel, C. Feldmeier, J. Cibulková, R. Pažout, J. Maixner, R.M. Gschwind, B. König, R. Cibulka, Aggregation effects in visible-light flavin photocatalysts: Synthesis, structure, and catalytic activity of 10-arylflavins, *Chem. A Eur. J.* 19 (2013) 1066–1075. doi:10.1002/chem.201202488.
- [29] M.H. Haindl, J. Hioe, R.M. Gschwind, The Proline Enamine Formation Pathway Revisited in Dimethyl Sulfoxide: Rate Constants Determined via NMR, *J. Am. Chem. Soc.* 137 (2015) 12835–12842. doi:10.1021/jacs.5b03420.
- [30] M.C. Holland, R. Gilmour, Deconstructing covalent organocatalysis, *Angew. Chemie Int. Ed.* 54 (2015) 3862–3871. doi:10.1002/anie.201409004.
- [31] C. Feldmeier, H. Bartling, K. Magerl, R.M. Gschwind, vLED-Illuminated NMR Studies of Flavin-Catalyzed Photooxidations Reveal Solvent Control of the Electron-Transfer Mechanism, *Angew. Chemie Int. Ed.* 54 (2015) 1347–1351. doi:10.1002/anie.201409146.
- [32] H. Bartling, A. Eisenhofer, B. König, R.M. Gschwind, The Photocatalyzed Aza-Henry Reaction of N-Aryltetrahydroisoquinolines: Comprehensive Mechanism, H⁻ versus H⁺-Abstraction, and Background Reactions, *J. Am. Chem. Soc.* 138 (2016) 11860–11871. doi:10.1021/jacs.6b06658.
- [33] K. Chen, N. Berg, R. Gschwind, B. König, Selective Single C(sp³)-F Bond Cleavage in Trifluoromethylarenes: Merging Visible-Light Catalysis with Lewis Acid Activation, *J. Am. Chem. Soc.* 139 (2017) 18444–18447. doi:10.1021/jacs.7b10755.
- [34] D. Petzold, P. Nitschke, F. Brandl, V. Scheidler, B. Dick, R.M. Gschwind, B. König, Visible-Light-Mediated Liberation and In Situ Conversion of Fluorophosgene, *Chem. A Eur. J.* 25 (2019) 361–366. doi:10.1002/chem.201804603.
- [35] S. Wang, L. Nanjundappa, J. Hioe, R.M. Gschwind, B. Koenig, Photoinitiated Carbonyl-Metathesis: Deoxygenative Reductive Olefination of Aromatic Aldehydes via Photoredox Catalysis, *Chem. Sci.* 10 (2019) 4580–4587. doi:10.1039/C9SC00711C.
- [36] E. Procházková, L. Čechová, J. Kind, Z. Janeba, C.M. Thiele, M. Dračinský, Photoswitchable Intramolecular Hydrogen Bonds in 5-Phenylazopyrimidines Revealed By In Situ Irradiation NMR Spectroscopy, *Chem. A Eur. J.* 24 (2018) 492–498. doi:10.1002/chem.201705146.
- [37] Y. Ji, D.A. DiRocco, C.M. Hong, M.K. Wismer, M. Reibarkh, Facile Quantum Yield Determination via NMR Actinometry, *Org. Lett.* 20 (2018) 2156–2159. doi:10.1021/acs.orglett.8b00391.
- [38] D. Lehnher, Y. Ji, A.J. Neel, R.D. Cohen, A.P.J. Brunskill, J. Yang, M. Reibarkh, Discovery of a Photoinduced Dark Catalytic Cycle Using in Situ LED-NMR Spectroscopy, *J. Am. Chem. Soc.* 140 (2018) 13843–13853. doi:10.1021/jacs.8b08596.
- [39] S. Hecht, N.D. Dolinski, Z.A. Page, J. Read de Alaniz, J. Niu, F. Eisenreich, C.J. Hawker, A Versatile Approach for In Situ Monitoring of Photoswitches and Photopolymerizations, *ChemPhotoChem.* 1 (2017) 125–131.

doi:10.1002/cptc.201600045.

- [40] J. Niu, Z.A. Page, N.D. Dolinski, A. Anastasaki, A.T. Hsueh, H.T. Soh, C.J. Hawker, Rapid Visible Light-Mediated Controlled Aqueous Polymerization with in Situ Monitoring, *ACS Macro Lett.* 6 (2017) 1109–1113. doi:10.1021/acsmacrolett.7b00587.
- [41] N.D. Dolinski, Z.A. Page, E.H. Discekici, D. Meis, I.H. Lee, G.R. Jones, R. Whitfield, X. Pan, B.G. McCarthy, S. Shanmugam, V. Kottisch, B.P. Fors, C. Boyer, G.M. Miyake, K. Matyjaszewski, D.M. Haddleton, J.R. de Alaniz, A. Anastasaki, C.J. Hawker, What happens in the dark? Assessing the temporal control of photo-mediated controlled radical polymerizations, *J. Polym. Sci. Part A Polym. Chem.* 57 (2019) 268–273. doi:10.1002/pola.29247.
- [42] S.B. Duckett, R.N. Perutz, P.M. Aguiar, B. Procacci, M.E. Halse, Photochemical pump and NMR probe to monitor the formation and kinetics of hyperpolarized metal dihydrides, *Chem. Sci.* 7 (2016) 7087–7093. doi:10.1039/c6sc01956k.
- [43] O. Torres, B. Procacci, M.E. Halse, R.W. Adams, D. Blazina, S.B. Duckett, B. Eguillor, R.A. Green, R.N. Perutz, D.C. Williamson, Photochemical pump and NMR probe: Chemically created NMR coherence on a microsecond time scale, *J. Am. Chem. Soc.* 136 (2014) 10124–10131. doi:10.1021/ja504732u.
- [44] J. Hore, R.W. Broadhurst, Photo-CIDNP of biopolymers, *Prog. Nucl. Magn. Reson. Spectrosc.* 25 (1993) 345–402. doi:10.1016/0079-6565(93)80002-B.
- [45] I. Ghosh, T. Ghosh, J.I. Bardagi, B. Konig, Reduction of aryl halides by consecutive visible light-induced electron transfer processes, *Science* 346 (2014) 725–728. doi:10.1126/science.1258232.
- [46] M. Khademalrasool, M. Farbod, M.D. Talebzadeh, The improvement of photocatalytic processes: Design of a photoreactor using high-power LEDs, *J. Sci. Adv. Mater. Devices.* 1 (2016) 382–387. doi:10.1016/j.jsamd.2016.06.012.
- [47] W.K. Jo, R.J. Tayade, New generation energy-efficient light source for photocatalysis: LEDs for environmental applications, *Ind. Eng. Chem. Res.* 53 (2014) 2073–2084. doi:10.1021/ie404176g.
- [48] S. Das, W.M.A. Wan Daud, A review on advances in photocatalysts towards CO₂ conversion, *RSC Adv.* 4 (2014) 20856–20893. doi:10.1039/c4ra01769b.
- [49] M. Goez, I. Sartorius, Photo-CIDNP investigation of the deprotonation of aminium cations, *J. Am. Chem. Soc.* 115 (1993) 11123–11133. doi:10.1021/ja00077a009.
- [50] D.E. Fast, A. Lauer, J.P. Menzel, A.M. Kelterer, G. Gescheidt, C. Barner-Kowollik, Wavelength-Dependent Photochemistry of Oxime Ester Photoinitiators, *Macromolecules.* 50 (2017) 1815–1823. doi:10.1021/acs.macromol.7b00089.
- [51] E. Stadler, A. Eibel, D. Neshchadin, G. Gescheidt, Toward Matching Optically and NMR Active Volumes for Optimizing the Observation of Photo-Induced Reactions by NMR, *Zeitschrift Fur Phys. Chemie.* 231 (2017) 625–636. doi:10.1515/zpch-2016-0854.
- [52] J.C. Zill, J. Matysik, C. Wilhelm, L. Köhler, M. Kansy, R. Goss, A. Alia, Photo-CIDNP in the Reaction Center of the Diatom *Cyclotella meneghiniana* Observed by ¹³C MAS NMR, *Zeitschrift Für Phys. Chemie.* 231 (2016) 347–367. doi:10.1515/zpch-2016-0806.

- [53] H.C. Siebert, R. Kaptein, J.J. Beintema, U.M. Soedjanaatmadja, C.S. Wright, A. Rice, R.G. Kleineidam, S. Kruse, R. Schauer, P.J.W. Pouwels, J.P. Kamerling, H.J. Gabius, J.F.G. Vliegthart, Carbohydrate-protein interaction studies by laser photo CIDNP NMR methods, *Glycoconj. J.* 14 (1997) 531–534. doi:10.1023/A:1018572023153.
- [54] O.B. Morozova, R. Kaptein, R.Z. Sagdeev, A. V. Yurkovskaya, Reduction of Guanosyl Radicals in Reactions with Proteins Studied by TR-CIDNP, *Appl. Magn. Reson.* 44 (2013) 233–245. doi:10.1007/s00723-012-0403-0.
- [55] O.B. Morozova, R. Kaptein, A. V. Yurkovskaya, Reduction of guanosyl radical by cysteine and cysteine-glycine studied by time-resolved CIDNP, *J. Phys. Chem. B.* 116 (2012) 8058–8063. doi:10.1021/jp301760b.
- [56] Y. Okuno, S. Cavagnero, Fluorescein: A Photo-CIDNP Sensitizer Enabling Hypersensitive NMR Data Collection in Liquids at Low Micromolar Concentration, *J. Phys. Chem. B.* 120 (2016) 715–723. doi:10.1021/acs.jpccb.5b12339.
- [57] A. De Marco, A.M. Petros, M. Llinás, R. Kaptein, R. Boelens, Ligand-binding effects on the kringle 4 domain from human plasminogen: a study by laser photo-CIDNP 1H-NMR spectroscopy, *Biochim. Biophys. Acta (BBA)/Protein Struct. Mol.* 994 (1989) 121–137. doi:10.1016/0167-4838(89)90151-9.
- [58] A. Mills, C. O'Rourke, In Situ, Simultaneous Irradiation and Monitoring of a Photocatalyzed Organic Oxidation Reaction in a TiO₂-Coated NMR Tube, *J. Org. Chem.* 80 (2015) 10342–10345. doi:10.1021/acs.joc.5b01001.
- [59] L. Bliumkin, R. Dutta Majumdar, R. Soong, A. Adamo, J.P.D. Abbatt, R. Zhao, E. Reiner, A.J. Simpson, Development of an in Situ NMR Photoreactor to Study Environmental Photochemistry, *Environ. Sci. Technol.* 50 (2016) 5506–5516. doi:10.1021/acs.est.6b00361.
- [60] X.L. Wang, W. Liu, Y. Yu, Y. Song, W.Q. Fang, D. Wei, X. Gong, Y. Yao, H.G. Yang, Operando NMR spectroscopic analysis of proton transfer in heterogeneous photocatalytic reactions, *Nat. Commun.* 7 (2016) 1–7. doi:10.1038/ncomms11918.
- [61] E.B. Gaeva, V. Pimienta, S. Delbaere, A.V. Metelitsa, N.A. Voloshin, V.I. Minkin, G. Vermeersch, J.C. Micheau, Spectral and kinetic properties of a red–blue pH-sensitive photochromic spirooxazine, *J. Photochem. Photobiol. A Chem.* 191 (2007) 114–121. doi:10.1016/j.jphotochem.2007.04.011.
- [62] J. Kind, L. Kaltschnee, M. Leyendecker, C.M. Thiele, Distinction of trans–cis photoisomers with comparable optical properties in multiple-state photochromic systems – examining a molecule with three azobenzenes via in situ irradiation NMR spectroscopy, *Chem. Commun.* 52 (2016) 12506–12509. doi:10.1039/C6CC06771A.
- [63] M.V. Gomez, A. Juan, F. Jiménez-Márquez, A. de la Hoz, A.H. Velders, Illumination of Nanoliter-NMR Spectroscopy Chips for Real-Time Photochemical Reaction Monitoring, *Anal. Chem.* 90 (2018) 1542–1546. doi:10.1021/acs.analchem.7b04114.
- [64] D.M. Schultz, F. Lévesque, D.A. DiRocco, M. Reibarkh, Y. Ji, L.A. Joyce, J.F. Dropinski, H. Sheng, B.D. Sherry, I.W. Davies, Oxyfunctionalization of the Remote C–H Bonds of Aliphatic Amines by Decatungstate Photocatalysis, *Angew. Chemie Int. Ed.* 56 (2017) 15274–15278. doi:10.1002/anie.201707537.

- [65] N. Mallo, P.T. Brown, H. Iranmanesh, T.S.C. MacDonald, M.J. Teusner, J.B. Harper, G.E. Ball, J.E. Beves, Photochromic switching behaviour of donor–acceptor Stenhouse adducts in organic solvents, *Chem. Commun.* 52 (2016) 13576–13579. doi:10.1039/C6CC08079K.
- [66] J. Bernarding, F. Euchner, C. Bruns, R. Ringleb, D. Müller, T. Trantzschel, J. Bargon, U. Bommerich, M. Plaumann, Low-cost LED-based Photo-CIDNP Enables Biocompatible Hyperpolarization of ¹⁹F for NMR and MRI at 7 T and 4.7 T, *ChemPhysChem.* 19 (2018) 2453–2456. doi:10.1002/cphc.201800570.
- [67] Y. Narukawa, M. Ichikawa, D. Sanga, M. Sano, T. Mukai, White light emitting diodes with super-high luminous efficacy, *J. Phys. D. Appl. Phys.* 43 (2010) 1–3. doi:10.1088/0022-3727/43/35/354002.
- [68] M. Bertolotti, *The History of the Laser*, Institute of Physics, Bristol, UK, Philadelphia, PA, 2005.
- [69] A.F. Haught, Lasers and Their Applications to Physical Chemistry, *Annu. Rev. Phys. Chem.* 19 (1968) 343–371. doi:10.1146/annurev.pc.19.100168.002015.
- [70] E. Microscopy, L. Reimer, *Lasers in Photomedicine and Photobiology*, Springer Berlin Heidelberg, Berlin, Heidelberg, 1980. doi:10.1007/978-3-540-38270-6.
- [71] V.S. Letokhov, Laser biology and medicine, *Nature.* 316 (1985) 325–330. doi:10.1038/316325a0.
- [72] J. Mattay, A. Griesbeck, *Photochemical Key Steps in Organic Synthesis: An Experimental Course Book*, VHC Verlagsgesellschaft mbH, Weinheim, 1994.
- [73] S.P. Road, T.C. Road, PHOTO-CIDNP OF BIOPOLYMERS, 25 (1993). doi:w796565p.
- [74] E. Daviso, S. Prakash, A. Alia, P. Gast, J. Neugebauer, G. Jeschke, J. Matysik, The electronic structure of the primary electron donor of reaction centers of purple bacteria at atomic resolution as observed by photo-CIDNP ¹³C NMR, *Proc. Natl. Acad. Sci.* 106 (2009) 22281–22286. doi:10.1073/pnas.0908608106.
- [75] M. Goetz, I. Sartorius, CIDNP Determination of the Rate of In-Cage Deprotonation of the Triethylamine Radical Cation, *J. Phys. Chem. A* 107 (2003) 8539–8546. doi:10.1021/jp030244g.
- [76] M. V. Fedin, Theoretical and experimental studies of chemically induced dynamic nuclear polarization kinetics in recombination of radical pairs by the method of switched external magnetic field. II. ¹³C CIDNP of micellized radical pairs, *J. Chem. Phys.* 111 (1999) 5491–5502. doi:10.1063/1.479862.
- [77] A. Yurkovskaya, O. Morozova, G. Gescheidt, Structures and Reactivity of Radicals Followed by Magnetic Resonance, in: *Encyclopedia of Radicals in Chemistry, Biology and Materials* (eds C. Chatgililoglu and A. Studer), Wiley, NJ, 2012. doi:10.1002/9781119953678.rad008.
- [78] M. Vacha, Y. Koide, M. Kotani, H. Sato, Single molecule detection and photobleaching study of a phosphorescent dye: Organometallic iridium(III) complex, *Chem. Phys. Lett.* 388 (2004) 263–268. doi:10.1016/j.cplett.2004.03.020.
- [79] P. Hartmann, M.J.P. Leiner, P. Kohlbacher, Photobleaching of a ruthenium complex in polymers used for oxygen optodes and its inhibition by singlet oxygen

- quenchers, *Sensors Actuators, B Chem.* 51 (1998) 196–202. doi:10.1016/S0925-4005(98)00188-9.
- [80] M. Rochkind, S. Pasternak, Y. Paz, Using dyes for evaluating photocatalytic properties: A critical review, *Molecules.* 20 (2015) 88–110. doi:10.3390/molecules20010088.
- [81] L. Bouslimi, E. Ben Braiek, Mongi, J.P. Cambronne, Georges, High Power Discharge Lamps and Their Photochemical Applications: An Evaluation of Pulsed Radiation, *Mol. Photochem. Var. Asp.* (2012). doi:10.5772/37769.
- [82] G.M. Miyake, J.C. Theriot, Perylene as an organic photocatalyst for the radical polymerization of functionalized vinyl monomers through oxidative quenching with alkyl bromides and visible light, *Macromolecules.* 47 (2014) 8255–8261. doi:10.1021/ma502044f.
- [83] I. Ghosh, B. König, Chromoselective Photocatalysis: Controlled Bond Activation through Light-Color Regulation of Redox Potentials, *Angew. Chemie Int. Ed.* 55 (2016) 7676–7679. doi:10.1002/anie.201602349.
- [84] D.A. Steigerwald, J.C. Bhat, D. Collins, R.M. Fletcher, M.O. Holcomb, M.J. Ludowise, P.S. Martin, S.L. Rudaz, Illumination with solid state lighting technology, *IEEE J. Sel. Top. Quantum Electron.* 8 (2002) 310–320. doi:10.1109/2944.999186.
- [85] Haitz's law, *Nat. Photonics.* 1 (2007) 23–23. doi:10.1038/nphoton.2006.78.
- [86] S.C. Singh, Basics of Light Emitting diodes, Characterizations and Applications, in: *Handbook of Light Emitting and Schottky Diode Research*, 1st ed., (eds. N.P. Chen) Nova Scientific Publisher, UK, 2009.
- [87] D. Barolet, Light-Emitting Diodes (LEDs) in Dermatology, *Semin. Cutan. Med. Surg.* 27 (2008) 227–238. doi:10.1016/j.sder.2008.08.003.
- [88] M.A. Garcia-Garibay, Advances at the frontiers of photochemical sciences, *J. Am. Chem. Soc.* 134 (2012) 8289–8292. doi:10.1021/ja301329b.
- [89] J.M.R. Narayanam, C.R.J. Stephenson, Visible light photoredox catalysis: applications in organic synthesis, *Chem. Soc. Rev.* 40 (2011) 102–113. doi:10.1039/B913880N.
- [90] N.A. Romero, D.A. Nicewicz, Organic Photoredox Catalysis, *Chem. Rev.* 116 (2016) 10075–10166. doi:10.1021/acs.chemrev.6b00057.
- [91] B.L. Feringa, R.A. van Delden, N. Koumura, E.M. Geertsema, Chiroptical Molecular Switches, *Chem. Rev.* 100 (2000) 1789–1816. doi:10.1021/cr9900228.
- [92] C. Cheng, J.F. Stoddart, Wholly Synthetic Molecular Machines, *ChemPhysChem.* 17 (2016) 1780–1793. doi:10.1002/cphc.201501155.
- [93] J.-P. Sauvage, From Chemical Topology to Molecular Machines (Nobel Lecture), *Angew. Chemie Int. Ed.* 56 (2017) 11080–11093. doi:10.1002/anie.201702992.
- [94] A.A. Beharry, G.A. Woolley, Azobenzene photoswitches for biomolecules, *Chem. Soc. Rev.* 40 (2011) 4422. doi:10.1039/c1cs15023e.
- [95] C. Feldmeier, H. Bartling, E. Riedle, R.M. Gschwind, LED based NMR illumination device for mechanistic studies on photochemical reactions - Versatile and simple,

- yet surprisingly powerful, *J. Magn. Reson.* 232 (2013) 39–44. doi:10.1016/j.jmr.2013.04.011.
- [96] M. Mompeán, R.M. Sánchez-Donoso, A. De La Hoz, V. Saggiomo, A.H. Velders, M.V. Gomez, Pushing nuclear magnetic resonance sensitivity limits with microfluidics and photo-chemically induced dynamic nuclear polarization, *Nat. Commun.* 9 (2018) 1–8. doi:10.1038/s41467-017-02575-0.
- [97] S. Coombes, D.T.E. Whittaker, A.M.R. Hall, R. Broomfield-Tagg, D.R. Carbery, A. Codina, U. Hintermair, M. Camilleri, J.P. Lowe, Online monitoring of a photocatalytic reaction by real-time high resolution FlowNMR spectroscopy, *Chem. Commun.* 54 (2017) 30–33. doi:10.1039/c7cc07059d.
- [98] Z. Wang, C. Li, K. Domen, Recent developments in heterogeneous photocatalysts for solar-driven overall water splitting, *Chem. Soc. Rev.* 48 (2019) 2109–2125. doi:10.1039/c8cs00542g.
- [99] K.L. Skubi, T.R. Blum, T.P. Yoon, Dual Catalysis Strategies in Photochemical Synthesis, *Chem. Rev.* 116 (2016) 10035–10074. doi:10.1021/acs.chemrev.6b00018.
- [100] Y. Nosaka, A.Y. Nosaka, Generation and Detection of Reactive Oxygen Species in Photocatalysis, *Chem. Rev.* 117 (2017) 11302–11336. doi:10.1021/acs.chemrev.7b00161.
- [101] M. Majek, U. Faltermeier, B. Dick, R. Pérez-Ruiz, A. JacobivonWangelin, Application of Visible-to-UV Photon Upconversion to Photoredox Catalysis: The Activation of Aryl Bromides, *Chem. A Eur. J.* 21 (2015) 15496–15501. doi:10.1002/chem.201502698.
- [102] H. Hennig, R. Billing, Advantages and disadvantages of photocatalysis induced by light-sensitive coordination compounds, *Coord. Chem. Rev.* 125 (1993) 89–100. doi:10.1016/0010-8545(93)85010-2.
- [103] C. Grewer, H.D. Brauer, Mechanism of the triplet-state quenching by molecular oxygen in solution, *J. Phys. Chem.* 98 (1994) 4230–4235. doi:10.1021/j100067a006.
- [104] P. Bonilla, Y.P. Rey, C.M. Holden, P. Melchiorre, Photo-Organocatalytic Enantioselective Radical Cascade Reactions of Unactivated Olefins, *Angew. Chemie - Int. Ed.* 57 (2018) 12819–12823. doi:10.1002/anie.201808183.
- [105] G. Goti, B. Bieszczad, A. Vega-Peñaloza, P. Melchiorre, Stereocontrolled Synthesis of 1,4-Dicarbonyl Compounds by Photochemical Organocatalytic Acyl Radical Addition to Enals, *Angew. Chemie Int. Ed.* 58 (2019) 1213–1217. doi:10.1002/anie.201810798.
- [106] J.A. Rincón, S. García-Cerrada, M. Barberis, O. de Frutos, J. Agejas, R.T. Smith, C. Mateos, X. Zhang, D.W.C. MacMillan, Metallaphotoredox-Catalyzed Cross-Electrophile C sp³–C sp³ Coupling of Aliphatic Bromides, *J. Am. Chem. Soc.* 140 (2018) 17433–17438. doi:10.1021/jacs.8b12025.
- [107] C. Wolff, J. Kind, H. Schenderlein, H. Bartling, C. Feldmeier, R.M. Gschwind, M. Biesalski, C.M. Thiele, Studies of a photochromic model system using NMR with ex-situ and in-situ irradiation devices, *Magn. Reson. Chem.* 54 (2016) 485–491. doi:10.1002/mrc.4403.

- [108] A. Seegerer, P. Nitschke, R.M. Gschwind, Combined In Situ Illumination-NMR-UV/Vis Spectroscopy: A New Mechanistic Tool in Photochemistry, *Angew. Chemie Int. Ed.* 57 (2018) 7493–7497. doi:10.1002/anie.201801250.
- [109] R. Kaptein, K. Dijkstra, F. Muller, C.G. Vanschagen, A.J.W.G. Visser, 60-MHZ LASER-Induced Photo-CIDNP In Photoreactions Of Flavins, *J. Magn. Reson.* 31 (1978) 171-176. doi: 10.1016/0022-2364(78)90180-4
- [110] R. Kaptein, K. Dijkstra, K. Nicolay, Laser photo-CIDNP as a surface probe for proteins in solution [37], *Nature.* 274 (1978) 293–294. doi:10.1038/274293a0.
- [111] R.J. Miller, G.L. Closs, Application of Fourier transform-NMR spectroscopy to submicrosecond time-resolved detection in laser flash photolysis experiments, *Rev. Sci. Instrum.* 52 (1981) 1876–1885. doi:10.1063/1.1136531.
- [112] G. Gescheidt, R. Herges, E. Stadler, P. Frühwirt, M. Dommaschk, Speeding up NMR by in Situ Photo-Induced Reversible Acceleration of T₁-Relaxation (PIRAT), *ChemPhysChem.* 19 (2017) 571–574. doi:10.1002/cphc.201701304.
- [113] M. Khademalrasool, M. Farbod, M.D. Talebzadeh, The improvement of photocatalytic processes: Design of a photoreactor using high-power LEDs, *J. Sci. Adv. Mater. Devices.* 1 (2016) 382–387. doi:10.1016/j.jsamd.2016.06.012.
- [114] J.E. Scheffler, C.E. Cottrell, L.J. Berliner, An inexpensive, versatile sample illuminator for photo-CIDNP on any NMR spectrometer, *J. Magn. Reson.* 63 (1985) 199–201. doi:10.1016/0022-2364(85)90169-6.
- [115] K. Maeda, C.E. Lyon, J.J. Lopez, M. Cemazar, C.M. Dobson, P.J. Hore, Improved photo-CIDNP methods for studying protein structure and folding, *J. Biomol. NMR.* 16 (2000) 235–244. doi:10.1023/A:1008351128089.
- [116] P.J. Hore, S.L. Winder, C.H. Roberts, C.M. Dobson, Stopped-flow photo-CIDNP observation of protein folding [8], *J. Am. Chem. Soc.* 119 (1997) 5049–5050. doi:10.1021/ja9644135.
- [117] K.H. Mok, T. Nagashima, I.J. Day, J.A. Jones, C.J.V. Jones, C.M. Dobson, P.J. Hore, Rapid sample-mixing technique for transient NMR and photo-CIDNP spectroscopy: Applications to real-time protein folding, *J. Am. Chem. Soc.* 125 (2003) 12484–12492. doi:10.1021/ja036357v.
- [118] C. Waldsich, *RNA Folding*, Humana Press, Totowa, NJ, 2014. doi:10.1007/978-1-62703-667-2.
- [119] T. Kühn, H. Schwalbe, Monitoring the kinetics of ion-dependent protein folding by time-resolved NMR spectroscopy at atomic resolution, *J. Am. Chem. Soc.* 122 (2000) 6169–6174. doi:10.1021/ja994212b.
- [120] J. Wirmer, T. Kühn, H. Schwalbe, Millisecond time resolved photo-CIDNP NMR reveals a non-native folding intermediate on the ion-induced refolding pathway of bovine α -lactalbumin, *Angew. Chemie Int. Ed.* 40 (2001) 4248–4251. doi:10.1002/1521-3773(20011119)40:22<4248::AID-ANIE4248>3.0.CO;2-I.
- [121] I. Kuprov, P.J. Hore, Uniform illumination of optically dense NMR samples, *J. Magn. Reson.* 171 (2004) 171–175. doi:10.1016/j.jmr.2004.08.017.
- [122] A. Breder, C.M. Thiele, K. Koszinowski, S. Ortgies, R. Rieger, J. Kind, K. Rode, J. Rehbein, Mechanistic and Synthetic Investigations on the Dual Selenium- π -Acid/Photoredox Catalysis in the Context of the Aerobic Dehydrogenative

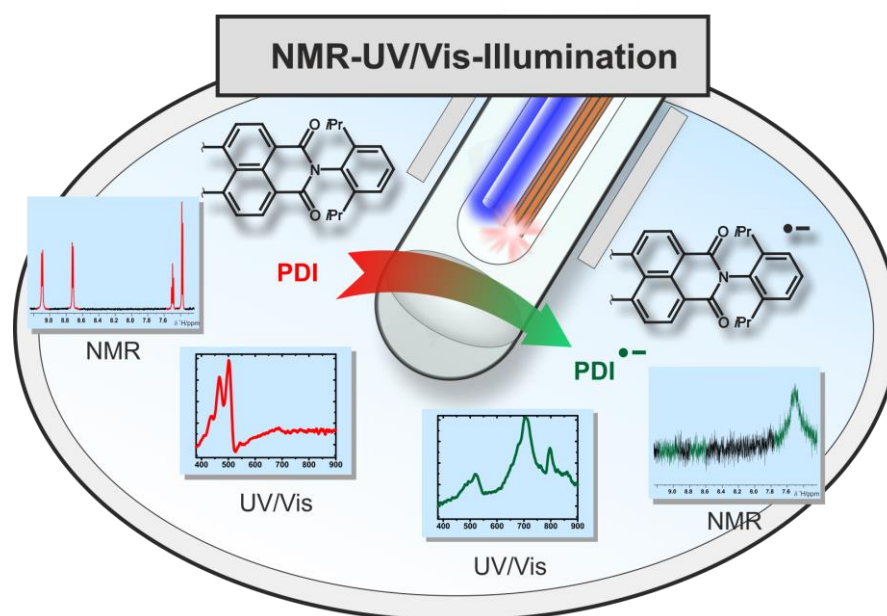
- Lactonization of Alkenoic Acids, *ACS Catal.* 7 (2017) 7578–7586. doi:10.1021/acscatal.7b02729.
- [123] S.J. Wezenberg, B.L. Feringa, Supramolecularly directed rotary motion in a photoresponsive receptor, *Nat. Commun.* 9 (2018) 1–7. doi:10.1038/s41467-018-04249-x.
- [124] P.M. Tolstoy, B. Koeppe, G.S. Denisov, H.H. Limbach, Combined NMR and UV/Vis Spectroscopy in the Solution State: Study of the Geometries of Strong OHO Hydrogen Bonds of Phenols with Carboxylic Acids, *Angew. Chemie Int. Ed.* 48 (2009) 5745–5747. doi:10.1002/anie.200806181.
- [125] B. Koeppe, P.M. Tolstoy, H.H. Limbach, Reaction pathways of proton transfer in hydrogen-bonded phenol-carboxylate complexes explored by combined UV-Vis and NMR spectroscopy, *J. Am. Chem. Soc.* 133 (2011) 7897–7908. doi:10.1021/ja201113a.
- [126] P. Giraudeau, F.X. Felpin, Flow reactors integrated with in-line monitoring using benchtop NMR spectroscopy, *React. Chem. Eng.* 3 (2018) 399–413. doi:10.1039/c8re00083b.
- [127] M.V. Gomez, A. De La Hoz, NMR reaction monitoring in flow synthesis, *Beilstein J. Org. Chem.* 13 (2017) 285–300. doi:10.3762/bjoc.13.31.
- [128] R. Dutta Majumdar, L. Blumkin, D. Lane, R. Soong, M. Simpson, A.J. Simpson, Analysis of DOM phototransformation using a looped NMR system integrated with a sunlight simulator, *Water Res.* 120 (2017) 64–76. doi:10.1016/j.watres.2017.04.067.
- [129] M. Li, D.P. Kim, Silicate glass coated microchannels through a phase conversion process for glass-like electrokinetic performance, *Lab Chip.* 11 (2011) 1126–1131. doi:10.1039/c0lc00522c.
- [130] G. Liu, S.H. Liou, N. Enkin, I. Tkach, M. Bennati, Photo-induced radical polarization and liquid-state dynamic nuclear polarization using fullerene nitroxide derivatives, *Phys. Chem. Chem. Phys.* 19 (2017) 31823–31829. doi:10.1039/c7cp06073d.
- [131] A. Mills, C. O'Rourke, Photocatalysis in an NMR tube: Carbon–carbon coupling of phenoxyacetic acid with N-substituted maleimides, *J. Photochem. Photobiol. A Chem.* 268 (2013) 7–16. doi:10.1016/j.jphotochem.2013.06.002.
- [132] A. Mills, C. O'Rourke, Photocatalytic organic synthesis in an NMR tube: CC coupling of phenoxyacetic acid and acrylamide, *Catal. Today.* 230 (2014) 256–264. doi:10.1016/j.cattod.2013.10.083.
- [133] A. Mills, C. O'Rourke, Photocatalytic oxidation of toluene in an NMR tube, *J. Photochem. Photobiol. A Chem.* 233 (2012) 34–39. doi:10.1016/j.jphotochem.2012.02.001.
- [134] S.-J. Hwang, C. Petucci, D. Raftery, In Situ Solid-State NMR Studies of Trichloroethylene Photocatalysis: Formation and Characterization of Surface-Bound Intermediates, *J. Am. Chem. Soc.* 120 (1998) 4388–4397. doi:10.1021/ja974192i.
- [135] S.-J. Hwang, C. Petucci, D. Raftery, In Situ Solid-State NMR Observations of Photocatalytic Surface Chemistry: Degradation of Trichloroethylene, *J. Am. Chem.*

- Soc. 119 (1997) 7877–7878. doi:10.1021/ja9703990.
- [136] I.D. Gay, A magic-angle spinner for vacuum-sealed samples, *J. Magn. Reson.* 58 (1984) 413–420. doi:10.1016/0022-2364(84)90145-8.
- [137] A.R. Pradhan, M.A. Macnaughtan, D. Raftery, Zeolite-coated optical microfibers for intrazeolite photocatalysis studied by in situ solid-state NMR, *J. Am. Chem. Soc.* 122 (2000) 404–405. doi:10.1021/ja992683s.
- [138] S. Pilkenton, S.-J. Hwang, D. Raftery, Ethanol Photocatalysis on TiO₂-Coated Optical Microfiber, Supported Monolayer, and Powdered Catalysts: An in Situ NMR Study, *J. Phys. Chem. B.* 103 (2002) 11152–11160. doi:10.1021/jp9927092.
- [139] S.J. Hwang, D. Raftery, In situ solid-state NMR studies of ethanol photocatalysis: Characterization of surface sites and their reactivities, *Catal. Today.* 49 (1999) 353–361. doi:10.1016/S0920-5861(98)00449-0.
- [140] E.A. Reyes-Garcia, Y. Sun, K. Reyes-Gil, D. Raftery, ¹⁵N solid state NMR and EPR characterization of N-doped TiO₂ photocatalysts, *J. Phys. Chem. C.* 111 (2007) 2738–2748. doi:10.1021/jp0652289.
- [141] S. Pilkenton, D. Raftery, Solid-state NMR studies of the adsorption and photooxidation of ethanol on mixed TiO₂-SnO₂ photocatalysts, *Solid State Nucl. Magn. Reson.* 24 (2003) 236–253. doi:10.1016/S0926-2040(03)00030-4.
- [142] W. Xu, D. Raftery, Photocatalytic oxidation of 2-propanol on TiO₂ powder and TiO₂ monolayer catalysts studied by solid-state NMR, *J. Phys. Chem. B.* 105 (2001) 4343–4349. doi:10.1021/jp004381e.
- [143] F. Engelke, D. Gräsing, J. Matysik, I.F. Céspedes-Camacho, T. Marquardsen, A. Alia, P. Bielytskyi, Field-cycling NMR with high-resolution detection under magic-angle spinning: determination of field-window for nuclear hyperpolarization in a photosynthetic reaction center, *Sci. Rep.* 7 (2017) 4–10. doi:10.1038/s41598-017-10413-y.
- [144] M. Hunger, W. Wang, Formation of cyclic compounds and carbenium ions by conversion of methanol on weakly dealuminated zeolite H-ZSM-5 investigated via a novel in situ CF MAS NMR/UV-Vis technique, *Chem. Commun.* 4 (2004) 584–585. doi:10.1039/b315779b.
- [145] M. Hunger, T. Horvath, A new MAS NMR probe for in situ investigations of hydrocarbon conversion on solid catalysts under continuous-flow conditions, *J. Chem. Soc. Chem. Commun.* (1995) 1423. doi:10.1039/c39950001423.
- [146] R. Miura, Versatility and specificity in flavoenzymes: control mechanisms of flavin reactivity, *Chem. Rec.* 1 (2001) 183–194. doi:10.1002/tcr.1007.
- [147] L. Shi, W. Xia, Photoredox functionalization of C-H bonds adjacent to a nitrogen atom, *Chem. Soc. Rev.* 41 (2012) 7687–7697. doi:10.1039/c2cs35203f.
- [148] J.W. Beatty, C.R.J. Stephenson, Amine functionalization via oxidative photoredox catalysis: Methodology development and complex molecule synthesis, *Acc. Chem. Res.* 48 (2015) 1474–1484. doi:10.1021/acs.accounts.5b00068.
- [149] E. Boess, D. Sureshkumar, A. Sud, C. Wirtz, C. Farès, M. Klusmann, Mechanistic studies on a Cu-catalyzed aerobic oxidative coupling reaction with N-phenyl tetrahydroisoquinoline: Structure of intermediates and the role of methanol as a solvent, *J. Am. Chem. Soc.* 133 (2011) 8106–8109. doi:10.1021/ja201610c.

- [150] J.J. Zhong, Q.Y. Meng, B. Liu, X.B. Li, X.W. Gao, T. Lei, C.J. Wu, Z.J. Li, C.H. Tung, L.Z. Wu, Cross-coupling hydrogen evolution reaction in homogeneous solution without noble metals, *Org. Lett.* 16 (2014) 1988–1991. doi:10.1021/ol500534w.
- [151] G. Zhao, C. Yang, L. Guo, H. Sun, C. Chen, W. Xia, Visible light-induced oxidative coupling reaction: Easy access to Mannich-type products, *Chem. Commun.* 48 (2012) 2337–2339. doi:10.1039/c2cc17130a.
- [152] Y. Zhou, J. Wang, Z. Gu, S. Wang, W. Zhu, J.L. Acenã, V.A. Soloshonok, K. Izawa, H. Liu, Next Generation of Fluorine-Containing Pharmaceuticals, Compounds Currently in Phase II-III Clinical Trials of Major Pharmaceutical Companies: New Structural Trends and Therapeutic Areas, *Chem. Rev.* 116 (2016) 422–518. doi:10.1021/acs.chemrev.5b00392.
- [153] M. Chen, M. Zhong, J.A. Johnson, Light-Controlled Radical Polymerization: Mechanisms, Methods, and Applications, *Chem. Rev.* 116 (2016) 10167–10211. doi:10.1021/acs.chemrev.5b00671.
- [154] A.K. Schönbein, J. Kind, C.M. Thiele, J.J. Michels, Full Quantification of the Light-Mediated Gilch Polymerization, *Macromolecules.* 51 (2018) 4678–4687. doi:10.1021/acs.macromol.8b00607.
- [155] F. Krohm, J. Kind, R. Savka, M. Alcaraz Janßen, D. Herold, H. Plenio, C.M. Thiele, A. Andrieu-Brunsen, Photochromic spiropyran- and spirooxazine-homopolymers in mesoporous thin films by surface initiated ROMP, *J. Mater. Chem. C.* 4 (2016) 4067–4076. doi:10.1039/c5tc04054j.
- [156] R. Klajn, Spiropyran-based dynamic materials, *Chem. Soc. Rev.* 43 (2014) 148–184. doi:10.1039/c3cs60181a.
- [157] B. Kuhn, P. Mohr, M. Stahl, Intramolecular hydrogen bonding in medicinal chemistry, *J. Med. Chem.* 53 (2010) 2601–2611. doi:10.1021/jm100087s.
- [158] B. Over, P. McCarren, P. Artursson, M. Foley, F. Giordanetto, G. Grönberg, C. Hilgendorf, M.D. Lee, P. Matsson, G. Muncipinto, M. Pellisson, M.W.D. Perry, R. Svensson, J.R. Duvall, J. Kihlberg, Impact of stereospecific intramolecular hydrogen bonding on cell permeability and physicochemical properties, *J. Med. Chem.* 57 (2014) 2746–2754. doi:10.1021/jm500059t.
- [159] S. Venkataramani, U. Jana, M. Dommaschk, F.D. Sonnichsen, F. Tuczec, R. Herges, Magnetic Bistability of Molecules in Homogeneous Solution at Room Temperature, *Science* 331 (2011) 445–448. doi:10.1126/science.1201180.
- [160] P. Renzi, J. Hioe, R.M. Gschwind, Decrypting Transition States by Light: Photoisomerization as a Mechanistic Tool in Brønsted Acid Catalysis, *J. Am. Chem. Soc.* 139 (2017) 6752–6760. doi:10.1021/jacs.7b02539.
- [161] T. Marcelli, P. Hammar, F. Himo, Phosphoric Acid Catalyzed Enantioselective Transfer Hydrogenation of Imines: A Density Functional Theory Study of Reaction Mechanism and the Origins of Enantioselectivity, *Chem. A Eur. J.* 14 (2008) 8562–8571. doi:10.1002/chem.200800890.
- [162] L. Simón, J.M. Goodman, Theoretical Study of the Mechanism of Hantzsch Ester Hydrogenation of Imines Catalyzed by Chiral BINOL-Phosphoric Acids, *J. Am. Chem. Soc.* 130 (2008) 8741–8747. doi:10.1021/ja800793t.

- [163] J.P. Reid, L. Simón, J.M. Goodman, A Practical Guide for Predicting the Stereochemistry of Bifunctional Phosphoric Acid Catalyzed Reactions of Imines, *Acc. Chem. Res.* 49 (2016) 1029–1041. doi:10.1021/acs.accounts.6b00052.

3 Combined in situ illumination-NMR-UV/Vis Spectroscopy: A New Mechanistic Tool in Photochemistry



Andreas Seegerer, **Philipp Nitschke**, and Ruth M. Gschwind*

Angew. Chem. Int. Ed. **2018**, *57*, 7493-7497

DOI: 10.1002/anie.201801250R1

The UVNMR-illumination setup was developed and realized by Andreas Seegerer. Together with Philipp Nitschke the setup was further improved and full automation was implemented. Philipp Nitschke recorded and analyzed the combined UVNMR reaction profiles and performed all NMR experiments except those for the assignments of the spiropyran species.

Adapted with permission from *Angew. Chem. Int. Ed.* Source of this chapter: <https://onlinelibrary.wiley.com/doi/full/10.1002/anie.201801250>.

3.1 Abstract

Synthetic applications in photochemistry are booming. Despite great progress in the development of new reactions, mechanistic investigations are still challenging. Therefore, we present a fully automated *in situ* combination of NMR spectroscopy, UV/Vis spectroscopy, and illumination to allow simultaneous and time-resolved detection of paramagnetic and diamagnetic species. This optical fiber-based setup enables the first acquisition of combined UV/Vis and NMR spectra in photocatalysis, as demonstrated on a conPET process. Furthermore, the broad applicability of combined UVNMR spectroscopy for light-induced processes is demonstrated on a structural and quantitative analysis of a photoswitch, including rate modulation and stabilization of transient species by temperature variation. Owing to the flexibility regarding the NMR hardware, temperature, and light sources, we expect wide-ranging applications of this setup in various research fields.

3.2 Introduction

Photocatalysis is one of the booming fields in organic synthesis and experienced a nearly exponential increase in publications of synthetic strategies and applications during the last decades.¹ Despite the high impact of new light-induced transformations on synthesis, detailed insights into photocatalytic mechanisms are still a real challenge. In photochemistry, ultrafast UV/Vis spectroscopy is so far the most commonly used method for detailed mechanistic studies, owing to its capability to detect the initial photoexcited states.² We and also other groups have recently shown that NMR spectroscopy can provide essential mechanistic information on photochemical and photocatalytic processes, despite its insensitivity and poor time resolution,³ by providing quantitative reaction profiles of reactants, products, and intermediates. Complementary to ultrafast UV/Vis, mechanistic features downstream from the initial photoexcitation, such as single- versus two-electron transfer processes,^{3b} proton transfer pathways, or multiple concurrent reaction mechanisms, can be elucidated by NMR spectroscopy.^{3a} Furthermore, owing to its high resolution spectra, NMR spectroscopy provides detailed structural information about intermolecular interactions⁴ and aggregation, revealing key information of activation or deactivation of substrates or catalysts in photocatalysis.⁵

However, besides the limited time resolution, NMR spectroscopy faces the additional challenge that single electron transfer (SET) processes, which are typical for photocatalysis, cause an interplay of paramagnetic and diamagnetic species. Often, the lifetime of these paramagnetic radical intermediates is so short that they do not even affect the NMR spectra of the diamagnetic species. The information on these transient radicals can often be accessed only by photo-chemically induced dynamic nuclear polarization (photo-CIDNP) through their diamagnetic recombination and disproportionation products.^{3b,6} In contrast, stable long-lived radicals can impose severe challenges to NMR spectroscopy. While in the case of several inorganic complexes or proteins paramagnetic NMR can be successfully applied,⁷ it is usually not possible to detect paramagnetic states of small organic molecules, such as those used as photocatalysts in photochemistry. Furthermore, for stable radical states of photocatalysts, chemical exchange often leads to severe line broadening even for the diamagnetic states.^{3b}

Because consecutive photoinduced electron transfer (conPET) processes⁸ (Figure 1) recently emerged as a hot topic to address the activation of strong bonds and higher redox potentials, detailed mechanistic investigations are highly demanded in the

photocatalysis community. In conPET processes, long-lived radical anions (usually elusive to NMR spectroscopy) are the central key intermediates generated by PET utilizing a sacrificial electron donor **D**. A second photoexcitation of this radical anion leads to a photoexcited state with reduction potentials up to -2.4 V.^{8,9} This provides an elegant way to increase the scope for metal-free photoredox catalysis under mild conditions using commercially available organic photocatalysts.

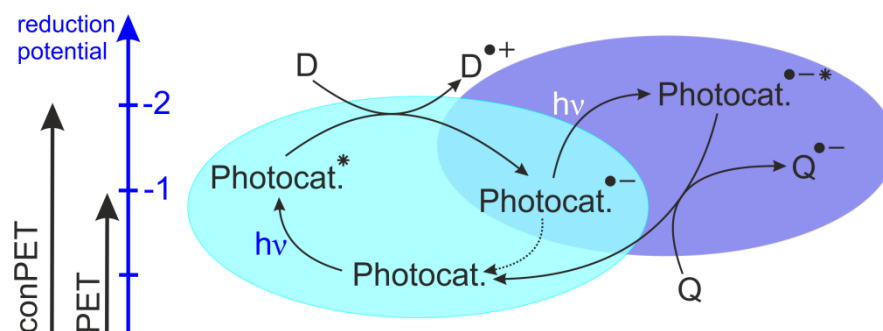


Figure 1. Schematic of a consecutive photoinduced electron transfer (conPET) process.^{8c} D = sacrificial electron donor, Q = quenching substrate.

To extend the scope of high-resolution NMR spectroscopic investigations in photocatalysis with stable radicals, a combined NMR and UV/Vis spectroscopic tool would be ideal.¹⁰ However, reaction profiles of photocatalytic processes featuring longer reaction times of up to several hours or even days impose severe challenges for separated setups. While also separated setups can match experimental conditions such as temperature and concentration, an exact match of light absorption/intensity, which depend on the geometry and positioning of light source and reaction vessel as well as parameters such as convection/diffusion properties, is best realized by using an *in situ* combination.

In addition to photocatalysis, an *in situ* setup combining of UV/Vis, NMR, and illumination would show a broad applicability in the field of photoswitches and molecular machines.¹¹ Herein, such a setup provides direct, quantitative correlations between absorbance and structure of switching states and can be used to track full conversion cycles.¹²

For static equilibria, Tolstoy *et al.* introduced an *in situ* combination of UV/Vis and high-resolution solution NMR spectroscopy (UVNMR) in 2009 to achieve absolute comparability of both methods.¹³ However, this setup cannot be applied for dynamic, light-induced (photo) chemical processes because of the hampered diffusion caused by a reflector between bulk solution for NMR spectroscopy and an aliquot for UV/Vis

spectroscopy. Furthermore, an additional light source for illumination is missing and the NMR probe has to be drilled to guide optical fibers to the tip of the NMR tube.

Therefore, in this paper we describe a fully automated triple combination of *in situ* illumination and UV/Vis and NMR spectroscopy. The potential of this setup is demonstrated by acquisition of combined UVNMR reaction profiles of a light-induced conPET process and a photoswitchable spiropyran.

3.3 Results and Discussion

Our new optical fiber-based UVNMR-illumination setup combines a UV/Vis-reflection dip probe (Avantes) with our *in situ* LED-illumination device¹⁴ inside an NMR spectrometer (see Figure 2A). The optical fiber for illumination (with a sandblasted tip) and the reflection dip probe for UV/Vis measurements are placed together inside a coaxial quartz glass insert within an amberized NMR tube. The optical fiber for illumination and the reflection dip probe (Figure 2B) were used for guiding the light of the LED-illumination device and the deuterium-halogen (D-Hal)-lamp directly into the NMR tube and to detect the reflected light. A PTFE insert inside the NMR tube acts as reflector (Figure 2B).

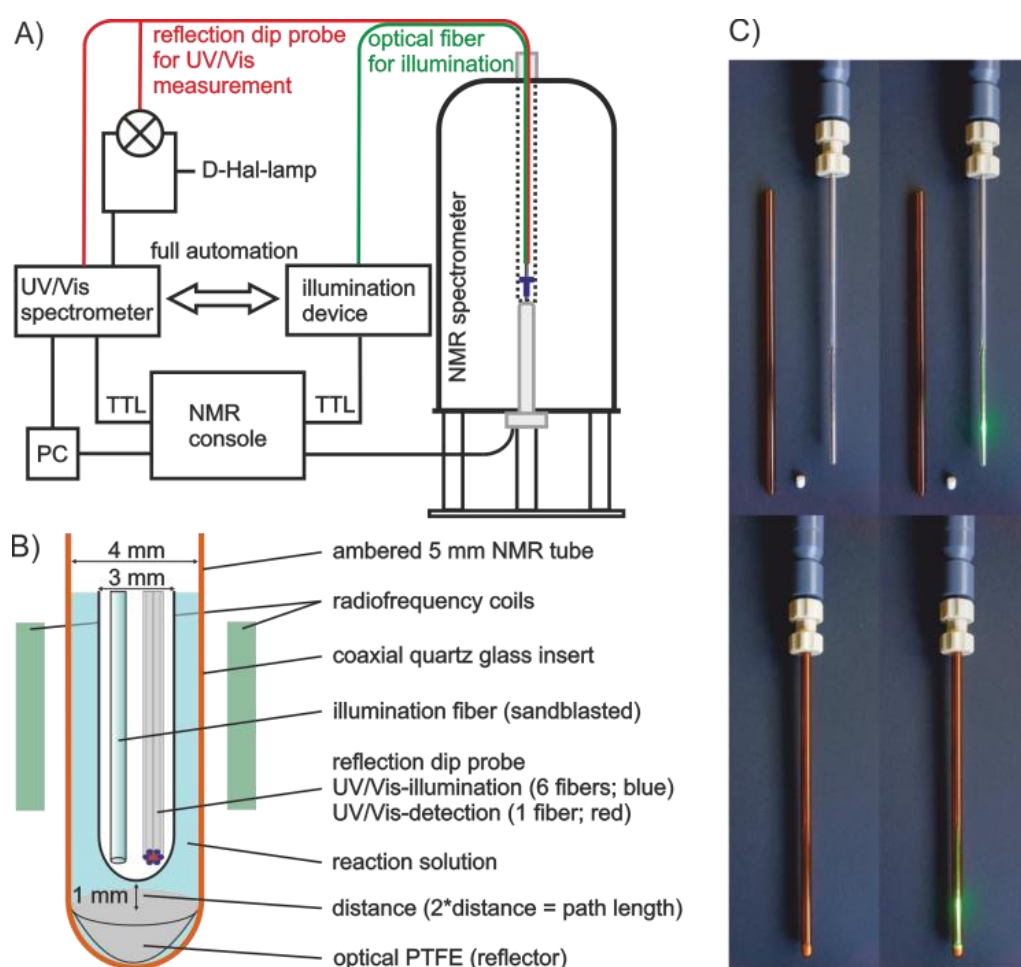


Figure 2. A) Schematic of UVNMR-illumination setup. B) Close-up of the illumination fiber and the reflection dip probe inside the NMR tube; C) Photos of the setup including the outer amberized NMR tube, PTFE reflector, screw cap, and coaxial insert with both optical fibers inside; (dis)assembled with/without light.

Owing to an outer diameter of the coaxial quartz glass insert of 3 mm and an inner diameter of 4 mm of the outer NMR tube, an active layer of 1 mm is given in the range of the NMR radio frequency (RF) coils (Figure 2B). To ensure homogeneity of the solution by diffusion, the distance between the tip of the insert and the PTFE reflector was set to approximately 1 mm (path length of approximately 2 mm). To adjust the path length, a customized screw cap was developed (Figure 2C, for details see the Supporting Information), which connects the NMR tube and the insert tightly, so even air-sensitive samples and (photo) reactions can be analyzed. The whole setup is portable, fully remote-controlled, and applicable to every conventional solution NMR spectrometer without any alteration. This allows for an extremely flexible application regarding the NMR setup (probe, field, temperature) adapted to the individual problems.

To enable combined, time-resolved UVNMR reaction profiles, an absolute time control of UV/Vis, NMR measurements, and illumination is required. Therefore, the NMR console was used as the central time control unit. It directly addresses the illumination device (LED transistor) and the UV/Vis spectrometer through TTL signals (Figure 2A), implemented as events in modified NMR pulse sequences (see Supporting Information). For a UV/Vis measurement, the UV/Vis spectrometer forwards the TTL signal of the NMR console to a D-Hal-light source to control its shutter, that is, the emitted light hits the sample exclusively during the UV/Vis-measurement.¹⁵

To demonstrate the power of our UVNMR-illumination setup combined *in situ* UV/Vis and NMR reaction profiles of a conPET process are presented. In this process, light (450 nm) transforms the photocatalyst N,N-bis(2,6-diisopropylphenyl)-perylene-3,4,9,10-bis(dicarboximide) (**PDI**) into the stable radical anion **PDI⁻** in presence of an electron donor **D** (in this case, NEt₃). A second photoexcitation of **PDI⁻** is proposed to allow for a reduction of aryl halides such as 4-bromo-benzaldehyde **Ald-Br** to the corresponding aryl **Ald** (Figure 1 and 3A/B and the Supporting Information).^{8a} In this reaction, **PDI** shows extreme line broadening effects in the NMR spectra (see Figure 3C). Even prior to illumination, all signals of **PDI** are significantly broadened most probably owing to an exchange with an electron donor acceptor complex between NEt₃ and **PDI** with the typical distance-dependent line broadening of radicals.^{3b} The protons **H₄** and **H₅** (Figure 3C, see the Supporting Information) attached to the central perylene core nearly vanished, **H₁** and **H₂** are broadened, and even proton **H₃** of the isopropyl groups on **PDI** are slightly affected.¹⁶ In contrast, without illumination the UV/Vis spectra show only small absorption bands of **PDI⁻** (Figure 3D; Supporting Information). This hints that in specific cases, NMR spectroscopy might be very sensitive for the detection of electron donor-acceptor complexes. Immediately after turning on the light, the NMR proton

signals of the **PDI** core (**H₄**, **H₅**) vanish completely. The other NMR proton signals of **PDI** are only detectable for seconds or minutes. However, even in the case of detection within the first minutes, for example, of **H₃**, the severe line broadening prevents any reliable quantification of both diamagnetic photocatalyst and paramagnetic intermediate (Figure 3C).

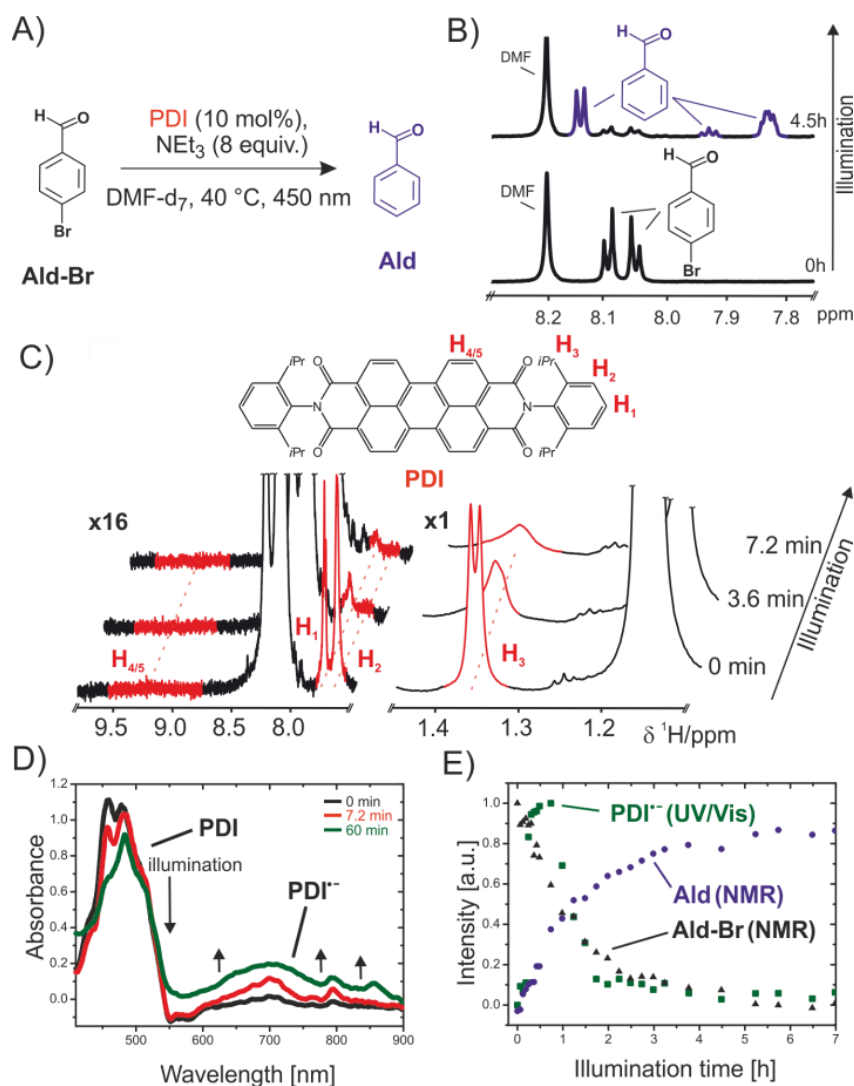


Figure 3. A) Photocatalytic reduction of 4-bromo-benzaldehyde **Ald-Br** to benzaldehyde **Ald** through a **PDI** catalyzed conPET process.^{8a} B) ¹H spectra of the reaction mixture, before and after illumination (450 nm) showing **Ald-Br** and **Ald** at 313 K in [D₇] DMF. C) Line broadening and vanishing of the **PDI** proton signals (red) upon illumination because of exchange with **PDI^{•-}**; D) conversion of **PDI** into **PDI^{•-}** monitored by *in situ* UV/Vis spectroscopy. E) Combined NMR and UV/Vis reaction profiles allow for *in situ* kinetic information of both paramagnetic (**PDI^{•-}**) and diamagnetic reactants (**Ald-Br**, **Ald**) in photocatalysis.

UV/Vis spectroscopy shows its power for the detection of stable radicals. After a few minutes of illumination at 450 nm, the absorption maxima of **PDI**^{•-} (698 and 794 nm)^{8a} rise, while the absorbance of **PDI** (455 and 482 nm) steadily decreases (Figure 3D). Besides its advantages in eliminating all previously described common issues associated with reaction conditions in separated setups, this study also reveals a general application of this combined UVNMR-illumination setup. In case of UV/Vis detectable intermediates/reactants, a relative quantification over time by UV/Vis is feasible. Studies towards an absolute quantification are in progress.

Thus, the UV/Vis data provides important, time-resolved information about reactants invisible to NMR spectroscopy, enabling a semiquantitative reaction profile for the evolution of **PDI**^{•-}. Complementary to the UV/Vis spectra, simultaneously recorded NMR spectra give full quantitative and structural insight into participating, diamagnetic reactants and reaction/decomposition products (Figure 3E).¹⁷

With this *in situ* combination of NMR and UV/Vis spectroscopy and illumination, complete reaction profiles of the whole progress of a reaction including paramagnetic and diamagnetic species can be obtained and important interactions as well as structural details can be investigated. This enables totally new possibilities to elucidate reaction mechanisms in photocatalysis. Further studies about this controversial mechanism are in progress.

Photoswitches are another promising field of applications for the *in situ* combination of NMR and UV/Vis spectroscopy and illumination. In our previous study about photoswitchable spiropyrans, deviations between the quantitative data of UV/Vis and NMR spectroscopy were found, demonstrating the importance of identical light intensities and reaction vessels in separated setups.¹⁸ To demonstrate the advantages of our UVNMR-illumination setup with only one illumination device and a common reaction vessel, a spectroscopic analysis of a similar photoswitchable spiropyran is presented. In this case, the colorless 1',3'-dihydro-1',3',3'-trimethyl-6-nitrospiro[2*H*-1-benzo-pyran-2,2'-(2*H*)-indole] **1** can be switched to its open, purple, zwitterionic state **2** (Figure 4A) by irradiation with UV light (365 nm) inside the NMR spectrometer at 300 K in [D₈]THF^{11a}. The *in situ* recorded UV/Vis spectrum (Figure 4B) shows new absorption maxima at 533 and 575 nm with continuous illumination. Complementary, the NMR spectrum (Figure 4C) gives immediate information about the quantity of the opened spiropyran **2** (21% after 2 minutes). However, upon switching off the light, **2** vanishes within circa 24 s in the NMR spectrum ($\tau_{1/2}$ (300 K) = 17.4 s determined by UV/Vis spectroscopy), which

prevents a detailed structural study by NMR spectroscopy at 300 K (Figure 4D and the Supporting Information).

By cooling the sample inside the NMR spectrometer to 180 K, without changing any other parameter of the setup, the thermal back-reaction rate was reduced significantly (Figure 4E and the Supporting Information). This enables more time-consuming NMR experiments to investigate both species without degradation products (see Supporting Information).

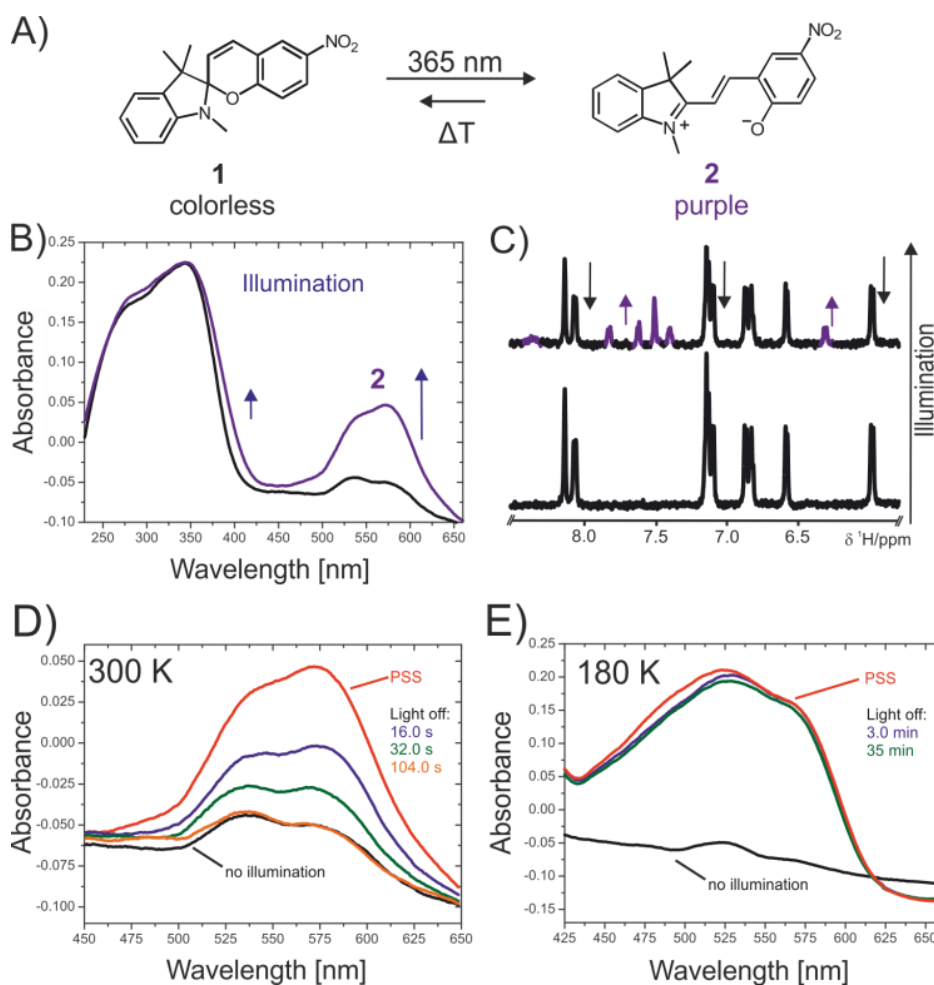


Figure 4. A) Equilibrium of spiropyran **1** and **2**. Upon excitation of **1** with a 365 nm LED, **1** switches into its open, colored form **2**. The photoswitch process can be detected by UV/Vis spectroscopy, while NMR spectroscopy unambiguously confirms the structure of the open form **2**. B) Absorption spectra under the influence of light (365 nm). C) Corresponding NMR spectra showing new signals of **2** after illumination at 300 K. D) UV/Vis spectra of the thermal back reaction of **2** to **1** at 300 K once the light is turned off. E) UV/Vis spectra of **2** at 180 K; the thermal back reaction is extremely slow, this enables a full investigation without the need of continuous illumination. PSS = photo stationary state.

Structural information about the preferred configuration and conformation can be essential to understand different binding properties of the isomers of photo switchable molecules, for example, in biochemical applications.¹⁹ Furthermore, the time-dependent conversion of different isomers can be tracked online by NMR and/or UV/Vis spectroscopy to show the active species present during a reaction. In general the low temperature applicability of the setup enables temperature-dependent rate modulation and stabilization to detect unstable intermediates by NMR and UV/Vis spectroscopy. In addition, combinations of UVNMR with advanced NMR techniques like DOSY to investigate aggregates or complexes are feasible.

3.4 Conclusion

To summarize, in this study we present a fully automated triple combination of *in situ* high-resolution NMR and UV/Vis spectroscopy and illumination in a new optical fiber-based setup. By merging two very important methods in the field of mechanistic investigations, it is now possible to monitor and quantify paramagnetic and diamagnetic species simultaneously and in a time-resolved manner during a light-induced photochemical transformation by NMR and UV/Vis spectroscopy. Besides the elimination of all common issues related to the use of separated systems, like concentration and temperature, the setup circumvents all deviations in terms of light intensity, reaction vessel, convection, and diffusion. Its applicability in a wide temperature range opens the opportunity to modulate the reaction rate of ongoing reactions or switching cycles to stabilize transient intermediates or conformers. Overall, the combined triple setup including high-resolution NMR and UV/Vis spectroscopy and illumination with different wavelengths will allow for detailed mechanistic and structural investigations in various research fields.

3.5 References

- (1) a) M. Majek, A. Jacobi von Wangelin, *Acc. Chem. Res.* **2016**, *49*, 2316–2327; b) I. Ghosh, L. Marzo, A. Das, R. Shaikh, B. König, *Acc. Chem. Res.* **2016**, *49*, 1566–1577; c) M. A. Garcia-Garibay, *J. Am. Chem. Soc.* **2012**, *134*, 8289–8292; d) J. M. R. Narayanam, C. R. J. Stephenson, *Chem. Soc. Rev.* **2011**, *40*, 102–113; e) K. Zeitler, *Angew. Chem. Int. Ed.* **2009**, *48*, 9785–9789; f) N. A. Romero, D. A. Nicewicz, *Chem. Rev.* **2016**, *116*, 10075–10166; g) B. König, *Eur. J. Org. Chem.* **2017**, *15*, 1979–1981.
- (2) a) Y. Zhang, J. Kubicki, M. S. Platz, *J. Am. Chem. Soc.* **2009**, *131*, 13602–13603; b) U. Megerle, M. Wenninger, R.-J. Kutta, R. Lechner, B. König, B. Dick, E. Riedle, *Phys. Chem. Chem. Phys.* **2011**, *13*, 8869–8880; c) J. Wang, G. Burdzinski, J. Kubicki, M. S. Platz, *J. Am. Chem. Soc.* **2008**, *130*, 11195–11209; d) P. K. Verma, F. Koch, A. Steinbacher, P. Nuernberger, T. Brixner, *J. Am. Chem. Soc.* **2014**, *136*, 14981–14989; e) E. Riedle, M. K. Roos, S. Thallmair, C. F. Sailer, N. Krebs, B. P. Fingerhut, R. de Vivie-Riedle, *Chem. Phys. Lett.* **2017**, *683*, 128–134; f) J. Xue, H. L. Luk, S. V. Eswaran, C. M. Hadad, M. S. Platz, *J. Phys. Chem. A* **2012**, *116*, 5325–5336.
- (3) a) H. Bartling, A. Eisenhofer, B. König, R. M. Gschwind, *J. Am. Chem. Soc.* **2016**, *138*, 11860–11871; b) C. Feldmeier, H. Bartling, K. Magerl, R. M. Gschwind, *Angew. Chem. Int. Ed.* **2015**, *54*, 1347–1351; c) M. V. Gomez, A. Juan, F. Jiménez-Márquez, A. de la Hoz, A. H. Velders, *Anal. Chem.* **2018**, *90*, 1542–1546; d) D. M. Schultz, F. Lévesque, D. A. DiRocco, M. Reibarkh, Y. Ji, L. A. Joyce, J.F. Dropinski, H. Sheng, B. D. Sherry, I. W. Davies, *Angew. Chem. Int. Ed.* **2017**, *56*, 15274–15278; e) N. Mallo, P. T. Brown, H. Iranmanesh, T. S. C. MacDonald, M. J. Teusner, J. B. Harper, G. E. Ball, J. E. Beves, *Chem. Commun.* **2016**, *52*, 13576–13579; f) J. Kind, L. Kaltschnee, M. Leyendecker, C. M. Thiele, *Chem. Commun.* **2016**, *52*, 12506–12509; g) E. Procházková, L. Čechová, J. Kind, Z. Janeba, C. M. Thiele, M. Dračinský, *Chem. Eur. J.* **2018**, *24*, 492–498; h) A. Bahamonde, P. Melchiorre, *J. Am. Chem. Soc.* **2016**, *138*, 8019–8030; i) A. Mills, C. O'Rourke, *J. Org. Chem.* **2015**, *80*, 10342–10345.
- (4) a) A. Seegerer, J. Hioe, M. M. Hammer, F. Morana, P. J. W. Fuchs, R. M. Gschwind, *J. Am. Chem. Soc.* **2016**, *138*, 9864–9873; b) N. Sorgenfrei, J. Hioe, J. Greindl, K. Rothermel, F. Morana, N. Lokesh, R. M. Gschwind, *J. Am. Chem. Soc.* **2016**, *138*, 16345–16354; c) J. Greindl, J. Hioe, N. Sorgenfrei, F. Morana, R. M. Gschwind, *J. Am. Chem. Soc.* **2016**, *138*, 15965–15971.
- (5) a) K. Chen, N. Berg, R. Gschwind, B. König, *J. Am. Chem. Soc.* **2017**, *139*, 18444–18447; b) J. Dadová, S. Kümmel, C. Feldmeier, J. Cibulková, R. Pažout, J. Maixner, R. M. Gschwind, B. König, R. Cibulka, *Chem. Eur. J.* **2013**, *19*, 1066–1075; c) A. Eisenhofer, J. Hioe, R. M. Gschwind, B. König, *Eur. J. Org. Chem.* **2017**, *15*, 2194–2204.
- (6) a) R. Kaptein, *J. Chem. Soc. D.* **1971**, *0*, 732–733; b) M. Goez, in *Annu. Reports NMR Spectrosc.*, Elsevier Ltd., **2009**, pp. 77–147; c) M. Goez, in *Hyperpolarization Methods NMR Spectroscopy.*, Springer-Verlag Berlin Heidelberg **2012**, pp. 1–32; d) I. Kuprov, M. Goez, P. A. Abbott, P. J. Hore, *Rev. Sci. Instrum.* **2005**, *76*, 084103-1 – 084103-7.
- (7) a) M. Enders, in *Model. Mol. Prop.* (Ed.: P. Comba), Wiley-VCH Verlag GmbH & Co. KGaA, Weinheim, Germany, **2011**, pp. 49–63; b) I. Bertini, C. Luchinat, G. Parigi, R. Pierattelli, *ChemBioChem* **2005**, *6*, 1536–1549; c) I. Bertini, C. Luchinat, G. Parigi, E. Ravera, *NMR of Paramagnetic Molecules: Applications to Metallobiomolecules and Models*, Elsevier B.V., **2017**; d) F. H. Köhler, in *Encycl. Magn. Reson.*, John Wiley &

Sons, Ltd, Chichester, UK, **2011**; e) F. Rastrelli, A. Bagno, *Chem. Eur. J.* **2009**, *15*, 7990–8004.

(8) a) I. Ghosh, T. Ghosh, J. I. Bardagi, B. König, *Science* **2014**, *346*, 725–728; b) L. Zeng, T. Liu, C. He, D. Shi, F. Zhang, C. Duan, *J. Am. Chem. Soc.* **2016**, *138*, 3958–3961; c) I. Ghosh, B. König, *Angew. Chem. Int. Ed.* **2016**, *55*, 7676–7679; d) M. Neumeier, D. Sampedro, M. Majek, V. de la Pena O’Shea, A. Jacobi von Wangelin, R. Pérez-Ruiz, *Chem. Eur. J.* **2017**, *23*, 1–5.

(9) a) A. Graml, I. Ghosh, B. König, *J. Org. Chem.* **2017**, *82*, 3552–3560; b) M. Poznik, B. König, *React. Chem. Eng.* **2016**, *1*, 494–500.

(10) Recently a laser/EPR/low resolution NMR combination was introduced to investigate photo-induced DNP on the solvent, a potential combination of radicals, diamagnetic species and light in solution.; G. Liu, S.-H.- Liou, N. Enkin, I. Tkach, M. Bennati *Phys. Chem. Chem. Phys.* **2017**, *19*, 31823-31829.

(11) a) J. Piard, *J. Chem. Educ.* **2014**, *91*, 2105–2111; b) J.-P. Sauvage, *Angew. Chem. Int. Ed.* **2017**, *56*, 1–15; c) C. Cheng, J. F. Stoddart, *ChemPhysChem* **2016**, *17*, 1780–1793; d) B. L. Feringa, R. A. van Delden, N. Koumura, E. M. Geertsema, *Chem. Rev.* **2000**, *100*, 1789–1816.

(12) Combination of illumination and *in situ* UVNMR in the field of photoswitches was already described by Gaeva *et al.* However, detailed information about the setup is missing; E. B. Gaeva, V. Pimienta, S. Delbaere, A. V. Metelitsa, N. A. Voloshin, V. I. Minkin, G. Vermeersch, J. C. Micheau, *J. Photochem. Photobiol. A Chem.* **2007**, *191*, 114–121.

(13) a) P. M. Tolstoy, B. Koeppe, G. S. Denisov, H.-H. Limbach, *Angew. Chem. Int. Ed.* **2009**, *48*, 5745–5747; b) B. Koeppe, P. M. Tolstoy, H. H. Limbach, *J. Am. Chem. Soc.* **2011**, *133*, 7897–7908.

(14) C. Feldmeier, H. Bartling, E. Riedle, R. M. Gschwind, *J. Magn. Reson.* **2013**, *232*, 39–44.

(15) During the UV/Vis measurements the light of the illumination fiber is turned off by the NMR console (pulse program).

(16) The methine proton of the isopropyl group is under one of the DMF solvent signals and hence not further discussed.

(17) Owing to the charge-transfer complex formation even without light, which causes severe line broadening of all PDI signals in NMR spectra, a quantitative analysis could not be performed.

(18) C. Wolff, J. Kind, H. Schenderlein, H. Bartling, C. Feldmeier, R. M. Gschwind, M. Biesalski, C. M. Thiele, *Magn. Reson. Chem.* **2016**, *54*, 485–491.

(19) A. A. Beharry, G. A. Woolley, *Chem. Soc. Rev.* **2011**, *40*, 4422-4437.

3.6 Supporting Information

3.6.1 Setup

3.6.1.1 General information

The setup presented in this publication was developed and optimized on a Bruker Avance III HD 600 (600.13 MHz) with a fluorine selective TBIF probe and Topspin 3.2. However this setup is applicable to any other modern NMR spectrometer with a 5 mm gradient probe head and the related software. All components of the UVNMR-illumination device were commercially available if not otherwise indicated. Customized parts are labeled with the corresponding article number of the vendor. In the following sections the setup is shown in three parts: the electronic setup outside the NMR spectrometer, the spectroscopy setup inside the NMR spectrometer and the corresponding pulse sequences and settings for a fully automated acquisition.

3.6.1.2 Electronic setup

The setup for simultaneous UV/Vis and NMR measurements under the influence of light from an external light source required a simple combination of mostly commercially available components (Figure S1). For the acquisition of NMR data an NMR spectrometer (here a Bruker Avance III HD 600; Bruker; Billerica, Massachusetts; USA) and a compatible NMR console (here: Avance III HD) is required. For fully automated measurements of UV/VIS and NMR spectra as shown in this publication two free Real-time Clock Pulse (RCP) outputs of the Intelligent Pulse Sequence Operator (IPSO) unit or the former Time Control Unit (TCU) are needed. These outputs can be found in all Bruker NMR consoles which are equipped with a TCU3 unit or newer versions of it. Unfortunately we do not have any information if the setup is also working fully automated with other NMR consoles since this setup was developed exclusively on Bruker machines and we did not have access to NMR consoles of different brands. However we do not see any problems to transfer the setup if the required RCP outputs are available. Manually triggered UVNMR experiments are possible with every setup.

The NMR console represents the central control unit of our device. Via the RCP outputs it is cable-connected to a commercially available UV/Vis spectrometer (Avaspec-ULS-2048-RS-USB2; Avantes; Apeldoorn, Netherlands) and an LED illumination device. This LED illumination device was already developed in our working group¹. The

corresponding highpower LEDs (365 nm and 450 nm) which were used in this publication were purchased by Lumitronix (Cree XT-E, royal blue, 500 mW, 68332) and Laser Components (LEUVA66X00RV00, 365 nm, 2.06 W). However any other commercially available LED can be used in this setup.

Due to the connection to the NMR console both components the LED illumination device as well as the UV/Vis spectrometer can be controlled fully automated by modified pulse programs via TTL signals [see section 3.6.1.4]. The UV/Vis spectrometer itself is further connected to a D-Hal-lamp (Avalight-DH-S-Bal; Avantes; Apeldoorn, Netherlands) by a customized Y-cable purchased by Avantes. Due to this connection between the UV/Vis spectrometer and the D-Hal-lamp the TTL signals from the NMR console can directly trigger an UV/Vis measurement and can open and close the internal shutter inside the D-Hal-lamp. This direct control of the shutter was an essential point in the development of our setup. If the shutter is opened outside the acquisition [ms] of an UV/Vis spectrum the light of the D-Hal-lamp (200-2500 nm) reaches unhampered the sample which can cause deviations in the results e.g. due to photodegradation by hard UV irradiation.

The NMR console and the UV/Vis spectrometer are furthermore connected to a PC with the corresponding software Bruker Topspin 3.2 (NMR) and Avasoft 8.6full (UV/VIS, Avantes; Apeldoorn, Netherlands). All measurements, UV/VIS as well as NMR are controlled by modified pulse programs in Topspin (see section 3.6.1.4).

To transfer the emitted light of the LED light source and the D-Hal-lamp into the sample inside the spectrometer and to read out the UV/Vis data with the UV/VIS spectrometer, all three components were connected to optical fibers which are guided into the NMR tube inside the NMR spectrometer (see following section).

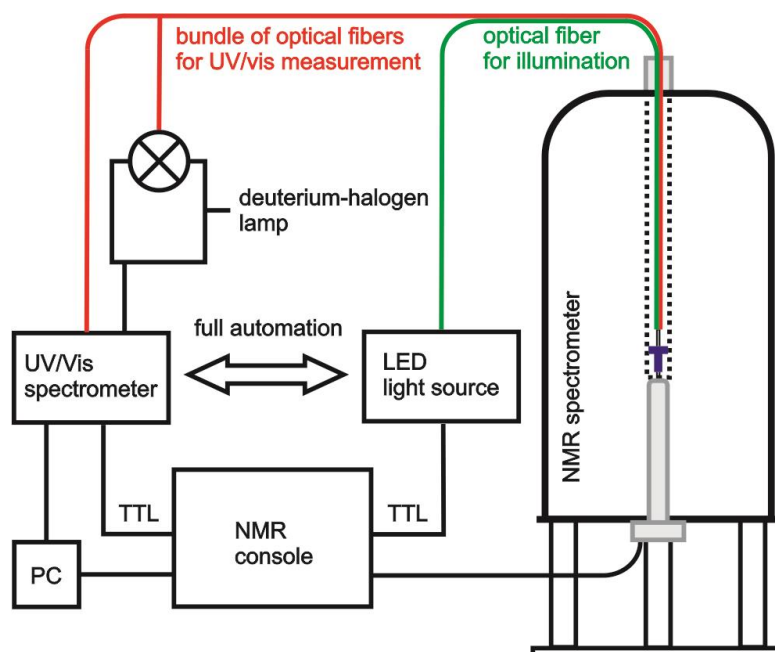


Figure S1. Schematic overview of all electronic and spectroscopic components of the UV/NMR-illumination setup including their wiring.

3.6.1.3 Spectroscopy setup

For measuring UV/Vis and NMR spectra under the influence of LED light inside a NMR spectrometer it was necessary to design a new device which was placed inside a standard 5 mm NMR tube. To make the setup applicable for any conventional NMR user, it was essential to us that no alteration of the NMR spectrometer and/or the NMR probe was required as it was described in a former publication about UVNMR combinations.^{2,3} Therefore a combination of different optical fibers was developed which was guided directly from the top of the NMR spectrometer into the NMR tube (Figure S1).

The LED light source (see section 3.6.1.2) is connected to a commercially available optical fiber with an outer diameter of 1000 μm (BFH48-1000high; Thorlabs). This illumination fiber is guided directly into the NMR sample (Figure S2A). To ensure a homogeneous illumination of the sample inside the NMR tube, the tip of the optical fiber was uncovered and roughened by sandblasting in the range of the NMR receiver coils. This setup for the illumination of NMR samples inside an NMR spectrometer was already described in an earlier publication of our working group.¹

The D-Hal-lamp and the UV/Vis spectrometer are connected to a bundle of 7 optical fibers with an outer diameter of 100 μm each purchased by Avantes (FCR-7UV200). In

the 230 mm long tip of this bundle the 7 optical fibers are arranged radial symmetrically (Figure S2B). The tip has outer diameter of 1000 μm .

The 6 outer fibers (Figure S2B, blue) are connected to the D-Hal-lamp, the central fiber (red) is connected to the UV/Vis spectrometer (changing the connection of the 6 outer fibers to the UV/Vis spectrometer instead to the D-Hal-lamp diminished the detected absorbance intensity). This "UV/Vis fiber" is also guided directly into the NMR tube inside the NMR spectrometer.

Here, the outer NMR tube is a standard thin wall tube with an outer diameter of 5 mm. To diminish the influence of light from the outside commercially available ambered tubes were used. To guide and to center the optical fibers (described above) inside the outer NMR tube a coaxial quartz glass insert (Norell NI5CCI-B-QTZ) with an outer diameter of 3 mm in the range of the stem was added. By nature natural quartz glass is transparent (90-95%) to light >210 nm which ensures the applicability of the setup even in the UV region.

On the bottom end of the tube a customized insert made of optical PTFE (RESTAN; www.image-engenieering.de) was put in place to reflect the light of the optical fibers which were connected to the D-Hal-lamp. The reflected light is afterwards detected by the central fiber (red) to give a UV/Vis spectrum of the solution inside the tube (Figure S2B).

Optical PTFE is a diffuse reflector and it is known to have a very high chemical and thermal resistance and can be shaped very easily. Furthermore the material is UV persistent and reflects more than 98% of incoming light in a range between 380-1700 nm. Due to its high thermal expansion coefficient it was necessary to test if the PTFE insert breaks the tube at higher temperatures. Therefore several "stress tests" with abrupt temperature changes were made. According to these tests our setup is at least applicable for a temperature range between 180-323 K. Outside this range no tests were made.

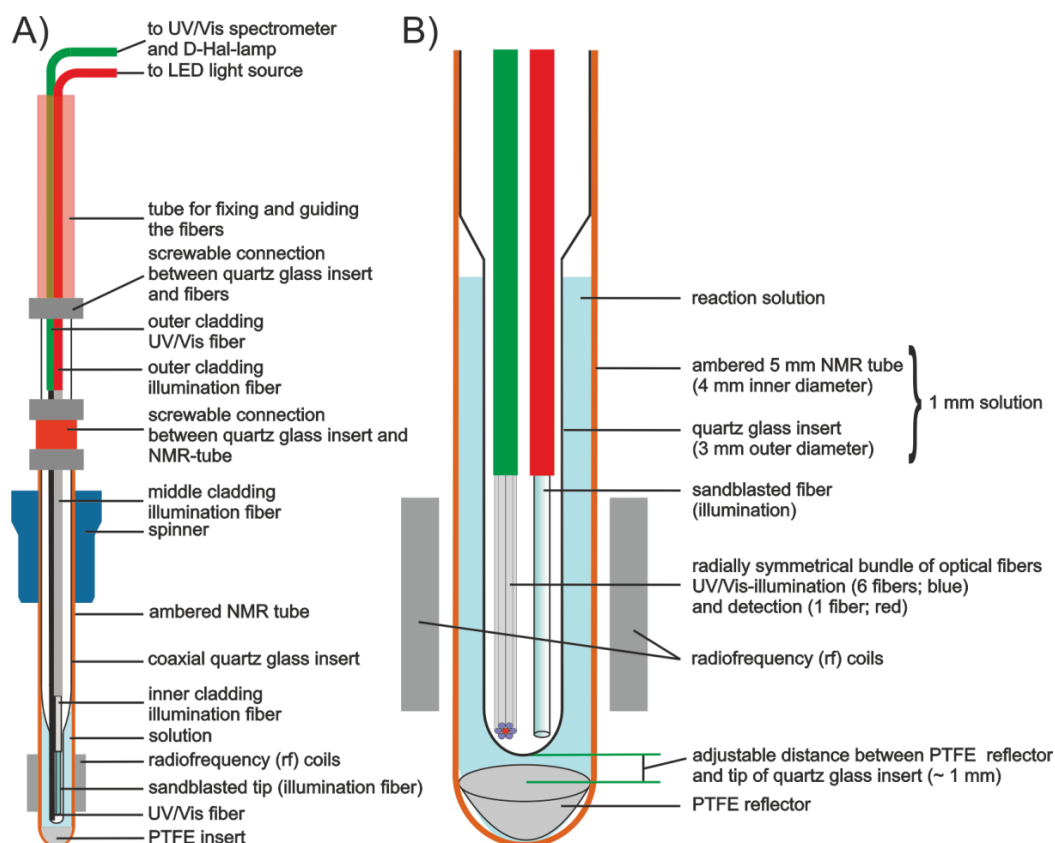


Figure S2. A) Depiction of all NMR tube related components B) Detailed setup of the UV/Vis related parameters.

To control the required pathlength for the UV/Vis measurements a new screw cap was developed (Figure S3). Depending on the concentration and the extinction coefficient according to the Lambert-Beer-law a particular distance between the PTFE reflector and the tip of the coaxial insert can be set to give an optimal UV/Vis spectrum. The screw cap is placed on the top of the outer ambered NMR tube and tightened by a customized union nut. Through a 4 mm channel inside the screw cap the quartz glass insert can be introduced into the NMR tube and can be fixed at a particular height by a second union nut. Furthermore it is used to place the stem of the coaxial insert perfectly inside the range of the radiofrequency (rf) coils of the NMR spectrometer. This is essential to achieve a good shimming quality in the NMR experiments and to get good results.

For quantification, we highly recommend to use the NMR results due to slight deviations in the distance settings between blank and sample. However, during the reaction the distance stays constant enabling a relative quantification of ratios by UV/Vis.

Since photochemical reactions and compounds are often influenced by the presence of oxygen two O-rings were added to make the screw cap air tight. Due to this enhancement, reactions under inert conditions are now open for investigation (as shown

in the recent PDI study in the manuscript). First tests showed an exclusion of air for at least 7 days.

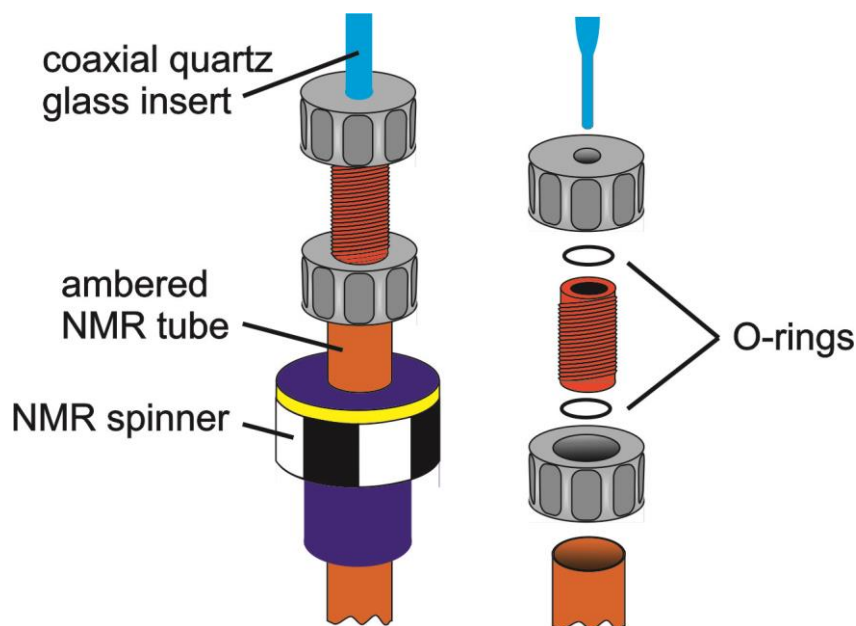


Figure S3. Detailed depiction of the airtight screw cap.

To link the optical fibers with the top end of the coaxial quartz glass insert a second screwable connector was developed. Similar to the airtight screw cap described before also here a union nut and an O-ring was used to connect the coaxial insert with a plastic tube in which both optical fibers were fastened. The tube is furthermore used to stabilize the whole setup and to inject it more easily into the NMR spectrometer.

3.6.1.4 Automation and modification of pulse sequences

As described in section 3.6.1.2 an automated measurement of UV/Vis spectra and LED illumination is achieved by a direct connection of the UV/Vis spectrometer and the LED transistor to the NMR console (Bruker Avance III HD). They are cable (BNC) connected via two RCP outputs of the T-Controller located in the Intelligent Pulse Sequence Organizer (IPSO; here IPSO 19'') unit, which synchronizes all acquisition related processes.

However to run a combined UV/Vis and NMR experiment under the influence of the external LED light source which is exclusively controlled by the NMR console, modified NMR pulse sequences are required. In general the IPSO unit provides a variety of RCP outputs, whereas most of them have a preset function. The free RCP outputs can be programmed by the user adding special events to the standard pulse sequence. The

outputs work on Transistor-transistor-logic (TTL) and are active low by default. By applying certain commands in the pulse program they can be switched from active low to inactive high and back.

Here, the free RCP outputs 28 and 29 were chosen to connect the LED light source and the UV/Vis spectrometer/D-Hal-lamp to the NMR console. According to the Bruker user manual, the following command syntaxes to control the devices were added to the pulse program.

d11 setnmr3^28 and **d11 setnmr3|28** turn the LED off and on

d11 setnmr3^29 and **d11 setnmr3|29** close/open the shutter of the UV/Vis spectrometer and initiate a measurement

(The minimum switching time d11 is given at 25 ns. Note: d11 can also be replaced by a fixed value (e.g. 1s))

To control the UV/Vis spectrometer with these commands, it was necessary to enable the external trigger mode in the related UV/Vis spectrometer software (Avasoft 8.6full).

Figure S4 schematically shows the resulting pulse sequence of a combined UVNMR illumination experiment. Here, the UV/Vis measurement is conducted prior to the NMR measurement under LED illumination. First the LED is turned off, then the shutter inside the D-Hal-lamp opens and the UV/VIS spectrometer initiates a measurement. After the UV/Vis measurement is completed the shutter is closed and the LED is turned on again. Then the common acquisition cycle starts (here: 1D ^1H spectrum), resulting in one UV/Vis spectrum and one NMR spectrum for this experiment. The delay $d_{\text{UV/Vis}}$ is of special interest here. This delay represents the integration time of the UV/Vis measurement (see Avasoft) and is acquired from the manual measurement of the blank sample prior to the actual experiment and has to be adjusted for every new sample.

For every measurement with this UV/NMR-illumination-setup a blank measurement under the same conditions was made previously to set the parameters for the UV/Vis and NMR measurements.

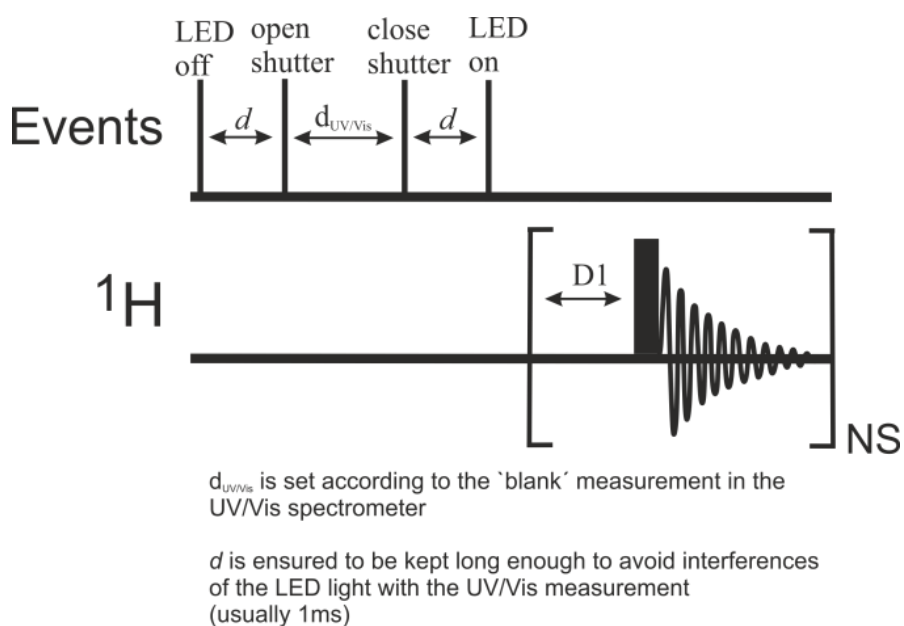


Figure S4. Modified pulse sequence of our combined UVNMR illumination experiment. A series of switching 5V TTL pulses of the T-Controller of the IPSO Unit directly control the UV/Vis spectrometer and the transistor of the illumination LED.

The corresponding pulse program to the pulse sequence shown in Figure S4 is:

```
;zg30_UV_light (based on zg30)
;avance-version (07/04/03)
;1D sequence
;using 30 degree flip angle
;performing one UV/Vis experiment before AQ cycle
;continous illumination during the whole experiment
;
;$CLASS=HighRes
;$DIM=1D
;$TYPE=
;$SUBTYPE=
;$COMMENT=

#include <Avance.incl>
```

```
"acqt0=-p1*0.66/3.1416"
```

```
1 ze
```

```
1m setnmr3^28 ;turn off illumination
```

```
d11 setnmr3|29 ;open shutter start UV/Vis experiment
```

```
1m setnmr3^29 ;close shutter
```

```
1m setnmr3|28 ;turn on illumination
```

```
2 30m
```

```
d1
```

```
p1*0.33 ph1
```

```
go=2 ph31
```

```
d21
```

```
30m mc #0 to 2 F0(zd)
```

```
exit
```

```
ph1=0 2 2 0 1 3 3 1
```

```
ph31=0 2 2 0 1 3 3 1
```

```
;p11 : f1 channel - power level for pulse (default)
```

```
;p1 : f1 channel - 90 degree high power pulse
```

```
;d1 : relaxation delay; 1-5 * T1
```

```
;d11: set d11 according to the blank measurement in the UV/Vis spectrum
```

```
;d21: delay between experiments
```

```
;NS: 1 * n, total number of scans: NS * TD0
```

```
;$Id: zg30,v 1.9 2007/04/11 13:34:31 ber Exp $
```

```
;d11: set d11 according to the integration time of the blank measurement in the UV/Vis spectrum.
```

For most measurements the d11 was determined to be around 400 ms.

The delay of one millisecond (1 m) for the events (setnmr3^28; setnmr3^29; setnmr3|28) ensures that the light emission of the LED is definitely zero to avoid interferences with the UV/Vis measurement.¹

In principle the command series for the UV/Vis measurement can be put anywhere in the pulse program e.g. before, after or during acquisition. Furthermore the command order can be changed at will if needed e.g. for experiments requiring light pulses instead of continuous illumination.

Since in our case the standby output level of the RCP used for the connection to the UV/Vis spectrometer and the D-Hal-lamp was high (~5 V) the shutter of the D-Hal-lamp was opened after every NMR experiment. To avoid the influence of the emitted light to the sample a customized TTL inverter between the NMR console and the UV/Vis spectrometer was added to set the standby TTL level low (~0 V).

3.6.1.5 Comparison of reaction rates – conventional LED illumination setup vs new combined LED UVNMR-illumination setup

To check for possible disadvantages of our new UVNMR-illumination setup we conducted a study about the illumination capabilities compared to our old illumination setup.¹ Figure S5 shows a schematic top view of our current illumination setup A) and our new UVNMR-illumination setup B) in the NMR tube. Our new systems have two major differences compared to our established illumination setup. First, instead of one fiber the glass insert is now filled with two fibers, the illumination fiber and the UV/Vis fiber. As the UV/Vis fiber is not transparent to light in horizontal axis this could lead to a 'dark area' (Figure S5B) in the sample which is not reached by the light emitted from the illumination fiber resulting in a hampered reaction rate. Secondly, two fibers require a bigger quartz glass insert (3 mm outer diameter), which in return reduces the layer thickness of the sample from 2 to 1 mm. This could lead to a faster reaction rate if the emitted light is not strong enough to thoroughly penetrate the whole sample in the old illumination setup. Either way, the differences of both setups are so pronounced when it comes to illumination that a comparison seems mandatory.

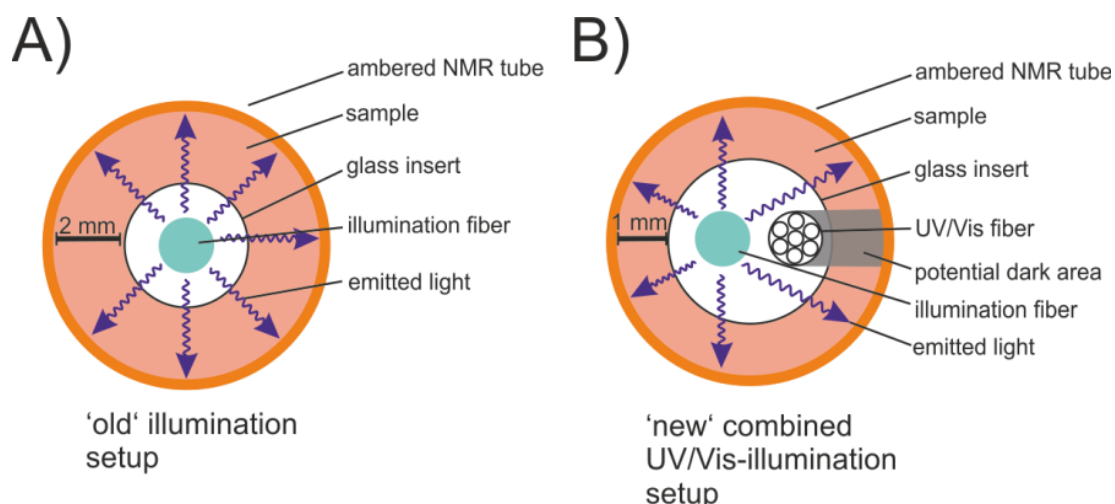


Figure S5. Schematic top view of the two LED illumination setups. A) Depiction of the old, conventional illumination setup with a layer thickness of 2 mm for the sample B) new combined UVNMR-illumination setup with a layer thickness of 1 mm for the sample. Due to the incorporation of the second UV/Vis fiber the issue of an unlit, dark area arises.

As a test reaction for the comparison of reaction rates the photocatalytic oxidation of 4-methylbenzyl alcohol (MBA) with riboflavin tetraacetate (RFTA) was chosen (Figure S6). This reaction was already thoroughly investigated in our working group and does not require the exclusion of oxygen.⁴ Hence, a stock solution can be prepared for all samples which greatly improves the comparability of all measurements.

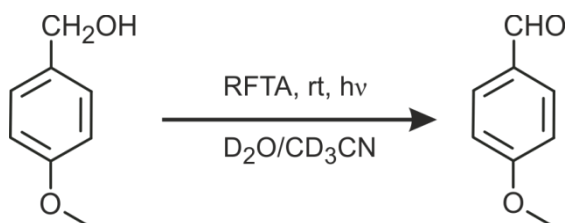


Figure S6. Photocatalytic oxidation of MBA is used as a test reaction for the comparison of reaction rates between the two illumination setups, shown in Figure S5.

Materials: The solvents D_2O and CD_3CN were purchased from Deutero GmbH and Sigma Aldrich. 4-Methoxybenzylalcohol was purchased from Sigma Aldrich and was used without further purification. The photocatalyst Riboflavin tetraacetate (RFTA) was synthesized according to the reported procedures.^{4,5}

Sample preparation: The NMR samples were prepared in pairs as a 1 mL solution of D_2O/CD_3CN (1:1) containing 2 mM riboflavin tetraacetate (RFTA) and 20 mM 4-methoxybenzyl alcohol (MBA). The solution was then split and filled into two ambered NMR tubes, each containing 350 μL of the stock solution. Afterwards the tubes were

connected to their illumination setup by inserting the respective glass insert (2 mm outer diameter for conventional; 3 mm outer diameter for the new quartz glass insert) and sealing everything airtight.

In situ NMR measurements: NMR experiments were conducted on a Bruker Avance 500 spectrometer with a 5 mm QXI probe. The resulting NMR spectra were processed and evaluated with Bruker Topspin 3.2. The samples were illuminated by a Cree XT-E royal blue high power LED with a center wavelength of 450 nm and 500 mW optical output power (Lumitronix, Cree XT-E, 68332). The light was guided directly into the sample with the help of an optical fiber as described previously.¹ After a first ¹H spectrum in the dark, all following spectra were recorded under continuous illumination. There was no need to record alternating illuminated and dark spectra since it was already shown that no signal is distorted by Photo-CIDNP effects in D₂O/CD₃CN. The kinetics were derived from the integrals of the ¹H aldehyde signal of 4-methoxybenzyl aldehyde (MBAld) since it does not overlap with other signals (Figure S7A). The integral of the ¹H MBAld signal was referenced to the aromatic protons of the starting material 4-methoxybenzyl alcohol (MBA).

Discussion: Figure S7A shows that MBAld is generated under continuous blue light illumination. The MBAld aldehyde signal does not overlap with any other signal and is hence suitable for integration. Figure S7B depicts the integral area of the MBAld aldehyde signal **1** under illumination over time for the two compared setups. Whereas the black kinetic corresponds to the conventional illumination setup containing only the illumination fiber and the smaller insert (2 mm) and the red kinetic belongs to the new setup incorporating the illumination and UV/Vis fiber in a bigger insert (3 mm). The reaction profiles clearly reveal that there is no significant difference between the two setups. One might even argue that the newer setup has a slightly higher reaction rate. This could be due to the smaller layer of thickness compared to the old setup (1 mm vs. 2 mm) which allows for a more potent illumination of the sample. But it could also be because of slight differences in the sandblasted fiber tips of the illumination fiber since every fiber tip is crafted individually. In summary, our new setup shows no significant variations in reaction rate compared to our old illumination setup, which implies that the 'dark area' (Figure S5B) caused by the UV/Vis fiber has no notable impact on the reaction rate or at least is canceled out by fast diffusion or by the thinner layer of solution allowing for a better illumination.

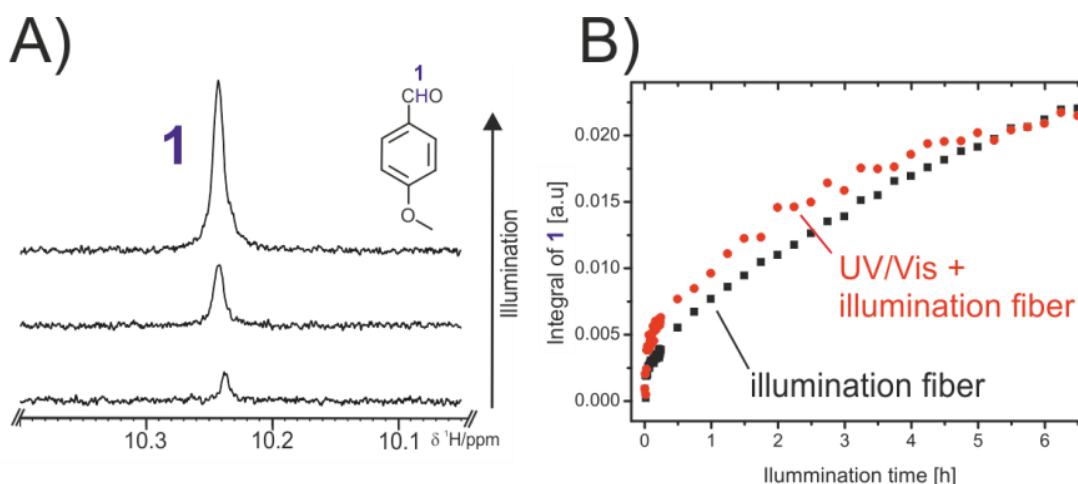


Figure S7. A) Photocatalytic generation of 4-methoxybenzaldehyde over time; the ^1H aldehyde signal 1 at 10.24 ppm poses a suitable signal for integration as it does not overlap with other signals B) Reaction profile of the ^1H aldehyde signal 1 at 10.24 ppm for the two illumination setups: Conventional illumination fiber (black) and UV/Vis fiber + illumination fiber (red).

3.6.2 Summary of conPET processes and investigators of aryl halides with PDI as photocatalyst

3.6.2.1 Summary of conPET processes

Recently, König *et al.* introduced the consecutive photoinduced electron transfer (conPET) process to achieve higher redox potentials.⁶⁻¹² Here aryl radicals can be obtained from aryl halides (**Q**) utilizing the excited states of stable radical anions (**Photocat⁻**) (Figure S8). These stable radical anions are generated via a classical photoinduced electron transfer (PET) process with the help of a sacrificial electron donor (**D**; e.g. NEt_3 , DIPEA). In conPET processes organic dyes (**Photocat.**; e.g. N,N-bis(2,6-diisopropylphenyl)-perylene-3,4,9,10-bis(dicarboximide) (PDI), rhodamine-6G and 9,10-Dicyanoanthracene) are used as photocatalysts as they form stable colored radicals under inert atmosphere.⁸⁻¹¹ Upon a second photoexcitation these stable radicals (**Photocat⁻**) are proposed to form a further excited state (**Photocat^{-*}**), which is able to transfer an electron to aryl halides resulting in an aryl radical precursor (**Q⁻**). After fragmentation this precursor can be trapped by various additives to yield the desired product.⁶⁻¹¹

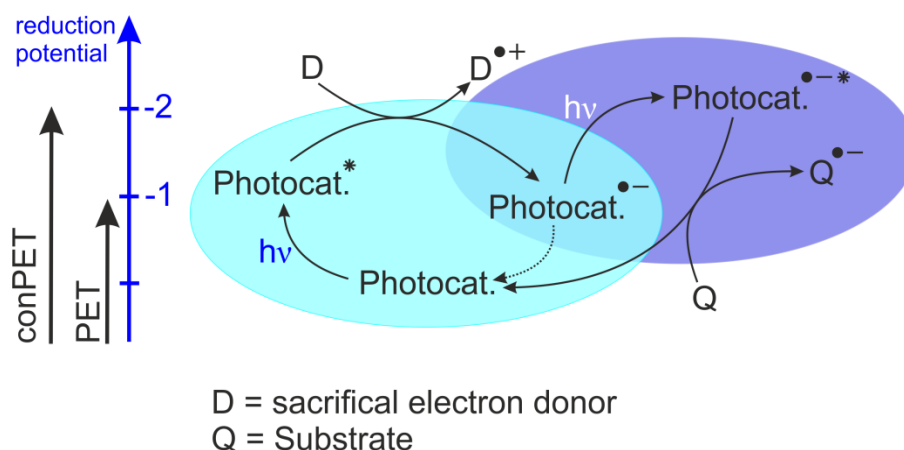


Figure S8. Schematic representation of a consecutive photoinduced electron transfer (conPET) process.

The first conPET process published in 2014 reported the photoreduction of aryl halides with blue light (455 nm) irradiation utilizing *N,N*-bis(2,6-diisopropylphenyl)-perylene-3,4,9,10-bis(dicarboximide) (PDI) as a photocatalyst.⁸ The general reaction conditions are illustrated in Figure S9.

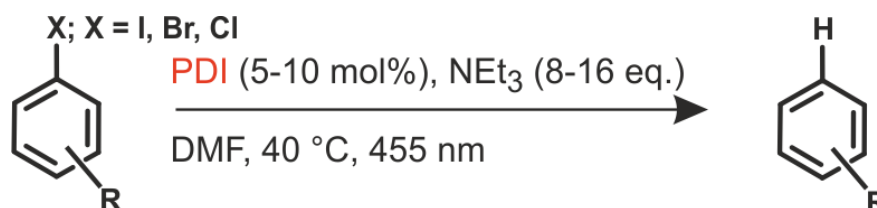


Figure S9. General conditions of the photoreduction of aryl halides via conPET.⁸

In the proposed and controversially discussed reaction mechanism (Figure S10), an initial photoexcitation of **PDI** with blue light (455 nm) yields the excited **PDI***, which gets reductively quenched by the sacrificial electron donor **NEt₃** to yield **PDI^{-•}** and **NEt₃^{•+}**. The stable **PDI^{-•}** radical anion is proposed to be excited by a second photon (455 nm) to give **PDI^{-•*}**. This photoexcited state is supposed to be able to reduce the given substrate (**Ald-Br**) resulting in an aryl radical precursor (**Ald-Br^{-•}**) and ground state **PDI**. **Ald-Br^{-•}** then fragments into **Br⁻** and the neutral radical **Ald[•]**, which can abstract a proton from either **NEt₃^{•+}** or the solvent (e.g. DMF) to give the final product **Ald**.⁸ If the proton was abstracted from **NEt₃** it will lead to a cationic imine species, which immediately reacts with water in solution to give diethylamine (**DEA**) and acetaldehyde.

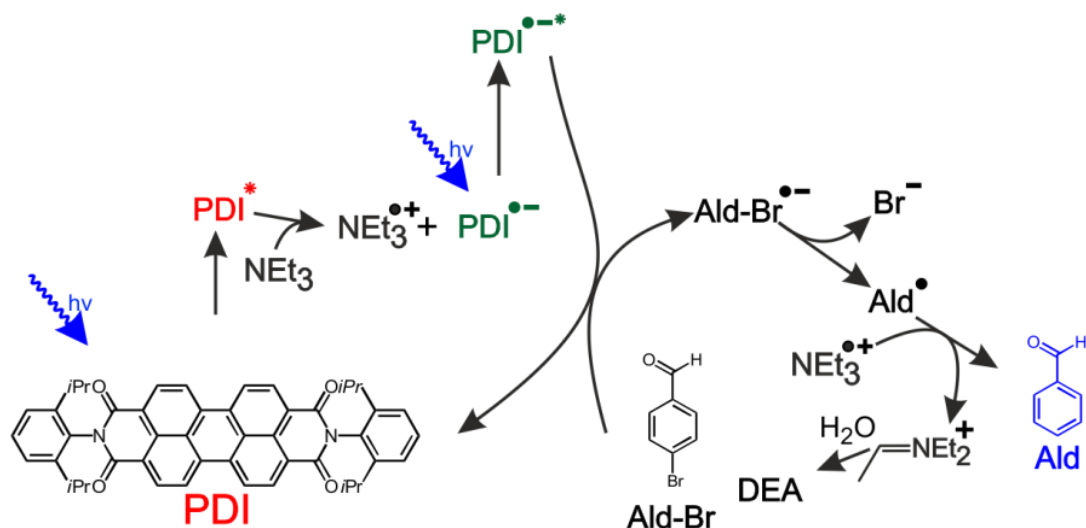


Figure S10. Catalytic mechanism of the first conPET process with PDI as proposed by König *et al.*⁸

3.6.2.2 Investigations of the photoreduction of aryl halides with PDI as photocatalyst

3.6.2.2.1 General information

Materials:

The solvents DMSO- d_6 and DMF- d_7 were purchased from Deutero GmbH. Both solvents were dried over 4 Å molecular sieves and deoxygenated via Freeze-Pump-thaw prior to use. N,N'-Bis(2,6-diisopropylphenyl)-3,4,9,10-perylenetetracarboxylic-diimide (PDI) was purchased from TCI chemicals and used without further purification. 4-bromo-benzaldehyde (Ald-Br) and triethylamine (NEt_3) were purchased from Merck. NEt_3 was dried over 4 Å molecular sieves prior to use and 4-bromo-benzaldehyde (Ald-Br) was used without further purification.

Combined UVNMR-illumination reaction profiles

All measurements were conducted on a Bruker Avance III HD 600 (600.13 MHz) spectrometer with a fluorine selective TBIF probe in combination with our new UVNMR-illumination device described in section 3.6.1. The samples were illuminated by a Cree XT-E royal blue high power LED (Lumitronix, 450 nm; 500 mW, 68332).

If not otherwise indicated, measurements were conducted at 313 K in 300 μ L solutions of DMF- d_7 or DMSO- d_6 containing 1 mM (0.1 eq.) N,N-bis(2,6-diisopropylphenyl)-perylene-

UVNMR-illumination

3,4,9,10-bisdicarboximide (PDI), 10 mM (1 eq.) 4-bromo-benzaldehyde (Ald-Br) and 80 mM (8 eq.) triethylamine (NEt₃).

Preparation blank:

Ald-Br and NEt₃ were dissolved in DMF-d₇ in an NMR tube under inert conditions. The quartz glass insert was added and the sample was sealed airtight with the customized screw cap (see setup).

Blank measurement:

The blank measurement was conducted prior to the combined reaction kinetic. The sample was injected into the NMR spectrometer to reach a temperature of 313 K. Then a blank UV/Vis spectrum was recorded. The resulting integration time given by the UV/Vis spectrometer determined the d11 delay in the NMR pulse program (section 3.6.1.4), which was necessary for later automation. An NMR spectrum was also taken as quality control, which ensured correct sample preparation.

Preparation sample:

Under argon atmosphere the required amount of PDI was added to the blank sample. The quartz glass insert was inserted and the sample was sealed with our customized screw cap. To dissolve the PDI completely the sample was sonicated.

Oxygen-test:

Prior to the kinetic investigations an oxygen-test sequence was conducted for every new sample to exclude the presence of oxygen. Therefore, the prepared sample was put into the NMR spectrometer to reach a temperature of 313 K. All **PDI** signals start to broaden once illumination starts. If oxygen is present in the reaction solution the **PDI** signals sharpen again once the light is turned off. This behavior can be exploited as a simple test to verify successful deoxygenation. Three single scan NMR spectra are measured in total. The first one before any illumination took place. The second one after an illumination time of 1.0 s and the third one two minutes after the illumination. As 1.0 s of illumination is already enough to induce the line broadening, the **PDI** signals are broader in spectrum two. If oxygen is present the **PDI** signals in spectrum three are sharp again, if deoxygenation was successful then spectrum two and three are identical.

Sample measurement:

For all NMR measurements the delay d11 in the pulse program was set to the required integration time determined in the blank UV/Vis measurement. The reaction profiles were generated by alternately recording non illuminated and illuminated ^1H NMR spectra. This ensured that no signal intensities were distorted by possible photo-CIDNP effects.⁴ One UV/Vis spectrum was automatically recorded prior to every NMR measurement (dark and light). After a first spectrum without illumination a row of ^1H spectra was collected alternating between illuminated and unilluminated proton spectra. Only spectra without illumination were used to generate reaction profiles. The NMR kinetics are derived from the aromatic proton integrals of **Ald-Br** and **Ald** (Signal **3**, Figure S11) and referenced to the respective signal in the first spectrum without illumination. Assignments were made by evaluating standard sets of 1D and 2D NMR spectra. The chemical shifts were referenced to the solvent signals (DMF- d_7). The UV/Vis kinetics are derived from the absorption maximum of the radical anion of **PDI** at 798 nm (see manuscript). Its intensity is referenced semi-quantitatively to its own maximum absorbance (=1.0). Referencing the radical anion to the ground state **PDI** was not possible because of the donor-acceptor complex of PDI and NEt_3 .

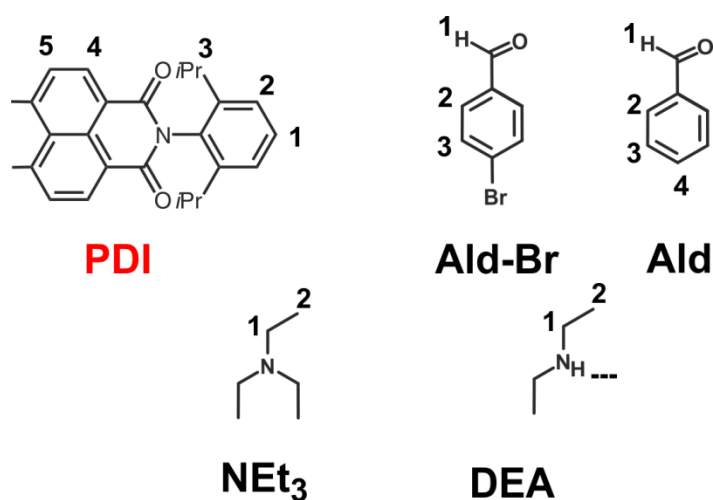


Figure S11. Numeration of PDI, Ald-Br, Ald, NEt_3 and DEA used for the assignment and further characterization.

3.6.2.2.2 Assignment of starting materials, photocatalyst and products

Assignments were made by evaluating standard sets of 1D and 2D NMR spectra.

Figure S12 shows the ^1H proton spectrum with an illustration of all reaction components before illumination under reaction conditions (PDI 1 mM, Ald-Br 10 mM, NEt_3 80 mM, deoxygenated in DMF-d_7 at 313 K) before illumination.

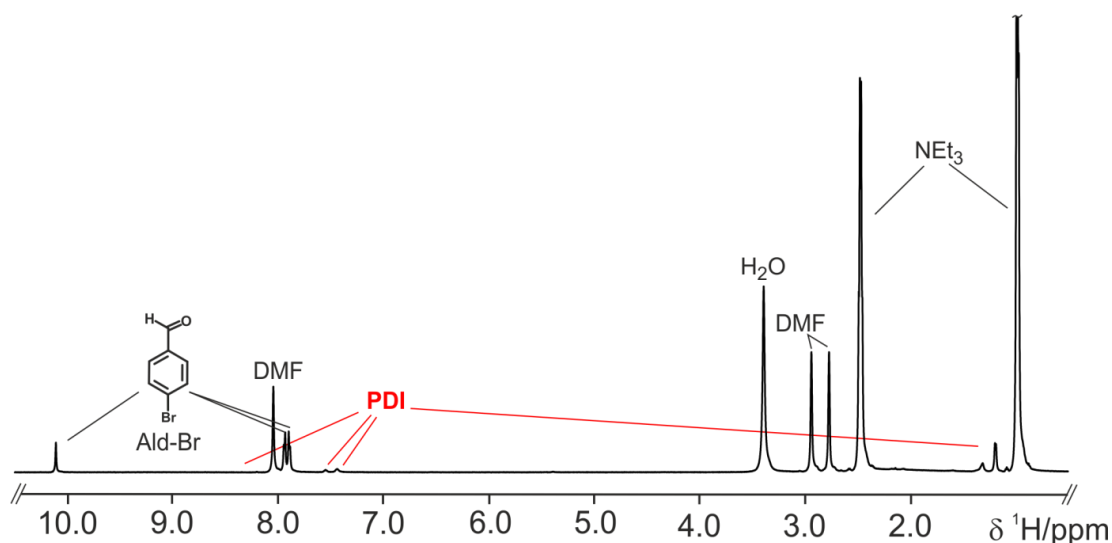


Figure S12. Full ^1H proton NMR spectrum of the reaction mixture at 313 K in DMF-d_7 before illumination. The reaction components PDI (1 mM), Ald-Br (10 mM) and TEA (80 mM) are illustrated.

Figure S13 depicts the assignments for the most prominent reaction components. As described in the manuscript all **PDI** signals are significantly broadened even prior to illumination with respect to their distance to the perylene core probably because of an acceptor-donor complex with NEt_3 . Especially the **PDI** proton signals **4** and **5** are broadened so much that they are only detectable as one broad signal just above the noise level (Figure S14). Hence the chemical shift for the **PDI** protons **4** and **5** can only be given in a chemical shift range from 9.7 to 8.6 ppm. The methine proton of the isopropyl group of **PDI** was not assignable as it is covered by the DMF signal at 2.92 ppm and is hence not discussed further. The remaining **PDI** proton signals could be readily assigned. The other reaction components (**Ald-Br**, **Ald**, NEt_3 and **DEA**) also can be assigned in a straightforward manner. The amine proton of **DEA** is not assignable probably due to exchange line broadening with the residual water in solution. The reaction product **Ald** is partially deuterated (ratio 1:2 H/D), since the reaction is carried out in fully deuterated DMF which can also act as a proton source besides NEt_3 .

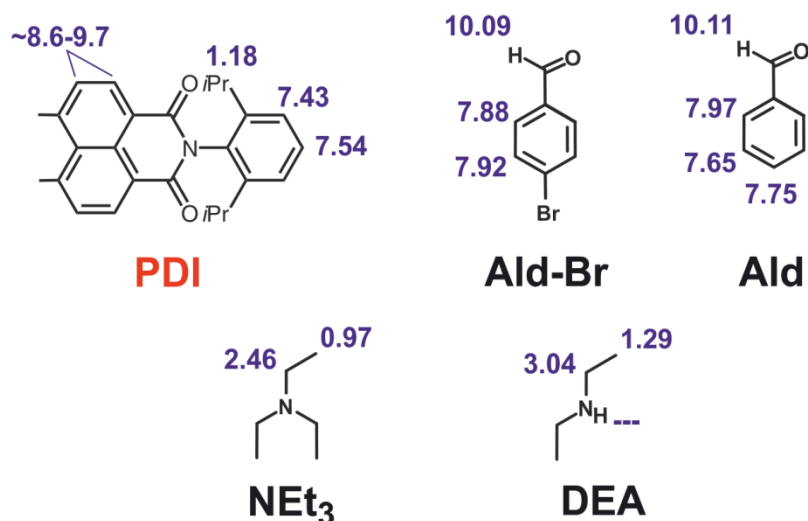


Figure S13. Assignment of PDI, Ald-Br, Ald, TEA and DEA in DMF-d₇. ¹H chemical shifts are highlighted blue and referenced to DMF (8.03 ppm). For the isopropyl groups only one chemical shift for the methyl groups is given because the methine proton is completely covered by the DMF solvent signal at 2.92 ppm.

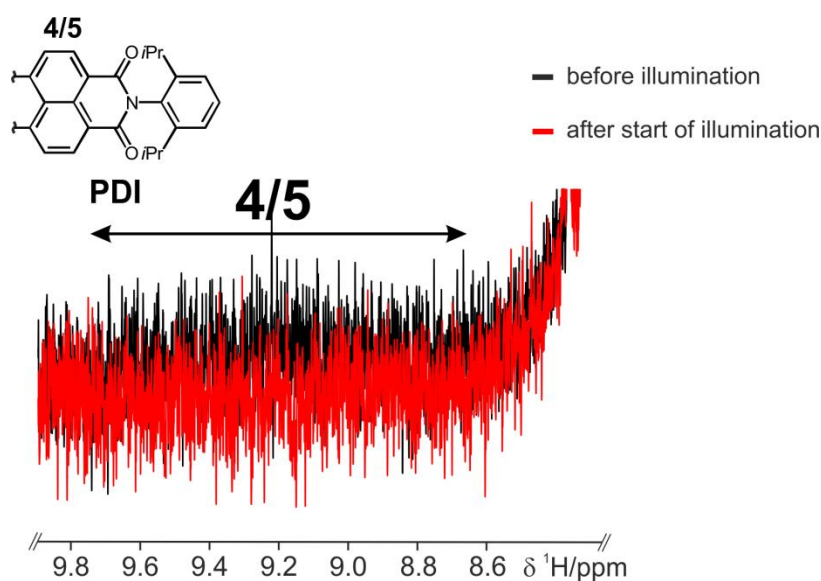


Figure S14. Excerpt of the ¹H proton spectrum region of the broadened PDI proton signals 4 and 5 prior to illumination (black) and after the light is turned on (red). The proton signals 4 and 5 appear as one broad signal just above the noise level and vanish immediately after the light is turned on.

3.6.3 Investigations of a common photoswitch

Materials:

The solvent THF-d₈ was purchased from Deutero GmbH. 1,3,3-Trimethylindlino-6'-nitrobenzopyrolospiran **1** was purchased from TCI chemicals and was used without further purification.

In situ UVNMR-illumination experiments:

All measurements were conducted on a Bruker Avance III HD 600 (600.13 MHz) spectrometer with a fluorine selective TBIF probe in combination with our new UVNMR-illumination device described in section 3.6.1. The samples were illuminated by a high power UV LED (Laser Components, 365 nm, 2.06 W, LEUVA66X00RV00).

The samples described here, all contained a solution of 1 mM 1,3,3-trimethylindlino-6'-nitrobenzopyrolospiran **1** in 300 µL of THF-d₈.

Preparation blank:

To measure the required UV/Vis spectrum of a blank sample, 300 µL THF-d₈ were transferred into the NMR tube, the glass insert was inserted and the tube was sealed airtight with our customized screw cap.

Blank measurement:

The blank measurement was conducted prior to the kinetic investigations. The blank was put into the NMR spectrometer to reach a temperature of 300 K or 180 K respectively. Then a blank UV/Vis spectrum was recorded. The resulting integration time given by the UV/Vis spectrometer determined the d11 delay in the NMR pulse program (section 3.6.1.4), which was necessary for latter automation. An NMR spectrum was also taken as quality control, which ensured correct sample preparation.

Preparation sample:

The 1,3,3-trimethylindlino-6'-nitrobenzopyrolospiran **1** was added to the blank sample, the glass insert was inserted into the sample and the tube sealed airtight with our customized screw cap.

Sample measurement:

After a first proton spectrum without illumination, the photoswitching process of **1** to its open form **2** was observed by a row of ¹H NMR spectra under continuous illumination

with 365 nm. One UV/Vis spectrum was automatically recorded prior to every NMR measurement (section 3.6.1.4). When the absorption maxima of the open species **2** reached a plateau at 300 K, the illumination was turned off and a row of ^1H NMR one scan spectra (one spectrum every 8 seconds with UV/Vis recordings) were recorded to follow the thermal back reaction to **1**. At 180 K a row of ^1H NMR spectra was taken every 20 min because of the drastically increased half-life $\tau_{1/2}$ of **2**. Quantification of the NMR signals was derived from the integrals of the methyl group (1) of **1** and the corresponding signal of **2**. Assignments were made by evaluating standard sets of 1D and 2D NMR spectra like ^1H , $^1\text{H}, ^1\text{H}$ -COSY, $^1\text{H}, ^1\text{H}$ -TOCSY, $^1\text{H}, ^1\text{H}$ -NOESY, $^1\text{H}, ^{13}\text{C}$ -HSQC, $^1\text{H}, ^{13}\text{C}$ -HMBC. For the numeration see Figure S15. The chemical shifts were referenced to the solvent signals. The UV/Vis absorption maximum at 533 nm was taken for half life determination of **2**. Evaluation of the half life $\tau_{1/2}$ was done by the exponential fit function of Origin 8.

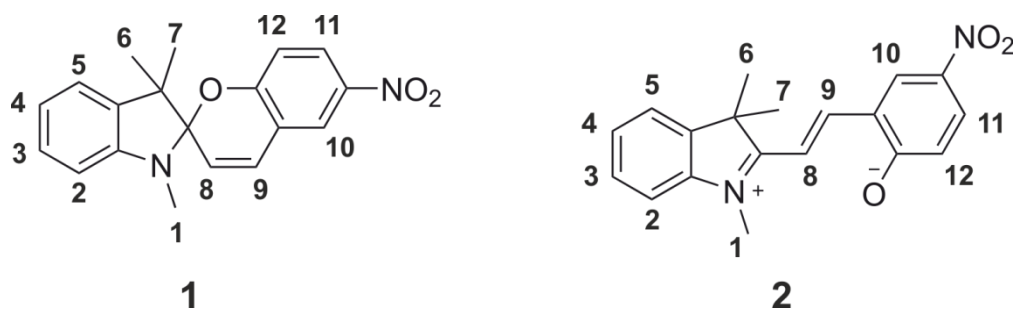


Figure S15. Numeration of 1,3,3-trimethylindolino-6'-nitrobenzopyrolospiran **1** and its open switched form **2** used for the assignment and further characterization.

3.6.3.1 Assignments of **1** and its open form **2**

Assignments were made by evaluating standard sets of 1D and 2D NMR spectra (see Figure S16).

The open form **2** could not be assigned at 300 K as it started to photodegrade very fast (< 30 min) under continuous illumination with 365 nm preventing a full 2D NMR set. All other species (**1** at 300 K, **1** at 180 K and **2** at 180 K) could be assigned in a straightforward manner.

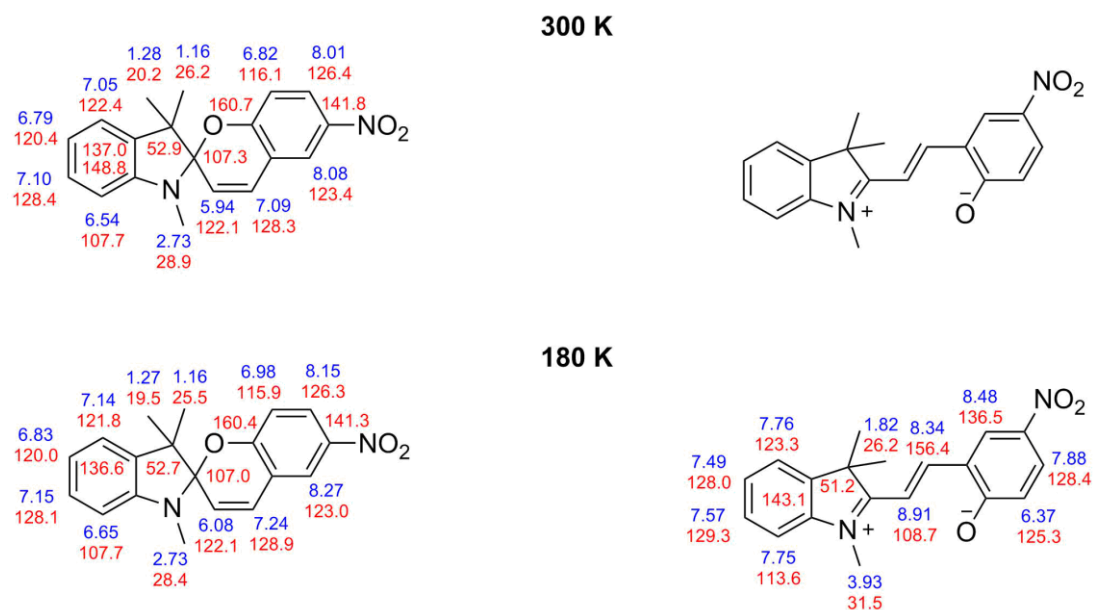


Figure S16. Assignment of **1** and its open form **2** in THF- d_8 at 300 K (top) and 180 K (bottom). ^1H chemical shifts are highlighted blue, ^{13}C chemical shifts are highlighted red. The assignment of the open form **2** at 300 K was not possible due to rapid degradation under continuous illumination with 365 nm.

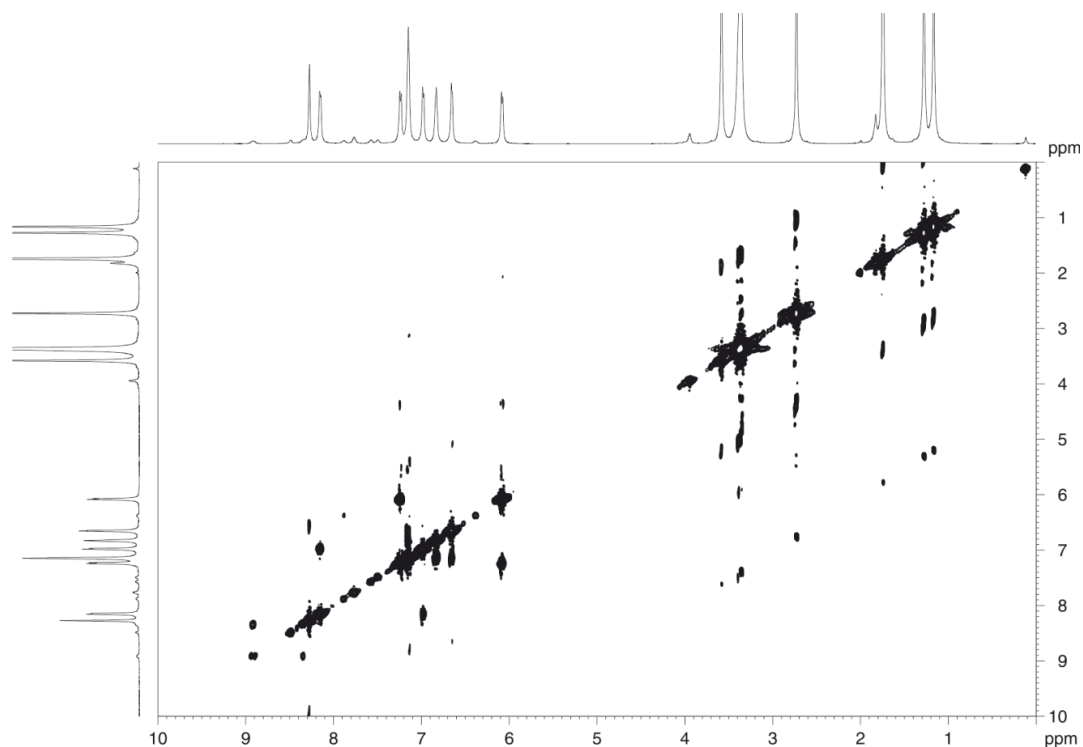


Figure S17. $^1\text{H}, ^1\text{H}$ -COSY of spiropyran **1** and its open form **2** in THF- d_8 at 180 K.

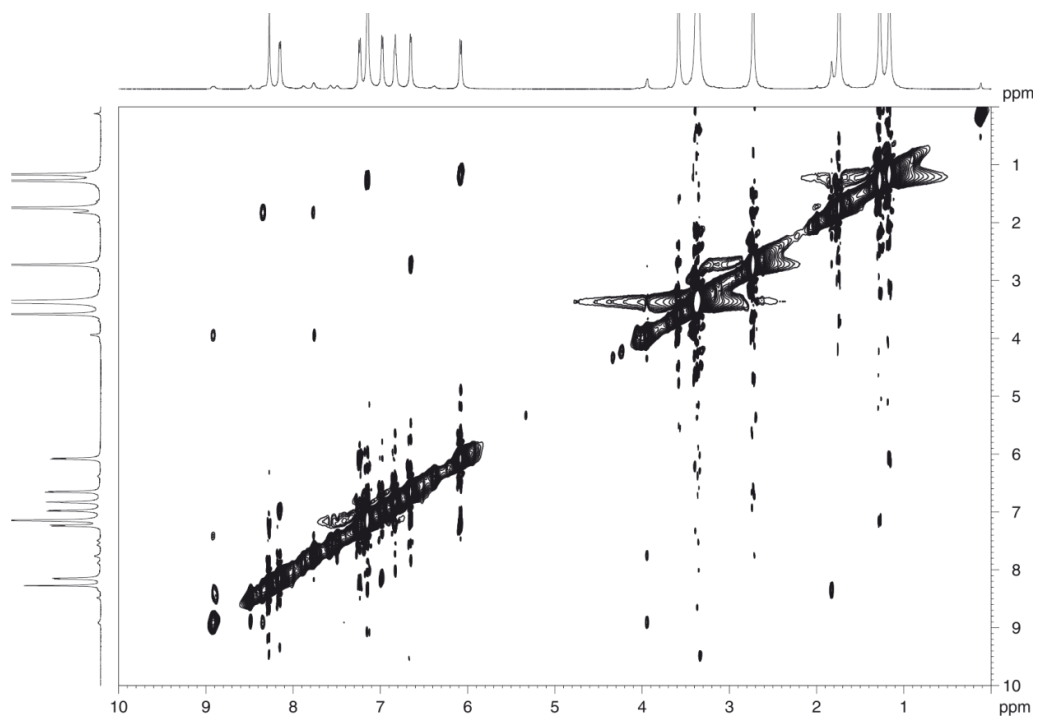


Figure S18. $^1\text{H},^1\text{H}$ -NOESY of spiropyran **1** and its open form **2** in THF-d_8 at 180 K. Mixing time 200 ms.

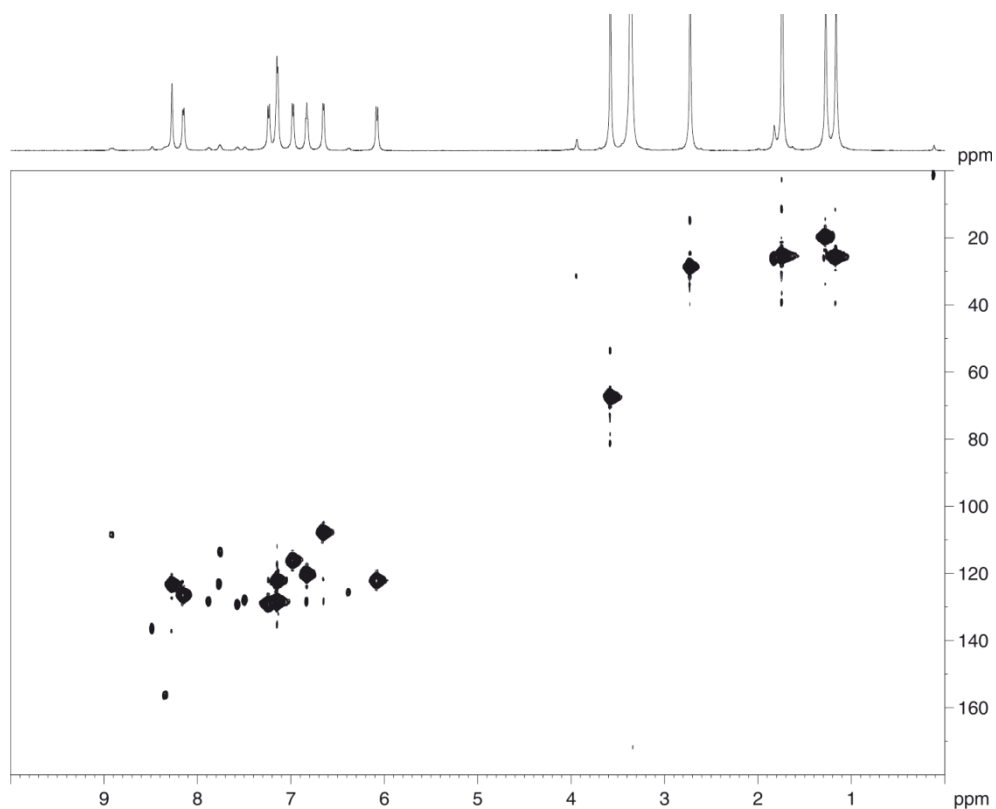


Figure S19. $^1\text{H},^{13}\text{C}$ -HSQC of spiropyran **1** and its open form **2** in THF-d_8 at 180 K.

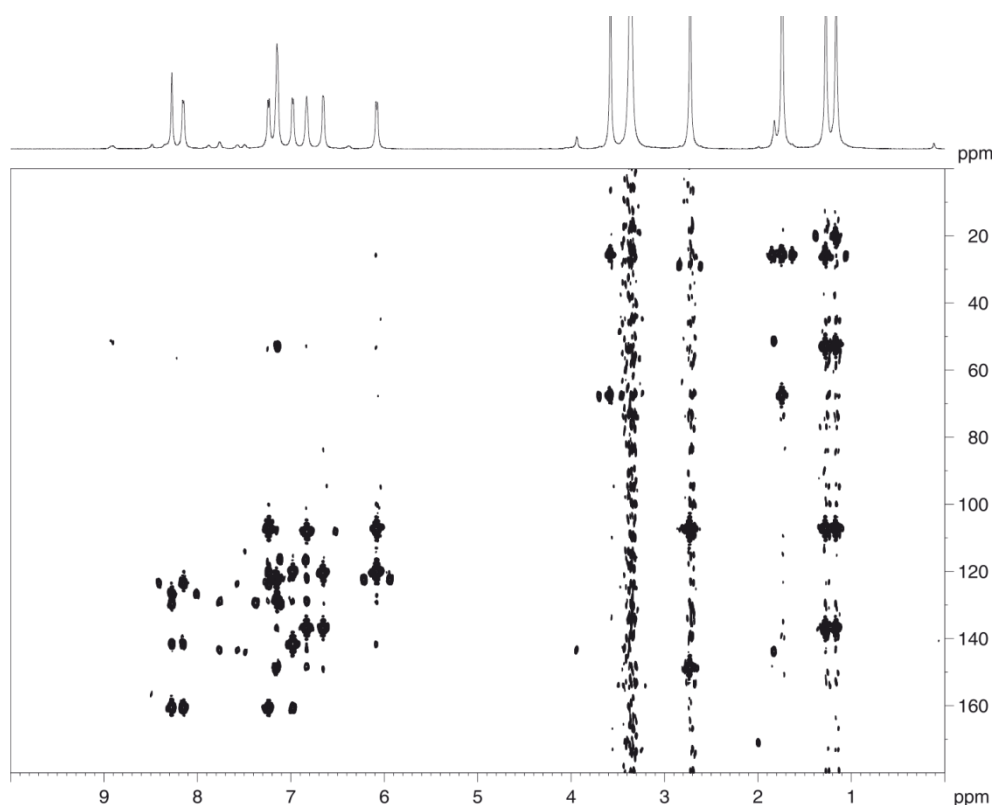


Figure S20. ^1H , ^{13}C -HMBC of spiropyran **1** and its open form **2** in THF-d_8 at 180 K.

3.6.3.2 NMR and UV/Vis build up and decay curves of **2**

3.6.3.2.1 Isomerization experiments at 300 K

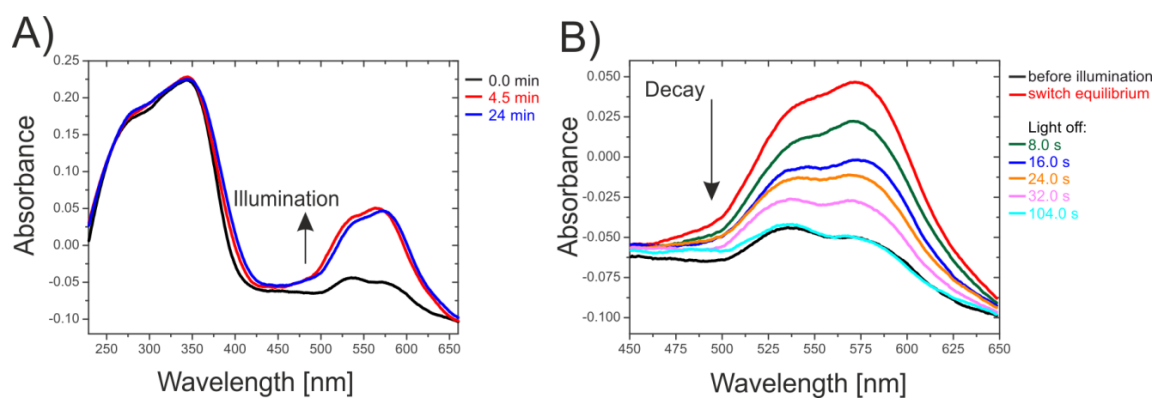


Figure S21. *In situ* recorded UV/Vis spectra of a solution of **1** in 300 μL THF-d_8 at 300 K
 A) buildup of the open form **2** under continuous illumination with 365 nm (increase of absorbance from 450-650 nm) B) excerpt of the UV/Vis spectrum from 450-650 nm showing the thermal back reaction of **2** to **1** once the light is turned off.

It is to be noted that the UV/Vis spectra recorded with the UVNMR-illumination setup sometimes show negative absorbances (as shown e.g. in S21). These negative absorbances are caused by slight deviations in the distance and/or positioning of the reflector and the dip probe between blank and actual measurement.

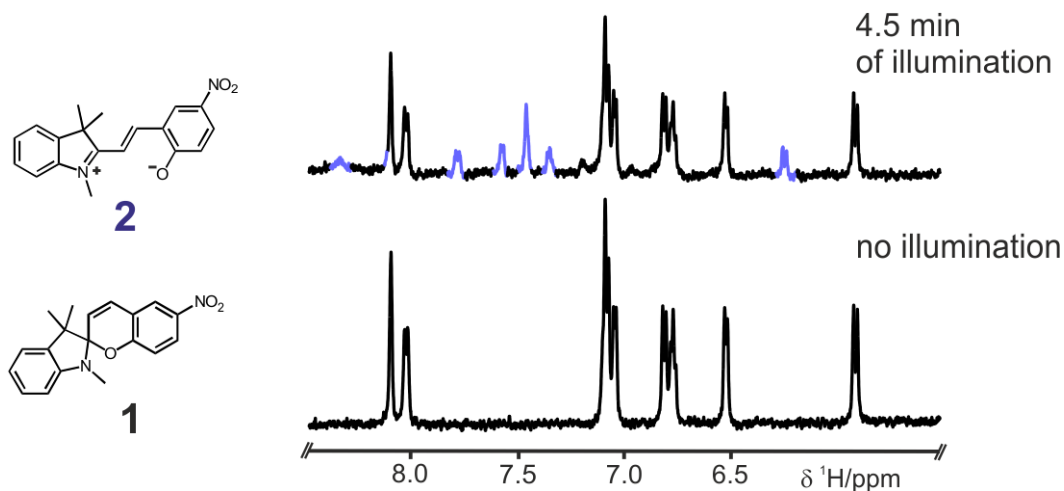


Figure S22. Excerpt of NMR spectra showing the photoswitch **1** in a solution of 300 μL THF- d_8 at 300 K prior to illumination (bottom) and the mixture of **1** and **2** once the photostationary state is reached (top) under illumination with 365 nm.

To evaluate the half-life $\tau_{1/2}$ of **2** in THF- d_8 at 300 K the light was turned off once the photostationary state was reached and one UV/Vis spectrum was taken every eight seconds. Afterwards the absorbance of the maximum at 533 nm (belonging to the open form **2**) was taken and plotted against the elapsed time (Figure S23). Those values were then fitted via exponential decay in Origin8 (ExpDec1). Using the equation shown in Figure S23 a half-life of 17.4 s was determined for **2** in THF- d_8 at 300 K.

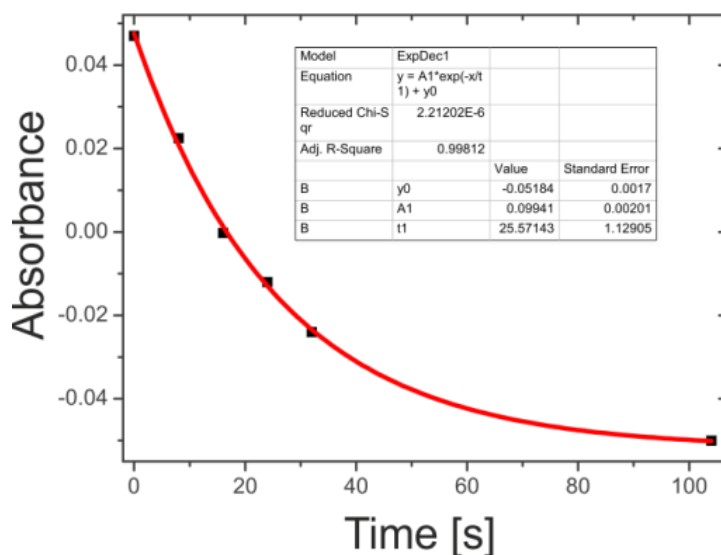


Figure S23. Plotted decay of the absorbance of **2**. After the photostationary state was reached the light was turned off to evaluate the half-life of **2** in THF- d_8 at 300 K. The absorbance values were taken from the maximum at 533 nm (see Figure S21B). Origin8 was used to fit the data via exponential decay (ExpDec1).

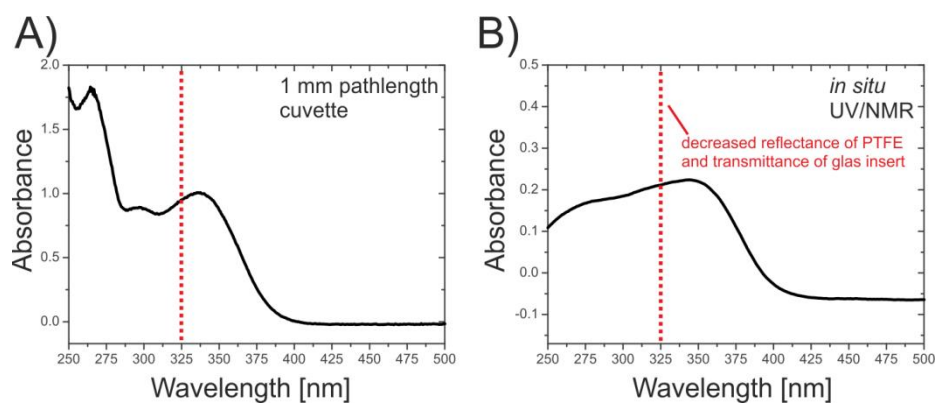


Figure S24. A) UV/Vis spectrum of **1** (1 mM) in THF in a 1 mm path length cuvette at ambient temperature. B) UV/Vis spectrum of **1** (1 mM) in THF with the in situ UVNMR-illumination device at 300 K. Until ~ 325 nm both spectra are comparable (respective absorbance maxima are 341 nm for A and 344 nm for B). Below 325 nm major differences can be observed between two methods probably because of the reduced reflectance of PTFE (from below 380 nm) and reduced transmittance of the glass insert at shorter wavelengths.

3.6.3.2.2 Isomerization experiments at 180 K

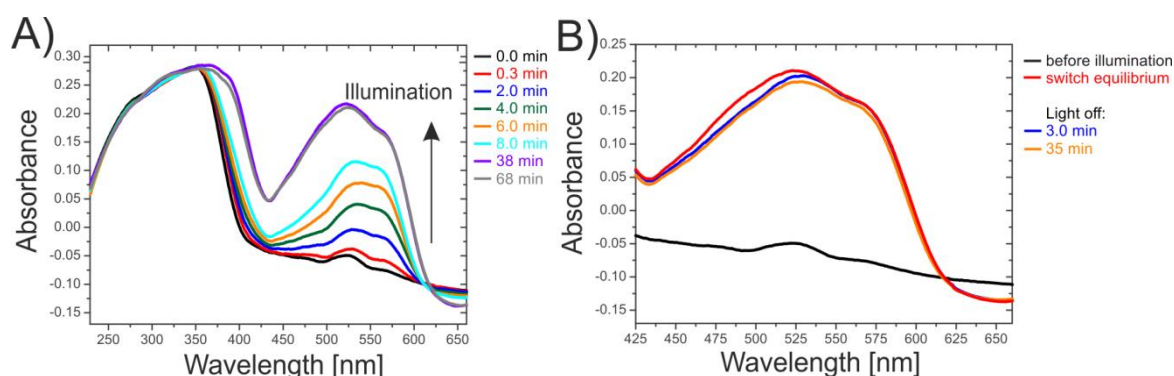


Figure S25. *In situ* recorded UV/Vis spectra of a solution of **1** in 300 μL THF- d_8 at 180 K A) buildup of the open form **2** under continuous illumination with 365 nm (increase of absorbance from 450-650 nm) B) excerpt of the UV/Vis spectrum from 425-655 nm showing that the thermal back reaction of **2** to **1** is prevented by the reduced temperature.

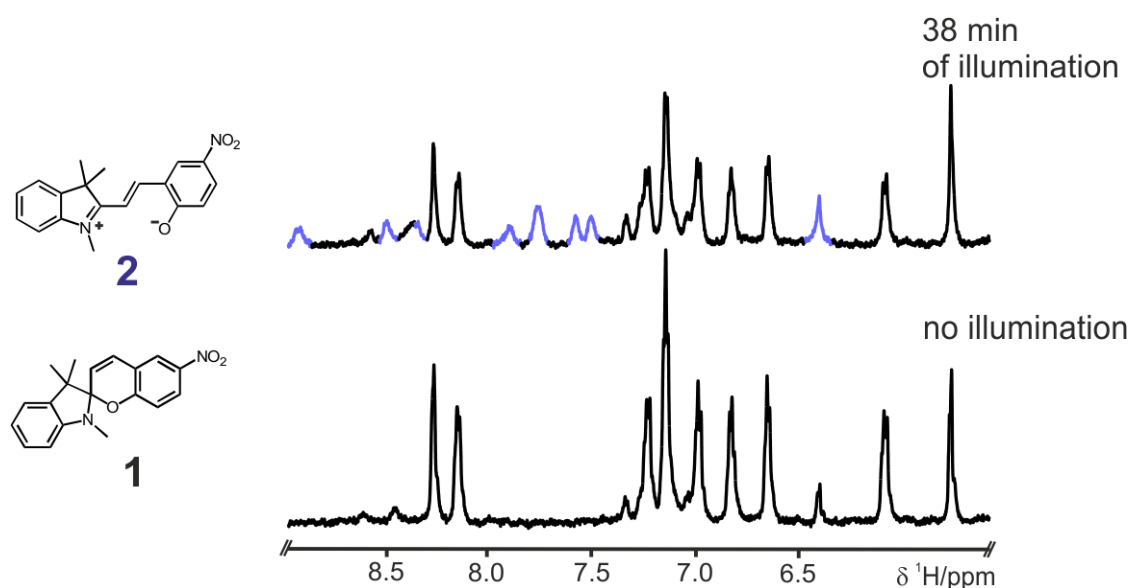


Figure S26. Excerpt of NMR spectra showing the photoswitch **1** in a solution of 300 μL THF- d_8 at 180 K prior to illumination (bottom) and the mixture of **1** and **2** once the photostationary state is reached (top) under illumination with 365 nm.

3.6.3.3 Photodegradation

It was observed that the photoswitch system of **1** and **2** is very prone to photodegradation at 365 nm. Both at 300 K and 180 K photodegradation starts after around 25-45 min preventing a study of the system under continuous illumination with 365 nm. Hence only **2** at 180 K could be structurally assigned unambiguously as the

thermal back reaction could be prevented by the reduced temperature and so the light could be turned off without the decrease in intensity of signals of **2**. Figure S27 shows the photodegradation of **1** and **2** under continuous illumination with 365 nm in THF- d_8 at 180 K. The UV/Vis spectrum (Figure S27A) loses the characteristic absorbance of the open form **2** from 425-625 nm and even the dominant absorbance of **1** loses some absorbance at around 375 nm indicating that not only **2** but also **1** gets photodegraded under continuous irradiation. Figure 27B shows a row of NMR spectra corresponding to the UV/Vis spectra of Figure S27A. Here the strength of NMR spectroscopy is showing as it immediately confirms that not only the open form **2** but also the initial photoswitch **1** is completely degraded after overnight illumination with 365 nm.

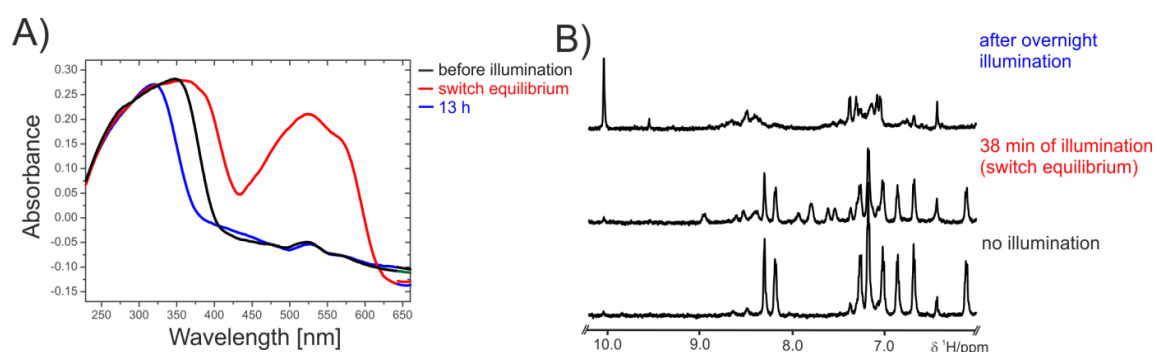
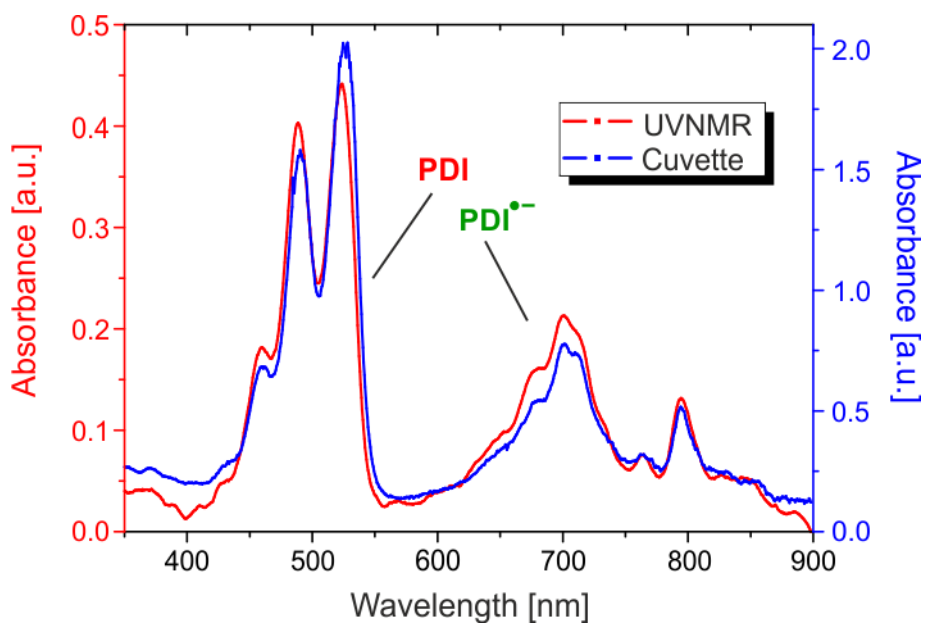


Figure S27. Degradation of the photoswitch **1** and its open form **2** under continuous illumination with 365 nm in THF- d_8 at 180 K. A) *in situ* recorded UV/Vis spectra show the combined absorbance of the photostationary state of **1** and **2** (red) is mostly gone after overnight illumination (blue) indicating photodegradation of **1** and **2**. B) row of NMR spectra corresponding to the UV/Vis spectra unambiguously confirm a full photodegradation of **1** and **2** under continuous illumination.

3.6.4 References

- (1) C. Feldmeier, H. Bartling, E. Riedle, R. M. Gschwind, *J. Magn. Reson.* **2013**, *232*, 39–44.
- (2) P. M. Tolstoy, B. Koeppe, G. S. Denisov, H.-H. Limbach, *Angew. Chemie Int. Ed.* **2009**, *48*, 5745–5747.
- (3) B. Koeppe, P. M. Tolstoy, H. H. Limbach, *J. Am. Chem. Soc.* **2011**, *133*, 7897–7908.
- (4) C. Feldmeier, H. Bartling, K. Magerl, R. M. Gschwind, *Angew. Chemie Int. Ed.* **2015**, *54*, 1347–1351.
- (5) D. B. McCormick, *J. Heterocycl. Chem.* **1970**, *7*, 447–450.
- (6) A. Graml, I. Ghosh, B. König, *J. Org. Chem.* **2017**, *82*, 3552–3560.
- (7) M. Poznik, B. König, *React. Chem. Eng.* **2016**, *1*, 494–500.
- (8) I. Ghosh, T. Ghosh, J. I. Bardagi, B. König, *Science* **2014**, *346*, 725–728.
- (9) M. Neumeier, D. Sampedro, M. Majek, V. de la Pena O'Shea, A. Jacobi von Wangelin, R. Pérez-Ruiz, *Chem. Eur. J.* **2017**, 1–5.
- (10) I. Ghosh, B. König, *Angew. Chemie Int. Ed.* **2016**, *55*, 7676–7679.
- (11) L. Zeng, T. Liu, C. He, D. Shi, F. Zhang, C. Duan, *J. Am. Chem. Soc.* **2016**, *138*, 3958–3961.
- (12) B. König, *European J. Org. Chem.* **2017**, *2017*, 1979–1981.

4 Photoinduced Dehalogenation of Aryl Halides with Perylene Bisimides Investigated by (UV)NMR Spectroscopy – What is the catalyst?



Philipp Nitschke, and Ruth M. Gschwind*

All NMR, UVNMR, and UV/Vis experiments were performed by Philipp Nitschke, except the *ex situ* NMR test, which were done by Veronica Scheidler. Philipp Nitschke and Ruth M. Gschwind wrote the manuscript. Ruth M. Gschwind supervised the project.

4.1 Abstract

Photo-induced electron transfer (PET) is one of the most common processes to initiate a photoreaction. But lately new techniques such as the consecutive photo-induced electron transfer (ConPET) were developed that push beyond the boundaries of conventional PET. ConPET employs small organic dyes and describes the ability of the photocatalyst to utilize the energy of two photons for a photochemical transformation. Although the mechanistic proposal of ConPET was recently verified for rhodamine 6G, the mechanism of the initial ConPET process, which describes the photo-induced dehalogenation of aryl halides by perylene bisimide (**PDI**) is still ambiguous. In fact, a recent study proposes a side reaction of **PDI** with the substrate to form a new catalytic species instead of ConPET. In this study, we further investigate this highly debated mechanism by means of comprehensive UVNMR illumination, *in situ* NMR illumination and UV/Vis spectroscopic studies. Here, we present various insights such as the presence of an electron donor acceptor (EDA) complex prior to illumination, tracking of the **PDI**^{•-} formation under illumination and overall behavior of starting material and products. NMR reaction profiles revealed an extensive initiating phase before the actual product formation starts. Further analysis of this initiating phase showed that **PDI** can interact with itself to most likely form the actual photocatalytic species by pre-arrangement of **PDI** and **PDI**^{•-}. At last we compare **PDI** to the closely related, aggregating **PTCDA**, which indicated that both are behaving similarly. With the combined results we propose a refined mechanistic proposals, which is based on the interaction of **PDI** with itself to generate a new photocatalytic species.

4.2 Introduction

Homogeneous photoredox catalysis has seen tremendous growth in the last decade [1–4] and is still a fast moving area[5–10]. The impressive amount of synthetic applications is usually propelled by photo-induced single electron transfer (PET) processes, with the inherent key feature that the employed catalysts can act in an oxidative or reductive way[4,11–14]. Here, metal organic and organic molecules are usually employed as photocatalysts, whereas metal organic catalysts pose the highest oxidation and reduction potentials when it comes to PETs[3,5,12]. But recently there have been some new approaches that go beyond the application of conventional PET. These yield higher reduction potentials due to inventive energy transfer pathways such as the liberation of hydrated electrons[15–17], triplet-triplet up-conversion[18], sensitization electron transfer[19] and consecutive photo-induced electron transfer (ConPET) processes (**Figure 1.**)[20].

Out of these, ConPET processes gained popularity, due to the ability of a small organic dye to utilize the energy of two photons in a single process to increase its reduction potential, which is a comparable principle to biological photosynthesis. The original ConPET process by Gosh *et al.*[20], first describes regular photoexcitation of *N,N*-bis(2,6-diisopropylphenyl)-3,4,9,10-perylenetetracarboxylic-diimide (**PDI**) and subsequent single electron transfer from a sacrificial electron donor (here: triethylamine; TEA) to yield the radical anion of **PDI** (**PDI^{•-}**; **Figure 1.**). This is analogous to a conventional PET process. But the **PDI^{•-}** can be excited again by a second photon resulting in a highly reducing, excited **PDI^{•-}**, which can readily reduce various aryl halides (**AH**). The resulting aryl halide radical anion (**AH^{•-}**), which then fragment into a halogen anion and a neutral radical (**A[•]**), abstracts a hydrogen from either TEA (or DMF⁵) to yield the final aryl compound **A** (**Figure 1.** right side).

Since, its original introduction by Gosh *et al.* in 2014, several other ConPET systems were proposed and refined[21–25] using other photocatalysts such as rhodamine 6G[22] and 9,10-dicyanoanthracene[23]. But in spite of the success of ConPET in synthetic applications, its mechanistic proposal of a true two photon excitation was highly discussed in the photocatalysis community. Though recently, Haimerl *et al.* could show the two photon excitation for the rhodamine 6G system by single molecule imaging

⁵ Only if DMF is used as a solvent (e.g. DMSO as solvent does not take part in the proton transfer step)

confirming the initial mechanistic proposal of ConPET as valid[26]. But especially the mechanistic proposal for the initial ConPET with **PDI** as photocatalyst is still highly challenged. In fact, in 2018, Marchini *et al.*[27] proposed that the ConPET process is most likely not happening and that the required excited **PDI^{•-}** for ConPET plays no major role in the reduction of aryl halides (see **Figure 1.**). Instead, they proposed a reaction of the excited **PDI^{•-}** with the respective aryl halide (**AH**), which results in the formation of a new catalytic species that drives the actual photoreaction. But despite the execution of extensive UV/Vis spectroscopic investigations as well as other approaches including EPR spectroscopy, NMR spectroscopy and mass spectrometry they were not able to describe the nature of the proposed new species[27]. In face of this confrontation, further mechanistic studies for the photo-induced dehalogenation of aryl halides with **PDI** seem in higher demand than ever.

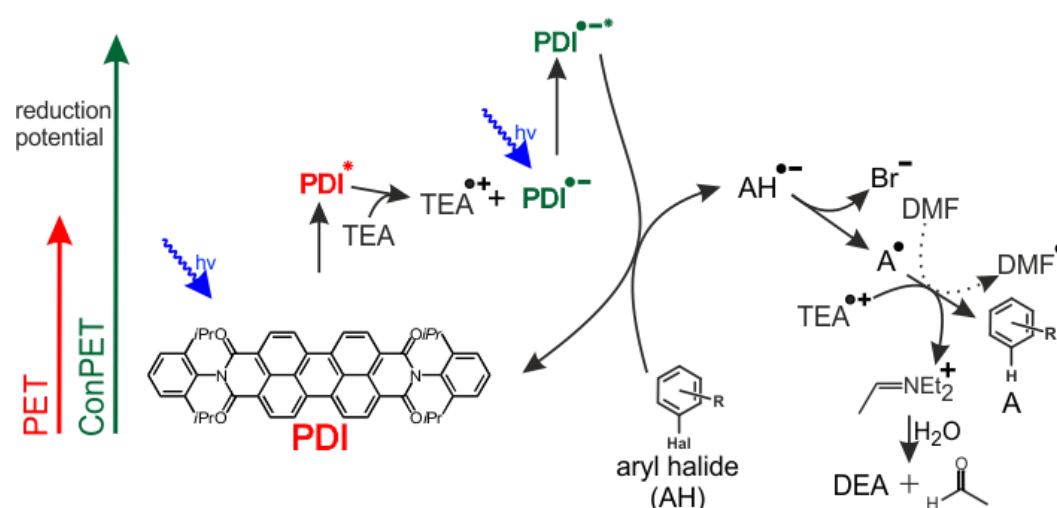


Figure 1. Schematic representation of the consecutive photo-induced electron transfer (ConPET) process with *N,N*-bis(2,6-diisopropylphenyl)-3,4,9,10-perylenetetracarboxylic-diimide (**PDI**) as photocatalyst[20]. After photoexcitation with blue light, **PDI** gets an electron from the sacrificial electron donor triethylamine (TEA) resulting in the radical anion of **PDI** and the radical cation of triethylamine (conventional PET). The generated **PDI^{•-}** can be excited a second time to yield the excited **PDI^{•-*}**, which possesses a much higher reduction potential than the regular **PDI^{•-}** (ConPET) and is able to reduce various aryl halides (**AH**). Subsequently AH fragments into a halide and the neutral radical **A[•]**. The neutral radical can either abstract a hydrogen atom from the TEA (TEA is then further converted to DEA and acetaldehyde) or the solvent to yield the respective aryl compounds (**A**).

In recent years, our group and others have shown that high resolution, solution NMR spectroscopy can be a powerful technique to investigate a broad range of photochemical reactions[28–36] besides established methods such as (ultrafast) UV/Vis[37–46] and EPR spectroscopy[47–50]. It was demonstrated that NMR can give valuable mechanistic information about the initial photoexcited state/radical pair by photo-chemically induced dynamic nuclear polarization (photo-CDINP)[36,51–53] as well as information about solvent effects[28], aggregation[54], chemical structure of critical intermediates[29,31], intermediate sequences in the catalytic cycle[32] and the presence of dark cycles[30,34] by means of classical NMR spectroscopy despite its inherent problems such as low sensitivity and time resolution. Furthermore, we recently presented a triple combination of UV/Vis, NMR spectroscopy and illumination, which allows for the detection of long lived paramagnetic species by UV/Vis spectroscopy simultaneously to NMR measurements[55]. Here, we presented the dehalogenation of aryl halides with **PDI** as a prove of concept reaction and showed that tracking of the long lived, paramagnetic **PDI**^{•-} by UV/Vis spectroscopy and detection of the main diamagnetic reaction components by NMR spectroscopy is readily possible with this UVNMR setup.

The applicability of the UVNMR illumination device and the active discussion about ConPET mechanisms compelled us to continue our mechanistic research towards the dehalogenation of aryl halides with **PDI**. Therefore in this publication, we conducted comprehensive NMR, UV/Vis and UVNMR spectroscopic investigations to get more insight into this unusual photocatalysis.

4.3 Results and Discussion

4.3.1 Test system

As the test system for the dehalogenation of aryl halides with **PDI** we chose 4-bromoacetophenone **1** as the main substrate for our investigations (**Figure 2**). This deviation to our previous work, in which we used 4-bromoacetaldehyde[55], is due to two reasons; first, we wanted to be able to compare our results to the investigations of Marchini *et al.* [27] and second, we found out that 4-bromoacetaldehyde can also react without photocatalyst under irradiation with blue light (therefore we tested **1** for possible background reaction see **Figure S1**). The remaining conditions are similar to our previous work and in accordance with the conditions used by Gosh *et al.*[20] employing **PDI** as the photocatalyst and TEA as a sacrificial electron donor. The reaction is carried out in DMF-*d*7 under inert argon atmosphere at 313 K. Photoexcitation of the photocatalyst was achieved with 450 nm blue light.

From our previous work and as already proposed by Gosh *et al.*[20] we knew that DMF-*d*7 also takes part in the proton transfer besides TEA to yield the final aryl halide **A** (see **Figure 1**.) (here: acetophenone **2**); hence **2** is also partially deuterated (**Figure 2**).

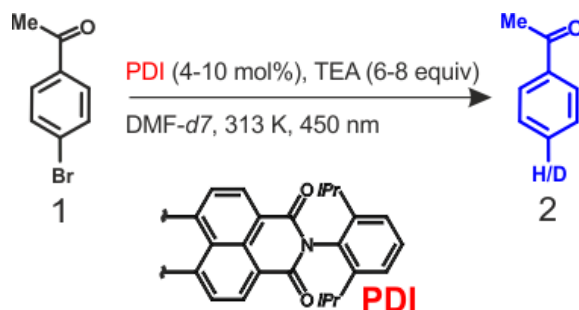


Figure 2. Test system for the mechanistic investigations of the reductive dehalogenation of aryl halides by **PDI**. 4-bromoacetophenone **1** was chosen as a substrate, TEA was used as sacrificial electron donor in 6-8 equiv. and the reaction was conducted in DMF-*d*7 under inert argon atmosphere at 313 K. The sample was irradiated with 450 nm blue light.

Besides the substrate 4-bromo-acetophenone, some measurements used 2-chloro-4-(trifluoromethyl)pyridine **4**, 2-chloro-benzonitrile **6** or 4-bromo-acetaldehyde as substrate. If the reaction conditions deviate from the mentioned conditions above in e.g. substrate, catalyst and/or TEA equivalents etc. it is directly mentioned in the text and/or under the

corresponding figures. ^1H assignments of starting materials and products under reaction conditions can be found in the supporting information (see **Figure S2.**).

4.3.2 *In situ* NMR and UV/Vis measurements under illumination

First, we performed a series of *in situ* illuminated NMR[56] and UVNMR measurements that alternate between NMR spectra, which are with or without illumination. Furthermore, for the UVNMR measurements, one UV/Vis spectrum was acquired before every NMR experiment. **Figure 3. A** depicts the proton spectrum of the whole reaction mixture inside the NMR before illumination. Even before the illumination starts, the **PDI** signals are heavily broadened. This is especially pronounced for the **PDI** signals 5 and 6, which are broadened so much that the signal intensity is almost below the detection limit (**Figure S3.**). In fact, the line broadening effect follows a distance dependent trend, at which signals close to the perylene core are stronger affected than signals which are far away (e.g. signals 3 and 4 are almost unaffected). This distance dependent line broadening was also previously observed in riboflavin derivatives and attributed to exchange processes with a radical species[28,57]. This indicates that the line broadening of the **PDI** signals is also due to exchange with a radical species; in this case **PDI \cdot^-** . To investigate this effect, we carried out a series of titration experiments, which showed that increasing amounts of TEA are the cause of this phenomenon (**Figure S4.**). This heavily indicates the formation of an electron donor acceptor (EDA) complex between **PDI** and TEA even prior to illumination.

This is further corroborated by a simultaneously acquired UV/Vis spectrum prior to illumination (**Figure 3. B**). First, one can clearly recognize the characteristic **PDI** absorbance bands from 400 – 550 nm. But closer inspection of the less intense absorbance in the region from 550 – 900 nm already reveals the presence of the main absorbance band of **PDI \cdot^-** at 705 nm (black line). The UV/Vis spectrum after five minutes of illumination is also superimposed (blue, dashed line) for comparison of the **PDI \cdot^-** absorbance bands. This discovery is directly in line with the NMR data, which suggests an EDA complex between **PDI** and TEA.

These combined results of NMR and UV/Vis spectroscopy indicate that NMR can be highly responsive to the formation of EDA complexes. The signals 5 and 6 of the **PDI** perylene core are already, clearly affected after the addition of 1 mM of TEA (see

Figure S4.), whereas in UV/Vis, high excess of TEA (at least 80 mM) was needed to detect the presence of **PDI^{•-}**.⁶

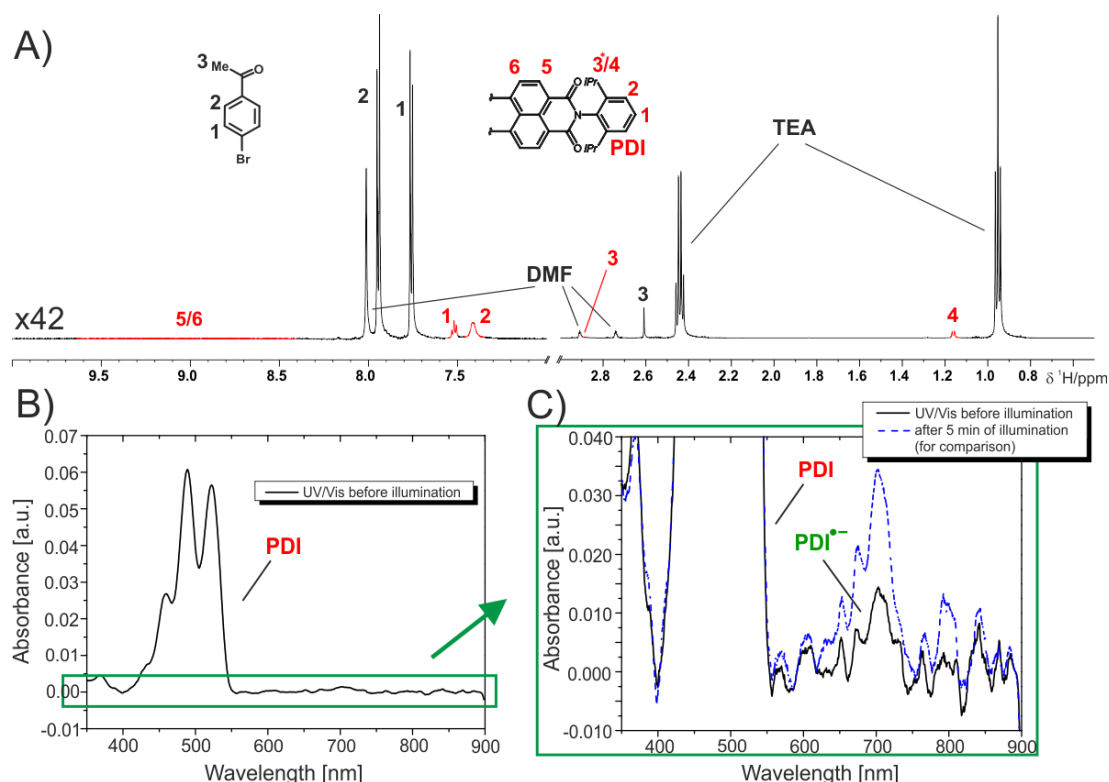


Figure 3. **A)** Proton spectrum depicting the low (left; zoomed in x 42) and high (right) field regions. The **PDI** signals (especially 5, 6 and 2) are already significantly broadened without illumination and the broadening is distance dependent with respect to the perylene core of **PDI**. This features indicate an exchange process with a radical species (**PDI^{•-}**) and strongly hints at an electron donor acceptor (EDA) complex of **PDI** and TEA. **B)** Simultaneously acquired UV/Vis spectrum of **PDI** before illumination. **C)** Zoomed in area of the UV/Vis spectra from B) shows already absorbance bands of the **PDI** radical anion (black line) further corroborating the presence of an EDA complex. The UV/Vis spectrum after 5 minutes of illumination is also superimposed (blue, dashed line) as reference for the **PDI^{•-}** absorbance bands. Reaction conditions: **1** (25 mM), **PDI** (1 mM), TEA (160 mM) in DMF-*d*7 under inert argon atmosphere at 313 K. Illumination with 450 nm blue light. *The methine proton 3 of **PDI** is rarely observable because it usually overlaps with the DMF signals and is not discussed any further.

⁶ The **PDI^{•-}** absorbances were also detected in regular UV/Vis measurements but only at high **PDI** (1 mM) and TEA (80 mM) concentrations in a 1 mm cuvette. In a standard 10 mm cuvette, we could never observe the **PDI^{•-}** absorbances (**PDI** 50 μ M, TEA 4 mM; data not shown) before illumination.

Once the light is turned on various changes in the NMR and UV/Vis spectra become immediately apparent. First, all signals of **PDI** gradually broaden even further and vanish completely after some time (**Figure 4. A**). This is in accordance with the observations for the EDA complex and indicate the transition of **PDI** into the paramagnetic **PDI^{•-}**. **Figure 4. B** depicts the simultaneously acquired UV/Vis spectra, which confirm the information indicated by NMR. With continuous illumination, the absorbance bands of **PDI^{•-}** gradually increase, while the absorbance bands of **PDI** decrease. Interestingly, all **PDI** NMR signals are gone after 50 min (**Figure 4. A**), although only low amounts of **PDI** radical anion ($\sim 10\%$ ⁷) have been generated; except **PDI** signal 4 which is heavily broadened and starts to overlap with TEA. This shows that in this case, NMR can contribute valuable qualitative information about the radical anion, which complements UV/Vis measurements (to confirm the quality of our recorded UV/Vis spectra with the UVNMR device we compared the spectra to a regular cuvette measurement; see **Figure S5**).

Next to the vanishing of the **PDI** signals, a new signal set appears only in the spectra with illumination but not in the spectra without illumination (**Figure 4. C**; top and middle spectrum) consisting of a doublet of doublets at 6.11 ppm and a quartet at 3.0 ppm (**Figure 4. C**; top spectrum highlighted blue). These signals could be identified as photo-CIDNP effects of the vinyl species **3** (N,N-diethyl-ethenamine) and were previously described by Goez *et al.*[51](see **Figure 4. C**; bottom spectrum). Because no negative photo-CIDNP phases were found, which would unambiguously confirm real photo-CIDNP effects, we conducted further experiments to confirm the effects as photo-CIDNP (**Figure S6**). It was previously described that a photo-CIDNP phase inversion can be observed after changing the concentration and/or the ratio of the participants (here: **PDI** and TEA) of the photo-CIDNP effects[58]. By varying the ratio of **PDI** to TEA (1:1 instead of usually at least 1:80) we could invert the photo-CIDNP signals to yield a negative phase for position 1 and 2 of species **3** confirming the observed signals as photo-CIDNP effects. According to the previous research by Goez *et al.*[51] the photo-CIDNP phases of the vinyl species **3** (same photo-CIDNP phase for position 1 and 2) show that the effects originate from the TEA radical cation, which in turn was formed in a radical pair with the photocatalyst **PDI**.

The photo-CIDNP results even further corroborate the data from the NMR and UV/Vis measurements and unambiguously fortify that the formation of **PDI^{•-}** immediately starts

⁷ Please note that the UVNMR setup device doesn't yield absolute quantitative UV/Vis data because of the diffuse polytetrafluorethylene (PTFE) reflector. But relative quantification works and hence we can make rough estimates for the amount of **PDI^{•-}** with respect to the absorbance of **PDI**.

to accelerate after illumination is turned on. Here, the radical anion most likely originates from the triplet pathway of the radical pair of **PDI** and TEA (**Figure 4. D**). Together with **PDI^{•-}**, the radical cation of TEA is produced, which partially in a reaction cascade turns into the vinyl species **3** and further into various secondary products. This reaction cascade of TEA can only be observed in the very beginning of the reaction. Once, product formation starts, the dominant degradation process of TEA is the proton transfer to the product **2**, which results in the subsequent formation of diethylamine (DEA) and acetaldehyde (see **Figure 1.**)

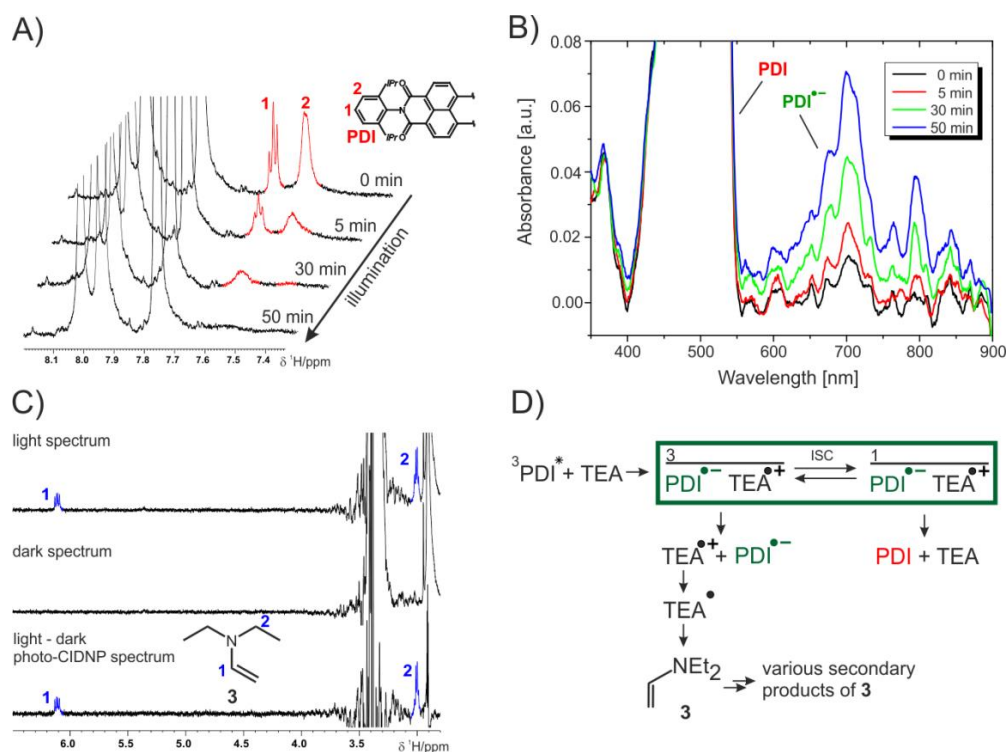


Figure 4. **A)** Series of ^1H NMR spectra focusing on the **PDI** signals 1 and 2 (red). With ongoing illumination, the signals gradually broaden and disappear after a while indicating the transition of **PDI** into a paramagnetic state. **B)** Series of UV/Vis spectra which represent the same time stamps as the NMR spectra in A). Upon illumination the absorbance band of the $\text{PDI}^{\bullet-}$ start to gradually increase. **C)** Photo-CIDNP spectrum of the vinyl species **3** (blue). The NMR spectrum in the dark is subtracted from the spectrum under illumination to yield the photo-CDINP spectrum. From the same photo-CDINP phase of signal 1 and 2 it can be concluded that the photo-CDINP effects originate from the TEA radical cation[51]. **D)** Proposed mechanism for the generation of the $\text{PDI}^{\bullet-}$ and the vinyl species **3**. Both originate from the triplet pathway of the radical pair of **PDI** and TEA. While the $\text{PDI}^{\bullet-}$ is stable in solution, the TEA radical cation participates in a reaction cascade, which yields **3** and various other secondary products. Reaction conditions: **1** (25 mM), **PDI** (1 mM), TEA (160 mM) in $\text{DMF-}d_7$ under inert argon atmosphere at 313 K. Illumination with 450 nm blue light.

After investigation of the initial behavior of the photocatalyst, we started the investigation of the starting material, products and other diamagnetic species with the help of NMR reaction profiles. **Figure 5. A** shows the ^1H NMR reaction profile of the starting material **1** over the course of 17 hours of illumination. Surprisingly, the integral values of **1** start to increase slightly once the illumination is turned on and continues to increase up to 4 hours of illumination where it reaches a plateau for around 4 hours. Afterwards the signal

intensity starts to decrease due to product formation of **2**. As it turns out, this initial buildup is not a “real” increase of **1** but rather a modulation of NMR relaxation properties of **1** due to changing reaction conditions. The aromatic signals of **1** (these were used for integration) have very long longitudinal relaxation times ($T_1 \geq 15$ s), which means an interscan delay of at least 52.5 s would be required⁸ for full relaxation of the signals. But the interscan delay in the presented reaction profile (**Figure 5. A**) is only around 7 s; hence, the integrals of **1** are not fully relaxed and are acquired in a steady-state. **Figure 5. B** depicts a series of simultaneously acquired UV/Vis spectra showing the continuous buildup of the paramagnetic **PDI^{•-}**, which hits a plateau after 4 hours of illumination. That this buildup of the **PDI^{•-}** is in line with the initial signal increase of **1** (both take 4 hours) is no coincidence, because the increased presence of the stable, paramagnetic **PDI^{•-}** facilitates the spin-lattice relaxation of **1**. This phenomenon is very much comparable to the well-known NMR method of paramagnetic relaxation enhancement, at which a paramagnetic compound is added to a solution, to actively reduce the spin-lattice relaxation time (T_1) of the investigated compounds[59]. To verify our paramagnetic relaxation enhancement hypothesis due to **PDI^{•-}**, we investigated the signal alteration of other slowly relaxing compounds in the reaction solution such as the solvent DMF-*d*7. The residual solvent of DMF-*d*7 signal relaxes extremely slow ($T_1 \gg 15$ s) due to inefficient relaxation to the neighboring deuterium nuclei. And in fact the same pseudo signal increase phenomenon can be observed for the residual signal of DMF-*d*7.

Figure 5. C plots the integral of DMF-*d*7 against the buildup of the **PDI^{•-}**-absorbance at 700 nm. It is evident that the increase of DMF-*d*7 signal and **PDI^{•-}** absorbance directly correlate to one another; they reach a plateau at the same time (~4 h) and stay constant for the remaining illumination time. Hence, in this special case, the intensity of the DMF-*d*7 signal can actually be used as an indirect tool to observe the presence and relative buildup/decrease of **PDI^{•-}**. Besides the various experimental findings, which demonstrate the formation and continuous buildup of **PDI^{•-}**, it is odd that the product formation of **2** doesn't also start immediately. In fact, the product formation is delayed by a very long initiating phase of ~8 h (**Figure 5. D**), although almost all **PDI** has been converted to **PDI^{•-}** after 4 h (**Figure 5. B**), which is supposed to promote the reaction. This indicates that the amount and availability of **PDI^{•-}** do not correlate with the product

⁸ Please note: At least five times the T_1 time is required for quantitative NMR measurements. This value gets modulated by a factor of ~0.7 because we acquired the spectra with a 30° instead of a 90° pulse ($15\text{ s} \times 5 \times 0.7 = 52.5$ s)

formation of **2**. Product formation of **2** is only observed after the very long initiating phase of 8 h, at which a linear product formation can be witnessed in the beginning.

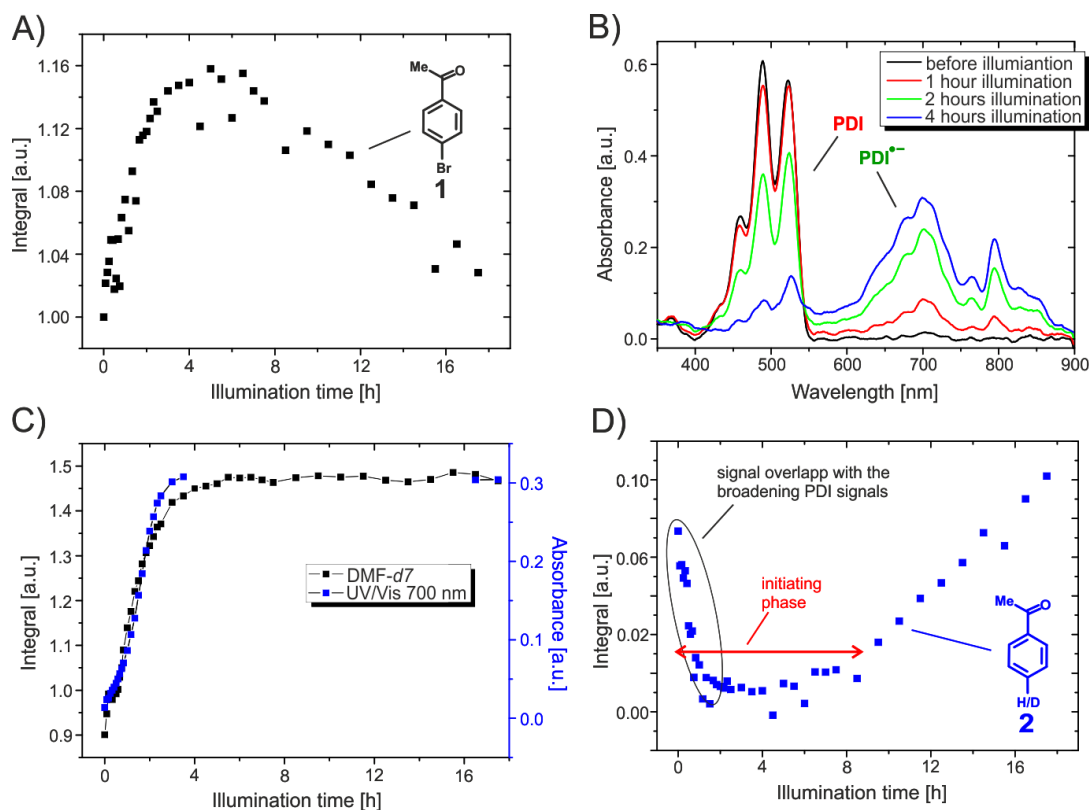


Figure 5. **A)** ^1H reaction profile of 4-bromoacetophenone **1**. The integral of **1** starts to pseudo increase once the light is turned on due to paramagnetic relaxation enhancement from the increasing $\text{PDI}^{\bullet-}$ concentration. The signal intensity of **1** starts to drop once product formation starts. **B)** Series of UV/Vis spectra showing the absorbance bands of **PDI** and $\text{PDI}^{\bullet-}$. With ongoing illumination, $\text{PDI}^{\bullet-}$ is continuously built up reaching a plateau after 4 h, while **PDI** is continuously decreasing. **C)** Combined UVNMR profile showing the directly correlated buildup of the residual DMF- d_7 solvent signal with the main absorbance bands of $\text{PDI}^{\bullet-}$ at 700 nm. The signal increase of DMF- d_7 is due to paramagnetic relaxation enhancement, which is induced by the increasing $\text{PDI}^{\bullet-}$ concentration and hence, DMF- d_7 can be used as an indirect tracer for the presence of the radical anion. **D)** ^1H reaction profile of the product acetophenone **2**. The product formation is preceded by an extremely long initiating phase (~8 h) although the maximum amount of $\text{PDI}^{\bullet-}$ has been reached after ~4 h indicating that product formation and $\text{PDI}^{\bullet-}$ presence are not directly correlated with one another. Reaction conditions: **1** (25 mM), **PDI** (1 mM), TEA (160 mM) in DMF- d_7 under inert argon atmosphere at 313 K. Illumination with 450 nm blue light.

To verify, if the strong effects of paramagnetic relaxation enhancement are due to the formation of **PDI^{•-}** and if the long initiating phase before the product formation is only a special case for the substrate 4-bromo-acetophenone **1**, we also investigated two more substrates; 2-chloro-4-(trifluoromethyl)pyridine **4** and 2-chloro-benzonitrile **6**. **Figure 6.** shows the *in situ* NMR illumination profile of **4** (black) and its conversion to the respective aryl compound **5** (blue) as well as the intensity change of the residual DMF-*d*₇ solvent signal (red) over time. In contrast to substrate **1** (see **Figure 5. A**), the starting material **4** (**Figure 6.** black) does not show a significant signal increase once the light is turned on. This is due the acquisition of ¹⁹F spectra for substrate **4**, because ¹⁹F has an inherently faster spin-lattice relaxation compared to protons (similar to substrate **1**, strong pseudo signal enhancements can be witnessed in the ¹H spectra of **4**; data not shown). But similarly to the first test system, the product formation of the aryl compound **5** (blue) is delayed by an extensive initiating phase of around 3.5 h. The residual DMF-*d*₇ solvent signal (red) shows strong paramagnetic relaxation enhancement. Considering this signal can be used as an indirect sensor for the presence and amount of **PDI^{•-}**, it can be reasoned that the maximum amount of **PDI^{•-}** is formed after 30 minutes and starts to decrease after ~3.5 h when the product formation starts. After 5.5 h the DMF signal intensity stays constant indicating that most if not all of **PDI^{•-}** is consumed/gone. Nevertheless, consumption of starting material **4** and formation of product **5** continues undisturbed with ongoing illumination. This further indicates that the presence of **PDI^{•-}** and the formation of the product are not in a direct relation to each other.

The reaction profile of 2-chloro-benzonitrile **6** also showed an initiating phase and paramagnetic relaxation enhancement effects; similar to substrate **1** and **4** (see supporting information **Figure S7.** and **Figure S8.** for a detailed description of conditions and reaction profiles).

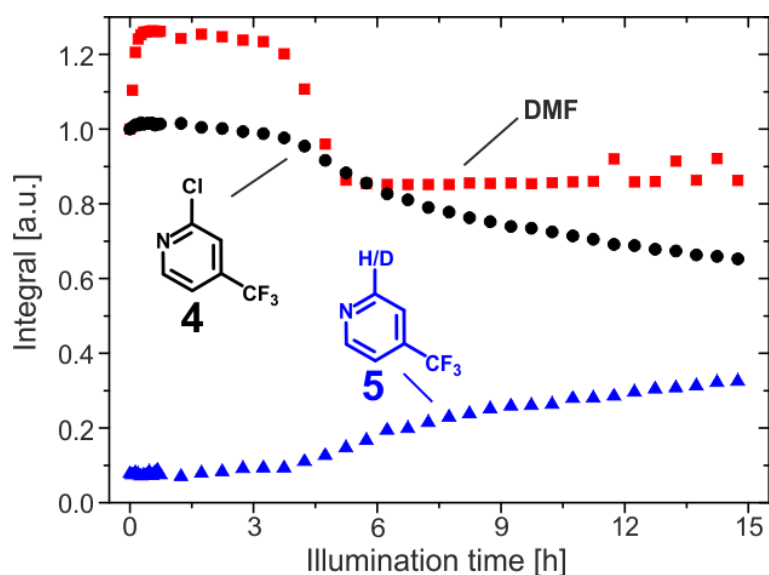


Figure 6. ^1H (for $\text{DMF-}d_7$) and ^{19}F (**4** and **5**) NMR reaction profile of substrate **4** (black) its product **5** (blue) and the residual solvent signal of $\text{DMF-}d_7$ (red) under blue light illumination. The starting material **4** (black) shows no significant signal increase due to paramagnetic relaxation enhancement because of the short spin-lattice relaxation time (T_1) of ^{19}F . The product formation (**5**, blue) is delayed by a very long initiating period of around 3.5 h. The signal intensity of $\text{DMF-}d_7$ (red) can be correlated to the amount of $\text{PDI}^{\bullet-}$ in solution. This shows, that product formation (**5**, blue) proceeds even though only minor amounts or no $\text{PDI}^{\bullet-}$ is present anymore after 5.5 h. Reaction conditions: **4** (10 mM), **PDI** (1 mM), TEA (80 mM) in $\text{DMF-}d_7$ under inert argon atmosphere at 313 K. Illumination with 450 nm blue light.

These findings are in line with observations by Marchini *et al.*, who also observed full depletion of $\text{PDI}^{\bullet-}$ in the early stages of the reaction by UV/Vis and HPLC analyses[27]. In addition, we also performed UV/Vis spectroscopic investigations in a 1 mm cuvette of the full reaction and also witnessed a fast depletion of $\text{PDI}^{\bullet-}$ and the appearance of broad undefined absorbance bands (see **Figure S9**).

The cumulative insight that $\text{PDI}^{\bullet-}$ seemingly does not directly promote product formation and the steady presence of an initiating phase prompted us to further scrutinize this early unproductive period of the reaction. First, we investigated the behavior of only the photocatalyst **PDI** under irradiation without presence of an aryl halide or TEA. **Figure 7. A** depicts a row of *in situ* recorded ^1H NMR spectra focusing on the signals of **PDI** (red). Similarly to the full reaction conditions with an aryl halide compound and TEA, all **PDI** signals start to broaden when illumination is turned on (albeit slower than with the presence of TEA). The signal broadening shows the same distance dependent behavior

with respect to the perylene core; i.e. the signals closer to the center are more affected (the signals attached to the perylene core disappear completely see **Figure S10.**). This suggests that **PDI** can turn into **PDI^{•-}**, even without the presence of TEA. Most probably **PDI** can interact with itself to generate **PDI^{•-}** because the remaining reaction components (DMF-*d*7 and residual water) are unlikely to participate as electron donors. As illumination continuous, new, broad signals start to appear slightly high field shifted in the aromatic region and nearly at the same chemical shift in the aliphatic region as the isopropyl signals. This indicates that **PDI** does not just only turn into **PDI^{•-}**, but also can engage further reactions and/or aggregation/stacking with itself, which is a well-known behavior for perylene bisimides under certain conditions[60–63]. In addition, we also tested the behavior of **PDI** in the presence of the aryl halide **1** and without TEA under illumination (see **Figure S11.**). Here, the **PDI** signals behave in the same manner as without the presence of **1** (i.e. they start to broaden and new signals appear), which suggests that the presence of **1** does not influence the inter-**PDI** interactions/reactions in solution. Subsequent re-aeration experiments showed (**Figure 7. A and B**) that the formation of the new signals is almost completely reversible⁹, at which the NMR reveals small amounts of side/degradation products (**Figure 7. B**; top spectrum and **Figure S12.**). In contrast, the UV/Vis spectrum remains unchanged (**Figure 7. C**). This further suggests that the broad resonances, which appear under prolonged illumination could be the result of some form of physical interactions (e.g. aggregation) between **PDI** and **PDI^{•-}** or an entirely new species. In fact, this process might include the formation of the actual photocatalytic species; because prolonged illumination of **PDI** in the presence of **1** actually leads to product formation of **2** even without the presence of TEA (see **Figure S13.**). Interestingly, the small side/degradation products observed by NMR (see **Figure S12.**) also vanish once illumination is turned back on, which suggests that the side products can still turn into a stable paramagnetic state; hence, the central perylene core is most likely still intact.

To verify the results from the *in situ* NMR measurements, we also performed UV/Vis spectroscopic investigations. **Figure 7. B** depicts a row of UV/Vis spectra of just **PDI** in DMF under blue light irradiation. As suggested by NMR, **PDI^{•-}** appears indeed with the start of illumination even in the absence of a suitable sacrificial electron donor (TEA). This further establishes the hypothesis that **PDI** can also interact with itself to generate **PDI^{•-}**. The absorbance bands of **PDI^{•-}** reach a maximum after approximately 30 s

⁹ Prolonged illumination (e.g. overnight/12 h) of pure **PDI** in DMF-*d*7 leads to the formation of irreversible degradation products of **PDI**, which appear as broad, undefined resonances in the NMR.

(Figure 7. B, blue spectrum). Surprisingly, afterwards the **PDI**^{•-} absorbance decreases again, while the **PDI** absorbance increases, despite continuous illumination with blue light (red spectrum). Then all absorbance bands start to decrease and broaden. Furthermore, the absorbance bands undergo a slight blue shift, which is an indication for H-aggregation in perylene bisimide systems[63]. After 45 min of illumination the absorbance bands have lost almost all definition and after 16 h of illumination **PDI** is fully decomposed¹⁰. The results from the UV/Vis experiments are in line with the NMR observations that **PDI** can induce the formation of **PDI**^{•-} and further reactions and/or aggregation/stacking with itself. It is possible that an aggregate forms, which is composed of **PDI** and **PDI**^{•-}. Furthermore, these reactions/aggregations can lead to further reactions, which lead to the decomposition of **PDI**. The UV/Vis experiments were also repeated in the presence of **1** and similarly to the NMR investigations, the presence of **1** did not influence the behavior of **PDI** in any way (see Figure S14.), which is in contrast to the investigations of Manchini et al., who proposed an inter action of **PDI** with the respective aryl halide[27].

¹⁰ Please note that the strength of illumination with 450 nm is much higher in the UV/Vis experiments than in the NMR experiments. In addition, the **PDI** concentration is much smaller in the UV/Vis experiments (50 μ M compared to 1 mM in NMR). Hence, only the overall behavior of **PDI** can be compared and not the time points directly to one another.

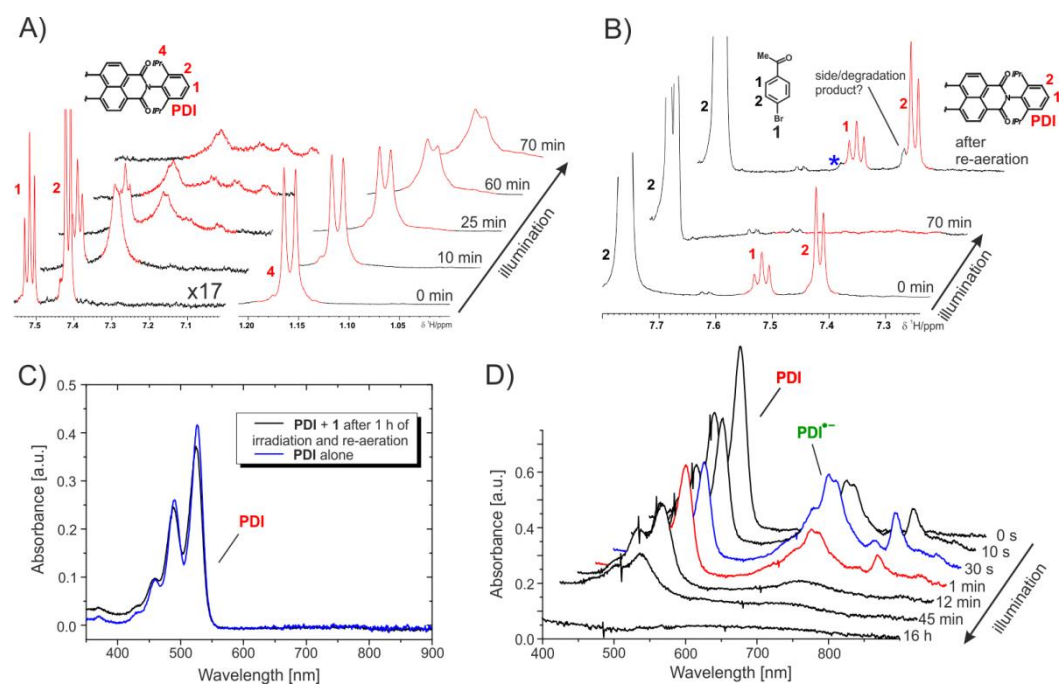


Figure 7. A) Row of ^1H spectra focusing on the aromatic signals 1 and 2 (red) of **PDI** (left; zoomed in $\times 17$) and methyl signals of the isopropyl groups (red) of **PDI** (right) under illumination. With ongoing light exposure, all **PDI** signals first start to broaden similarly to the full reaction conditions with an aryl halide substrate and TEA (see **Figure 4. A**). As illumination continuous, several other signals start to appear slightly high field shifted in the aromatic region and at approximately the same chemical shift in the aliphatic region. **B)** Re-aeration test of **PDI** after prolonged illumination without TEA. The line broadening of the **PDI** signals is almost completely reversible, although minor side products can be detected. **C)** Corresponding UV/Vis spectrum of the re-aeration experiments of **PDI** after illumination. In contrast to NMR, the UV/Vis spectrum remains completely unchanged. **D)** Series of UV/Vis spectra of **PDI** under prolonged illumination with 450 nm. Similarly to the full reaction conditions with aryl halide and TEA (see **Figure 4. B** and **Figure S9.**), **PDI $^{\bullet-}$** immediately appears once illumination start. Under prolonged illumination all **PDI** and **PDI $^{\bullet-}$** absorbance bands start to broaden and lose their profile. Interestingly, at one point the **PDI $^{\bullet-}$** absorbance bands decrease, while the **PDI** absorbances rise again (blue vs red spectrum) despite ongoing illumination. After 16 h **PDI** is fully decomposed. Reaction conditions NMR: **PDI** (1 mM) in $\text{DMF-}d_7$ under inert atmosphere at 313 K. Illumination with 450 nm. Reaction conditions UV/Vis: **PDI** (50 μM) in DMF under inert conditions at ambient temperature. Illumination with 450 nm. *The blue star in **B)** belongs to the product **2**, which already started to form in this experiment.

The insight that **PDI** can interact with itself and induce the formation of **PDI^{•-}** and other interactions, prompted us to further investigate, whether these phenomena lead to the generation of the actual catalytic species. Therefore, first **PDI** was pre-irradiated on its own (no aryl halide or TEA in solution) for one hour inside the NMR (**Figure 8. A**, bottom spectrum). This leads to the appearance of broad **PDI** resonances and various other signals, which were discussed above (**Figure 8 A**, bottom spectrum; red and orange highlighted signals). Then the aryl halide **1** and TEA are added to reaction mixture. This leads to an even increased broadening of the **PDI** signals and some of the additionally appeared signals disappear (**Figure 8 A**, middle spectrum). This is probably, because the remaining **PDI** in solution engages in an EDA complex with the TEA as mentioned before. Now, after the blue light irradiation is turned on, product formation of **2** starts immediately and all **PDI** resonances disappear (**Figure 8. A**, top spectrum). This is a tremendous difference to the general reaction conditions (with **1** and TEA from the start), which showed hour long initiating periods prior to product formation (see **Figure 5. D**). **Figure 8. B** shows the ¹H reaction profile of **1** and **2**. It is evident that once the light is turned on, **1** and **2** immediately follow a linear decrease/increase in the beginning without hints of an initiating phase. These results are in line with the hypothesis that pre-irradiation of **PDI** leads to the generation of the actual photoactive species due to interaction of **PDI** with itself. Additionally, one more experiment was carried out to determine if the photoactive species rather emerges from inter **PDI** reactions or emerges out of **PDI** aggregates/stacking. First, **PDI** was pre-irradiated without the presence of **1** and TEA (**Figure 8. C**). Then the mixture was re-aerated, put under inert conditions again, **1** and TEA were added and the light was turned on. **Figure 8. C** shows the corresponding reaction profile, where it is evident that product formation is yet again preceded by an initiating period. Furthermore, the pseudo signal increase of **1** can also be detected. These results indicate that the photoactive species does not stem from a new compound after a chemical reaction of **PDI** because this process should be irreversible. Hence, the reaction should start immediately, because the actual photocatalyst is already present. Due to the presence of the initiating phase, the photoactive species is likely the result of aggregates/stacking of **PDI** and **PDI^{•-}**. This is also in line with the fact, that most observed changes of the pre-irradiation are reversible by the addition of oxygen, which can quench **PDI^{•-}** (see **Figure 7.. B**). In addition, we also pre-irradiated **PDI** in the presence of TEA for 24 h. **Figure S15**. depicts the corresponding ¹H reaction profile after the addition of **1** to the pre-illuminated **PDI**-TEA

solution¹¹. Similarly to the pre-irradiation of just **PDI**, the reaction starts immediately once the illumination is turned on. In fact the reaction proceeds even slightly faster with pre-illumination of **PDI** and TEA instead of just **PDI** (see **Figure S16**). This further establishes that a formation or pre-arrangement of the actual photocatalytic species happens before the product formation is initiated.

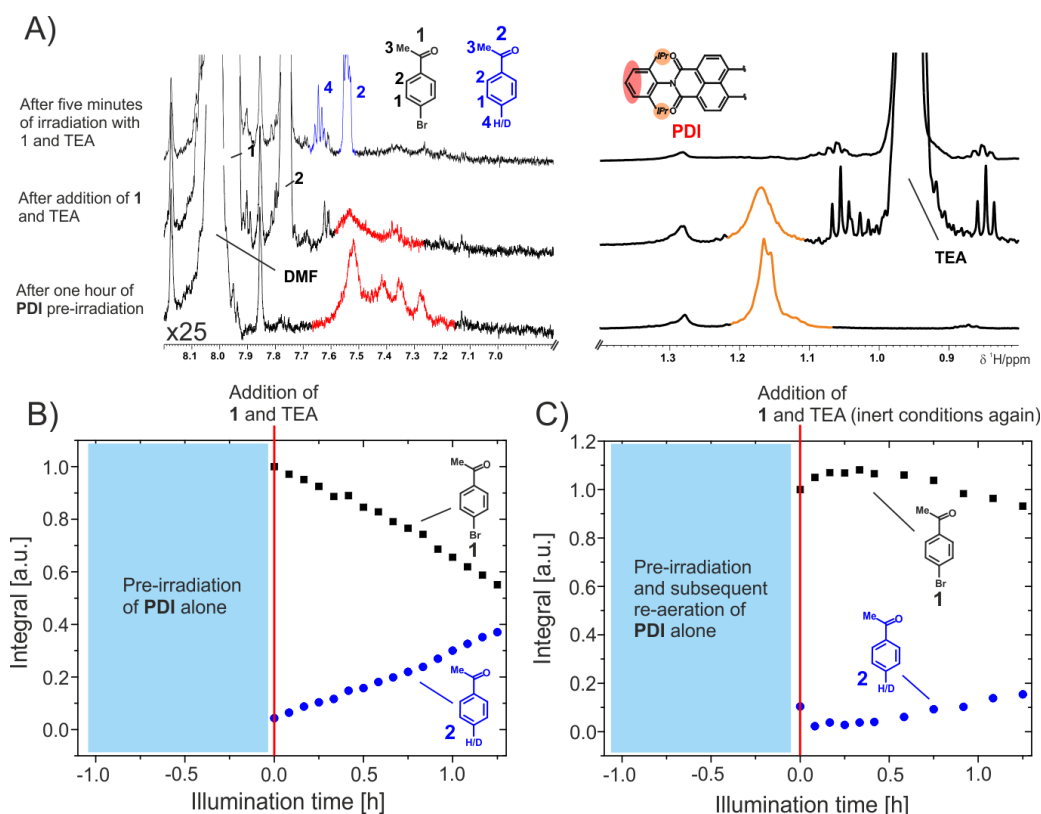


Figure 8. A) ¹H NMR spectra depicting high field (left, zoomed in x 25) and low field (right) regions, which contain relevant signals of **PDI** (red and orange), **1** and **2** (blue). After one hour of pre-irradiation (bottom spectrum), the **PDI** signals are broadened and various other signals appear in conjunction with the original resonances (see also **Figure 7. A**). The middle spectrum shows the solution after the addition of **1** and TEA. The **PDI** signals are further broadened and some of the other resonances disappear (probably due to an EDA complex formation of **PDI** with TEA). The top spectrum shows the reaction solution after the start of illumination. Product formation of **2** (blue) starts immediately, while all **PDI** signals disappear and no initiating phase can be observed in contrast to the general reaction conditions (**PDI**, **1** and TEA from the start), which has a long initiating phase (see **Figure 5. A**) **B)** ¹H reaction profile of **1** and **2** after one hour of pre-irradiation of **PDI** alone. The reaction starts immediately once the light is turned on

¹¹ Although, the **PDI** radical anion is stable once generated it has to be mentioned that **PDI** can also be photodegraded in the presence of TEA under prolonged illumination. This indicates that the reactions that **PDI** can perform with itself also occur in the presence of TEA.

the **1** and **2** decrease/increase linearly in the beginning. **C)** Trial if the pre-irradiation of **PDI** results in a reversible or irreversible process. Pre-irradiated **PDI** is re-aerated, put under inert conditions again and **1** and TEA are added. A initiating phase can be observed indicating a reversible process such as aggregation/stacking. Reaction conditions: **PDI** (1 mM), TEA (160 mM; after addition) and **1** (20 mM; after addition) in DMF-*d*7 under inert atmosphere at 313 K. Illumination with 450 nm.

To corroborate the results gained from the investigation of the initiating phase, which suggest that **PDI** can interact with itself to form pre-arranged aggregates/stacks of **PDI** and **PDI^{•-}**, we compared **PDI** to perylene-3,4,9,10-tetracarboxylic-dianhydride (**PTCDA**) (**Figure 9. A**). **PTCDA** is the common precursor for the synthesis of perylene bisimides[64] but is usually not applied as photocatalyst because **PTCDA** is not soluble in organic solvents due to the formation of extensive aggregates. But in general, **PTCDA** should possess similar photophysical properties as **PDI**, because the perylene core is the active chromophore. Hence, we compared the performance of **PDI** and the aggregate forming **PTCDA** under reaction conditions. **Figure 9. B** shows the ¹H *in situ* NMR reaction profile of the reaction of **1** to the corresponding product **2** for **PDI** (black and blue progression) and **PTCDA** (red and green progression). In case of **PDI**, one can observe the long initiating phase before the product formation of **2** starts and the pseudo signal increase of **1** due to paramagnetic relaxation enhancement from the generated **PDI^{•-}**. In contrast, the reaction with **PTCDA** as photocatalyst starts immediately and no initiating phase can be observed, although **PTCDA** also forms its respective radical anion once illumination starts¹². This observation is in line with the hypothesis that aggregates consisting of mixtures of the neutral photocatalyst and the radical anion are required to drive the photoreaction. Whereas, for **PDI** this pre-arrangement has to supposedly build up in the reaction, it is already in place in case of **PTCDA** and as a result **PTCDA** shows the better performance as photocatalyst.

In fact, we also compared **PDI** and **PTCDA** in *ex situ* NMR tests for the substrates **1**, **4** and **6** and **PTCDA** outperformed **PDI** in every experiment with respect to conversion over time (see **Figure S16.-S18.**)

¹² In the beginning the reaction solution with **PTCDA** is a dark red suspension and it turns blue when the illumination starts (similar to **PDI**; orange solution in the beginning, which turns dark green/blue when the illumination starts)

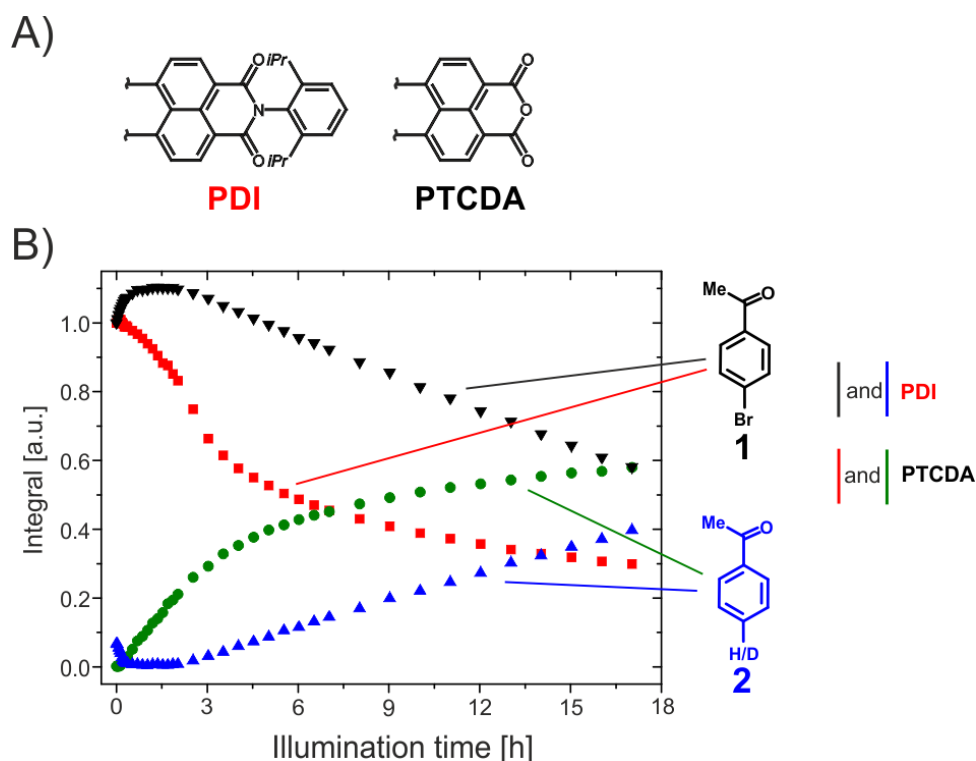


Figure 9. A) Structure of **PDI** and **PTCDA** B) ^1H NMR reaction profiles for substrate **1** and its reaction product **2**. The black progression of **1** and the blue progression of **2** correspond to the reaction with **PDI**. The red and green progressions of **1** and **2** correspond to the reaction with **PTCDA** as photocatalyst. In contrast to **PDI**, **PTCDA** shows no initiating phase and promotes a faster conversion of **1** to **2**. Reaction conditions: **PDI** (2 mM) or **PTCDA** (2 mM), **1** (26.6 mM) and TEA (160 mM) in $\text{DMF-}d_7$ under inert atmosphere at 313 K. Illumination with 450 nm.

In addition, Marchini *et al.* mentioned in their investigation that once **PDI** $^{\bullet-}$ is formed, the reaction can also be promoted with red light irradiation. We also tested the property of **PDI** to perform the reaction with 690 nm red light illumination and compared it to **PTCDA** by performing *ex situ* NMR tests. The top spectrum of **Figure 10. A** shows the ^1H NMR of **PDI** in presence of **1** and TEA in $\text{DMSO}/\text{DMSO-}d_6$ (9:1) after 17 h of irradiation with 690 nm. None surprisingly, no product formation is observed, since the absorbance bands of **PDI** do not span beyond 550 nm and hence no **PDI** $^{\bullet-}$ is produced with irradiation at 690 nm. The middle spectrum of **Figure 10. A** depicts the same reaction solution after 25 minutes of blue light irradiation. Product formation has started¹³ and **PDI** $^{\bullet-}$ should still be present in solution. If the reaction solution is now irradiated 690 nm

¹³ Please note that these reactions were performed in $\text{DMSO}/\text{DMSO-}d_6$ (9:1), which leads to two consequences. First, the product **2** is fully protonated because DMSO does not take part in the proton transfer step (see **Figure 1**). And second, the dimer product **8** is formed in minor amounts because of the reduced amount of proton donors in solution (absence of $\text{DMF-}d_7$ as source)

red light, further product formation (albeit slowly) can be indeed observed (**Figure 10. A**, bottom spectrum). In contrast, **PTCDA** does not require pre-illumination with blue light and can directly promote the reaction under illumination with 690 nm (**Figure 10. B**), because the pre-arranged **PTCDA** aggregates absorb throughout the whole VIS region. We would assume this is also the case for the **PDI**/**PDI^{•-}** aggregates that potentially form under blue light irradiation explaining why the reaction can be promoted at 690 nm after pre-illumination with blue light.

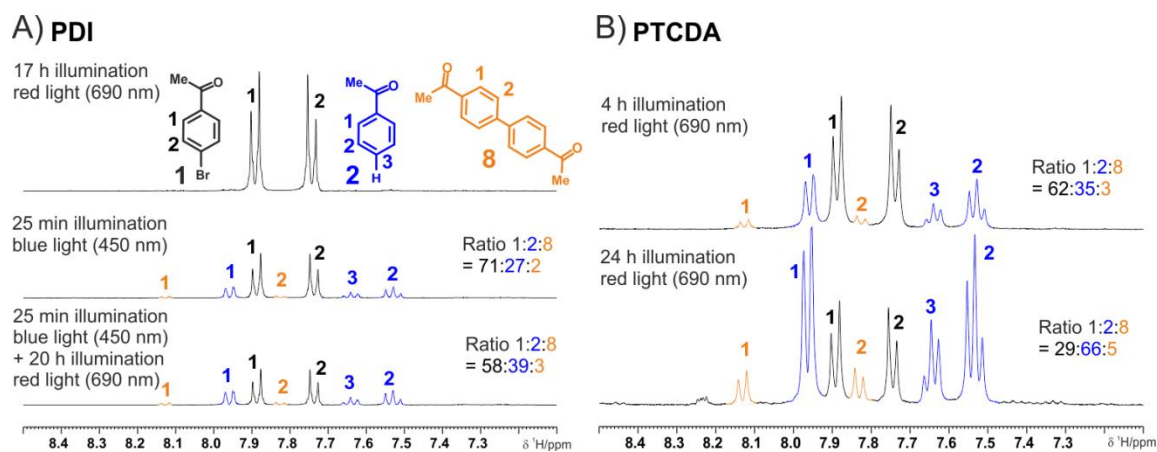


Figure 10. A) *Ex situ* NMR experiments to probe the ability of **PDI** to promote the photoreaction of **1** to **2** under red light (690 nm) illumination. Under direct illumination with red light the reaction does not work (top spectrum). But if **PDI** is pre-irradiated with blue light and hence the **PDI^{•-}** is present in solution (middle spectrum), then the reaction can slowly continue under red light illumination (bottom spectrum). **B)** *Ex situ* NMR experiments to probe the ability of **PTCDA** to promote the photoreaction of **1** to **2** under red light (690 nm) illumination. **PTCDA** can readily start the photoreaction under red light illumination because the **PTCDA** aggregates absorb throughout the whole VIS region.

4.4 Conclusion

To summarize in this study, we present extensive UVNMR illumination, *in situ* NMR illumination and UV/Vis spectroscopic investigations of the **PDI** promoted dehalogenation of aryl halides. This interesting photoreaction was initially proposed as a ConPET process, which uses the energy of two photons to drive the photoreaction. The general ConPET mechanism was recently verified with the photocatalyst rhodamine 6G, but the initial ConPET with **PDI** was lately questioned by a new proposal, which suggests that the **PDI^{•-}** forms a new catalytic species upon reaction with the substrate. We continued this research and present a series of new mechanistic insights and novel proposals.

First, by means of UVNMR illumination measurements, we showed the existence of an EDA complex between the photocatalyst **PDI** and the sacrificial electron donor TEA, which is formed even prior to illumination. This showed that in some cases, NMR can be very sensitive for the detection of EDA complexes by line width analyses.

Second, the first couple of minutes of the reaction were investigated in detail and the combination of regular NMR, photo-CIDNP NMR and UV/Vis spectroscopy could unambiguously show that **PDI^{•-}** is immediately generated once the illumination with blue light is turned on. Here, it could be demonstrated that the transition of a photocatalyst into a stable, paramagnetic state can be roughly followed by NMR through line broadening effects.

Investigation of UVNMR illumination reaction profiles yielded two important insights. First, the generation of the stable **PDI^{•-}** leads to a pseudo signal increase of slowly relaxing reaction components due to paramagnetic relaxation enhancement. As a result, the residual proton signal of the deuterated solvent can be used as an indirect tracer for the presence and relative amount of the paramagnetic **PDI^{•-}**. The second insight is the detection of an extensive initiating phase before the reaction actually starts. This also showed that the presence of **PDI^{•-}** and product formation do not correlate at all and indicated that the sole **PDI^{•-}** (or the excited **PDI^{•-}**) does not promote the photoreaction.

In detail study of the initiating phase, which included selective irradiation experiments revealed that **PDI** on its own can interact with itself to yield **PDI^{•-}**. Furthermore, **PDI** seemingly can also interact with itself to form aggregates/stacks, which are eventually composed of **PDI** and the **PDI^{•-}**. Pre-irradiation experiments could confirm that the selective irradiation of pure **PDI** can get rid of the extensive initiating phase, which

occurs in the regular reaction. This indicates that the interactions of **PDI** with itself lead to the generation of the actual photocatalytic species. Furthermore, pre-irradiation – re-aeration experiments showed that the pre-irradiation process is reversible and no new photocatalytic species is generated by an irreversible chemical reaction.

To check this hypothesis, **PDI** was compared to the highly aggregating **PTCDA**, which possess similar photophysical properties. Here, it could be shown that **PTCDA** also forms its respective radical anion but does not show any initiating phases and the reaction starts immediately. In addition, it could also be demonstrated that the **PTCDA** aggregates and after pre-irradiation of **PDI** at 450 nm, the investigated reaction can also be promoted with irradiation at 700 nm.

With these combined results, we can state that we could not confirm the two existent proposals for the dehalogenation of aryl halides by **PDI**, which are the highly reducing, excited **PDI^{•-}** after a second photoexcitation of **PDI** to promote the reaction or the occurrence of a side reaction, where **PDI^{•-}** reacts with the corresponding substrate to generate a new photocatalytic species. Instead we would make a new proposal, which suggests that **PDI** can interact with itself to form a new catalytic species i.e. a pre-arrangement of **PDI** and **PDI^{•-}** in some form of aggregate/stack.

Finally we hope that these insights encourage further investigations focusing on the interactions of **PDI** with itself to finally fully uncover the nature of the catalytic species, which promotes this unusual photoreaction.

4.5 References

- [1] M.A. Garcia-Garibay, *Advances at the frontiers of photochemical sciences*, *J. Am. Chem. Soc.* 134 (2012) 8289–8292. doi:10.1021/ja301329b.
- [2] K. Zeitler, *Photoredox Catalysis with Visible Light*, *Angew. Chemie Int. Ed.* 48 (2009) 9785–9789. doi:10.1002/anie.200904056.
- [3] B. König, *Photocatalysis in Organic Synthesis - Past, Present, and Future*, *European J. Org. Chem.* 2017 (2017) 1979–1981. doi:10.1002/ejoc.201700420.
- [4] L. Marzo, S.K. Pagire, O. Reiser, B. König, *Visible-Light Photocatalysis: Does It Make a Difference in Organic Synthesis?*, *Angew. Chemie - Int. Ed.* 57 (2018) 10034–10072. doi:10.1002/anie.201709766.
- [5] L. Buzzetti, G.E.M. Crisenza, P. Melchiorre, *Mechanistic Studies in Photocatalysis*, *Angew. Chemie Int. Ed.* (2019) 3730–3747. doi:10.1002/anie.201809984.
- [6] B. Schweitzer-Chaput, M.A. Horwitz, E. de Pedro Beato, P. Melchiorre, *Photochemical generation of radicals from alkyl electrophiles using a nucleophilic organic catalyst*, *Nat. Chem.* 11 (2019) 129–135. doi:10.1038/s41557-018-0173-x.
- [7] R.C. McAtee, E.J. McClain, C.R.J. Stephenson, *Illuminating Photoredox Catalysis*, *Trends Chem.* 1 (2019) 111–125. doi:10.1016/j.trechm.2019.01.008.
- [8] N.P. Ramirez, B. König, J.C. Gonzalez-Gomez, *Decarboxylative Cyanation of Aliphatic Carboxylic Acids via Visible-Light Flavin Photocatalysis*, *Org. Lett.* 21 (2019) 1368–1373. doi:10.1021/acs.orglett.9b00064.
- [9] J. Schwarz, B. König, *Visible-light mediated C–C bond cleavage of 1,2-diols to carbonyls by cerium-photocatalysis*, *Chem. Commun.* 55 (2019) 486–488. doi:10.1039/C8CC09208G.
- [10] S. Cuadros, M.A. Horwitz, B. Schweitzer-Chaput, P. Melchiorre, *A visible-light mediated three-component radical process using dithiocarbamate anion catalysis*, *Chem. Sci.* (2019) 2–6. doi:10.1039/C9SC00833K.
- [11] J.M.R. Narayanam, C.R.J. Stephenson, *Visible light photoredox catalysis: applications in organic synthesis*, *Chem. Soc. Rev.* 40 (2011) 102–113. doi:10.1039/B913880N.
- [12] M. Majek, A. Jacobi von Wangelin, *Mechanistic Perspectives on Organic Photoredox Catalysis for Aromatic Substitutions*, *Acc. Chem. Res.* 49 (2016) 2316–2327. doi:10.1021/acs.accounts.6b00293.
- [13] N.A. Romero, D.A. Nicewicz, *Organic Photoredox Catalysis*, *Chem. Rev.* 116 (2016) 10075–10166. doi:10.1021/acs.chemrev.6b00057.
- [14] I. Ghosh, L. Marzo, A. Das, R. Shaikh, B. König, *Visible Light Mediated Photoredox Catalytic Arylation Reactions*, *Acc. Chem. Res.* 49 (2016) 1566–1577. doi:10.1021/acs.accounts.6b00229.
- [15] R. Naumann, F. Lehmann, M. Goetz, *Generating Hydrated Electrons for Chemical*

- Syntheses by Using a Green Light-Emitting Diode (LED), *Angew. Chemie Int. Ed.* 57 (2018) 1078–1081. doi:10.1002/anie.201711692.
- [16] C. Kerzig, M. Goetz, Combining energy and electron transfer in a supramolecular environment for the “green” generation and utilization of hydrated electrons through photoredox catalysis, *Chem. Sci.* 7 (2016) 3862–3868. doi:10.1039/c5sc04800a.
- [17] C. Kerzig, M. Goetz, Generating hydrated electrons through photoredox catalysis with 9-anthrolate, *Phys. Chem. Chem. Phys.* 17 (2015) 13829–13836. doi:10.1039/c5cp01711d.
- [18] M. Majek, U. Faltermeier, B. Dick, R. Pérez-Ruiz, A. JacobivonWangelin, Application of Visible-to-UV Photon Upconversion to Photoredox Catalysis: The Activation of Aryl Bromides, *Chem. A Eur. J.* 21 (2015) 15496–15501. doi:10.1002/chem.201502698.
- [19] I. Ghosh, R.S. Shaikh, B. König, Sensitization-Initiated Electron Transfer for Photoredox Catalysis, *Angew. Chemie Int. Ed.* 56 (2017) 8544–8549. doi:10.1002/anie.201703004.
- [20] I. Ghosh, T. Ghosh, J.I. Bardagi, B. König, Reduction of aryl halides by consecutive visible light-induced electron transfer processes, *Science* 346 (2014) 725–728. doi:10.1126/science.1258232.
- [21] L. Zeng, T. Liu, C. He, D. Shi, F. Zhang, C. Duan, Organized Aggregation Makes Insoluble Perylene Diimide Efficient for the Reduction of Aryl Halides via Consecutive Visible Light-Induced Electron-Transfer Processes, *J. Am. Chem. Soc.* 138 (2016) 3958–3961. doi:10.1021/jacs.5b12931.
- [22] I. Ghosh, B. König, Chromoselective Photocatalysis: Controlled Bond Activation through Light-Color Regulation of Redox Potentials, *Angew. Chemie Int. Ed.* 55 (2016) 7676–7679. doi:10.1002/anie.201602349.
- [23] M. Neumeier, D. Sampedro, M. Májek, V.A. de la Peña O’Shea, A. Jacobi von Wangelin, R. Pérez-Ruiz, Dichromatic Photocatalytic Substitutions of Aryl Halides with a Small Organic Dye, *Chem. A Eur. J.* 24 (2018) 105–108. doi:10.1002/chem.201705326.
- [24] M. Poznik, B. König, Fast colorimetric screening for visible light photocatalytic oxidation and reduction reactions, *React. Chem. Eng.* 1 (2016) 494–500. doi:10.1039/C6RE00117C.
- [25] A. Graml, I. Ghosh, B. König, Synthesis of Arylated Nucleobases by Visible Light Photoredox Catalysis, *J. Org. Chem.* 82 (2017) 3552–3560. doi:10.1021/acs.joc.7b00088.
- [26] J. Haimerl, I. Ghosh, B. König, J. Vogelsang, J.M. Lupton, Single-molecule photoredox catalysis, *Chem. Sci.* 10 (2019) 681–687. doi:10.1039/C8SC03860K.
- [27] M. Marchini, A. Gualandi, L. Mengozzi, P. Franchi, M. Lucarini, P.G. Cozzi, V. Balzani, P. Ceroni, Mechanistic insights into two-photon-driven photocatalysis in organic synthesis, *Phys. Chem. Chem. Phys.* 20 (2018) 8071–8076. doi:10.1039/c7cp08011e.

- [28] C. Feldmeier, H. Bartling, K. Magerl, R.M. Gschwind, vLED-Illuminated NMR Studies of Flavin-Catalyzed Photooxidations Reveal Solvent Control of the Electron-Transfer Mechanism, *Angew. Chemie Int. Ed.* 54 (2015) 1347–1351. doi:10.1002/anie.201409146.
- [29] H. Bartling, A. Eisenhofer, B. König, R.M. Gschwind, The Photocatalyzed Aza-Henry Reaction of N-Aryltetrahydroisoquinolines: Comprehensive Mechanism, H-versus H+-Abstraction, and Background Reactions, *J. Am. Chem. Soc.* 138 (2016) 11860–11871. doi:10.1021/jacs.6b06658.
- [30] D. Petzold, P. Nitschke, F. Brandl, V. Scheidler, B. Dick, R.M. Gschwind, B. König, Visible-Light-Mediated Liberation and In Situ Conversion of Fluorophosgene, *Chem. A Eur. J.* 25 (2019) 361–366. doi:10.1002/chem.201804603.
- [31] K. Chen, N. Berg, R. Gschwind, B. König, Selective Single C(sp³)-F Bond Cleavage in Trifluoromethylarenes: Merging Visible-Light Catalysis with Lewis Acid Activation, *J. Am. Chem. Soc.* 139 (2017) 18444–18447. doi:10.1021/jacs.7b10755.
- [32] N. Lokesh, A. Seegerer, J. Hioe, R.M. Gschwind, Chemical exchange saturation transfer in chemical reactions: A mechanistic tool for NMR detection and characterization of transient intermediates, *J. Am. Chem. Soc.* 140 (2018) 1855–1862. doi:10.1021/jacs.7b12343.
- [33] N.D. Dolinski, Z.A. Page, E.H. Discekici, D. Meis, I.H. Lee, G.R. Jones, R. Whitfield, X. Pan, B.G. McCarthy, S. Shanmugam, V. Kottisch, B.P. Fors, C. Boyer, G.M. Miyake, K. Matyjaszewski, D.M. Haddleton, J.R. de Alaniz, A. Anastasaki, C.J. Hawker, What happens in the dark? Assessing the temporal control of photo-mediated controlled radical polymerizations, *J. Polym. Sci. Part A Polym. Chem.* 57 (2019) 268–273. doi:10.1002/pola.29247.
- [34] D. Lehnherr, Y. Ji, A.J. Neel, R.D. Cohen, A.P.J. Brunskill, J. Yang, M. Reibarkh, Discovery of a Photoinduced Dark Catalytic Cycle Using in Situ LED-NMR Spectroscopy, *J. Am. Chem. Soc.* 140 (2018) 13843–13853. doi:10.1021/jacs.8b08596.
- [35] A. Mills, C. O'Rourke, In Situ, Simultaneous Irradiation and Monitoring of a Photocatalyzed Organic Oxidation Reaction in a TiO₂-Coated NMR Tube, *J. Org. Chem.* 80 (2015) 10342–10345. doi:10.1021/acs.joc.5b01001.
- [36] M. Goez, Elucidating Organic Reaction Mechanisms Using Photo-CIDNP Spectroscopy, in: *Hyperpolarization Methods NMR Spectrosc.*, 2012: pp. 1–32. doi:10.1007/128_2012_348.
- [37] C.G.S. Lima, T.D.M. Lima, M. Duarte, I.D. Jurberg, M.W. Paixão, Organic Synthesis Enabled by Light-Irradiation of EDA Complexes: Theoretical Background and Synthetic Applications, *ACS Catal.* 6 (2016) 1389–1407. doi:10.1021/acscatal.5b02386.
- [38] B. Liu, C.H. Lim, G.M. Miyake, Visible-light-promoted C-S cross-coupling via intermolecular charge transfer, *J. Am. Chem. Soc.* 139 (2017) 13616–13619. doi:10.1021/jacs.7b07390.
- [39] J. Sun, Y. He, X. De An, X. Zhang, L. Yu, S. Yu, Visible-light-induced iminyl radical formation: Via electron-donor-acceptor complexes: A photocatalyst-free

- approach to phenanthridines and quinolines, *Org. Chem. Front.* 5 (2018) 977–981. doi:10.1039/c7qo00992e.
- [40] Y. Zhang, J. Kubicki, M.S. Platz, Ultrafast UV–Visible and Infrared Spectroscopic Observation of a Singlet Vinylcarbene and the Intramolecular Cyclopropanation Reaction, *J. Am. Chem. Soc.* 131 (2009) 13602–13603. doi:10.1021/ja905992p.
- [41] J. Wang, G. Burdzinski, J. Kubicki, M.S. Platz, Ultrafast UV–Vis and IR Studies of *p*-Biphenyl Acetyl and Carbomethoxy Carbenes, *J. Am. Chem. Soc.* 130 (2008) 11195–11209. doi:10.1021/ja803096p.
- [42] P.K. Verma, F. Koch, A. Steinbacher, P. Nuernberger, T. Brixner, Ultrafast UV-Induced Photoisomerization of Intramolecularly H-Bonded Symmetric β -Diketones, *J. Am. Chem. Soc.* 136 (2014) 14981–14989. doi:10.1021/ja508059p.
- [43] E. Riedle, M.K. Roos, S. Thallmair, C.F. Sailer, N. Krebs, B.P. Fingerhut, R. de Vivie-Riedle, Ultrafast photochemistry with two product channels: Wavepacket motion through two distinct conical intersections, *Chem. Phys. Lett.* 683 (2017) 128–134. doi:10.1016/j.cplett.2017.02.086.
- [44] U. Megerle, M. Wenninger, R.-J. Kutta, R. Lechner, B. König, B. Dick, E. Riedle, Unraveling the flavin-catalyzed photooxidation of benzylic alcohol with transient absorption spectroscopy from sub-pico- to microseconds, *Phys. Chem. Chem. Phys.* 13 (2011) 8869. doi:10.1039/c1cp20190e.
- [45] J. Xue, H.L. Luk, S. V. Eswaran, C.M. Hadad, M.S. Platz, Ultrafast infrared and UV-vis studies of the photochemistry of methoxycarbonylphenyl azides in solution, *J. Phys. Chem. A.* 116 (2012) 5325–5336. doi:10.1021/jp3025705.
- [46] I. Ghosh, R.S. Shaikh, B. Kçnig, Communications Photocatalysis Very Important Paper Sensitization-Initiated Electron Transfer for Photoredox Catalysis *Angewandte*, (2017) 8544–8549. doi:10.1002/anie.201703004.
- [47] K.C. Christoforidis, M. Louloudi, E.R. Milaeva, Y. Sanakis, Y. Deligiannakis, EPR study of a novel [Fe-porphyrin] catalyst, *Mol. Phys.* 105 (2007) 2185–2194. doi:10.1080/00268970701749260.
- [48] M. Goswami, A. Chirila, C. Rebreyend, B. de Bruin, *EPR Spectroscopy as a Tool in Homogeneous Catalysis Research*, Springer US, 2015. doi:10.1007/s11244-015-0414-9.
- [49] T. Risse, D. Hollmann, A. Brückner, Chapter 1. In situ electron paramagnetic resonance (EPR) – a unique tool for analysing structure and reaction behaviour of paramagnetic sites in model and real catalysts, in: *Catalysis*, 2015: pp. 1–32. doi:10.1039/9781782622697-00001.
- [50] G. Liu, S.-H. Liou, N. Enkin, I. Tkach, M. Bennati, Photo-induced radical polarization and liquid-state dynamic nuclear polarization using fullerene nitroxide derivatives, *Phys. Chem. Chem. Phys.* 19 (2017) 31823–31829. doi:10.1039/C7CP06073D.
- [51] M. Goez, I. Sartorius, CIDNP Determination of the Rate of In-Cage Deprotonation of the Triethylamine Radical Cation, *J. Phys. Chem. A* 107 (2003) 8539–8546.
- [52] M. Goez, I. Sartorius, Photo-CIDNP investigation of the deprotonation of aminium

- cations, *J. Am. Chem. Soc.* 115 (1993) 11123–11133. doi:10.1021/ja00077a009.
- [53] M. Goetz, Chapter 3 Photo-CIDNP Spectroscopy, in: *Annu. Reports NMR Spectrosc.*, 1st ed., Elsevier Ltd., 2009: pp. 77–147. doi:10.1016/S0066-4103(08)00403-1.
- [54] J. Dařová, S. Kümme, C. Feldmeier, J. Cibulková, R. Pařout, J. Maixner, R.M. Gschwind, B. König, R. Cibulka, Aggregation Effects in Visible-Light Flavin Photocatalysts: Synthesis, Structure, and Catalytic Activity of 10-Arylflavins, *Chem. A Eur. J.* 19 (2013) 1066–1075. doi:10.1002/chem.201202488.
- [55] A. Seegerer, P. Nitschke, R.M. Gschwind, Combined In Situ Illumination-NMR-UV/Vis Spectroscopy: A New Mechanistic Tool in Photochemistry, *Angew. Chemie Int. Ed.* 57 (2018) 7493–7497. doi:10.1002/anie.201801250.
- [56] C. Feldmeier, H. Bartling, E. Riedle, R.M. Gschwind, LED based NMR illumination device for mechanistic studies on photochemical reactions - Versatile and simple, yet surprisingly powerful, *J. Magn. Reson.* 232 (2013) 39–44. doi:10.1016/j.jmr.2013.04.011.
- [57] D.D. Macmurchie, R.J. Cushley, Paramagnetic effects in flavin spectroscopy. A ¹³C nuclear magnetic resonance study, *Can. J. Chem.* 56 (1978) 1045–1051. doi:10.1139/v78-177.
- [58] M. Goetz, G. Eckert, Photoinduced electron transfer sensitization investigated by chemically induced dynamic nuclear polarization (CIDNP), *Phys. Chem. Chem. Phys.* 8 (2006) 5294. doi:10.1039/b609026e.
- [59] G.M. Clore, J. Iwahara, Theory, Practice, and Applications of Paramagnetic Relaxation Enhancement for the Characterization of Transient Low-Population States of Biological Macromolecules and Their Complexes, *Chem. Rev.* 109 (2009) 4108–4139. doi:10.1021/cr900033p.
- [60] F. Würthner, Perylene bisimide dyes as versatile building blocks for functional supramolecular architectures, *Chem. Commun.* 4 (2004) 1564–1579. doi:10.1039/B401630K.
- [61] R.O. Marcon, S. Brochsztain, Aggregation of 3,4,9,10-perylenediimide radical anions and dianions generated by reduction with dithionite in aqueous solutions, *J. Phys. Chem. A.* 113 (2009) 1747–1752. doi:10.1021/jp808383e.
- [62] H. Miao, J. Yang, Y. Wei, W. Li, Y. Zhu, Visible-light photocatalysis of PDI nanowires enhanced by plasmonic effect of the gold nanoparticles, *Appl. Catal. B Environ.* 239 (2018) 61–67. doi:10.1016/j.apcatb.2018.08.009.
- [63] Z. Cheng, F. Xing, Y. Bai, Y. Zhao, S. Zhu, M. Li, Aggregation Behavior and Electron-Transfer Reaction of Dendritic Perylene Bisimide, Accompanied by the Formation of Highly Stable Anionic Radical Species, *Asian J. Org. Chem.* 6 (2017) 1612–1619. doi:10.1002/ajoc.201700334.
- [64] A. Nowak-Król, F. Würthner, Progress in the synthesis of perylene bisimide dyes, *Org. Chem. Front.* 6 (2019) 1272–1318. doi:10.1039/C8QO01368C.

4.6 Supporting Information

4.6.1 Materials

The solvents DMSO- d_6 and DMF- d_7 were purchased from Deutero GmbH. Both solvents were either dried over 4 Å molecular sieves and deoxygenated via Freeze-Pump-thaw prior to use or used without further treatment. The non-deuterated solvents DMF and DMSO were all p.A. grade and used without further purification. N,N'-bis(2,6-diisopropylphenyl)-3,4,9,10-perylenetetracarboxylic-diimide (**PDI**) was purchased from TCI chemicals and used without further purification. Perylene-3,4,9,10-tetracarboxylic-dianhydride (**PTCDA**) was purchased from Sigma-Aldrich and used without further purification. The substrates 2-chloro-4-(trifluoromethyl)pyridine **4** and 2-chloro-benzonitrile **6** were purchased from Sigma-Aldrich and the substrate 4-bromo-acetophenone **1** was purchased from Merck. All were used without further purification. Triethylamine (TEA) was stored over KOH pellets and filtrated prior to use.

4.6.2 Combined UVNMR-illumination measurements

All measurements were conducted on a Bruker Avance III HD 600 (600.13 MHz) spectrometer with a fluorine selective TBIF probe in combination with our UVNMR-illumination device[55]. The samples were illuminated by either a Cree XT-E royal blue (Lumitronix, 450 nm; 500 mW) or an Osram Oson SSL80 (455 nm; 500 mW) high power LED. UV/Vis spectra were acquired with an Avantes2048 spectrometer.

If not otherwise indicated, measurements were conducted at 313 K in 300 μ L solutions of DMF- d_7 or DMSO- d_6 . The specific composition and concentration of the reaction components (photocatalysts, aryl halide, sacrificial electron donor etc.) is mentioned under the figures of the corresponding experiment.

4.6.2.1 Preparation of the blank sample for the UVNMR-illumination measurements

The corresponding aryl halide was dissolved in DMF- d_7 in an NMR tube (amberized) and the solution was argon bubbled for 10 minutes. Then TEA was injected into the solution and the quartz glass insert was added and the sample was sealed airtight with the customized screw cap (see setup).

4.6.2.2 Blank sample measurements

The blank measurement was conducted prior to the combined UVNMR experiments. The sample was injected into the NMR spectrometer to reach a temperature of 313 K. Once the temperature equilibrated, a blank UV/Vis spectrum was recorded. The resulting integration time given by the UV/Vis spectrometer determined the d11 delay in the NMR pulse program (the d11 is the duration of the UV/Vis measurement; for more info see [55]), which is necessary for later automation. An NMR spectrum was also taken as quality control, which ensured correct blank preparation.

4.6.2.3 Sample preparation

Under argon atmosphere the required amount of **PDI** was added to the blank sample. The quartz glass insert was inserted and the sample was sealed with our customized screw cap. To dissolve the **PDI** completely the sample was sometimes sonicated.

4.6.2.4 UVNMR-illumination measurements

For all NMR measurements the delay d11 in the pulse program was set to the required integration time determined in the blank sample measurement. The reaction profiles were generated by alternately recording non illuminated and illuminated ^1H NMR spectra. This ensured that no signal intensities were distorted by possible photo-CIDNP effects. One UV/Vis spectrum was automatically recorded prior to every NMR measurement (dark and light). After a first spectrum without illumination a row of ^1H spectra was collected alternating between illuminated and unilluminated proton spectra. Only spectra without illumination were used to generate reaction profiles.

The NMR kinetics are derived from the aromatic proton integrals of **1** and **2** (Signal **1**, see **Figure 10**) and referenced to the respective signal in the first spectrum without illumination. Assignments were made by evaluating standard sets of 1D and 2D NMR spectra. The chemical shifts were referenced to the solvent signals (DMF-*d*7 or DMSO-*d*6). For DMF one of the two methyl group signals was used for integration (depending on the reaction conditions and/or progress of the reaction, one of the signals is sometimes overlapped by TEA or secondary products of TEA). The raw UV/Vis spectra, which were acquired with the UVNMR illumination device, were processed with OriginPro 8 by smoothing them (Savitzky-Golay) and performing a baseline correction (spline).

4.6.3 Regular *in situ* NMR illumination measurements

All measurements were conducted either on a Bruker Avance III HD 600 (600.13 MHz) spectrometer with a fluorine selective TBIF probe or on a Bruker Avance 500 (500.13 MHz) spectrometer with a 5 mm QXI probe or a 5 mm prodigy TCI cryo-probe in combination with our previously described *in situ* NMR illumination device[56]. The samples were illuminated by either a Cree XT-E royal blue (Lumitronix, 450 nm; 500 mW) or an Osram Oson SSL80 (455 nm; 500 mW) high power LED.

If not otherwise indicated, measurements were conducted at 313 K in 450 μ L solutions of DMF- d_7 or DMSO- d_6 . The specific composition and concentration of the reaction components (photocatalysts, aryl halide, sacrificial electron donor etc.) is mentioned under the figures of the corresponding experiment.

4.6.3.1 Sample preparation

The corresponding aryl halide and/or photocatalyst (**PDI** or **PTCDA**) were dissolved in DMF- d_7 in an NMR tube (amberized) and the solution was argon bubbled for 10 minutes. Then TEA was injected into the solution and the quartz glass insert was added and the sample was sealed airtight. No TEA was added for the investigation without sacrificial electron donor.

4.6.3.2 *In situ* NMR measurements

Reaction profiles were generated by alternately recording non illuminated and illuminated ^1H NMR spectra (and/or ^{19}F NMR spectra for aryl halide **4**). This ensured that no signal intensities were distorted by possible photo-CIDNP effects. After the first spectra without illumination a row of ^1H and/or ^{19}F spectra was collected illuminating alternating between illuminated and non-illuminated spectra. Only spectra without illumination were used to generate reaction profiles.

The NMR kinetics are derived from the aromatic proton integrals of **1** and **2** (Signal 1, **Figure 10 A**) or **6** and **7** (Signal 4 and 2, respectively, see **Figure S18.**) and the ^{19}F signal of the CF_3 moiety of **4** and **5** and referenced to the respective signal in the first spectrum without illumination. Assignments were made by evaluating standard sets of 1D and 2D NMR spectra. The chemical shifts were referenced to the solvent signals (DMF- d_7 or DMSO- d_6). For DMF one of the two methyl group signals was used for integration (depending on the reaction conditions and/or progress of the reaction, one of the signals is sometimes overlapped by TEA or secondary products of TEA).

4.6.4 Photo-CIDNP Experiments

The presented photo-CIDNP effects were all steady state photo-CIDNP effects. They were directly extracted from the recorder UVNMR or *in situ* NMR illumination reaction profiles. For the photo-CIDNP spectra, one NMR spectrum in the dark was subtracted from the previous NMR spectrum under illumination (light minus dark) yielding the photo-CIDNP difference spectrum.

4.6.5 *Ex situ* NMR end point measurements

The photocatalyst (**PDI** or **PTCDA**) (0.004 mmol) and aryl halide (**1**, **4** or **6** 0.04 mmol) were weight into a 5 mL crimp cap vial with a stirring bar and 2 ml of DMSO/DMSO-*d*₆ (9:1) were added. Then the vial was sealed with a crimp cap with septum and argon bubbled for 10 minutes. Then TEA (0.32 mmol) was added and the vial was placed approximately 1 cm above a 450 nm LED inside a cooling block and stirred under irradiation. After the respective illumination time, 600 – 700 μ L were directly pulled from the reaction solution and filled into an NMR tube. The sample was then measured straight forwardly.

For the measurements at 690 nm irradiation the photocatalyst and the aryl halide were directly weight into the NMR tube and the tube was filled with 600 μ L of DMSO/DMSO-*d*₆ (9:1). After ten minutes of argon bubbling the sample was sealed airtight and the 690 nm LED was brought in close contact with the NMR tube and LED + NMR tube were wrapped in aluminum foil (in some cases for **PDI** as photocatalyst the sample was first succumbed to illumination with 450 nm light for 1.5 hours). The NMR sample was measured straight forward after the respective illumination time. Red light illumination was conducted with a 1W Fedy Tech. (FD-15R-Y1) 690-700 nm LED (measured maximum 688 nm; data not shown).

4.6.6 UV/Vis measurements (under illumination)

All UV/Vis spectra acquired with an Avantes2048 spectrometer. The illuminated UV/Vis spectra were either acquired in 10 mm or 1 mm \varnothing quartz glass cuvettes. Illumination was performed with either a Cree XT-E royal blue (Lumitronix, 450 nm; 500 mW) or an Osram Oson SSL80 (455 nm; 500 mW) high power LED, which was brought into close proximity (~1 cm) of the cuvette for irradiation. At the respective time point the light was turned off and a UV/Vis spectrum was acquired straight-forwardly.

4.6.7 Test background reaction of 4-bromo-acetophenone

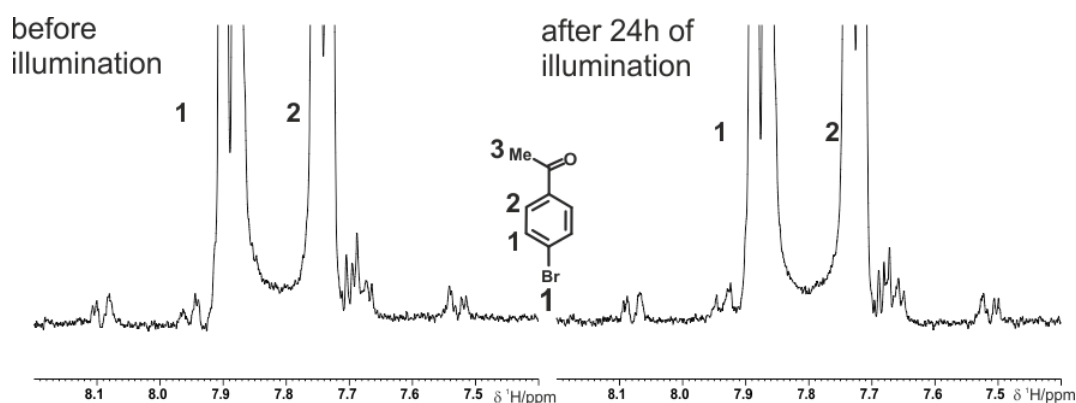


Figure S1. ^1H NMR spectrum of 4-bromo-acetophenone **1** before illumination (left) and after 24 hours of illumination (right). It is evident that **1** does not react without photocatalyst. Reaction conditions: **1** (20 mM) and TEA (160 mM) in 600 μL DMSO/DMSO- d_6 (9:1) at 313 K. Irradiation was conducted with 450 nm blue light.

4.6.8 ^1H assignments of relevant starting materials and products

Figure S2. lists the ^1H (and ^{19}F ; red) assignments of the relevant starting materials and products, which are discussed within this publication. Please note that the chemical shifts are under reaction conditions and can vary depending on the reaction progression. This is especially the case for TEA and DEA, which continuously shift to lower field as the reaction progresses, because they can interact with the liberated halide anion (Cl^- or Br^-). The chemical shift for **1**, **4**, **PDI** and TEA is given for the start of the reaction in DMF- d_7 and for **6** in DMSO- d_6 before the illumination is turned on. The chemical shift of **2**, **5**, DEA and acetaldehyde is given at the end of the reaction in DMF- d_7 and for **7** in DMSO- d_6 after the light was turned off. The chemical shift of the vinyl species **3** was picked from the first illuminated spectrum because the only signals visible are the photo-CDINP enhanced signals under illumination. No signals could be detected for the photocatalyst **PTCDA** because at reaction conditions (1 mM and above) **PTCDA** forms extensive aggregates and is not detectable with solution NMR spectroscopy. The chemical shifts of dimer **8** are in DMSO/DMSO- d_6 (9:1) because it is a special case as it only appears in detectable amounts in DMSO. ^{13}C chemical shifts were not investigated in detail because all presented compounds are commercially available and/or literature known.

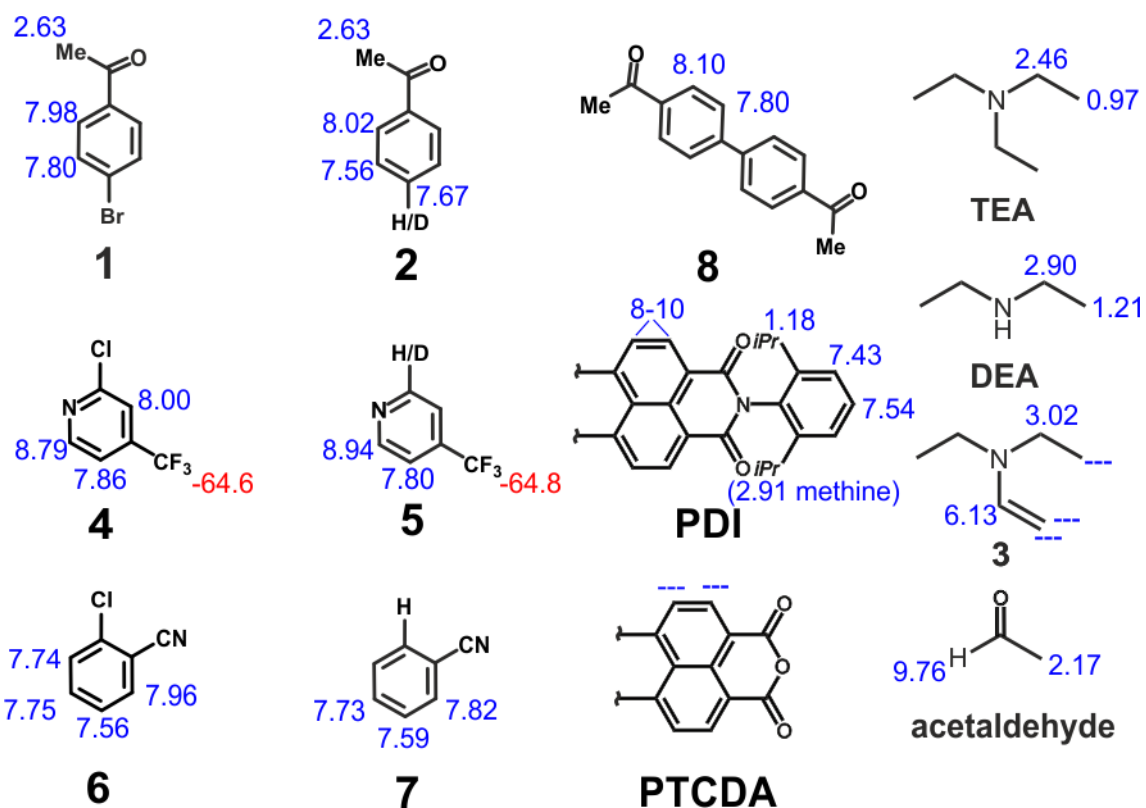


Figure S2. ^1H (and ^{19}F , red) chemical shifts of relevant starting materials and reaction products. Please note that all chemical shifts are given under reaction conditions. Therefore, the chemical shifts can heavily vary depending on the respective conditions and the overall progression of the reaction.

Broadened PDI signals 5 and 6

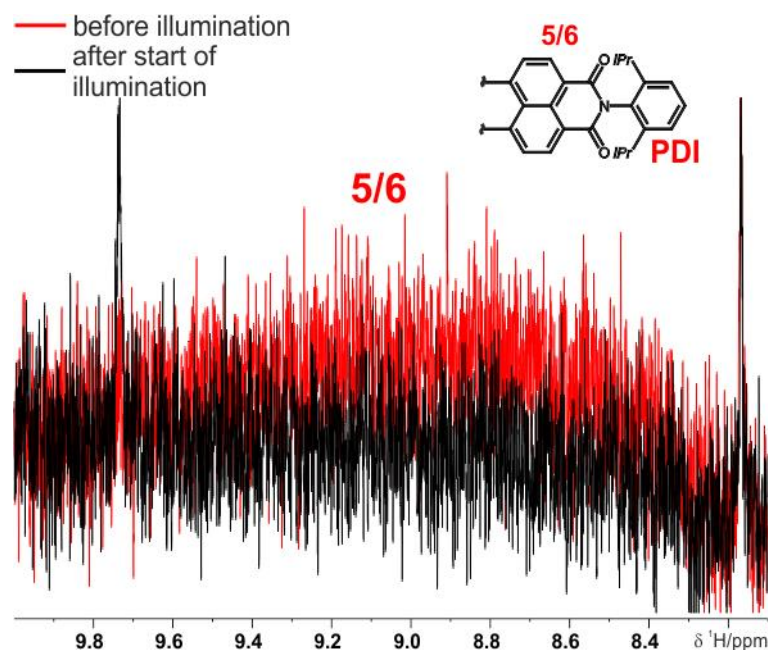


Figure S3. The **PDI** signals 5 and 6 are heavily broadened even before illumination due to an EDA complex (red spectrum). After the illumination starts the signals vanish completely in an instant due to the formation of the **PDI^{•-}** (black spectrum). Reaction conditions: **1** (25 mM), **PDI** (1 mM), TEA (160 mM), in DMF-*d*₇ under inert atmosphere at 313 K. Irradiation was conducted with 450 nm blue light.

4.6.9 Titration experiments

For the titration experiment, a solution of 1 mM **PDI** was exposed to an increasing concentration of TEA. **Figure S4.** shows a series of proton spectra highlighting the aromatic region. With increasing TEA concentration, the **PDI** signals start to broaden significantly and the broadening is distance dependent with respect to the perylene core of **PDI**. The **PDI** signals 5 and 6 are clearly more affected than 1 and 2 and the signals of the isopropyl moiety are almost not affected at all (data not shown). Similar distance dependent line broadening was also previously reported for riboflavin derivatives and was attributed to the formation of radical species[1,2]. Furthermore, the line broadening is not accompanied by significant chemical shift differences ($\Delta\delta > 5$ Hz for 0-90 mM TEA) excluding the formation of novel diamagnetic species. Hence, this behavior is indicative of an exchange process with a radical species (here: **PDI^{•-}**) due to the formation of an electron donor acceptor (EDA) complex between TEA and **PDI**. In addition, the titration experiments were not carried out under inert conditions showing

that the EDA complex is permanently formed although the oxygen in solution can quench $\text{PDI}^{\bullet-}$ back into its ground state[3].

It is to be noted, that the TEA signals show a similar distant dependent line broadening behavior to the center (the CH_2 group of the ethyl residues is more affected than the CH_3 group and in the vinyl residue the $=\text{CH}$ is stronger affected than the $=\text{CH}_2$), which further indicates the formation of an EDA complex between **PDI** and TEA. But the line broadening of TEA can only be observed at very low TEA concentrations ($> 5 \text{ mM}$; data not shown). Under reaction conditions ($\text{TEA} \geq 80 \text{ mM}$) the TEA signals are not visibly affected anymore due to the high excess.

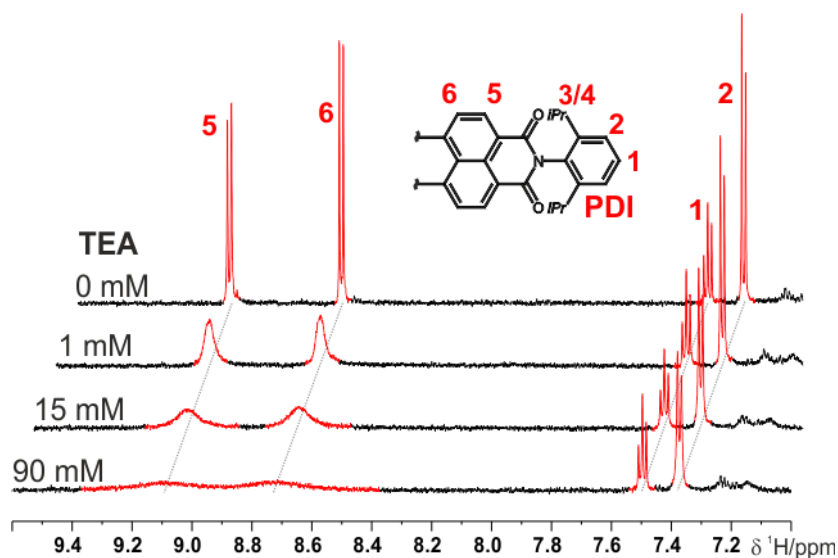


Figure S4. Titration series adding increasing concentrations of TEA (1-90 mM) to a solution of 1 mM **PDI** in $\text{DMSO-}d_6$ under ambient atmosphere at 313 K. The **PDI** signals clearly broaden upon addition of TEA, at which the broadening shows a distance dependent behavior with respect to the perylene core.

4.6.10 UVNMR compared to regular UV/Vis

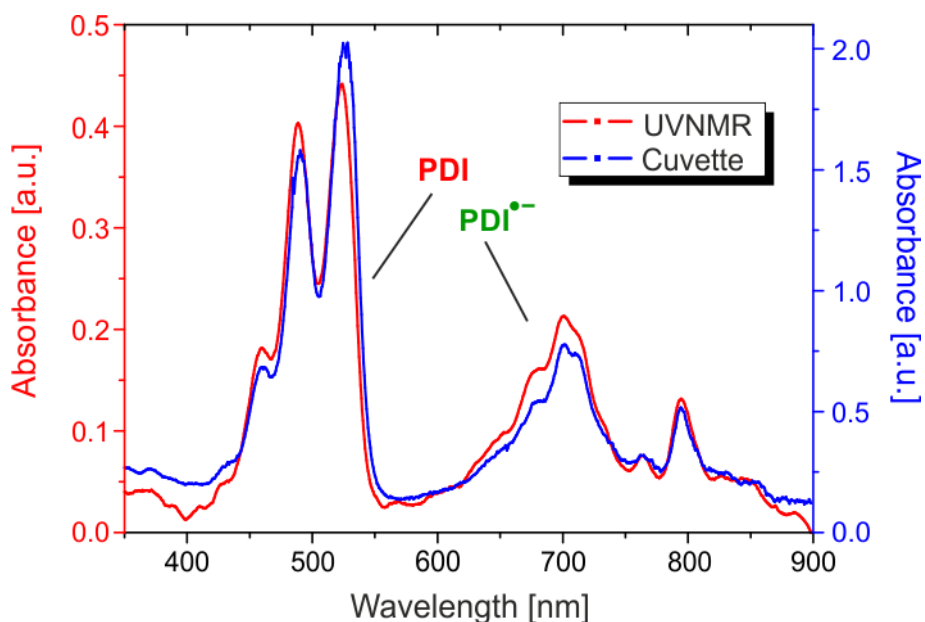


Figure S5. Qualitative comparison of UV/Vis spectra acquired by the UVNMR setup (red) and a conventional UV/Vis measurement inside a regular 10 mm cuvette (blue) showing the absorbance bands of **PDI** and **PDI^{•-}**.

4.6.11 Photo-CIDNP effects of the vinyl species **3**

Since we could observe that the vinyl species **3** reacts into further secondary products it was not unambiguous if the overserved signals are real photo-CIDNP effects (only positive photo-CDINPs were detected) or if the signals are regular NMR signals and **3** is just so short lived that it already reacted further in the dark spectra. Hence, we conducted further experiments to confirm the validity of the photo-CDINP effects. It was previously reported in literature (Goez *et al.*[4]) that changing concentrations and/or ratio of the participants of the photo-CIDNP effect can lead to a sign inversion of the photo-CDINP effect. And indeed at a 1:1 ratio of PDI to TEA (3 mM each; ratio in the reaction is usually at least 1:80) in DMSO-*d*₆, we could achieve a sign inversion of signal 1 and 2, which unambiguously confirms the observed signals as photo-CDINP effects. **Figure S6.** shows the corresponding light, dark, and photo-CDINP difference spectrum.

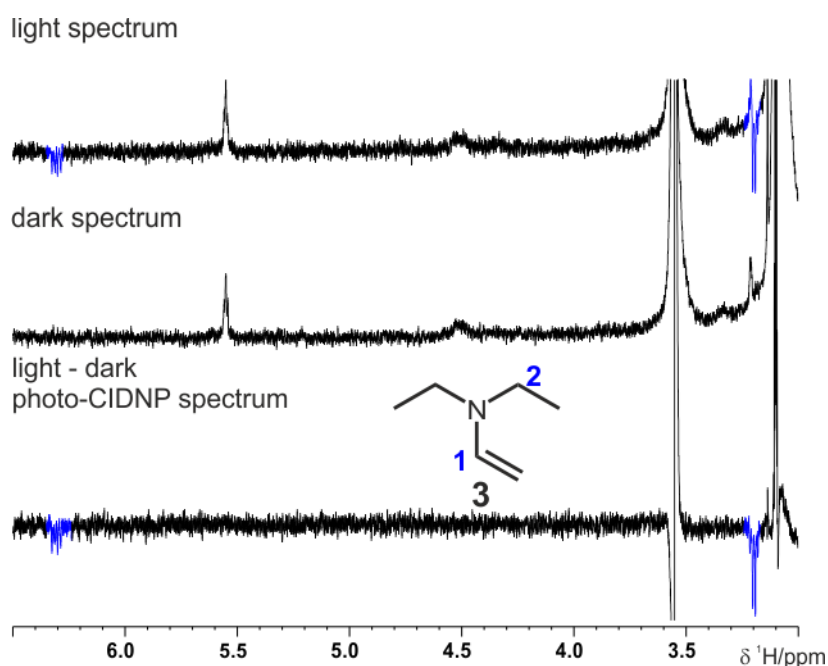


Figure S6. Photo-CIDNP spectrum of the vinyl species **3** showing the negative photo-CIDNP phases of signal **1** and **2** (blue). The light and dark spectra are recorded consecutively and then subtracted from one another to yield the photo-CIDNP difference spectrum. Reaction conditions: **PDI** (3 mM), TEA (3 mM), 4-bromo-benzaldehyde in DMF-*d*7 under inert atmosphere at 313 K. Irradiation was conducted with 450 nm blue light.

4.6.12 *In situ* NMR profiles of 2-chloro-benzonitrile **6**

Besides the substrates **1** and **4**, *in situ* NMR illumination reaction profiles were also recorded for 2-chloro-benzonitrile **6**. **Figure S7.** shows the corresponding ^1H NMR reaction profile. Similar to substrate **1**, a pseudo signal increase can be observed for the starting material **6** (black) due to paramagnetic relaxation enhancement, which is induced by rising **PDI** $^\bullet$ -concentrations. There is also an extensive initiating phase (~1.5 h) before the product formation of **7** starts. It should be noted, that this reaction was conducted in DMSO-*d*6, which is also a suitable solvent for the reaction, instead of DMF-*d*7. Since, DMSO-*d*6 can't participate in the proton donation event (in contrast to DMF-*d*7) for the final product **7**, **7** is fully protonated. **Figure S8.** depicts the integral intensity of the residual DMSO-*d*6 solvent signal. Similar to DMF-*d*7, the signal intensity increases with ongoing illumination (corresponds to amount of **PDI** $^\bullet$ -in solution) and hits a plateau after 1 h. Unfortunately, after around 5 h the DMSO signals is overlapped with

the continuously low field shifting CH₂- moiety of TEA¹⁴ and the DMSO signal intensity cannot be accounted for anymore.

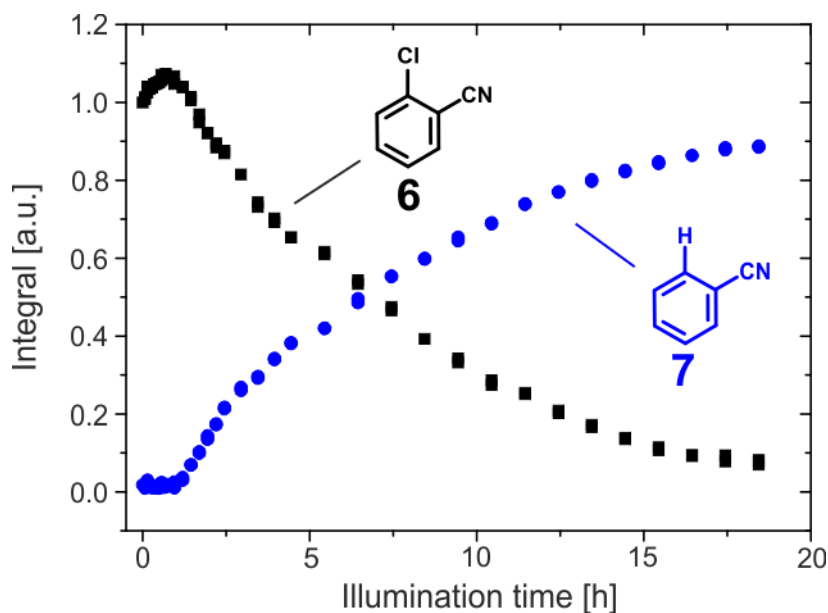


Figure S7. ¹H NMR reaction profile for substrate **6** and its reaction product **7**. The integral value of **6** (black) increases once the light is turned on, due to paramagnetic relaxation enhancement resulting from increasing **PDI**^{•+} concentration. The product formation of **7** (blue) is preceded by a long initiating phase. Reaction conditions: **6** (10 mM), **PDI** (2 mM), TEA (80 mM), in DMSO-*d*₆ under inert atmosphere at 313 K. Irradiation was conducted with 450 nm blue light.

¹⁴ TEA shifts downfield once product formation starts because of increasing amounts of anions (halides) in solution.

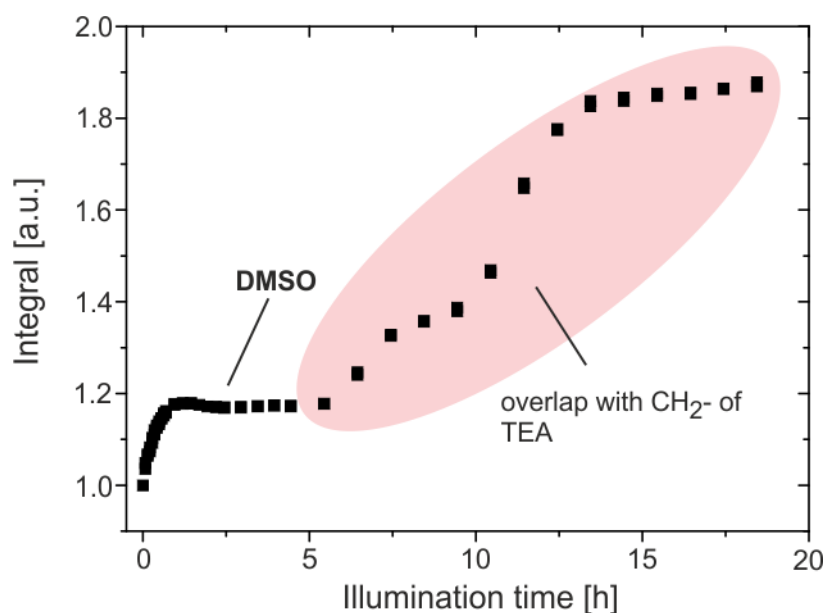


Figure S8. ^1H NMR reaction profile of the residual DMSO- d_6 solvent signal. Analogous to DMF- d_7 , the DMSO- d_6 signal increases with ongoing illumination, which is corresponding to rising $\text{PDI}^{\bullet-}$ concentration. The DMSO- d_6 signal is overlapped by the CH_2 - group of TEA after 5 – 6 h, preventing further evaluation of the DMSO- d_6 signal. Reaction conditions: **6** (10 mM), **PDI** (2 mM), TEA (80 mM), in DMSO- d_6 under inert atmosphere at 313 K. Irradiation was conducted with 450 nm blue light.

4.6.13 UV/Vis experiments

Figure S9. depicts a row of UV/Vis spectra from the reaction of 4-bromo-acetaldehyde (10 mM) to the corresponding aryl compound acetaldehyde in the presence of **PDI** (1 mM) and TEA (80 mM) in DMF under inert atmosphere in a 1 mm cuvette. The solution was continuously irradiated with 450 nm blue light and UV/Vis spectra were taken at the time points given in **Figure S9**. (0 min, black; 5 min, red; 8 min, blue and 40 min, green). The $\text{PDI}^{\bullet-}$ absorbance bands immediately appear when the illumination starts (600 – 1000 nm). But with ongoing illumination, these bands decrease again and they start to broaden and lose their distinctive features. Similarly, the absorbance bands of **PDI** (400 – 550 nm) also start to decrease and lose their definition. After 40 min. of illumination (**Figure S9**. green spectrum) only very broad absorbances remain, which probably stem from degradation products of **PDI** and/or can also indicate aggregation. These findings are in line with the results of Marchini *et al.*, who also reported a fast disappearance of the $\text{PDI}^{\bullet-}$ and the appearance of broad, undefined absorbances in UV/Vis investigations under continuous illumination with blue light[5].

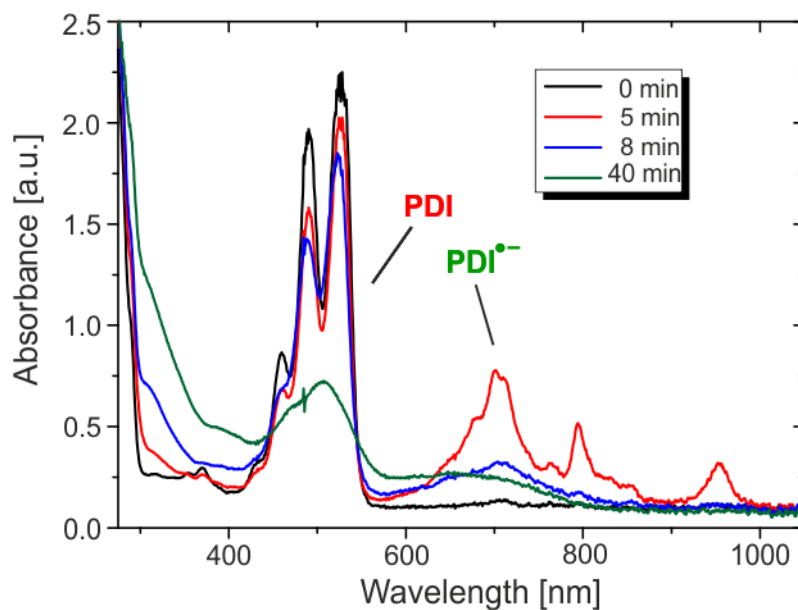


Figure S9. Series UV/Vis spectra of the reaction of 4-bromo-acetaldehyde (10 mM) in the presence of **PDI** (1 mM) and TEA (80 mM) in DMF under inert atmosphere, under continuous 450 nm irradiation at room temperature in a 1 mm cuvette. Once the illumination begins, **PDI^{•-}** starts to form (absorbance bands 600 – 1000 nm). With ongoing illumination all absorbance bands (of **PDI** and the **PDI^{•-}**) start to change and transform into broad, undefined absorbance bands.

4.6.14 Signal broadening of the perylene core signals of PDI under illumination

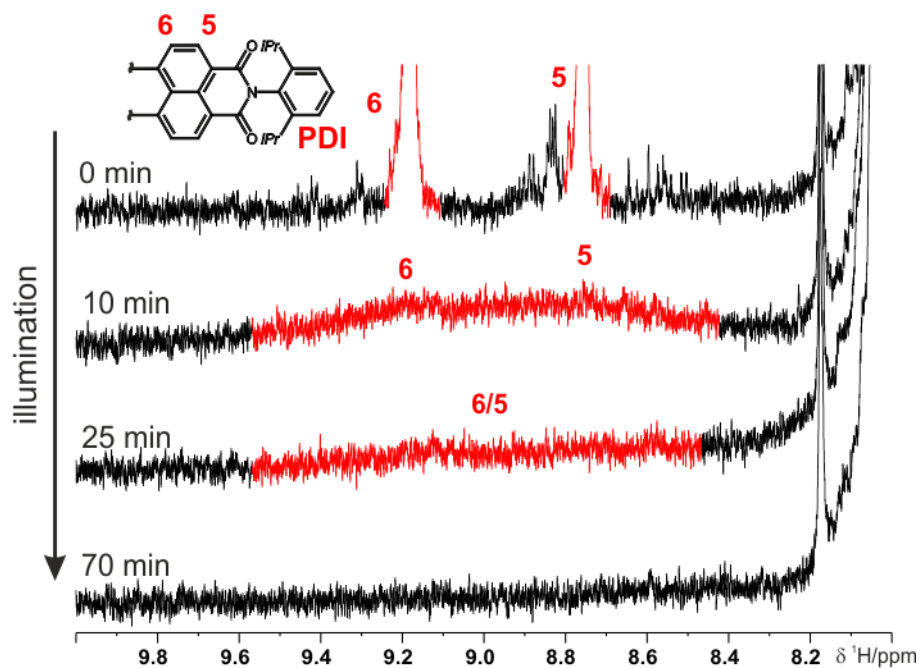


Figure S10. Series of ^1H spectra focusing on the perylene core signals 5 and 6 (red) of **PDI** under illumination. Once illumination is turned on, the signals start to quickly broaden and fully disappear after some time. This suggests that **PDI** can transition into its paramagnetic radical anion state even without the presence of a sacrificial electron donor such as TEA. Reaction conditions: **PDI** (1 mM) in $\text{DMF-}d_7$ under inert atmosphere at 313 K. Illumination with 450 nm.

4.6.15 NMR behavior of PDI with and without the presence of 1 under illumination

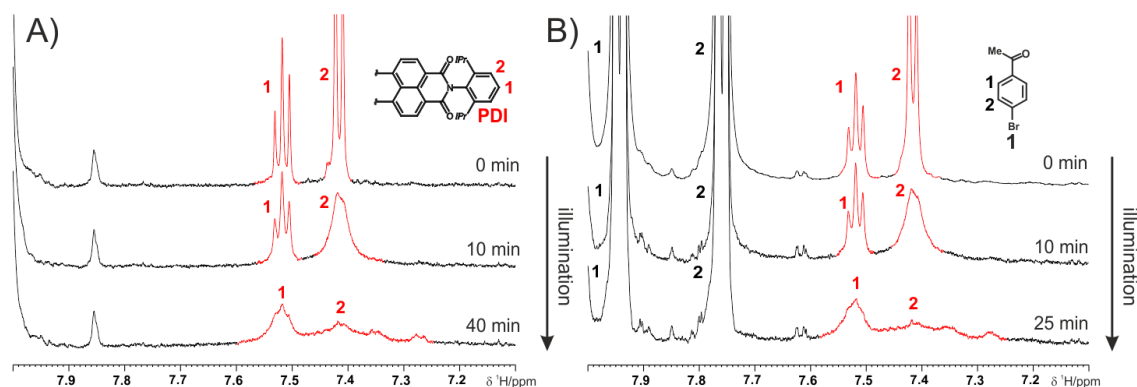


Figure S11. A) Row of ¹H spectra focusing on the signals 1 and 2 of **PDI** (red) under illumination B) Row of ¹H spectra focusing on the signals 1 and 2 of **PDI** (red) under illumination in the presence of the aryl halide **1**. Whether **1** is present or not, the **PDI** signals behave in the same manner under prolonged illumination. First, they start to broaden and as illumination progresses new, broad signals start to appear slightly upfield shifted. This suggests that **1** does not influence the inter-**PDI** interactions/reactions. Reaction conditions: **PDI** (1 mM), **1** (20 mM; only for B) in DMF-*d*₇ under inert atmosphere at 313 K. Illumination with 450 nm.

4.6.16 Re-aeration experiments

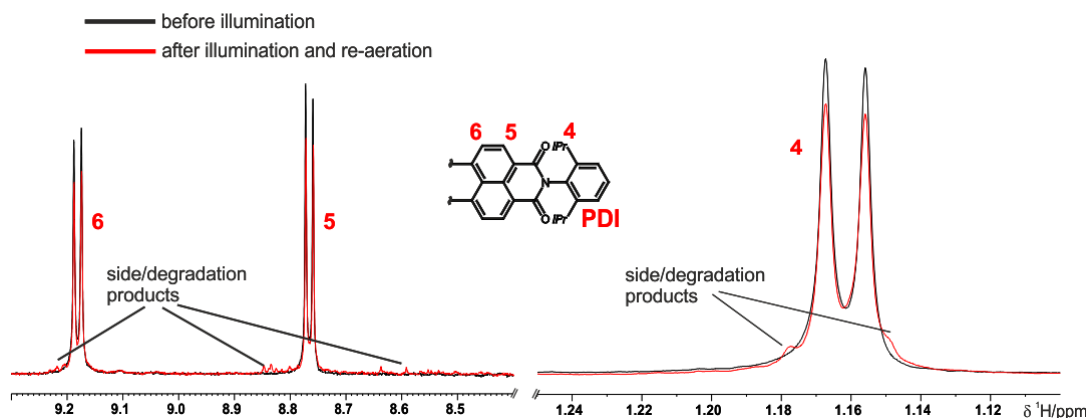


Figure S12. NMR re-aeration experiments of **PDI**. The spectra depict the low field region (left) focusing on the **PDI** signals 5 and 6 and the high field region (right) with the **PDI** signal 4, before (black) and after illumination and subsequent re-aeration. After re-aeration minor side/degradation products can be observed for all signals. Reaction conditions: **PDI** (1 mM) in DMF-*d*₇ under inert atmosphere at 313 K. Illumination with 450 nm.

4.6.17 Prolonged illumination of PDI in the presence of 4-bromoacetophenone 1

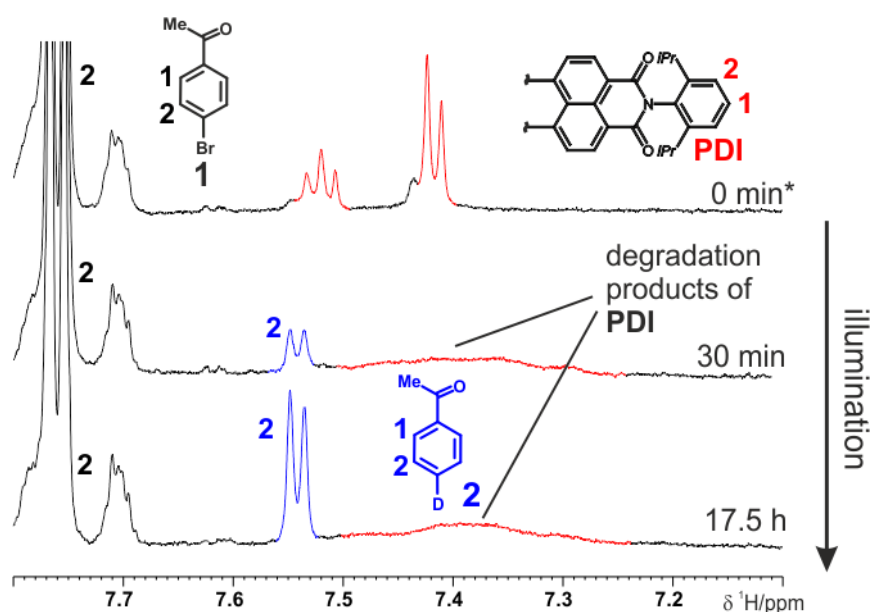


Figure S13. *In situ* NMR illumination of **PDI** in the presence of **1**. The top spectrum shows the **PDI** signals 1 and 2 (red) before illumination. The middle and bottom spectrum show the same reaction solution after 30 min and 17.5 h of blue light illumination, respectively. It is evident that under prolonged illumination, product formation of **2** occurs (blue) despite the absence of TEA. Furthermore, broad, undefined degradation resonances of **PDI** appear with ongoing irradiation. Please note, since the absence of TEA, $\text{DMF-}d_7$ is the only proton source and hence product **2** is fully deuterated in the *para*-position. Reaction conditions: **PDI** (1 mM), **1** (20 mM) in $\text{DMF-}d_7$ under inert atmosphere at 313 K. Illumination with 450 nm. *The top spectrum is the same as the top spectrum in **Figure S12 A**, but was put under inert atmosphere again.

4.6.18 UV/Vis measurements of PDI in the presence of 4-bromo-acetophenone 1

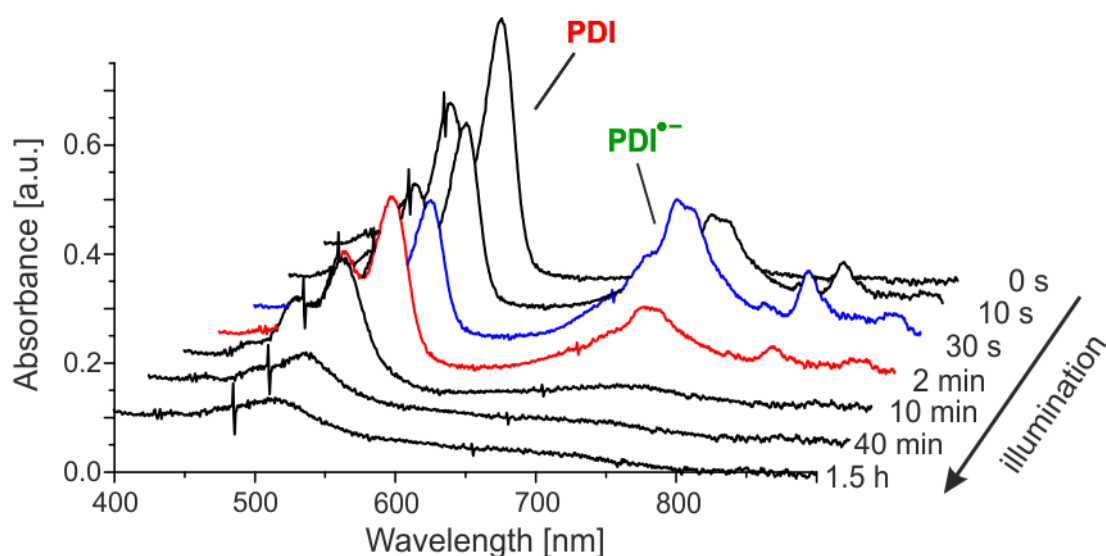


Figure S14. Series of UV/Vis spectra of **PDI** in the presence of **1** under prolonged illumination with 450 nm. Similarly to the full reaction conditions with aryl halide and TEA (see **Figure 4. B** and **Figure S9.**) or the experiments of just **PDI** (see **Figure 7. B**), the **PDI•⁻** immediately appears once illumination starts. Under prolonged illumination all **PDI** and **PDI•⁻** absorbance bands start to broaden and lose their profile. Interestingly, at one point the **PDI•⁻** absorbance bands decrease, while the **PDI** absorbances rise again (blue vs red spectrum) despite ongoing illumination. After 10 min of irradiation **PDI** starts to decompose and broad, undefined absorbances appear. Reaction conditions: **PDI** (50 μM) and **1** (500 μM) in DMF under inert conditions at ambient temperature. Illumination with 450 nm.

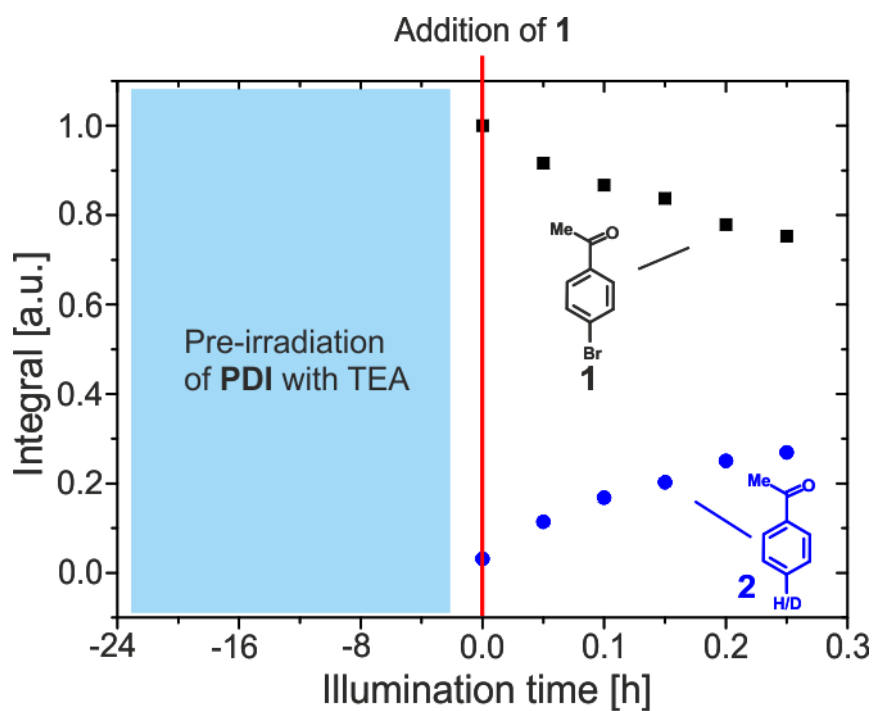
4.6.19 ^1H reaction profiles with PDI-TEA pre-irradiation

Figure S15. ^1H reaction profile of **1** and **2** after 24 hours of pre-irradiation of **PDI** in solution with TEA. The reaction starts immediately once the light is turned on, **1** and **2** decrease/increase linearly in the beginning. Reaction conditions: **PDI** (1 mM), TEA (160 mM) **1** (20 mM; after addition) in $\text{DMF-}d_7$ under inert atmosphere at 313 K. Illumination with 450 nm.

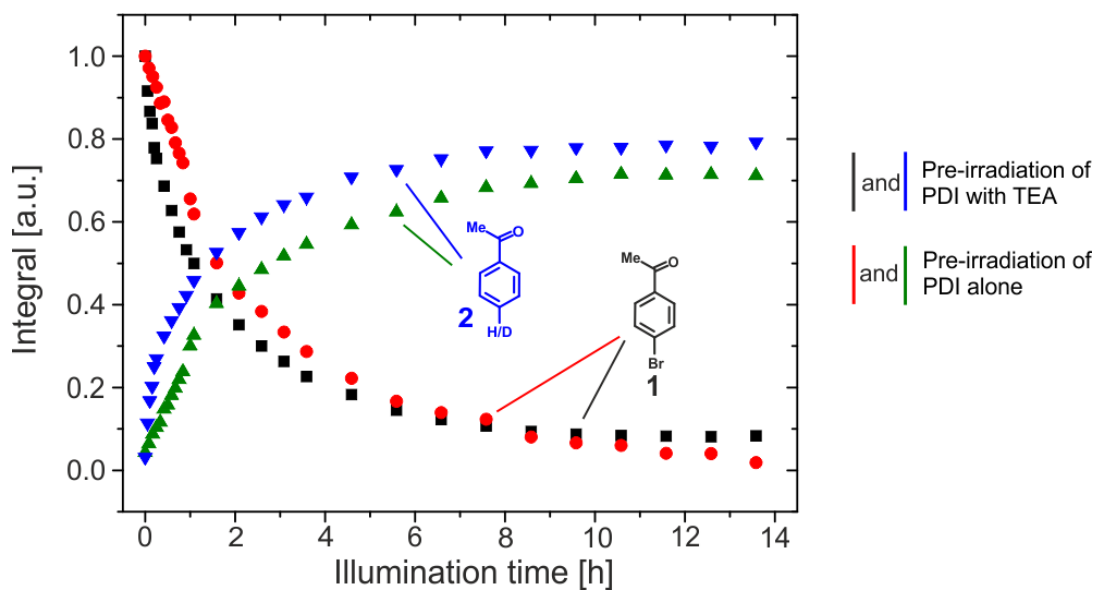
4.6.20 Comparison of the ^1H reaction profiles with PDI and PDI-TEA pre-irradiation

Figure S15. ^1H NMR reaction profiles for substrate **1** and its reaction product **2**. The black progression of **1** and the blue progression of **2** correspond to the reaction with **PDI** pre-irradiation in presence of TEA before **1** was added. The red and green progression of **1** and **2** correspond to the reaction where only **PDI** was pre-irradiated before **1** and TEA was added. It is evident that pre-irradiation of **PDI** and TEA leads to a faster reaction than just pre-irradiation of **PDI**. Reaction conditions: **PDI** (1 mM) or PTCDA (1 mM), **1** (20 mM) and TEA (160 mM) in $\text{DMF-}d_7$ under inert atmosphere at 313 K. Illumination with 450 nm.

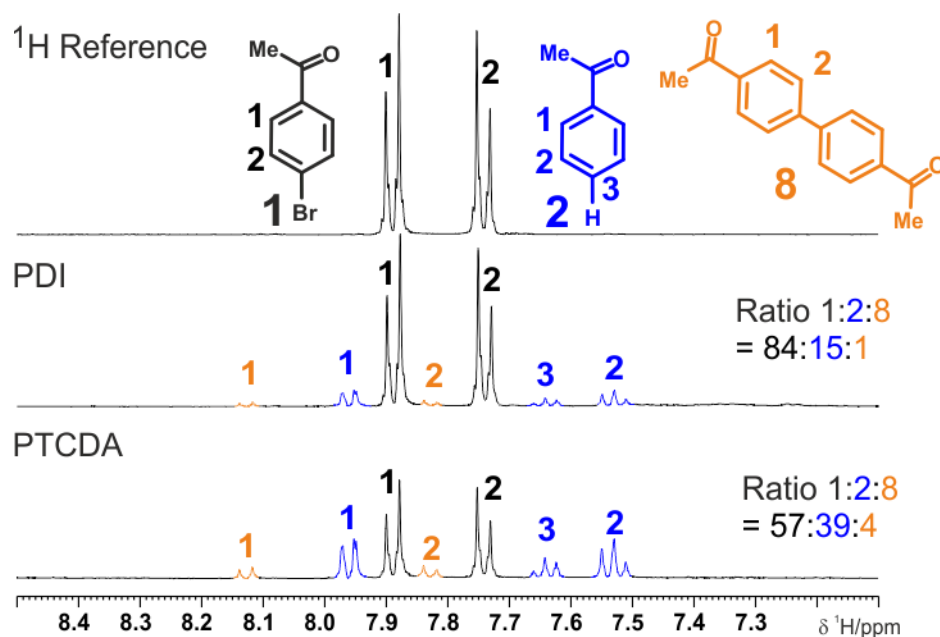
4.6.21 *Ex situ* NMR measurements to compare the performance of the photocatalysts PDI and PTCDA

Figure S16. *Ex situ* NMR tests to compare the performance of the photocatalysts **PDI** and **PTCDA** for the photocatalytic dehalogenation of **1** to **2** (and **8**). Top spectrum: ^1H reference of **1** (aromatic region). Middle spectrum: Results for **PDI** after four hours of illumination. Bottom spectrum: Results for **PTCDA** after four hours of illumination. **PTCDA** yields superior conversion after 4 hours of illumination than **PDI**. Reaction conditions: Photocatalyst (**PDI** or **PTCDA**; 2 mM), **1** (20 mM), TEA (160 mM) in DMSO/DMSO- d_6 (9:1) under inert atmosphere at 313K (NMR measurement at 299 K). Illumination with 450 nm.

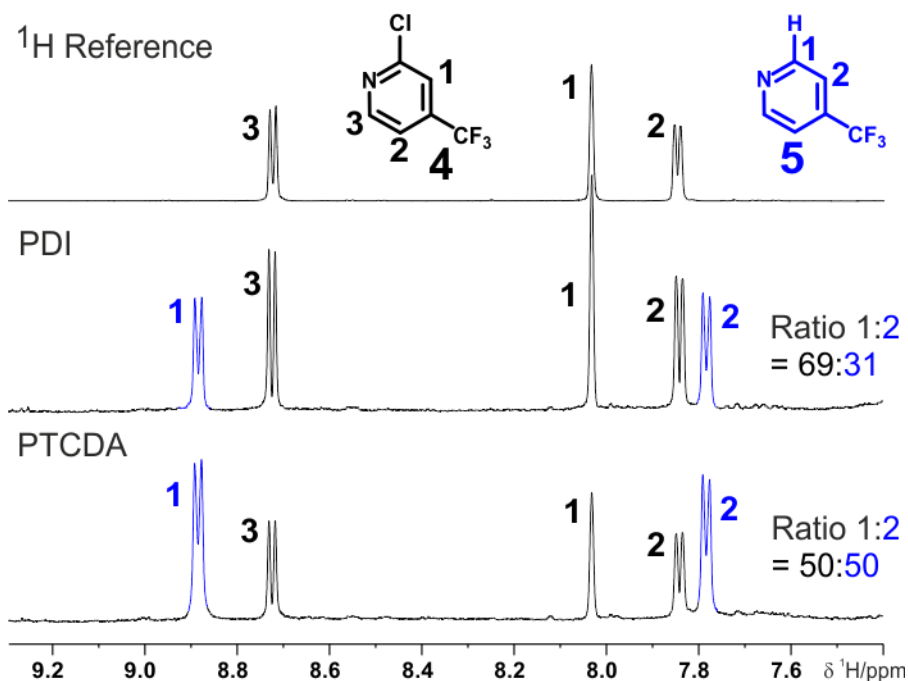


Figure S17. *Ex situ* NMR tests to compare the performance of the photocatalysts **PDI** and **PTCDA** for the photocatalytic dehalogenation of **4** to **5**. Top spectrum: ^1H reference of **4**. Middle spectrum: Results for **PDI** after four hours of illumination. Bottom spectrum: Results for **PTCDA** after four hours of illumination. **PTCDA** yields superior conversion after 4 hours of illumination than **PDI**. Reaction conditions: Photocatalyst (**PDI** or **PTCDA**; 2 mM), **4** (20 mM), TEA (160 mM) in DMSO/DMSO- d_6 (9:1) under inert atmosphere at 313K (NMR measurement at 299 K). Illumination with 450 nm.

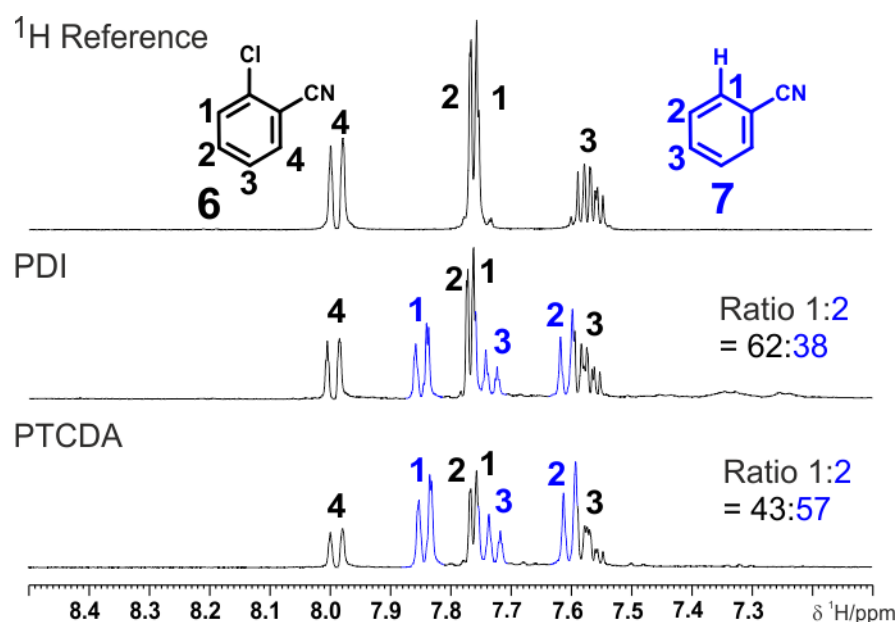
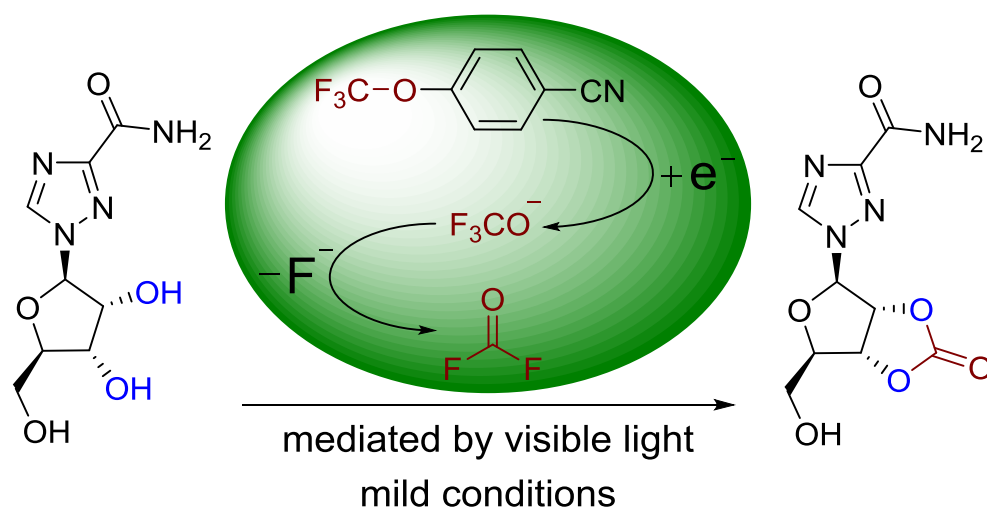


Figure S18. *Ex situ* NMR tests to compare the performance of the photocatalysts **PDI** and **PTCDA** for the photocatalytic dehalogenation of **6** to **7**. Top spectrum: ^1H reference of **6**. Middle spectrum: Results for **PDI** after four hours of illumination. Bottom spectrum: Results for **PTCDA** after four hours of illumination. **PTCDA** yields superior conversion after 4 hours of illumination than **PDI**. Reaction conditions: Photocatalyst (**PDI** or **PTCDA**; 2 mM), **6** (20 mM), TEA (160 mM) in DMSO/DMSO- d_6 (9:1) under inert atmosphere at 313K (NMR measurement at 299 K). Illumination with 450 nm.

4.6.22 References

- [1] C. Feldmeier, H. Bartling, K. Magerl, R.M. Gschwind, vLED-Illuminated NMR Studies of Flavin-Catalyzed Photooxidations Reveal Solvent Control of the Electron-Transfer Mechanism, *Angew. Chemie Int. Ed.* 54 (2015) 1347–1351. doi:10.1002/anie.201409146.
- [2] D.D. Macmurchie, R.J. Cushley, Paramagnetic effects in flavin spectroscopy. A ^{13}C nuclear magnetic resonance study, *Can. J. Chem.* 56 (1978) 1045–1051. doi:10.1139/v78-177.
- [3] I. Ghosh, T. Ghosh, J.I. Bardagi, B. König, Reduction of aryl halides by consecutive visible light-induced electron transfer processes, *Science* 346 (2014) 725–728. doi:10.1126/science.1258232.
- [4] M. Goetz, G. Eckert, Photoinduced electron transfer sensitization investigated by chemically induced dynamic nuclear polarization (CIDNP), *Phys. Chem. Chem. Phys.* 8 (2006) 5294. doi:10.1039/b609026e.
- [5] M. Marchini, A. Gualandi, L. Mengozzi, P. Franchi, M. Lucarini, P.G. Cozzi, V. Balzani, P. Ceroni, Mechanistic insights into two-photon-driven photocatalysis in organic synthesis, *Phys. Chem. Chem. Phys.* 20 (2018) 8071–8076. doi:10.1039/c7cp08011e.

5 Visible-Light-Mediated Liberation and *In Situ* Conversion of Fluorophosgene



Daniel Petzold, **Philipp Nitschke**, Fabian Brandl, Veronica Scheidler, Bernhard Dick, Ruth M. Gschwind, Burkhard König

Chem. Eur. J. **2019**, 25, 361-366

DOI: 10.1002/chem.201804603

Daniel Petzold and Philipp Nitschke contributed equally to this work. Daniel Petzold developed the project, optimized the reaction, prepared the substrate scope and the manuscript. Philipp Nitschke performed the NMR measurements and evaluations and contributed to the mechanistic part of the manuscript. Fabina Brandl performed the transient spectroscopy experiments and evaluations. Veronica Scheidler assisted with the NMR measurements. Bernhard Dick, Ruth M. Gschwind and Burkhard König supervised the project and the preparation of the manuscript.

Adapted with permission from *Chem. Eur. J.* Source of this chapter: <https://onlinelibrary.wiley.com/doi/full/10.1002/chem.201804603>.

5.1 Abstract

The first example for the photocatalytic generation of a highly electrophilic intermediate that is not based on radical reactivity is reported. The single-electron reduction of bench-stable and commercially available 4-(trifluoromethoxy)benzotrile by an organic photosensitizer leads to its fragmentation into fluorophosgene and benzotrile. The in situ generated fluorophosgene was used for the preparation of carbonates, carbamates, and urea derivatives in moderate to excellent yields via an intramolecular cyclization reaction. Transient spectroscopic investigations suggest the formation of a catalyst charge-transfer complex-dimer as the catalytic active species. Fluorophosgene as a highly reactive intermediate, was indirectly detected via its next downstream carbonyl fluoride intermediate by NMR. Furthermore, detailed NMR analyses provided a comprehensive reaction mechanism including a water dependent off-cycle equilibrium.

5.2 Introduction

Carbonates, carbamates and urea derivatives are privileged structures in organic synthesis and common motifs in pharmaceuticals, pesticides and plastics (Figure 1 A).¹ Many methods for the synthesis of these compounds have been described.² The direct and most hazardous way is the use of gaseous phosgene or its less reactive derivatives diphosgene and triphosgene.³ However, handling of those compounds in the lab or in industry plants requires special safety precautions due to their severe toxicity.⁴ Alternative procedures utilize activated or non-activated carbonates or ureas, which are either prepared by reaction with phosgene or less efficiently from CO₂ (Figure 1 B).^{2a, 5} Some of these procedures require harsh reaction conditions or suffer from low reactivity and poor atom economy.² Therefore, there is still a significant demand for a less hazardous, practical and easily controllable generation of reactive C1 building blocks.

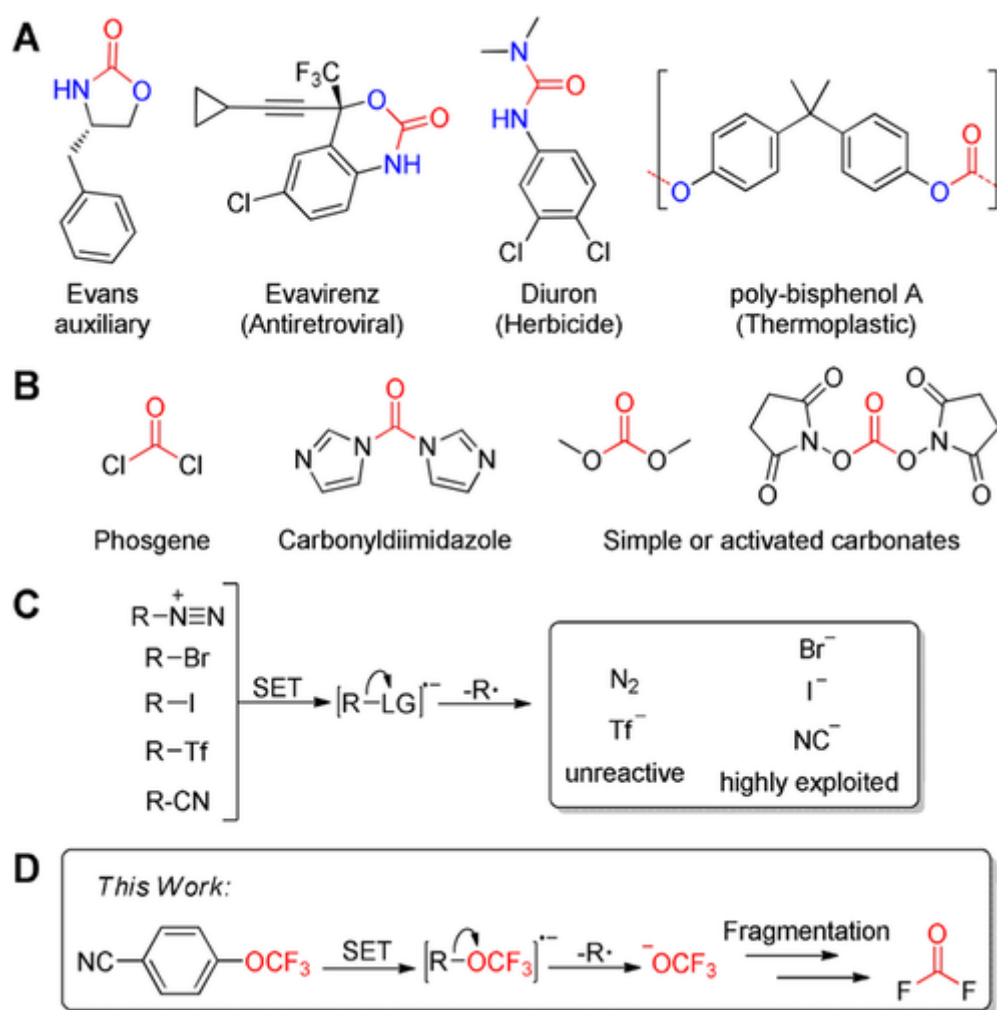


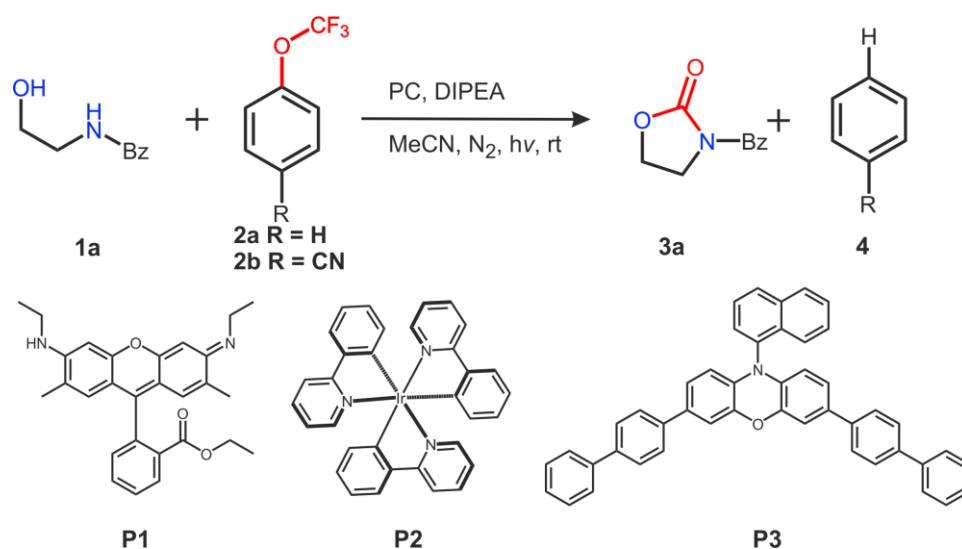
Figure 1. **A)** Structures of prominent carbamate or urea containing molecules used in synthesis, pharmacy, agriculture and daily life. **B)** Structures of phosgene and commonly employed alternatives. **C)** Typical leaving groups and their reactivity profile in photoredox catalysis. **D)** Overview of the photocatalytic fluorophosgene generation; Tf=trifluoromethanesulfonate, R=benzonitrile.

Photoredox catalysis with organic photosensitizers has received tremendous attention in the past years.⁶ Many useful transformations without the need of metal catalysts were discovered, exploiting the versatile reduction and oxidation potentials of organic photocatalysts.⁷ The common requirement for a typical photocatalytic reaction is the generation of a radical species which can either react with another radical, a sp^2/sp center, a nucleophile or a metal complex.⁸ However, the photocatalytic generation of intermediates with pure ionic reactivity remains elusive because energy and single electron transfer are the predominant reaction paths of all common photocatalysts.⁹ But especially under photo-reductive conditions most leaving groups are ionic species, for example, halides, pseudo halides or cyanide, which are neglected in the course of the

reaction because they possess only limited reactivity and/or were already exploited in thermal and photochemical reactions (Figure 1 C).¹⁰ On the other hand, the C–OCF₃ bond could only be activated electrochemically or under harsh reaction conditions so far.¹¹ However, the photocatalytic *N*-OCF₃ cleavage of complex starting materials was reported very recently.¹² To address the need of a hazard- and metal-free access to highly reactive C1 building blocks, we envisioned to cleave the C–OCF₃ bond of a simple, commercially available aryl trifluoromethoxy ether by photoredox catalysis. We identified 4-(trifluoromethoxy)- benzonitrile as a suitable starting material, which can be cleaved quantitatively into benzonitrile and fluorophosgene by an organic photosensitizer (Figure 1 D). Furthermore, we investigated the reaction mechanism by NMR kinetic and structural analyses and propose a photo-reductive mechanism based on the results of radical trapping experiments and excited state quenching experiments monitored by transient spectroscopy.

5.3 Results and Discussion

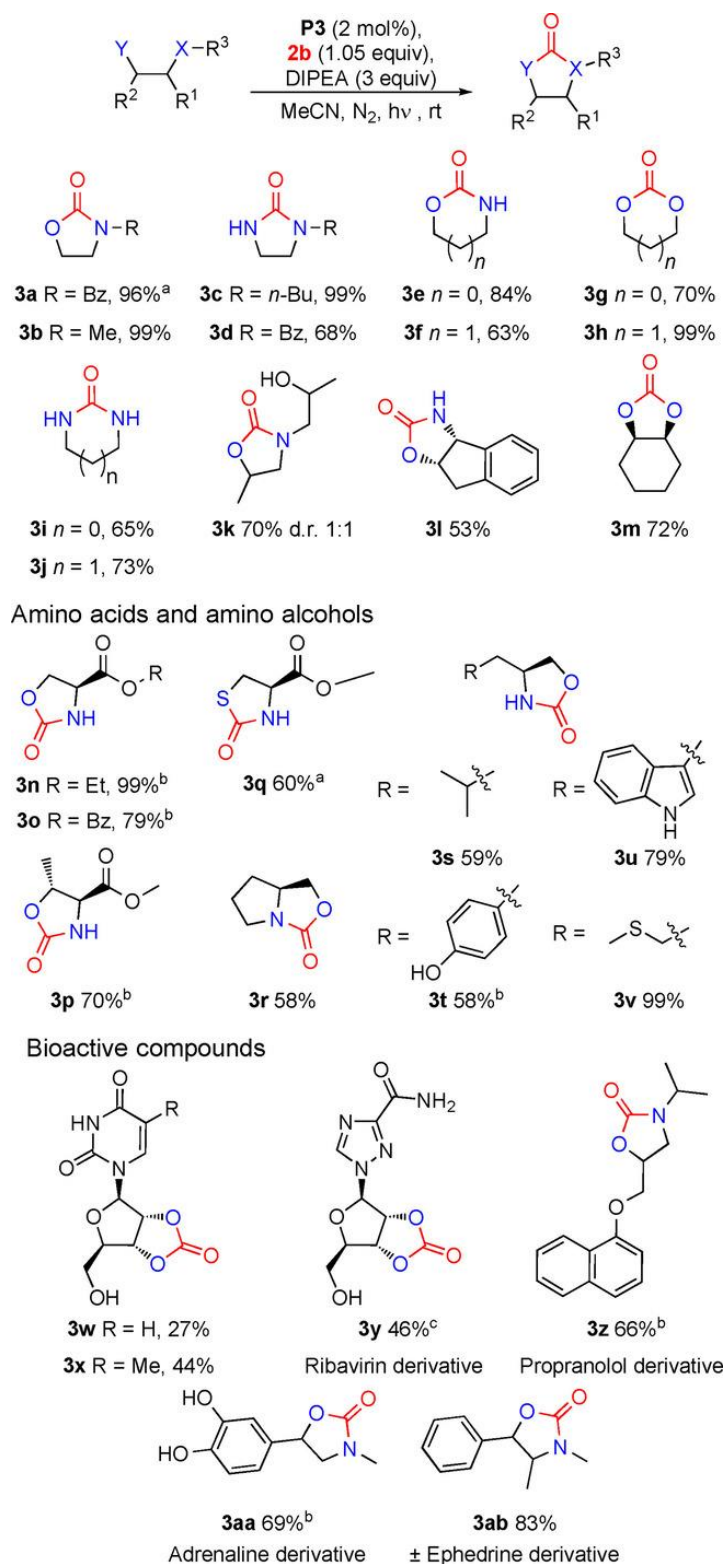
We began our investigation using 2-benzylaminoethanol (**1 a**) as a model substrate, rhodamine 6G (**P1**) as a strongly reducing photosensitizer, diisopropylethylamine (DIPEA) as electron donor and trifluoromethoxybenzene (**2 a**) as fluorophosgene precursor in neat acetonitrile.¹⁴ However, no conversion of **2 a** was observed (Table 1 entry 1). Switching to commonly employed Ir(ppy)₃ (**P2**) or to the recently reported, phenoxazine based photosensitizer **P3** did also not lead to fragmentation of **2 a** (entries 2–3).¹³ Therefore, trifluoromethoxybenzene derivative **2 b** bearing an electron withdrawing nitrile group was employed. Hence, the redox potential of **2 b** was much more accessible ($E_{\text{red}}(\mathbf{2 a})=-3.0$ V vs. SCE compared with $E_{\text{red}}(\mathbf{2 b})=-2.1$ V vs. SCE, see Figure S1) and **2 b** showed slow conversion in the presence of photosensitizer **P2** (entry 4). The reaction was significantly improved by switching to **P3** giving full conversion of **2 b** and **1 a** (entry 5). Further optimization of the reaction lead to conditions giving **3 a** in an excellent isolated yield (entry 6). Control experiments revealed that without catalyst, light or DIPEA no or only trace amounts of product could be obtained (entries 7–9). Finally, we observed that the cleavage of **2 b** was independent of the presence of **1 a** (entry 10).

Table 1. Optimization of the reaction conditions.

Entry	PC (mol%) / λ	Conversion of 2a/2b ^a	Conversion of 1a ^a
1	P1 (10) / 455 nm	2a 0%	0%
2	P2 (2) / 455 nm	2a 0%	0%
3	P3 (5) / 400 nm	2a 0%	0%
4	P2 (2) / 455 nm	2b 51%	40%
5	P3 (5) / 400 nm	2b 100%	100%
6 ^b	P3 (2) / 400 nm	2b 100%	100% [96%]
7 ^b	400 nm	2b 0%	0%
8 ^{b, c}	P3 (2)	2b 0%	0%
9 ^{b, d}	P3 (2) / 400 nm	2b traces	traces
10 ^{b, e}	P3 (2) / 400 nm	2b 100%	0%

General conditions: A mixture of 0.1 mmol of **1a**, 2 equiv of **2b**, the indicated amount of PC, 4 equiv of DIPEA in neat MeCN (0.1 m) under N₂ atmosphere were irradiated for 24 h with 400 nm light (or 455 nm for **P1** and **P2**). [a] Conversion determined by GC-FID, isolated yield of **3a** in brackets. [b] A mixture of 0.1 mmol of **1a**, 1.05 equiv of **2b**, 2 mol % **P3**, 3 equiv of DIPEA in dry MeCN (0.1 m) under N₂ atmosphere were irradiated for 24 h at 400 nm. [c] no light, 48 h. [d] no DIPEA. [e] no **1a**. Bz=benzyl.

In the next step, the synthetic scope of the method was investigated (Scheme 1). *N*-substituted, five membered cyclic carbamates and ureas were prepared in good to excellent yield (Scheme 1, **3 b–3 d**). Unsubstituted, five and six membered cyclic carbamates, carbonates and ureas also showed good to excellent conversion (**3 e–3 j**). More complex carbamate **3 k** was isolated in good yield with a diastereomeric ratio of 1:1. 1,2-*cis*-Configured carbamate **3 l** and carbonate **3 m** were prepared in moderate to good yield without racemization. Subsequently, amino acids and amino alcohols were investigated. The ethyl and benzyl ester of serine (**3 n** and **3 o**), as well as the methyl ester of threonine (**3 p**) gave good to excellent yields. Noteworthy, **3 p** was obtained diastereomerically pure indicating that no racemization of the reactive α -position took place. The methyl ester of cysteine (**3 q**) gave a moderate yield, but demonstrated that also thiocarbamates can be obtained by this method. The corresponding carbamates of the amino alcohols prolinol, valinol and tyrosinol were isolated in moderate yields (**3 r–3 t**), whereas tryptophanol and methioninol showed good to excellent conversion to **3 u** and **3 v**, respectively. Finally, some bioactive compounds were subjected to this method. Uridine and ribothymidine as well as the antiviral drug ribavirin were converted to **3 w**, **3 x** and **3 y** with low to moderate yields. Finally, the beta-blocker propranolol, the neurotransmitter adrenalin and the sympathomimetic ephedrine gave good yields of the cyclized products (**3 z–3 ab**). To demonstrate the synthetic utility of the reaction, a gram scale reaction, using **1 a** as substrate, was performed. The corresponding product **3 a** was isolated with 70 % yield after a prolonged reaction time of 48 h.



Scheme 1. General conditions: A mixture of 0.1 mmol of substrate, 1.05 equiv of **2b**, 2 mol % **P3**, 3 equiv of DIPEA in neat MeCN (0.1 m) under N₂ atmosphere were irradiated for 24 h with 400 nm light. **a**: 70 % isolated yield on 7 mmol (gram)scale. **b**: 4 equiv of DIPEA were used because the starting material was a hydrochloride salt. **c**: DMF (0.1 m) was used as the solvent. Bz=benzyl, Me=methyl, *n*Bu=*n*-butyl, Et=ethyl.

To investigate the mechanism, transient spectroscopy, cyclic voltammetry as well as radical trapping experiments and *in situ* and *ex situ* NMR analyses were performed. To get insight into the photocatalytic mechanism, the quenching of the excited state of **P3** was investigated by transient spectroscopy. The measurements revealed that both, addition of DIPEA ($E_{\text{ox}}=+0.8$ V vs. SCE) and **2 b** ($E_{\text{red}}=-2.1$ V vs. SCE) had no influence on the triplet lifetime of **P3** ($E_{\text{ox}}=+0.4$ V; $E_{\text{red}}=-1.7$ V, see Figure S2).¹⁴ However, during measurements at catalyst concentrations of 30 μM and above (compared to 2 mM under the reaction conditions), we observed a charge-transfer band originating from the radical cation part in the catalyst CT-complex dimer.¹⁵ The lifetime of this band decreases significantly by addition of DIPEA (Figure 2 A). This indicates, that the charge recombination might be slowed down by interaction of the radical cation part of the CT-complex with DIPEA. As a consequence, the radical anion part can reduce **2 b** to restore its uncharged ground state. This assumption is supported by cyclic voltammetry of **P3** revealing a ground state reduction potential of the **P3** radical anion of about -2.5 V vs. SCE in MeCN (see Figure S1 and see the Supporting Information for more data about the mechanistic investigation). Currently, further transient spectroscopic investigations on **P3** and this catalytic transformation are ongoing in our lab.

To find evidence for the presence of a benzonitrile radical originating from a photo-reductive mechanism, we performed radical trapping experiments in presence of **1 a**. We observed 48 % conversion of **2 b** to the corresponding *N*-methylpyrrole adduct **5 a** (Figure 2 B). Moreover, the aryl radical could be trapped with the isolated double bond of allylbenzene giving adduct **5 b** in 45 % yield. The different radical trapping conditions did not influence the conversion of **1 a** significantly, as **3 a** was isolated in high yields. The formation of **5 a** and **5 b** is a good indication for the intermediacy of an aryl radical and the operation of a photo-reductive mechanism.¹⁶ *In situ* ^1H and ^{19}F NMR profiles further corroborate this mechanistic step monitoring a clean transformation of **2 b** into **4** upon illumination of **P3** in the presence of DIPEA (see Figure S4-13 and S4-14). Next, an *ex situ* NMR profile of the whole reaction with substrate **1 a** was recorded (Figure 2 C). Upon illumination, **2 b** (black) and **1 a** (violet) start to decrease, while the two main products **3 a** (green) and **4** (red) can be readily detected. Furthermore, two more reaction intermediates could be identified (**F-I**, magenta and **OC-I**, cyan). Instead of the highly reactive free fluorophosgene itself, the formation of its next downstream more stable reaction intermediate (**F-I**) with **1 a** was observed. Using advanced 1D and 2D NMR techniques for the ^1H , ^{19}F and ^{13}C assignment the intermediate was identified as a carbonyl fluoride adduct (**F-I**) of **1 a**. The immediate formation of **F-I** combined with the lag-phase of **3 a** in the illuminated *in situ* NMR profile (Figure 2 D) suggested **F-I** as direct

precursor of **3 a**. This is further solidified by the fact that once the light is turned off, a distinct conversion of **F-I** into **3 a** can be observed (for spectra see the Supporting Information).

In addition, a second, off-cycle intermediate (**OC-I**, Figure 2 C) could be assigned. The emergence of **OC-I** is the reason for the evidently faster decrease of **1 a** with respect to **2 b** (Figure 2 C), as it stems from a side reaction of **1 a** with acetaldehyde, which in turn is liberated after downstream reactions from DIPEA (see the Supporting Information). From the three-hour mark on in Figure 2 C, it is evident, that **1 a** and **F-I** are already gone, whilst **OC-I** is slowly decreasing and **1 a** is still slowly increasing. This suggests that **OC-I** and **1 a** are in a slow off-cycle equilibrium. It could also be shown that this equilibrium is heavily water dependent (see the Supporting Information). This results in **3 a** still being generated even after **1 a** is fully consumed as long as fluorophosgene is still liberated. Furthermore, addition of water can effectively reduce the formation of **OC-I** and increase the reaction rates significantly (See the Supporting Information for further details on the NMR analyses).

In situ liberation and conversion of fluorophosgene

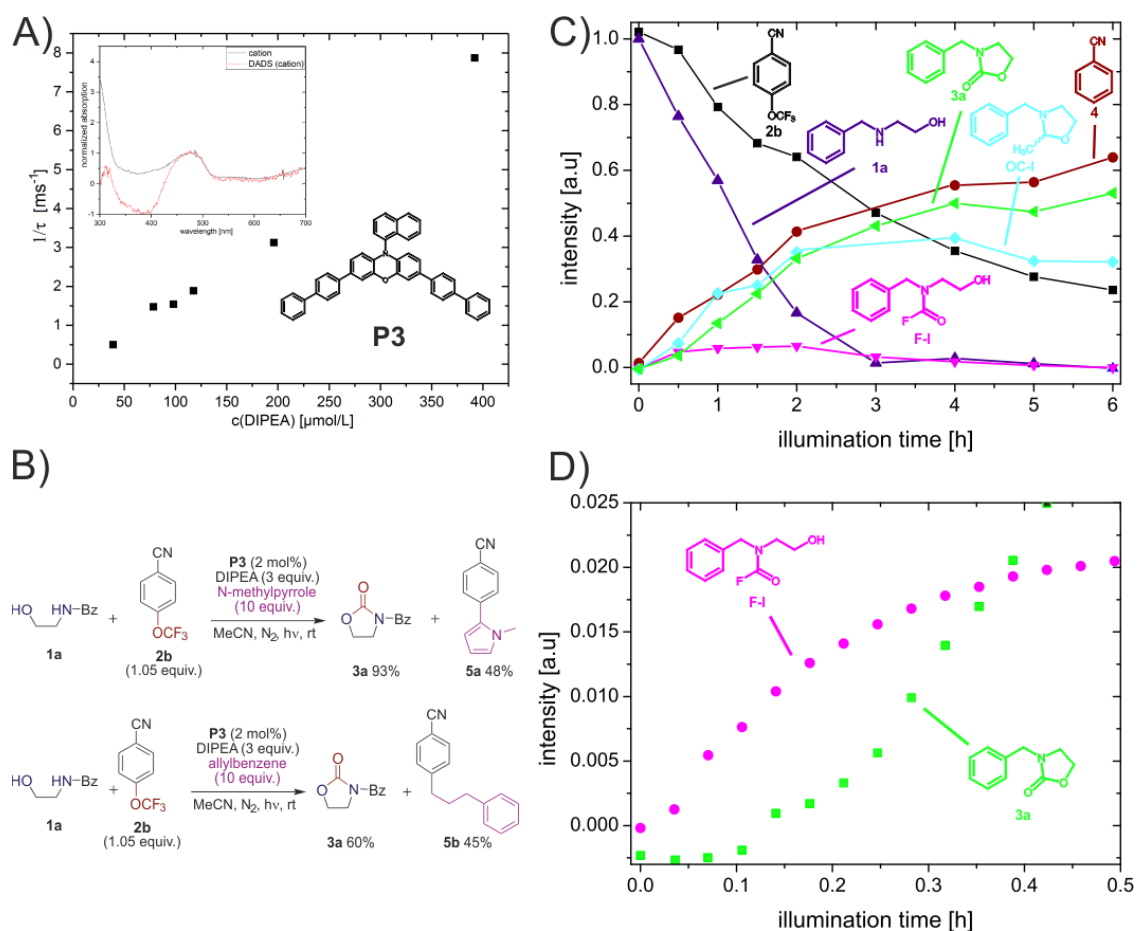


Figure 2. A) Stern–Volmer plot of quenching of the **P3** radical cation with DIPEA; inset: comparison of **P3** radical cation spectrum obtained via transient spectroscopy and spectro-electro chemistry (See the Supporting Information for details). **B)** Radical trapping experiments with *N*-methylpyrrole and allylbenzene. **C)** *Ex situ* reaction profile of **1a** (100 mM), **2b** (105 mM), **P3** (2 mM) and DIPEA (300 mM) in CD₃CN. Next to the major products **3a** (green) and **4** (red), two intermediates can be detected; **F-I** (magenta), which is the next downstream intermediate of fluorophosgene and the direct precursor of **3a** and **OC-I** (cyan). **OC-I** presents an off-cycle intermediate being in an ongoing water dependent equilibrium with **1a**. As long as fluorophosgene is generated, **OC-I** is slowly converted into **3a** through **1a**. **D)** Excerpt of the *in situ* reaction profile of **1a** (100 mM), **2b** (110 mM), **P3** (2 mM) and DIPEA (300 mM) in CD₃CN showing the initial trend of **3a** (green) and **F-I** (magenta). The formation of **3a** is preceded by an initial lag-phase whilst the intermediate **F-I** is generated immediately after the light is turned on as the direct precursor of **3a**.

Therefore, we propose the following mechanism for the liberation of fluorophosgene from **2 b** (Figure 3). **P3** is excited by the light of 400 nm LEDs. One excited photocatalyst molecule (**P3***) and one ground state **P3** molecule form a CT-complex dimer which disproportionates to the corresponding **P3⁺** and **P3⁻**. The **P3⁻** reduces **2 b** leading to its fragmentation into the aryl radical and trifluoromethanolate. Trifluoromethanolate decomposes into F⁻ and fluorophosgene, which readily reacts with amine- or alcohol-based nucleophiles resulting in a carbonyl fluoride intermediate (see **F-I**).¹⁷ Subsequent cyclization leads to the desired product. To regenerate **P3**, the **P3⁺** oxidizes DIPEA and the aryl radical abstracts a hydrogen atom from DIPEA^{•+} or the solvent to give benzonitrile. Next to the main pathway, a second off-cycle pathway is in progress. Downstream reactions of DIPEA lead to the liberation of acetaldehyde, which can readily react with **1 a** to yield the off-cycle intermediate **OC-I**. The resulting equilibrium of **OC-I** and **1** is heavily dependent on the water concentration. As long as fluorophosgene is provided, **OC-I** is slowly converted into **3 a** through **1 a**. Addition of extra water can virtually suppress the off-cycle equilibrium, which in turn accelerates the reaction.

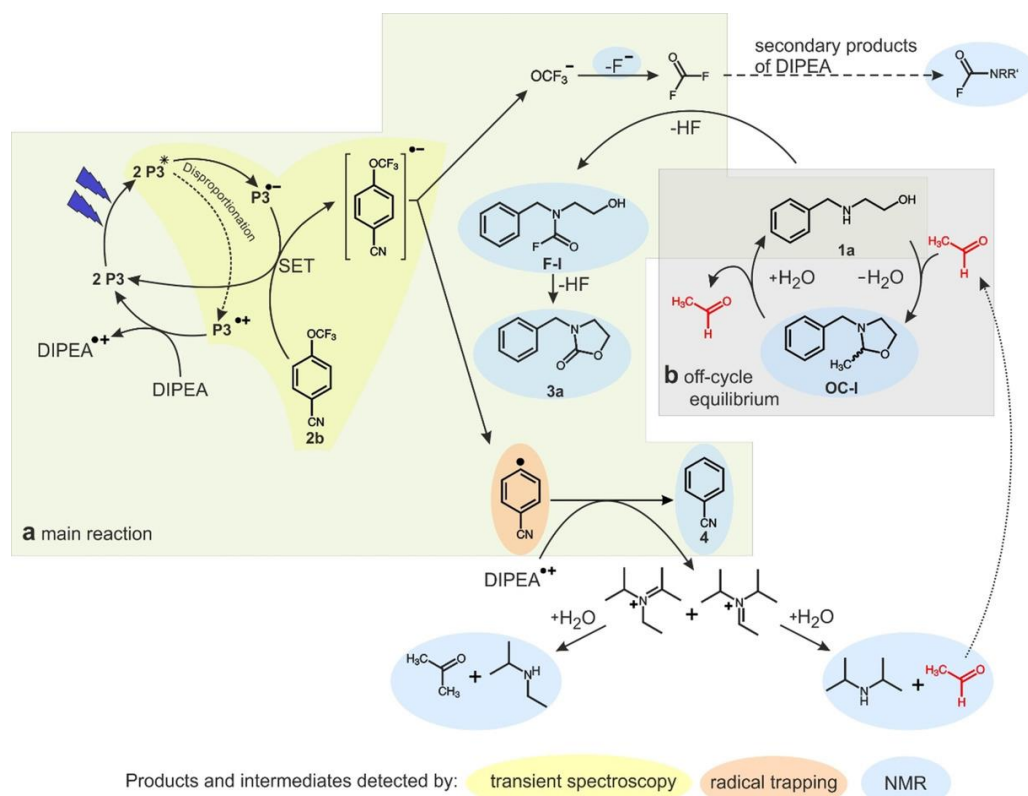


Figure 3. Proposed catalytic cycle for the photocatalytic liberation of fluorophosgene for substrate **1 a**, based on the conducted mechanistic studies. The mechanism can be differentiated into two segments: **a**: The main reaction, which comprises the photocatalytic liberation of fluorophosgene by reducing **2 b** and the subsequent reaction of fluorophosgene with **1 a** over **F-I** to yield **3 a**. **b**: The off-cycle equilibrium (gray background), which describes the water dependent equilibrium between **1 a** and **OC-I** through addition and cleavage of acetaldehyde (secondary product of DIPEA). Detected products and intermediates are highlighted.

5.4 Conclusion

In summary, we have developed the first, visible light mediated procedure for the cleavage of an aryl trifluoromethoxy ether and the controlled liberation and *in situ* conversion of fluorophosgene for the synthesis of carbamates, carbonates and urea derivatives. The method shows regioselectivity for aliphatic amines and/or alcohols in presence of aromatic ones. No racemization of amino acid stereocenters was observed. Transient spectroscopy suggests the formation of a catalyst CT-complex dimer as the catalytic active species. NMR measurements identified key intermediates consolidating a stepwise fragmentation into fluorophosgene as the most likely mechanistic pathway; while also uncovering a water dependent off-cycle equilibrium, which can be effectively modulated to accelerate the reaction. Notably, this method expands the toolbox of photoredox catalysis by the generation of an extremely reactive species which is not based on radical reactivity under mild reaction conditions.

5.5 References

- (1) a) M. M. Heravi, V. Zadsirjan, B. Farajpour, *RSC Adv.* **2016**, *6*, 30498–30551; b) M. A. Rodrigo, N. Oturan, M. A. Oturan, *Chem. Rev.* **2014**, *114*, 8720–8745; c) J. Magano, J. R. Dunetz, *Chem. Rev.* **2011**, *111*, 2177–2250; d) Y. Zhou, J. Wang, Z. Gu, S. Wang, W. Zhu, J. L. Aceña, V. A. Soloshonok, K. Izawa, H. Liu, *Chem. Rev.* **2016**, *116*, 422–518.
- (2) a) A. K. Ghosh, M. Brindisi, *J. Med. Chem.* **2015**, *58*, 2895–2940; b) J. P. Parrish, R. N. Salvatore, K. W. Jung, *Tetrahedron* **2000**, *56*, 8207–8237; c) D. J. Díaz, A. K. Darko, L. McElwee-White, *Eur. J. Org. Chem.* **2007**, 4453–4465.
- (3) L. Pasquato, G. Modena, L. Cotarca, P. Delogu, S. Mantovani, *J. Org. Chem.* **2000**, *65*, 8224–8228.
- (4) a) W. Schneider, W. Diller in *Ullmann's Encyclopedia of Industrial Chemistry*, Vol. 26, Wiley-VCH: Weinheim, **2000**, pp. 623–632; b) L. Cotarca, T. Geller, J. Répási, *Org. Process Res. Dev.* **2017**, *21*, 1439–1446.
- (5) T. Sakakura, K. Kohnoa, *Chem. Commun.* **2009**, 1312–1330.
- (6) N. A. Romero, D. A. Nicewicz, *Chem. Rev.* **2016**, *116*, 10075–10166.
- (7) a) D. Petzold, B. König, *Adv. Synth. Catal.* **2018**, *360*, 626–630; b) I. Ghosh, T. Ghosh, J. I. Bardagi, B. König, *Science* **2014**, *346*, 725–728; c) I. Ghosh, B. König, *Angew. Chem. Int. Ed.* **2016**, *55*, 7676–7679; d) S. J. S. Düsel, B. König, *J. Org. Chem.* **2018**, *83*, 2802–2807; e) N. A. Romero, K. A. Margrey, N. E. Tay, D. A. Nicewicz, *Science* **2015**, *349*, 1326–1330.
- (8) a) J. Twilton, C. Le, P. Zhang, M. H. Shaw, R. W. Evans, D. W. C. MacMillan, *Nat. Rev. Chem.* **2017**, *1*, 0052; b) H. Seo, M. H. Katcher, T. F. Jamison, *Nat. Chem.* **2016**, *9*, 453–456; c) A. Studer, D. P. Curran, *Nat. Chem.* **2014**, *6*, 765–773; d) M. N. Hopkinson, A. Tlahuext-Aca, F. Glorius, *Acc. Chem. Res.* **2016**, *49*, 2261–2272.
- (9) a) A. Neubauer, G. Grell, A. Friedrich, S. I. Bokarev, P. Schwarzbach, F. Gärtner, A.-E. Surkus, H. Junge, M. Beller, O. Kühn, S. Lochbrunner, *J. Phys. Chem. Lett.* **2014**, *5*, 1355–1360; b) A. Singh, C. J. Fennell, J. D. Weaver, *Chem. Sci.* **2016**, *7*, 6796–6802; c) Z. Lu, T. P. Yoon, *Angew. Chem. Int. Ed.* **2012**, *51*, 10329–10332.

- (10) a) M. H. Shaw, J. Twilton, D. W. C. MacMillan, *J. Org. Chem.* **2016**, *81*, 6898–6926; b) M. Majek, A. Jacobi von Wangelin, *Acc. Chem. Res.* **2016**, *49*, 2316–2327; c) D. A. Petrone, J. Ye, M. Lautens, *Chem. Rev.* **2016**, *116*, 8003–8104.
- (11) a) A. Iijima, H. Amii, *Tetrahedron Lett.* **2008**, *49*, 6013–6015; b) K. K. K. Goh, A. Sinha, C. Fraser, R. D. Young, *RSC Adv.* **2016**, *6*, 42708–42712; c) C. Combellas, F. Kanoufi, A. Thiébault, *J. Electroanal. Chem.* **1997**, *432*, 181–192.
- (12) a) B. Sahoo, M. N. Hopkinson, *Angew. Chem. Int. Ed.* **2018**, *57*, 7942–7944; b) A. Togni, B. J. Jelier, P. F. Tripet, E. Pietrasiak, I. Franzoni, G. Jeschke, *Angew. Chem. Int. Ed.* **2018**, *57*, 13784.
- (13) a) R. M. Pearson, C. Hooi-Lim, B. G. McCarthy, C. B. Musgrave, *J. Am. Chem. Soc.* **2016**, *138*, 11399–11407; b) Y. Du, R. Pearson, C. Hooi-Lim, S. Sartor, M. Ryan, H. Yang, N. Damrauer, G. Miyake, *Chem. Eur. J.* **2017**, *23*, 10962–10968.
- (14) B. G. McCarthy, R. M. Pearson, C.-H. Lim, S. Sartor, N. H. Damrauer, G. M. Miyake, *J. Am. Chem. Soc.* **2018**, *140*, 5088–5101.
- (15) S. M. Sartor, B. G. McCarthy, R. M. Pearson, G. M. Miyake, N. H. Damrauer, *J. Am. Chem. Soc.* **2018**, *140*, 4778–4781.
- (16) D. P. Hari, P. Schroll, B. König, *J. Am. Chem. Soc.* **2012**, *134*, 2958–2961.
- (17) M. Nguyen, M. H. Matus, V. Ngan, R. Haiges, K. O. Christe, D. A. Dixon, *J. Phys. Chem. A* **2008**, *112*, 1298–1312.

5.6 Supporting Information

5.6.1 Materials and methods

Starting materials and reagents were purchased from commercial suppliers (Sigma Aldrich, Alfa Aesar, Acros, TCI) and were used without further purification. 4-(trifluoromethoxy)benzotrile was purchased from abcr GmbH. Solvents were used as *p.a.* grade. Industrial grade of solvents was used for automated flash column chromatography. Dry nitrogen was used as inert gas atmosphere. Liquids were added *via* syringe, needle and septum technique unless stated differently.

5.6.2 Nuclear magnetic resonance spectroscopy

All NMR spectra were measured at room temperature using a Bruker Avance 300 (300 MHz for ^1H , 75 MHz for ^{13}C) or a Bruker Avance 400 (400 MHz for ^1H , 101 MHz for ^{13}C) NMR spectrometer. All chemical shifts are reported in δ -scale as parts per million [ppm] (multiplicity, coupling constant J , number of protons) relative to the solvent residual peaks as the internal standard.¹ The spectra were analyzed by first order and coupling constants J are given in Hertz [Hz]. Abbreviations used for signal multiplicity: ^1H -NMR: br = broad, s = singlet, d = doublet, t = triplet, q = quartet, quint = quintet, dd = doublet of doublets and m = multiplet.

5.6.3 Gas chromatography and gas chromatography coupled with mass spectrometry

GC measurements were performed on a GC 7890 from Agilent Technologies. Data acquisition and evaluation was done with Agilent ChemStation Rev.C.01.04.

GC-MS measurements were performed on a 7890A GC system from Agilent Technologies with an Agilent 5975 MSD Detector. Data acquisition and evaluation was done with MSD ChemStation E.02.02.1431.

A capillary column HP-5MS/30 m x 0.25 mm/0.25 μm film and helium as carrier gas (flow rate of 1 mL/min) were used. The injector temperature (split injection: 40:1 split) was 300 °C and the detection temperature was 300 °C for the flame ionization detector (FID). GC measurements were performed and investigated via integration of the signals obtained. The GC oven temperature program was adjusted as follows: initial temperature 40 °C

was kept for 3 min, the temperature was increased at a rate of 25 °C/min over a period of 10.4 min until 300 °C was reached and kept for 5 min.

5.6.4 Mass spectrometry

The mass spectrometric measurements were performed at the Central Analytical Laboratory of the University of Regensburg. All mass spectra were recorded on a Finnigan MAT SSQ 710 A, ThermoQuest Finnigan TSQ 7000, Jeol AccuTOF GCX or an Agilent Q-TOF 6540 UHD instrument.

5.6.5 Preparation of the photocatalyst P3

P3 was prepared according to a reported literature procedure.^[19] All photoreactions and NMR investigations were performed with self-made catalyst. CV, online UV-VIS, spectro-electro chemistry and transient spectroscopic measurements were performed with a commercial catalyst (Sigma-Aldrich).

5.6.6 General procedure of the preparation of carbonates and urea derivatives

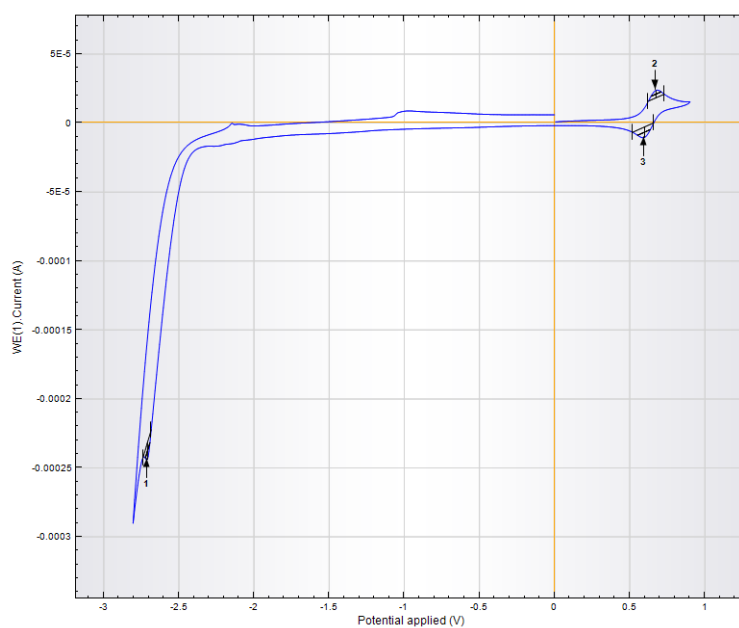
The photocatalyst (1.2 mg, 0.002 mmol, 0.02 equiv.) and the substrate (0.1 mmol) were weight into a 5 mL crimp cap vial. A stirring bar, 1 mL of dry MeCN, 15.6 μ L (0.105 mmol, 1.05 equiv.) 4-(trifluoromethoxy)benzotrile and 51.0 μ L (0.3 mmol, 3 equiv.) DIPEA were added into the vial *via* syringe. The vial was sealed with a crimp cap with septum and set under nitrogen atmosphere by three consecutive freeze-pump-thaw cycles. The vial was placed approximately 1 cm above a 400 nm LED and stirred under continuous irradiation for 24 h. After completion, two equal reaction mixtures were combined and quenched by addition of 0.5 mL of H₂O. Silica was added, the solvent was evaporated from the suspension and the residue was used as dry load for column chromatography on a Biotage[®] Isolera[™] Spektra One using a petrol ether and ethyl acetate or a dichloromethane/methanol mixture as the mobile phase. A 10 g column was employed with silica gel of type 60 M (40-63 μ m, 230-440 mesh) by Merck as stationary phase.

For the gram scale reaction, the photocatalyst (86 mg, 0.14 mmol, 0.02 equiv.) and **1a** (1.1 g, 7.0 mmol, 1.0 mL) were weight into a 250 mL Schlenk flask. A stirring bar, 70 mL of dry MeCN, 1.1 mL (7.4 mmol, 1.05 equiv.) 4-(trifluoromethoxy)benzotrile and 3.6 mL (21 mmol, 3 equiv.) DIPEA were added into the flask *via* syringe. The flask was set under nitrogen atmosphere by three consecutive freeze-pump-thaw cycles. The vial was

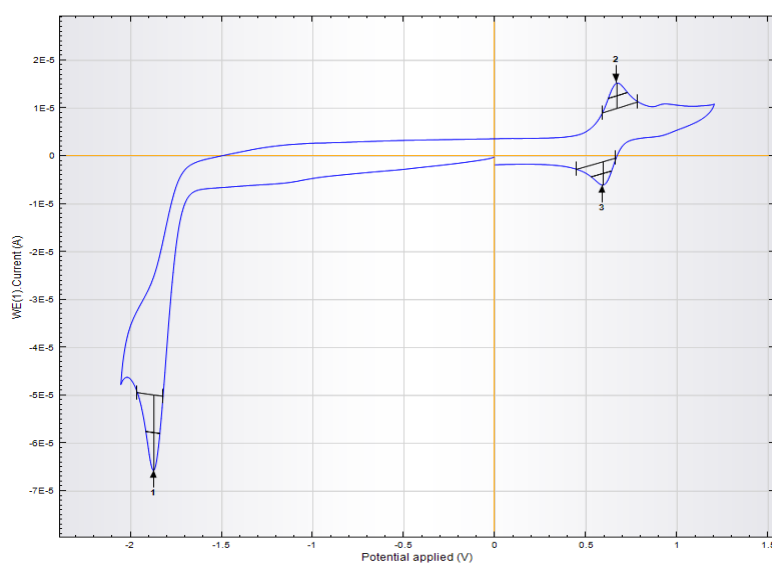
In situ liberation and conversion of fluorophosgene

placed approximately 1 cm above two 400 nm LEDs and stirred under continuous irradiation for 48 h. The reaction was quenched by addition of 5 mL water and concentrated *in vacuo*. Purification was done as described above but a 25 g column was used instead of a 10 g column.

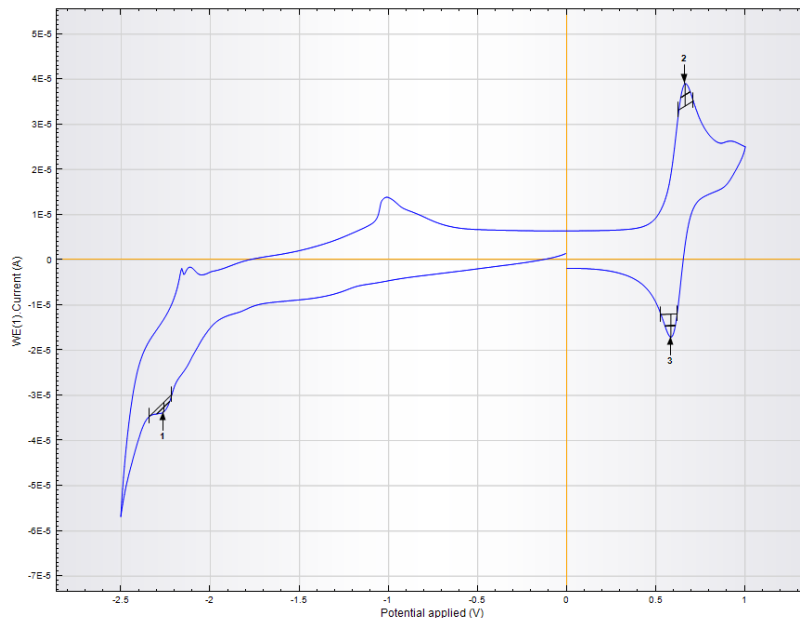
5.6.7 Cyclovoltammetric data of P3, 2a and 2b (in MeCN) – Figure S1-3



Index	Peak position	
1	-2.709 V	2a
2	0.675 V	Ferrocene
3	0.599 V	Ferrocene



Index	Peak position
1	-1.873 V 2b
2	0.670 V Ferrocene
3	0.594 V Ferrocene



Index	Peak position
1	-2.261 V P3
2	0.665 V Ferrocene
3	0.584 V Ferrocene

5.6.8 Transient spectroscopy and further mechanistic discussion

5.6.8.1 2D transient absorption spectrum

The measurements were performed with a Pump-Probe Setup. The Pump source is the third Harmonic of a Nd:YAG laser (Surelite II, Continuum). The wavelength of 355 nm, with a pulse width of about 5 nm. The typical pulse duration is 8 ns. The repetition rate is 10 Hz and pulses are selected by a shutter (LS055, nmLaser). The white probe light is generated by a pulsed xenon flash lamp (MSP-05, Müller Elektronik-Optik) and passes the sample orthogonal to the Pump beam. Toroidal mirrors (aluminum-coated blanks of eyeglass lenses, Rodenstock) are used to focus and guide the probe light without chromatic aberrations. A shutter (LS6ZM, Uniblitz) is used to block the continuous light of the xenon lamp. A spectrograph (Bruker 200is) disperses the probe light after it passed the sample. The probe light is then passed on to a streak camera (C7799, Hamamatsu

Photonics), a spectral and temporal resolved picture is projected on a phosphor screen and recorded by a CCD camera (ORCA-CR, Hamamatsu Photonics). The temporal window of the streak camera can be set between 0.5 ns and 10 ms. The time resolution in each window is about 0.5% of the temporal window width. All components are controlled by a home-built delay controller (DC).

A 2D transient absorption data matrix ($\Delta\mathbf{A}$) is generated from 4 separate images (I) recorded by the CCD camera.

$$\Delta\mathbf{A} = -\frac{(I_{LP} - I_L)}{(I_P - I_D)}$$

I_{LP} is an image where both the pump (**L**) and probe (**P**) light is used

I_L records only the emission and scattered light caused by a laser pulse

I_P records the probe light passing through the sample without a pump pulse.

I_D is a dark picture and records only the sensor noise without any pump or probe light.

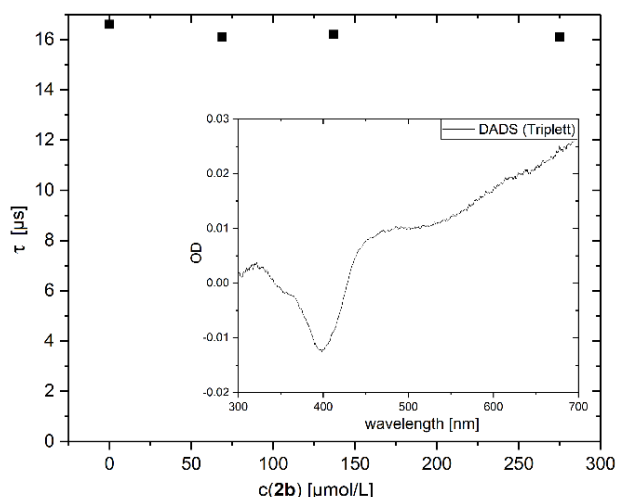
5.6.8.2 Data analysis

Data were analyzed with homemade software to obtain decay associated difference spectra (DADS). This analysis corresponds to the least-squares fit:

$$\left| \Delta OD(t, \lambda) - \sum_k^N f_k(t) DAD S_k(\lambda) \right|^2 = \min,$$

where $\Delta OD(t, \lambda)$ is the measured data matrix and the $f_k(t)$ are exponential (or more complex) decay functions convoluted with a Gaussian function as the apparatus response function.

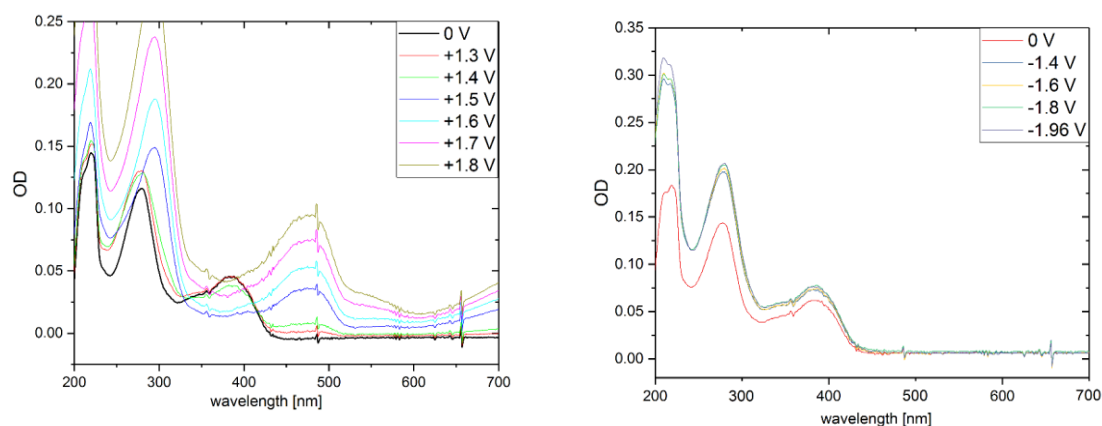
For each manifold $\{f_k$ the DADS display the spectral changes associated with particular decay times. The DADS are in turn linear combinations of the species spectra where increasing species have negative coefficients and decreasing species have positive coefficients.



Quenching of the **P3** triplet state with **2b** in a 30 μM solution of **P3** in MeCN. Inset: Transient spectrum of the triplet state of a 30 μM solution of **P3** in MeCN.

The lifetime of the triplet state remains unchanged upon addition of **2b** indicating that the reduction of **2b** does not proceed *via* direct SET the triplet state.

5.6.9 Verification of the radical cation and radical anion spectra of **P3** via spectro-electro chemistry

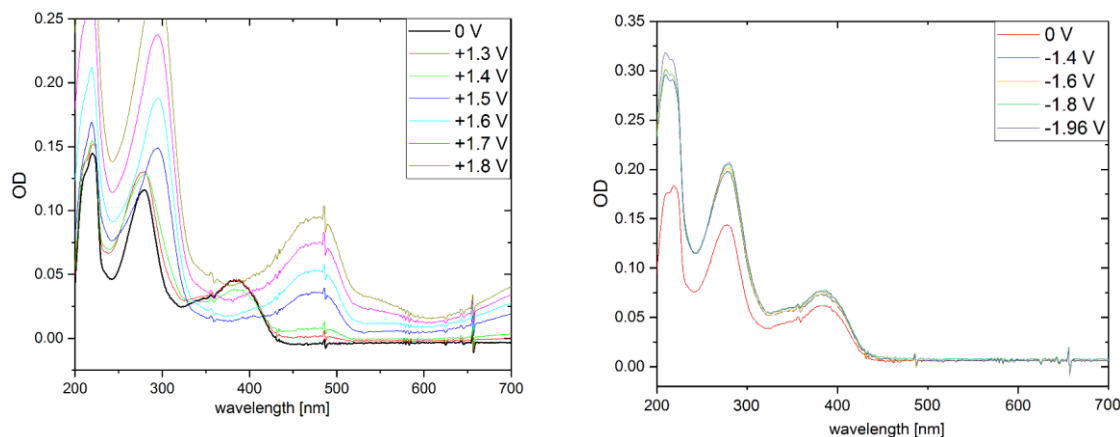


Left: Absorption spectra of **P3** at various positive potentials in MeCN. **Right:** Absorption spectra of **P3** at various negative potentials in MeCN.

At positive potentials a strong absorption at 475 nm occurs, while the absorption peak at 380 nm fades, indicating the formation of the **P3** radical cation. The same band was observed during the transient spectroscopic measurements of **P3** at concentrations around 30 μM (compared to 2 mM in the reaction mixture) which lead to the assumption of the formation of a charge-transfer complex dimer as catalytic active species. However, the direct observation and/or quenching of the **P3** radical anion could not be observed

due to the very minuscule shift of the absorption peak at 280 nm compared to the ground state absorption spectrum.

5.6.10 Investigation of the catalytic active species via online irradiation



Left: Absorption spectra of **P3** at various positive potentials in MeCN. **Right:** Absorption spectra of **P3** at various negative potentials in MeCN.

At positive potentials a strong absorption at 475 nm occurs, while the absorption peak at 380 nm fades, indicating the formation of the **P3** radical cation. The same band was observed during the transient spectroscopic measurements of **P3** at concentrations around 30 μM (compared to 2 mM in the reaction mixture) which lead to the assumption of the formation of a charge-transfer complex dimer as catalytic active species. However, the direct observation and/or quenching of the **P3** radical anion could not be observed due to the very minuscule shift of the absorption peak at 280 nm compared to the ground state absorption spectrum.

5.6.11 NMR spectroscopic investigations

5.6.11.1 Materials

The solvent CD_3CN was purchased from Deutero GmbH. The solvent was dried over 4 Å molecular sieves and deoxygenated by Freeze-Pump-Thaw cycling prior to use. Starting materials (2-benzylaminoethanol (**1a**) and 4-(trifluoromethyl)benzotrinitril (**2b**)) and reagents (DIPEA) were purchased from commercial suppliers (Sigma Aldrich, Alfa Aesar, Acros or Fluka) and were used without further purification.

5.6.11.2 Sample preparation for *in situ* NMR illumination measurements

For the measurements in CD₃CN 450 μ L solutions of 100 mM starting material **1a**, 110 mM **2b**, 2 mM photocatalyst **P3** and 300 mM DIPEA were directly prepared in amberized NMR tubes to minimize the influence of ambient light in the reaction solution. The solvent was deoxygenated either by Freeze-Pump-Thaw cycling and then transferred to the NMR tube under argon atmosphere or purged with argon (10 min) directly inside the NMR tube. Then a transparent glass insert containing the glass fiber, was inserted and everything was sealed airtight.

5.6.11.3 Sample preparation for *ex situ* NMR illumination measurements

1 mL or 2 mL reaction solutions in CD₃CN were prepared in a 5 mL crimp cap vial with a stirring bar. Under standard conditions these solutions contained 2 mM of the photocatalyst **P3**, 100 mM of substrate **1a**, 105 mM of **2b** and 300 mM DIPEA. Deviating conditions are directly mentioned in the text. The vial was sealed with a crimp cap with septum and deoxygenated by three consecutive Freeze-Pump-Thaw cycles or bubbled with argon for 10 minutes. The vial was placed approximately 1 cm above a 400 nm LED inside a cooling block and stirred under irradiation. An aliquot (50 μ L or 100 μ L) was taken from the solution and diluted with 350 μ L DMSO-d₆ or 300 μ L CD₃CN to give a total volume of 400 μ L for the NMR measurements.

5.6.11.4 NMR measurements

All measurements were conducted on a Bruker Avance III HD 600 (600.13 MHz for ¹H; 564.59 MHz for ¹⁹F) spectrometer with a fluorine selective TBIF probe or on a Bruker Avance 500 (500.13 MHz) spectrometer with a 5 mm QXI probe. Temperature control was ensured by a Bruker BVTE 3000 unit (298 K). The spectra were processed, evaluated and plotted with Bruker TopSpin 3.2. The *in situ* samples were illuminated by a NCSU279AT high power LED (Nichia, 405 nm; 950 mW).

5.6.11.5 *In situ* NMR illumination measurements

For the *in situ* reaction profiles an *in situ* illumination device previously reported by our working group was employed.^[20] The reaction profiles were generated by either alternately recording non-illuminated and illuminated ¹H NMR spectra (and/or ¹⁹F NMR spectra) or continuous illumination throughout the measurement. In some cases, the ¹H NMR spectra were recorded with a T2 spin echo filter (300 μ s echo time, looped 128

times) to suppress broad, shifting signals like the water signal, which can significantly distort the integrals of other signals. After the first spectra without illumination a row of ^1H and/or ^1H and ^{19}F spectra were collected either illuminating continuously or alternating between illuminated and non-illuminated spectra.

5.6.11.6 *Ex situ* NMR illumination measurements

The *ex situ* reaction profiles were recorded in a straightforward manner by putting the sample into the NMR spectrometer. The down time from taking an aliquot from the batch reaction to the NMR measurement was approximately 5 minutes. In some cases, the ^1H NMR spectra were recorded with a T2 spin echo (300 μs echo time, looped 64-128 times) filter to suppress broad, shifting signals like the water signal, which can significantly distort the integrals of other signals

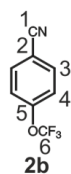
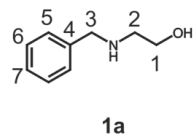
5.6.11.7 Processing and evaluation

The NMR kinetics are derived from signal C3-H for **2b** and **4**, C3-H for **1a**, **3a** and the two conformations of the fluorointermediate (**F-I1** and **F-I2**) and C2-H for **OC-I** in the ^1H proton spectra and C6-F₃ for **2b** in the ^{19}F spectra and referenced to the respective signal in the first spectrum without illumination (Fig. S-4-1). Inversion recovery experiments (for ^1H and ^{19}F) were performed prior to illumination to ensure full relaxation of the reaction components of interest for correct quantification. Assignments were made by evaluation of full sets of 1D and 2D NMR spectra (Fig. S-4-2). For ^1H NMR spectra chemical shifts were referenced to the solvent signals of CD_3CN . For ^{19}F NMR spectra trifluoro acetic acid (-76.55 δ (ppm) vs $\text{CFCl}_3 = 0.00$ ppm) was added after the reaction was finished/ illumination was stopped.

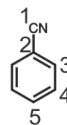
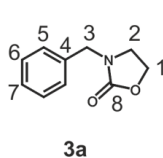
Pulse sequences and important parameters (O, transmitter frequency offset [ppm]; TD, size of FID; SW, spectral width [ppm]; D1, recycling delay [s]; NS, number of scans; DS; number of dummy scans) for the $^1\text{H}^{19}\text{F}$ -HMBCs and the $^{19}\text{F}^{13}\text{C}$ -edHSQC are listed below the corresponding spectrum.

Numeration for integration and further assignments

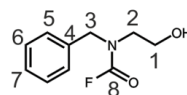
starting materials:



products:



off-cycle intermediate (OC-I)



fluorointermediate (F-I)

detectable as two conformations (F-I1 and F-I2)

Figure S-4-1. Numeration of starting materials and relevant reaction products as used for the assignments and further characterization.

5.6.11.8 NMR assignments

Assignments were made by sets of 1D NMR spectra consisting of ^1H , ^{13}C , ^{19}F , and 2D NMR spectra consisting of $^1\text{H}^1\text{H}$ -COSY, $^1\text{H}^1\text{H}$ -TOCSY, $^1\text{H}^1\text{H}$ -NOESY, $^1\text{H}^{13}\text{C}$ -HSQC, $^1\text{H}^{13}\text{C}$ -HMBC, and in specific cases selective 1D $^1\text{H}^1\text{H}$ -TOCSY, selective 1D $^1\text{H},^1\text{H}$ -NOESY, $^1\text{H}^{19}\text{F}$ -HMBC and $^{19}\text{F}^{13}\text{C}$ -HSQC spectra were recorded.

The ^{13}C chemical shifts of **1a** weren't assigned because all 1D ^{13}C and 2D spectra were usually recorded after illumination when 2-benzylaminoethanol (**1a**) was already fully consumed. It was forgone to assign the ^{13}C chemical shifts in an additional measurement, as **1a** is commercially available and literature known. The chemical shift of the hydroxyl functionality of **1a** is heavily dependent on the water content of the reaction and is in some instances not detectable at all due to exchange. If detectable, it can be witnessed as either a triplet or broad singlet, again dependent on the water content. After illumination starts, it rapidly broadens and usually vanishes after a couple of minutes due to further interactions/exchange. Hence, its chemical shift was put in parentheses in Figure S-4-2.

The ^1H and ^{13}C chemical shifts of position 6 and 7 for the off-cycle intermediate (**OC-I**) and the two conformations of the fluorointermediate (**F-I1** and **F-I2**) couldn't be assigned unambiguously, owing to heavy overlap with other signals from the starting material **1a** and the main product **3a**. Hence, only a chemical shift region is given for **OC-I**, **F-I1** and **F-I2** for signals 6 and 7 in Figure S-4-2.

Fluoride can be detected as a broad singlet at \sim 125 ppm as the reaction progresses. Its chemical shift is heavily dependent on the initial water content and progress of the

reaction and shifts from high to low field during the reaction. Only small amounts of fluoride are detectable since most of the fluoride precipitates as insoluble salts.

The off-cycle intermediate OC-I is cyclized for substrate **1a**, but for other substrates it can also appear in its open form, which can also have at least two conformations probably similar the fluorointermediate conformations (**F-I1** and **F-I2**) detected for **1a** (data not shown).

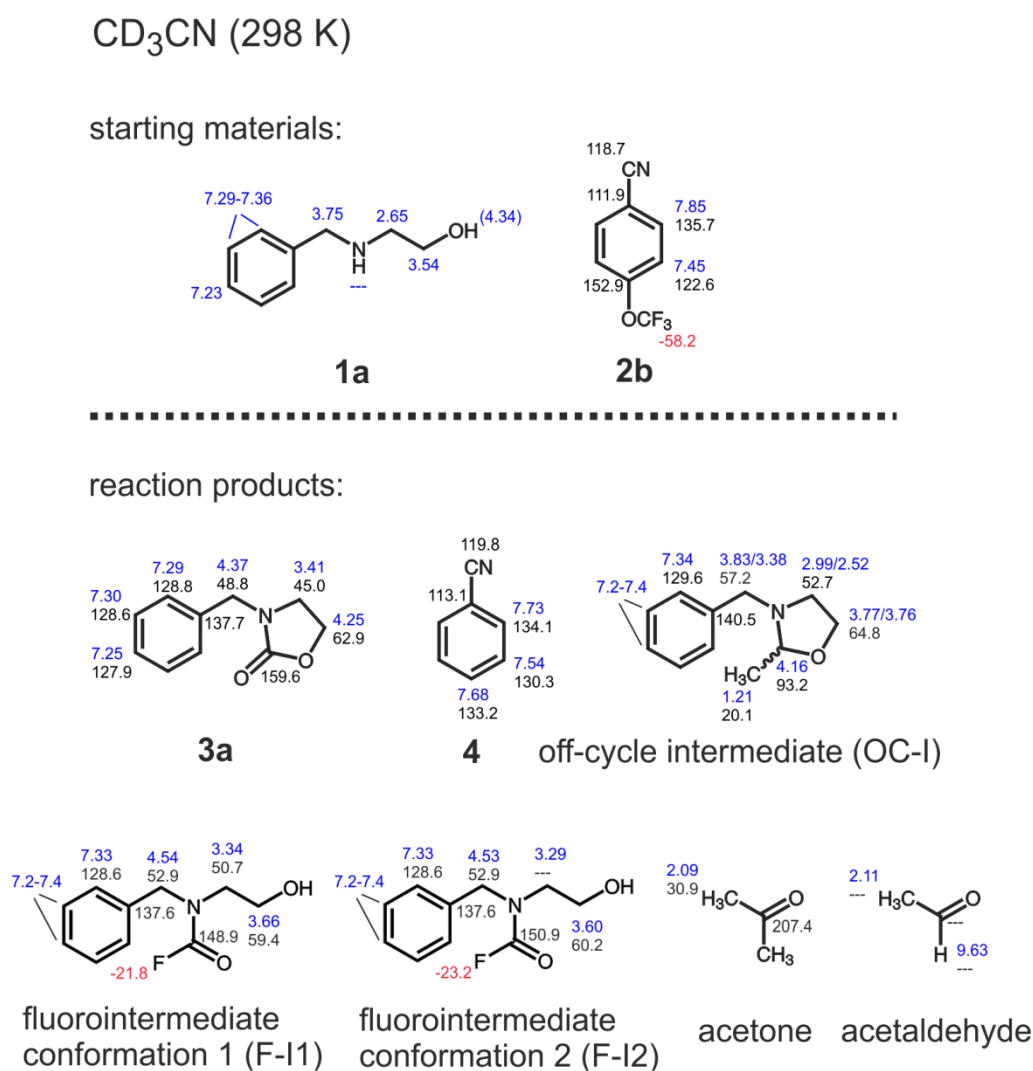


Figure S-4-2. Assignment of starting materials and relevant reaction products in CD₃CN at 298 K. ¹H chemical shifts are highlighted blue and ¹³C chemical shifts are highlighted black and referenced to CD₃CN (1.94 ppm ¹H; 1.32 ppm ¹³C). ¹⁹F chemical shifts are highlighted red and are referenced to trifluoro acetic acid (-76.55 ppm).

5.6.11.9 Relevant spectra for the assignments of the two conformations of the key fluorointermediate (F-I1 and F-I2)

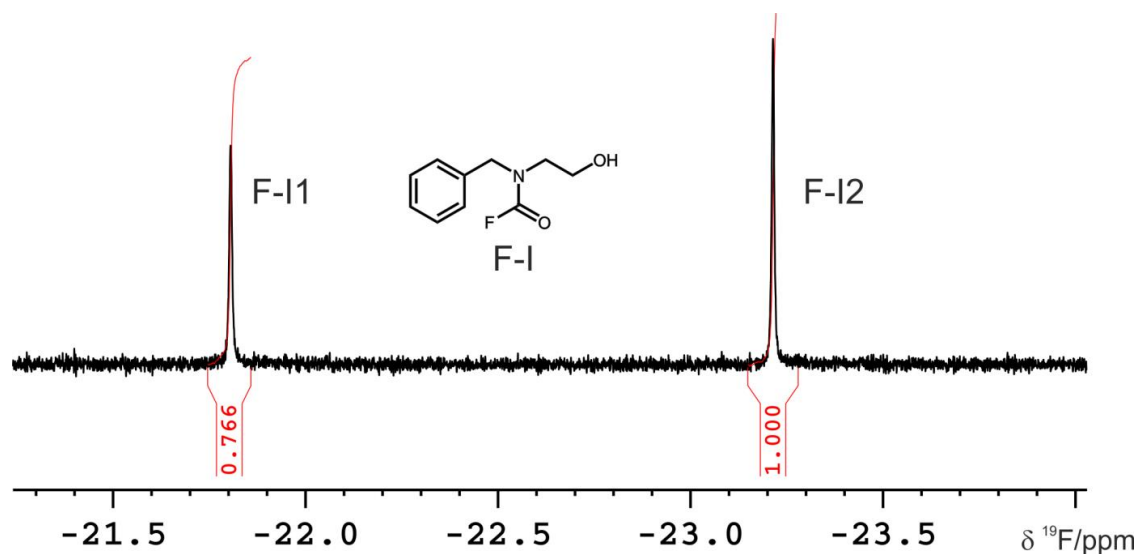


Figure S-4-3. Excerpt of the ^{19}F proton spectrum after 50 minutes of continuous illumination. The two conformations of the fluorointermediate **F-I** (**F-I1** and **F-I2**) both yield one singlet in the ^{19}F spectrum.

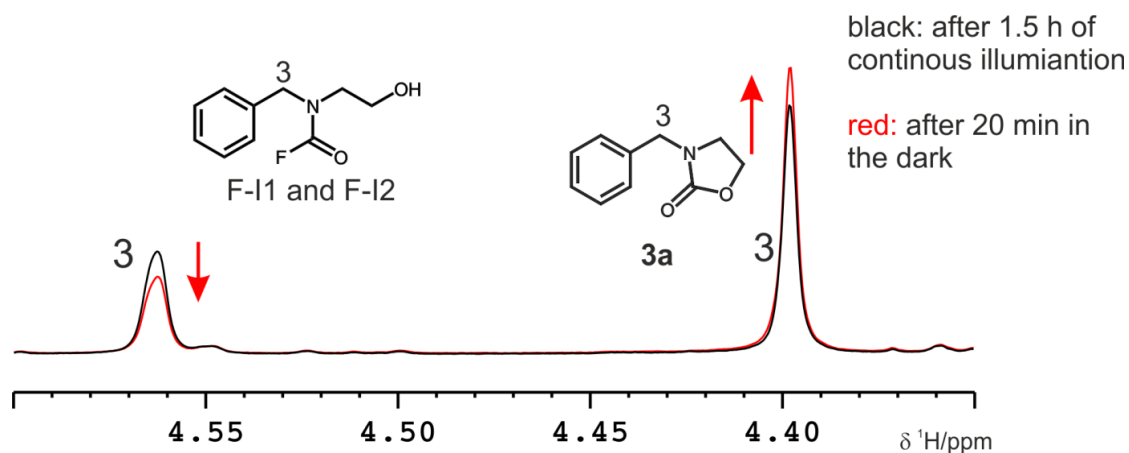


Figure S-4-4. Excerpt of the ^1H proton spectrum after 1.5 hours of continuous illumination (black) and the reaction mixture in the dark after 20 minutes (red). **F-I1** and **F-I2** convert into the desired product **3a** by a dark reaction. The position C3-H of **F-I1** and **F-I2** usually overlap, hence it appears as one singlet in the NMR spectrum. All other signal sets in the NMR spectrum stay constant within the observed time frame.

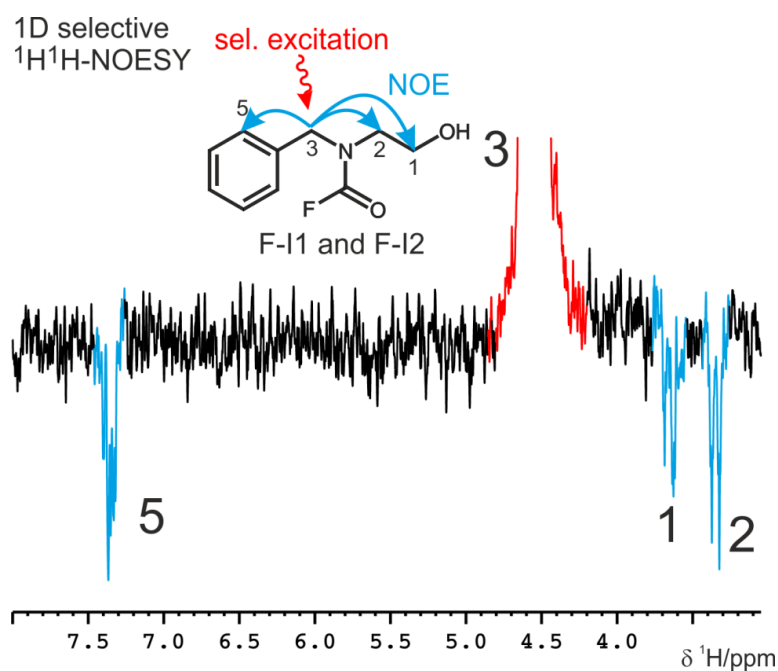


Figure S-4-5. 1D $^1\text{H}^1\text{H}$ -NOESY spectrum with selective excitation of the C3-H position at 4.54 ppm of F-I1 and F-I2 (red). The selective NOESY yields three distinctive NOE sets (blue) to the signals C1-H, C2-H and C5-H of both conformations F-I1 and F-I2, due to spectral overlap at the C3-H position. $t_m = 600$ ms.

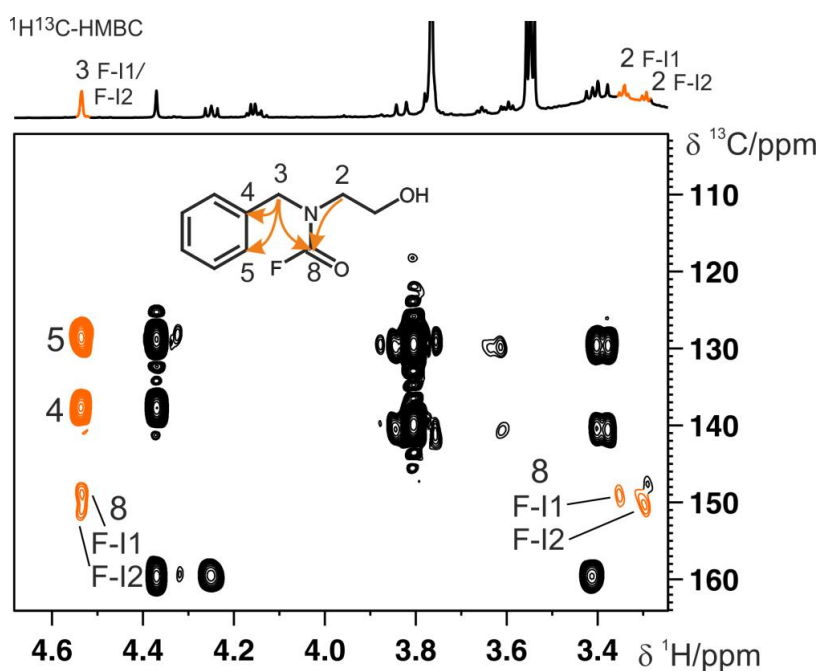


Figure S-4-6. $^1\text{H}^{13}\text{C}$ HMBC highlighting the relevant cross correlations (orange) for both conformations of the fluorointermediate (F-I1 and F-I2).

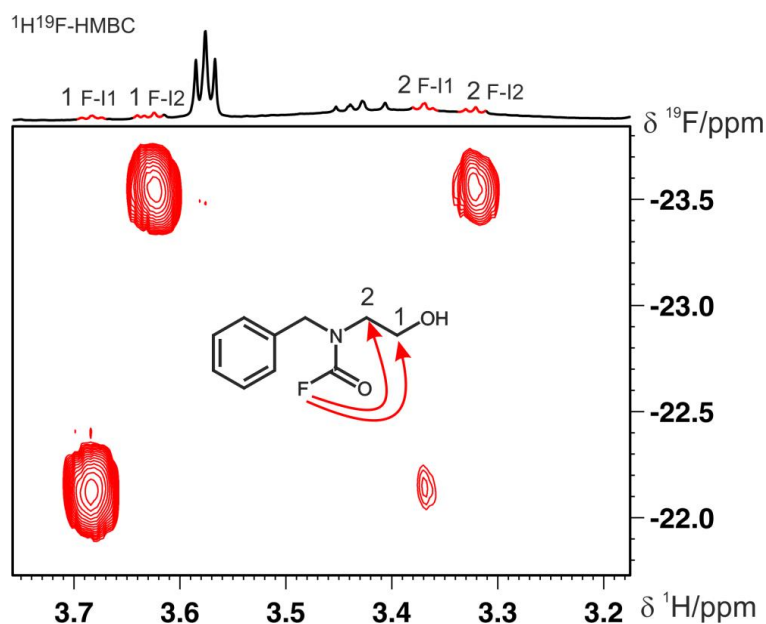


Figure S-4-7. ¹H¹⁹F-HMBC highlighting the relevant cross correlations (red) for both conformations of the fluorointermediate (**F-I1** and **F-I2**). Parameters: PP = *hmbcgpndqf*; NS = 64; DS = 16; TD-F1 = 16; TD-F2 = 2048; D1 = 1; SW-F1 = 5; SW-F2 = 12; O-F1 = -23; O-F2 = 5; evolution long range coupling = 71.4 ms.

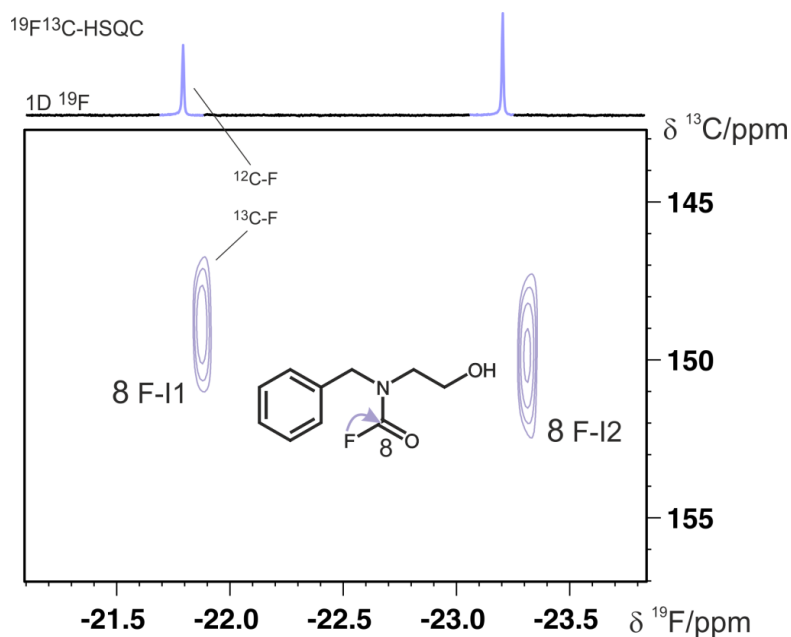


Figure S-4-8. Edited ¹⁹F¹³C-HSQC highlighting the relevant cross correlations (purple) for both conformations of the fluorointermediate (**F-I1** and **F-I2**). The cross signals in the HSQC are high field shifted in F2 with respect to the 1D ¹⁹F projection because of the strong isotope effect of ¹⁹F (¹²C-F in regular 1D ¹⁹F vs ¹³C-F in the HSQC). Parameters: PP = *hsqcedhpph*; NS = 1024; DS = 16; TD-F1 = 16; TD-F2 = 512; D1 = 1; SW-F1 = 50; SW-F2 = 10; O-F1 = 140; O-F2 = -23; adjusted for ¹J_{CF} = 283 Hz.

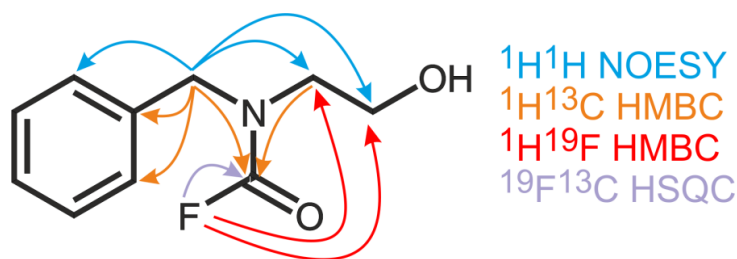


Figure S-4-9. Summary of important cross correlations for the assignment of both conformations of the fluorointermediate (**F-I1** and **F-I2**) consisting of $^1\text{H}^1\text{H}$ -NOESY (blue), $^1\text{H}^{13}\text{C}$ -HMBC (orange), $^1\text{H}^{19}\text{F}$ -HMBC (red) and $^{19}\text{F}^{13}\text{C}$ -HSQC (purple).

5.6.11.9.1 Conformations of F-I1 and F-I2

Figure S-4-10 depicts two conceivable options for the conformational nature of **F-I1** and **F-I2**. Option 1 shows the (*s-cis*)- and (*s-trans*)-conformers of **F-I**. These could be possible due a hindered rotation around the NC(O) amide bond. But an inversion around the amide bond would also lead to an inversion of coupling constants e.g. the $^4J_{\text{HF}}$ couplings from position 8 to 3 and 8 to 2. The $^1\text{H}^{19}\text{F}$ -HMBC spectrum in Figure S-4-7 clearly shows that both conformations have clear cross signals to position 2 (and 1), but signals to position 3 have never been observed greatly diminishing the likelihood of option 1. Option 2 suggests an intramolecular hydrogen bond leading to a seven membered ring within the molecule. This option splits into two more possibilities as there could be either a slow equilibrium between the open form and the seven membered ring or the seven membered ring structure itself can engage two conformations. This would also be in line with the $^1\text{H}^{19}\text{F}$ -HMBC spectrum in Figure S-4-7 as the fluorine has cross signals to position 2 and 1 for both conformations, albeit slightly different in intensity. Option 2 is further supported when investigating other substrates (e.g. *N*-benzylethylenediamine leading to product **3d**) where only one conformation could be detected (data not shown). In summary, option 2 seems the more likely option, although it could never be proven unambiguously

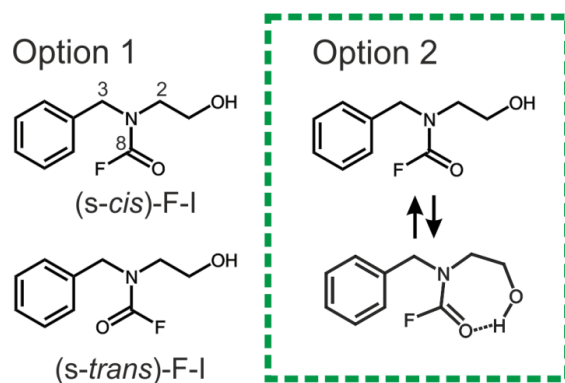


Figure S-4-10. Conceivable options for the two detectable conformers of **F-I**. Option 1, **F-I1** and **F-I2** are the (*s-cis*)- and (*s-trans*)-conformers of **F-I** due to a hindered rotation around the NC(O) amide bond. Option 2, **F-I** can form a stable intramolecular hydrogen bond between the hydroxyl group and the NC(O) carbonyl group leading to a seven membered structure. Exchange between the open form and the seven membered structure can lead to two conformers. The seven membered structure could also have two stable conformations of the seven membered ring. Option 2 is the more likely option as option 1 doesn't fit the experimental NMR data ($^1\text{H}^{19}\text{F}$ -HMBC) and is hence, highlighted. (for details see text above)

5.6.11.10 Illuminated NMR reaction profiles

5.6.11.10.1 *In situ* NMR reaction profiles

Figure S-4-11 illustrates the full *in situ* ^1H NMR reaction profile of the photoreaction of **1a** (100 mM), **2b** (110 mM), DIPEA (300 mM) and **P3** (2 mM) in CD_3CN at 298 K with illumination at 405 nm. Immediately after turning on the light, both starting materials (**1a** violet and **2b** black) start to decrease. Next to the starting materials the formation of two main products can be observed. First the fragmentation product of **2b**, benzonitrile **4** (red) can be assigned, whose formation is directly correlated with the decrease of **2b** (see also Fig. S-4-13). Secondly the desired product **3a** (green) can be designated, whose formation is also strongly correlated with the decrease of **2b** and the increase of **4**. Furthermore, a third major species could be assigned as the chiral off-cycle intermediate **OC-I** (cyan), resulting from a side reaction of **1a** with acetaldehyde, which in turn is a fragmentation product of DIPEA. Next to those three products one other significant intermediate species (**F-I**, magenta) could be readily assigned. This intermediate is a result from the reaction of the starting material **1a** with *in situ* generated fluorophosgene (COF_2) and thus presents a key intermediate supporting the proposed mechanism. **F-I** can be detected as two conformers (**F-I1** and **F-I2**) in solution albeit the

unambiguous nature of both conformers could not be determined (see relevant spectra for the assignments of **F-I1** and **F-I2**). Owing to the heavy signal overlap and the overall small intensity of both conformers they are treated as one species (**F-I**) in the reaction profiles. Figure S-4-12 shows the initial combined build-up of **F-I1** and **F-I2** (**F-I**, magenta), and product **3a** (green). The formation of product **3a** is slightly delayed, whereas the formation of **F-I** starts immediately. After around 6 minutes the signals of **3a** start to increase as the intermediates are converted into **3a** in a concurrent dark reaction. This was further confirmed by turning the light off in some instances, leading to a steady decrease of **F-I1** and **F-I2** while **3a** is constantly generated solidifying the role of **F-I1** and **F-I2** as a precursor of **3a**.¹⁵

In Figure S-4-11 it can be observed that the starting material **1a** decreases faster than **2b** and is fully consumed after ~6 hours, which also halts product conversion of **3a** (and **OC-I** as well as **F-I**) at ~40 %. This big difference compared to the batch reaction (96 % isolated yield) is due to heavy precipitation of a yellow solid. It could be demonstrated that this precipitate contains a significant amount of product **3a** next to DIPEA and probably fluoride salts (see Fig. S-4-14). It can also be assumed that parts of this solid could still participate in the reaction as it also contains photocatalyst **P3**. Next to the main products presented in Figure S-4-11 several other fragmentation products originating from DIPEA could be assigned (data not shown). These are diisopropylamine, *N*-ethylisopropylamine, acetaldehyde and acetone. These fragmentation products support the function of DIPEA as a hydrogen source for the formation of **4**. But it is to be noted that several other, unknown side products, originating from DIPEA are also present in solution in low amounts.

¹⁵ It is to be noted that besides the signal sets of **3a**, **F-I1** and **F-I2**, all remaining signal sets stay constant within the observed time frame without illumination (10-20 minutes)

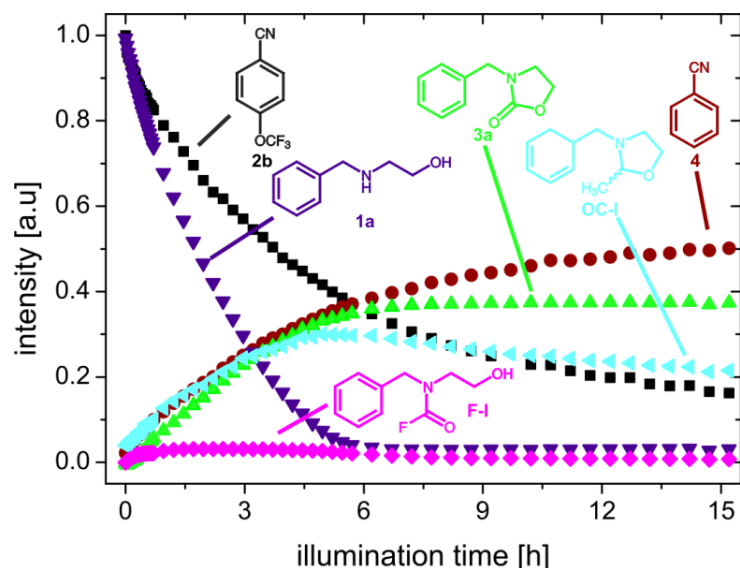


Figure S-4-11. ¹H NMR reaction profile recording the photoreaction of **1a** (100 mM), **2b** (110 mM), DIPEA (300 mM) and **P3** (2 mM) in CD₃CN at 298 K with illumination at 405 nm. The build-up of the desired product **3a** (green) correlates with the formation of the fragmentation product **4** (red) of **2b** (black). Moreover, two intermediates (**F-I**, magenta and **OC-I**, cyan) could be readily assigned. **F-I** is the direct precursor of **3a** stemming from the reaction of **1a** with *in situ* generated fluorophosgene whereas **OC-I** is the result from the reaction of **1a** with acetaldehyde, which in turn is a fragmentation product of DIPEA.

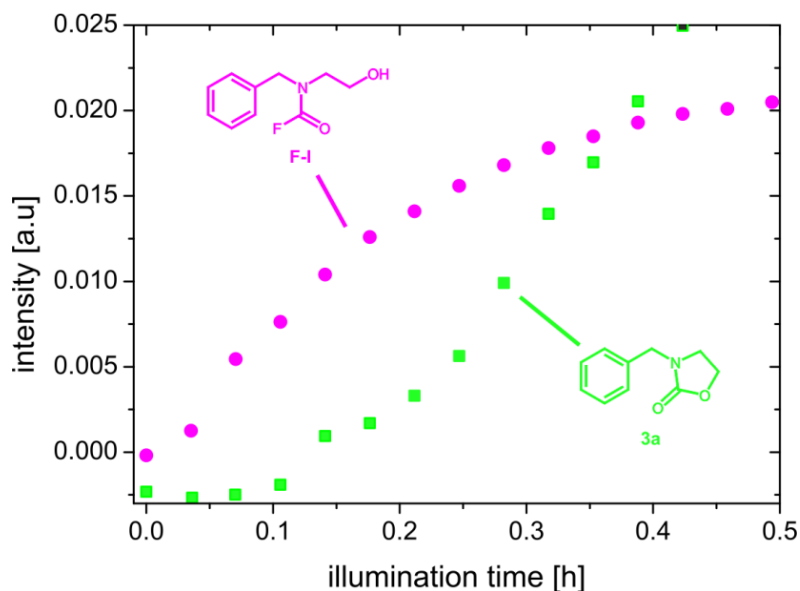


Figure S-4-12. ¹H NMR reaction profile showing the initial trend of **3a** (green) and **F-I** (**F-I1** + **F-I2**, magenta). The formation of **3a** is preceded by an initial lag-phase whilst the intermediate **F-I** is generated immediately after the light is turned on as the direct precursor of **3a** solidifying its role as a direct precursor to **3a**.

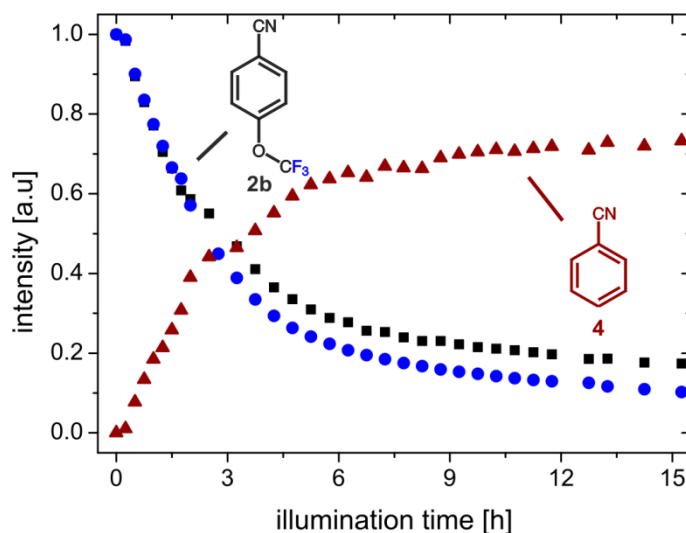


Figure S-4-13. ^1H and ^{19}F NMR reaction profile. Increase and decrease in signal intensity of the starting material **2b** (^1H black; ^{19}F blue) and the corresponding reaction product **4** (red). The profile shows a clean conversion of **2b** into **4**. The deviation of the ^1H and ^{19}F intensities for **2b** comes from overlapping signals in the ^1H NMR spectrum

Figure S-4-14 shows the ^{19}F NMR reaction profile of the photoreaction of **1a** (100 mM), **2b** (110 mM), DIPEA (300 mM) and **P3** (2 mol %) in CD_3CN at 298 K with illumination at 405 nm. Although **2b** (blue) decreases continuously, there is only a slight increase of other fluorine species over time (green). At the end of illumination all other fluorine species only amount to ~12% of the total signal intensity (compared to **2b** in the beginning). As the proposed mechanism (Figure 3) suggest that fluoride (F^-) gets liberated not only from the OCF_3^- fragment from **2b** but also from the reaction of fluorophosgene with **1a** and the subsequent intramolecular cyclization to yield **3a**, it can be assumed that most of the fluorine in the reaction is F^- , which then mostly precipitates as some sort of insoluble salt, that can be witnessed as a yellowish solid at the bottom of the NMR tube after illumination. Only small amounts of free F^- can be observed in solution (broad singlet at ~-125 ppm).

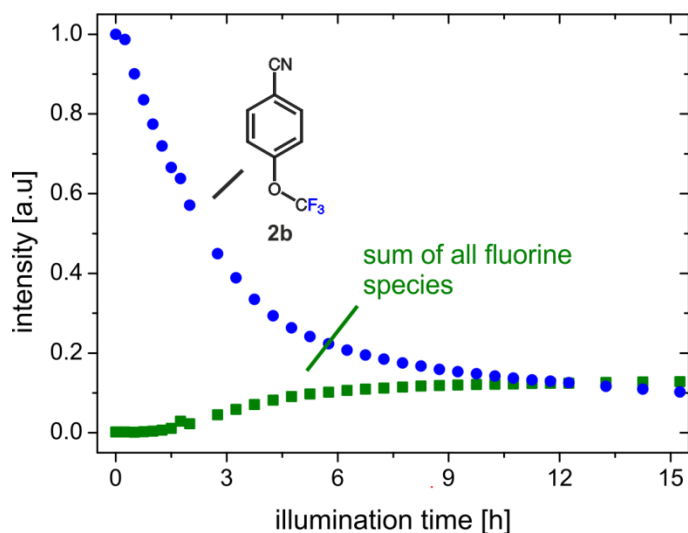


Figure S-4-14. ^{19}F NMR reaction profile showing the decrease of the starting material **2b** (blue) and the increase of all detectable fluorine species (green). The combined observable fluorine species only amount to ~12 % because the bulk of fluorine probably precipitates as various fluoride salts, as F^- is the main fluorine species generated in the reaction.

5.6.11.10.2 *Ex situ* reaction profiles

Ex situ NMR reaction profiles were also recorded, besides the *in situ* reaction profiles. Figure S-4-15 shows the reaction profile of diluted 100 μL aliquots (final volume 400 μL ; backfilled with CD_3CN) from the photoreaction of **P3** (2 mM), **2b** (110 mM), **1a** (100 mM) and DIPEA (300 mM) in 2 mL CD_3CN at 298 K under continuous illumination with 400 nm. Similar to the *in situ* reaction profile two main products (**3a**, green and **4**, red) and two significant intermediates (**F-I**, magenta and **OC-I**, cyan) can be assigned next to the two starting materials **2b** (black) and **1a** (blue). The decrease of **2b** and the increase of its fragmentation product **4** (red) directly correlate to one another, similar to *in situ* approach. Furthermore, the increase of the main product **3a** (green) also correlates with the decrease of **2b** and the increase of **4**. But it is evident that the conversion rate of **1a** to **3a** is significantly higher compared to the *in situ* reaction owing to the higher light intensity. The two conformations of the important fluorointermediate (**F-I1** and **F-I2**) can also be assigned. Analogous to the *in situ* reaction profile **F-I1** and **F-I2** are treated as one entity (**F-I**) in the reaction profile. Like in the *in situ* reaction, one can detect the chiral side product **OC-I** originating from a side reaction of **1a** with *in situ* generated acetaldehyde. Furthermore, large amounts of precipitate can be again witnessed. The precipitate contains product **3a**, photocatalyst **P3** and fluoride salts, similar to the *in situ* reaction. To sum up, the overall trend of the *ex situ* approach is very much comparable

to the *in situ* approach, albeit the *ex situ* approach lead to significantly increased product conversion and shows increased reaction rates. However, there is still a noteworthy, observable difference between the results of the *ex situ* reaction kinetic and the *in situ* reaction kinetics. At the 3 hour mark it is evident that substrate **1a** and **F-I** are fully consumed. Nevertheless, product **3a** is still generated, whereas **OC-I** is decreasing steadily. This is due to a water off-cycle equilibrium between **1a** and **OC-I**. As a result, **OC-I** gets slowly converted back to **1a**, which can then react further on to yield **3a** (and **F-I**) as long as fluorophosgene is still liberated.

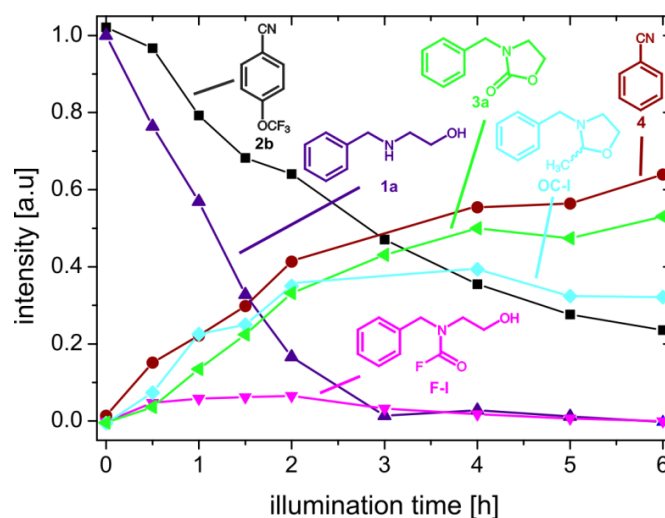


Figure S-4-15. *Ex situ* ^1H NMR reaction profile showing the photoreaction of **1a** (100 mM), **2b** (105 mM), DIPEA (300 mM) and **P3** (2 mM) in 2 mL CD_3CN at 298 K with illumination at 405 nm. The build-up of the desired product **3a** (green) correlates with the formation of the fragmentation product **4** (red) of **2b** (black). Furthermore, two intermediates (**F-I**, magenta and **OC-I**, cyan) can be detected. **F-I** is the direct precursor of **3a** stemming from the reaction of **1a** with *in situ* generated fluorophosgene whereas **OC-I** is the result from the reaction of **1a** with acetaldehyde, which in turn is a fragmentation product of DIPEA. **OC-I** and **1a** are in a water dependent off-cycle equilibrium leading to an ongoing generation of **3a** even after **1a** and **F-I** are consumed as long as fluorophosgene is still liberated.

5.6.11.10.3 *In situ* reaction profiles without **1a**

Next to reaction profiles of the full photoreaction, NMR reaction profiles without the starting material **1a** were recorded as well.

Figure S-4-16 illustrates the full ^1H and ^{19}F NMR reaction profile of the photoreaction of **2b** (110 mM), DIPEA (300 mM) and **P3** (2 mM) in CD_3CN at 300 K with illumination at

405 nm. Immediately after turning on the light all signals of **2b** (^1H ; black and ^{19}F ; blue) start to decrease. Simultaneously a new signal set belonging to **4** (red) appears in the ^1H NMR spectra. The decrease of **2b** and the increase of **4** show that both are directly correlated, as **4** presents the fragmentation product of **2b**. Similar to the full reaction mixture only low amounts of other fluorine signals can be observed in the ^{19}F NMR spectra. Next to a ^{19}F signal of fluoride, several carbonylfluoride signals could be detected. Most of the fluorine again reacts to F^- (broad singlet at ~ -125 ppm) and precipitates as an insoluble salt at the bottom of the NMR tube (see *in situ* NMR reaction profiles with **1a**).

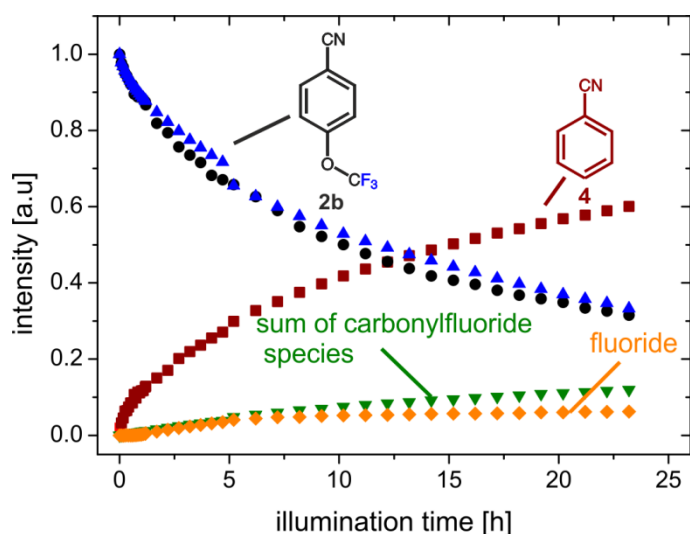


Figure S-4-16. ^1H and ^{19}F NMR reaction profile recording the photoreaction of **2b** (110 mM), DIPEA (300 mM) and **P3** (2 mM) in CD_3CN at 300 K with illumination at 405 nm. The decrease of **2b** (^1H black; ^{19}F blue) directly correlates with the formation of the fragmentation product **4** (red). The combined observable fluorine species only amount to $\sim 13\%$ because the bulk of fluorine probably precipitates as various fluorides.

Figure S-4-17 shows an excerpt of the reaction mixture of **2b** (110 mM), DIPEA (300 mM) and **P3** (2 mM) in CD_3CN at 300 K after illumination with 405 nm. Overall three ^{19}F signals can be detected (F1-F3; all singlets) next to the starting material **2b** and fluoride¹⁶, $^1\text{H}^{19}\text{F}$ -HMBC spectra show clear cross signals in the HMBC spectrum for all three signals (Fig. S-4-18). Hence, concerning the proton chemical shifts (3.2 to 1.2 ppm), it can be concluded that F1 to F3 are side products from the reaction with DIPEA and/or its fragmentation products (diisopropylamin, N-ethylisopropylamine, etc).

¹⁶ Fluoride usually appears as a broad singlet at around ~ -125 ppm, but the chemical shift heavily depends on the reaction conditions and the progress of the reaction.

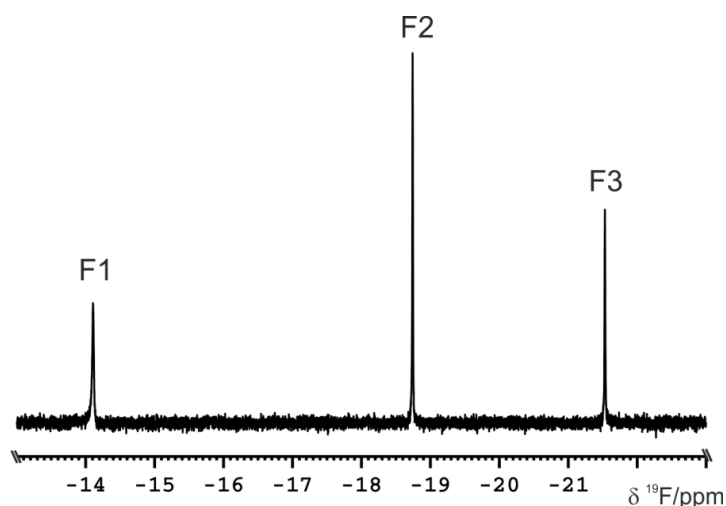


Figure S-4-17. Excerpt of the ^{19}F fluorine spectrum region of the signals in the chemical shift range of carbonylfluorides. Up to three ^{19}F signals (F1-F3) can be clearly identified. Reaction conditions: **2b** (100 mM), DIPEA (300 mM) and **P3** (2 mM in CD_3CN at 300 K after illumination with 405 nm).

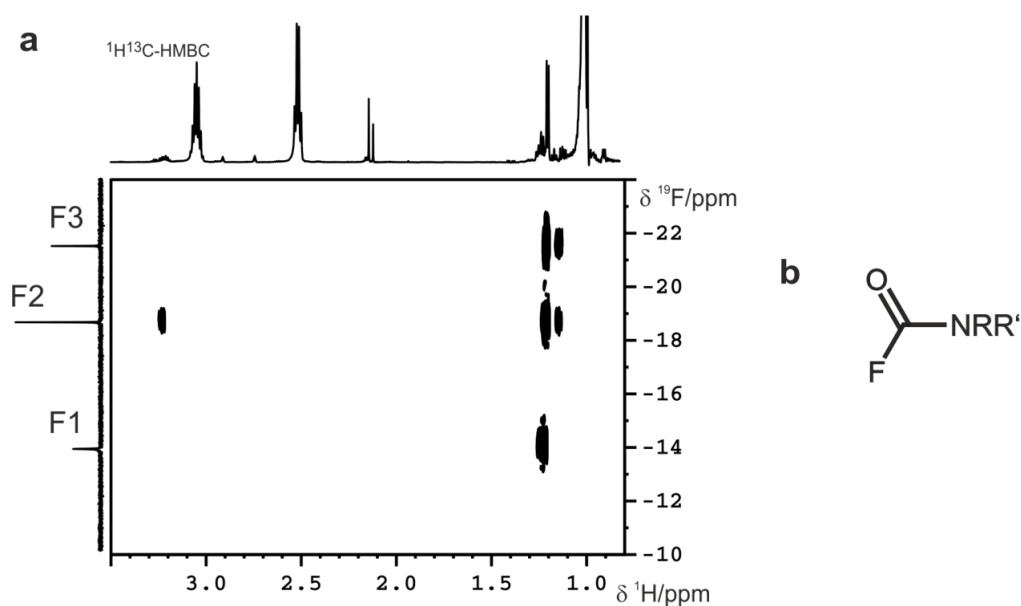


Figure S-4-18. a, $^1\text{H}^{19}\text{F}$ -HMBC. All fluorine signals (F1-F3) in the carbonylfluoride region show clear HMBC cross signals to protons of secondary DIPEA products. Parameters: PP = *hmbcgpndqf*; NS = 16; DS = 16; TD-F1 = 128; TD-F2 = 4096; D1 = 1; SW-F1 = 120; SW-F2 = 12; O-F1 = -10; O-F2 = 5; evolution long range coupling = 71.4 ms. b, Likely framework of the secondary products from the reaction of COF_2 with fragmentation products of DIPEA.

5.6.11.11 Off cycle equilibrium and role of water

Next to the NMR reaction profiles, further NMR studies were conducted to corroborate the proposed mechanism (Figure 3). Figure S-4-19 depicts a proposal for the water dependent off-cycle equilibrium between **1a** and **OC-I**. Acetaldehyde is released through fragmentation after secondary reactions of DIPEA, which hereupon can react with starting material **1a** under dehydration to yield the off-cycle intermediate **OC-I**. In turn, addition of water to **OC-I** yields **1a** and acetaldehyde again. The proposed water dependent off-cycle equilibrium leads to two conclusions. First, as long as fluorophosgene is liberated from **2b**, the reaction towards **3a** should continue if **OC-I** is in solution, independent of **1a** and/or **F-I** still being present in detectable amounts. Second, addition of water should shift the equilibrium presented in Figure S-4-19 towards **1a**, eventually suppressing **OC-I**.

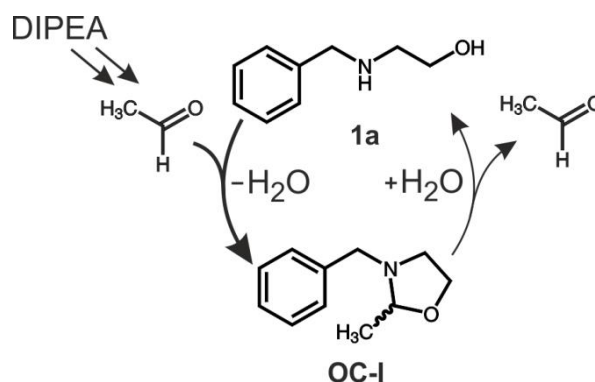


Figure S-4-19. Proposed water dependent off-cycle equilibrium between **1a** and **OC-I**. Secondary reactions of DIPEA lead to the liberation of acetaldehyde, which readily reacts with starting material **1a** to yield **OC-I**. Afterwards **OC-I** and **1a** are in a slow water dependent equilibrium, which can be shifted towards **1a** by the addition of extra water.

Figure S-4-20 shows excerpts of the ¹H NMR spectra of the aliphatic region for position 3 of **F-I**, position 3 and 1 of **3a** and position 8 for **OC-I**. Spectrum **a** at the bottom depicts the reaction mixture under standard conditions after 24 hours of illumination. Both starting materials (**2b** and **1a**) and **F-I** are fully consumed. Hence, no reaction is running anymore and only **3a** and **OC-I** are present in solution as relevant reaction products. Spectrum **b** at the top shows the same reaction mixture from spectrum **a** after addition of 5 μ L of **2b** and 1 hour of continuous illumination (total illumination 25 h). It can be clearly witnessed that the intermediate **F-I** is again present in solution, while **OC-I** has decreased in intensity, despite the absence of **1a** and **2b** (product **3a** also increased but concerning the big intensity difference of **3a** and **OC-I** it is hardly presentable). This

experiment demonstrates that there has to be an equilibrium between **1a** and **OC-I**, as **OC-I** presents the only conceivable source to provide **1a**.

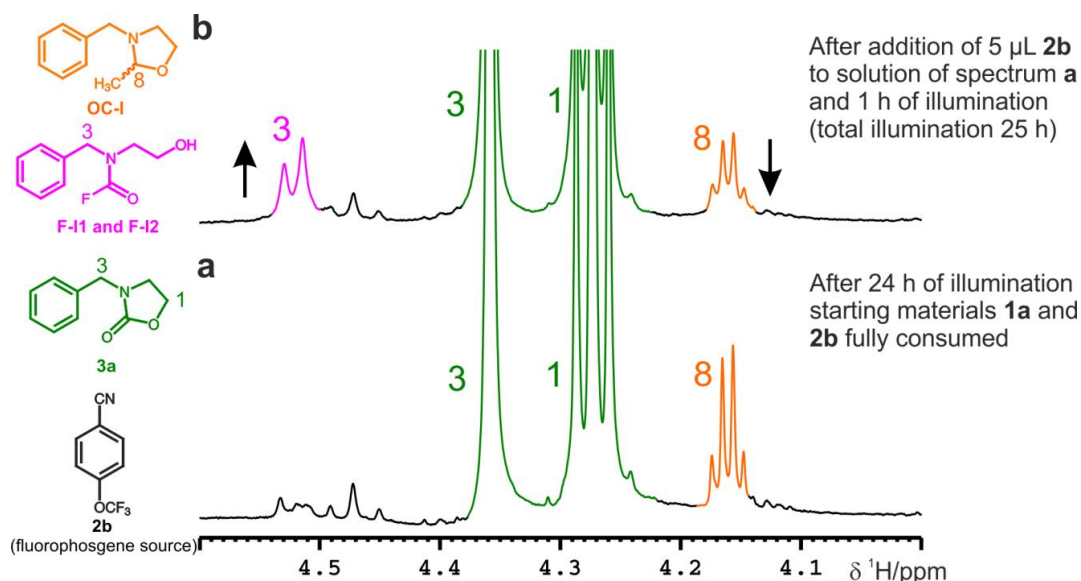


Figure S-4-20. Excerpts of the ¹H NMR spectra of the aliphatic region for position 3 of **F-I**, position 3 and 1 of **3a** and position 8 for **OC-I** of the reaction mixture under standard conditions. **Spectrum a**, reaction solution after 24 hours of illumination. **1a**, **2b** and **F-I** are fully consumed, hence no reaction is progressing. **Spectrum b**, reaction solution after addition of 5 µL **2b** to the mixture of spectrum **a** and 1 hour of further illumination (total illumination time 24 h). **F-I** and **3a** start to be generated again, while **OC-I** is decreasing affirming the proposed off-cycle equilibrium.

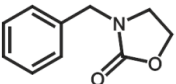
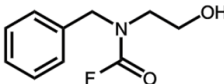
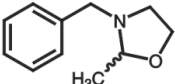
To further investigate on how to influence the off-cycle equilibrium *ex situ* NMR measurements were performed testing different reaction conditions with respect to the general conditions (general conditions: **1a** 100 mM, **2b** 105 mM, **P3** 2 mM, DIPEA 300 mM, in CD₃CN). Next to the general conditions, three modified reaction conditions were tested which were derived from the off-cycle proposal (Fig. S-4-19).¹⁷ Samples were taken after two hours of continuous illumination comparing the amount of **3a**, **F-I** (comprising of **F-I1** and **F-I2**) and **OC-I**. The results are summarized in Table S-4-1. First the general conditions yield the same result as the regular *ex situ* NMR reaction kinetics with a comparable amount of **3a** and **OC-I** and low amounts of **F-I**. For the first modified condition, the concentration of **2b** was doubled from 105 mM (1.05 eq) to 210 mM (2.10 equiv.) with the idea that more **2b** should lead to a longer and increased supply of

¹⁷ All reactions within the *ex situ* NMR measurements including the general conditions also contained 12 equiv. of 1,4-cyclohexadiene, which leads to a partial recovery of DIPEA. But it didn't notably affect any kinetics or yields.

fluorophosgene. The result shows a heavily increased amount of generated **F-I**, while **OC-I** is already suppressed by around 50 % with respect to the general conditions whereas the amount of **3a** stays rather constant. For the second modified reaction condition, the influence of water on the off-cycle equilibrium between **1a** and **3a** was investigated. Here, the solvent mixture was changed to CD₃CN/H₂O (9:1) instead of pure CD₃CN. The results in Table S-4-1 indicate a distinct shift in the off-cycle equilibrium towards **1a** as well as a much faster reaction. After two hours the sum of **3a** and **F-I** already reaches above 90 % and **OC-I** is almost fully suppressed. This shows that the water amount influences the off-cycle equilibrium considerably and can be used to effectively accelerate the reaction. The last modification of reaction conditions is basically a combination of the two modifications already described. The concentration of **2b** is increased from 105 mM (1.05 equiv.) to 210 mM (2.1 equiv.) and the solvent was changed from pure CD₃CN to CD₃CN/H₂O (9:1). Under these conditions, generation of **OC-I** can be completely suppressed, while conserving the high amount of **3a + F-I**.

The results presented in Table S-4-1 allow the conclusion that the reaction can be very much optimized substrate specific by tuning the amount of **2b** and the water content.

Table S-4-1. Influence of **2b** and water on product and intermediate formation investigated by *ex situ* NMR measurements.

Conditions	amount after two hours of continuous illumination		
	 3a	 F-I	 OC-I
General conditions	38 %	5 %	32 %
2.1 eq. of 2b instead of 1.05 eq.	34 %	33 %	15 %
Solvent CD ₃ CN/H ₂ O(9:1) instead of pure CD ₃ CN	70 %	21 %	6 %
Solvent CD ₃ CN/H ₂ O (9:1) and 2.1 eq. of 2b	57 %	31 %	>1 %

The amount of **3a + F-I** can be viewed as 'potential' amount of product **3a**, because **F-I** converts into **3a** by a self-propagating dark reaction and serves as better comparison between the different reaction conditions (red bracket).

The appearing precipitate during the reaction was also investigated, because a considerable amount was observed in both the *ex situ* and *in situ* reaction approaches. Figure S-4-21 shows an excerpt of the ^1H NMR spectrum of the precipitate dissolved in DMSO. It is evident that the reaction product **3a** is one of the main constituents within the precipitate apart from fluoride which isn't observable in the proton NMR spectrum. The presence of **3a** in the precipitate is one likely reason that the conversion of **1a** to **3a** is never fully completed in the *in situ* ^1H NMR reaction profiles (and sometimes also *ex situ* ^1H NMR measurements). Next to **3a**, DIPEA and secondary products of DIPEA were also found in small amounts within the precipitate. Furthermore, the photocatalyst **P3** could be identified probably owing to its poor solubility in CD_3CN even at low concentrations. Due to the precipitate being dissolved in non-deuterated DMSO, a double solvent suppression comprising of presaturation and excitation sculpting was employed to get rid of the DMSO and water signals.

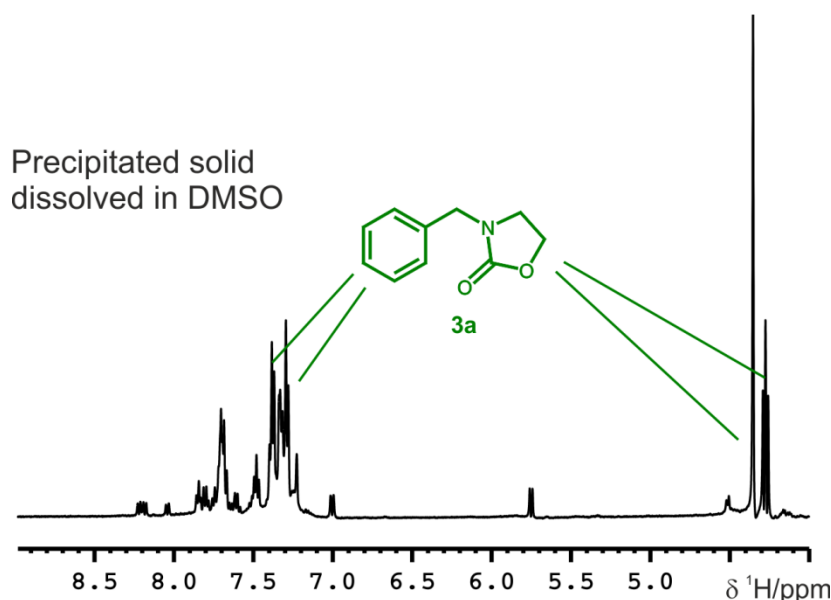


Figure S-4-21. Excerpt of the ^1H proton spectrum of the precipitated solid during the reaction dissolved in DMSO. The signals clearly show product **3a** as one of the prominent components besides the photocatalyst **P3**, DIPEA and secondary products of DIPEA. The DMSO and water peaks were suppressed *via* a combination of excitation sculpting and presaturation.

5.6.12 References

- (1) a) M. M. Heravi, V. Zadsirjan, B. Farajpour, *RSC Adv.* **2016**, *6*, 30498-30551; b) M. A. Rodrigo, N. Oturan, M. A. Oturan, *Chem. Rev.* **2014**, *114*, 8720-8745; c) J. Magano, J. R. Dunetz, *Chem. Rev.* **2011**, *111*, 2177-2250; (d) Y. Zhou, J. Wang, Z. Gu,

S. Wang, W. Zhu, J. L. Aceña, V. A. Soloshonok, K. Izawa, H. Liu, H. *Chem. Rev.* **2016**, *116*, 422-518.

(2) a) A. K. Ghosh, M. Brindisi, *J. Med. Chem.* **2015**, *58*, 2895-2940; b) J. P. Parrish, R. N. Salvatore, K. W. Jung, *Tetrahedron* **2000**, *56*, 8207-8237; c) D. J. Díaz, A. K. Darko, L. McElwee-White, *Eur. J. Org. Chem.* **2007**, 4453-4465.

(3) L. Pasquato, G. Modena, L. Cotarca, P. Delogu, S. Mantovani, *J. Org. Chem.* **2000**, *65*, 8224-8228.

(4) a) W. Schneider, W. Diller in *Ullmann's Encyclopedia of Industrial Chemistry*, Vol. 26, Wiley-VCH: Weinheim, **2000**, pp 623-632; b) L. Cotarca, T. Geller, J. Répási, *Org. Process Res. Dev.* **2017**, *21*, 1439-1446.

(5) T. Sakakura, K. Kohnoa, *Chem. Commun.* **2009**, 1312-1330.

(6) N. A. Romero, D. A. Nicewicz, *Chem. Rev.* **2016**, *116*, 10075-10166.

(7) a) D. Petzold, B. König, *Adv. Synth. Catal.* **2018**, *360*, 626-630; b) I. Ghosh, T. Ghosh, J. I. Bardagi, B. König, *Science* **2014**, *346*, 725-728; c) I. Ghosh, B. König, *Angew. Chem. Int. Ed.* **2016**, *55*, 7676-7679; d) S. J. S. Düsel, B. König, *J. Org. Chem.* **2018**, *83*, 7676; e) N. A. Romero, K. A. Margrey, N. E. Tay, D. A. Nicewicz, *Science* **2015**, *349*, 1326-1330.

(8) a) J. Twilton, C. Le, P. Zhang, M. H. Shaw, R. W. Evans, D. W. C. MacMillan, *Nat. Rev. Chem.* **2017**, *1*, 0052; b) H. Seo, M. H. Katcher, T. F. Jamison, *Nat. Chem.* **2017**, *9*, 453-456; c) A. Studer, D. P. Curran, *Nat. Chem.* **2014**, *6*, 765-773; d) M. N. Hopkinson, A. Tlahuext-Aca, F. Glorius, *Acc. Chem. Res.* **2016**, *49*, 2261-2272.

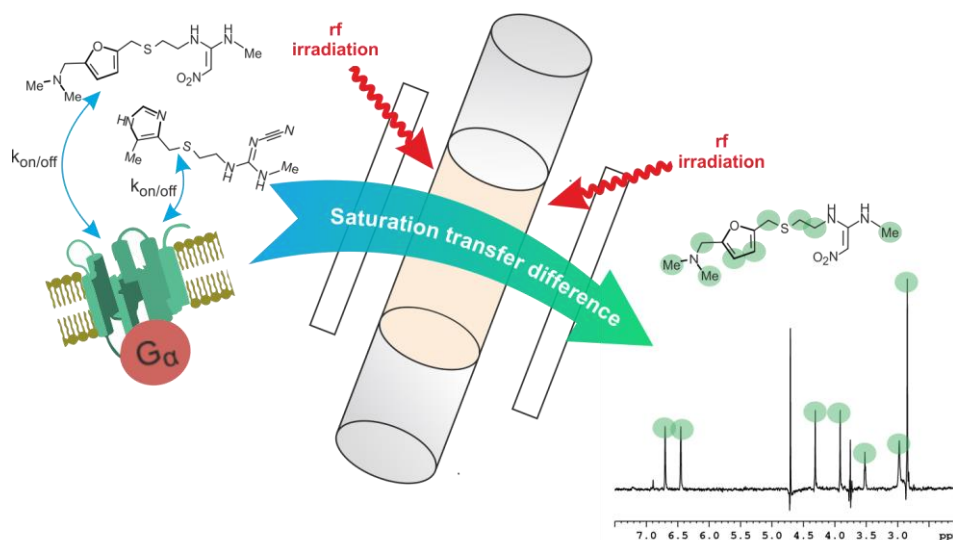
(9) a) A. Neubauer, G. Grell, A. Friedrich, S. I. Bokarev, P. Schwarzbach, F. Gärtner, A.-E. Surkus, H. Junge, M. Beller, O. Kühn, S. Lochbrunner, *J. Phys. Chem. Lett.* **2014**, *5*, 1355-1360; b) A. Singh, C. J. Fennell, J. D. Weaver, *Chem. Sci.* **2016**, *7*, 6796-6802; c) Z. Lu, T. P. Yoon, *Angew. Chem. Int. Ed.* **2012**, *51*, 10329-10332.

(10) a) M. H. Shaw, J. Twilton, D. W. C. MacMillan, *J. Org. Chem.* **2016**, *81*, 6898-6926; b) M. Majek, A. Jacobi von Wangelin, *Acc. Chem. Res.* **2016**, *49*, 2316-2327; c) D. A. Petrone, J. Ye, M. Lautens, *Chem. Rev.* **2016**, *116*, 8003-8104.

(11) (a) A. Iijima, H. Amii, *Tetrahedron Lett.* **2008**, *49*, 6013-6015; b) K. K. K. Goh, A. Sinha, C. Fraser, R. D. Young, *RSC Adv.* **2016**, *6*, 42708-42712; c) C. Combellas, F. Kanoufi, A. Thiébault, *J. Electroanal. Chem.* **1997**, *432*, 181-192.

- (12) a) B. Sahoo, M. N. Hopkinson, *Angew. Chem. Int. Ed.* **2018**, *57*, 7942-7944; b) B. J. Jelier, P. F. Tripet, E. Pietrasiak, I. Franzoni, G. Jeschke, A. Togni, *Angew. Chem. Int. Ed.*, **2018**, *57*, 13784-13789
- (139) a) R. M. Pearson, C. Hooi-Lim, B. G. McCarthy, C. B. Musgrave, *J. Am. Chem. Soc.* **2016**, *138*, 11399-11407; b) Y. Du, R. M. Pearson, C. Hooi-Lim, S. M. Sartor, M. Ryan, H. Yang, N. H. Damrauer, G. M. Miyake, *Chem. Eur. J.*, **2017**, *23*, 10962-10968.
- (14) B. G. McCarthy, R. M. Pearson, C. Hooi-Lim, S. M. Sartor, N. H. Damrauer, G. M. Miyake, *J. Am. Chem. Soc.* **2018**, *140*, 5088-5101.
- (15) S. M. Sartor, B. G. McCarthy, R. M. Pearson, G. M. Miyake, N. H. Damrauer, *J. Am. Chem. Soc.* **2018**, *140*, 4778-4781.
- (16) D. P. Hari, P. Schroll, B. König, *J. Am. Chem. Soc.* **2012**, *134*, 2958-2961.
- (17) M. Nguyen, M. H. Matus, V. Ngan, R. Haiges, K. O. Christe, D. A. Dixon, *J. Phys. Chem. A* **2008**, *112*, 1298-1312.
- (18) a) G. R. Fulmer, A. J. M. Miller, N. H. Sherden, H. E. Gottlieb, A. Nudelman, B. M. Stoltz, J. E. Bercaw, K. I. Goldberg, *Organometallics* **2010**, *29*, 2176-2179; b) H. E. Gottlieb, V. Kotlyar, A. Nudelman, *J. Org. Chem.* **1997**, *62*, 7512-7515.
- (19) R. M. Pearson, R. M.; Lim, C.-H.; McCarthy, B. G.; Musgrave, C. B.; Miyake, G. M. *J. Am. Chem. Soc.* **2016**, *138*, 11399-11407.
- (20) A. Seegerer, P. Nitschke, R. M. Gschwind, *Angew. Chem. In. Ed.* **2018**, *57*, 7493-7497.

6 Investigation of Ligand Receptor interactions by Small Molecule Guided NMR spectroscopy: Interactions of Histamine and H2R Antagonists with membrane bound H2R



All NMR measurements (including STD, WaterLOGSY and INPHARMA) and experiment preparations were performed by Philipp Nitschke and Dr. Maxime Melikian. All buffer solutions were prepared by Philipp Nitschke. Preparation of the SF9 membrane suspensions were done by the working group Buschauer (mainly Maria Beer-Krön) and Philipp Nitschke. The GTPγS assays were carried out by Maria Beer-Krön and Philipp Nitschke.

6.1 Introduction

Gastroesophageal reflux disease (GERD) is a prevalent, ubiquitous digestive disorder.^[1] GERD usually results from an impaired function of the lower esophageal sphincter (LES), which is a ring of muscle located between the esophagus and the stomach^[1–6]. Insufficient function of this muscle leads to a surging of stomach acid into the esophagus. This acid reflux will gradually burn the esophagus over time and the resulting inflammations and irritated tissue can further develop into esophageal bleeding, ulcers, chronic scarring, Barrett's esophagus and esophageal cancer^[1–12]. With approximately 20 % of western culture and around 5 % of eastern culture being affected by GERD (Figure1) there is a high demand for effective long term treatments of the disease^[2,6,9,12].

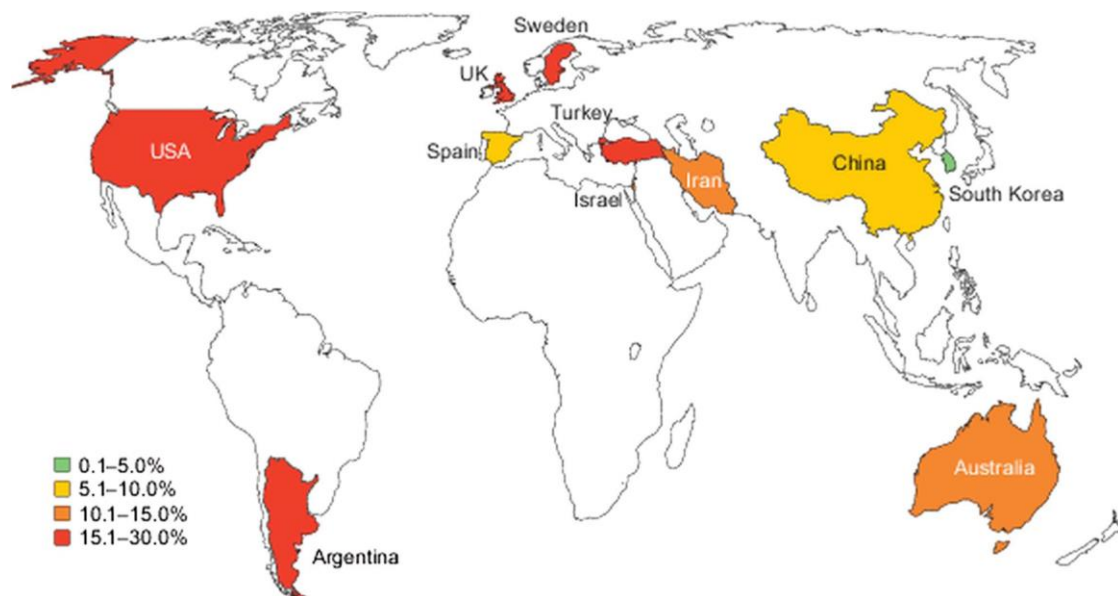


Figure 1: Global epidemiology of GERD according to El-Serag *et al.*^[9] Reproduced with permission from^[9].

The LES itself can only be treated with highly invasive surgical procedures like fundoplication.^[1,2,5,6] To avoid heavy strain on patients and to decrease risks, GERD is usually treated with medications that decrease or neutralize stomach acid^[1,6,7,11,12]. Hence, less stomach acid can reflux into and damage the esophagus. Especially two drug classes established themselves for the medical treatment of GERD. First, proton-pump inhibitors (PPI) such as Esomeprazole and Lansoprazole, which irreversibly block the gastric proton pump (H^+/K^+ ATPase) located in the stomach (Figure 2; left)^[13,14]. And second, Histamin-2-receptor (H2R) blockers such as Cimetidine, Ranitidine and Famotidine, which competitively occupy the active center of the H2R instead of the acid proliferating hormone Histamine (Figure 2; right)^[15,16]. Both are used for different degrees

of GERD, whereas treatment with proton-pump inhibitors leads to a stronger stomach acid reduction than H2R antagonists^[6].

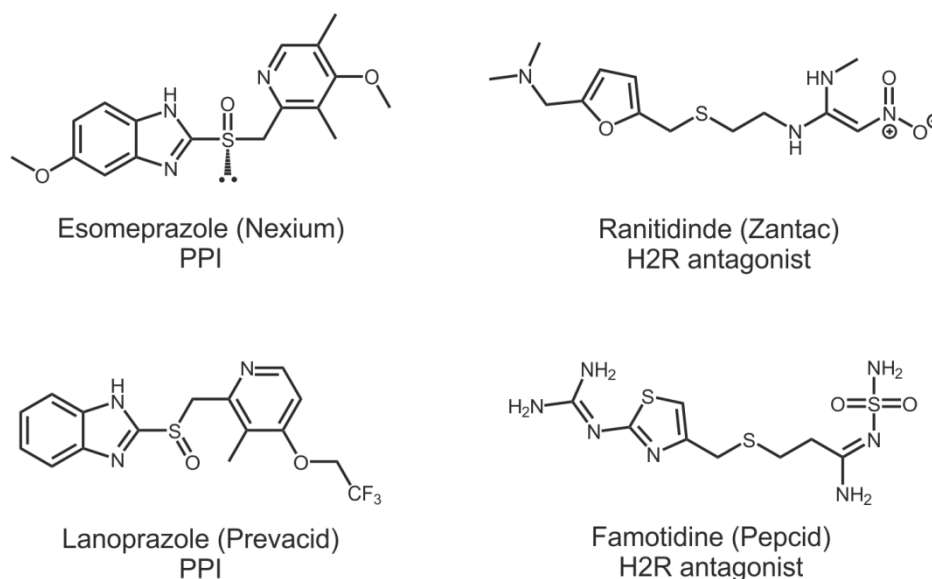


Figure 2: Common drugs for the treatment of GERD including proton-pump inhibitors (PPI) and histamin-2-receptor (H2R) antagonists.

Although decent amounts of drugs for the treatment of GERD exist, there is still a large scope for improvement in terms of new more effective, pharmacologic structures and for in detail elucidation of their active mechanisms. Especially investigations of the H2R in terms of pharmacodynamics are useful, because the H2R belongs to the family of G-protein coupled receptors (GPCRs)^[17,18]. Hence understanding the pharmacodynamics of H2R antagonists and the H2R do not only promote treatment of GERD, but can also give deeper insight into other GPCR systems. According to Stevens and Overington *et al.*, GPCRs present around 25 % of all biological targets for commercial drugs in use^[19,20]. Hence, there is a tremendous demand to understand the structure and the mechanisms of these biological structures. GPCRs are transmembrane proteins, which are ubiquitous within our body and to date over 800 GPCRs could be identified^[21]. They can be divided into five main families: The **G**lutamate, **R**hodopsin, **A**dhesion, **F**rizzled/Taste2 and **S**ecretin family (GRAFS), whereas the Rhodopsin family contains most known GPCRs^[22]. All of them consist of seven characteristic transmembrane α -helix domains, which provide various domains (e.g. inside the transmembrane helices or at the extracellular domains) that can act as active centers for various ligands (Figure 3)^[23]. The transmembrane domain is in close spatial proximity to a hetero-trimeric (α , β and γ sub-domains) guanine nucleotide-binding protein (G-protein). Upon ligand binding, the GPCR

undergoes conformational changes that lead to an activation of the G-protein domain^[24]. This triggers signal cascades, which can lead to various cellular responses^[25].

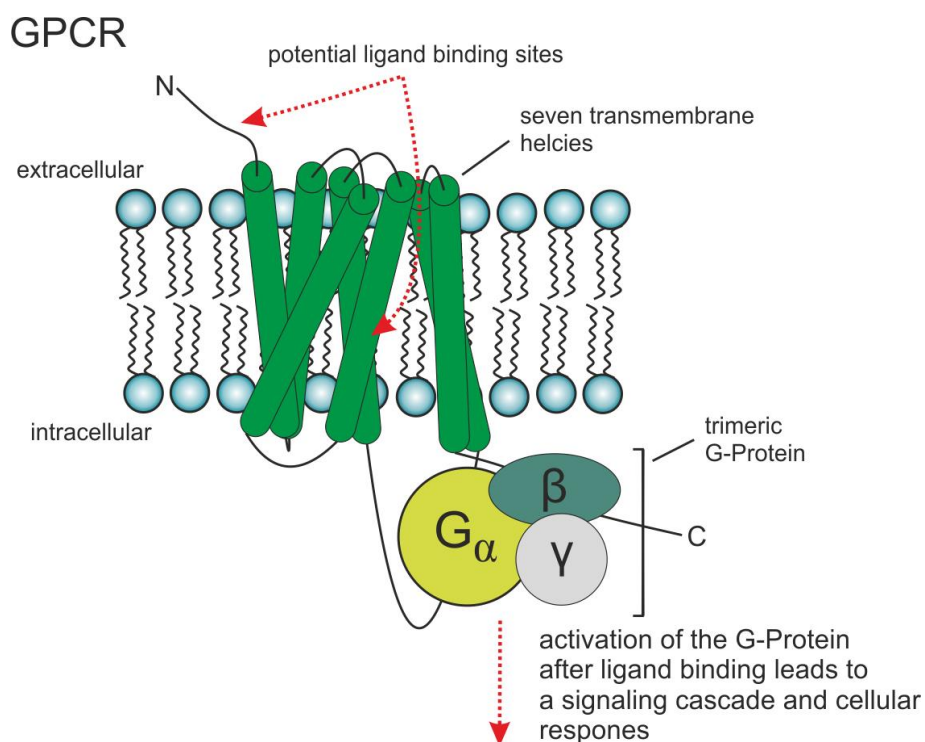


Figure 3: Schematics of a G-Protein coupled receptor (GPCR). A GPCR is a transmembrane protein, which consists of seven α -helical domains (green). The extracellular N terminus and the transmembrane domain can act as binding sites for various ligands. The random coil region of the GPCR from transmembrane domain 5 and 6 is bound to a hetero-trimeric α (yellow, β pale green, γ grey) guanine nucleotide-binding protein (G-protein). Ligand binding to the GPCR induces conformational changes that activate the G-protein resulting in further signal cascades and cellular responses.

Over the decades, many methods were developed to investigate GPCRs, ligands or receptor-ligand interactions^[26–30]. These include X-Ray crystallography^[31,32], surface plasmon resonance (SPR)^[33–35], fluorescence microscopy^[36–38] and low tech assays such as radio-ligand binding assays, competition assays etc.^[39–46]. But in the last decades, nuclear magnetic resonance (NMR) has emerged as versatile and as one of the most used techniques (Figure 4), which can be applied in every phase of drug discovery ranging from early screening (high throughput screening, HTS; fragment based drug design, FBDD) to late clinical trials (metabolic NMR; NMR imaging)^[47–50]. NMR methods in drug discovery include macromolecular NMR^[48] (structure elucidation of macromolecules/biological targets), ligand based NMR^[48] (information about solubility, charge etc.), metabolic NMR^[47] and NMR imaging^[49].

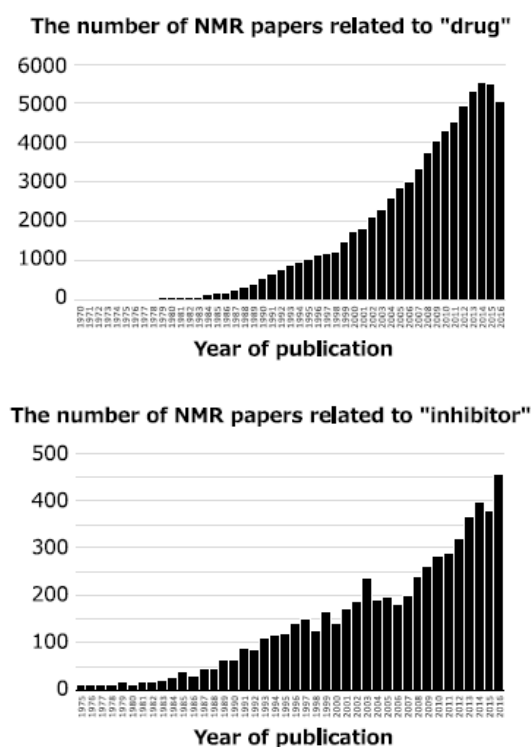


Figure 4: The amount of NMR focused publications including the key word “drug” and “inhibitor” during the years 1975-2016^[50]. Reproduced with permission from ^[50].

NMR also established a series of techniques, which can unravel receptor-ligand interactions aiding NMR based drug design. In principle, these techniques can be divided into two categories, receptor based NMR methods and ligand based NMR methods^[48]. Receptor based methods such as chemical shift perturbation HSQCs, isotope editing (or full assignment of the biological target) can give detailed information about position of active sites and orientations as well as conformation^[48,50,51]. But they are usually not suited to early fragment screening in drug discovery due to several reasons. First, the target molecule has to be fully or at least partially ¹³C and ¹⁵N (and eventually also partially ²H) labeled to enable a full assignment, or to ensure the acquisition of good quality spectra in reasonable time frames. Second, the receptor based methods in general require around ten times the amount of the biological target for the measurements (receptor based 20 – 200 μM; ligand based low μM – nM range). Third, the size of the target is typically limited to 30 – 40 kDa for these methods, because assignments become increasingly more difficult at higher molecular weights due to line broadening and increased signal overlap; although, advances in Bio-NMR increase the availability of high molecular structures and continuously push the boundaries of the size limitation in solution NMR^[52–56]. As a result, receptor based NMR techniques are usually employed at the later stages of drug discovery for structure activity relation (SAR)

studies^[50,51] (with exception of full assignments, which naturally are sometimes the very first step). Unfortunately, SAR can only rarely be used for the investigations of GPCRs due to the mentioned limitations of these methods and the increased challenge of overexpressing stable GPCR systems for solution NMR. Hence, GPCRs are usually investigated by more indirect receptor based methods such as ¹⁹F studies and spin labeling^[57]. On the other hand, ligand based NMR methods for receptor-ligand interactions solely focus on the ligand signals. As a result, the investigated biological target doesn't have to be labelled and ligand based methods are not restricted by any receptor size limits, which makes them very attractive for scarce, structurally unknown and very big (>30 kDa) targets such as GPCRs. Some of the methods can also be conducted with very low receptor concentrations (down to nM range^[58]). The used methodologies include magnetization transfer techniques such as saturation transfer difference (STD), water-ligand observed via gradient spectroscopy (WaterLOGSY), and inter-ligand NOE for pharmacophore mapping (INPHARMA), diffusion based techniques, relaxation based techniques (trNOE, T1ρ, T2), ¹⁹F measurements and titration experiments^[49]. Although these methods usually don't yield the detailed information about active sites like the receptor based methods, they still reveal important information about complex stoichiometry, binding kinetics and ligand orientation. Due to the challenges of GPCRs for receptor based methods, they are an interesting target for ligand based methods in NMR drug design. Hence, the most prevalent ligand based receptor-ligand interactions techniques are described in detail in the following.

6.1.1 Ligand based NMR methods in drug discovery for the investigation receptor – ligand interactions

6.1.1.1 Saturation transfer difference (STD)

Saturation transfer difference (STD) NMR has evolved into the most commonly used ligand based NMR technique for the detection of receptor ligand interactions.^[59–84] It can be and is applied in high throughput screening (HTS), fragment based drug design (FBDD) and can also be used to determine K_D values or to make spatial estimations of the ligand in the active center (group epitome mapping^[75,77,83,85,86]). In general, STD makes use of two properties: First, the dissociation constant (K_D) of the ligand resulting in a bound (to the receptor) and free state of the ligand and second, the NMR intrinsic nuclear Overhauser effect^[84]. Figure 5 illustrates the principles of STD NMR. For an STD experiment two spectra are acquired: One spectrum termed on-resonance (Figure 5; top) and an off-resonance spectrum (Figure 5; bottom). In the on-resonance spectrum,

signals of the investigated receptor are directly irradiated at resonances that are far away from all ligand resonances (2000-3000 Hz; if irradiation is too close, the ligand signals will be directly saturated) [84]. This leads to a full saturation of the receptor due to spin diffusion. Selective saturation is usually achieved by a train of Gauss pulses, but can also be achieved with cw irradiation or trains of any other pulses such as BURB, SINC, SQUARE etc. [86]. If a ligand binds to the fully saturated receptor (Figure 5; red GPCR), saturation is directly transferred to the ligand resonances by NOE during the residence time resulting in reduced ligand signals in the NMR spectrum. The effectiveness of this reduction is determined by the spatial proximity of the ligands' protons to the receptor while being bound and this reduction in line with NOE attenuation by r^{-6} . The off-resonance spectrum is acquired similarly to the on-resonance spectrum with one difference: direct saturation is neither focused on the receptor or the ligand but aimed at frequencies, which do not contain any NMR signals at all (usually around 5000-10000 Hz away from the closest resonances of ligand or receptor). Hence, in the off-resonance spectrum no saturation transfer takes place and the spectrum should look like a regular 1D proton experiment. Subtraction of the on-resonance and off-resonance spectra yields the STD difference spectrum, which only contains the signals affected by the saturation transfer.

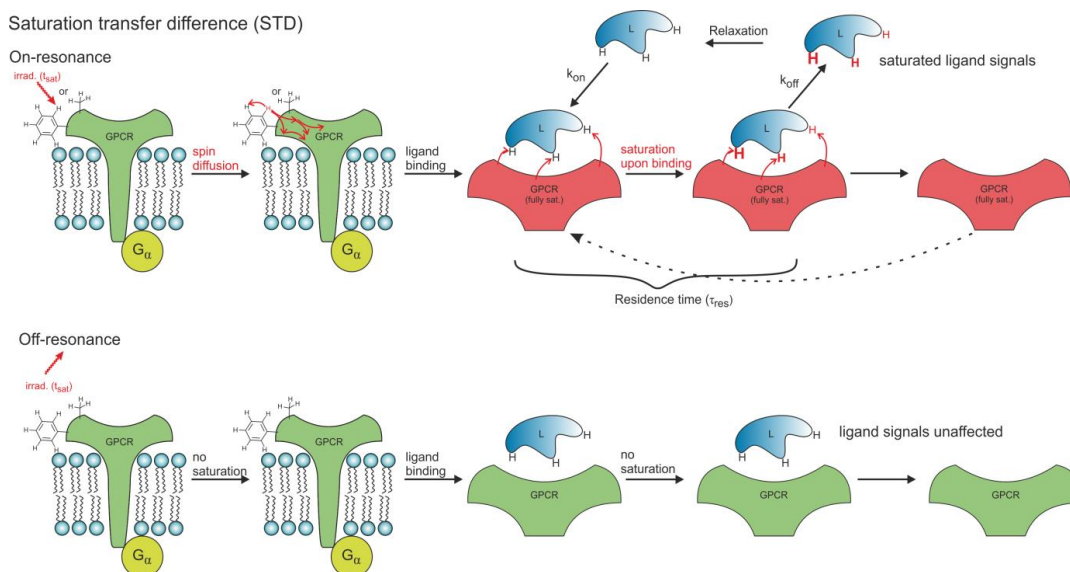


Figure 5: Principle of STD NMR. Acquisition of two spectra is required: on- and off-resonance. In the on-resonance spectrum (top), some receptor signals distant to the ligand signals are selectively saturated. Spin diffusion promotes effective saturation through the receptor. Upon ligand binding, saturation is transferred via NOE on the ligand resulting in saturated/diminished ligand signals in the spectrum. The off-resonance spectrum is similar to the on-resonance spectrum but the irradiation

frequency is far away from ligand and receptor resonances. Hence, no saturation of any signals occurs. The acquired on- and off-resonance spectra can be subtracted from one another to yield the STD spectrum, which only shows the saturated signals.

STD NMR is a very robust and straight forward method, which can also be seen in the pulse sequences (Figure 6). The top sequence shows the most basic version for STD NMR with solvent suppression. The sequence is similar to the equally popular chemical exchange saturation transfer (CEST) sequence, which can be used to detect various exchange processes in proteins^[87] or small molecules^[88]. It basically only consists of a 90° pulse, which is preceded by a train of shape pulses (usually Gauss) for selective irradiation (Figure 6 top; green pulse). Hence, the main challenge in setting up an STD experiment is the selection of the on-resonance frequency to only hit the receptor and not the ligand. Of course, optimization of other parameters such as choosing the shape pulse, its duration and power as well as overall saturation time can improve STD performance but usually don't determine the successful outcome of a measurement. The pulse sequence on the bottom of Figure 5 presents a more elaborate version for STD NMR. Besides solvent suppression it also contains a spoil sequence to destroy residual transversal magnetization and the option of a spin lock (SL) to suppress the broad receptor resonances. As a result the STD spectra only show the ligand signals. The robust saturation principle of STD NMR can also be added to any other sequences including COSY, TOCSY, NOESY, HSQC etc.^[49]

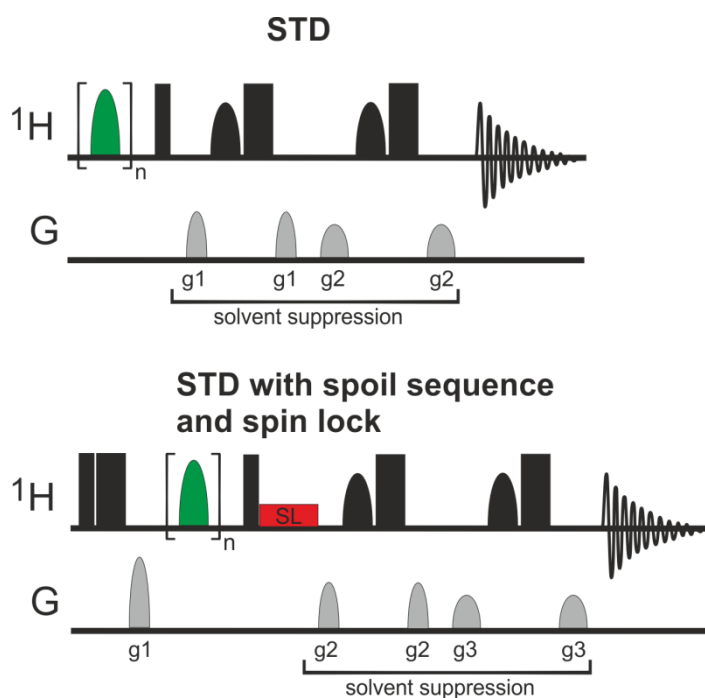


Figure 6: Common STD pulse sequences. Top: Most basic STD pulse sequence (including solvent suppression) Bottom: Elaborated STD pulse sequence, which contains a spoil sequence to destroy unwanted transversal magnetization and a spin lock (SL) to suppress broad receptor signals.

On a practical aspect, STD can generally be used for every biological target and has no molecular weight/size restrictions^[49]. In fact, the saturation of the receptor due to spin diffusion becomes more efficient for slower tumbling, which benefits STD measurements. In addition, STD NMR is very flexible regarding the molecular weight of the ligand and can also be performed with small peptides^[89]. STD can also be used for a broad range of ligand affinities including K_D values from 10^{-3} to 10^{-9} M^[49] and due the high efficiency and easy read out of saturation transfer, STD NMR allows for very low receptor concentrations in the nM^[67,68,76,90].

6.1.1.2(Exchange) transferred NOE (trNOE)

(Exchange) transferred NOE is another popular NMR method to probe receptor-ligand interactions. Apart from binder \leftrightarrow non-binder information of the ligands, trNOE can also yield information about the bound conformation of the ligand inside the receptor^[91–93]. Unlike STD and WaterLOGSY, the trNOE does not require any special pulse sequences and is based on the acquisition of regular 2D $^1\text{H}, ^1\text{H}$ NOESY spectra. The principle of trNOE is based on the dependence of the NOE with respect to molecular motion (Figure 7), i.e. positive NOEs for small molecules in the extreme narrowing limit and negative

NOEs for big molecules in the slow tumbling limit. Small ligands show positive NOEs if they are free in solution. But in presence of a receptor, they can engage binding, which in turn results in a sign change of the ligands' NOEs because it “adapts” the correlation time properties of the large receptor, if the K_D is fast enough (fast exchange on the NMR time scale i.e. only one signal set for bound and free ligand is required for trNOE). Therefore, two measurements have to be carried out for trNOE. The first one contains only the ligand and yields small positive NOEs. The second measurement, acquires data of ligand and receptor in solution and if binding occurs, the small positive NOEs of the free ligand are overridden by the strong positive NOEs of the bound portion to the receptor. Via in detail investigations of the obtained trNOEs, one can extract information about the bound conformation of the investigated ligand. In addition, just like other ligand based NMR methods, trNOE has no size restrictions for the investigated target receptor.

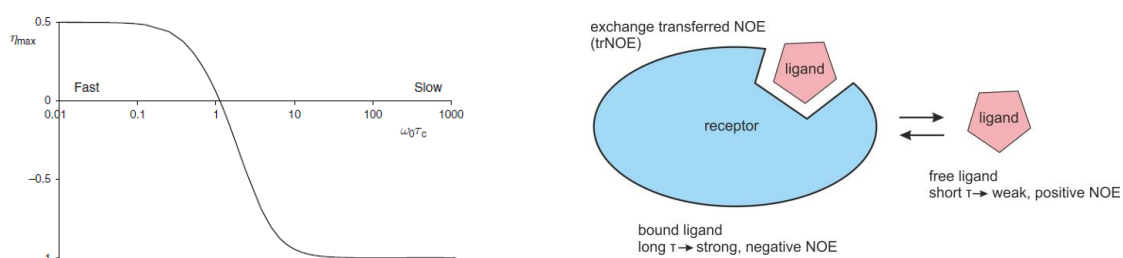


Figure 7: A) Variation of the NOE sign as a function of molecular tumbling rate. For small molecules in the extreme narrowing limit one obtains positive NOEs, while negative NOEs are obtained for big molecules in the spin-diffusion limit. B) Principle of the exchange transferred NOE (trNOE). A free, small ligand yields weak, positive NOEs. Upon presence of a binding receptor, the NOE sign changes because the ligand inherits the properties of the large slow tumbling receptor. A) Reproduced with permission from [94].

6.1.1.3 Water-ligand observed via gradient spectroscopy (WaterLOGSY)

Water-ligand observed via gradient spectroscopy (WaterLOGSY) is based on NOE driven magnetization transfer to the investigated ligand and is mostly applied to distinguish binding and non-binding ligands to a biological target^[95–105]. But instead of magnetization transfer from the biological target to the ligand like in STD, WaterLOGSY uses selective excitation of the bulk water inside the solution to transfer the magnetization and takes advantage of the inherently different properties of small and big molecules in NOE experiments (comparable to trNOE)^[95,101]. The bulk water magnetization is transferred intermolecular during the NOESY mixing time towards the

bound ligand by different mechanisms (Figure 8): First, magnetization transfer from water, which is potentially squeezed between the receptor-ligand binding sites. Second, magnetization transfer from water, which is located in different receptor cavities. Third, chemical exchange between H₂O and the NH and OH protons of the receptor and fourth, direct excitation of the H_α protons of the receptor (similar chemical shift to the H₂O signal resulting in magnetization propagation through the receptor via spin diffusion). All four processes are active during the mixing time and lead to discrimination of binding and non-binding ligands due to different NOE signs. Binders adapt the long correlation times of the receptor and hence, show negative NOE signs. In contrast, non-binders keep their inherently fast correlation times and as a result their intermolecular NOEs to water will be positive. It is to be noted, that to keep the negative NOE of the binder their longitudinal relaxation time (T₁) has to be bigger than their K_{Doff} from bound to unbound state.

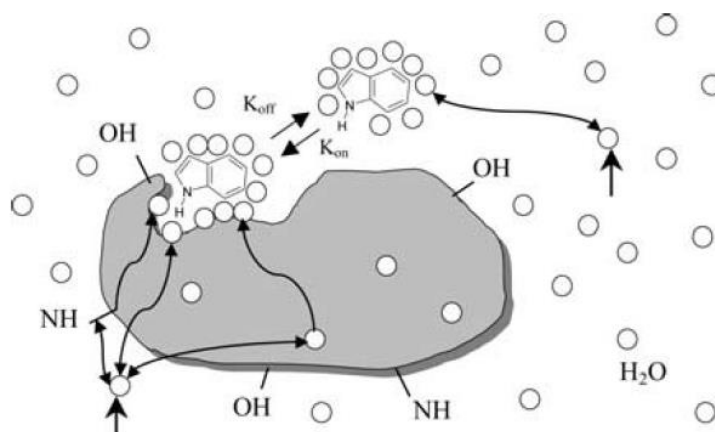


Figure 8: Schematic representation of Water-ligand observed via gradient spectroscopy (WaterLOGSY). Excitation of the bulk water (circles) and potential magnetization transfer pathways are indicated with black arrows. Reproduced with permission from ^[101].

In principle, WaterLOGSY operates like a regular selective 1D ¹H¹H NOESY (Figure 9 top) achieving selective excitation of the water by pulsed field gradients and a selective 180 refocusing pulse (e.g. Gauss or re-BURP). The NOESY mixing time is usually rather long and most reported values are between 1-2 seconds^[96,98,102,105]. Solvent suppression of the water signal is necessary as WaterLOGSY needs the H₂O in solution and does not work with deuterated solvents such as D₂O. For the standard Bruker pulse sequence solvent suppression is achieved via excitation sculpting, but versions using WET or Watergate have been reported as well^[96,97].

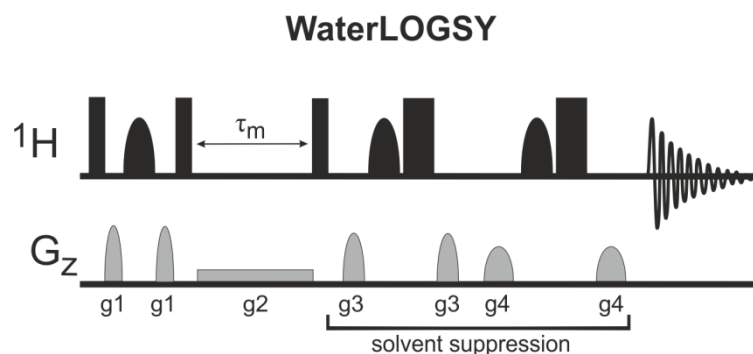


Figure 9: Exemplary pulse sequence for water-ligand observed via gradient spectroscopy (WaterLOGSY).

WaterLOGSY is more sensitive than STD NMR experiments by at least a factor of two and can be more sensitive up to an order of magnitude depending on the system^[60] and can also be used for a broad range of ligand affinities (K_D values from 10^{-3} to 10^{-9} M). In contrast, WaterLOGSY usually doesn't give any insight into the binding mode of the investigated ligand(s), although some binding information could be figured out in some cases^[99].

6.1.1.4 Inter-ligand NOE pharmacophore mapping (INPHARMA)

Inter-ligand NOE pharmacophore mapping (INPHARMA) presents one of the newest methods for the detection of receptor-ligand interactions by NMR^[90,106–116]. It allows to determine the relative binding mode of competitively binding ligands inside an active center^[110]. Similar to trNOE, INPHARMA doesn't require special pulse sequences and solely relies on the interpretation of regular 2D ^1H , ^1H NOESY spectra^[111]. An INPHARMA measurement is usually conducted with two competitively binding ligands that possess modest to weak binding properties (K_D 10^{-3} - 10^{-6}) in presence of a common biological target (Figure 10; A)^[90,107]. During the NOESY mixing time, the first ligand (ligand 1) binds to the target and transfers magnetization to the receptor via NOE (Figure 10 B). After the residence time, the ligand 1 dissociates from the receptor, while the receptor retains the magnetization from ligand 1 and spreads it via spin diffusion (Figure 10; C). Then the second ligand (ligand 2) binds to the target and receives the magnetization from ligand 1 through the receptor via NOE (Figure 10; D). The resulting NOESY spectrum (Figure 10; E schematic representation) yields interligand NOEs between ligand 1 and 2 in addition to the regular intramolecular NOEs, although both ligands were never in direct spatial proximity to one another. The interligand NOEs can be used to determine the relative position of ligand 1 and 2 inside the active center.

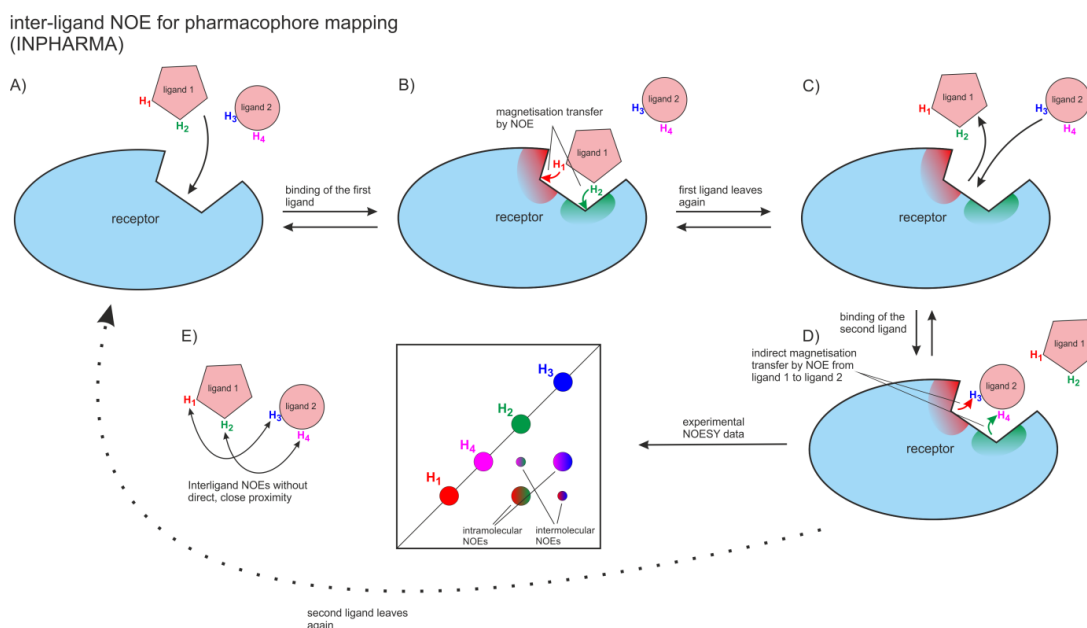


Figure 10: Schematic presentation of the inter-ligand NOE pharmacophore mapping (INPHARMA). The method requires two competitively binding ligands (with similar affinity) which bind to the biological target alternately. A) Both ligands (1 and 2) are in solution with the receptor. B) Ligand 1 binds to the receptor and transfers magnetization via NOE. C) Ligand 1 dissociates and ligand 2 can bind (magnetization of ligand 1 is retained inside the receptor). D) Ligand 2 receives the magnetization of ligand 1 indirectly through magnetization transfer with the receptor. D) The resulting NOESY spectrum shows interligand NOEs in addition to intramolecular NOEs due to the indirect magnetization transfer of ligand 1 to ligand 2 inside the binding pocket.

On a practical note, INPHARMA requires at least two competitively binding ligands with K_D s' of the same order of magnitude (the more similar the better)^[90]. Furthermore, INPHARMA measurements take long measurement times (up to days) and hence, require very stable biological systems^[90]. But in spite of these requirements, INPHARMA has one major advantage over any other ligand based NMR method for the detection of receptor-ligand interactions; it is unaffected by non-specific interactions. In addition, INPHARMA is also unaffected by the molecular size of the biological target molecule.

6.1.1.5 Relaxation based methods: T1p and T2

Similar to WaterLOGSY and trNOE measurements, relaxation based methods take advantage of intrinsically different properties of fast tumbling (small) and slow tumbling (big) molecules^[49,50]. Figure 11 shows the dependence of spin-lattice (T1) and spin-spin relaxation on molecular tumbling rates (molecular size/weight). Whereas T1 is pretty

much insensitive to slow motion, T_2 is continuously affected and shortens with increasing molecular size. Hence, ligands usually have a long T_2 time, while the investigated receptors have very short T_2 times. Analogous to trNOE measurements, the properties of the large molecule can be inherited by the small molecule upon interaction. Therefore, two measurements are performed for relaxation based NMR methods to investigate receptor-ligand interactions. The first one is a regular T_2 measurement (CPMG) of only the ligand. The second one is a measurement with ligand and receptor. If binding occurs, the ligand should yield a significantly lower T_2 value because of interaction with the receptor (sometimes this interaction can be seen immediately due to line broadening of the ligand signals upon addition of the receptor because T_2 heavily contributes to the line width of a signal). $T_1\rho$ measurements act by the same principle but focus on the different relaxation properties of molecules in a spin lock and should yield similar results to the T_2 measurements. Just like other ligand based NMR methods, the relaxation techniques have no size restrictions for the investigated target receptor. In addition, it can be applied over a large range of K_D values ranging from 10^{-3} - 10^{-7} M.^[49]

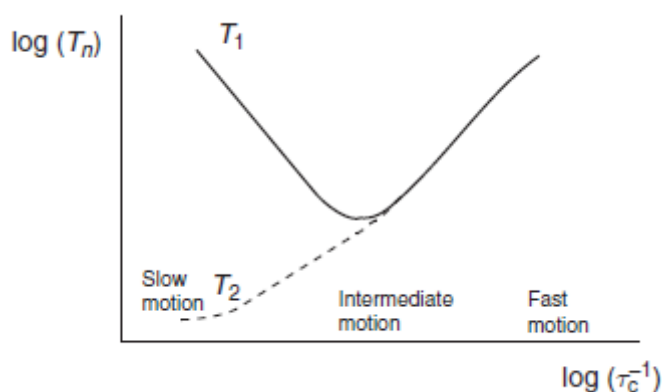


Figure 11: Dependence of spin-lattice (T_1) and spin-spin (T_2) relaxation on molecular tumbling rates (molecular size/weight). Reproduced with permission from ^[94].

6.2 Results and Discussion

6.2.1 Investigations of the Histamine-H2 receptor by ligand based NMR methods

Despite the recent success of NMR in the field of drug discovery, GPCRs and other membrane bound structures (e.g. ion channels, tyrosine kinases etc.) have not been in the center of attention for investigations yet. This is due to several reasons. First, GPCRs are not easily expressed in cell systems in high quantities. Second, stability of the expressed GPCRs in e.g. SF9 or HEK cells is most often only guaranteed for a couple of hours. Third, extraction of the expressed GPCRs out of the parental membrane and subsequent incorporation of the GPCRs into artificial membranes or lipid-bilayer nanodiscs to guarantee their stability is extremely challenging and can take years. Nevertheless, some reports in literature describe the successful investigation of GPCRs in parental membrane systems by NMR^[90,117]. In face of these challenges and recent advancements for NMR guided GPCR investigations, our group also tackled an ambitious project to survey GPCR-ligand interactions by NMR in parental membrane systems. The project was organized in close cooperation with the working group Buschauer (Department of Pharmacy), which focusses on the investigation of Histamine receptors (Histamine H1-H4 receptors; all GPCRs). The main goal was defined as the investigation of overexpressed Histamine-receptors (GPCRs) in parental membrane systems (obtained from cells overexpressing the receptor) by STD, WaterLOGSY and INPHARMA ligand based receptor-ligand interaction NMR methods.

6.2.2 The Histamine receptor test system for the ligand based NMR experiments

The recombinant, human Histamin-H2 receptor (hH2R) linked to a G_{saS}-protein was chosen as receptor system for overexpression. This fusion protein (hH2R-G_{saS} / H2R) was available in the Department of Pharmacy and could be readily overexpressed in baculovirus infected SF9 insect cells. The cells were broken down according to membrane preparation instructions described in section 6.4.1. The resulting parental cell membranes were stored in 1 mL solutions with a 2-amino-2-(hydroxymethyl)propane-1,3-diol (TRIS-based) buffer at -80 °C. Furthermore, membrane preparations, which did not incorporate hH2R-G_{saS}, were prepared for blank tests and/or for comparison. Determination of the total protein content yielded 1115 µg/mL for the membranes with receptor and 1126 µg/mL for the membranes without receptor, respectively. Prior investigations in the Department of Pharmacy showed that the expressed receptors usually constitute ~3-6 % of the total protein content. Stability of the receptor inside the

parental membrane preparation was determined by GTP γ S-assays (see 6.4.2) yielding a stable receptor for 6-9 hours at a temperature range from 4-37 °C.

The ligands chosen for the investigation consisted of Histamine (natural neurotransmitter of the H₂R) and a selection of commercially available H₂R antagonists (Figure 12). These included Ranitidine, Cimetidine and Famotidine¹⁸. All ligands have binding properties that are within K_D-limitations for common receptor-ligand based NMR methods (ligands 10⁻⁷-10⁻⁸ M (requirement for NMR methods 10⁻³-10⁻⁸ M; see 6.1.1).^[118] In addition, due to the presentation of the H₂R antagonists as commercial drugs, in depth investigations and literature can be consulted to validate the obtained results from the NMR experiments.

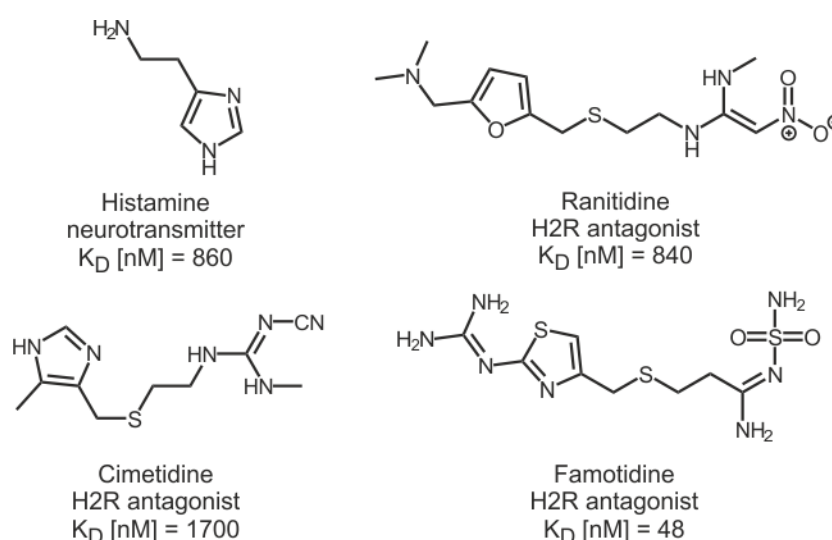


Figure 12: H₂R ligands, which were chosen for the investigation of hH₂R-G_{saS} incorporated in parental membrane preparations by NMR. Histamine presents the natural occurring neurotransmitter in our body for H₂R, while Ranitidine, Cimetidine and Famotidine are available as commercial H₂R antagonists on the market.

Due to the weak solubility of the ligands in H₂O/D₂O, stem solutions containing 100 mM of the respective ligand in DMSO-_{d6} were prepared for all NMR experiments. Structure and purity of all ligands was determined straight forwardly by NMR (see 6.4.3).

¹⁸ In the beginning of the project, Buriamide was also one of the investigated ligands but was discarded because it's not commercially available (at reasonable cost) and was only available in low amounts via synthesis. Furthermore, Buriamide did not yield any more insights/results compared to the other H₂R antagonists.

6.2.3 Ligand based NMR investigations of the membrane bound hH2R-G_{sas}

6.2.3.1 INPHARMA experiments

INPHARMA experiments (see 6.1.1.4) were conducted as a first approach to investigate the membrane preparations by NMR. Most INPHARMA measurements were executed by Dr. Maxime Melikian. The experimental design was based on the procedures presented by Bartoschek *et al.*, which investigated receptor-ligand interactions of the GPR40 fatty acid binding receptor by INPHARMA^[90]. Here, ligand concentrations were in the μM range (100-200 μM) and the K_D values of the investigated ligands were 340 and 280 nM respectively. For our experiments, we chose Ranitidine and Cimetidine as a first ligand pair for investigation. The concentration of both ligands was set to 500 μM . The experiment used one vial of the membrane solution (=1115 $\mu\text{g}/\text{mL}$ protein content), which was thawed and directly transferred to the NMR tube with addition of 5 % D_2O for the NMR lock. Unfortunately, this INPHARMA experiments showed no interligand NOEs. Subsequent INPHARMA experiments, in which ligand and membrane concentrations were varied also did not yield any interligand signals. This was probably due one major reason. The membrane stability was not high enough to carry out the relative insensitive INPHARMA experiments successfully. According to Bartoscheck *et al.* and personal communication the NOESY spectra were acquired with at least 128 scans and at least 512 points in the direct dimension^[90]. Rough estimations of the measurement time yield an experiment duration of ~2 days for one NOESY spectrum, which vastly exceeds the stability of our membrane system (6 – 9 hours). As a consequence, successful INPHARMA experiments were deemed inaccessible for our system and the project focus was switched towards STD as a more sensitive method for the detection of receptor-ligand investigations.

6.2.3.2 Experimental considerations for STD experiments with the H2R membrane system

The initial INPHARMA experiments revealed some serious preparative issues with the membrane system. Next to the low stability of the receptor inside the membranes (6-9 h), the thawed membrane “soup” would rapidly precipitate and “clump” together at the bottom of the NMR tube (Figure 13; top). As a result, even the more sensitive STD could hardly be conducted for reproducible investigations. Therefore, various steps for the sample preparation were added and iterated to prevent the rapid membrane precipitation. First, the membranes were extensively homogenized (3 times with of 0.9

mm syringe and 20 times with a 0.35 mm diameter syringe) prior to the transfer into the NMR tube. An extruder system, which used 400 nm and 100 nm membranes, was also tested to increase homogenization. This approach led to highly homogeneous solutions but the method was hardly reproducible, because the membrane solution was not suited for our extruder system. As a result, high amounts of protein were lost and got “stuck” inside the extruder apparatus. Therefore, this approach was not followed up upon. Secondly, Venkitakrishnan *et al.* mentioned that the initial membrane preparation (see 6.4.1) can leave residual DNA strands in solution, which heavily proliferate the clumping process of the membranes^[59]. As a countermeasure, they added DNase to break down the residual DNA strands. We adapted this approach and also added 1 μL of DNase into the final solution (additionally 1 mM $\text{MgCl}_2 \cdot 6\text{H}_2\text{O}$ or $\text{CaCl}_2 \cdot 2\text{H}_2\text{O}$ was added to the respective buffer system for ideal performance of the DNase). And third, the regular 5 mm NMR tube was replaced by a 5 mm Shigemi tube. This also led to reduced membrane precipitation and additionally allowed for higher membrane concentration due to the decreased solvent requirements (300 μL instead of 450 μL). The culmination of homogenization, DNase and Shigemi tube resulted in a homogeneous membrane suspension, which only showed first signs of precipitation after 12 h (Figure 13; bottom). The time frame was enough to conduct STD experiments and well exceeded the stability of the receptor inside the membrane anyway. Hence, the sample preparation was not improved any further.

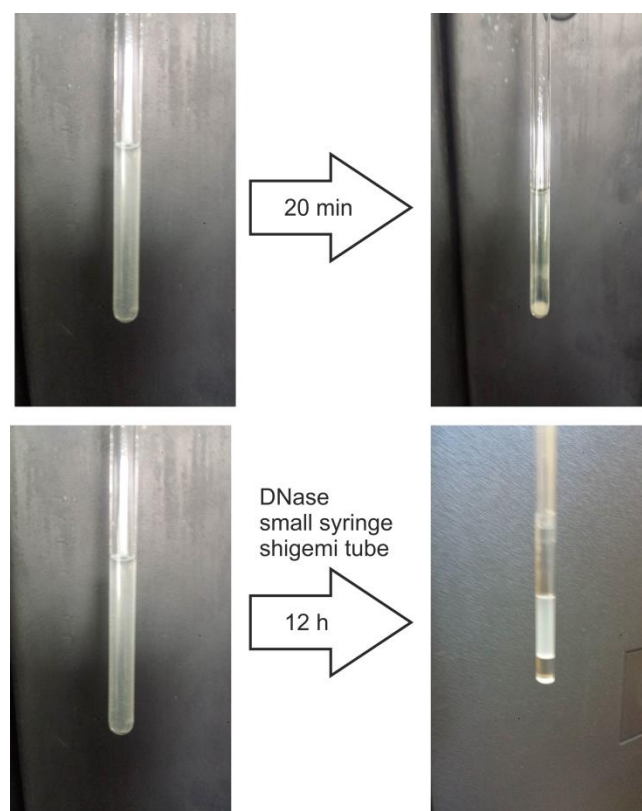


Figure 13: Top: Straight forward NMR sample preparation of the membranes via simple transfer and rough homogenization leads to a quick sedimentation and “clumping” of the membranes within a few minutes. Bottom: improved sample preparation. Use of a DNase to remove residual DNA strands from the membrane preparation (see 6.4.1), improved homogenization with a 0.35 mm diameter syringe and switching from a regular 5 mm NMR tube to a 5 mm Shigemi tube lead to a homogeneous suspension for ~12 hours.

Besides the preparative aspect of sample preparation, the first INPHARMA experiments also revealed that the composition of the storage buffer of the membranes was not ideal for NMR measurements. The membrane preparations are stored in binding buffer, which contains a high amount of non-deuterated tris-(hydroxymethyl)-aminoethane (TRIS) (see 6.4.1). As a result, the NMR spectra always contained a very intense signal from TRIS and the full NMR sensitivity could not be utilized due to a significantly reduced receiver gain (Figure 14). Double solvent suppression of the water and TRIS signals was successfully tested; but was not deemed ideal because the TRIS signal is very close to some ligand resonances, which also get suppressed or diminished as a result. Therefore, the buffer system was completely switched out for a phosphate (PBS) based buffer, which contained 137 mM NaCl, 10 mM Na₂HPO₄, 2.7 mM KCl and 1 mM KH₂PO₄ (and 1 mM MgCl₂·6H₂O or CaCl₂·2H₂O for the DNase) in D₂O. The composition was

chosen according to Venkitakrishnan *et al.*, which successfully investigated membrane bound receptors in parental membrane preparations before^[59]. With this change the receiver gain could be increased by an order of magnitude. Furthermore, it was previously reported that switching from H₂O to D₂O increases the saturation effect in STD experiments by at least a factor of two due to reduced spin diffusion from the bulk water to the investigated biological target^[60,119,120].

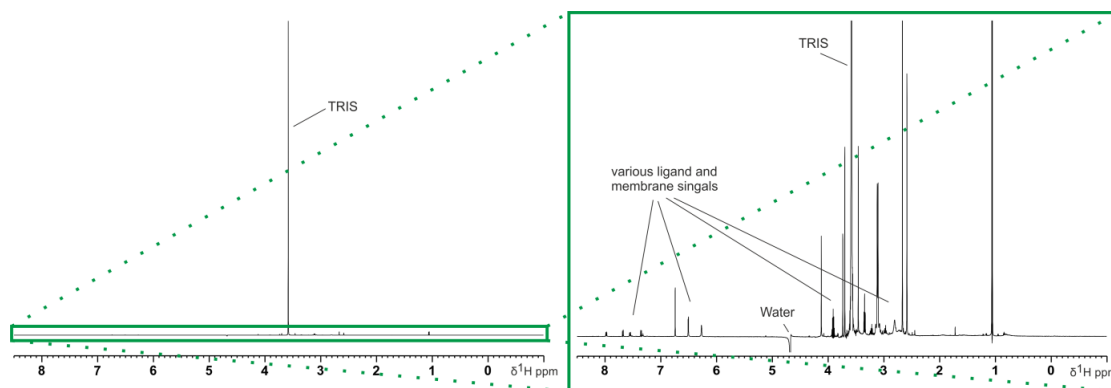


Figure 14: Left: Exemplary ¹H NMR spectrum of the membrane preparation inside the binding buffer after direct transfer into the NMR. Right: Cutout of the spectrum on the left showing the inconvenience of TRIS inside the solution.

6.2.3.3 STD experiments with the H2R membrane system

Frist STD NMR experiments were carried out with the ligand Ranitidine in presence of membranes which incorporate the fusion protein hH2R-G_{saS}. The sample was prepared in PBS buffer according to the general procedure for STD NMR (final total protein concentration: 1115 µg/mL) and Ranitidine concentration was chosen to be 1 mM, which is in the common concentration range for STD experiments^[59,68,76,80,82,120]. For the STD measurements an on-resonance frequency (f_{on}) of 0 Hz and an off-resonance (f_{off}) of -16000 Hz was chosen. Saturation time was set to 2 seconds and consisted of a train of forty 50 ms Gauss pulses. The left side of Figure 15 shows the resulting STD difference spectrum and the proton reference spectrum of Ranitidine in the membrane suspension. The STD difference spectrum shows clear STD signals for most Ranitidine resonances. Control experiments showed that the STD effects are not due to direct saturation of Ranitidine (data not shown). Nevertheless, for the investigation of membrane bound receptors it is necessary to repeat the STD experiment with membranes which don't contain the investigated biological target to determine if some or all of the STD signals are due to non-specific interaction with the membrane or other components in the membrane suspension. The right side of Figure 15 shows the corresponding control

experiment of Ranitidine in the presence of membranes which don't incorporate hH2R-G_{saS}. All experimental procedures (preparation; and NMR acquisition) were similar to the experiments with hH2R-G_{saS}. Unfortunately, the STD spectrum with hH2R-G_{saS} is nearly identical to the spectra without the receptor (Figure 15). In fact the STD signals in the system without H2R are even slightly stronger than with H2R. This indicates that all STD signals are dominated by non-specific interactions with the membrane or other compounds in the membrane suspension and not, or just in minor amounts due to selective binding to H2R. Furthermore, although the protein content of both membrane preparations is nearly equal, the amount of phospholipids was never determined. Hence, the membranes without H2R could have higher amounts of phospholipids, which could explain the stronger STD signals due to non-specific interactions with (negatively charged) phospholipids. This would also make sense in terms of affinity; the bio lipids are generally charged negatively and Ranitidine possesses various hydrogen bond donors and is most likely charged positively at pH 7.4. Unfortunately, all other investigated ligands (Famotidine, Cimetidine and Histamine) also possess strong hydrogen donor capabilities and are most likely charged positively at pH 7.4. In addition, even measuring samples, which were several month old still yielded similar STD signals and intensities, further indicating that only non-specific interactions are the reason for the STD effects.

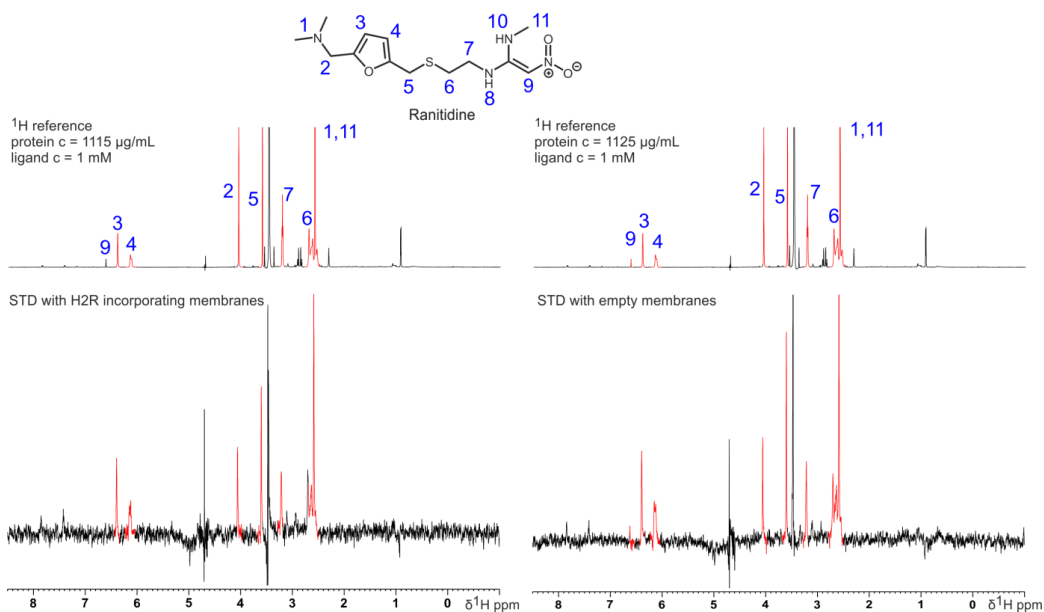


Figure 15: ^1H reference spectra (top) and corresponding STD difference spectra (bottom) of membranes with (left) and without (right) incorporation of hH2R- G_{saS} (overall protein content 1115 $\mu\text{g}/\text{mL}$ for membranes with hH2R- G_{saS} and 1125 $\mu\text{g}/\text{mL}$ for membranes without hH2R- G_{saS}) in PBS buffer. The experiments were carried out in presence Ranitidine (1 mM) STD parameters: NS = 1024; DS = 4; $t_{\text{sat}} = 2$ s D1 = 4 s; f_{on} : 0 Hz; f_{off} : -16000 Hz.

The issue of non-specific binding turned out to be the biggest issue of this project. Unfortunately, STD NMR cannot distinguish between specific and non-specific binding in any way. The same issue applies to other ligand-based techniques such as WaterLOGSY and relaxation based experiments as well¹⁹. Hence, switching the method was not a viable option. Although the first experiment didn't produce the desired results we continued with varying experimental conditions in hope to see differences between the membrane preparations with and without receptor. These included:

- High total protein concentration (>1200 $\mu\text{g}/\text{mL}$) with high ligand concentrations (> 1 mM)
- High total protein concentration (>1200 $\mu\text{g}/\text{mL}$) with low ligand concentrations (< 500 μM)
- Low total protein concentration (< 250 $\mu\text{g}/\text{mL}$) with high ligand concentrations (> 1 mM)

¹⁹ Albeit we also tested WaterLOGSY and relaxation methods; but to no surprise they yielded the same results as the STD measurements.

- Low total protein concentration (< 250 µg/mL) with low ligand concentrations (< 500 µM)
- Competition experiments of various ligands with the membranes, which included H2R
- Different temperatures to modulate the residence time of the ligands in the active center (283 – 310 K)
- Variation of all STD relevant STD parameters (f_{on} , +11 – -4 ppm; f_{off} , +300 – -40 ppm; relaxation delays, 2 – 90 s; saturation power and duration)
- Additional buffer systems (e.g. PBS sucrose buffer) and pH variations (pH 6 – 8)
- Further experiments not related to the H2R – H2R-ligand system presented above (e.g. living cells, which did or did not incorporate H2R; measurement of small peptides as ligands; STD screening of random small molecules to estimate which properties result in non-specific membrane interactions)

But in spite of these efforts, the problem of non-specific interactions could never be resolved and in it was never possible to clearly distinguish the membrane systems with and without receptor. Even competition experiments (see 6.2.3.3.5) did not show any effect. Chapter 6.2.3.3.1 – 6.2.3.3.5 shows exemplary spectra of the bullet points 1 – 5 and discusses them briefly. But in spite of not accomplishing the main goal, we could still deduct some relevant information for possible future systems and investigations. Especially the buffer screening and the STD screening of random molecules gave some hints for working systems. The PBS sucrose buffer did not show any non-specific interactions for the sucrose with the membrane, which suggests that sugar receptors would be a good target system for further investigations. The small molecule screening showed that especially highly functionalized and all positively charged molecules have non-specific interactions with the membrane. On the other hand, lowly functionalized molecules, which are neutral or negatively charged showed non-specific interactions with the membrane only rarely or none at all. These results are very much in line with previously successful systems of membrane preparations or living cells using sweetener molecules^[59], sugars^[68], fatty acid receptor agonists^[90] and steroidal compounds^[72] as ligands for the NMR investigations. All ligands were lowly functionalized and are neutral or negatively charged at pH 7.4. This further underlines that the absence of non-specific interaction is the most important prerequisite for investigations of biological targets in parental membranes with NMR. In addition, we could show that membranes, which do

not possess the investigated receptor are not necessarily ideal blank tests, because if non-specific binding is present it can vary between two different membrane preparations, because the total protein and bio lipid concentration can be entirely different. Hence, competition experiments with a literature known or the natural ligand seem to be the best choice to exclude non-specific interactions. In total for STD studies we would recommend a series of four STD experiments to completely rule out non-specific interactions and/or direct saturation of the ligands.

- First, only the ligand in the buffer system to rule out any direct saturation effects etc.
- Second, the ligand in presence of empty membranes to check for non-specific interactions.
- Third, the ligand in presence of membranes, which contain the respective receptor to investigate the ligand-receptor interactions.
- And fourth, ligand-ligand competition experiments with a second, ideally literature known ligand in presence receptor containing membranes to verify that the specific binding is at the correct active site.

Additionally, we would recommend neutral lowly functionalized ligands for the investigation of receptors in parental membrane suspension and/or living cells. Unfortunately, to our knowledge, all H2R ligands are positively charged at pH 7.4 and/or are highly functionalized and possess various hydrogen donor and acceptor capabilities.

6.2.3.3.1 STD with high protein and high ligand concentration

The STD experiments with high protein (>1200 µg/mL) and high ligand (> 1 mM) concentrations yielded by far the strongest STD signals. Figure 16 depicts the ¹H and STD spectra of 5 mM Famotidine in presence of membranes containing H2R (total protein concentration 2649 µg/mL) and empty membranes (total protein concentration 2675 µg/mL). Already after 32 scans one can detect clear STD signals, but they show similar intensities for the measurements with and without receptor.

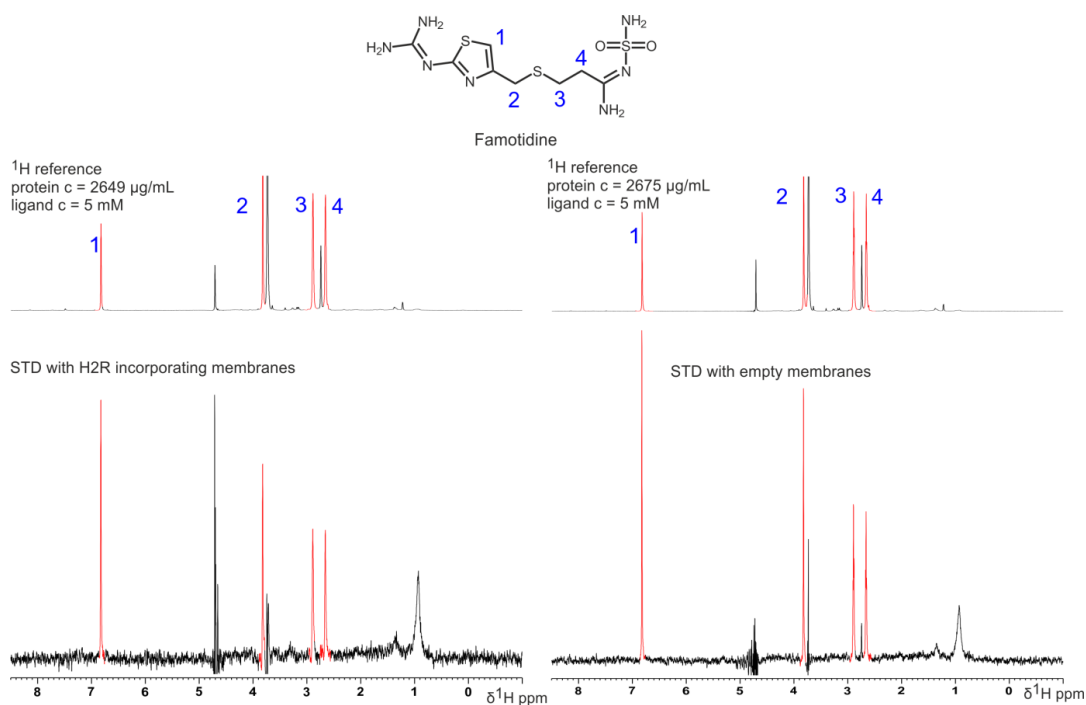


Figure 16: ¹H reference spectra (top) and corresponding STD difference spectra (bottom) of membranes with (left) and without (right) incorporation of hH2R-G_{saS}. The experiments were carried out in presence of a high Famotidine concentration (5 mM) and high overall protein content (2649 µg/mL for membranes with hH2R-G_{saS} and 2675 µg/mL for membranes without hH2R-G_{saS}) in PBS buffer. STD parameters: NS = 32; DS = 4; t_{sat} = 3 s D1 = 6 s; f_{on}: 735 Hz; f_{off}: 32000 Hz.

6.2.3.3.2 STD with high protein and low ligand concentration

The STD experiments with high protein (>1200 µg/mL) and low ligand (< 500 µM) concentrations. Figure 17 depicts the ¹H and STD spectra of 300 µM Ranitidine in presence of membranes containing H2R (total protein concentration 3319 µg/mL) and empty membranes (total protein concentration 3351 µg/mL). It can be clearly seen that for both conditions similar STD effects are detected.

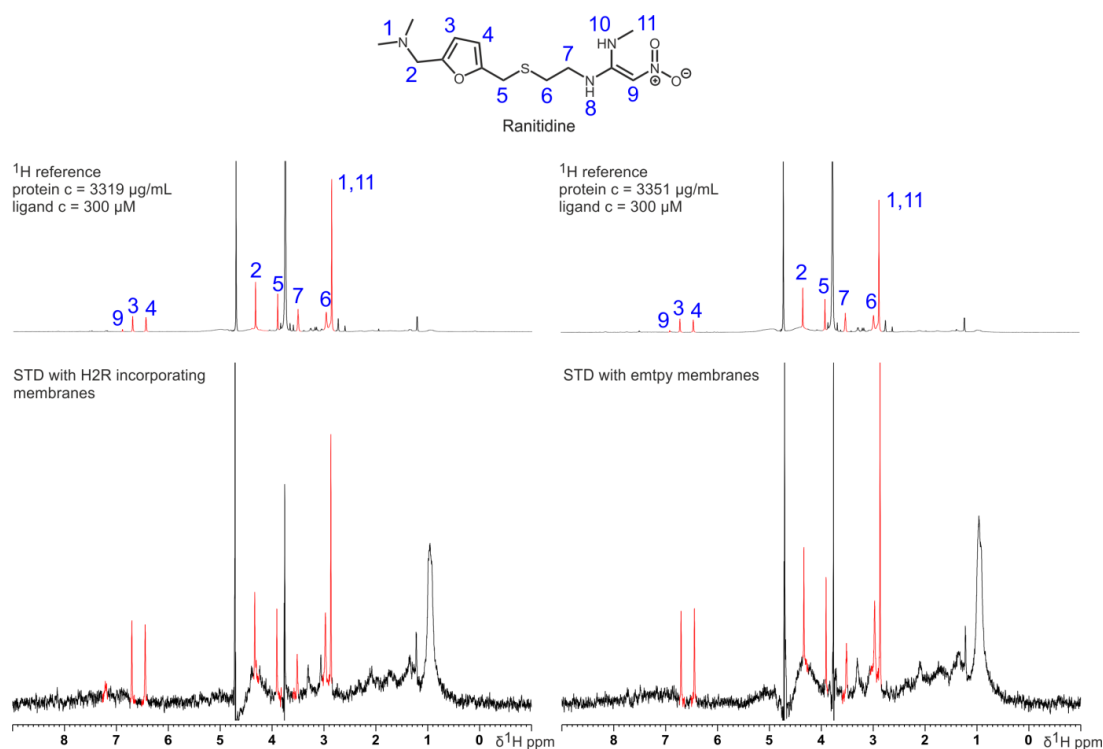


Figure 17: ¹H reference spectra (top) and corresponding STD difference spectra (bottom) of membranes with (left) and without (right) incorporation of hH2R-G_{saS}. The experiments were carried out in presence of a low Ranitidine concentration (300 μM) and high overall protein content (3319 μg/mL for membranes with hH2R-G_{saS} and 3351 μg/mL for membranes without hH2R-G_{saS}) in PBS buffer. STD parameters: NS = 64; DS = 4; t_{sat} = 3 s D1 = 7.5 s; f_{on}: 735 Hz; f_{off}: 32000 Hz.

6.2.3.3.3 STD with low protein and high ligand concentration

Figure 18 depicts the ¹H and STD spectra of 1 mM Ranitidine in presence of membranes containing H2R (total protein concentration 223 μg/mL) and empty membranes (total protein concentration 230 μg/mL). It can be clearly seen that for both conditions similar STD effects are detected.

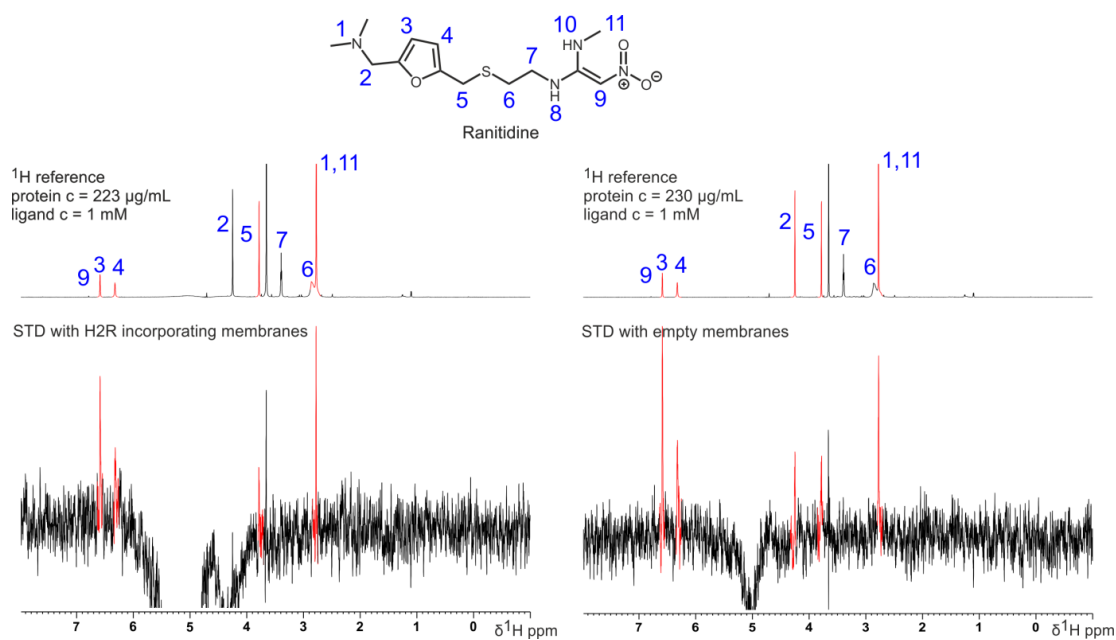


Figure 18: ^1H reference spectra (top) and corresponding STD difference spectra (bottom) of membranes with (left) and without (right) incorporation of hH2R-GsaS. The experiments were carried out in presence of a high Ranitidine concentration (1 mM) and low overall protein content (223 $\mu\text{g}/\text{mL}$ for membranes with hH2R-G_{saS} and 230 $\mu\text{g}/\text{mL}$ for membranes without hH2R-G_{saS}) in PBS buffer. STD parameters: NS = 1024; DS = 4; $t_{\text{sat}} = 2$ s D1 = 4 s; f_{on} : 0 Hz; f_{off} : -16000 Hz.

6.2.3.3.4 STD with low protein and low ligand concentration

Figure 19 depicts the ^1H and STD spectra of 300 μM Cimetidine in presence of membranes containing H2R (total protein concentration 112 $\mu\text{g}/\text{mL}$) and empty membranes (total protein concentration 113 $\mu\text{g}/\text{mL}$). It can be clearly seen that for both conditions similar STD effects are detected.

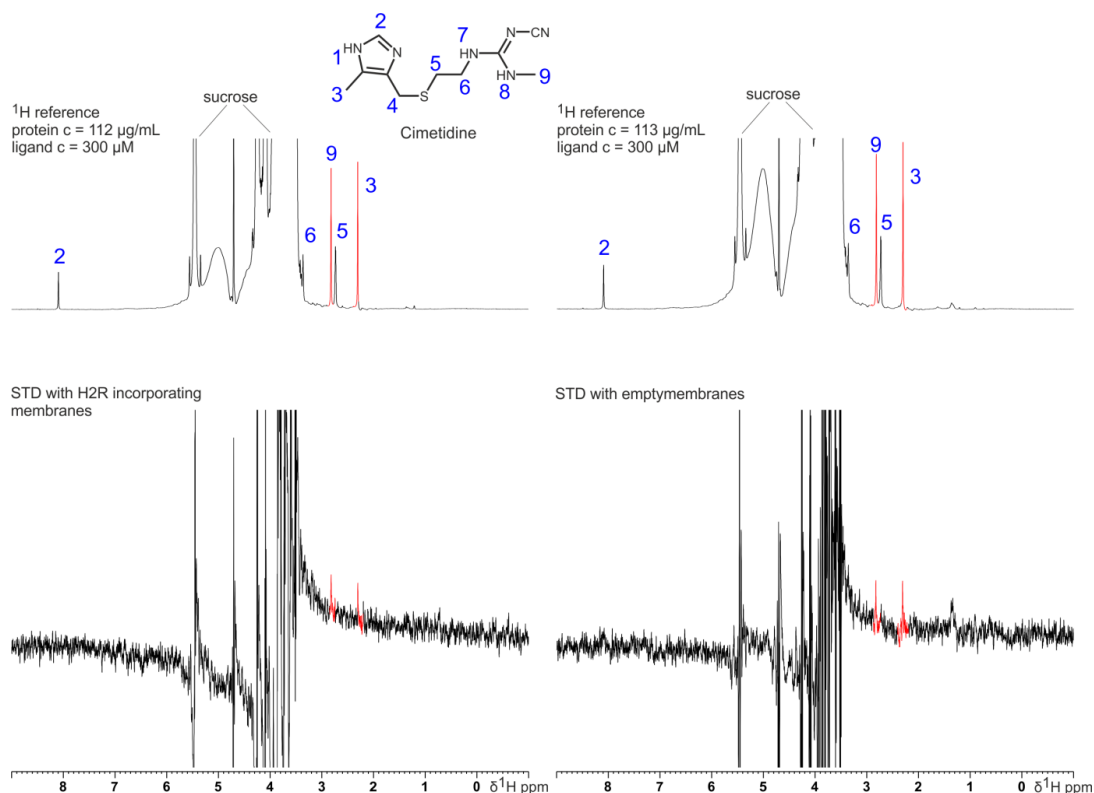


Figure 19: ^1H reference spectra (top) and corresponding STD difference spectra (bottom) of membranes with (left) and without (right) incorporation of hH2R-G_{saS}. The experiments were carried out in presence of a low Cimetidine concentration (300 μM) and low overall protein content (112 $\mu\text{g}/\text{mL}$ for membranes with hH2R-G_{saS} and 113 $\mu\text{g}/\text{mL}$ for membranes without hH2R-G_{saS}) in PBS buffer with 100 mM sucrose. STD parameters: NS = 64; DS = 2; t_{sat} = 3 s D1 = 60 s; f_{on} : 0 Hz; f_{off} : 24000 Hz.

6.2.3.3.5 STD competition experiments

One of the seemingly most promising approaches to see any difference in terms of specific and non-specific interactions were STD competition experiments. First, a STD spectrum of the first ligand (here: Ranitidine at 5 mM) is acquired in the presence of membranes with and without H2R (Figure 20; bottom spectra). Afterwards, a second ligand (here: Famotidine at 5 mM) is added and another STD spectrum is acquired for both samples with and without H2R (Figure 20; top spectra). Although, Famotidine is a by far stronger ligand than Ranitidine (K_D Famotidine 48 nM; K_D Ranitidine 840 nM) for the H2R and should completely “remove” Ranitidine from the active site of H2R, the STD spectra show no reduced STD intensities for the Ranitidine signals at all. This suggests that the contribution of specific binding is below the detection limit for the investigated conditions and is further confirmed by similar STD signals in the spectra with and without

H2R. In addition, it also shows that the options for non-specific interactions are not saturated even at a total ligand concentration of around 10 mM in solution.

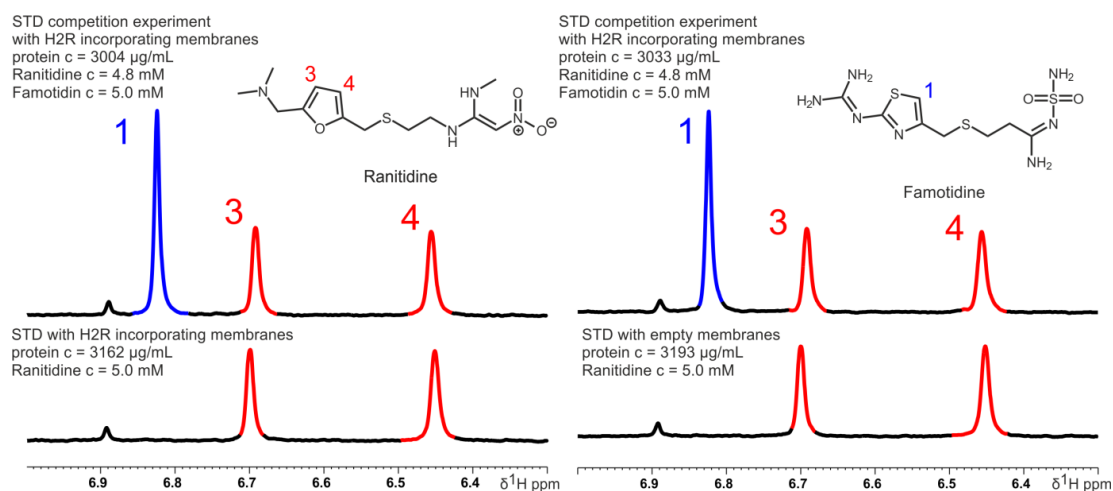


Figure 20: STD competition experiments showing the final STD difference spectra for membranes with (left) and without (right) incorporation of hH2R-G_{saS}. The bottom spectra depict the STD difference spectra of only Ranitidine (5 mM) in presence of membranes in PBS buffer. Upon addition of 5 mM Famotidine the STD difference spectra are not affected with or without receptor overexpression. STD parameters: NS = 64; DS = 4; $t_{\text{sat}} = 3$ s D1 = 7.5 s; f_{on} : 735 Hz; f_{off} : 32000 Hz.

6.3 Conclusion and outlook

In summary the main goal of the investigation of overexpressed Histamine-receptors (GPCRs) in parental membrane systems (obtained from cells overexpressing the receptor) by (STD, WaterLOGSY) and (INPHARMA) ligand based receptor-ligand interaction NMR methods was not successful. Here, the main issue was lacking membrane receptor stability and the incapability of STD, WaterLOGSY, T1 ρ and T2 experiments to distinguish specific and non-specific interactions. Nevertheless, we greatly improved sample preparation and reduced membrane precipitation and clumping significantly. As result we gained homogeneous membrane suspensions for ~12 hours. In addition, we gained some clear insight into why the project did not work. Positive charges and highly functionalization of ligands resulting in various hydrogen donor and acceptor properties are absolutely detrimental for the investigation of receptors in parental membrane systems and living cells. Furthermore, we got some hints that neutrally charged and lowly functionalized molecules are ideal candidates and necessary for investigations of those systems by NMR.

6.4 Supporting Information

6.4.1 Membrane preparation of the SF9 cell membranes

Cell culture: 50 mL cell suspension containing 3 Mio. cells/mL is infected with 500 µL (1:100) baculovirus stock solution. Afterwards the suspension is shaken for 48 h and examined via optical microscopy.

Membrane preparation: The infected cell suspension is centrifuged 100 rpm, 10 min. at 4 °C. Then the supernatant is discarded and PBS-buffer is added to the remaining cell pellet. The PBS-buffer-cell mixture is suspended and centrifuged again for 10 min. at 4 °C. The resulting pellet is suspended in 15 mL Lysin-buffer and homogenized in a Dounce-homogenizator under ice cooling (note: from here on every step is conducted under ice cooling). Afterwards, the obtained suspension is centrifuged 500 rpm, 10 min. at 4 °C. The supernatant is collected and again centrifuged 18.000 rpm, 20 min at 4 °C. Here, the obtained supernatant is discarded, the pellet is suspended again in 20 mL Lysin-buffer and centrifuged 18.000 rpm, 20 min. at 4 °C. Afterwards, the supernatant is discarded yet again and pellet is suspended and homogenized with Binding-buffer. The resulting mixture was stored in 1 mL vials at -80 °C.

Protein concentration: Determination of protein concentration was achieved with DC-Protein-Assays (Bio-Rad.).

PBS-buffer: NaCl (100 mM), Na₂HPO₄ (80 mM), NaH₂PO₄ (20 mM).

Lysin-buffer: Tris/HCl (10 mM), PMSF (200 µM), Benzamidine (80 µM), Leupeptin (25 µM), protease-inhibitor (1 pill/100mL).

Binding-buffer: Tris (45 mM), MgCl₂ x 6 H₂O (500 µM), EDTA (1.25 mM), adjusted to pH = 7.5, stored at 4 °C.

6.4.2 GTPγS-assays

The membrane preparation for the [³⁵S]GTPγS assay was thawed. Reaction mixtures (total volume, 1 ml) contained Sf9 membranes expressing hH2R-G_{saS} proteins in binding buffer or PBS buffer (see membrane preparation) supplemented with 0.05% (w/v) bovine serum albumin, 1 mM GDP, and 1 nM [³⁵S]GTPγS. Reaction mixtures additionally contained water and Histamine or Famotidine at a saturating concentration (100 µM for Histamine and 10 µM for Famotidine respectively). Incubations were

conducted for 90 min. at 25°C and shaking at 250 rpm. Bound [^{35}S]GTP γ S was separated from free [^{35}S]GTP γ S by filtration through GF/C filters, followed by a washing procedure (3x2 ml of binding buffer at 4°C). Filter-bound radioactivity was determined by liquid scintillation counting.

The results indicated the same stability of the membranes in PBS and binding buffer at around 6-9 hours.

Further tests surveying different buffers, varying temperature (rt – 37°C), incubation of the ligand from the start, different concentration or no ion worsened or did not affect the stability of the receptor.

6.4.3 NMR reference spectra of the ligands for assignment and purity control

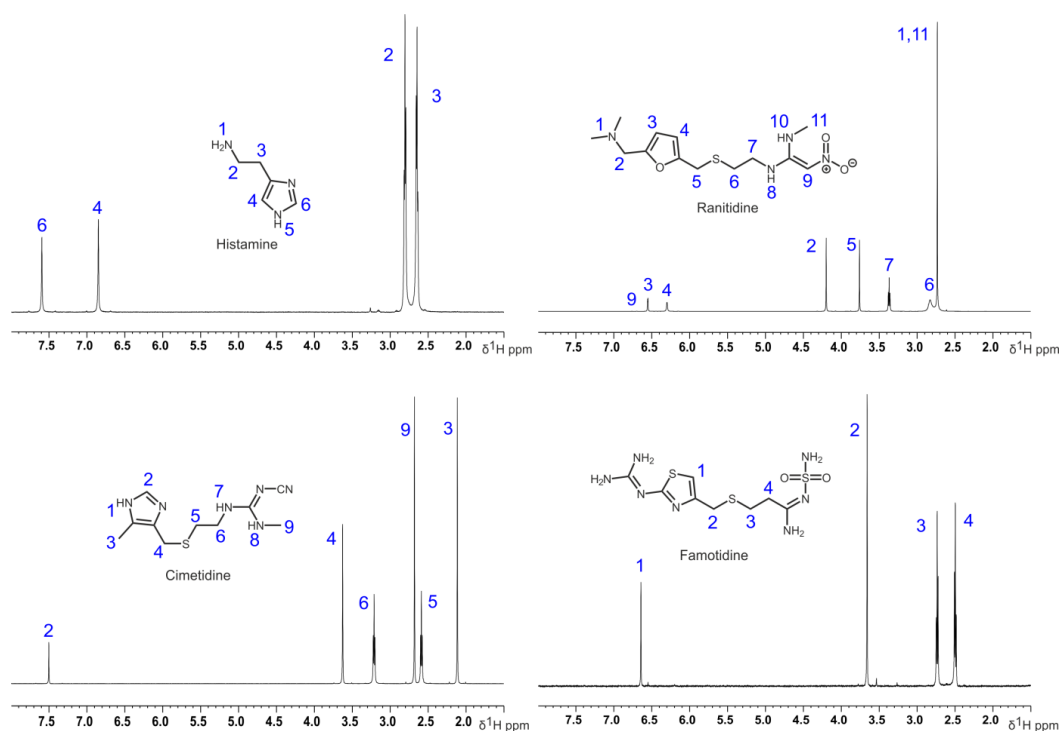


Figure 21: Assignment and numeration of the ligands Histamine, Ranitidine, Cimetidine, and Famotidine in D_2O . It is to be noted, that some ligands show more signals in H_2O because the exchanging protons become detectable to some degree.

6.4.4 General membrane sample preparation for NMR

6.4.4.1 General procedure

One 1 mL vial containing the membranes (see membrane prep 6.4.1) was quickly thawed in warm water. Afterwards, the mixture was centrifuged for 2 min. at 300 rpm. The supernatant was discarded and the residual membranes were suspended in the respective amount (100 μ L – 1 mL) of desired buffer system (usually PBS-D₂O; see below). The mixture was homogenized with a regular 0.9 mm syringe three times and 20 times with a 0.35 mm diameter syringe. Then the mixture was transferred into a 5 mm shigemi NMR tube and the respective amount of ligand stem solution(s) was added. Measurement of the sample was conducted directly after the sample preparation.

PBS buffer: NaCl (137 mM), Na₂HPO₄ (10 mM), KCl (2.7 mM), KH₂PO₄ (sometimes 1 mM MgCl₂·6H₂O or CaCl₂·2H₂O) in H₂O or D₂O. The PBS buffer was adjusted to pH 7.4 using highly diluted amounts of HCl or NaOH (pH was not corrected for isotopic effect for D₂O)

6.4.4.2 Other procedures

In some cases the 1 mL vial containing the membranes (see membrane prep. 6.4.1) was thawed and the solution was directly transferred into the NMR tube. Then ligand stem solution(s) and 5 % D₂O were added. Measurement of the sample was conducted directly after the sample preparation.

In some cases, the homogenization step was expanded with the introduction of an extruder. Here, the membranes were additionally pressed through 100 – 400 nm filter membranes. But a lot of membrane is lost in this process and the approach didn't show a high degree of reproducibility.

6.4.5 STD experiments

The standard STD pulse sequences *stdiffesgp*, *stdiffesgp.2* and *stdiffesgp.3* from Bruker were used for all investigations. The experiments were either conducted on a Bruker Avance 600 MHz NMR equipped with a forward BBO prodigy cryo-probehead or on a Bruker Avance 800 MHz equipped with an inverse TCI cryo-probe. Selective saturation of the receptor was achieved by a train of 50 ms Gauss pulses at frequencies from (-4 – +11ppm; at least 1600 Hz away from the nearest ligand frequency) for a total saturation time of 0.1 – 6 seconds. Off-resonance irradiation was usually set at (-16000-

32000 Hz or up to +240000 Hz). An excitation sculpting block ensured suppression of the water signal. On- and off-resonance spectra were acquired in a pseudo 2D fashion with a total number of scans ranging from 16 – 2048.

6.5 References

- [1] D. M. Clarrett, *Mo Med.* **2018**, *115*, 214–218.
- [2] E. Savarino, A. J. Bredenoord, M. Fox, J. E. Pandolfino, S. Roman, C. P. Gyawali, *Nat. Rev. Gastroenterol. Hepatol.* **2017**, *14*, 665–676.
- [3] S. J. Spechler, R. M. Genta, R. F. Souza, *Am. J. Gastroenterol.* **2007**, *102*, 1301–1306.
- [4] P. Sharma, S. Wani, Y. Romero, D. Johnson, F. Hamilton, *Am. J. Gastroenterol.* **2008**, *103*, 2669–2680.
- [5] F. K. Friedenberg, M. Xanthopoulos, G. D. Foster, J. E. Richter, *Am. J. Gastroenterol.* **2008**, *103*, 2111–2122.
- [6] D. S. Sandhu, R. Fass, *Gut Liver* **2018**, *12*, 7–16.
- [7] C. P. Gyawali, P. J. Kahrilas, E. Savarino, F. Zerbib, F. Mion, A. J. P. M. Smout, M. Vaezi, D. Sifrim, M. R. Fox, M. F. Vela, et al., *Gut* **2018**, *67*, 1351–1362.
- [8] N. J. Talley, G. Richard Locke, M. McNally, C. D. Schleck, A. R. Zinsmeister, L. Joseph Melton, *Am. J. Gastroenterol.* **2008**, *103*, 12–19.
- [9] H. B. El-Serag, S. Sweet, C. C. Winchester, J. Dent, *Gut* **2014**, *63*, 871–880.
- [10] L. Patrick, *Altern. Med. Rev.* **2011**, *16*, 116–33.
- [11] M. A. C. de A. Henry, *ABCD. Arq. Bras. Cir. Dig. (São Paulo)* **2014**, *27*, 210–215.
- [12] M. F. Vaezi, *Diagnosis and Treatment of Gastroesophageal Reflux Disease*, Springer International Publishing, Cham, **2016**.
- [13] D. S. Strand, D. Kim, D. A. Peura, *Gut Liver* **2017**, *11*, 27–37.
- [14] C. Tosetti, I. Nanni, *World J. Gastrointest. Pharmacol. Ther.* **2017**, *8*, 180.
- [15] M. J. Smit, R. Leurs, A. E. Alewijnse, J. Blauw, G. P. Van Nieuw Amerongen, Y. Van De Vrede, E. Roovers, H. Timmerman, *Proc. Natl. Acad. Sci.* **2002**, *93*, 6802–6807.
- [16] K. Adelborg, J. Sundbøll, M. Schmidt, H. E. Bøtker, N. S. Weiss, L. Pedersen, H. T. Sørensen, *Clin. Epidemiol.* **2018**, *10*, 521–530.

- [17] J. W. Black, W. A. M. Duncan, C. J. Durant, C. R. Ganellin, E. M. Parsons, *Nature* **1972**, 236, 385–390.
- [18] S. Dove, S. Elz, R. Seifert, A. Buschauer, *Mini-Reviews Med. Chem.* **2012**, 4, 941–954.
- [19] R. C. Stevens, V. Cherezov, V. Katritch, R. Abagyan, P. Kuhn, H. Rosen, K. Wüthrich, *Nat. Rev. Drug Discov.* **2013**, 12, 25–34.
- [20] J. P. Overington, B. Al-lazikani, A. L. Hopkins, *Nat Rev Drug Discov.* **2006**, 5, 993–996.
- [21] J. L. Sharman, H. E. Benson, A. J. Pawson, V. Lukito, C. P. Mpamhanga, V. Bombail, A. P. Davenport, J. A. Peters, M. Spedding, A. J. Harmar, *Nucleic Acids Res.* **2013**, 41, 1083–1088.
- [22] H. B. Schiöth, M. C. Lagerström, *Nat. Rev. Drug Discov.* **2008**, 7, 339–357.
- [23] K. Kristiansen, *Pharmacol. Ther.* **2004**, 103, 21–80.
- [24] R. Fredriksson, M. C. Lagerström, L.-G. Lundin, H. B. Schiöth, *Mol. Pharmacol.* **2003**, 63, 1256–72.
- [25] L. M. Luttrell, *Mol. Biotechnol.* **2008**, 39, 239–264.
- [26] X. Du, Y. Li, Y.-L. Xia, S.-M. Ai, J. Liang, P. Sang, X.-L. Ji, S.-Q. Liu, *Int. J. Mol. Sci.* **2016**, 17, 144.
- [27] A. D. Attie, R. T. Raines, *J. Chem. Educ.* **1995**, 72, 119.
- [28] I. Guryanov, S. Fiorucci, T. Tennikova, *Mater. Sci. Eng. C* **2016**, 68, 890–903.
- [29] S. W. Hla, *Reports Prog. Phys.* **2014**, 77, 56502.
- [30] M. S. Dietz, F. Fricke, C. L. Krüger, H. H. Niemann, M. Heilemann, *ChemPhysChem* **2014**, 15, 671–676.
- [31] S. B. Gacasan, D. L. Baker, A. L. Parrill, *AIMS Biophys.* **2017**, 4, 491–527.
- [32] J. García-Nafría, Y. Lee, X. Bai, B. Carpenter, C. G. Tate, *Elife* **2018**, 7, 1–19.
- [33] S. Huber, F. Casagrande, M. N. Hug, L. Wang, P. Heine, L. Kummer, A. Plückthun, M. Hennig, *PLoS One* **2017**, 12, 1–19.
- [34] C. A. Shepherd, A. L. Hopkins, I. Navratilova, *Prog. Biophys. Mol. Biol.* **2014**, 116,

- 113–123.
- [35] S. Locatelli-Hoops, A. A. Yeliseev, K. Gawrisch, I. Gorshkova, *Biomed. Spectrosc. Imaging* **2013**, 2, 155–181.
- [36] A. Sergé, S. De Keijzer, F. Van Hemert, M. R. Hickman, D. Hereld, H. P. Spaink, T. Schmidt, B. E. Snaar-Jagalska, *Integr. Biol.* **2011**, 3, 675–683.
- [37] I. Böhme, A. G. Beck-Sickinger, *Cell Commun. Signal.* **2009**, 7, 1–22.
- [38] F. Ciruela, K. A. Jacobson, V. Fernández-Dueñas, *ACS Chem. Biol.* **2014**, 9, 1918–1928.
- [39] A. Kumar, A. Plückthun, *PLoS One* **2019**, 14, 1–25.
- [40] K. Liu, N. Southall, S. A. Titus, J. Inglese, R. L. Eskay, P. Shinn, C. P. Austin, M. A. Heilig, W. Zheng, *Assay Drug Dev. Technol.* **2010**, 8, 362–374.
- [41] R. Zhang, X. Xie, *Acta Pharmacol. Sin.* **2012**, 33, 372–384.
- [42] R. Geyer, U. Nordemann, A. Strasser, H. J. Wittmann, A. Buschauer, *J. Med. Chem.* **2016**, 59, 3452–3470.
- [43] Z. Yang, S. Han, M. Keller, A. Kaiser, B. J. Bender, M. Bosse, K. Burkert, L. M. Kögler, D. Wifling, G. Bernhardt, et al., *Nature* **2018**, 556, 520–524.
- [44] K. K. Kuhn, T. Ertl, S. Dukorn, M. Keller, G. Bernhardt, O. Reiser, A. Buschauer, *J. Med. Chem.* **2016**, 59, 6045–6058.
- [45] K. K. Kuhn, T. Littmann, S. Dukorn, M. Tanaka, M. Keller, T. Ozawa, G. Bernhardt, A. Buschauer, *ACS Omega* **2017**, 2, 3616–3631.
- [46] S. Dukorn, T. Littmann, M. Keller, K. Kuhn, C. Cabrele, P. Baumeister, G. Bernhardt, A. Buschauer, *Bioconjug. Chem.* **2017**, 28, 1291–1304.
- [47] R. Powers, *J. Med. Chem.* **2014**, 57, 5860–5870.
- [48] D.J. Abraham, *Burger's Medicinal Chemistry and Drug Discovery*, John Wiley & Sons, Inc., Hoboken, NJ, USA, **2003**.
- [49] B. Ross, T. Tran, P. Bhattacharya, D. M. Watterson, N. Sailasuta, *Curr. Top. Med. Chem.* **2011**, 11, 93–114.
- [50] T. Sugiki, K. Furuita, T. Fujiwara, C. Kojima, *Molecules* **2018**, 23, 1–27.

- [51] Y. Li, C. Kang, *Molecules* **2017**, *22*, 1399.
- [52] D.-W. Sim, Z. Lu, H.-S. Won, S.-N. Lee, M.-D. Seo, B.-J. Lee, J.-H. Kim, *Molecules* **2017**, *22*, 1347.
- [53] D. P. Frueh, A. C. Goodrich, S. H. Mishra, S. R. Nichols, *Curr. Opin. Struct. Biol.* **2013**, *23*, 734–739.
- [54] M. Mund, J. H. Overbeck, J. Ullmann, R. Sprangers, *Angew. Chem. Int. Ed.* **2013**, *52*, 11401–11405.
- [55] M. Mund, A. Neu, J. Ullmann, U. Neu, R. Sprangers, *J. Mol. Biol.* **2011**, *414*, 165–176.
- [56] C. Huang, C. G. Kalodimos, *Annu. Rev. Biophys.* **2017**, *46*, 317–336.
- [57] I. Shimada, T. Ueda, Y. Kofuku, M. T. Eddy, K. Wüthrich, *Nat. Rev. Drug Discov.* **2019**, *18*, 59–82.
- [58] C. Dalvit, A. Vulpetti, *J. Med. Chem.* **2019**, *62*, 2218–2244.
- [59] R. P. Venkitakrishnan, O. Benard, M. Max, J. L. Markley, F. M. Assadi-Porter, in *Membr. Protein Struct. Dyn.* (Eds.: N. Vaidehi, J. Klein-Seetharaman), Humana Press, Totowa, NJ, **2012**, pp. 47–63.
- [60] A. Antanasijevic, B. Ramirez, M. Caffrey, *J. Biomol. NMR* **2014**, *60*, 37–44.
- [61] Z. Ji, Z. Yao, M. Liu, *Anal. Biochem.* **2009**, *385*, 380–382.
- [62] M. Kramer, E. Kleinpeter, *J. Magn. Reson.* **2010**, *202*, 245–249.
- [63] J. L. Burger, K. M. Jeerage, T. J. Bruno, *Anal. Biochem.* **2016**, *502*, 64–72.
- [64] A. Bhunia, G. L. Chua, P. N. Domadia, H. Warshakoon, J. R. Cromer, S. A. David, S. Bhattacharjya, *Biochem. Biophys. Res. Commun.* **2008**, *369*, 853–857.
- [65] D. Bini, R. Marchetti, L. Russo, A. Molinaro, A. Silipo, L. Cipolla, *Carbohydr. Res.* **2016**, *429*, 23–28.
- [66] C. Chatterjee, B. Majumder, C. Mukhopadhyay, *J. Phys. Chem. B* **2004**, *108*, 7430–7436.
- [67] D. Potenza, F. Vasile, L. Belvisi, M. Civera, E. M. V Araldi, *ChemBioChem* **2011**, *12*, 695–699.

- [68] S. Mari, D. Serrano-Gómez, F. J. Cañada, A. L. Corbí, J. Jiménez-Barbero, *Angew. Chem. Int. Ed.* **2005**, *44*, 296–298.
- [69] Y. Xia, Q. Zhu, K. Jun, J. Wang, X. Gao, *Magn. Reson. Chem.* **2010**, *48*, 918–924.
- [70] P. Groves, K. E. Kövér, S. André, J. Bandorowicz-Pikula, G. Batta, M. Bruix, R. Buchet, A. Canales, F. J. Cañada, H. Gabius, et al., *Magn. Reson. Chem.* **2007**, *45*, 745–748.
- [71] B. D. Cox, A. K. Mehta, J. O. Diraddo, D. C. Liotta, L. J. Wilson, J. P. Snyder, *Biochem. Biophys. Res. Commun.* **2015**, 1–5.
- [72] A. Pereira, T. A. Pfeifer, T. A. Grigliatti, R. J. Andersen, *ACS Chem. Biol.* **2009**, *4*, 139–144.
- [73] M. T. Quirós, J. Angulo, M. P. Muñoz, *Chem. Commun.* **2015**, *51*, 10222–10225.
- [74] J. Ribeiro, T. Diercks, J. Jiménez-Barbero, S. André, H. Gabius, F. Cañada, *Biomolecules* **2015**, *5*, 3177–3192.
- [75] O. Cala, I. Krimm, *J. Med. Chem.* **2015**, *58*, 8739–8742.
- [76] A. Antanasijevic, C. Kingsley, A. Basu, *J. Biomol. NMR* **2016**, *64*, 255–265.
- [77] B. K. Gilsbach, A. C. Messias, G. Ito, M. Sattler, D. R. Alessi, A. Wittinghofer, A. Kortholt, *J. Med. Chem.* **2015**, *58*, 3751–3756.
- [78] A. Shirzadi, M. J. Simpson, Y. Xu, A. J. Simpson, *Environ. Sci. Technol.* **2008**, *42*, 1084–1090.
- [79] B. Claasen, M. Axmann, R. Meinecke, B. Meyer, *J. Am. Chem. Soc.* **2005**, *127*, 916–919.
- [80] A. Mallagaray, C. Rademacher, F. Parra, G. Hansman, T. Peters, *Glycobiology* **2017**, *27*, 80–86.
- [81] H. Coelho, T. Matsushita, G. Artigas, H. Hinou, F. J. Cañada, R. Lo-Man, C. Leclerc, E. J. Cabrita, J. Jiménez-Barbero, S.-I. Nishimura, et al., *J. Am. Chem. Soc.* **2015**, *137*, 12438–12441.
- [82] A. Bhunia, S. Bhattacharjya, S. Chatterjee, *Drug Discov. Today* **2012**, *17*, 505–513.
- [83] A. Albohy, M. R. Richards, C. W. Cairo, *Glycobiology* **2015**, *25*, 284–293.

- [84] A. Viegas, J. Manso, F. L. Nobrega, E. J. Cabrita, *J. Chem. Educ.* **2011**, *88*, 990–994.
- [85] B. Meyer, T. Peters, *Angew. Chem. Int. Ed.* **2003**, *42*, 864–890.
- [86] K. FURIHATA, S. SHIMOTAKAHARA, Y. SHIBUSAWA, M. TASHIRO, *Anal. Sci.* **2010**, *26*, 1107–1110.
- [87] D. Long, C. B. Marshall, G. Bouvignies, M. T. Mazhab-Jafari, M. J. Smith, M. Ikura, L. E. Kay, *Angew. Chem. Int. Ed.* **2013**, *52*, 10771–10774.
- [88] N. Lokesh, A. Seegerer, J. Hioe, R. M. Gschwind, *J. Am. Chem. Soc.* **2018**, *140*, 1855–1862.
- [89] M. F. Mesleh, W. A. Shirley, C. E. Heise, N. Ling, R. A. Maki, R. P. Laura, *J. Biol. Chem.* **2007**, *282*, 6338–6346.
- [90] S. Bartoschek, T. Klabunde, E. Defossa, V. Dietrich, S. Stengelin, C. Griesinger, T. Carlomagno, I. Focken, K. U. Wendt, *Angew. Chemie Int. Ed.* **2010**, *49*, 1426–1429.
- [91] C. Post, *Curr. Opin. Struct. Biol.* **2003**, *13*, 581–588.
- [92] M. Simčič, M. Hodošček, J. Humljan, K. Kristan, U. Urleb, D. Kocjan, S. G. Grdadolnik, *J. Med. Chem.* **2009**, *52*, 2899–2908.
- [93] B. Fritzing, I. Moreels, P. Lommens, R. Koole, Z. Hens, J. C. Martins, *J. Am. Chem. Soc.* **2009**, *131*, 3024–3032.
- [94] T. D. W. Claridge, *High-Resolution NMR Techniques in Organic Chemistry*, Elsevier Science, Oxford, UK, **2008**.
- [95] C. Dalvit, P. Pevarello, M. Tatò, M. Veronesi, A. Vulpetti, M. Sundström, *J. Biomol. NMR* **2000**, *18*, 65–68.
- [96] J. Hu, P.-O. Eriksson, G. Kern, *Magn. Reson. Chem.* **2010**, *48*, 909–911.
- [97] A. D. Gossert, C. Henry, M. J. J. Blommers, W. Jahnke, C. Fernández, *J. Biomol. NMR* **2009**, *43*, 211–217.
- [98] H. Lei, C. Jones, T. Zhu, K. Patel, N. M. Wolf, L. W. Fung, H. Lee, M. E. Johnson, *Bioorg. Med. Chem.* **2016**, *24*, 596–605.
- [99] C. Ludwig, P. J. A. Michiels, X. Wu, K. L. Kavanagh, E. Pilka, A. Jansson, U.

- Oppermann, U. L. Günther, *J. Med. Chem.* **2008**, *51*, 1–3.
- [100] C. F. Martinez-farina, N. McCormick, A. W. Robertson, H. Clement, A. Jee, A. Ampaw, N. Chan, T. Syvitski, D. L. Jakeman, *Org. Biomol. Chem.* **2015**, *13*, 10324–10327.
- [101] C. Dalvit, G. Fogliatto, A. Stewart, M. Veronesi, B. Stockman, *J. Biomol. NMR* **2001**, *21*, 349–359.
- [102] R. Huang, A. Bonnichon, T. D. W. Claridge, I. K. H. Leung, *Sci. Rep.* **2017**, *7*, 1–6.
- [103] C. Dalvit, M. Fasolini, M. Flocco, S. Knapp, P. Pevarello, M. Veronesi, *J. Med. Chem.* **2002**, *45*, 2610–2614.
- [104] R. T. Syvitski, D. L. Jakeman, *Org. Biomol. Chem.* **2015**, *13*, 3347–3350.
- [105] E. A. Batuev, A. Y. Lisunov, E. A. Morozova, V. V. Klochkov, N. V. Anufrieva, T. V. Demidkina, V. I. Polshakov, *Mol. Biol.* **2014**, *48*, 896–905.
- [106] I. Onila, T. ten Brink, K. Fredriksson, L. Codutti, A. Mazur, C. Griesinger, T. Carlomagno, T. E. Exner, *J. Chem. Inf. Model.* **2015**, *55*, 1962–1972.
- [107] J. Sikorska, L. Codutti, L. Skjærven, B. Elshorst, R. Saez-Ameneiro, A. Angelini, P. Monecke, T. Carlomagno, *Medchemcomm* **2015**, *6*, 1501–1507.
- [108] J. Pilger, A. Mazur, P. Monecke, H. Schreuder, B. Elshorst, S. Bartoschek, T. Langer, A. Schiffer, I. Krimm, M. Wegstroth, et al., *Angew. Chem. Int. Ed.* **2015**, *54*, 6511–6515.
- [109] J. Orts, S. Bartoschek, C. Griesinger, P. Monecke, T. Carlomagno, *J. Biomol. NMR* **2012**, *52*, 23–30.
- [110] J. Orts, J. Tuma, M. Reese, S. K. Grimm, P. Monecke, S. Bartoschek, A. Schiffer, K. U. Wendt, C. Griesinger, T. Carlomagno, *Angew. Chem. Int. Ed.* **2008**, *47*, 7736–7740.
- [111] J. Orts, C. Griesinger, T. Carlomagno, *J. Magn. Reson.* **2009**, *200*, 64–73.
- [112] M. Reese, V. M. Sánchez-Pedregal, K. Kubicek, J. Meiler, M. J. J. Blommers, C. Griesinger, T. Carlomagno, *Angew. Chem. Int. Ed.* **2007**, *46*, 1864–1868.
- [113] L. Skjærven, L. Codutti, A. Angelini, M. Grimaldi, D. Latek, P. Monecke, M. K. Dreyer, T. Carlomagno, *J. Am. Chem. Soc.* **2013**, *135*, 5819–5827.

- [114] M. Fruth, A. Plaza, S. Hinsberger, J. H. Sahner, J. Hauptenthal, M. Bischoff, R. Jansen, R. Müller, R. W. Hartmann, *ACS Chem. Biol.* **2014**, *9*, 2656–2663.
- [115] I. Krimm, *Medchemcomm* **2012**, *3*, 605.
- [116] K. Ono, K. Takeuchi, H. Ueda, Y. Morita, R. Tanimura, I. Shimada, H. Takahashi, *Angew. Chemie Int. Ed.* **2014**, *53*, 2597–2601.
- [117] M. Mayer, B. Meyer, *J. Am. Chem. Soc.* **2001**, *123*, 6108–6117.
- [118] P. Hendrik, Species-Selective Interactions of Histamine H₂ Receptors with Guanidine-Type Agonists : Molecular Modelling , Site- Directed Mutagenesis and Pharmacological Analysis, *Thesis*, **2007**.
- [119] B. Cuttin, S. V. Shelke, Z. Dragic, B. Wagner, H. Gathje, S. Kelm, B. Ernst, *Magn. Reson. Chem.* **2007**, *45*, 720-724.
- [120] M. Mayer, T. L. James, *J. Am. Chem. Soc.* **2002**, *124*, 13376–13377.

Conclusion

Nowadays, photocatalysis is one of the major topics in chemistry with tremendous success in synthetic applications. But to sustain this growth, a profound understanding of the underlying mechanisms is required. In recent years, NMR spectroscopy has established itself as a powerful method, which can give insights into every aspect of a photoreaction ranging from the initial photoexcitation by photo-CIDNP (nanosecond time scale) to various downstream processes such as intermediate formation and their sequence in the reaction as well as aggregations, unproductive pathways and solvent effects (second to hour time scale). But despite the recent success of NMR spectroscopy in photochemistry, there is still much room for improvement in terms of new experimental setups and approaches.

The aim of this thesis was the introduction of a new method for NMR, which combines illumination, UV/Vis spectroscopy and NMR as well as the investigation of photocatalytic reactions to further increase the applicability scope of NMR spectroscopy in the research field of photochemistry. In addition, apart from photochemical investigations, ligand based NMR methods for drug discovery are surveyed, which probe ligand-receptor interactions of Histamine-H2 receptor (H2R) antagonists in the presence of the H2R incorporated in SF9 cell membranes.

The second chapter presented an elaborate introduction of NMR in combination with illumination. First, it discussed and compared commonly applied illumination sources in illuminated NMR spectroscopy. Furthermore, the chapter surveyed *in situ* and *ex situ* illumination approaches and illumination apparatus as well as special purpose illumination setups. In a second part, case studies of photo-NMR in the research fields of photocatalysis, photoswitches, photopolymerizations and various new concepts for *in situ* illumination NMR were presented in detail.

In chapter three, a fully automated triple combination of UV/Vis spectroscopy, NMR spectroscopy and *in situ* illumination (UVNMR-illumination) was developed. This optical fiber based setup merges two major, analytical methods for the investigation of (photo)chemical reactions; i.e. it enables the time-resolved, simultaneous detection of diamagnetic (NMR) and paramagnetic (UV/VIS) species in the same (photo)system. Therefore, this UVNMR-illumination setup eliminates issues that arise from separated UV/Vis – NMR systems such as concentration and temperature. Furthermore, the setup also provides the same reaction vessel, light intensity, convection and diffusion. In

Conclusion

addition, the setup is portable and can be used at every solution NMR spectrometer, independent of the magnetic field or the installed probe (including cryo-probes). The applicability of the setup was tested for a large temperature range (180 – 323 K), which can be exploited to modulate exchange rates; e.g. it was shown that a spiropyran based photoswitch, which has a fast thermal back isomerization and photodegrades under prolonged illumination, could be easily stabilized at low temperatures (180 K). As a result, the otherwise short lived isomer could be easily assigned, while also gaining quantitative information and absorbance spectra. In addition, the UVNMR-illumination setup was put to the test in photocatalysis for the investigation of a consecutive photoinduced electron transfer (ConPET) process. Since ConPET processes rely on the presence of stable radical species (paramagnetic), they presented an ideal system to demonstrate the potential of the UVNMR-illumination device. Here, during preliminary investigations of the reaction it was indeed possible, to acquire simultaneous reaction profiles of paramagnetic and diamagnetic species under the same conditions, for the first time.

Chapter four follows up on the preliminary ConPET investigations, which were presented in chapter three. The studies focus on the mechanistic investigation of the first, proposed ConPET process; the visible light mediated dehalogenation of aryl halides with perylene bisimide (PDI). The mechanistic foundation of ConPET is the ability of the photocatalyst to utilize the energy of two photons for a chemical reaction and was recently confirmed for the ConPET reaction with rhodamine 6G as photocatalyst. But the PDI promoted ConPET was recently challenged by a new proposal, which suggest a reaction of PDI with the substrate to yield a new photocatalytic species. Chapter four continued the research of the contested PDI ConPET process by means of extensive UVNMR-illumination, *in situ* NMR illumination and UV/Vis spectroscopic investigations, which lead to new mechanistic insights resulting in a new mechanistic proposal for the reaction. First, UVNMR-illumination measurements detected an electron-donor-acceptor (EDA) complex of PDI and triethylamine (TEA) prior to illumination indicating that NMR can be very sensitive for the detection of EDAs in some cases. Second, combined results of NMR, photo-CIDNP and UV/Vis spectroscopy showed that PDI is effectively turned into its radical anion (PDI^{•-}) once the light is turned on. Combined UVNMR-illumination reaction profiles revealed unexpected paramagnetic relaxation enhancements due to the formation of the stable PDI^{•-}, which lead to a pseudo signal increase of slowly relaxing compounds. As a result it could be shown that in this case, the residual solvent signal can be used as an indirect tracer to track the evolution and relative amount of the PDI^{•-}. In addition, the presence of an initiating phase that preceded product formation was

detected. UVNMR-illumination reaction measurements showed that this initiating phase persisted although the maximum amount of $\text{PDI}^{\cdot-}$ was already formed ($\text{PDI}^{\cdot-}$ was supposed to promote the reaction). Hence, it could be concluded that the radical anion concentration and product formation do not correlate. In detail examinations of the initiating phase by means of UV/Vis spectroscopy and *in situ* NMR illumination revealed that PDI can also interact with itself and does not require TEA to generate $\text{PDI}^{\cdot-}$. In addition, pre-irradiation experiments revealed that PDI can interact with itself beyond the formation of $\text{PDI}^{\cdot-}$ by physical interactions. Presumably, these interactions result in $\text{PDI}/\text{PDI}^{\cdot-}$ stacks/aggregates because the observed effects could be reversed by the addition of oxygen. Furthermore, this pre-irradiation of PDI got rid of the initiating phase before the product formation, which indicated that the interactions of PDI with itself result in the formation of the actual photocatalytic species. These combined results led to a new mechanistic proposal, which deviates from the two existing proposals for the PDI promoted dehalogenation of aryl halides by light. This new proposal suggests that PDI can interact with itself to yield a new catalytic photoactive species under illumination; i.e. some sort of stack/aggregate consisting of PDI and $\text{PDI}^{\cdot-}$.

Chapter 5 surveyed the development and mechanistic investigations of the very first synthetic approach to cleave C-OCF₃ bonds (here: an aryl trifluoromethyl ether), which resulted in a controlled liberation and *in situ* conversion of fluorophosgene for the synthesis of various substrates such as carboantes, carbamates and urea derivatives. The mechanistic studies combined *ex situ* and *in situ* NMR illumination studies, transient spectroscopy and radical trapping experiments. Here, transient spectroscopy suggested the formation of a charge-transfer (CT) dimer complex of the photocatalyst as the initial photoexcitation step. The photo-NMR measurements identified a carbonyl fluoride compound as key intermediate solidifying the mechanistic proposal of a fluorophosgene promoted reaction. In addition, NMR could unravel an unproductive, second reactive pathway in the dark, which can be almost completely suppressed by the addition of water. With the combined mechanistic studies, an elaborate mechanistic proposal could be made, which covers all aspects of the reaction ranging from the initial photoexcitation, to intermediate detection and the assignment of numerous relevant products and side products.

The last chapter of this thesis focused on the execution of ligand based NMR techniques in the field of drug discovery. Here, especially saturation transfer difference (STD) was applied to a system of Histamine-H₂ receptor (H₂R) antagonists in the presence of H₂R, which were overexpressed in a parental membrane system. These investigations showed that ligand based NMR methods are very unreliable if non-specific interactions

Conclusion

besides the ligand-receptor interactions are present. Therefore, albeit numerous efforts were made, it was not possible to distinguish specific and non-specific binding of H2R antagonists in the presence of H2R, which was incorporated in a membrane system. Nevertheless, sample preparation and composition was tremendously improved by changing out the buffer system and optimization of the sample formulation. In addition, a proposal could be devised, which describes applicable systems for membrane preparations.

In summary, this thesis first presented an elaborate review, which surveys the evolution of NMR in combination. Second, the development of a new triple combination consisting of NMR spectroscopy, UV/Vis spectroscopy and *in situ* illumination (UVNMR-illumination) is described and its applicability as a mechanistic investigation tool in photochemistry is shown for two test systems in the fields of photoswitches and photocatalysis. Third, extensive UVNMR-illumination, *in situ* NMR illumination and UV/Vis spectroscopic examinations were conducted to unravel the mechanism of a seemingly ConPET driven reaction, in which a novel mechanistic proposal could be made. In addition, in a cooperative project, a photoreaction, which does not rely on radical reactivity, was developed and the underlying mechanism was investigated in detail yielding information about the initial photoexcitation as well as the assignment of key intermediates and the detection of an unproductive dark cycle. The last chapter focused on ligand based NMR methods in drug discovery. Here, valuable information concerning sample preparation and composition could be gathered. Furthermore, it was shown that non-specific interactions are a major issue for ligand based NMR methods; hence, they are only applicable for a minuscule amount of ligands (uncharged ligands with few functionalization) for the investigation transmembrane receptors, which are incorporated in a parental membrane system.

Glossary

2,4-DNBA: 2,4-dinitrobenzaldehyde

ASAP: acceleration by sharing adjacent polarization

ATRP: atom transfer radical polymerization

B₂pin₂: (Bis(pinacolato)diboron)

BIRD: bilinear rotation decoupling

BnSH: benzyl thiol

BTA: benzene-1,3,5-tricarboxamide

BTPA: 2-(butylthiocarbonothioyl) propionic acid

cat: catalyst

ccc: cis-cis-cis (all cis)

CCD: charge-coupled device

CDC: cross-dehydrogenative coupling

CEST: chemical exchange saturation transfer

ConPET: consecutive photoinduced electron transfer

COSY: correlation spectroscopy

CRP: controlled radical polymerization

CT: charge transfer

CV: cyclic voltammetry

DADS decay obtained difference spectra

DCE: 1,2-dichloroethane

DCM: dichloromethane

DEA: N,N'-diethylacrylamide; diethylamine

Glossary

dim: dimer

DIPEA: N,N-diisopropylethylamine

DMA: N,N'-dimethylacrylamide

DMF: dimethyl formamide

DMSO: dimethyl sulfoxide

DNA: deoxyribonucleic acid

DOSY: diffusion ordered spectroscopy

DS: number of dummy scans

DTS-hv: decrypting transition states by light

EBiB: ethyl α -bromoisobutyrate

EDA: electron donor-acceptor

ee: enantiomeric excess

EPR: electron paramagnetic resonance

EtBPA: ethylthiobutyraldehyde

EXSY: exchange spectroscopy

FBDD: fragment based drug design

FID: free induction decay

FMN: flavin mononucleotide

FO: fiber optics

GC: gas chromatography

GC-MS: gas chromatography – mass spectrometry

GERD gastroesophageal reflux disease

GPCR: G-protein coupled receptor

GTP: guanosine-5'-triphosphate

H2R: Histamine-H2 receptor

HAT: hydrogen atom transfer

HBpin/Bpin: pinacolborane

HMBC: heteronuclear multiple bond correlation

HPLC: high performance liquid chromatography

HSQC: heteronuclear single quantum coherence

HTS: high throughput screening

$h\nu$: light (pulse)

Hz: hertz

IMHB: intramolecular hydrogen bond

inc.: incorporated

INPHARMA: inter-ligand NOE pharmacophore mapping

IPSO: intelligent pulse sequence organizer

IR: infrared

LASER: light amplification by stimulated emission of radiation

LD: LASER Diode

LED: light-emitting diode

LES lower esophageal sphincter

MA: methyl acrylate

MAS: magic angle spinning

MBA: 4-methoxy benzyl alcohol

MBAld: 4-methoxy benzyl aldehyde

Me6TREN: tris[2-(dimethylamino)ethyl]amine

MHz: megahertz

Glossary

MMA: methyl methacrylate

MRI: magnetic resonance imaging

NA: not available

NaASC: sodium ascorbate

NAM: N-acryylmorpholine

ND:YAG: neodymium-doped yttrium aluminum garnet

NFSI: N-fluorobenzenesulfonimide

NMI: N-substituted maleimide

NMR: nuclear magnetic resonance

NOESY: nuclear Overhauser effect spectroscopy

NS: number of scans

PAA: phenoxyacetic acid

PBS: phosphate-buffered saline

PCB: printed circuit board

PDI: N,N'-bis(2,6-diisopropylphenyl)-3,4,9,10-perylenetetracarboxylic-diimide

PDMS: polydimethylsiloxane

PEGA: poly(ethylene glycol) methyl ether acrylate

PET: photoinduced electron transfer

PET-RAFT: photoelectron transfer reversible addition–fragmentation chain transfer

PHIP: para-hydrogen induced polarization

photo-CIDNP: photo-chemically induced dynamic nuclear polarization

PIRAT: Photo-Induced Reversible Acceleration of T1-Relaxation

PLA: polylactic acid

PPI: proton-pump inhibitor

ppm: parts per million

PRE: paramagnetic relaxation enhancement

PSS: photo stationary state

PTCDA: perylene-3,4,9,10-tetracarboxylic-dianhydride

PTFE: polytetrafluoroethylene

PTH: phenothiazine

RCP: Real-time Clock Pulse

rf: radiofrequency

RFTA: riboflavin tetraacetate

rpm: revolutions per minute

RSH: aryl thiol

SAR: structure activity relationship

SCE: saturated calomel electrode

SET: single electron transfer

SM: substrate material

S/N: signal to noise

SNR: signal to noise (in adapted figures)

SPC: semiconductor photocatalyst

SPR: surface plasmon resonance

SL: spin lock

STD: saturation transfer difference

SW: spectral width

tcc: trans-cis-cis

TCU: time control unit

Glossary

TD: time domain

TEA: triethylamine

THIQ: N-aryltetrahydroisoquinolines

TMP: 2,2,6,6-tetramethylpiperidine

TRIP: 3,3'-Bis(2,4,6-triisopropylphenyl)-1,1'-binaphthyl-2,2'-diyl hydrogenphosphate

TRIS: tris(hydroxymethyl)aminoethane

trNOE: (exchange) transferred NOE

ttc: trans-trans-cis

TTL: transistor-transistor logic

ttt: trans-trans-trans (all trans)

UV: ultraviolet

V: volt

Vis: visible

WaterLOGSY: water-ligand observed via gradient spectroscopy

ZQ: zero quantum

Curriculum Vitae

Personal Information

Name: Philipp Nitschke
Date of birth : 10.08.1989
Address: Haselweg 11
84036 Landshut, Germany
Phone: +49 1577 1450373
E-Mail: philipp.nitschke@ur.de

Experience

02/2016 – present

PhD Student, Institute of Organic Chemistry, University of Regensburg

Activities:

- Mechanistic and structural investigations in the field of photochemistry/photocatalysis by NMR and UV/Vis
- Ligand based NMR approaches to investigate ligand-receptor interactions (STD, WaterLOGSY)
- Maintenance and improvement of NMR-illumination hardware

Education

10/2013 – 10/2015

M.Sc. Medicinal Chemistry, University of Regensburg

Grade: 1.4 (Master Thesis Grade: 1.0; Mechanistic studies
NMR and execution of low tech assays)

by

09/2009 – 04/2013

B.Sc. Pharmaceutical Chemistry, University of Applied Sciences Isny

Grade: 1.9 (Bachelor Thesis Grade: 1.3; Natural product
synthesis; University of Würzburg from 09/2012 –04/2013)

Publications

A. Seegerer, P. Nitschke, R. M. Gschwind, *Combined In Situ Illumination-NMR-UV/Vis Spectroscopy: A New Mechanistic Tool in Photochemistry*, *Angew. Chem.* **2018**, *57*, 7493-7497.

D. Petzold, P. Nitschke, F. Brandl, V. Scheidler, B. Dick, R. M. Gschwind, B. König, *Visible Light Mediated Liberation and in situ Conversion of Fluorophosgene*, *Chem. Eur. J.* **2019**, *25*, 361-366.

P. Nitschke, N. Lokesh, R. M. Gschwind, *Combination of Illumination and High Resolution NMR Spectroscopy: Key Features and Practical Aspects, Photochemical Applications and New Concepts*, *Prog. Nucl. Magn. Reson. Spectrosc.* **2019**, accepted.

Talks at international conferences

Combined in situ NMR-UV/Vis-Illumination Spectroscopy: A Novel Mechanistic Approach in Photochemistry; SMASH, 9/2019, Philadelphia, USA.

Combined in situ NMR-UV/Vis-Illumination Spectroscopy: A Novel Mechanistic Approach in Photochemistry; 40th FGMR Meeting, 9/2019, Leipzig, Germany.

Awards

Ernst Award of the Division of Magnetic Resonance Spectroscopy of the German Chemical Society - 2018

Research award of the "Max-Buchner-Forschungstiftung" for chemical engineering at Universities of Applied Sciences - 2013

Additional Skills

Bruker Topspin (Versions 2.x – 4.x, + Bruker IconNMR)

NMR Hardware (Avance II – Avance NEO)

Microsoft Office

OriginPro 8G (data analysis and graphing software)

CorelDraw (graphic design, illustration and technical software)

AvaSoft (UV/Vis software)

HPLC (Avantes)

Languages

German (native), English (business fluent)

Eidesstattliche Erklärung

(1) Ich erkläre hiermit an Eides statt, dass ich die vorliegende Arbeit ohne unzulässige Hilfe Dritter und ohne Benutzung anderer als der angegebenen Hilfsmittel angefertigt habe; die aus anderen Quellen direkt oder indirekt übernommenen Daten und Konzepte sind unter Angabe des Literaturzitats gekennzeichnet

(2) Bei der Auswahl und Auswertung haben mir die zu Beginn des jeweiligen Kapitels aufgeführten Personen in der jeweils beschriebenen Weise unentgeltlich geholfen.

(3) Weitere Personen waren an der inhaltlich-materiellen Herstellung der vorliegenden Arbeit nicht beteiligt. Insbesondere habe ich hierfür nicht die entgeltliche Hilfe eines Promotionsberaters oder anderer Personen in Anspruch genommen. Niemand hat von mir weder unmittelbar noch mittelbar geldwerte Leistungen für Arbeiten erhalten, die im Zusammenhang mit dem Inhalt der vorgelegten Dissertation stehen.

(4) Die Arbeit wurde bisher weder im In- noch im Ausland in gleicher oder ähnlicher Form einer anderen Prüfungsbehörde vorgelegt.

Regensburg, den _____

Philipp Nitschke